

UNIVERSIDADE FEDERAL DO RIO GRANDE DO SUL
ESCOLA DE ENGENHARIA
PROGRAMA DE PÓS-GRADUAÇÃO EM ENGENHARIA CIVIL: CONSTRUÇÃO E INFRAESTRUTURA

STUDY OF THUNDERSTORM WIND OUTFLOWS
AND PROPOSITION OF MEAN WIND PROFILES

ELIAS GALVAN DE LIMA

Porto Alegre

2022

ELIAS GALVAN DE LIMA

ELIAS GALVAN DE LIMA

STUDY OF THUNDERSTORM WIND OUTFLOWS
AND PROPOSITION OF MEAN WIND PROFILES

This Thesis was presented to the Postgraduate Program in Civil Engineering of the Universidade Federal do Rio Grande do Sul as part of the requirements for the degree of Doctor in Engineering.

Supervisor: Prof. Acir Mércio Loredo-Souza

Porto Alegre

2022

CIP - Catalogação na Publicação

Galvan de Lima, Elias
Study of Thunderstorm Wind Outflows and Proposition
of Mean Wind Profiles / Elias Galvan de Lima. -- 2022.
333 f.
Orientador: Acir Mércio Loredo-Souza.

Tese (Doutorado) -- Universidade Federal do Rio
Grande do Sul, Escola de Engenharia, Programa de
Pós-Graduação em Engenharia Civil: Construção e
Infraestrutura, Porto Alegre, BR-RS, 2022.

1. Thunderstorm Winds. 2. Severe weather. 3.
Downbursts. 4. Modeling. 5. Wind profiles. I.
Loredo-Souza, Acir Mércio, orient. II. Título.

Elaborada pelo Sistema de Geração Automática de Ficha Catalográfica da UFRGS com os
dados fornecidos pelo(a) autor(a).

ELIAS GALVAN DE LIMA

STUDY OF THUNDERSTORM WIND OUTFLOWS
AND PROPOSITION OF MEAN WIND PROFILES

This doctoral thesis was assessed by the Board of Examiners and considered suitable for obtaining the title of DOCTOR IN ENGINEERING. Its final version was approved by the supervising professor and the Postgraduate Program in Civil Engineering of the Universidade Federal do Rio Grande do Sul.

Porto Alegre, 2nd of December 2022

Prof. Acir Mércio Loredou Souza
Ph.D. University of Western Ontario

Dr. Ângela de Moura Ferreira Danilevicz
Coordinator of PPGCI/UFRGS

Board of Examiners

Dr. Ângela Borges Masuero
Universidade Federal do Rio Grande do Sul

Dr. Adrián Roberto Wittwer
Universidade Federal do Rio Grande do Sul

Dr. Gustavo Javier Zani Núñez
Universidade Federal do Rio Grande do Sul

Dr. Mario Gustavo Klaus Oliveira
Universidade Federal do Rio Grande do Sul

ACKNOWLEDGMENTS

To Prof. Ph.D. Acir Mércio Loredou-Souza to encourage and mentor me throughout this long journey of my graduate studies. I am grateful for his time and dedication to supervise this research. His friendship and compassion helped me persevere through adversities encountered to achieve such milestone.

To UFRGS, PPGCI, PPGECC, and PROMEC to welcome my diverse background on a journey of innovative thinking, enriching experiences, and development of meaningful relationships. I will always be proud to be an alumnus of such institutions of excellence in Brazil.

To Prof. Dr. Angela Borges Masuero, Prof. Dr. Adrián Roberto Wittwer, Prof. Dr. Gustavo Javier Zani Núñez, and Dr. Mario Gustavo Klaus Oliveira for being part of the panel and helping me with insightful ideas and valuable contributions to improve this document.

To the team of the Laboratório de Aerodinâmica das Construções (LAC) for friendship and exceptional learning experiences.

To my partner Charles, my family, and beloved friends I owe my utmost appreciation for their support throughout this journey. I cannot thank them enough for their daily encouragement and for helping me stay grounded despite my absences.

To my inspiring work colleagues – in particular, Dr. Mowry, Luis Soto, Cecilia Martensson, Carlos Tamayo, and Ines Mato – for opening doors to me in foreign places and disciplines. I am grateful for their support in helping me stay focused and advancing my professional development, as well as guiding me through these years of intense engineering practice in the infrastructure design field.

To my employers along these years – City of Miami Beach, WSP, and Microdesk/Symetri – for providing the flexibility I needed to work on professional development and conclude my doctorate studies.

In memory of Prof. Joaquim Blessmann and Prof. Giovanni Solari, whose pioneering contributions to the development of Wind Engineering have helped create a safer and more resilient society.

ABSTRACT

The impact of thunderstorm (TS) winds on the built environment has been extensively reported in recent years showing that current wind standards do not properly represent all types of extreme wind events. This document discusses the characteristics of TS winds in depth, focusing on existing vertical full-scale measurements, modeling approaches and their occurrence worldwide. Firstly, the development of the downburst research worldwide is reviewed and, due to Brazil's vulnerability to this type of event, reported cases in national news and scientific literature are investigated. This study showed that most of Brazil is vulnerable to downbursts, having the Amazon region the larger amount of occurrences and the Southern states the most susceptible for extreme winds generated by TS outflows or simply downbursts. The Southeastern states are also prone to extreme downburst occurrence. Northeast and central north states present downburst events with lower intensity, which are caused mostly by isolated thunderstorms. Modeling techniques are commonly adopted to study the effects of these events on the built environment. A systematic review of 122 publications on downburst modeling identified four main clusters of alternative approaches to simulating these events: analytical modeling, experimental laboratory simulations, computer fluid dynamics (CFD) and data-driven models. An analytical method is proposed to describe the mean wind speed profiles at their maximum stage based on full-scale measurements considering the storm organization, time averaging and terrain categories. The proposed fitted curve profile functions are valid only for the original measured average intervals. Results showed that most of the proposed fitted curve profile functions had a "nose-like" shape, highly defined by the terrain roughness, with peak velocities typically observed at lower levels in TS winds – between 50 and 250 meters – allowing the profile fitting by a third-degree polynomial function, instead of the traditional power law function as adopted for synoptic winds. Seventeen profiles originated from full-scale measurements were selected and carefully analyzed. However, in order to propose a practical application that can be coupled with a general extreme wind climatology, only seven fitted curve profile functions were taken for further analysis. Six out of seven fitted curve profiles demonstrated good adherence to Ponte Junior (2005) model and the TS wind profile proposed by the international code ISO 4354. These proposed profiles were further analyzed along with the typical NBR-6123 boundary layer velocity profiles. For Terrain Category II, the fitted curve profile function based on the maximum profile of Gunter and Schroeder (2015) "PEP Event" for 1-min time averaging presented the most conservative case at all elevations. For Terrain Category III, results were mixed, but the fitted curve profile function based on the maximum profile measured by Lombardo et al. (2014) "03-Aug-2010 Event" presented maximum values at lower levels for 3-s time averaging and is therefore considered the maximum profile for this terrain category. Finally, for Category IV, it is suggested to use as reference the fitted curve profile based on the maximum profile of Zhang *et al.* (2019) "15:01 Meas.", since this is a more realistic TS wind profile dataset for 30-s time averaging due to the particular effects of the terrain on that specific measurement.

Keywords: Thunderstorm Winds, severe weather, downbursts, modeling, wind profiles.

RESUMO

O impacto dos ventos gerados por tempestades (TS) no ambiente construído tem sido amplamente relatado nos últimos anos, revelando que as normas de vento atuais não representam adequadamente todos os tipos de ventos extremos. Neste documento se discute em profundidade as características dos ventos TS, com foco em medições verticais de escala real, abordagens de modelagem e sua ocorrência no mundo. Primeiramente, é revisado o desenvolvimento mundial das pesquisas sobre *downbursts* e, devido à vulnerabilidade do Brasil a esse tipo de evento, é feita uma investigação de casos relatados em notícias e literatura científica. Este estudo mostrou que a maior parte do Brasil é extremamente vulnerável a *downbursts*, tendo a região Amazônica o maior número de ocorrências e os estados da região Sul os mais suscetíveis a ventos extremos gerados por tormentas TS ou simplesmente *downbursts*. Os estados do Sudeste são também propensos à ocorrência de *downbursts* severos. Os estados do Nordeste e Centro-Norte apresentam eventos de menor intensidade, causados principalmente por tempestades isoladas. Técnicas de modelagem são comumente adotadas para estudar os efeitos desses eventos no ambiente construído. Uma revisão sistemática de 122 publicações sobre modelagem de *downbursts* identificou quatro grupos principais de abordagens para simular esses eventos: modelos analíticos, simulações experimentais em laboratório, dinâmica de fluidos computacional (CFD) e modelos baseados em dados. Um método analítico é proposto para descrever os perfis médios de velocidade de vento em seu estágio máximo com base em medições em escala real, considerando-se organização da tempestade, intervalo de tempo e categorias de terreno. As funções de perfil de curva ajustada propostas são válidas apenas para os intervalos de tempo medidos originais. Os resultados mostraram que a maioria das funções propostas de perfis de curvas ajustadas tinham forma de "nariz", fortemente definida pela rugosidade do terreno e com velocidades de pico tipicamente observadas em níveis mais baixos em ventos TS – entre 50 e 250 metros – permitindo o ajuste do perfil por uma função polinomial de terceiro grau, em vez da função de potência tradicional, como utilizado para ventos sinóticos. Dezesete perfis oriundos de medições reais foram selecionados e analisados minuciosamente. Porém, para possibilitar a proposição de uma aplicação prática capaz de incorporar resultados de climatologias gerais de ventos extremos TS, somente sete curvas ajustadas foram levadas adiante para análise. Seis dos sete perfis ajustados demonstraram boa aderência ao modelo de Ponte Junior (2005) e ao perfil de vento TS proposto pelo código internacional ISO 4354. Esses perfis propostos foram posteriormente analisados juntamente com os perfis de velocidade de camada limite típicos da NBR-6123. Para a categoria de terreno II, a função do perfil ajustada com base nos valores máximos obtidos por Gunter e Schroeder (2015) no "PEP Event" para intervalo de tempo de 1-min apresentou o caso mais conservador em todas as elevações. Para a categoria de terreno III, os resultados foram mistos, mas considerou-se como evento extremo o perfil ajustado baseado no evento extremo de "03-ago-2010" de Lombardo et al. (2014) para o intervalo de média de tempo de 3-s. Finalmente, para a Categoria IV, sugere-se utilizar como referência o perfil de curva ajustado ao evento extremo registrado por Zhang et al. (2019) "15:01 Meas.", uma vez que o perfil de vento TS resultante é mais realista para média de tempo de 30-s devido aos efeitos do terreno específicos deste caso.

Palavras-chave: Ventos TS, tempo severo, ventos não sinóticos, modelagem, perfis de vento.

TABLE OF CONTENTS

COVER	1
ACKNOWLEDGMENTS	5
RESUMO	7
TABLE OF CONTENTS	8
LIST OF FIGURES	11
LIST OF TABLES	28
LIST OF ABBREVIATIONS AND ACRONYMS	29
LIST OF SYMBOLS	33
1. INTRODUCTION	35
1.1. RELEVANCE OF THIS STUDY.....	35
1.2. OBJECTIVES.....	38
1.3. ASSUMPTIONS AND LIMITATIONS	40
1.4. THESIS STRUCTURE.....	40
2. ELEMENTS OF THUNDERSTORM WINDS	43
2.1. SEVERE WEATHER OVERVIEW.....	43
2.1.1. Deep Moist Convective System Types	43
2.1.2. The Severe Weather in South America	50
2.2. WIND CLASSIFICATIONS	56
2.3. THE DOWNBURST DISCOVERY	59
2.3.1. Downburst Field Studies.....	59
2.3.2. Downburst Classifications	70

2.3.3.	Downdraft Currents.....	81
2.3.4.	Forecasting Favorable Downburst Environments	86
2.4.	IMPACT OF THUNDERSTORM WINDS TO THE BUILT ENVIRONMENT IN THE WORLD	89
3.	PHYSICAL PROPERTIES OF NON-TORNATIC THUNDERSTORM WIND EVENTS	94
3.1.	VERTICAL PROFILES FULL-SCALE MEASUREMENTS OF NON-TORNADIC TS WINDS	94
3.2.	TURBULENCE CHARACTERISTICS OF NON-TORNATIC THUNDERSTORM WINDS.....	131
3.3.	THUNDERSTORM WIND CODES PROVISIONS AND STANDARD SPECIFICATIONS	140
3.4.	DISTINGUISHING AND CLASSIFYING THUNDERSTORM WIND SIGNALS FROM MIXED DATASETS	144
3.5.	THE CASE FOR THE DEVELOPMENT OF BRAZIL'S EXTREME WIND CLIMATOLOGY	153
4.	PROPOSITION OF MAXIMUM THUNDERSTORM WIND FITTING CURVE PROFILE FUNCTIONS FOR MEAN VELOCITY BASED ON FULL-SCALE MEASUREMENTS.....	160
4.1.	DESCRIPTION OF METHOD DEVELOPED.....	160
4.2.	ANALYSIS OF VERTICAL FULL-SCALE PROFILE DATASETS AND PROPOSED CURVE FITTING FUNCTIONS.....	164
4.2.1.	Sherman (1987)	164
4.2.2.	Hjelmfelt <i>et al.</i> (1988)	165
4.2.3.	Choi and Hidayat (2002).....	166
4.2.4.	Paluch <i>et al.</i> (2003).....	167
4.2.5.	Gast (2003) – RFD and Derecho Events.....	168
4.2.6.	Choi (2004)	170
4.2.7.	Lombardo <i>et al.</i> (2014).....	171

4.2.8.	Gunter and Schroeder (2015).....	173
4.2.9.	Burlando <i>et al.</i> (2017).....	174
4.2.10.	Repetto (2018)	175
4.2.11.	Zhang <i>et al.</i> (2019).....	176
4.3.	ANALYSIS OF FULL-SCALE THUNDERSTORM WIND PROFILES AND RESPECTIVE PROPOSED FITTING PROFILE CURVE FUNCTIONS.....	178
4.3.1.	Proposed fitted curves meeting allowable requirements.....	183
4.3.2.	Proposed fitted curves at levels below 10 meters.....	185
4.4.	COMPARASION OF PROPOSED FITTED CURVE PROFILES TO EXISTING ANALYTICAL THUNDERSTOM WIND MODELS	187
4.5.	PROPOSED FITTING CURVE PROFILE FUNCTIONS COMPARED TO EXISTING WIND CODES	189
4.5.1.	Results comparison to TS wind codes and standards: ISO 4354 and AS/NZS 7000	189
4.5.2.	Results investigation against NBR 6123 profiles	191
4.6.	PROPOSED FITTED CURVE MODEL DISCUSSIONS	197
5.	CONCLUSIONS.....	200
5.1.	SUGGESTION FOR FUTURE WORK.....	208
	REFERENCES	210
	APPENDIX A - INVESTIGATION OF DOWNBURTS-LIKE EVENTS INCIDENCE IN BRAZIL	223
	APPENDIX B - MODELING TECHNIQUES OF THUNDERSTORM WIND OUTFLOW	241

LIST OF FIGURES

Figure 1. The Alan G. Davenport Wind Loading Chain. Source: Davenport (1961).....	35
Figure 2. Steps towards the codification of thunderstorms winds. Source: Author.....	39
Figure 3. Research flow adopted to structure this document. Source: Author.....	40
Figure 4. Schematics indicating the structure of this thesis. Source: Author.	42
Figure 5. Scale definitions and characteristics on time and horizontal length scales of atmospheric systems. Source: Markowski and Richardson (2010).....	43
Figure 6. Schematic of an ordinary single-cell thunderstorm at different life stages: a) cumulus stage, b) mature stage, and c) dissipating stage. Source: Wallace and Hobbs (2006).	45
Figure 7. Structure of typical tornadic supercell storm and expected inflows and outflows. Source: Wallace and Hobbs (2006).	46
Figure 8. Schematic of an idealized multicell storm developing in a strong shear environment. The typical equivalent temperature and wind profile are presented to the left. Arrows show the direction of the flow. Source: Wallace and Hobbs (2006).....	47
Figure 9. Cross section through an idealized squall line. Source: Houze (1993) adapted by Wallace and Hobbs (2006).	48
Figure 10. Evolution of bow echoes proposed by Fujita. In this model, the horizontal flow of a weakening downburst induces a mesoscale circulation, which reshapes the initial line echo called tall echo to a bow echo and then Comma Echo Stage. Downburst and tornadoes are expected at the front end of these systems. Source: Fujita (1981) adapted by Wolfson (1988).	49
Figure 11. Venn diagram of typical dimensions and relations of mesoscale convective systems. Source: Markowski and Richardson (2010).....	50
Figure 12. Typical atmospheric dynamic interaction of LLJ and the SJ in a) South America and LLJ and PJ in b) North America: Source: Nascimento (2005).	51
Figure 13. Atmospheric systems at low and high troposphere that influence the Climate of South America. At the low tropospheric levels: Mesoscale Convective Complex (MCC), Northeast Trade	

Winds (NTW), Subtropical Anticyclone of the South Atlantic (SASA), Intertropical Convergence Zone (ITCZ), Instability Lines (IL), Cold Front (CF), Warm Front (WF), Subtropical Anticyclone of the South Pacific (SASP), Low Level Jet (LLJ) at east of the Andes, Chaco Low (CL), Trade Winds from the Southeast (TWS), Low Pressure System(L), Region of Thermal Low in Northwestern Argentina (LNA), Prefrontal Squall Line (PSL), Comma Cloud (CC), Cyclogenetic Regions (CR), Convergence Zone South Atlantic (CZSA). At the high levels tropospheric, Cyclonic Vortices of High Tropical Levels (CVHL), Bolivia High (BH), Atmospheric Blockage Area (AB), Brazilian Northeastern Dug (BND), Subtropical Jet (SJ), Polar Jet (PJ). AB and BND are systems which get set up only during the winter. Source: Adapted from Reboita et al. (2010)	52
Figure 14. The longest lightning ever registered in the world in terms of extension and duration per WMO. Source: Nullis (2020).....	53
Figure 15. Average of days per year that has environments favorable for the tornadic supercells were convection to for. Including strong shear, deep tropospheric layer, and CAPE. Source: Brooks et al. (2003).	54
Figure 16. Map indicating Small, Moderate, and Heavy damages caused by Hurricane Catarina at landfall. Source: Pereira Filho et al. (2010).....	55
Figure 17. Characteristic time instants mean downburst speed time histories. Source: Chen (2005) apud Gast (2003).	58
Figure 18. Depicted a) a time series of an EPS wind event and b) another wind speed time series where it indicates the characteristic spike in wind speed caused by a downburst event. Source: Chowdhury (2018).	59
Figure 19. Damage patterns caused by tornados: In is shown a) a traveling tornado forming a sort of spiral damage; in b) a stationary tornado that had caused a spiral and punctual damage to the corn field; and c) a traveling tornado crossing a long extension of land. Source: Fujita (1985b).....	62

Figure 20. Aerial images of the damage caused by downburst winds. A starburst pattern of uprooted trees (left) on the field and building damage by downburst winds from the lower left corner of the picture to the upper right corner. Source: Fujita (1985b).	62
Figure 21. This picture displays CP-3 Radar Doppler Analysis of the exact moment a downburst had occurred. The orange area represents wind speed ranging 21 to 27 m/s at 70 m above the ground. Source: Fujita (1990).	64
Figure 22. Cross-section of microburst winds depicted by CP-3 Doppler Radar During NIMROD Project in 1978. In a) is shown the maximum vertical wind speed and b) is shown the maximum horizontal wind speeds. Source: Fujita (1990).	65
Figure 23. Doppler Radar triangulation used in NIMROD Project. Source: Fujita (1985).	65
Figure 24. Map of the JAWS Project study area. The Doppler Radars used in this effort were positioned at vertexes of the triangle in the middle of the Figure with a smaller spacing when compared to the previous field project (NIMROD). Denver's Stapleton International Airport is at CP-4. Source: Fujita (1985).	67
Figure 25. a) NIMROD (left) and JAWS (right) microbursts captured velocities and in b) is indicated expected return period for each of the projects along with the regression equation. Source: Fujita (1985a).	68
Figure 26. Histogram of full-scale peak wind longevity. Source: Lin et al. (2007). Data extracted from Fujita (1985b)	69
Figure 27. Typical soundings for a) high based, shallow-depth clouds that are associated with dry microbursts and b) heavily precipitating thunderstorms that produce wet downbursts. Source: Wolfson (1988).	71
Figure 28. A typical a) dry microburst coming from a virga cloud and a b) typical wet microburst being produced by a convective system. Source: Wolfson (1988).	72
Figure 29. Three types of microbursts clouds identified during NIMROD, JAWS, and MIST Projects. Source: Fujita (1990).	73

Figure 30. Typical components of a downburst event based on damage patterns proposed by Fujita. Source: Fujita and Wakimoto (1981).	75
Figure 31. Microburst line schematic of a) Discrete and homogeneous outflow and b) perspective cross section views of vertical structures of microburst line structure. Source: Hjelmfelt (1988).	76
Figure 32. Typical wind vectors observed during a) discrete and b) in-line downburst event. Source: Hjelmfelt (1988).	77
Figure 33. A stationary downburst is depicted on the left and a typical traveling downburst on the right. Source: Fujita (1981).	78
Figure 34. Model of a microburst descending from the cloud base presenting rotating downdrafts. Source: Wolfson (1988).	79
Figure 35. A laboratory experiment at the Wind Research Laboratory at the University of Chicago, indicating the evolution of a microburst airflow. The downburst phases are 1) Descending stage; 2) Contact Stage; 3) Touchdown Stage; 4) Spreading Stage; and 5) Ring-vortex Stage. Source: Fujita (1990).	80
Figure 36. Four stages of a downburst event/ Descending Stage, Contact Stage, Mature Stage and Breakup Stage. Source: Wolfson (1988).	80
Figure 37. Idealized representation of microburst wind fields. Where a) represents an open terrain, b) represents the impact of a downburst within an urban area causing pockets of wind because of the irregularity of the surface. Source: Pita and de Schwarzkopf (2016).	81
Figure 38. Sketch of a downdraft formation (dark blue) within the cloud during the maturation (right) period of the storm, when downdrafts and updrafts coexist at the same time and downburst can be developed at the front end of the storm, commonly along with precipitation. Source: Wolfson (1988).	83
Figure 39. Bernoulli's Theorem showing the total pressure is equal to the sum of static pressure (blue) and dynamic pressure (red). Source: Fujita (1985a).	85

Figure 40. Schematic sectional representation through a model of downburst outflow event indicating regions of high wind speed, progression of the outflow in different times (t and $t + \Delta t$). Source: Mason (2017)	85
Figure 41. Simplified model showing the use of indexes to track the characteristics of the morning and evening atmospheric soundings favorable for dry-microburst activity over the high Plains in the United States. Source: Wakimoto (1985).....	87
Figure 42. Natural disaster occurrences per category from early 20 th Century to 2020. Data extracted from EMDAT (2020) chart created by the Author.....	89
Figure 43. Illustration of a downburst event that occurred in the City of Porto Alegre on 29/01/2016. Source: Author.	93
Figure 44. Aircraft accident caused by a downburst at the John F. Kennedy International Airport (JFK) on June 24, 1975. In this illustration, Fujita draws the Aircraft being pushed down due to a strong downdraft. Source: Fujita (1976).	96
Figure 45. Rare microburst event registered at the Andrews Air Force Base on 1 st August 1983. Wind 3-s instant gust peak of 67 m/s (150 knots) followed by a back-side peak wind gust of 42 m/s (84 knots), reading from right to left. Source: Fujita (1985a).	97
Figure 46. Doppler high resolution, vertical profiles of the radial wind differential velocity for three microbursts and the average curve for six cases. Source: Wilson et al. (1984).....	98
Figure 47. Typical schematic of a downburst per radar reflectivity. Source: Hjelmfelt (1988).	99
Figure 48. Schematics of typical JAWS microburst structure at maximum intensity. Source: Hjelmfelt (1988).	100
Figure 49. In a) is shown the maximum radial velocity profiles for the microburst cases investigated by Hjelmfelt (1988) and in b) the maximum diameter for each event. Source: Hjelmfelt (1988).....	101
Figure 50. Different analysis of typical downburst profiles, where in a) is showed time variation to reach normalized V_{max} ; in b) is showed microburst velocity profile normalized to V_{max} ; in c) is showed normalized radial velocity along the V_{max} azimuth versus scaled to the radius at maximum velocity	

(<i>r_{vmax}</i>); and in d) typical time of expansion and dissipation of downbursts. Source: Hjelmfelt (1988).	103
Figure 51. Typical microburst lifespan. Source: Hjelmfelt (1988).	104
Figure 52. Graphs of wind speed (l-sec instant values) at each level on the tower around the time of passage of the downburst. Source: Sherman (1987).	105
Figure 53. in a) shown the wind speed for three different heights for both 30-s and 10-min intervals, and in b) the same is presented but for wind. Source: Choi and Hidayat (2002).	107
Figure 54. Velocity-time record during a TS event in Passo Fundo – RS at a) 20 meters; b) 30 meters, and c) 40 meters and change in wind direction. Source: Paluch et al. (2003) apud Ponte and Riera (2010).	108
Figure 55. Seven towers configuration utilized in Gast (2003) during the register of the RFD and Derecho. Source: Chen and Letchford (2006).	109
Figure 56. Isometric view of wind speed for a) RFD and b) Derecho at various at 10 m in height. Source: Chen and Letchford (2006).	109
Figure 57. RFD event Vertical mean wind profile (U_{mean}) at different time steps. Height is given in natural logarithm. Source: Gast (2003).	111
Figure 58. Derecho event vertical Wind Profile (U_{mean}) at different time steps. Height is given in natural logarithm. Source: Gast (2003).	111
Figure 59. Four types of TS wind profiles (dashed line) proposed comparatively to non-thunderstorm events (continuous line). Source: Choi (2004).	113
Figure 60. Typical TS outflow profiles identified by Choi (2004). Source: Adapted from Choi (2004).	114
Figure 61. Various dual-Doppler mean 1-min mean wind speed profiles from and 10-min mean profiles for a) Syracuse – Kansas (SYR), b) Truscott – Texas (TRUS) and c) Pep – Texas (PEP). Source: Gunter and Schroeder (2015)	116

- Figure 62. Maximum gust profiles for averaging times of 3s, 8s, 34s, 68s, and 136s. The maximum profile is the far right and increasing averaging times continue to the left. In a) is shown the profile for the event in 08. Source: Lombardo et al. (2014)..... 118
- Figure 63. LiDAR profiler measurements in the Port of Livorno, 13 September 2015: a) velocity at 120 m above ground; b) evolutionary vertical wind velocity profile at time 295-s, for different time averaging, and c) wind direction at time 295-s. Source: Burlando et al. (2017a)..... 119
- Figure 64. Intense non-synoptic event detected by LIDAR in Port of Livorno on June 14th, 2014. In the Left is shown 10-min mean vertical wind velocity and, in the right, it is shown the 10-min mean horizontal wind velocity. The hollow triangles and circles are the 1 sec measurements along the 10 maximum min average. Source: Repetto et al. (2018). 120
- Figure 65. Elevation of test section with measurement points. Source: Stengel and Thiele (2017).. 121
- Figure 66. Wind speed time history on 12 positions along the time during a downburst event in Northern Germany in the fall of 2015. Source: Stengel and Thiele (2017)..... 121
- Figure 67. Picture of the urban environment in Beijing where the anemometric tower used to capture the TS wind profile event in Zhang et al. (2019). Source: Zhang et al. (2019). 122
- Figure 68. Shown the 30-min long record of the thunderstorm outflow in Beijing on June 10, 2016. In a) the data is shown in an isometric chart with the tower's height increasing in the z axis h(m) (colored graphs), time is presented in the x axis and velocity in the y axis. In b) the same data but presented in a 2D graph for different time steps of the outflow and c) is shown the evolution of the profile direction over time. Source: Zhang et al. (2019). 124
- Figure 69. Compilation of four maximum TS wind outflow profiles. Where black lines are Hjelmfelt et al. (1989) TS wind profiles from various events; blue lines are Lombardo et al. (2014) TS wind profiles; green lines are Gunter and Schroeder (2015), where dash lines represent the divergent flow velocities; and orange line refers to Repetto et al. (2017) profile. Source: Mason (2017)..... 125

Figure 70. Typical wind records over the length of the record in which a) is showed the random fluctuation of velocity around the mean and in b) is showed the typical frequency distribution where the highest frequency of values is found within the center part of the curve. Source: Liu (1990). ...	131
Figure 71. Long-term and short-term probability distributions of wind speed. Source: Liu (1990)..	132
Figure 72. Turbulence Intensity for the RFD and Derecho Events. In a) the TI time series (120s s mean) and in b) the I of both events compared for different I . Source: Orwig-gast and Schroeder (2005).	135
Figure 73. Ensemble of the diagrams of μt for all thunderstorm records investigated and their mean values (thick line). Source: Solari et al. (2015a).	136
Figure 74. PSD reduced turbulent fluctuation v' as a function of the reduced frequency f for all thunderstorms records detected in Solari et al. (2015a). Source: Solari et al. (2015a).....	138
Figure 75. Estimated PSD as stationary process for a) RFD and b) derecho overlaid with Karman-Harris PSD (thicker line) Source: Chen and Letchford (2006).	139
Figure 76. Envelope wind speed profiles from ISO 4350 and AS/NZS 7000 compared to three full-scale measurements of TS winds. Source: Mason (2017) apud Holmes et al. (2008); Lombardo et al. (2014); Gunter and Schroeder (2015).	143
Figure 77. Typical wind speed pattern is used to illustrate the method aimed at identifying downburst winds within surface wind records. Source: Fujita (1985b).	145
Figure 78. A sample of a dataset in which a) the time-varying mean that has been removed, b) the density function of such series and c) the residual turbulence after removing the stationary residual turbulence. Source: Lombardo et al. (2009).	147
Figure 79. In a) are shown the assessments of wind speeds for various return period for the Newark Airport using a mixed distribution (M), thunderstorms winds (T), non-thunderstorm winds (NT), and commingled winds (C) in b) are shown the same analysis for the La Guardia Airport. Source: Lombardo et al. (2009).	147
Figure 80. Three distinct cases of a typical 1-hour record of a) a stationary gaussian event; in b) it is almost perfectly superimposed histogram density function of the recorded wind speed. This event	

corresponds to a neutral atmospheric event; in c) a non-stationary and non-gaussian event and in d) the histogram density function changed because a gust peak relative to the mean wind speed, corresponding to a Thunderstorm. In d) a typical 1-hour record of a Stationary Non-Gaussian event and a moderately non-Gaussian distribution, corresponding to an unstable gust front. Source: Gaetano et al. (2014).....	150
Figure 81. Conceptual scheme of transforming datasets associated with the different wind events. Source: Gaetano et al. (2014).	151
Figure 82. Two wind records of a) EPS event and b) downburst event from the Port of the Northern Tyrrhenian Sea during the Project Wind and Ports. Where the blue line represents the mean wind speed, the red line the moving average speed, and the red dot the maximum wind record captured. Source: Gaetano et al. (2014).	152
Figure 83. Mean recurrence period in year for extreme wind velocities in sector groups for a) Bagé, and b) Porto Alegre. Source: Riera and Nanni (1989)	154
Figure 84. Summary of four phases adopted to perform the dataset classification proposed by Vallis (2019). Source: Author. Data extracted from Vallis (2019).....	155
Figure 85. Climatic regions are based on the type of associated phenomena that originate them. Source: Loredo-Souza et al. (2021).	158
Figure 86. Isopleth map for basic velocity V_0 (m/s) considering proposed “transitioning map” approach. Source: Loredo-Souza et al. (2021).	159
Figure 87. Visual representation of the process to obtain the profiles proposed here. Source: Author.	161
Figure 88. Proposed model (continuous blue line) and field data (dashed orange line) from vertical TS wind event extracted from Sherman (1987). Source: Author.	165
Figure 89. Proposed model (continuous blue line) and field data (dashed orange line) from vertical TS wind event extracted from Hjelmefelt (1988). Source: Author.	166

Figure 90. Proposed model (continuous blue line) and field data (dashed orange line) from vertical TS wind event extracted from Choi and Hidayat (2002). Source: Author.	167
Figure 91. Proposed model (continuous blue line) and field data (dashed orange line) from vertical TS wind event extracted from Paluch et al. (2003). Source: Author.	168
Figure 92. Proposed model (continuous blue line) and field data (dashed blue line) from vertical TS wind event extracted from Gast (2003) for RFD event and proposed model (continuous orange line) and field data (dashed orange line) from vertical TS wind event extracted from Gast (2003) for Derecho event. Source: Author.	169
Figure 93. Thunderstorm events observed by Choi (2004). Each dashed line represents a different event observed. The two continuous lines represent best fit models proposed for two maximum et 29/01/2001 and 21/05/2022 events. Source: Author.	170
Figure 94. Two maximum profiles based on Lombardo et al. (2014) datasets. In this case the Maximum Profile 1 is showed in Blue, and the Maximum Profile 2 is showed in orange. In both cases the proposed model is given by the continuous line and the field data is given by the dashed line. Source: Author.	172
Figure 95. Two maximum profiles based on Gunter and Schroeder (2015) datasets. In this case the Maximum Profile 1 is showed in Blue, and the Maximum Profile 2 is showed in orange. In both cases the proposed model is given by the continuous line and the field data is given by the dashed line. Source: Author.	173
Figure 96. Proposed model (continuous blue line) and field data (dashed orange line) from vertical TS wind event extracted from Burlando et al. (2017). Source: Author.	174
Figure 97. Profile measurements of Repetto et al. (2018) at maximum stage for both 1-s (blue) and 10 min (orange) averaging time. where the dashed lines represent field measurements and the continuous line represent the proposed models. Source: Author.	176
Figure 98. Proposed model (continuous blue line) and field data (dashed orange line) from vertical TS wind event extracted from Zhang et al. (2019). Source: Author.	177

Figure 99. Composite illustration of wind outflow profiles field measurements investigated in this study. Each color represents the maximum profile from each source. It also showed time averaging and terrain category as per NBR 6123 in which each dataset was acquired from. Source: Author...	180
Figure 100. Illustration of proposed TS wind profile fitted curves based on full-scale measurements considered in this study. Source: Author.	184
Figure 101. Illustration of proposed TS wind profile fitted curves based on full-scale measurements considered in this study. Datasets are normalized to their wind speed at 10 m. Source: Author.	185
Figure 102. Illustration of proposed TS wind profile fitted curves based on full-scale measurements considered in this study. Datasets are normalized to their wind speed at 10 m. Only the lower portion of the profile is shown. Source: Author.	186
Figure 103. Illustration of proposed TS wind profile fitted curves based on full-scale measurements considered compared to other existing TS wind models normalized to V_{10} . Source: Author.	188
Figure 104. Illustration of proposed TS wind profile fitted curves based on full-scale measurements considered in this study compared to TS profiles on ISO 4354 and AS/NZS 7000. Source: Author. ...	190
Figure 105. Comparison of proposed fitted curve profiles to category II profiles of NBR 6123 and various time averaging. Source: Author.	192
Figure 106. Comparison of proposed fitted curve profiles to category III profiles of NBR 6123 and various time averaging. Source: Author.....	193
Figure 107. Comparison of proposed fitted curve profiles to category IV profiles of NBR 6123 and various time averaging. Source: Author.....	195
Figure 108. Maximum proposed fitted curve profiles found in this study for Terrain Categories II, III, and IV and time averaging 1-min, 3-s, and 30-s, respectively. Source: Author.	199
Figure 109. Location and season of tornadoes and waterspouts reports. December–February (DJF) is summer, March–May (MAM) is fall, June–August (JJA) is winter, and September–November (SON) is spring. Source: Silva Dias (2011).	224

Figure 110. In a) shows Garstang (1998) estimation of downburst distribution in the Amazon based on satellite analysis and in b) a more recent work from Taszarek et al. (2021) shows the annual mean climatology of severe thunderstorm environments in hours. Note how the blowdowns analysis matches very closely the more recent climatologic studies. Source: Adapted from Taszarek et al. (2021) and Garstang (1998).....	226
Figure 111. Agribusiness Research and Rural Extension Company of Santa Catarina (EPAGRI/SC) news article, discuss the pattern of damages after a severe storm in the State. Source: EPAGRI (2010)...	227
Figure 112. Capture of a downburst event in Presidente Prudente – SC. Notice the divergent wind pattern highlighted in the Radar capture. Source: O Município (2018).	227
Figure 113. Existing radar network in Brazil colored according to their respective managing entities. Source: Created by Author. Data extracted from: Naccarato and Camargo (2019) and Tropical Atlantico (2020).	229
Figure 114. Damage survey after a downburst event in President Prudente – SC. Photo by Marcos Fernandes. Source: O Município (2018).....	230
Figure 115. Picture of a downburst event in Morro Agudo on 12/11/19. Source: Climaavivo.com (2019)	230
Figure 116. Downburst event photographed in Torres – RS. Source: saojoaquimonline.com (2019).	231
Figure 117. In a) is shown the full-scale damage caused by a downburst event in Porto Alegre and in b) the laboratory testing showing records of the same building, where the red and orange areas represent the side that was mostly damaged by the same thunderstorm event. Source: Loredou-Souza et al. (2019).	232
Figure 118. Downburst cases reported in Brazil within different year ranges. Source: Author.	233
Figure 119. Downburst cases reported in Brazil until 2020 per State. Source: Author.	234
Figure 120. Downburst reports maximum wind gust speed overlayed above population density in Brazil. Focus is given to southern portion of Brazil since is where most part of the cases are located.	

Source: Author. Data extracted from: Wind data extracted from several downburst events analysis and population density information from WorldPop.org (WORLDPOP, 2021).	235
Figure 121. Summary of downburst modeling approaches clusters (first level), methods (second level), and specific techniques (third level). Source: Author.	242
Figure 122. Depictures a a) gravity current (or density current) simulated in a laboratory experiment utilizing the fluid release approach and in b) the structure of a gust front event. Source: a) Simpson (1969) and b) Charba (1974).	244
Figure 123. Recording stage of PIV system deployed for circular water jet flow impinging on a flat plate. Source: Landreth and Adrian (1990).	245
Figure 124. Representation of the fluid release structure used in Alahyari and Longmire (1994). Source: Alahyari and Longmire (1994).	246
Figure 125. Schematic layout of the deployed thunderstorms wind tunnel in Wood et al. (2001) and Wood and Kwok (1998). Source: Wood et al. (2001).	248
Figure 126. Radial development of the mean velocity profile for wall jet experiment. Source: Wood et al. (2001).	249
Figure 127. The moving jet wind tunnel. Source: Letchford and Chay (2002).	250
Figure 128. Sarkar and Haan (2002) downburst wind simulator in a) the jet simulator and in b) the jet with added smoke to allow visualization of the flow. Source: Sarkar and Haan (2002).	250
Figure 129. Graph comparing Gast's full-scale microburst wind record measurement at 10 m above ground (blue line) and Sarkar and Hann's record considering and experimentally jet at $X/D = 0.75$ and $Z/D = 0.01$ (representing approximately 15 m in full scale). Source: Mason et al. (2005).	251
Figure 130. Pulsing aperture in a) open position and in b) close position. Source: Mason et al. (2005).	252
Figure 131. Schematic arrangement of an impinging wall jet experimental setup. Source: Xu and Hangan (2008).	253

Figure 132. Nozzle height arrangements utilized in McConville et al. (2009) experiment. In a) the nozzle is located a 1.0D, in b) 1.5D, and in c) 2.0D. Source: McConville et al. (2009).	254
Figure 133. A schematic picture of the impinging wall jet simulator used Zhang et al. (2013b). Source: Zhang et al. (2013b).	254
Figure 134. Results obtained by Zhang et al. (2013a) showing good agreement at lower levels to different X/D comparing to the cooling source model, other previous experiments, and full-scale measurement. Source: Zhang et al. (2013a).	256
Figure 135. Modeled buildings geometry of a) Cube, b) grain bin, c) gable-roofed building (16° degrees roof slope) and d) gable-roofed building (35° roof slope). Gable roofs and conic-shaped roof experience lower drag uplift in the outburst region. The geometric parameters of the roof did not seem to influence significantly the wind load. Source: Zhang et al. (2014).	257
Figure 136. Photograph taken internally of the WindEEE wind tunnel. Source: Hangan et al. (2017).	258
Figure 137. Downburst flow visualization in WindEEE. Source: Hangan et al. (2017).	259
Figure 138. Normalized velocity profiles from full scale events from Hjelmfelt (1989) and Fujita (1978). Source: Junayed et al. (2019).	260
Figure 139. Sideview depicting the slot jet tunnel proposed by Lin et al. (2007). In a) is depicted the bottom of the tunnel, in b) and c) are shown the slots in close and open position. Source: Lin et al. (2007).	261
Figure 140. Elevation view of the wind tunnel used in Lin et al. (2015) experiment. Source: Lin et al. (2015).	262
Figure 141. The prototype of the pivoted flat plate at the Miyazaki University used by Butler and Kareem (2007). D in this figure represents the height of the distance from the ground to the flat plate. Source: Butler and Kareem (2007).	263
Figure 142. a) Profile development beyond a flat plate at 30° incidence and b) boundary layer profile compared during simulation attempt. Source: Butler and Kareem (2007).	264

Figure 143. Configuration of the 3-D multiple fan wind tunnel. Source: Butler et al. (2010).....	264
Figure 144. ABL velocity profile gust flow field compared to the full-scale data from Hjelmfelt (1988). In b) turbulence intensity profile of both the initial boundary layer profile and gust flow field. Source: Butler et al. (2010).	265
Figure 145. Multiple louvers capable of rotating at high speed to different angles in a) is shown the system with blades rotated at +50° and b) – 30° positions. Source: Aboutabikh et al. (2019).	266
Figure 146. In a) are shown vertical wind profiles of the maximum running-mean wind speed, and in b) shown the turbulence intensity profile compared to the ESDU open exposure profile. Source: Aboutabikh (2019).....	267
Figure 147. In a) is shown the small-scale win tunnel of the Northeastern university with multi-blade transient flow device to redirect and simulate flow at angle and in b) shown another view of the same experiment with blades in different angle. Source: Le and Caracoglia (2019).	268
Figure 148. Comparison of the velocity profile obtained at the modified wind tunnel along with other full-scale measurements and downburst simulations. Source: Le and Caracoglia (2019).....	269
Figure 149. A graphic representation of classic analytical model a) wall jet and b) ring vortex models: Source: Savory et al. (2001).	270
Figure 150. Comparison of Oseguera and Bowles (1988) Model to TASS, NIMROD full-scale measurements and proposed Analytical Model. Source: Oseguera and Bowles (1998).....	271
Figure 151. Vicroy (1991) outputs compared to Oseguera/Bowles's Model, NIMROD, and JAWS full-scale measurements. It is noticeable how the new model proposed presented a better fit for both a) normalized vertical profile of horizontal winds and in b) normalized horizontal wind profiles along a radial development comparing to the full-scale measurements. Source: Vicroy (1991).	272
Figure 152. Contours of maximum wind speed footprint generated by the downburst passage. Source: Holmes and Oliver (2000).....	273
Figure 153. Vectorial summation of the downburst displacement in the horizontal plane and the radial velocity generated by the downburst thunderstorm itself. Source: Holmes and Oliver (2000).....	273

Figure 154. Results from Homes and Oliver's model. In a) is presented the Mode's profile radial windspeed and in b) a comparison of the equation proposed to full-scale measurements. Source: Holmes and Oliver (2000).....	274
Figure 155. The vertical profile of horizontal radial outflow wind speed associated with microburst. Source: Savory et al. (2001).	275
Figure 156. Flow line in the downdraft. Source: Adapted from Ponte and Riera (2010).	275
Figure 157. Path of 20 TS events in the region of interest. Source: Miguel and Riera (2013).....	278
Figure 158. In a) is shown the sketch of a thunderstorm system embedded in an extratropical cyclone and in b) is shown a sketch of a theoretical vectorial sum of speed from the EPS with the thunderstorm system moving, and TS outflow speed. Source: Author.	279
Figure 159. Horizontal component of a downburst event registered at the Porto La Spezia in 25/11/2011, where the red line represents the 10-min average flow, which is equivalent to the velocity of the thunderstorm system. Source: Solari et al. (2015b).....	280
Figure 160. Horizontal wind velocity at the reference height ($z=10\text{m}$) during a typical squall line event. Source Riera (2016).....	281
Figure 161. Evolution in time of TS component for $V_t = 38.7 \text{ m/s}$ and five different characteristic time T. Source: (RIERA, 2020).....	282
Figure 162. Simulation results of model proposed by Xhelaj et al. (2020) are presented (magenta line) and compared against full-scale measurements at two different spots (blue line). In a) and b) is showed the results obtained for velocity and direction, respectively, in Anemometer SP03; and in c) and d) the same parameters are shown for Anemometer SP 02.....	284
Figure 163. Ring Vortex Model. Source: Vicroy (1992).	286
Figure 164. The simulated downburst wind speed time history at a height of 101.7 is shown in a) and in b) is shown the downburst fluctuation wind speed component for the same simulation. Source: Chen and Letchford (2004).....	290

Figure 165. Results of Chen and Letchford' NDESH Model for utilizing a) Wood's vertical profile and b) Holmes's spatial function. Source: Chen and Letchford (2007).....	291
Figure 166. Outputs of Nicholls et al. (1993) LES model a) and c) streamlines outflows and b) and d) pressure perturbations over a building. Source: Nicholls et al. (1993).....	295
Figure 167. CM1 Model 3D volume rendering of a) a cloud developing a downburst and b) isopleths of enclosed horizontal streamline winds exceeding 25 m/s. Source: Orf et al. (2012).....	296
Figure 168. 3D renderings of the two colliding downbursts at different time steps in the 2km grid. Source: Anderson et al. (1992).....	298
Figure 169. Comparison of results from Mason et al. (2009, 2010) to other experiments and full-scale measurements form the JAWS experiment. Source: Mason et al. (2009; 2010).	300
Figure 170. Schematic of the computational domain used for the CFD simulation. Source: Shehata et al. (2005).	302
Figure 171. In a) are presented vectors coming out from a numerically simulated jet impinging a flat surface. In b) is shown one of the profiles for a radio jet diameter and maximum velocities ratio of an empirically tested downburst at TTU. Source: Chay et al. (2006).....	303
Figure 172. Vorticity and vector snapshots of vortex-ring and secondary vortex evolution at the non-dimensional time step $T=12.8$, for a) $RE=20,000$ and b) $RE=100,000$. Source: Kim and Hangan (2007).	303
Figure 173. Effects of the roughness to the instantaneous and envelope peak radial velocity profiles. Source: Aboshosha et al. (2015).	305
Figure 174. Application of the stationary wavelet transform to process the RFD data, where in a) is shown the original full-scale measured data; b) is shown the stationary decomposition approximation function and c) for different detail coefficient levels. Source: Orwig and Schroeder (2007).	308
Figure 175. Schematic diagram of the new gust front factor framework proposed by Kwon and Kareen (2009). Source: Kwon and Kaeem (2019).....	310

LIST OF TABLES

Table 1. Major Aircraft accidents caused by downburst induced winds. Source: Potts (2007), Wikipedia (2018) and NOAA (2020A).....	61
Table 2. Table of vertical profile measurements of TS wind outflows available in the literature discovered within the scope of this research. Source: Author.	128
Table 3. Summary of extreme values analysis methods and distribution methods considered by Vallis (2019) for the analysis of Brazil's extreme wind climatology. Source: Author. Data extracted from Vallis (2019).	156
Table 4. Summary of all full-scale measurements and proposed fitted curve profile considerations. Source: Author.	181
Table 5. Factors based on proposed TS wind fitted curve profiles. The highlighted gray cells show the normalized maximum values for the obtained profiles. Source: Author.....	196
Table 6. Parameters of five downbursts categories for various downbursts V_0 proposed by Riera (2016). Source: Riera (2016).....	282

LIST OF ABBREVIATIONS AND ACRONYMS

1D	One-dimensional
2D	Two-dimensional
3D	Three-dimensional
AAFB	Andrews Air Force Base
AB	Atmospheric Blockage Area
ABL	Atmospheric Boundary Layer
ANSI	American National Standards Institute
ARMA	Auto regressive moving average
AS/NZS	Australia/New Zealand
ASCE	American Association of Civil Engineers
ASWS	Automated weather stations data
BAM	Federal Institute for Materials Research and Testing in Germany
BH	Bolivia High
BLUE	Best Linear Unbiased Estimator
BND	Brazilian Northeastern Dug
BrasilDAT	Brazil's Lighting Network Data
BTD	Brightness Temperature Difference
CAPE	Convective Available Potential Energy
CAS	Chinese Academy of Sciences
CBDI	Cloud-Base Detrainment Instability
CC	Comma Clouds
CEMADEN	National Center for Monitoring and Early Warning of Natural Disasters
CF	Cold Front
CFD	Computational Fluid Dynamics
CFSR	Climate Forecast System Reanalysis
CFSv2	Climate Forecast System Version 2
CL	Chaco Low
CLAW	Classify, Locate, and Avoid Wind Shear
CM1	Bryan Cloud Model
CM1	Bryan Cloud Model Version 13
CR	Cyclogenetic Regions
CSU-RAMS	Colorado State University – Regional Atmospheric Modeling System
CVHL	Cyclonic Vortices of High Tropical Levels
CWE	Computational Wind Engineering
CZSA	Convergence Zone South Atlantic
DAEE	Department of Water and Electricity in the State of São Paulo
DECEA	Department of Airspace Control
DJF	December to February
DPVI	Particle Image Velocimeter
EMD	Empirical Mode Decomposition
EMD	Empirical Mode Decomposition
EM-DAT	International Disaster Database

EPAGRI/CIRAM	Agricultural Research and Rural Extension of the State of Santa Catarina
EPAGRI/SC	Agribusiness Research and Rural Extension Company of Santa Catarina State
EPS	Extended Pressure Systems
EPSD	Evolutionary Power Spectral Density
ESDU	Engineering Sciences Data Unit
EVAM	Extreme Value Analysis Method
FACE	Florida Area Cumulus Experiment
FFD	Forward-flank downdraft
FFT	Fast Fourier Transform
FIM	Fixed interval method
FUNCEME	Foundation for Meteorology and Water Resources in the State of Ceará
GDF	Gaussian Density Function
Geo-Rio	Geotechnical Institute Foundation in the State of Rio de Janeiro
GEVD	Generalized Extreme Value Distribution
G	Gust Factors
GIS	Global Information System
GOES	Geostationary Operational Environmental Satellite
GPD	Generalized Pareto Distribution
GRF	Gust response factor method
hp	House Power
IL	Instability Lines
INEA	State Environmental Institute in the State of Rio de Janeiro
INPE	National Institute for Space Research
IPMET-UNESP	Institute for Meteorological Research of the University of the State of São Paulo
ISO	International Organization for Standardization
ITCZ	Intertropical Convergence Zone
JAWS	Joint Airport Weather Studies
JF	Jet Outflow
JFK	John F. Kennedy International Airport
JJA	June to August
L	Low Pressure System
LAC	Laboratório de Aerodinâmica das Construções
LES	Large Eddy Simulation
LLJ	Low-Level Jets
LLWAS	Anemometer-based Low-Level Wind Shear Alert Systems
LLWAS	Low-Level Wind Shear Alert Systems
LNA	Region of Thermal Low in Northwestern Argentina
LSPSV	Large Scale Streak Velocimeter
MAM	March to May
MCC	Mesoscale Convective Complex
MCS	Mesoscale Convective Systems
MIS-BR	Method of Independent Storms
MIST	Microburst and Severe Thunderstorm Project
MJO	Madden Julian Oscillation

MMM	Mesoscale meteorological models
MSC	Mesoscale Convective Systems
MWPI	Microburst Windspeed Potential Index
N.A.	Not Applied
N.I.	Not Informed
NBR	Brazilian Wind Code (Norma Brasileira)
NCAR	United States National Center for Atmospheric Research
NDESH	Nonparametric deterministic-stochastic hybrid
NIMROD	Northern Illinois Meteorological Research in Downbursts
NOAA	United States National Weather Service
NSSP	National Severe Storm Project
NTS	Non-thunderstorm Event
NTW	Northeast Trade Winds
PAM	Portable Automated Mesonet
PJ	Polar Jet
PJ	Polar Jet
POD	Proper orthogonal decomposition
PSD	Power spectral function
PSL	Prefrontal Squall Line
R	Radial Coordinate
RE	Reynold's Number
RFD	Rear-flank downdraft
S2iD	Brazilian Integrated Disaster Database
SAS	Adaptive Scale Simulation
SASA	Subtropical Anticyclone of the South Atlantic
SASP	Subtropical Anticyclone of the South Pacific
SDF	Spectral density function
SF	Straight-line flow
SI	Stability Index
SIMEPAR	Meteorological System in the State of Paraná
SIPAM	Amazon Surveillance System
SJ	Subtropical Jet
SON	September to November
SRM	Spectral representation method
SRM	Spectral representation method
SWS	Surface weather stations
SWTI	Severe Weather Threat Index
TASS	Termina Area Simulation System
TS	Thunderstorm
TTU	Texas Tech University
TTU	Texas Tech University
TTUKa	ka band Mobile Doppler Radars Mobile Doppler
TVAR	Vector time-varying autoregressive
TWS	Trade Winds from the Southeast

UPF	Universidade de Passo Fundo
URANS	Reynolds Averaged Navier-Stokes
US	United States
VAI	Averaging interval method
WERFL	Wind Engineering Research Field Laboratory
WF	Warm Front
WindEEE	Wind Engineering Energy and Environment
WINDEX	Wind Index
WiST	Wind Simulator and Testing
WME	Wisconsin Model Engine
WMO	World Meteorological Organization
XEPSD	Evolutionary cross-power spectral density (XEPSD) functions
XPSD	Cross-power spectral density

LIST OF SYMBOLS

\hat{v}	1-s Peak Wind Velocity
$A_M(t)$	Approximation Function
\bar{V}_{max}	Average Maximum Velocity
U_{Mean}	Average Wind Speed
T	Averaging Period
Z_m	Axial Coordinates Of The Jet Flow
H	Axial Distance (Height) Between Jet And Impinging Surface.
θ	Azimuthal Coordinates
ρ_o	Basic State Density
V_o	Basic Wind Velocity
dBZ	Decibels
ρ	Density of the Fluid
z_h	Depth of the Outflow
$D_j(t)$	Detail Function Level in Wang <i>et al.</i> (2013, 2014)
D	Diameter
Z_{DR}	Differential Reflectivity
R_n	Distance From the Center of the Cloud to the Point of Interest
V_{EPS}	EPS Wind Speed
R_o	Equivalent Spherical Radius Of The Cylindrical Fluid Release
u', v', w'	Fluctuating Wind Components
n	Frequency
X/D	Function of distance of Impingement Zone and Nozzle Height
g	Gravitational Acceleration
G_{G-F}	Gust-front factor
z_{max}	Height of Maximum Wind Speed
V_{inl}	Inlet Velocity
D_{Jm}	Jet Diameter
K	Kelvins (Temperature)
Km	Kilometers
v	Kinematic Viscosity
κ	Kurtosis
k	Background wind contribution in Ponte Junior (2005)
<i>i</i>	Mass Mixing Ratios of Liquid Ice
<i>l</i>	Mass Mixing Ratios of Liquid Water
u_{max}	Maximum Horizontal Velocity
$U_{r,max}$	Maximum Horizontal Wind Speed At Different Radial
v_{max}	Maximum Sampled Value
\bar{v}_{max}	Maximum Value of the Slowly Varying Mean Wind Velocity
w_{max}	Maximum Vertical Velocity

V_{max}	Maximum Wind Velocity
$\bar{u}, \bar{v}, \bar{w}$	Mean Wind Component
$\bar{\phi}_i$	Mean Wind Speed
m	Meters
m/s	Meters per Second
Mb	Milibars
τ	Moving Average Period
τ	Moving Average Period
$\mu(t)$	Non-Dimensional Function Named
\bar{w}_+	Post-Peak Mean
\bar{w}_+	Post-Peak Wind Mean Speed
θ_e	Potential Temperature
\bar{w}_-	Pre-Peak Mean
\bar{w}_-	Pre-Peak Wind Mean Speed
P'	Pressure Perturbation from Hydrostatic Basic Rate
r_m	Jet Flow Radial Coordinate
V_r	Radial Velocity
R	Radio or Radial Coordinates
r_{vmax}	Radius of Maximum Velocity
f	Reduced Frequency Function
R^2	R-squared
Y	Skewness
σ_v	Slowly Varying Standard Deviation
$\bar{U}_i(t)$	Spatial Function
u_{seg}'	Stationary Residual Turbulence a Wind Record Segment
u_{seg}	Stationary Residual Turbulence of Each Segment
T	Environment Temperature/Moving Average Time Period
ΔT	Temperature Variation Between the Parcel or air and The Environment
T_o	Time Scale
$\tilde{u}_{t, seg}$	Time Varying Mean of a Record Segment
\tilde{u}_t	Time-Varying Residual Turbulence
V_{TS}	TS Wind Speed
I	Turbulence Intensity
z	Vertical Coordinate of a 3D space
w	Vertical Wind Component
$K_{z,G-F}$	Velocity Pressure Coefficient
dW	Vertical Velocity of an Air Parcel
$\bar{\Phi}_i(z)$	Vertical Wind Profile Function
V	Wind Speed (Not Decoposed)

1. INTRODUCTION

1.1. RELEVANCE OF THIS STUDY

The Davenport Wind Load Chain is one of the most critical efforts in wind engineering as it proposes a multidisciplinary study involving the fields of meteorology, micrometeorology, climatology, aerodynamics, and structural dynamics and aims to synthesize the structural effects of wind loads in structures. In Figure 1, a representation of the proposed approach is shown where each of the links represent an essential component of the system to correctly calculate the wind load/response of structures.

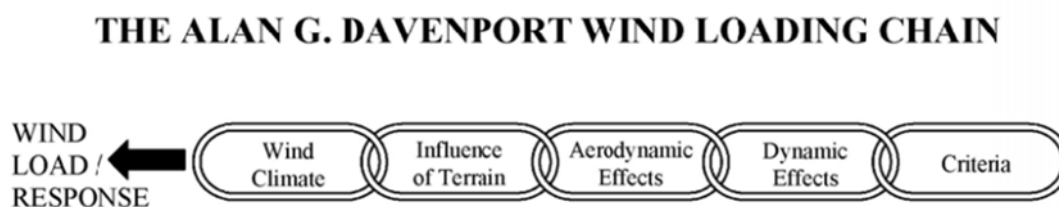


Figure 1. The Alan G. Davenport Wind Loading Chain. Source: Davenport (1961).

In Davenport's approach, a "weak link" leads to the unreliability of the entire system since each link is intimately interconnected to each other (DAVENPORT, 1961). Davenport's approach is exceptional, and it has been used world-wide for the development of wind codification. The first link, "wind climate" is considered the most complex component once it defines the loads that will act upon structures over their entire lifetime. However, the assumption made so far that all winds are the same and follow one unique and simple model is no longer valid given a series of advances in wind climatology studies.

Following the creation of Davenport's work, Gomes and Vickery (1977, 1978) developed an climatologic analysis of the Australian extreme winds and showed that approximately half of the extreme winds at that country had as causing mechanisms non-synoptic weather events, such phenomena such as thunderstorms (TS), tropical storms, and tornados. This would go in contrary to the assumption that the most extreme winds would always be caused by Extended Pressure System (EPS) events. EPS winds are generated by major weather systems found in a stratified and neutral Atmospheric Boundary Layer (ABL); they are characterized by sustained winds that vary little in time and spatial scales and can be described using typical averaging times that vary from 10 min to 1 hour (depending on the approach of the analysis and

definitions of local code provisions) and the turbulent field is considered to be approximately a stationary and Gaussian process. In contrast, non-synoptic winds are defined as convectively induced wind gusts that recede rapidly, varying significantly from one event to another, lasting usually less than 10 minutes, and typically presenting a characteristic wind speed "nose" profile (ZHANG, *et al.* 2013a). These type of winds generate significant wind shear and extreme speed values near ground, putting at risk structures designed solely to comply with conventional wind loading theories (KWON AND KAREEM, 2009). In this work, downburst winds are commonly referred to as non-synoptic winds or TS winds whereas these terms are used interchangeably. Similarly, synoptic and EPS winds will be used to refer to the same phenomena interchangeably in this work.

When studying the climatology of TS winds, Gomes and Vickery (1977, 1978) found that in some geographical locations, extreme winds may be caused by synoptic or non-synoptic events, or they can be a product of the combination of both. Places that have extreme winds generated by either TS or EPS events have they extreme wind climate called *mixed extreme wind climates*. Since these extreme winds present such distinct characteristics, there is a clear need to separate them as per the type of originating phenomena mechanism as well understanding the contribution parcel of each phenomenon to the final wind speed.

In summary, thunderstorm winds can be described as the product of extreme weather events caused by local and intense convective zones. Thunderstorms are local storms produced by cumulonimbus clouds always accompanied by one or more of these events: lightning, thunder, heavy rain, hail, producing strong wind gusts, sometimes tornadoes and/or downbursts or other types of TS winds (FUJITA, 1990). For instance, tornados generate a type of TS wind defined as an upstream and swirl current that normally occurs during the maturing phase of the thunderstorm. In the other end, downbursts are often called anti-tornadoes, once they generate TS winds that are the product of a consist, intense, slightly rotating column of cold descending air downwards from the clouds, which bursts out violently once it reach the surface (FUJITA, 1990). Downbursts are very localized and are the result of the evaporation process within the originating cloud called *evaporative cooling*, which occurs because of the entrainment of cold dry air in the mid-atmospheric level, causing a strong column of negative buoyancy air to fall towards the ground.

Downbursts became an important piece of investigation with the scientific community after it was found they have caused dozens of airplane accidents and structure failures resulting in numerous deaths and financial damages even nowadays. Fujita started to investigate these events after a series of mysterious wind accidents in the 70s and proposed the Theory of The Downburst, which initially was taken with skepticism from the scientific community, but after several field studies in the United States, downbursts became recognized as a phenomenon that differs in many ways of their counterpart's non-synoptic winds, such as gust fronts and tornadoes.

Further research has shown that in areas prone to severe weather an average of one microburst is observed per day. If this analysis is extended to all larger areas with similar characteristics in the United States, is estimated that 100 microbursts happen every day in that country (MCCANN, 1994). In fact, downbursts are reported to be observed more often than tornadoes in the United States and for that reason they are appointed to be more destructive than tornadoes (FUJITA, 1990). The same is seen in other places in the world, but the lack of knowledge and misinformation about downbursts makes numerous events go unnoticed, confused by other types of phenomena such as tornadoes, or simply generically defined as intensive windstorms.

Independently of which type of TS wind is being discussed, for wind engineering it is of major importance to define the frequency and vertical properties of all endangering phenomena that happen in the lower levels of the atmosphere encompassing the built environment. A major obstacle to advance the understanding of such winds and reducing imposed safety risks to structures is the lack of reliable full-scale measurements of these phenomena in both vertical and horizontal scales, this is mostly because TS wind events are scarce, rapid, and the right instrumentation to capture these events is costly.

Besides full-scale measurements, modeling can be an effective alternative to understand the properties of TS winds through simulation, although vertical high quality full-scale measurements need to be made available to further validate outputs. Substantial research has been developed and various methods have been proposed, they include physical models, Computational Fluid Dynamics (CFD) models, analytical models, and data driven models. Given the traditional approach of wind codes provisions and standard specifications, analytical

solutions are an attractive approach since they can be easily implemented in further engineering applications.

Some TS wind provisions have already been proposed by national codes and standard specifications associations, but there is some criticism to such initiatives because of the lack in agreement to characterize the properties of these winds. Therefore, a securely, agreeable, established, and proved method to simulate thunderstorm winds, similarly to what once was proposed by Davenport for synoptic winds, is still a major challenge deserving more attention of the scientific community. Additionally, little has been done to systematically review the extensive literature in the TS wind/downburst modeling and comparatively analyze full-scale measurements; representing important knowledge gaps that aim to be covered in this present document.

1.2. OBJECTIVES

Considering the aspects mentioned above, it is clear the need to expand the understanding of TS winds characteristics, as well their modeling approaches and techniques, whereas this is an essential step to create a reliable TS wind codification and consequently improve structural safety. In Figure 2, six steps are identified to be necessary to advance the towards the development of the codifications of extreme wind climatology of TS winds. Steps one and two refer to capturing, filtering, and treating TS measurements, conventionally these datasets are captured at the standard height of 10, whereas this can be seen as the horizontal description of wind measurements and other meteorological parameters. The final product is a general extreme wind climatology that distinguishes the basic velocity (V_o) for each type of meteorological event (TS, EPS, or others) for the regions analyzed.

The present work focuses mostly on steps three and four. These steps focus on identifying the vertical properties of TS winds which can be performed using a myriad of vertical measurements approaches and propose TS wind models, such as Radar, LiDAR, and anemometric towers. In step five, TS winds properties are modeled and interactions with structures are then analyzed utilizing through the deployment of various methods. For the last step (six), further studies are developed aiming to propose strategies (i.e., aerodynamic coefficients) to implement wind codes that can ultimately guide engineers to designing structures to the action of winds.



Figure 2. Steps towards the codification of thunderstorms winds. Source: Author.

Considering the discussions above and the 6 steps towards codification, five questions are proposed and listed below:

1. How TS winds are a endanger the built environment in the world and in Brazil. How often and where do they occur?
2. What is the background of downbursts as a meteorological phenomenon? How was it discovered? How did downbursts become an important subject of study for the wind engineering?
3. What are the common properties of non-tornadic TS winds?
4. What are the current strategies to model TS wind? What is the most accurate method to perform such an analysis? How to choose a method?
5. How to create a simpler TS wind model that can represent TS wind profiles at their maximum stage that can be easily integrated to TS wind codes?

Considering the research questions above, the following objectives were identified and are listed below:

1. Develop a literature review of severe weather characteristics in South America and discuss the impacts of severe weather due to thunderstorms in Brazil.
2. Present an overview of the development in the downburst research since its discovery in 70's and analyze their impacts on the built environment in Brazil and in the world.
3. Characterize physical properties of TS winds focusing on velocity and turbulence. Furthermore, it aimed to discuss methods used to identify TS winds within mixed datasets, analyze existing wind codes that have already adopted TS wind analysis in their provisions, and quickly examine the case of efforts done in Brazil to characterize its extreme wind climate.

4. Chronologically and systematically review the state-of-art in thunderstorm wind outflows modeling (generically referred as downbursts) aiming to cluster and explore different approaches and techniques to simulate these types of winds.
5. Identify relevant full-scale measurements of TS outflows for wind engineering applications and propose best fit curve functions that can best describe TS wind profiles at their maximum stage. These datasets will be then classified according to different types of terrains and time averaging methods. Selected profiles are then analyzed against existing downburst models, TS wind profiles proposed in existing TS wind codes, and finally looked against the profiles proposed in the NBR 6123.

With the accomplishment of these objectives, it is expected to produce a contribution that will significantly add to the understanding of thunderstorm winds, their consequences to the built environment, and ultimately helping to mitigate the risk that these winds impose to the structural safety.

1.3. ASSUMPTIONS AND LIMITATIONS

During the development of this work, it was found various terminologies commonly used to define TS winds. In this work is assumed that thunderstorms winds are any type of non-synoptic winds that is primarily driven by convective forces. The focus of this work are downwards straight-line outflow winds, which is the reversed terminology commonly used to define "upwards swirl winds" that refer to tornado winds, therefore in this work tornadoes-type winds are put aside, and the focus is taken to downwards convectively generated wind events, commonly referred as downbursts.

1.4. THESIS STRUCTURE

The objective herein is to identify, analyze, classify, and model TS winds with the wind engineering outlook applications. This workflow is summarized in Figure 3.



Figure 3. Research flow adopted to structure this document. Source: Author.

Initially, in the **Identification Phase**, the aspects concerning TS winds as a phenomenon derived from severe weather are surveyed. The aim in this phase is to justify the importance of this research subject by understanding their impact on the built environment in the world and in Brazil, additionally, in Appendix A an investigation on downburst-like events incidence in Brazil is presented. In the **Analyze Phase**, physical properties of TS wind are expanded and discussed; in this phase four main topics were found to be of major relevance, these are full-scale wind profiles measurements, turbulence analysis, development of methods aimed to identifying TS winds in mixed climate datasets, and examination of present efforts to implementing TS analysis to wind to codes and standards. Finally, in the last session, the case of the efforts developed to define Brazil's extreme wind climate and approaches for codification are briefly discussed.

In the **Modeling Phase**, an extensive literature review is developed regarding ways to model TS winds, comparative analysis of methods and approaches is developed. This research is presented in details Appendix B. Analytical models are given emphasis in the discussion since in **Proposition Phase** is proposed a derived method to defined TS wind profiles based full-scale measurements.

In Figure 4 is showed a graphic describing the structure of this thesis. Note that each chapter represents to approximately each of the development phases presented in Figure 3. Also, the arrows indicate the sequence in which the topics are discussed in the text, exemplifying the interconnections amongst the various topics discussed in this work. Note that due to the extension of the Model discussions portion, these are presented in Appendix B.

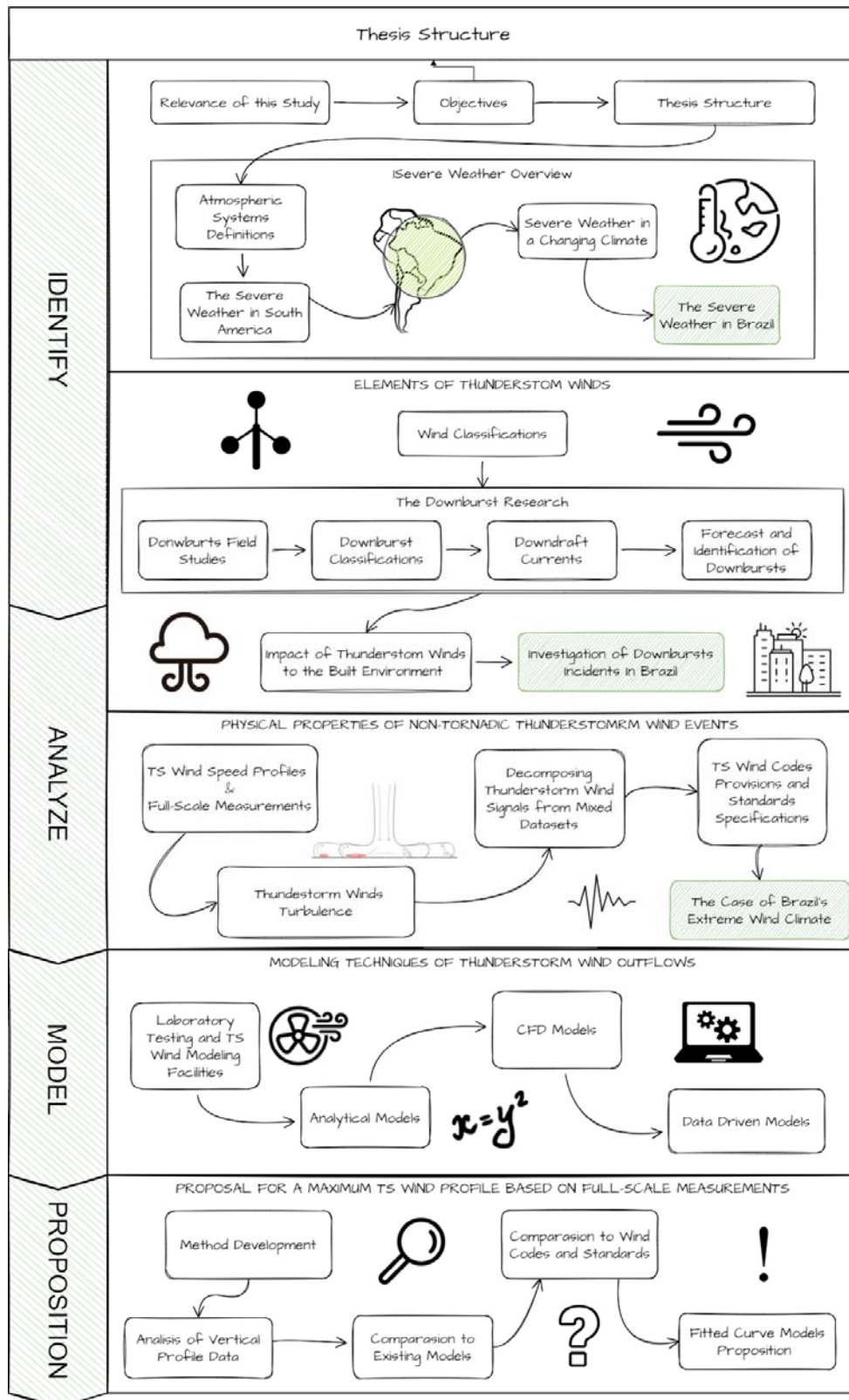


Figure 4. Schematics indicating the structure of this thesis. Source: Author.

2. ELEMENTS OF THUNDERSTORM WINDS

2.1. SEVERE WEATHER OVERVIEW

A common practice in meteorology is to classify atmospheric systems as per their time and space scales. There are several classifications proposed in the literature to name these scales. In this section the most monthly used nomenclatures are discussed. In Figure 5, is shown classifications proposed by Fujita (1981) and Orlanski (1975) and how they relate to each other in terms of horizontal length scale (x-axis) and timescale (y-axis). In the same figure are shown the typical corresponding weather phenomena schematically represented according to their typical dimensions and durations. These various scales are summarized into four main categories: **Planetary, Synoptic, Mesoscale, and Microscale Scales**. Considering these aspects, in this session it will be discussed the various types of deep moist convective systems causing severe weather.

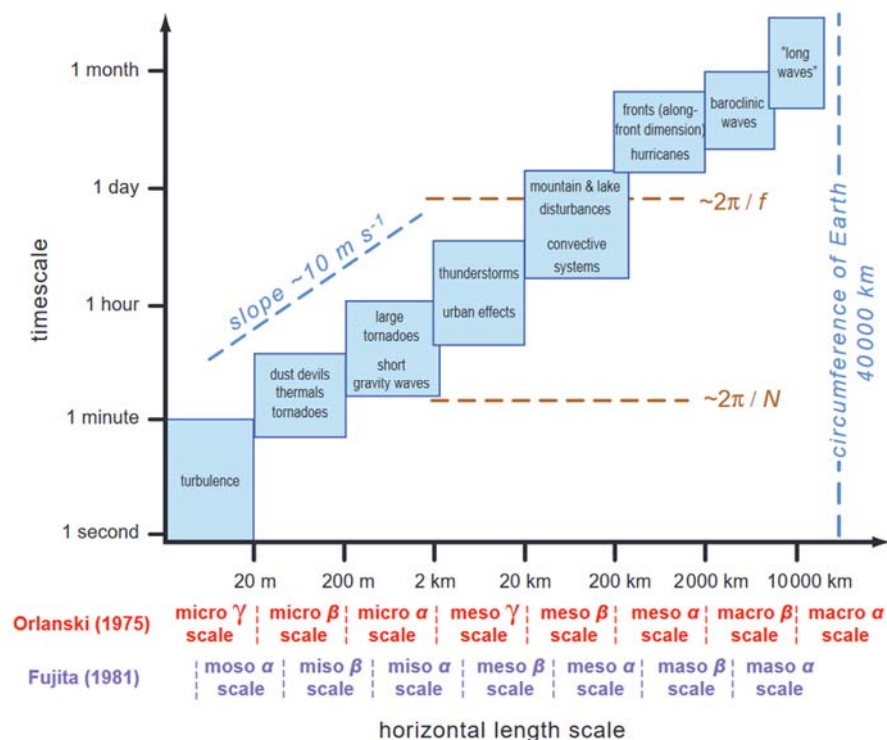


Figure 5. Scale definitions and characteristics on time and horizontal length scales of atmospheric systems. Source: Markowski and Richardson (2010).

2.1.1. Deep Moist Convective System Types

Even though there may be a blurry line in terms of space and time between these various events, this research focuses on mainly deep moist convective systems. These systems are

usually considered to be mesoscale weather systems, which may produce weather events such as tornadoes, downbursts, or other Severe Thunderstorm Events. The most accepted definition of severe thunderstorm was proposed by Johns and Doswell (1992), in which they are defined as events that produce hail with a diameter larger than 2 cm, intense windstorms higher than 50 kt (about 26 m/s) or tornados. Note that these systems are extremely dynamic, they interact with other events of other dimensions, and their strength is influenced by other smaller or larger scale weather systems, the terrain, and even human activities.

Deep moist convection systems or **convective storms** are a common way to refer to atmospheric systems that can generate severe thunderstorms (MARKOWSKI AND RICHARDSON, 2010). These systems are a relief response of atmospheric to vertical instabilities by bringing middle tropospheric air down to the surface or surface air upwards through convection (MCCANN, 1994). **Convection** is defined as the heating and rising process of an air parcel because of thermodynamic processes imposed by the ground and low-level winds. This process can generate extreme winds either during the process of formation, causing upwards winds, or dissipation of the storm cell (s), causing downwards winds.

Thunderstorms comprise one or multiple cells. They develop, mature and decay over a short period of time (BYERS AND HULL, 1949). Convective storms can be classified as ordinary thunderstorm, multicell storms, and supercell storms (WALLACE AND HOBBS, 2006). **Ordinary thunderstorms** or air mass thunderstorm result from local convection in an unstable air mass rather than by fronts or instability lines. These cells grow rapidly, fueling moisture and energy available in the atmosphere until they reach the mature stage. When in equilibrium state, the raising air parcels are no longer buoyant, and the downdraft circulation starts with the drag force caused by water drops. In this case the cloud cells spread out to the form of an anvil at the top dissipating after the fact. This process is illustrated in Figure 6.

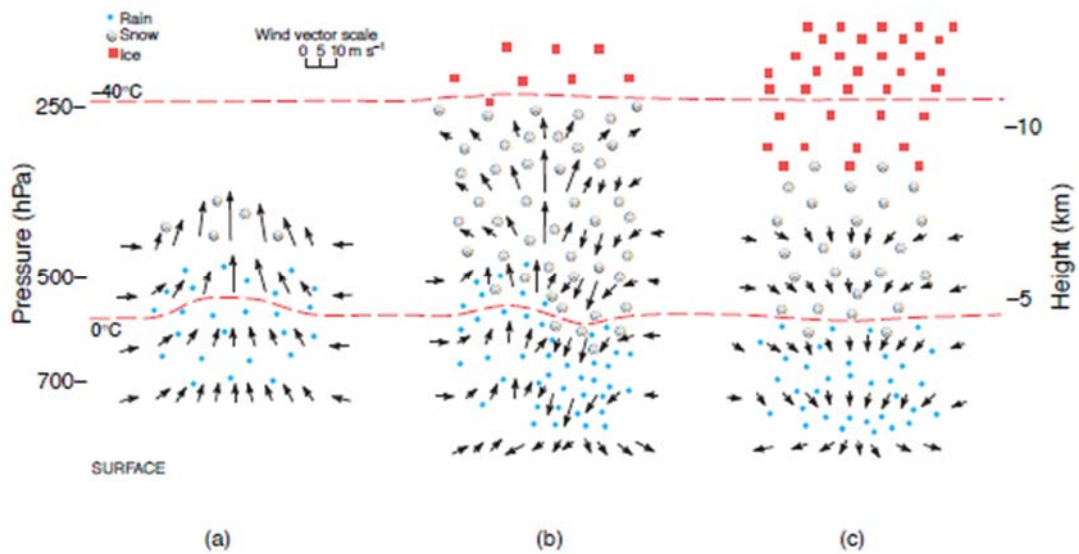


Figure 6. Schematic of an ordinary single-cell thunderstorm at different life stages: a) cumulus stage, b) mature stage, and c) dissipating stage. Source: Wallace and Hobbs (2006).

Single-cell thunderstorms are short lived and rarely generate extreme wind events in surface since it contains a self-destructive mechanism (namely downdraft circulation) induced by the own precipitation within the cloud. The dissipation of single-cell thunderstorms also happens quicker in environments without other major weather systems. This happens because normally these systems add up strong wind shears to the environment which acts as a factor to increase air buoyancy within the storm cloud, which helps sustain it.

Multicell Storms are characterized by a succession of cells evolving through its own cycle as in a single storm promoting the development of new cells (WALLACE AND HOBBS, 2006). These storms can be poorly organized under weak windshear, but when under strong wind shear, they can develop to a larger scale and longer-lived cell.

Supercell Storms are characterized by rotation renders induced by a *mesolow* within the upward region, which are superimposed upon the hydrostatically balanced pressure fields that exist because of the density gradients. There are two main regions in a supercell, the forward-flank downdraft (FFD) and rear-flank downdraft (RFD). The FFD contains most of the precipitation within the storm and the RFD downdraft rotates around the backside of the mesocyclone, contributing to formation of up whirl winds (tornados) and eventually down whirl winds causing a downburst (CHEN, 2005). In Figure 7, is shown the typical elements of a supercell storm.

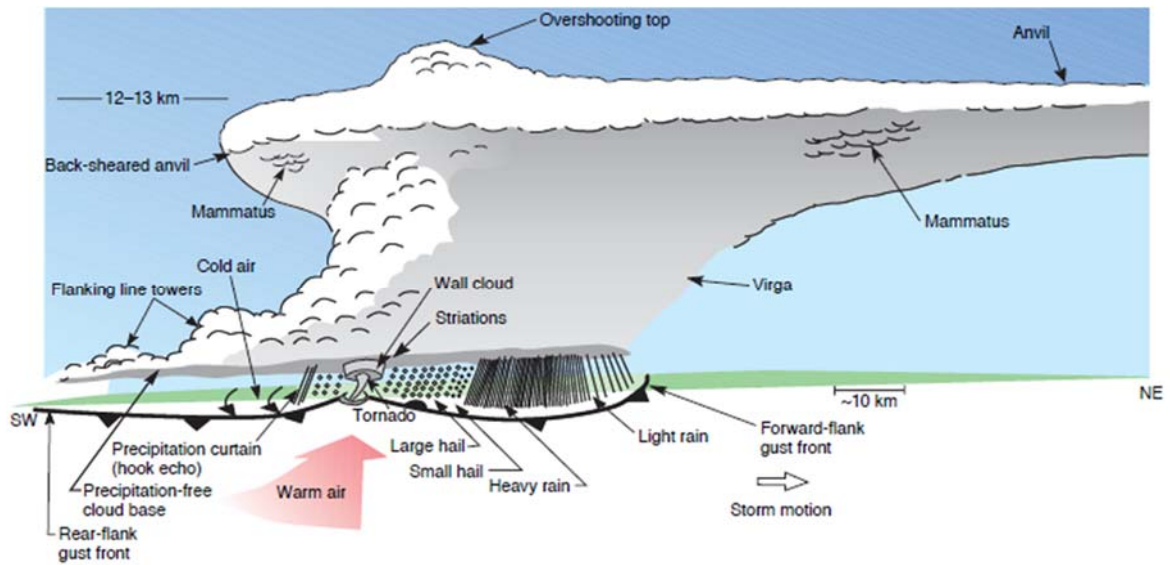


Figure 7. Structure of typical tornadic supercell storm and expected inflows and outflows. Source: Wallace and Hobbs (2006).

These storm formations can be often referred to by the following terms: Gust Fronts, Derechos, Mesoscale Convective Systems (MSC), Squall Line, Bow Echoes, Mesoscale Convective Vortices, and Downslope Winds. See below a brief explanation of each of these components.

Gust fronts are associated with either multicell or supercell storms, they announce the approach of the storm and occur because of the warm and moist boundary-layer lifted at the leading edge of the evaporatively cooled air from the base of the cloud. This lift forms new cells frontward of the multicell storm which can persist to sustain the cloud. A schematic illustration of this process is shown in Figure 8, note that the gust front follows the direction of motion of the multicell.

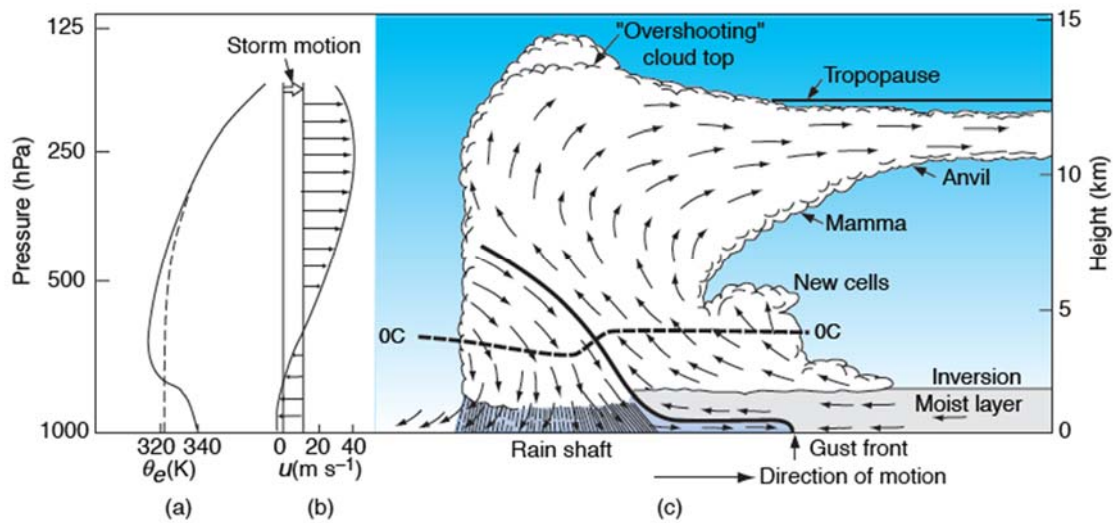


Figure 8. Schematic of an idealized multicell storm developing in a strong shear environment. The typical equivalent temperature and wind profile are presented to the left. Arrows show the direction of the flow. Source: Wallace and Hobbs (2006).

The presence of latent heat helps to define the persistence of a thunderstorm system. In highly convective areas, air masses tend to rise, and latent heat is released, maintaining the horizontal temperature gradients within the storm, which leads to the increase in supply of potential energy available for conversion to kinetic energy. Therefore, precipitating storms in moister environment tend to deepen rapidly and achieve greater intensities leading to the development of storms even in drier environments (WALLACE AND HOBBS, 2006).

Gust fronts are commonly mistaken by downbursts (LIN *et al.*, 2007). Even though both present a similar dynamic and are convective winds, gust fronts are much more spread event, and due to its scale presents lower wind speeds (FUJITA, 1990). Similarly to downburst, though, the can described as gravity currents model (CHARBA, 1974). Gusts fronts are normally taken as the announcement of a storm approaching, as they tend to form along the leading edges of large domes of rain-cooled air that result from the amalgamation (CARACENA *et al.*, 1989). Gust fronts winds are extensively discussed in Goff (1976). Additionally, Byers and Braham (1949) identified 4 stages of gust front evolution, named formative, mature, late mature, and dissipative. Extreme wind events with convective origin are normally observed in the formative stage (GOFF, 1976).

Derechos can result from the association of gust fronts, especially strong, acting over large distances and long convention lifespan (MARKOWSKI AND RICHARDSON, 2010). Extreme

winds produced by derechos are usually at the leading edge of downdrafts, where a series of strong thunderstorms coalesce to form an unbroken line of high and long-lived winds.

Mesoscale Convective Systems (MCS) transcends the single or multi-cell patterns and presents much larger spatial dimensions and longer lifespans. They also present the coexistence of convective and stratiform precipitation (HOUZE, 2004).

Mesoscale Convective Complex (MCC) is a unique kind of mesoscale convective system. They are long-lived, extended, often form nocturnally, and commonly contain heavy rainfall, wind, hail, lightning, and possibly tornadoes.

Squall Lines are a type of MCS that is frequently observed over midlatitudes and tropical regions and is known for causing more damages than isolated cells because of the sum of the background wind and downburst winds (PONTE AND RIERA, 2010). They usually appear in satellite or radar scans as thin long lines of cone-shaped clouds with overshooting tops. They are long-lived and slow moving. Lilly (1979) proposed significant advances in the understanding of thunderstorm properties and the development of an idealized isolated storm model, which was able to show the typical formation of organized squall lines.

Figure 9 shows a typical cross section of a squall line. Note the coexistence of stratiform and convective rain, which is a classic characteristic of these events.

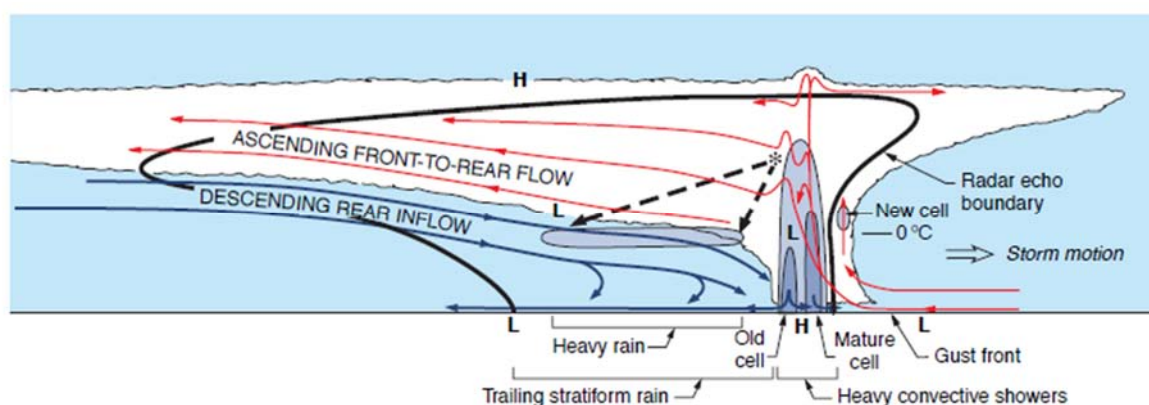
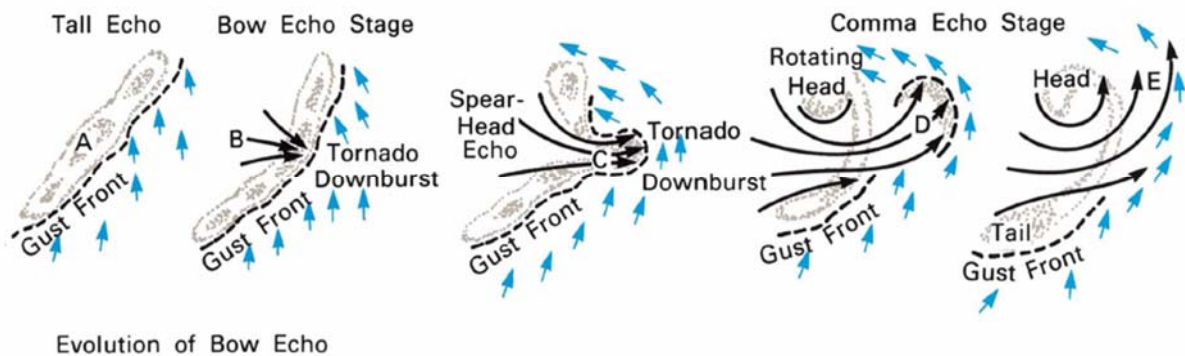


Figure 9. Cross section through an idealized squall line. Source: Houze (1993) adapted by Wallace and Hobbs (2006).

Bow Echo are cloud formations characterized by an echo wave pattern that can be observed from radar or satellite imagery and induce meso-scale downbursts. In Figure 10 is showed a model representation of the horizontal flow of a mesoscale circulation, which reshapes the

initial line echo called tall echo to a bow echo, and then comma echo stage. With the development of the system, tornadoes and downbursts are consistently observed at the front end of the system called spear-head echo. As the system acquires rotation, it dissipates itself and extreme winds are no longer expected.



Evolution of Bow Echo

Figure 10. Evolution of bow echoes proposed by Fujita. In this model, the horizontal flow of a weakening downburst induces a mesoscale circulation, which reshapes the initial line echo called tall echo to a bow echo and then Comma Echo Stage. Downburst and tornadoes are expected at the front end of these systems. Source: Fujita (1981) adapted by Wolfson (1988).

Mesoscale Convective Vortices are remarkably like squall lines, but it presents a significant rotational component that sustains convection to within the system, making it last longer.

Downslope Winds or katabatic winds are formed because of terrain effects and can also generate TS Winds, creating very localized storms windward. In Figure 11 is presented the Venn Diagram proposed by Markowski and Richardson (2010) with typical relative dimensions of the convective systems mentioned above.

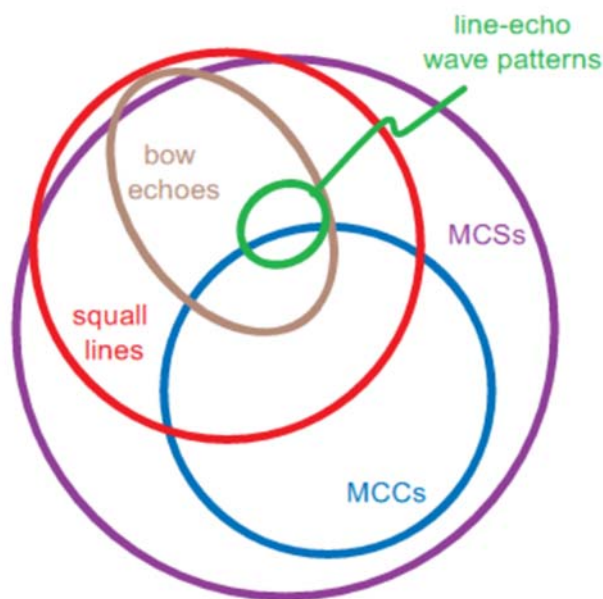


Figure 11. Venn diagram of typical dimensions and relations of mesoscale convective systems. Source: Markowski and Richardson (2010).

2.1.2. The Severe Weather in South America

South America's middle latitudes and subtropical latitudes at eastern of the Andes Mountains Range are one of the most favorable regions in the world for severe weather and extreme wind events (BROOKS *et al.*, 2003; NASCIMENTO, 2005A). Extensive research in the patterns of extreme weather in Brazil shows that the higher frequency of deep convection systems in subtropical latitudes of South America – covering most part of the Basin de La Plata and including the southern portion of Brazil – is mostly because of the establishment of low-level jet circulation east of the Andes (NASCIMENTO, 2005). The Low-Level Jets (LLJ) is a conceptualized as an "aerial river" that flows south along the Andes Mountains Ranges, and it contributes to the atmospheric destabilization of the weather in the Basin de La Plata Region through the transport of moisture and energy from the Amazon Region, especially during the austral spring and fall.

The occasional coupling between LLJ and the Subtropical Jet (SJ), which is found at higher-levels of the atmosphere jets, forms deeper and common low-pressure system in the Basin de La Plata Basin region and this dynamic coupling mechanism frequently results in severe storm events (NASCIMENTO, 2005A; SALIO *et al.*, 2007). A similar configuration is observed in North America, which the LLJ coupling with the higher-level Polar Jet (PJ) is known for producing

severe weather over the Central United States. In these events, downbursts and tornadoes outbreaks are commonly observed and are known for killing dozens and leaving extensive structural damages. Both weather dynamic structures mentioned above are show with their typical location in Figure 12 for a) South America and in b) North America.

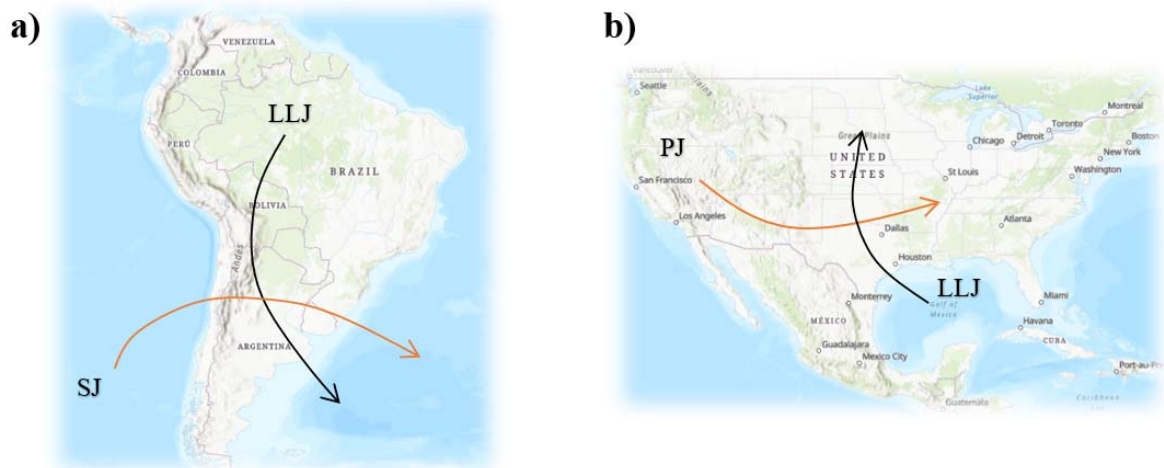


Figure 12. Typical atmospheric dynamic interaction of LLJ and the SJ in a) South America and LLJ and PJ in b) North America: Source: Nascimento (2005).

Besides the influence of the LLJ and SJ, other systems promote the precipitation regime in South America and affect severe weather patterns over the whole continent. In Figure 13, these elements are shown for the a) Low Levels Troposphere and b) High Level Troposphere. The areas that tend to present higher incidence of extreme wind events are the areas within the schematic representation of Mesoscale Convective Complexes (MCC), Instability Lines (IL) or squall lines, and Comma Clouds (CC). These low tropospheric systems can be intensified when coupled with higher tropospheric systems, such as the mentioned JS and the Cyclonic Vortices of High Tropical Levels (CVHL).

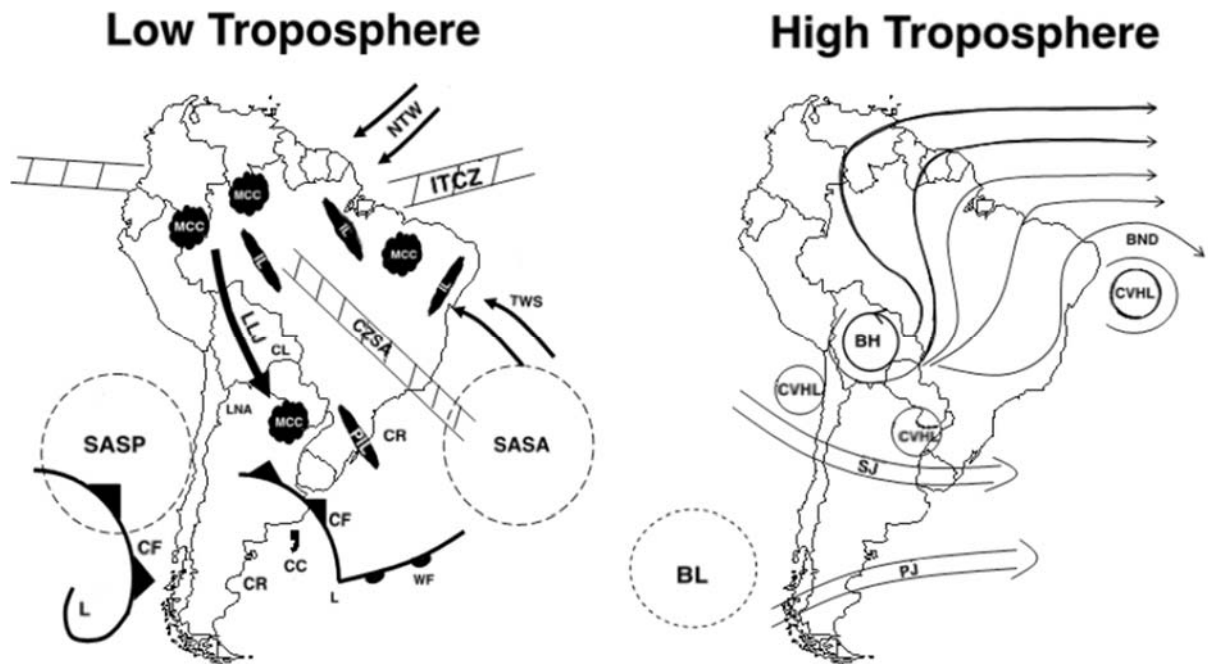


Figure 13. Atmospheric systems at low and high troposphere that influence the Climate of South America. At the low tropospheric levels: Mesoscale Convective Complex (**MCC**), Northeast Trade Winds (**NTW**), Subtropical Anticyclone of the South Atlantic (**SASA**), Intertropical Convergence Zone (**ITCZ**), Instability Lines (**IL**), Cold Front (**CF**), Warm Front (**WF**), Subtropical Anticyclone of the South Pacific (**SASP**), Low Level Jet (**LLJ**) at east of the Andes, Chaco Low (**CL**), Trade Winds from the Southeast (**TWS**), Low Pressure System (**L**), Region of Thermal Low in Northwestern Argentina (**LNA**), Prefrontal Squall Line (**PSL**), Comma Cloud (**CC**), Cyclogenetic Regions (**CR**), Convergence Zone South Atlantic (**CZSA**). At the high levels tropospheric, Cyclonic Vortices of High Tropical Levels (**CVHL**), Bolivia High (**BH**), Atmospheric Blockage Area (**AB**), Brazilian Northeastern Dug (**BND**), Subtropical Jet (**SJ**), Polar Jet (**PJ**). **AB** and **BND** are systems which get set up only during the winter. Source: Adapted from Reboita et al. (2010)

Atmospheric electricity can be a key element to show severe weather patterns. During the austral spring and summer is much more active than in other seasons, reaching a maximum in January and a minimum in July (ANSELMO, 2015). The Basin de La Plata is bounded west by the southern and central parts of Brazil, and it presents the second highest atmospheric electric activity in the world, producing 195% to 323% more thunderstorms than the rest of the Brazil (ANSELMO, 2015). For instance, in the years of 2018 and 2019 two record-breaking lightning flashes were observed in that region, as per the World Meteorological Organization–WMO. The one in for the greatest duration was in Northern Argentina and another for the greatest extension was in Southern Brazil (NULLIS, 2020). In Figure 14 is shown the extension of these events in red.

The impact of these events to several communities in South America promoted several field projects such as the Relampago Project (Remote Sensing of Electrification, Lighting, and

Mesoscale/microscale Process with adaptive Ground Observations) and Brazil's Lighting Network Data (BrasilDAT) (NACCARATO AND MACHADO, 2019), creating an international effort to understand and forecast severe weather in these Countries.



Figure 14. The longest lighting ever registered in the world in terms of extension and duration per WMO. Source: Nullis (2020).

Besides being highly convective active, the southern portion of Brazil, Northern Argentina, and Uruguay were found to be the most favorable environment for the development of favorable tornadic super-cells in the globe, comparable to the environment seen in the highlands of the United States (BROOKS *et al.*, 2003). In Figure 15 is shown the annual mean tornadic environment period from 1970 to 1999. In this analysis several factors, such as presence of strong convective factors, shear, deep tropospheric layer, and Convective Available Potential Energy - CAPE values, high relative humidity; therefor the closer to color red the more favorable days are observed to the occurrence of tornadoes. It is worth mentioning that this conclusion can be extended to the favorable days of occurrence of downbursts as well, since the triggering factors are very similar.

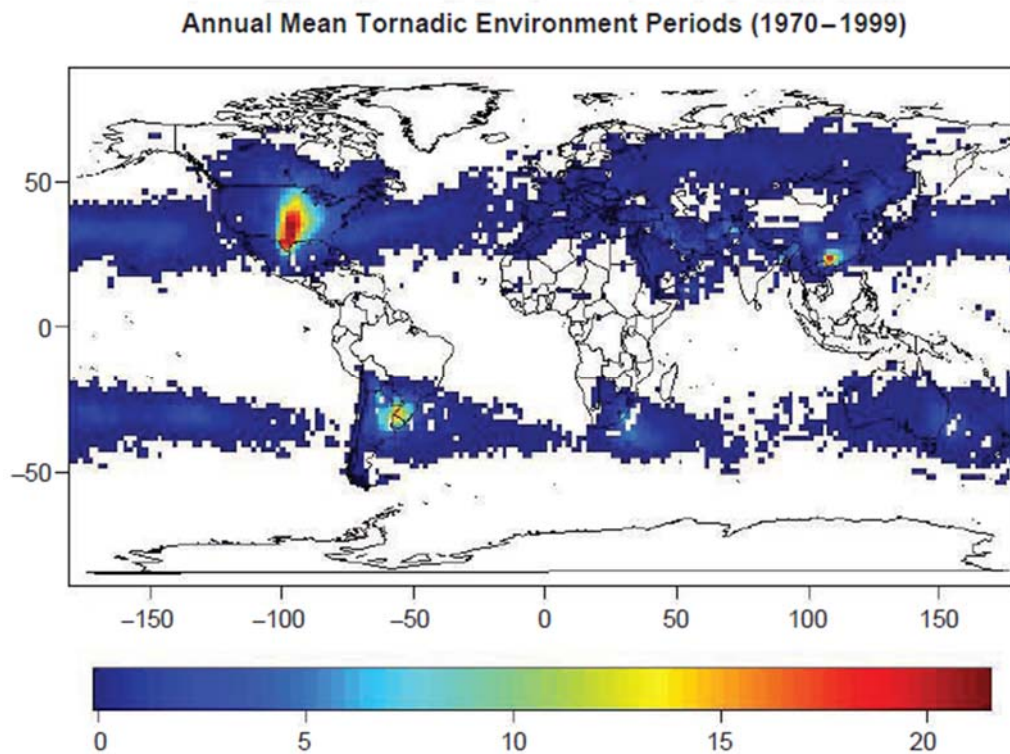


Figure 15. Average of days per year that has environments favorable for the tornadoic supercells were convection to for. Including strong shear, deep tropospheric layer, and CAPE. Source: Brooks et al. (2003).

In Brazil, extreme weather is more often defined as convectively induced weather, although it is Brazil can also be vulnerable to mild cyclones events and more recently, as such the Hurricane Catarina, considered to be a Category 2 event having hit the Southern State of Santa Catarina in 28/04/2004, killing 11 people, and caused approximately 500 million dollars in damages. Figure 16 shows the municipalities mostly affected by the hurricane at the landfall in the southern portion of Santa Catarina State.

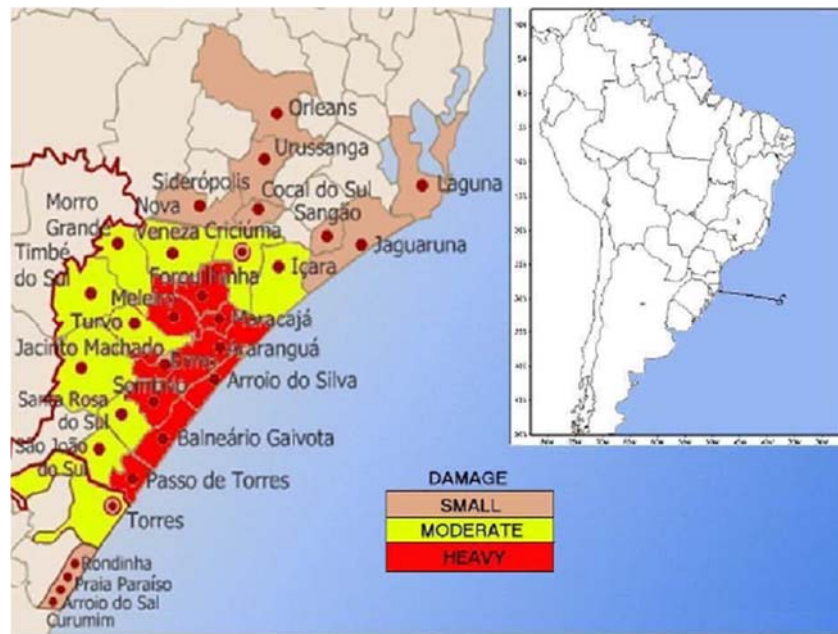


Figure 16. Map indicating Small, Moderate, and Heavy damages caused by Hurricane Catarina at landfall. Source: Pereira Filho et al. (2010).

Intense extratropical cyclones in Brazil can also cause severe weather being the result of frequent advance of intense, dry, and cold fronts coming from the south (weekly to biweekly) that clashes with hot tropical wet systems formed in lower latitudes. Together, these cold and hot fronts define a portion of the extreme weather events that generate intense winds in the southern portion of Brazil. Additionally, mesoscale and more localized well organized storm systems are responsible for the other portion of extreme weather events commonly observed in the country, they normally present higher intensity in the southern and lower intensity northern part of the country, although for the latter these convective storms are found to be more frequent, especially when coupled with the ITCZ then causing major extreme weather events in the northern states.

It is important to highlight that the intensity and frequency of severe weather in Brazil can also be defined by larger scale anomalies, such as El Niño/La Niña, Madden Julian Oscillation (MJO), heat islands effects, and others (VIANA et al., 2009). These events might contribute to intensify or weaken weather systems that cause severe weather in the country; therefore, their study, classification, and prediction is an extremely important factor to consider when studying extreme weather in Brazil.

2.2. WIND CLASSIFICATIONS

Similarly to the process of classifying various weather systems as per their characteristics, the advent of wind engineering brought to the light the need to classify wind according to their properties as well. Gomes and Vickery (1978) proposed to categorize winds according to their significant meteorological phenomena that generated them. The authors also proposed to identify wind gust types based on probabilistic distributions of extreme values, aiming to provide more accuracy to the calculations of loads because of extreme winds in structures and therefore increase resilience to severe wind events.

Gomes and Vickery defined four main wind categories: extensive, extratropical pressure systems (EPS) winds, tropical cyclones winds, tornadoes, and thunderstorms (TS winds) in which downbursts are part of. In the following a description of each of these wind types is presented.

Extensive Pressure Systems (EPS) winds are generated by larger scale (or synoptic) weather events, such as extra-tropical cyclones or frontal depressions. These systems are formed in temperate climates where they generate strong wind gusts as they move forward to the equatorial areas where they become weaker until dissipating. They are thermally neutral and normally defined by the weather for a larger area and longer time—typically 3 to 4 days and 1000 km or greater (LETCHEFORD AND LOMBARDO, 2015). EPS Winds are also commonly referred to as atmospheric boundary layer winds (ABL Winds).

Tropical Cyclone Winds receive different denominations depending on the location they occur. They are called hurricanes in the North Atlantic, central North Pacific, and eastern North Pacific; typhoons are the terminology used in the Northwest Pacific; and in the South Pacific and Indian Ocean, the generic term "tropical cyclone" is used regardless of the wind speed associated with the weather system. These winds are considered being the most disruptive type of extreme weather event, not necessarily for presenting the highest instant speeds, but for their persistent and spread out characteristics (GOMES AND VICKERY, 1978).

Thunderstorms (TS) Winds result from intense downdrafts carrying cold air from higher levels of the atmosphere. As the warmer and wet air lifts, it condenses, forming dense clouds. This process is called precipitation-cooling (evaporation, melting, and sublimation). The movement

is typically sustained until the uplifting strength cannot hold the precipitated water and iced droplets load, resulting in an intense downdraft outflow, which can be non-divergent straight-line winds or highly divergent straight or curved winds (FUJITA, 1981).. Thunderstorm winds may be classified as **Non-tornadic TS Winds** (straight-line) or **Tornadic Winds**.

Tornadic Winds are short-lived meteorological phenomenon caused by an expressive low-pressure core caused by sustained uplift of warmth and wet air and imposes major threat to human lives and structures. When these phenomena occur in the water, they are called waterspouts and when occurring in the desert – usually of mild nature – they are referred as whirlwinds or dust devils. Tornados winds may commonly be referred also as TS Winds.

After Gomes and Vickery (1978) have proposed this new method to classify wind, several other research with the similar scope acquired traction other alternative nomenclatures were developed to winds according to their originating phenomena, including: TS winds or non-TS winds (CHOI AND HIDAYAT 2002B; LOMBARDO *et al.* 2009); frontal depressions vs TS winds (KASPERSKI 2002; GAETANO *et al.* 2014), gust front winds (KASPERSKI 2002; GAETANO *et al.* 2014; DURAÑONA 2015), winds determined by local conditions or topography (RIERA *et al.*, 1977), convectively induced wind gusts (FERREIRA AND NASCIMENTO, 2016), rear-flank (RFD) or forward-flank downdrafts (FFD) (GAST, 2003), Ramp-up events (LOMBARDO *et al.* 2014). Independently of the classification used by each author in this research field TS winds are essentially defined as a transient, non-Gaussian and stochastic phenomenon, that evolves rapidly, having a downward transfer of moment showing major differences when compared to the typical ABL log-profile (LOMBARDO *et al.*, 2014). TS winds may present rotation or not (tornadic or non-tornadic), and they are characterized by short durations and wind speed and turbulence characteristics that differ from EPS winds.

The typical behavior of a TS horizontal wind record is idealized in Figure 17 along with typical conventional nomenclature used to characterize and defines these records. At the beginning of the event, the backflow of the storm is abruptly interrupted by a noticeable decrease in the wind speed reaching to a point of stagnation, then a sudden peak gust increases the instant wind velocity till it reaches a maximum, this event is called the front-side peak gust. After that, a sudden decline in the wind speed is observed, reaching to a minimum, which is then called

"the eye" of the microburst. Sometimes, it is observed that a second peak in the wind speed, called "back-side peak gust", being usually less intense than the first peak.

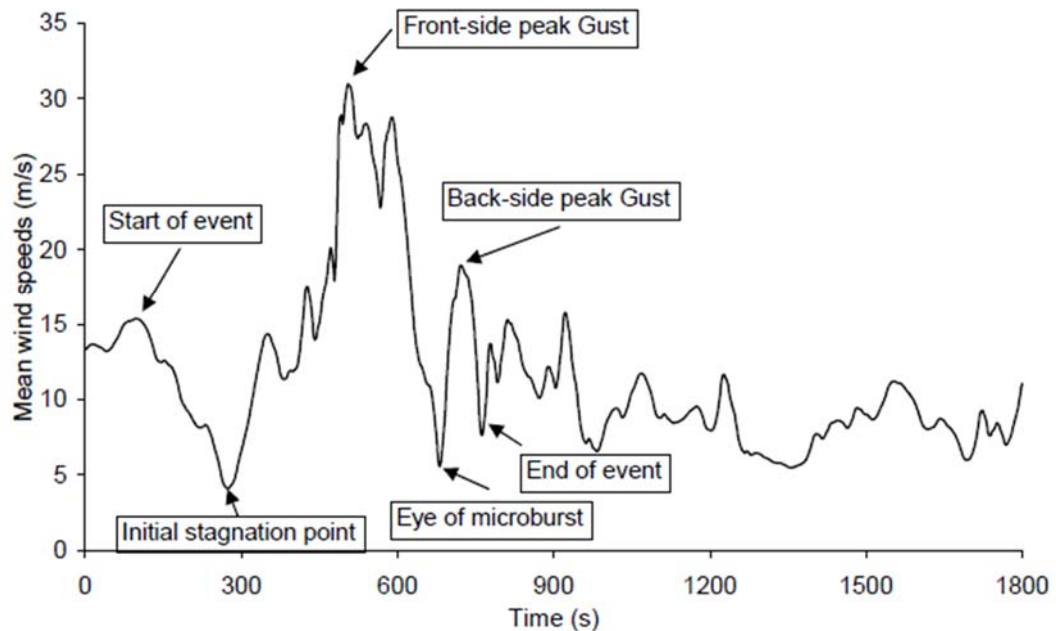


Figure 17. Characteristic time instants mean downburst speed time histories. Source: Chen (2005) apud Gast (2003).

These so-called ramp-up events also substantially differ in both kinematic and thermodynamic properties from EPS winds. Therefore, typical engineering properties used on the design of structures, such as the power law, the turbulence intensity, and gust factor, cannot be expected to be applied in the same way as they are for EPS winds to describe TS winds (LOMBARDO *et al.*, 2014; MASON, 2017). To illustrate these differences, in Figure 18 are shown typical horizontal wind time series of an a) EPS wind register and b) a downburst event (CHOWDHURY, 2018). It is evident the spike observed in Figure 18 b) imposes unexpected static and dynamic loads to structures designed to under ABL wind provisions.

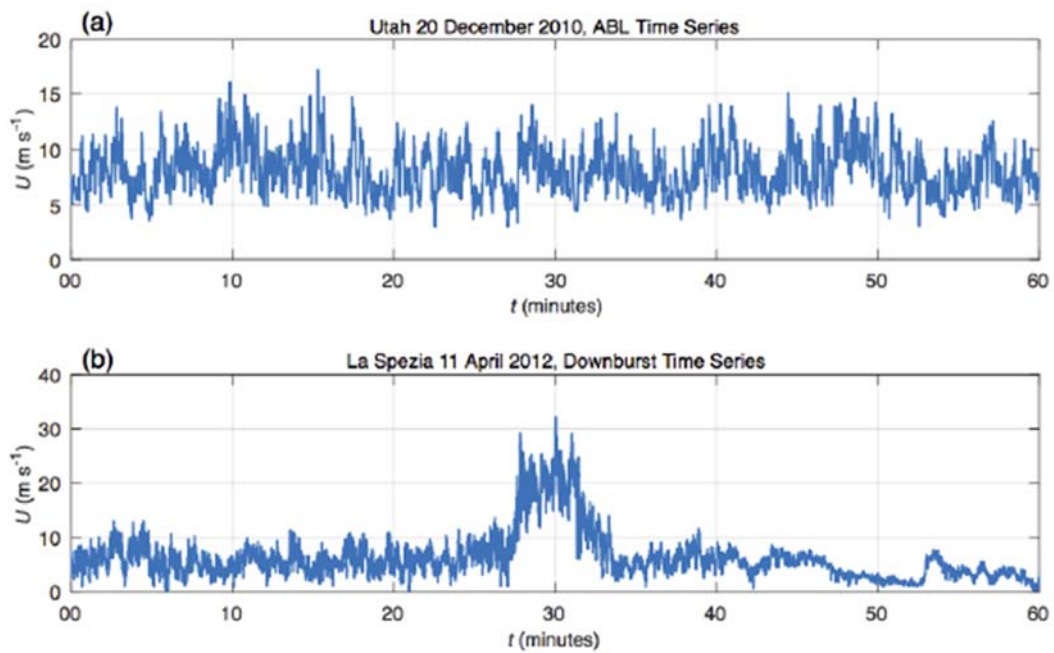


Figure 18. Depicted a) a time series of an EPS wind event and b) another wind speed time series where it indicates the characteristic spike in wind speed caused by a downburst event. Source: Chowdhury (2018).

2.3. THE DOWNBURST DISCOVERY

Fujita defined downbursts as "A natural event that occurs because of thunderstorms produced by a cumulonimbus cloud causing a strong downdraft which induces an outburst of damaging winds on or near the ground" (FUJITA AND BYERS, 1977). Fujita's efforts to investigate these events led to the discovery of the downburst phenomena to receive increased attention in both wind engineering and meteorology fields. Since non-tornadic TS winds have the unique characteristic of varying significantly from one event to another, downbursts became an idealized way to understand TS winds as a common denominator of other non-tornadic TS winds. In this session it is discussed the development of the research in downbursts.

2.3.1. Downburst Field Studies

2.3.1.1. Thunderstorm Project

The Thunderstorm Project was not specifically developed to investigate downbursts, but the discoveries sourced from this project were extensively useful to gather further insights about the phenomena downbursts. The Thunderstorm Project was a major effort developed during

1946 to 1947 which aimed to better understand the characteristics and structures of thunderstorms (BYERS AND BRAHAM, 1949). This research focused on exploring the knowledge development and morphology of several types of storm cells. It also helped to characterize meteorological parameters, such as temperature, wind, and rain generated by these events.

In the Thunderstorm Project several approaches to investigate thunderstorms were deployed. In altitude, it included airplanes equipped with radars, airspeed, altimeters, airborne electric fields meters, and temperature instruments, balloon-borne vertical airspeed indicators, radio soundings. In surface, complete meteorological stations set with a 1-2 mile spacing, plus radar measurements. In this research, it was highlighted the importance of proper network resolution to analyze various sized wind systems.

Their finds identified nine main elements that define the processes within thunderstorms, they are: 1) Vertical motions (updraft and downdraft); 2) Horizontal motions (inflow, outflow, vorticity); 3) Horizontal and vertical temperature gradients; 4) Electrical fields (indicative of thunderstorm intensity); 5) Rainfall distribution and intensity 6) Temperature changes at the ground; 7) Pressure changes at the ground; 8) Surface wind fluctuations (related to 2); 9) General turbulence or gustiness.

These finds inspired in the Fujita in the 50s first to define the wording "meso-scale" systems as noises in synoptic maps that could cause local extreme meteorological conditions (FUJITA *et al.*, 1956) and characterize the typical scales of thunderstorm winds exist. It was also proposed that a proper weather network resolution should be deployed to perform an analysis of meteorological phenomena that happens on this specific scale. Fujita proposed that a surface network of 1 to 10 km resolution would only be able to capture the dynamic of these events along with extensive aerial photogrammetry survey.

2.3.1.2. National Severe Storm Project (NSSP)

From the 1940's to the 2010's at least 575 people have died because of aircraft accidents caused by extreme winds induced by downbursts (WOLFSON, 1988). A summary of aircraft accidents with the most fatalities because of downbursts in the world is shown in Table 1 along

with the numbers of fatalities associates with to the occurrence of these events normally at lower levels of the atmospheric, which these planes were taking off or landing.

Table 1. Major Aircraft accidents caused by downburst induced winds. Source: Potts (2007), Wikipedia (2018) and NOAA (2020A).

Fight	Date	Fatalities	Place
American Airlines Flight 63 (Flagship Ohio)	07/28/1943	20	United States
1956 Kano Airport BOAC Argonaut	24/07/1956	32	Nigeria
Ozark Air Lines Flight 809	23/07/1973	38	United States
Pan Am Flight 806	30/01/1974	96	American Samoa
Fokker F-27	31/05/1974	0	Australia
Eastern Air Lines Flight 66	24/06/1975	113	United States (JFK)
Aeroflot Flight 4225	08/07/1980	166	Kazakhstan
Pan Am Flight 759	09/07/1982	145	United States
Delta Air Lines Flight 191	08/02/1985	137	United States
Mandala Airlines Flight 660	24/07/1992	70	Indonesia
Martinair Flight 495	21/12/1992	56	Portugal
USAir Flight 1016	07/02/1994	68	United States
2011 United Nations Bombardier CRJ-100	04/04/2011	32	Rep. of Congo
Bhoja Air Flight 213	20/04/2012	127	Pakistan
Aeroméxico Connect Flight 2431	31/07/2018	0	Mexico

After several aircraft accidents have already occurred, the government of the United States invested heavily in an extensive research project called the National Severe Storm Project (NSSP) in 1961 (LEE, 1962). With greater availability of resources, this effort aimed to investigate severe thunderstorms and awoke the interest in using Doppler Radars for the purpose of meteorological research (BROWN AND LEWIS, 2005).

During an aerial survey after a tornadoes *superoutbreak* in 1974, Fujita noticed during the inspection of the pictures a swirling outburst divergent pattern of uprooted trees pattern, much different from what it would be expected from tornadoes (FUJITA, 1985b). In Figure 19, some of his finds are presented showing patterns from the tornadoes. In a) a traveling tornado forming sort of spiral damage; in b) a stationary tornado that had caused a spiral and punctual damage to the corn field; and in c) a traveling tornado crossing a long extension of land.

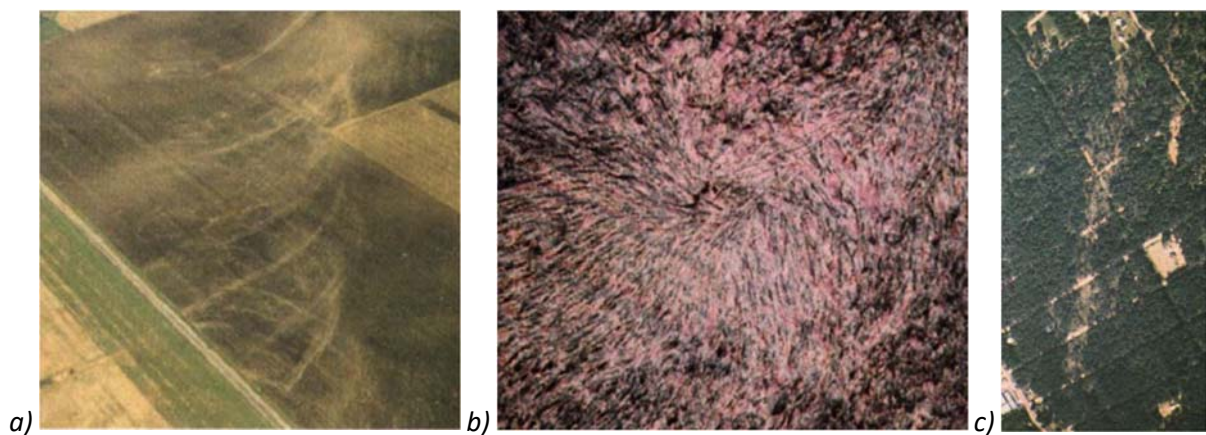


Figure 19. Damage patterns caused by tornados: In is shown a) a traveling tornado forming a sort of spiral damage; in b) a stationary tornado that had caused a spiral and punctual damage to the corn field; and c) a traveling tornado crossing a long extension of land. Source: Fujita (1985b).

In Figure 20, the aerial survey shows the damage caused by downburst winds. In a) is shown a starburst pattern of strongly divergent uprooted trees in the field because of the divergent forces of downburst induced winds from the upper left corner of the picture to the lower right corner. The same is valid for the damage pattern in b) note the clear difference in pattern when comparing downburst and tornadoes damages.

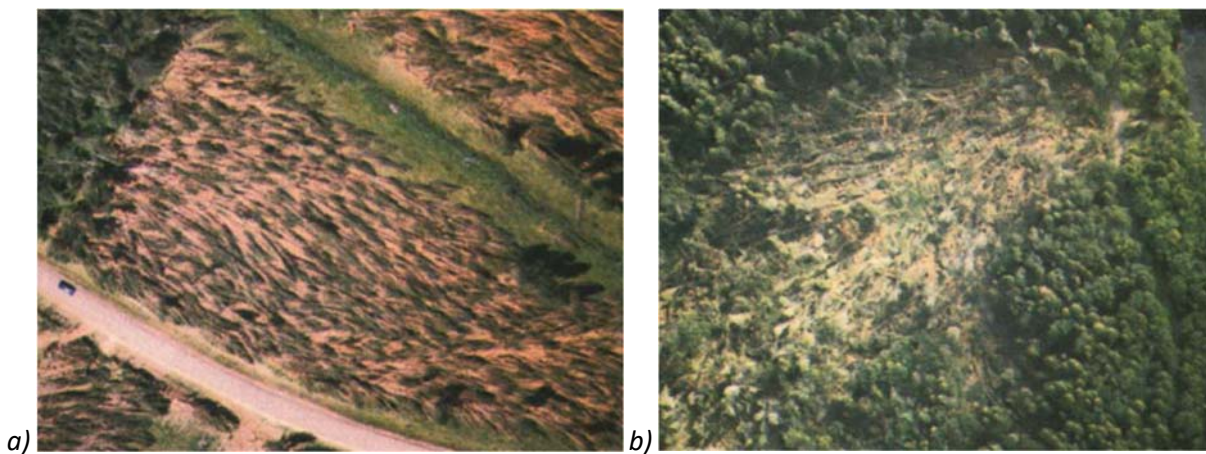


Figure 20. Aerial images of the damage caused by downburst winds. A starburst pattern of uprooted trees (left) on the field and building damage by downburst winds from the lower left corner of the picture to the upper right corner. Source: Fujita (1985b).

When investigating the aircraft accident in 1975 at the John F. Kennedy International (JFK) Airport in New York City Fujita coined the term Downburst as a unique and discrete phenomenon, that presents intense downdraft from regular downdrafts, but there were still not enough scientific arguments to prove his theory. Fujita's diligence in investigating and publishing his finds in a timely manner helped the whole aviation community save many lives. Initially the term was taken as controversial by the scientific community. Although, Fujita's

persistence in proving the existence of downbursts led to the development of three fact-finding field programs in 1978, 1982, and 1986 to track downbursts using the United States National Center for Atmospheric Research (NCAR) Doppler Radars (FUJITA, 1990). All the field programs mobile and stationary Doppler Radars were deployed to scan the downburst events and generate estimations of the characteristics of the wind generated by such events.

2.3.1.3. Florida Area Cumulus Experiment (FACE) (1975)

The **Florida Area Cumulus Experiment (FACE)** was an effort to investigate downburst recurrence in hot and humid environments as found in Florida State in 1975. Several finds on this mission for wet environment downbursts confirmed previous results obtained in Fujita's campaigns, including the theory that a downburst is likely to occur when precipitation is unloaded under a when in an elevated dry layer with the presence of moist adiabatic lower troposphere, propitious synoptic conditions, and increased in the lower troposphere (CARACENA AND MAIER, 1987).

The Convection initiation and Downburst Experiment (CINDE) (WAKIMOTO, 1994); the FAA-Lincoln Laboratory Operational Weather Studies (FLOWS) Project in 1984 (WOLFSON, 1988); and the Cooperative Huntsville Meteorological Experiment (COHMEX) (WOLFSON AND IACONO, 1987) are other remarkable field experiments intended to develop research on thunderstorms outflows in the United States.

These finds came agreed with the investigation done by Sinclair *et al.* (1973) in terms of the variation of low-level winds during a thunderstorms in Tampa, US. In this observation, the authors tracked 81 thunderstorms and found that the main predictors parameters for downburst occurrence are dry instability index, maximum cloud height at the time of the peak gust, and average wind speed prior to the maximum wind gust.

2.3.1.4. Northern Illinois Meteorological Research in Downbursts (NIMROD) (1978)

This field study aimed to investigate downbursts specifically was called **Northern Illinois Meteorological Research in Downbursts (NIMROD)**. This study was executed during the spring of 1978 and conducted by Fujita and Srivastava. The primary aim was to validate the existence of downbursts and to collect meteorological data over the US (FUJITA, 1985a). In this experiment, they captured the radar signature of 42 downburst and depicted their

structure. They also created the terms “*microburst*” and “*macroburst*”, distinguishing downburst based on their horizontal extension.

In Figure 21 is presented a Doppler Radar scan of a downburst event captured during the NIMROD Project, where the orange area represents wind speed ranging 21 to 27 m/s at 70 m above the ground (FUJITA, 1990). In Figure 22 is presented a typical cross section of the downburst previously mentioned. In a) is shown the maximum vertical wind speed and in b) is shown the maximum horizontal wind speeds. The dashed areas represent regions expected to present higher reflectivity (≈ 65 dB) and consequently higher wind speeds. Fujita (1981) defined this area as the "pressure nose" of the downburst.

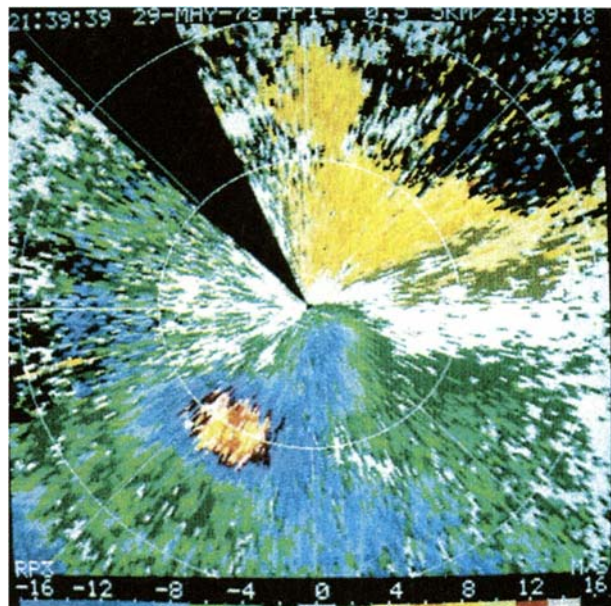


Figure 21. This picture displays CP-3 Radar Doppler Analysis of the exact moment a downburst had occurred. The orange area represents wind speed ranging 21 to 27 m/s at 70 m above the ground.
Source: Fujita (1990).

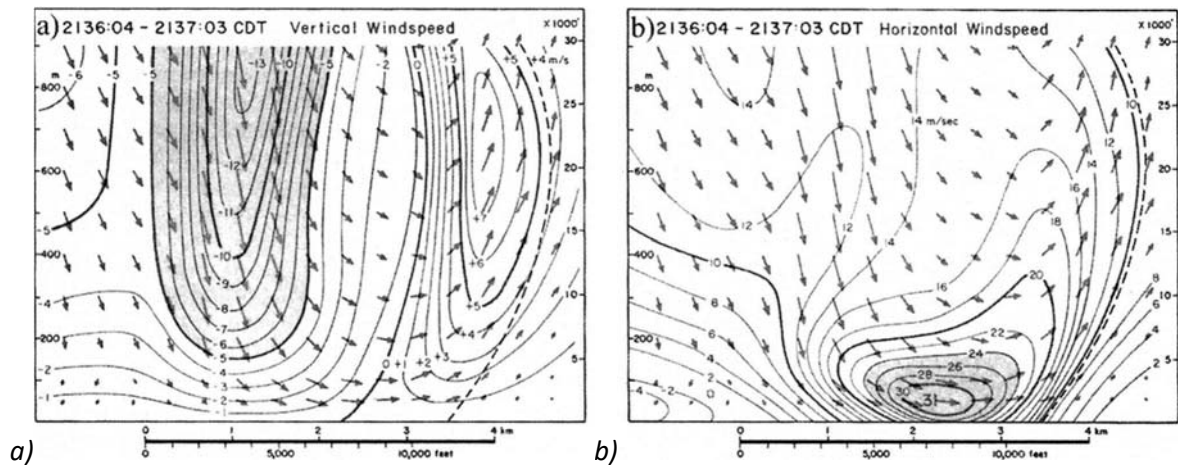


Figure 22. Cross-section of microburst winds depicted by CP-3 Doppler Radar During NIMROD Project in 1978. In a) is shown the maximum vertical wind speed and b) is shown the maximum horizontal wind speeds. Source: Fujita (1990).

In Figure 23, is shown the first Doppler Radar triangulation utilized by the authors of about 60 km. Even though many downburst events were captured, the authors found that the distancing between radars was excessive to capture the time and spacing scale variability of these downburst events, leading to the reduction in distancing for next experiments.

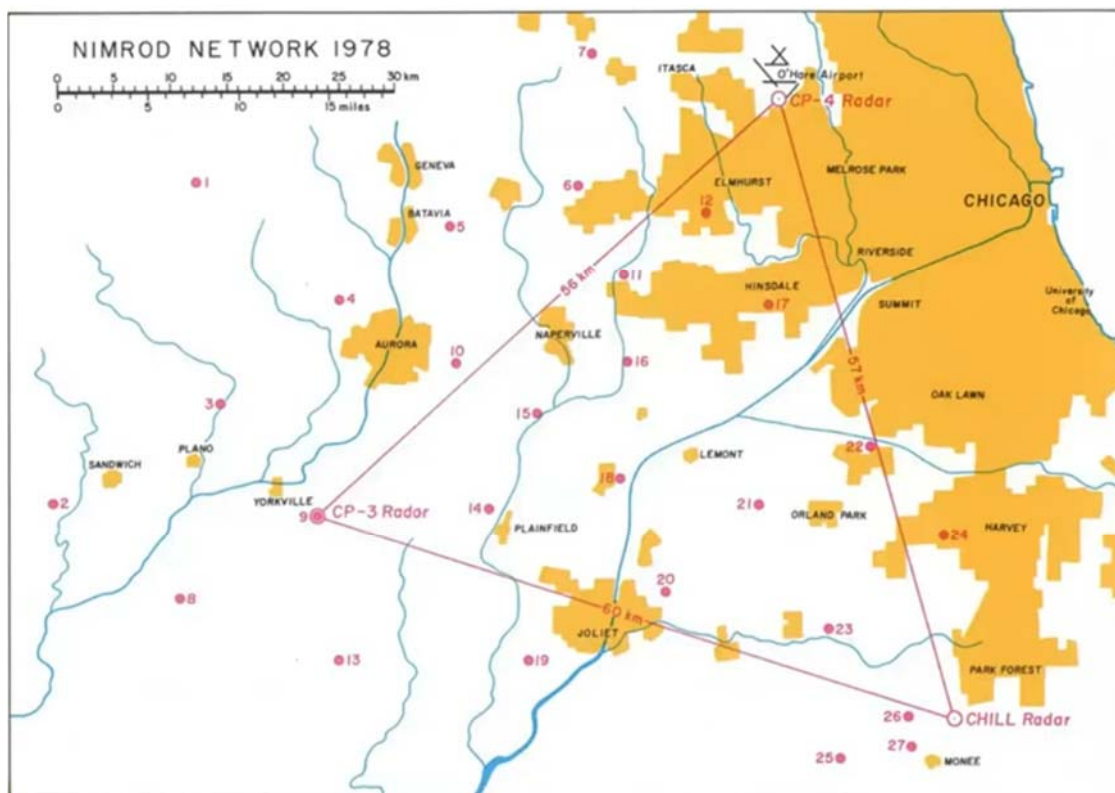


Figure 23. Doppler Radar triangulation used in NIMROD Project. Source: Fujita (1985).

2.3.1.5. Joint Airport Weather Studies (JAWS) (1982)

The next major field study to investigate downbursts was called **Joint Airport Weather Studies (JAWS)**. This experiment was conducted by Fujita, McCarthy and Wilson, in Colorado, during the hot season of 1982. The objective of this project was to fine-tune the understanding of the structure of thunderstorms dynamics and kinematics near a major airport, helping to comprehend the effects of the low-level wind shear on aircraft safety and proposing real-time testing of low level wind shear detection, warning techniques, and display of the phenomena (MCCARTHY AND WILSON, 1982).

Since the existing airport radars were not fully adequate to the needs of this meteorological study, other Dual-Doppler Radars were deployed to analyze the kinematic structure of downbursts in low-level of the atmosphere. This time, the researchers decreased the spacing between the radars to about 20 to 30 km, allowing them to capture the three-dimensional fields of 186 downbursts. These studies also led to the development of an important aviation guideline called "Low-altitude Wind Shear and its Hazard to Aviation", which it was a manual for pilots when landing or taking within 100 meters from the ground in areas prone to downbursts (NATIONAL RESEARCH COUNCIL, 1983).

During the JAWS project, it was proven that one or more downbursts can occur during the same storm. Another output of JAWS mission was the discovery of "wet" and "dry" downbursts, which depends mostly on the prese or not of rain during the occurrence of the downburst (FUJITA, 1985b). Dry downbursts represents a major threat for aviation in dry areas, they can be as frequent as wet downburst (83% of recurrence during JAW Project) and because of the absence of rain in the ground, they are not as easily to be visually identified. (PROCTOR, 1988).

The find of dry downbursts also agree with previous analytical models based on physical properties that showed how in a dry-adiabatic sub-cloud environments even a light rainfall can cause intense downdrafts, which can produce high winds, but no rain as the downdraft reaches the ground (SRIVASTAVA, 1985, 1987). Hjelmfelt (1988) developed extensive analysis of the data obtained from the JAWS experiment and presented great contribution to the modeling of downbursts.

Figure 24 shows the schematic map of the JAWS Project Study Area and the Radar triangulation CP-2 (S-Band), CP-3 and CP-4 (C-Bands) deployed (white triangles). The red circles represent the Portable Automated Mesonet (PAM) Network spaced in average 4 km and the red triangle represents the vertexes of the new triangulation used in this study. Note how the triangulation spacing is much smaller than the previous showed in Figure 23.

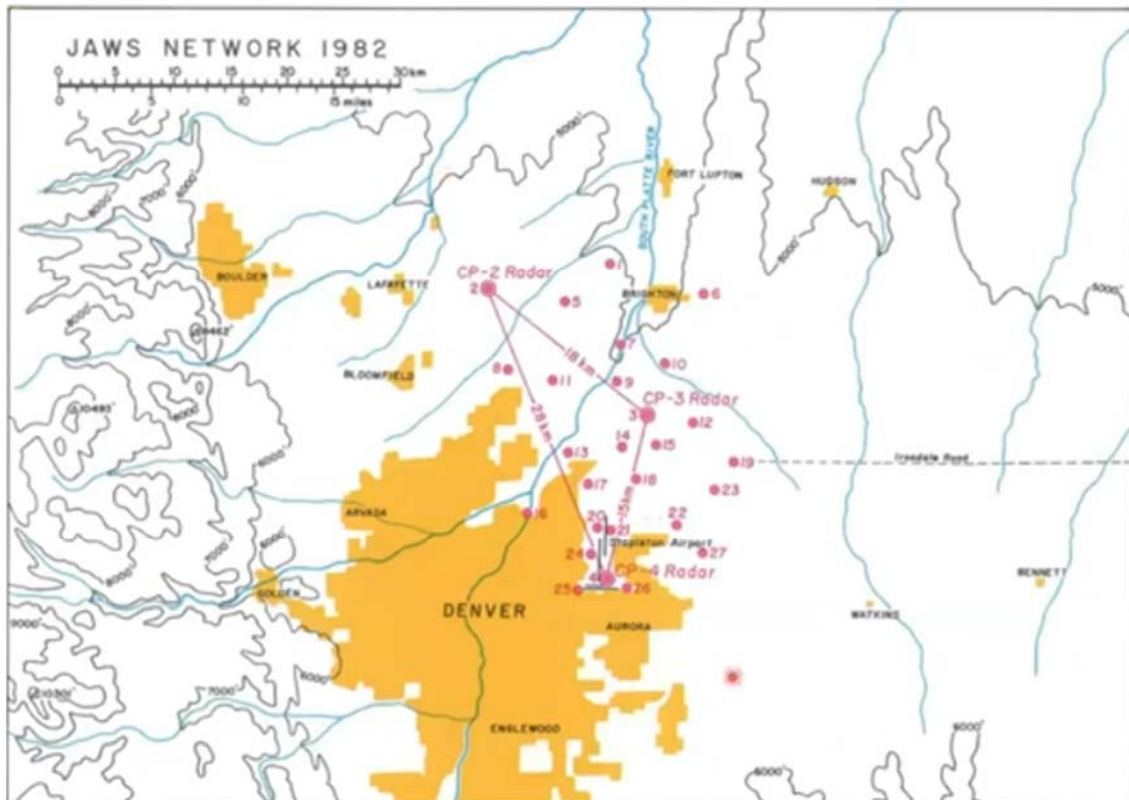


Figure 24. Map of the JAWS Project study area. The Doppler Radars used in this effort were positioned at vertexes of the triangle in the middle of the Figure with a smaller spacing when compared to the previous field project (NIMROD). Denver's Stapleton International Airport is at CP-4. Source: Fujita (1985).

NIMROD and JAWS experiments were extremely successful missions and extensive relevant datasets were obtained from these field studies. Climatological analysis revealed that downbursts events presented similar recurrence period for both areas, producing in average wind speeds ranging from 12 to 14 m/s in surface, they also unexpectedly found that downburst to be more recurrent than tornadoes for the studied areas (FUJITA, 1985b). In Figure 25 are presented NIMROD (left) and JAWS (right) microbursts velocities analysis, in a) is shown the microburst frequency plotted as a function of their peak wind speeds and in b) shown the regression expressions that best described the return-period given in years of downburst events for each of study efforts.

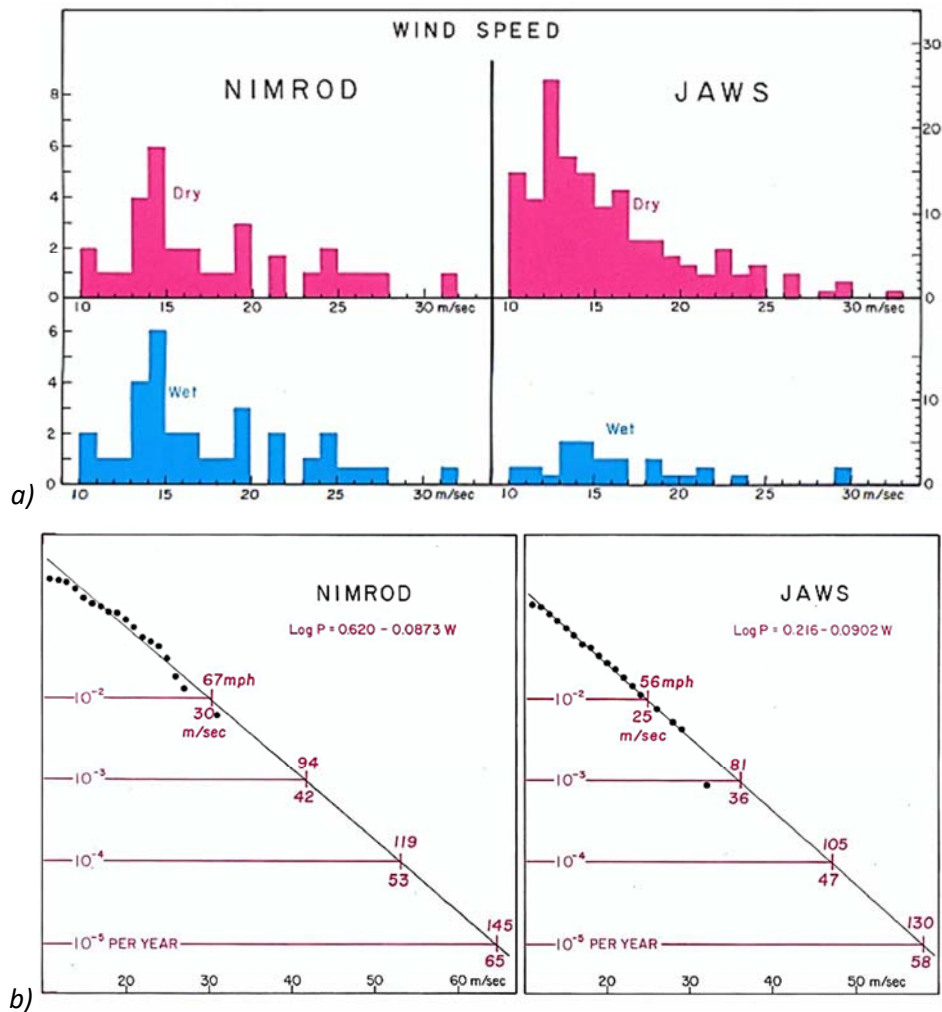


Figure 25. a) NIMROD (left) and JAWS (right) microbursts captured velocities and in b) is indicated expected return period for each of the projects along with the regression equation. Source: Fujita (1985a).

In Figure 26 is presented a histogram with the typical duration that took downburst flow to reach the peak velocity during JAWS and NIMROD projects, which normally happens beneath of the primary vortex. Note that for both projects, the peak velocities happen from 2 to 3 minutes.

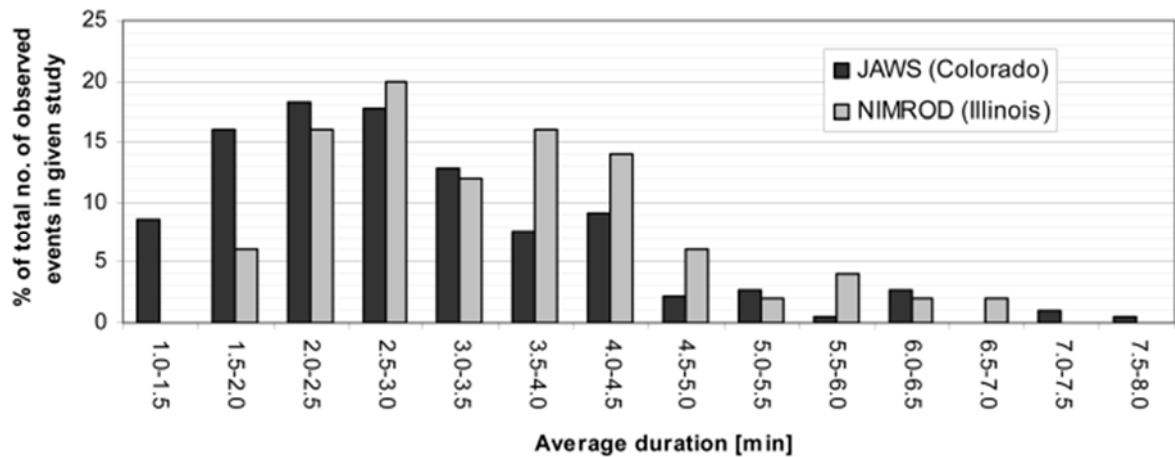


Figure 26. Histogram of full-scale peak wind longevity. Source: Lin et al. (2007). Data extracted from Fujita (1985b)

During the summer of 1984 NCAR conducted in Denver two other field projects called Classify, Locate, and Avoid Wind Shear (CLAW) Project (MCCARTHY *et al.*, 1986) and the Convection Initiation Project (HJELMFELT, 1988). The intent of these projects was to continue the track and understanding the morphology of a microburst, after conclusion of JAWS project.

Recent critics to the downburst data obtained mentions that radars scans at the time could not capture with high resolutions data 50 m above the ground, questioning the application of such datasets for the development of accurate models with major applicability for wind engineering application. For this purpose, more recently detailed field experiments have been conducted looking to obtain datasets on thunderstorm outflows with higher time/space resolution specially at lower levels, new approaches started to be adopted such as the use of LiDAR, anemometric towers, and mesoscale SWS networks.

2.3.1.6. Microburst and Severe Thunderstorm Project (MIST) (1986)

The last major field project lead by Fujita aimed to investigate downbursts was in 1986 and it was called **Microburst and Severe Thunderstorm Project (MIST)**. The main outcomes of this project was to confirm the importance of higher water content within the cloud as prominent precipitation core, which was found to be the main cause on the production of strong downdrafts in environments that are more statically stables (SRIVASTAVA, 1985; PROCTOR, 1989; KINGSMILL AND WAKIMOTO, 1991).

Through the radar analysis of lower levels of the atmosphere and with the deployment of advanced and denser surface weather stations (SWS) networks in the three projects

mentioned above, Fujita and his team was able to identify and idealize outflows models coming from parent clouds and finally prove to the scientific community the existence of downbursts and it threaten to the aviation industry and the build environment.

2.3.1.7. Wind and Ports and Wind, Ports”, and Sea Programs

Since the 80s, other field experiments were developed to investigate thunderstorm winds helping to develop the understanding of these phenomena but this time more focused on the effects of these winds to the built environment. More recently, the "**Wind and Ports**" and "**Wind, Ports and Sea**" in Italy – financed by the European Cross-border Programme – focused on monitoring and forecasting extreme wind events in the Northern Tyrrhenian and Ligurian Seas aiming to promote the safety and management of activities near ground of the commercial ports. This project has already turned in hundreds of high-quality datasets of thunderstorm winds near ground, bringing major advancements for thunderstorm properties research. In this effort, it was mobilized an in situ high frequency weather monitoring network, multi-scale numerical modeling, simulation of wind and wave fields, and climate analysis. To help with the data analysis a WebGIS platform that captures local and global meteorological information was developed, allowing data modeling to further identify, predict, and report adverse wind conditions that may impact the port activities (REPETTO *et al.*, 2018). This effort is a great example of cross-discipline efforts to tracking, forecasting, and defining climatology in TS winds (BURLANDO *et al.*, 2017).

2.3.2. Downburst Classifications

Thunderstorms winds may vary significantly from one event to another, and downbursts are one of the most common ways to refer to these types of TS winds; they are also the most well studied nature phenomena that can generate non-tornadic convectively induced wind and a wide range of approaches to classifying them has been proposed in the literature, which are further discussed in this section.

2.3.2.1. Environmental Conditions

Downbursts can be classified according to the height and the environmental humidity in which they occur. Amongst several tools ways developed to identify downbursts, vertical atmospheric soundings capable to capture information of moisture and temperature profiles

are efficient mechanisms developed to identify environments propitious for the development of such winds (WILSON *et al.*, 1984). In Figure 27 are presented typical atmospheric vertical soundings of in environments in which downburst had been observed, where in a) is presented a high-based, shallow-depth clouds above a very dry layer of air that are associated with dry microbursts and in b) is shown a heavily precipitating thunderstorms with mid-level dry and cold air entrainment into a towering cumulus, which leads to speed up the air downwards, configuring to be the main mechanism of downdraft enhancement in warm-based air mass thunderstorm leading to produce wet downbursts.

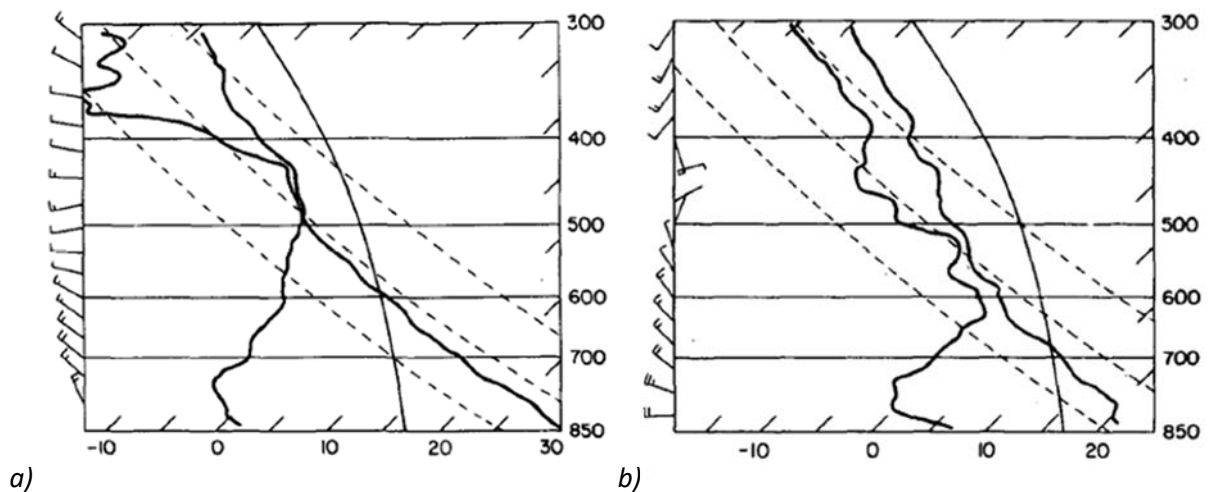


Figure 27. Typical soundings for a) high based, shallow-depth clouds that are associated with dry microbursts and b) heavily precipitating thunderstorms that produce wet downbursts. Source: Wolfson (1988).

Figure 28 shows a typical a) dry microburst coming from a virga cloud at high levels and a b) typical wet microburst produced by a convective system generating intense rain at lower tropospheric levels and presenting the typical spreading out configuration, clearly visible from the ground. Note the clear distinction between both phenomena even though the phenomena are driven by very similar features.

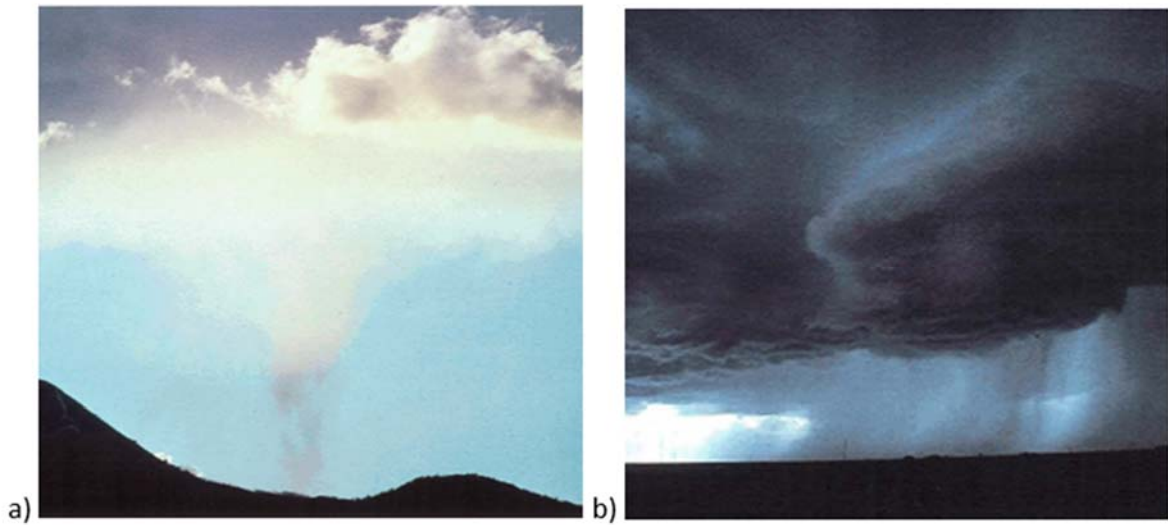


Figure 28. A typical a) dry microburst coming from a virga cloud and a b) typical wet microburst being produced by a convective system. Source: Wolfson (1988).

Dry microbursts are characterized by a deep and vertical boundary layer, with a nearly dry adiabatic rate of temperature. In mid-levels (500 mb) it is observed a moist layer that can eventually precipitate over this very dry layer, triggering the evaporative cooling of that parcel of air, resulting in negative buoyancy and rapid downdraft towards the ground (FUJITA, 1985a).

Even though Fujita has coined the Dry microbursts term, such phenomenon had been before hypothesized as "dry thunderstorm" (BRAHAM, 1952). These high intense winds are accompanied by little or no rain and are usually associated with virga clouds, which derives from altocumuli or shallow high-based cumulonimbus. Snowflakes are a type of precipitation that seems to first trigger the generation of downburst specifically since they promptly evaporate once entering a dry atmospheric layer (WAKIMOTO, 1985). These downbursts usually present smaller magnitude, being commonly called only as "dry microburst" and are normally not a major threat to the wind engineering since they then to happen at higher tropospheric altitudes.

Wet microbursts, in contrast, result from several forcing mechanisms presenting themselves in a wide variety of sizes and shapes. The vertical atmospheric sounding for a typical wet microburst is closer to the moist-adiabatic lapse rate. The relative humidity of the environment below the cloud base presents substantial water vapor, which serves as fuel for the evaporative cooling process within the cloud and for that reason, a wet downburst can

produce much higher wind speeds than dry microbursts (Srivastava, 1985). Wet downbursts are commonly associated with precipitation (not necessarily heavy) in areas with higher relative humidity values. The strength of the low-altitude downdrafts associated with precipitations is highly depended of the size and intensity of precipitation, environmental dryness and stability in mid-levels (KNUPP, 1985).

When a dry, cold air layer entrains in storms at midlevel, they become superposed with air from the cloud. This liquid water finds in unstable conditions, originating "penetrative downdrafts", which subsequently produces wet downbursts. For wet downbursts, ice-phase precipitation is the main forcing of low altitude melting and evaporation. Evaporation cooling at mid-tropospheric levels acts as a second forcing in this process, as suggested by (EMANUEL, 1981).

Additionally, Fujita (1990) proposed the existence of an "intermediate" environment downbursts, which as the name suggests, it is special case when downburst occur at intermediate levels, producing little or no precipitation at the surface as showed in Figure 29.

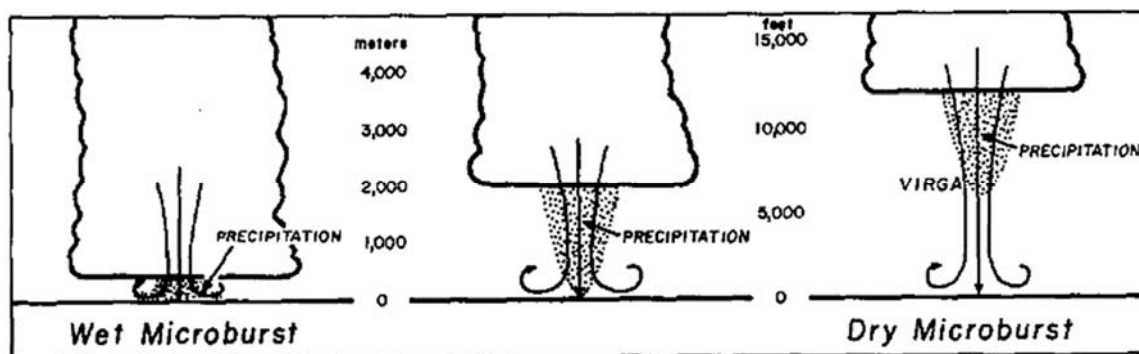


Figure 29. Three types of microbursts clouds identified during NIMROD, JAWS, and MIST Projects. Source: Fujita (1990).

In contrast, Knupp (1985) proposed four distinct types of downbursts:

1. **Penetrative downdrafts**, common to non-precipitating clouds and upper region of precipitating clouds.
2. **Upper-level downdrafts**, observed when updraft air surpasses an equilibrium level, cooling down at upper levels and descending from the cloud top.

3. **Middle-level cloud-edge downdrafts**, forced primarily by negative buoyancy associated with evaporation and melting of the cloud's precipitation within just outside of bottom of the cloud.
4. **Low level precipitation associated with downdraft**, forced at low levels by precipitation loading, evaporation and melting. This specific type of downdraft can get relatively large scales of downdraft and outflows.

Heat bursts are a rare downburst event that can cause intense outflow winds in lower levels of the atmosphere. Also, they are dependent on the environmental conditions since these intense mesoscale downdrafts are caused by the evaporation of rain from a virga cloud into a cold, dry, and stable thin layer of air at high levels. This process generates a parcel of air much denser than its surroundings that speeds up downwards and warms up due to the atmospheric compression, producing hot and intense wind gusts near the ground (JOHNSON *et al.*, 1989).

2.3.2.2. Morphology Classifications

Spatial and time dimensions of downburst are another common classification method that takes mostly into consideration the strength and extension of the impact caused by the extreme winds in surface. Fujita coined the term **Macroburst** for downburst events with an outburst larger than 4 km and lasting from 5 to 20 minutes; and the term **microburst** for downburst events with its outburst extension not higher than 4 km and larger than is 0.8 km and typically lasting from 2 to 5 minutes.

Macrobursts are always observed in wet environments. They are accompanied by a dome of high pressure induced by rain-cooled air. **Microbursts** normally present higher wind speed, because of a strong concentrated cold downdraft that descends very closer to the ground before spreading horizontally. The air warms up dry-adiabatically to the ground, unless raindrops evaporate fast enough to maintain a moist-adiabatic descent, which is very unlikely. The air temperature and pressure can either increase or decrease because the outburst winds tend to lose their pressure head while accelerating from the microburst center (FUJITA 1985b).

In the event of a downburst, a few components can be typically categorized depending on the size of the event. In Figure 30 these components are identified, where in a) is shown a **masohigh pressure system** or anti-cyclone, these damages are spread out and not to be too

intense. In b) is shown a **mesohigh pressure system** or pressure dome (BYERS AND BRAHAM, 1949), these damages are usually embedded within which anticyclones and present significant straight-line damages patterns usually caused by gust fronts at the front boundary of cold fronts. In c) is shown a **miso-high** system, these systems include major downbursts. Lastly, in d) is shown a **mosohigh pressure system**, which presents typical damage patterns observed within downbursts outflows called burst swath. These damages are typically long and narrow, not surpassing 100 m in length and 40 m in width. A burst swath damage pattern can also be caused by tornados (FUJITA AND WAKIMOTO, 1981).

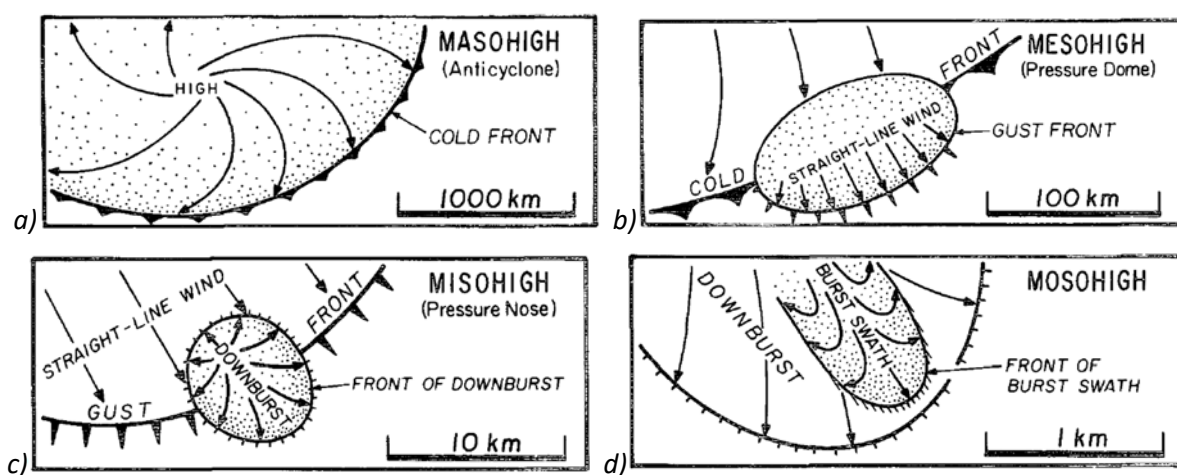


Figure 30. Typical components of a downburst event based on damage patterns proposed by Fujita. Source: Fujita and Wakimoto (1981).

2.3.2.3. Discrete Downbursts or Homogeneous Embedded Downburst Lines

Utilizing the information described in Figure 5 in terms of scale definitions and characteristic on time and horizontal length scales of atmospheric systems, Fujita and Wakimoto (1981) defined a family of Downbursts as a meso- β scale weather system that contains a series of downburst clusters. Downburst clusters are a meso- α scale weather system, which comprises two or more downbursts, considered to be a meso- β scale system. Microbursts are miso- α scale systems that are smaller than the downbursts and contain burst swatches, considered to be miso- β systems.

Hjelmfelt (1988) observed that downbursts typically begin as a single discrete event and can depending on the intensity of the storm, they can continuously persist along as a line of events embedded in one unique divergent segment that can last up to 57 min. These events are found to be most intense type of events of thunderstorms outflows (RIERA, 2016). In Figure 31 in a)

is shown a representation of a discrete (right) and homogeneous (left) downburst event; furthermore in b) is shown typical cross sections representations of the wind speed observed in homogeneous events. Note that when two downburst events overlap each other's outflow, the wind speed profiles change from discrete and isolated to a homogeneous event, intensifying in some areas and destroying the velocity at other areas. In Figure 32 are presented two real full-scale measurements of the outburst winds generated by in a) a discrete downburst cases are shown and in b) a homogenous/line downburst captured during JAWS field experiment. Hjelmfelt (1988) found large difference in maximum averages wind speed for homogeneous and discrete events; for instance for the former, downburst events wind speed is about 26 m/s, meanwhile for the later, they are less expressive at about 12 m/s.

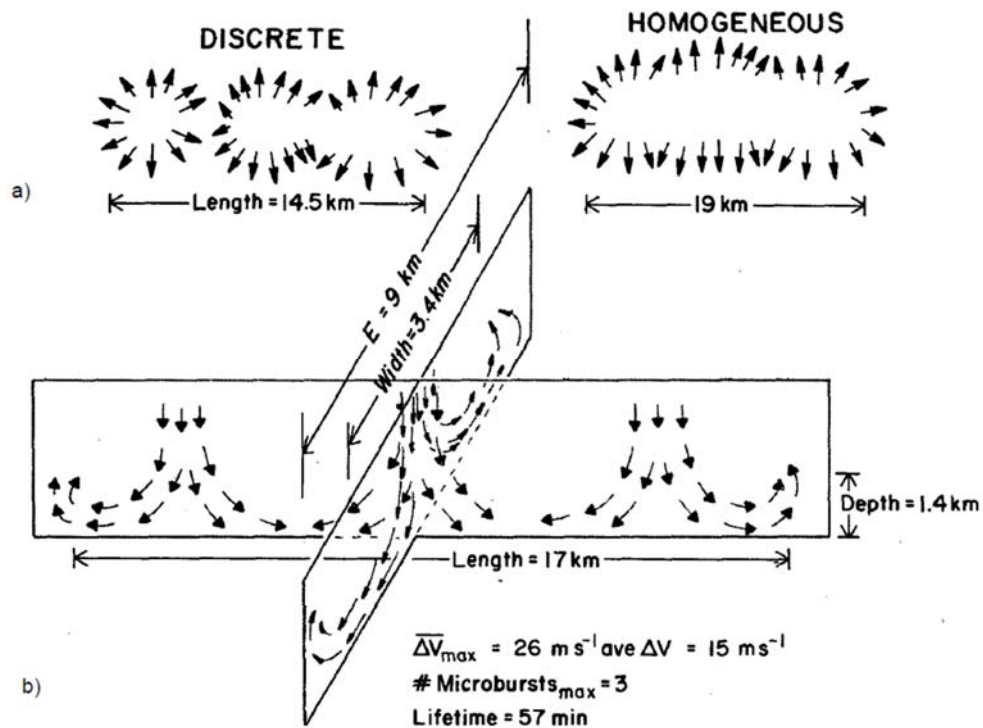


Figure 31. Microburst line schematic of a) Discrete and homogeneous outflow and b) perspective cross section views of vertical structures of microburst line structure. Source: Hjelmfelt (1988).

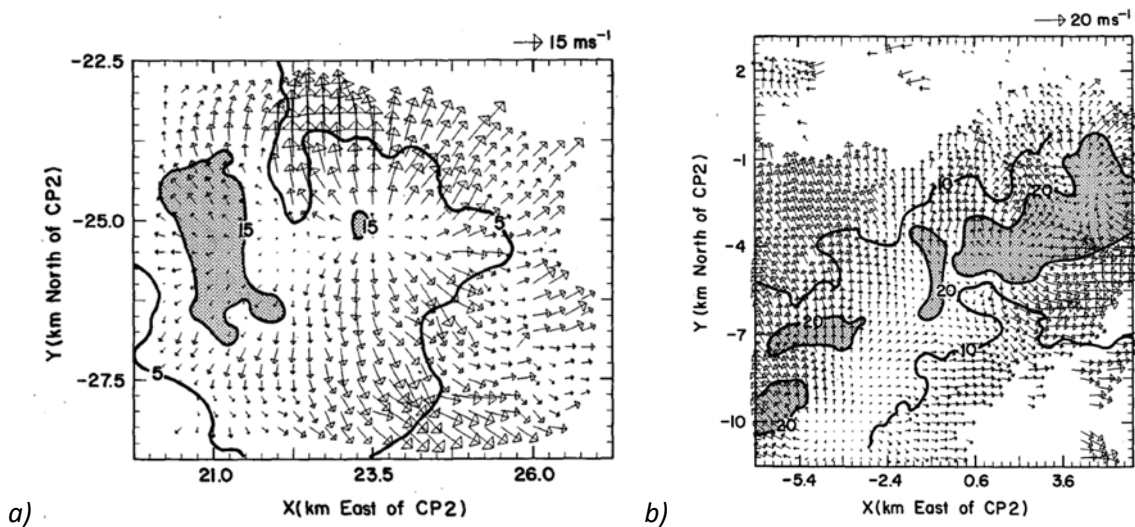


Figure 32. Typical wind vectors observed during a) discrete and b) in-line downburst event. Source: Hjelmfelt (1988).

2.3.2.4. Stationary or Traveling Downbursts

Another common classification of downbursts takes into consideration their stationarity. Downbursts can be stationary or traveling (transient). Traveling downbursts usually generate a typical line pattern of damage (Hjelmfelt, 1988) and are commonly observed within the presence of a backflow wind, such as a squall line. Similarly to the homogeneous downbursts, traveling or transient downbursts tend to present higher wind speeds since they are represented by the vectorial sum of background wind plus outflow wind speed (RIERA, 2016). Stationary downbursts usually descend as a straight line to the ground at contact stage, spreading out evenly. This process is depicted in Figure 33, where in a) a cold air downdraft is brought down by the microburst and accumulates within the ground, after that a cushion of the cold air prevents the descending air from reaching the surface, imposing strong winds at a higher height comparing to the case of a traveling downburst. As depicted in Figure 33, in b) a traveling downburst keeps descending with the cold air, which is left behind to form a mesoscale pressure dome. It is likely that the slanted surface of the cold air deflects the outburst winds forward, generating a typical asymmetric damage pattern.

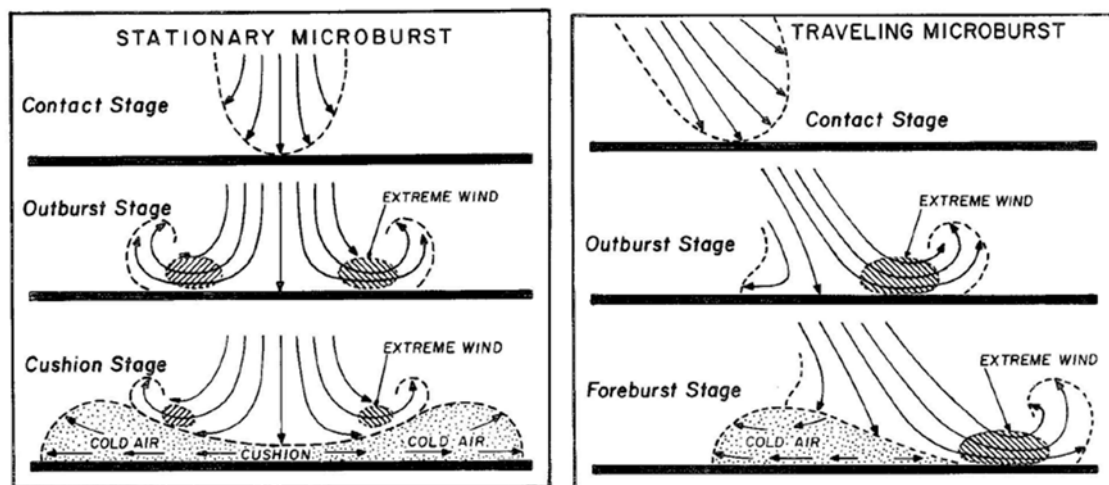


Figure 33. A stationary downburst is depicted on the left and a typical traveling downburst on the right. Source: Fujita (1981).

2.3.2.5. Outflow Symmetry

Downburst winds can be highly uneven because of the presence of higher background winds imposed by the thunderstorm movement which may or may not be caused by its stationarity. The mean winds in the ground are highly affected by the angle to which the downdraft departs (HJELMFELT, 1988). Eilts and Doviak (1986) suggests that besides the damage patterns induced by a downburst, radar reflectivity is also used to check downburst symmetry.

Three-dimensional experiments have indicated that even when there is a non-symmetric outflow, the outburst tends to be symmetric, suggesting that external environment factors superimpose small scale downdrafts shapes (HJELMFELT, 1988). Wolfson (1988) points out that the downburst velocity strength is mostly defined by the downward flux and the linearity geometry. As defined by the continuation equation, the cases in which the downdrafts are the narrowest downdrafts the outflows will be shown to be most divergent at the ground.

2.3.2.6. Twisting or Straight-Line Downbursts

Downburst wind usually occur as straight lines, but it is not uncommon to see winds suffering the influence of weather systems such as hook echoes leading to producing rotational motion to downbursts inducing swirling winds (FUJITA AND CARACENA, 1977), these downbursts are also called rotor dominant (MASON, 2017) as depicted in Figure 34. The rotation feature reduces entrainment and allows the vertical momentum to be preserved as it approaches the surface. Vertical vorticity is produced by the interaction of the storm with the environmental vertical wind shear and it is transmitted to the accelerating downdraft (WAKIMOTO, 1985).

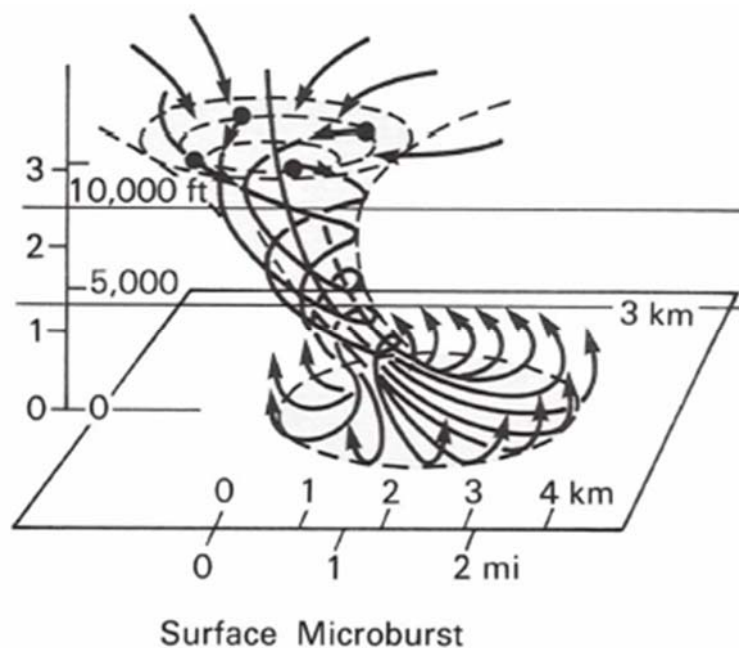


Figure 34. Model of a microburst descending from the cloud base presenting rotating downdrafts.
Source: Wolfson (1988).

2.3.2.7. Downburst Stages and Development

Goff (1976) analyzed 20 gust fronts between 1971 and 1973 on a 461 m high tower in Oklahoma–US. These convective outflows largely depend on the properties of the originating thunderstorms and follow a similar logic of the thunderstorms model proposed by Byers and Braham (1949), which can be described in three stages, defined as **First stage**, the thunderstorm stage, when the outflows are characterized by accelerating properties and correspond to the period of intensification of the storm. **Second stage**, when outflows present the quasi-steady properties corresponding to the originating moment of the thunderstorm. And finally, the **third stage**, when the outflows present decelerating properties and the storms are dissipating, corresponding to the end of the thunderstorm life cycle.

Fujita (1985a) extended the interpretation of Goff (1976) to downbursts and described the development of phenomena in five stages described as, **first stage**, the descending stage; **second stage**, the contact stage; **third stage**, the touchdown stage; **fourth stage**, the spreading stage; and **fifth stage**, the ring-vortex stage. Fujita (1990) developed a wall jet experiment developed to show each stage of the development of a downburst. In Figure 35 is shown the cross-sections photographs of simulated microbursts exemplifying the development of such event.

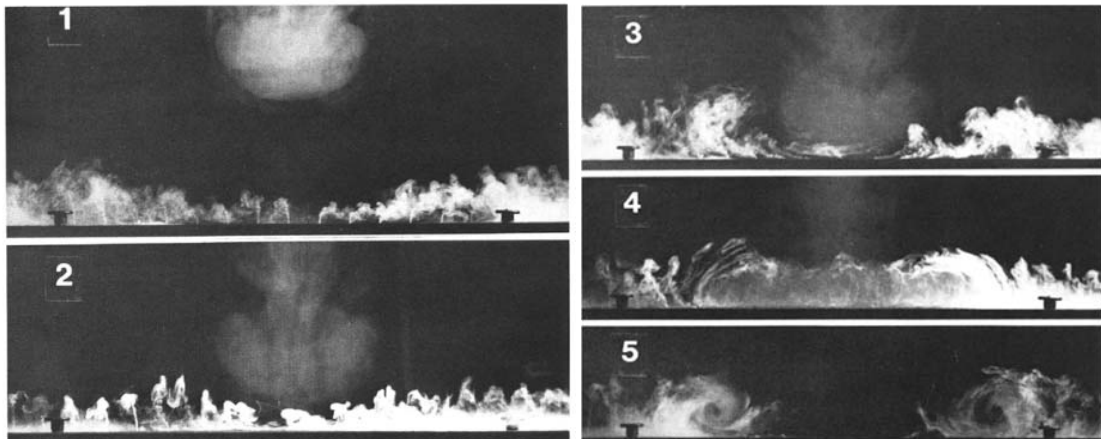


Figure 35. A laboratory experiment at the Wind Research Laboratory at the University of Chicago, indicating the evolution of a microburst airflow. The downburst phases are 1) Descending stage; 2) Contact Stage; 3) Touchdown Stage; 4) Spreading Stage; and 5) Ring-vortex Stage. Source: Fujita (1990).

An alternative analysis showed in Figure 36 proposed by Wolfson (1988) defines the development of a downburst the flow in four stages: **first stage**, descending stage, referring to the midair microburst descending; **second stage**, contact stage, when the microburst hits the ground; **third stage**, mature stage, referring to the stretching of the ring vortex; and **fourth stage**, breakup stage, which refers to the runaway vortex rolls induce burst swaths.

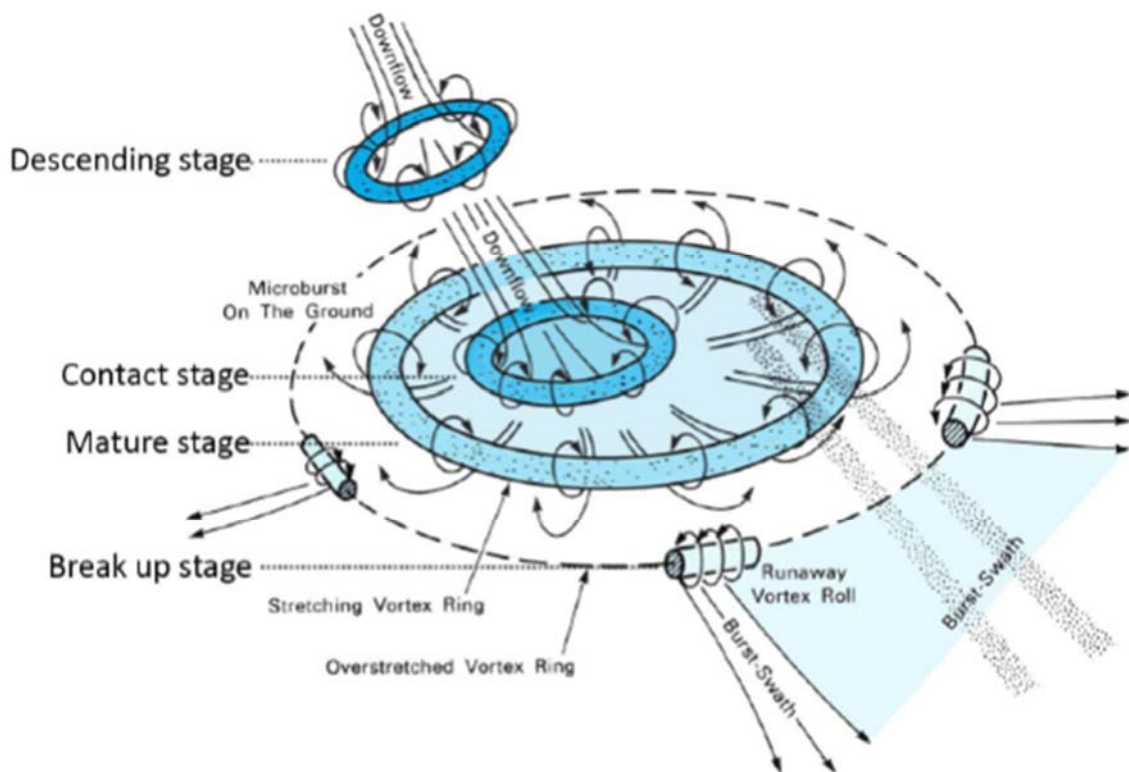


Figure 36. Four stages of a downburst event/ Descending Stage, Contact Stage, Mature Stage and Breakup Stage. Source: Wolfson (1988).

2.3.2.8. Influence of the Terrain

The terrain characteristics are an important topic of research on downbursts winds. Damage patterns caused by downbursts in open space areas tend to be more intense and observed as more homogenous and in straight lines. In Figure 37 a) is shown an idealized downburst with different ranges of wind speeds where in b) is shown a representation of how terrain irregularities and roughness can affect patterns (PITA AND DE SCHWARZKOPF, 2016).

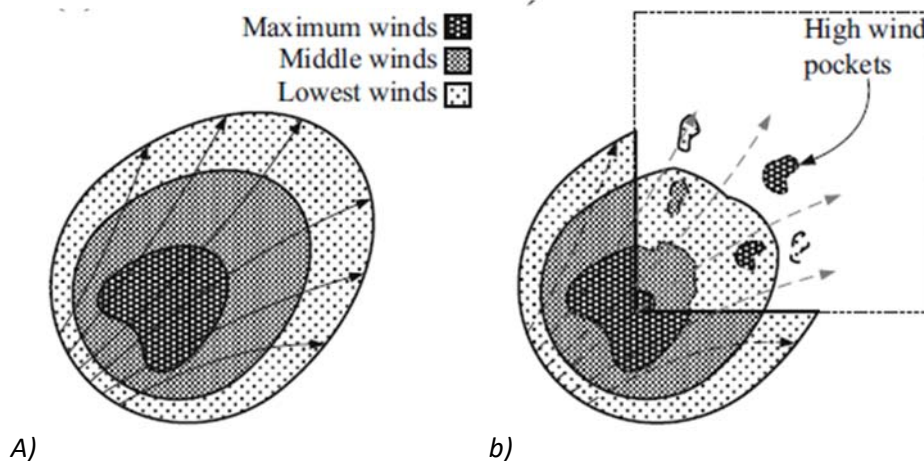


Figure 37. Idealized representation of microburst wind fields. Where a) represents an open terrain, b) represents the impact of a downburst within an urban area causing pockets of wind because of the irregularity of the surface. Source: Pita and de Schwarzkopf (2016).

2.3.3. Downdraft Currents

Foster (1958) developed a model from atmospheric soundings and found that wind gusts in surface are the result of negative buoyancy acting on a dry parcel of air entrained into a thunderstorm. This process resulted from some upper level and cooled by evaporation until it becomes denser and cooler than the environment, descends to the ground as a strong current, and diverging once it hits the surface (BARRETT AND RIEHL, 1948; BYERS AND HULL, 1949; SQUIRES, 1958).

Emanuel (1981) used the similarity theory to describe the properties of unsaturated penetrative downdrafts started at the top of deep and inert clouds. The results of such investigation showed that when the cloud-top instability criteria were met, unsaturated downdrafts may penetrate at the base of the cloud. This phenomenon is called Cloud-Base Detrainment Instability (CBDI), which may be visually interpreted by identified mamma or ice clouds formations that can announce the formation of downburst thunderstorms. DiStefano

(1983) proposed a similar model and confirmed the importance of the unsaturated thermal entrainment for the development of a downdraft, stating that evaporation of falling precipitation into relatively undiluted, unsaturated downdrafts are responsible for larger velocities and low temperature at the surface.

Srivastava (1985) developed a one-dimensional (1D) model and confirmed that the combination of deep, dry, neutrally stable sub-cloud layer produces, and the evaporative cooling process are the features that precedes downbursts. Srivastava (1987) analyzed the role of ice-phase microphysics in determining the downdraft and outflow strength. It was found that precipitation in the form of ice increases the intensity of the downdrafts when compared to precipitation in form of rain, therefore the higher the mixing ratio in the cloud, the higher is the availability of water to evaporate. In this research was also identified that, rain drops with smaller radii have higher evaporation area (related to volume) and consequently present a much higher evaporation rate once small particles are condensed quickly and are depleted by evaporation, leading to increase negative buoyancy (SRIVASTAVA, 1985). Figure 38 presents a sketch of a downdraft formation (dark blue) within the cloud during the maturation (right) period of the storm, when downdrafts and updrafts coexist at the same time and downburst can be developed at the front end of the storm commonly along with precipitation.

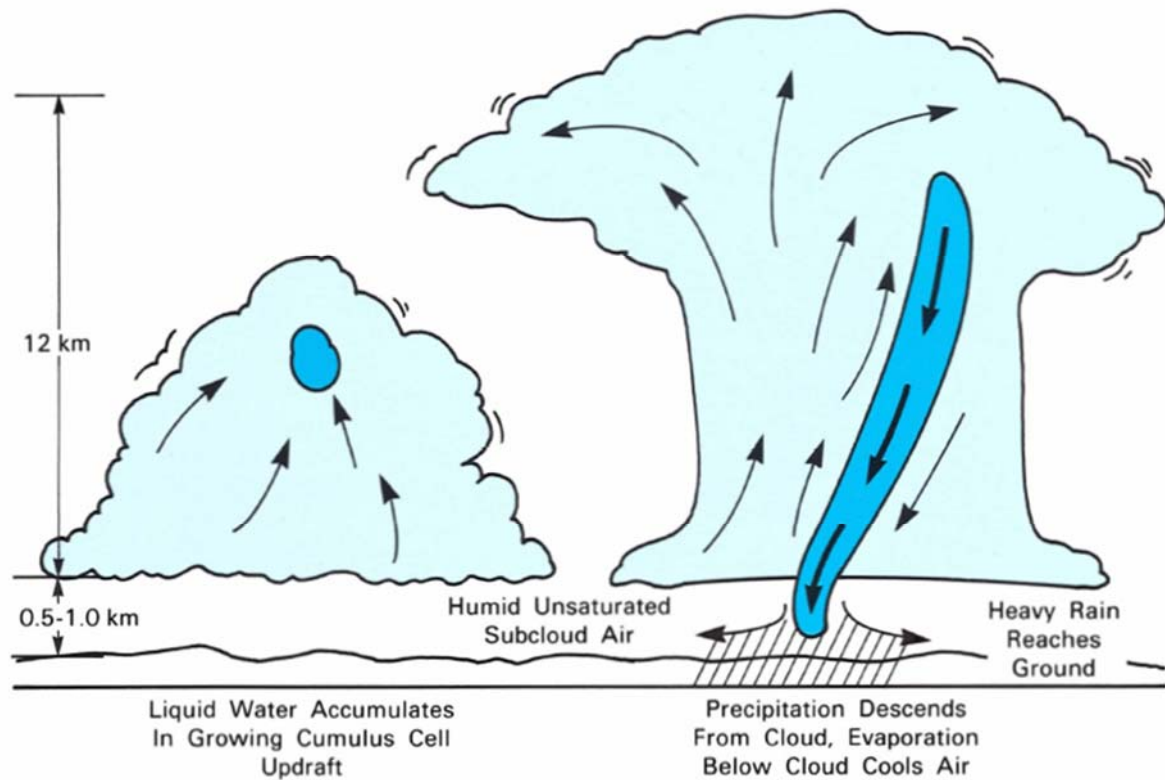


Figure 38. Sketch of a downdraft formation (dark blue) within the cloud during the maturation (right) period of the storm, when downdrafts and updrafts coexist at the same time and downburst can be developed at the front end of the storm, commonly along with precipitation. Source: Wolfson (1988).

The speed of the downdraft current depends on the forces that accelerate them vertically. Foster (1958) defines vertical acceleration of the downdraft equals to the thermal buoyancy minus precipitation loading minus the non-hydrostatic pressure gradient in the absence of Coriolis Forces because of the typical scale of these phenomena, as shown in Equation 1:

$$\frac{dw}{dt} = g \frac{\Delta T}{T} - g(l + i) - \frac{\delta P'}{\delta z \rho_o} \quad \text{Equation 1}$$

Where $\frac{dw}{dt}$ is the vertical acceleration of the air parcel; g is the gravitational acceleration; T is the temperature of the environment; ΔT is the temperature variation between the parcel or air and the environment; l and i are mass mixing ratios of liquid water and ice respectively, $g(l + i)$ represents the drag because due to the hydrometeors; z is the vertical coordinate of the system; P' is the pressure perturbation from hydrostatic basic rate; and ρ_o is the basic state density.

In Equation 1, the first term on the right side shows that if the thunderstorm air parcel is colder than the environment, the thermal buoyancy is negative and the acceleration is downwards.

The precipitation is defined by the second term; it defines how the increase of water within the parcel leads to accelerate the thunderstorm parcel downwards. The thermodynamic forcing is considered the main forcing to contribute to the downdraft development. For instance, Garstang *et al.* (1998) found that a potential temperature (θ_e) variation of 4.00K between lower atmospheric levels and dry layer in mid-levels, may be enough to induce the downburst wind in surface. The perturbation pressure is represented by the third element of the equation, the force on the thunderstorm air parcels is direct downward and increases with height.

These forces over time build up the negative vertical acceleration of the downdraft outflow, which eventually plummets to the surface, forming a small scale mesohigh at the stagnation point leading to a divergent horizontal outflow, where winds are reported to reach maximum speed. For smaller sized downburst, increased surface pressure is expected in the inside area because of a strong downflow that impinges upon the surface. This leads to the increase of ranges varying usually from 2 to 3 mb (Fujita, 1985a).

As shown in Figure 39, at the eye of the downburst (or impinging point) the surface pressure reaches its maximum and the wind presents a predominant downwards movement and the high total pressure at the microburst center accelerates the air outward. The atmospheric pressure decreases as the outflow speed increases, reaching a minimum at the location of the maximum windspeed. Assuming a frictionless terrain and ignoring the outflow turbulence, Bernoulli's theorem can be applied, which shows that the total pressure is equal to the sum of static pressure (blue) and dynamic pressure (red). In Figure 40 a representation of the phenomena is showed along with estimated horizontal velocity profiles.

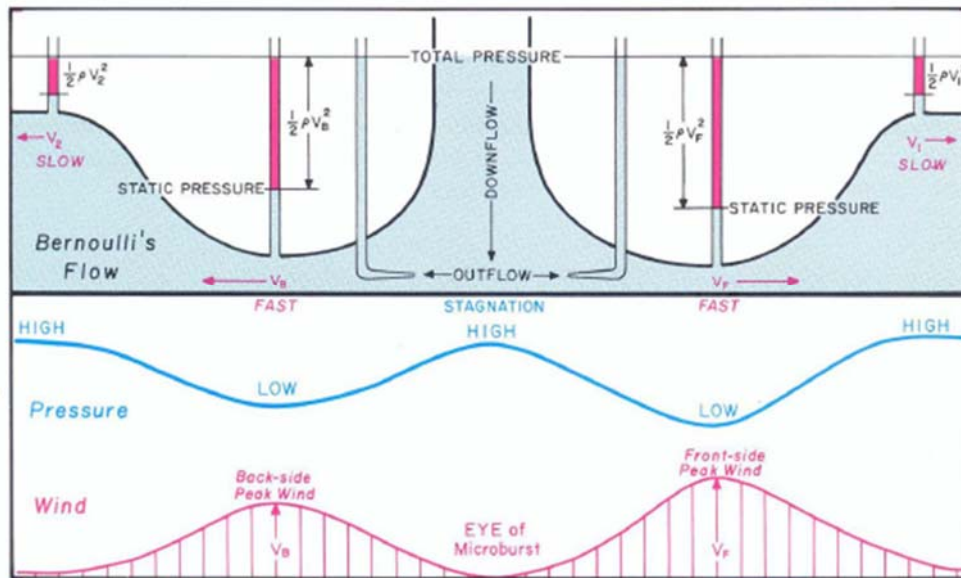


Figure 39. Bernoulli's Theorem showing the total pressure is equal to the sum of static pressure (blue) and dynamic pressure (red). Source: Fujita (1985a).

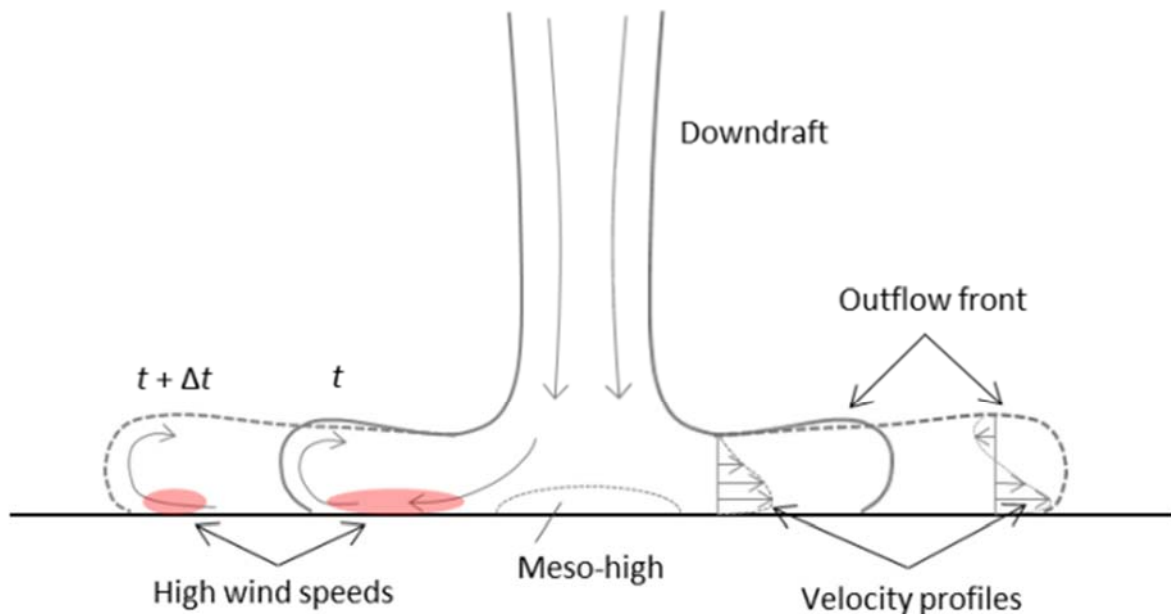


Figure 40. Schematic sectional representation through a model of downburst outflow event indicating regions of high wind speed, progression of the outflow in different times (t and $t + \Delta t$). Source: Mason (2017)

The phase changes during the development of the downdrafts characterize the interrelation of the two first components to the right of Equation 1. When the ice in the cloud melts because of the latent heat of fusion, as the air parcels move vertically through the freezing level, liquid water evaporates releasing latent heat of vaporization, causing moderate to heavy rain for

wet downbursts. This process occurs when midlevel air entrains into the thunderstorm or when rain falls into the unsaturated air below the cloud base, usually because of the gusty fronts of the background wind.

2.3.4. Forecasting Favorable Downburst Environments

After Fujita and Byers (1977) have pointed out the danger that downbursts impose to aircraft during landing and taking off, several approaches were developed to rapidly analyze if the environmental conditions were downburst prone and manage with focus on safety airport control operations. Data from Doppler Radars (MCCARTHY AND WILSON, 1982), lidar, satellite soundings (ELLROD, 1989), anemometer-based low-level wind shear alert systems (LLWAS) (WOLFSON *et al.*, 1994), and wind profilers radars (ELLROD *et al.*, 2000) were deployed to allow the predictability of extreme shear winds like downbursts (WILSON *et al.*, 1984; PRYOR AND ELLROD, 2004; PRYOR, 2011).

Stability Index (SI) developed by Showalter (1953) was the first index to be proposed and it was based on four basic elements that defined the likelihood for the development of thunderstorm outflows:

1. Enough convergence, frontal activity, or orographic lifting to cause a convective exchange of potentially unstable air between the 850 hPa and 50 hPa levels.
2. Condensation occurs at temperatures above freezing in convective clouds that extend to levels with temperatures below freezing.
3. Rising and moist reaches the level of Free Convection below 500 hPa.
4. Enough cooling aloft or warming with increasing moisture at low levels.

After stability index was proposed and established, other approaches for the instability predictors, such as the Lift Index, Convective Available Potential Energy (CAPE), Wind Index (WINDEX), Severe Weather Threat Index (SWEAT), Total Totals Index, K Index, Bulk Richardson, Dry Instability Index and several other regional approaches (Solari, 2020).

Sinclair *et al.* (1973) found a strong correlation between strength for the peak wind gust, the average surface wind speed prior to the gust as theorized by the Instability Index. Wakimoto (1985) identified the standard evolution along the day of environments favorable for the

development of dry downbursts by using atmospheric soundings in the high plains region of the United States. The correct analysis of the atmospheric conditions earlier in the day could define or not the observations of dry downbursts later.

In Figure 41 is presented a simplified model focusing on the typical environmental changes for dry downburst favorable days proposed by Wakimoto. In the figure is showed the diagram at two different times, the morning and the afternoon. In the morning there is a shallow radiation inversion at the surface beneath a deep dry-adiabatic layer, which extends up to 500 mb. The mean sub cloud missing ratio is about 3 to 5 g/kg with mid-level moisture. Later during the day, convection activates allowing the typical formation of virga clouds that will be causing dry downbursts.

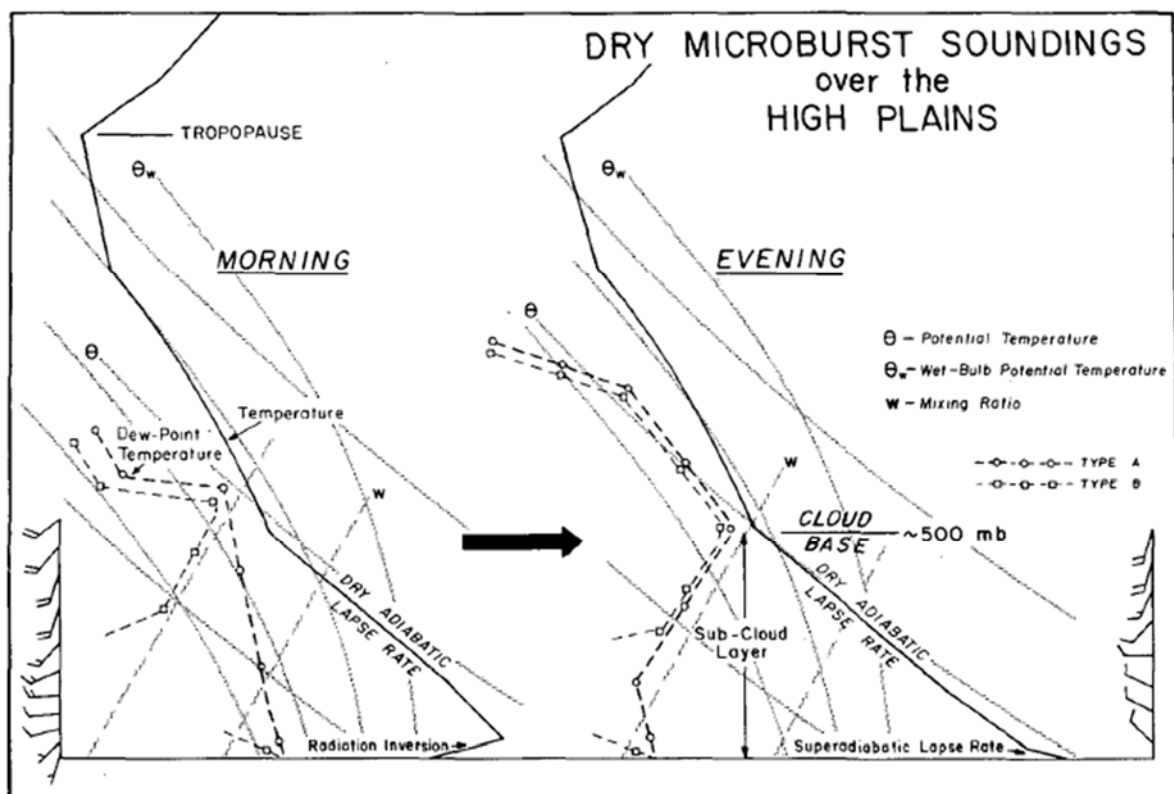


Figure 41. Simplified model showing the use of indexes to track the characteristics of the morning and evening atmospheric soundings favorable for dry-microburst activity over the high Plains in the United States. Source: Wakimoto (1985).

Wakimoto and Bringi (1988) outlined the importance of understanding the differences between convective storms that produce downbursts from those that do not and presented a study case on identifying microburst-producing storms by analyzing together cloud photogrammetry and radar observations during the life cycle. They noted that a near zero

differential reflectivity (Z_{DR}) surrounded by large positive Z_{DR} values in the main precipitation core may produce downbursts. This feature is named Z_{DR} -Hole, implying a localized downdraft composed of melting hail.

Caracena and Maier (1987) expanded the downburst studies from drier and temperate climates of northern United States to the wet subtropical climate of Florida. The focus was to obtain vertical atmospheric data with upper-air soundings prior the thunderstorms, characterize favorable environments that trigger the downbursts formation, and obtain the maximum wind speed in surface by applying thermodynamic atmospheric parameters to the buoyancy equation (FOSTER, 1958).

Atkins and Wakimoto (1991) investigated the thermodynamic properties of wet microburst producing days. Analysis of rawinsonde data indicated that low-level moisture is presented and is capped by a midlevel dry layer. The authors found that downbursts tend to occur during the diurnal cycle and that thunderstorm environments that present a difference between the surface and the lowest value in equivalent potential temperature (θ_e) greater than 20 K days can produce downbursts.

Microburst nowcasting applications for the Geostationary Operational Environmental Satellite (GOES) were developed to generate short term forecasting of downburst potential. The Microburst Wind Speed Potential Index (MWPI), the bi-spectral GOES imager Brightness Temperature Difference (BTD) (PRYOR, 2008, 2010, 2011) and the WINDEX (MCCANN, 1994) are examples of downburst forecast products created. A complete overview of these products is found in (PRYOR, 2015).

2.4. IMPACT OF THUNDERSTORM WINDS TO THE BUILT ENVIRONMENT IN THE WORLD

Natural disasters caused by severe weather events have been the most frequent type of incident in the world since the beginning of the 20th Century. Severe weather (hail, tornadoes, extreme wind) accounts for 40% of all catastrophic losses in the world (MUNICH RE, 2019), when accounted along with flood events these two categories together account for almost 70% of the natural disasters occurred in the world and causing the most financial damage out of all natural hazards (SOLARI *et al.*, 2015b). In Figure 42 is shown the frequency of natural disasters from the International Disaster Database (EM-DAT) for various categories reported in the world since it was accounted for in the beginning of the 20th Century.

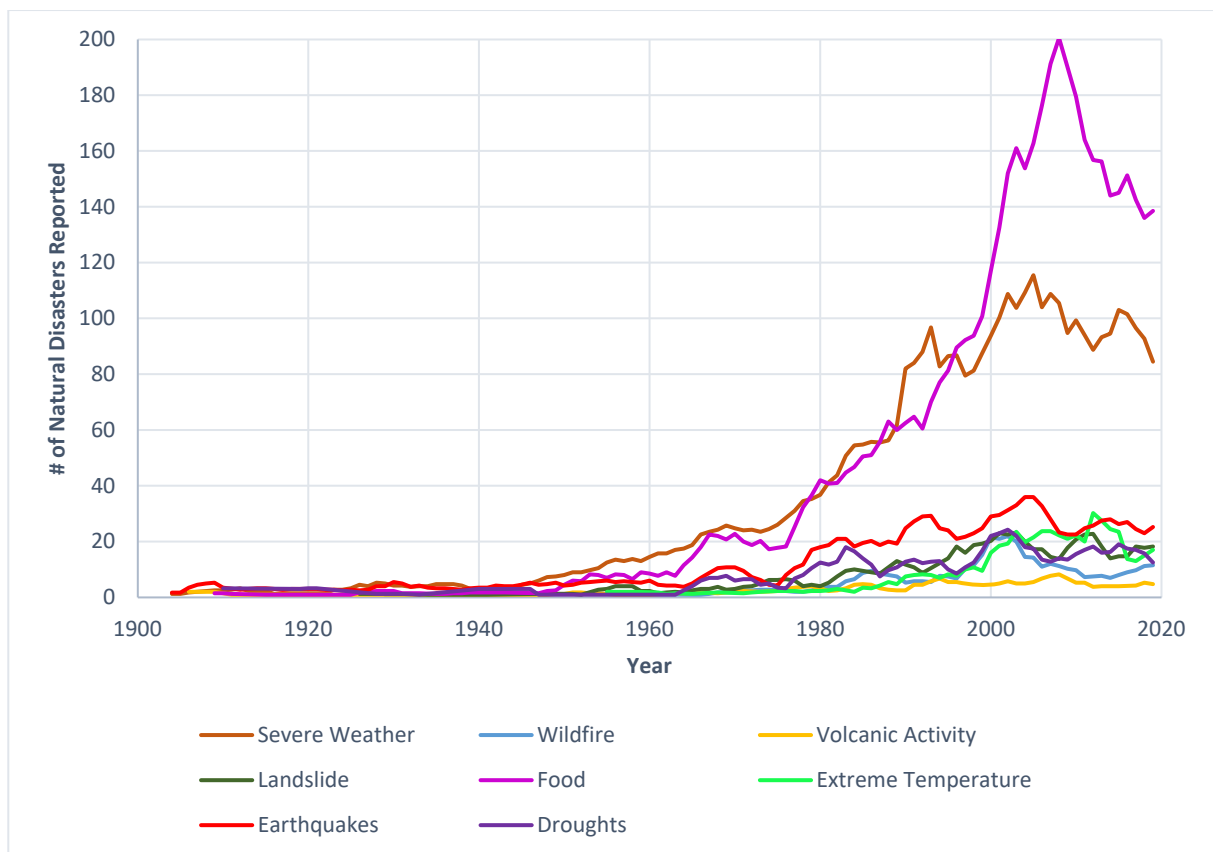


Figure 42. Natural disaster occurrences per category from early 20th Century to 2020. Data extracted from EMDAT (2020) chart created by the Author.

The analysis of Figure 42 shows a concerning growing trend in the number of natural disasters in the world for the most recent year especially for severe weather-related events. These events tend to cause lesser fatalities than other types of calamities, but they cause the most financial damage comparatively to other types of calamities.

Solely in the United States has caused \$1.5 billion in insured losses because of severe weather and it has left a death toll of 74 from 2001 to 2010 (LETFORD AND LOMBARDO, 2015). In the same country, convective severe storms cause as much insurance losses as hurricane events (INSURANCE INFORMATION INSTITUTE, 2020). The White House estimates thunderstorms have caused \$18 to 33 billion in economic losses only due to power outages between 2003 and 2012 (DAMATTY *et al.*, 2016).

In the world, high intensity winds are found to be the main cause for transmission towers failures and small-scale and rapid durations TS winds have been shown to cause most of these accidents (SAVORY *et al.*, 2001; LI, 2000). This is because of large momentum differences between points within a short longitudinal space imposes cause load patterns not typically considered in these types of structures, which may lead to the failure of even the most well-designed transmission towers. For instance, synoptic winds may be just as extreme as TS winds, but the typical homogenous characteristic of EPS winds acting upon an extensive portion of these transmission systems dispersing wind loads evenly (LI, 2000).

Dempsey and White (1996) *apud* Damatty *et al.* (2016) estimates that high intensity winds are responsible for causing 80% of all transmission lines accidents in the World. Thunderstorm winds are the main reason for transmission line failures in areas where icing is not observed (GHENO *et al.*, 2015). In Australia, for instance, 94 structures failures were recorded in the 90s, whereas over 90% of these events were caused by TS winds (LI, 2000). Wood *et al.* (2001) points out that 50% of the extreme wind gusts in Australia are found outside of the tropical cyclone region, showing that severe thunderstorms are the main precursor of these events.

In China, it was identified that 90% of the transmission lines accidents were caused by downbursts (HAWES, 1993) and 18 transmission towers accidents were linked with thunderstorms winds, including downbursts. Recently a cruise ship in China was stroke by a sudden squall line of downbursts, resulting in 442 casualties (ZHANG *et al.*, 2019). In Canada, downbursts are reported to cause the failure of 19 transmission towers in Canada (MCCARTHY AND MELSNESS, 1996). In Slovak, 18 transmission line towers failed because of downbursts winds (KAŇÁK *et al.*, 2007). In Romania, TS winds were responsible for the collapse of 19 high voltage towers in 2017, after wind gusts of up to 20 m/s were registered (CALOTESCU, 2018).

In Europe, Gardiner *et al.* (2010) point out that mechanical damages imposed by storms are responsible for 50% of the deforestation in that continent. Roberts *et al.* (2014) developed a windstorm catalogue tracking the 50 most extreme windstorm events in Europe from 1979 to 2012. In Italy, downbursts are known for causing innumerable infrastructure accidents because of specific conditions imposed by the Mediterranean Sea. Port areas are important but extremely vulnerable economic components to extreme TS winds. Due to the risk to the workers' lives and frequent ceases to avoid accidents have increase economic impact (REPETTO *et al.*, 2018). One of the major accidents caused by TS winds induced by downbursts was the collapsed of the Morandi Viaduct in Genoa in 2018, killing 43 people, with most of them living in buildings underneath that bridge (VILLANI, 2019; POVOLEDO, 2020).

In Central America, Fujita (1990) showed evidences that intense dry microbursts winds could have caused several shipwrecks in the Bermuda Triangle along the Golf Stream. In South America Nelson *et al.* (1994) and Garstang *et al.* (1998) found that downbursts are an essential turnover feature to the maintenance tropical forests in the Brazilian Amazon and Puerto Rico. These extreme wind events are an important component of biotic dynamics defined by a deforesting process which contributes to the availability of biomass in the soil (NELSON, 1994). It is estimated that the western and central areas of amazon are more affected by these events, reaching to 4.5×10^6 km² every year (BORDON, 2012). In contrast, windstorms in the southern portion of South America are found to be the most common eventuality count of natural disasters (MARCELINO *et al.*, 2005; VARGAS JR AND CAMPOS, 2015).

The analysis of the impacts of TS wind events on the built environment raises up the question how a changing climate will eventually affect the intensity and frequency of thunderstorm events as well as their intrinsic patterns, such as rainfall, thundering, and winds. For instance, while significant increases in rainfall have been observed over the last 50 years over summers seasons in the world (PENALBA AND ROBLEDO, 2010), extreme rainfall events are not conditionally associated with intense wind events. In reality, low rainfall efficiency storms are better correlated with high values of wind shear (DOSWELL, 2001). Solari (2020) points out that the warming of the earth's poles could even reduce the wind shear in mid-latitude, making these areas less prone to severe thunderstorms, but no conclusions are yet extensively accepted by the scientific community.

Other phenomena such as the Multi-decadal Cycles of the Pacific and Indian Ocean Sea Surface Temperature evolutions are found to be highly influential to the rainfall and circulation over Southern Brazil, but it is still not determined if such phenomena (that began to be observed in the 70s) is already a direct product of global warming or it is in fact a natural phenomenon (SILVA DIAS, 2011). The same is valid for the El Niño/La Niña phenomena (HANSEN *et al.*, 2010), whereas the coupling of both phenomena is found to change expected trends in precipitation around the globe.

In the scenario of climate changes, global warming should increase the temperature and moisture of the air intensifying man-induced atmospheric energy unbalances, such as heat islands. These two components (heat and moisture) are a major source of available potential energy and together complementarily feed thunderstorms when larger systems are present. Taking into consideration this outlook, it is expected that severe meteorological events will become more intense and actual patterns might change (BRAUN AND AWRUCH, 2011; SOLARI 2020), putting even more at risk larger urban conglomerates that already stumble with the effects of severe weather.

In South America, it is generally accepted that climate changes will substantially impact the subtropical portion of the continent more causing record-breaking intense storms (ZIPSER *et al.*, 2006). For instance, a downburst event observed in the City of Porto Alegre, in the State of Rio Grande do Sul (RS), in Brazil in 29/01/2016 is believed to have been intensified due to the heat island effect caused by the urban conglomerate. In such case, a larger synoptic system was intensified above the city during summer, causing damage estimated at R\$50 million. This event endangered millions of people, leaving thousands of structures severely damaged, and entire areas of the city without electricity or potable water. The downburst was estimated to have occurred close to downtown area as it is illustrated in Figure 43. The squall line advancing over the city is shown in depicted by the overlaid figures taken at different points if the city indicated by the arrows.



Figure 43. *Illustration of a downburst event that occurred in the City of Porto Alegre on 29/01/2016.*
Source: Author.

3. PHYSICAL PROPERTIES OF NON-TORNATIC THUNDERSTORM WIND EVENTS

In this chapter is discussed the fundamental physical properties of non-tornadic thunderstorm wind events with focus on their vertical properties. Also, herein are discussed methods to identify TS winds within mixed datasets, existing attempts to include these analyses in engineering codes and/or standards, and finally the case of Brazil in terms of efforts developed to include TS winds consideration into the country's extreme wind climate studies.

3.1. VERTICAL PROFILES FULL-SCALE MEASUREMENTS OF NON-TORNADIC TS WINDS

The variation in the wind speed with height is one of the most important properties of the wind when evaluating their interactions with structures. EPS winds are traditionally described following the Power Law or the Logarithmic Law within the ABL, which normally extends for about 1 km from the earth's surface.

The shape of this profile is usually defined by the influence of the turbulence that is generated thermodynamically (i.e., heating, cloud microphysics) or mechanically (i.e., surface roughness). Therefore, the power-law or logarithmic exponents approach assumes values that vary due to the type of terrain, which defines the effects of quantity of movement exchange through turbulence effects due to the surface roughness (BLESSMANN, 1995).

Due to the intrinsic differences between TS winds and EPS winds, the ABL theory is not valid any longer for TS winds and still to date there is no well-defined agreement of how to describe these winds vertically. Full-scale measurements are in consequence the main mechanism to empirically understand and validate the typical properties of thunderstorm wind profiles wind near the ground.

Some of the reasons full-scale measurements are rare and scarce, include roadblocks such as difficulty to acquire these datasets, such as typical weather networks, which in most cases are composed of synoptic stations, meaning that they are not in fact designed to capture with precision the rapid varying characteristics of TS winds. Therefore, special apparatus that captures precisely high-resolution datasets near-ground is often required, these apparatuses include mesoscale analysis equipped weather networks, meteorological towers with anemometers at different levels, and of course Doppler Radars. In the attempt to access existing profiles, in this section is presented exhaustive research of existing efforts

chronologically organized aimed to capture measurements of TS wind speed vertical profiles. Some of the profiles are further discussed and analyzed in Chapter 4 in the attempt to propose empirical models based on full-scale measurements.

As early as 1937 Sherlock and Stout (1937) was already investigating the effect of wind loading in electric power lines during high wind events. Empirical techniques to estimate maximum surface wind speed were then proposed by Fawbush and Miller (1954). Foster (1958) focused to understand the correlation between the strength of the downward currents and the speed of the convective-induced wind gusts measured in the ground, by integrating the buoyancy equation to obtain the downward wind speed of an air parcel that becomes cooler than the surrounding in mid-atmospheric levels. The theory was validated against an extensive dataset of thunderstorm downdrafts captured from about one hundred vertical atmospheric soundings.

Sinclair et al. (1973) analyzed the structure of 6 gust fronts from data obtained using a 150 m tall tower in Florida and Oklahoma. For the gust fronts analyzed, the logarithmic wind law showed to be valid for the first 100 m for those events, above this level more complex wind shears are observed. Although, as previously discussed, these analyzes were made focused on aeronautical applications, having limited applications for wind engineering.

Fujita (1976) investigated an aircraft accident caused by a downburst at the John F. Kennedy International Airport (JFK) on June 24, 1975; and estimated the vertical component of the downdraft from radar, satellite, SWS, and the wind speed register by the airplane. In Figure 44 are presented the vertical components estimated by Fujita that led to cause the aircraft accident. Note that the vertical downdraft velocities reached an instantaneous peak value of 28 knots making the plane lose altitude and crashing.

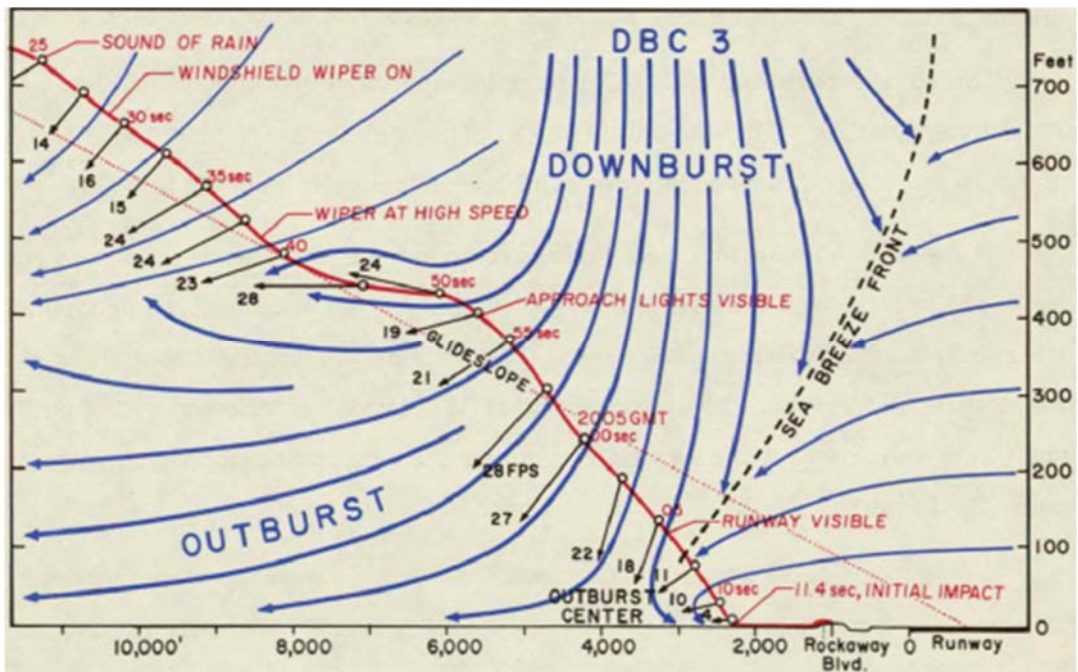


Figure 44. Aircraft accident caused by a downburst at the John F. Kennedy International Airport (JFK) on June 24, 1975. In this illustration, Fujita draws the Aircraft being pushed down due to a strong downdraft. Source: Fujita (1976).

Fujita and Wakimoto (1981) used Doppler Radars triangulation to study damage patterns after several windstorms in the 70s. Radar and ballistic analysis were developed to help understand the profiles of the TS wind events revealing a maximum wind speed obtained based on the projectiles was 63 ± 10 m/s.

The highest wind speeds generated by a downburst event ever captured was at the Andrews Air Force Base, in 1st August, 1983 (FUJITA, 1983). In Figure 45 reading from right to left, the black line represents the 3-s instant gust peak wind velocity and the magenta line represents the 1-min mean wind speed. The maximum peak of wind speed registered was 67 m/s (130 knots), followed by a sudden change in wind direction (showed on the bottom of the graph). The second wind speed peak gust was registered at 42 m/s (84 knots). Both measurements were taken at the standard height of 10 m from the ground. Unfortunately, there are no vertical measurements of this event.

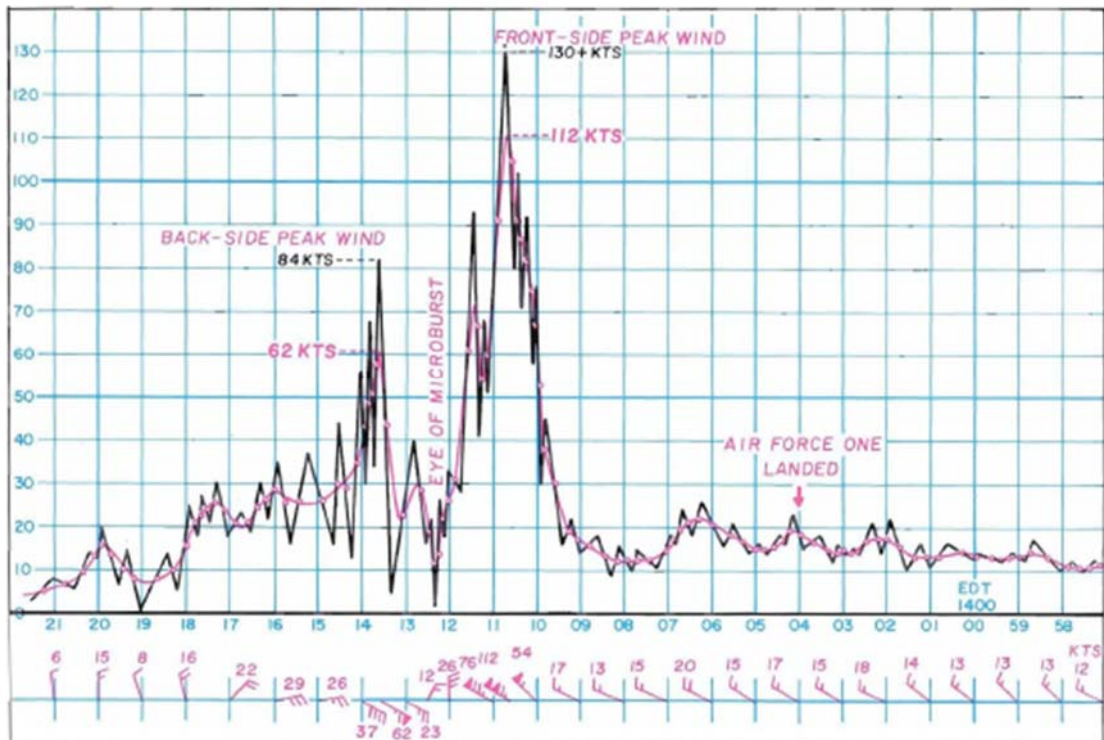


Figure 45. Rare microburst event registered at the Andrews Air Force Base on 1st August 1983. Wind 3-s instant gust peak of 67 m/s (150 knots) followed by a back-side peak wind gust of 42 m/s (84 knots), reading from right to left. Source: Fujita (1985a).

In Fujita (1985a) finds from both JAWS and NIMROD projects were presented in an extensive technical report at the University of Chicago. Several methods were deployed to measure those thunderstorm outflows, including radars, SWS networks, ballistic analysis, and aerial photographs. Other relevant publications on these finds include Fujita (1985b, 1985c) and Wilson *et al.* (1984). It is important to reiterate that these studies were not developed for wind engineering applications and the information on wind properties at lower levels is very limited in terms of spatial and time resolution. For instance, in Figure 46 is shown the radial wind velocity across three microburst events with velocities captured from high-resolution Doppler observations at close range (4-10 km). The average curve is for six cases between four wider radar triangulation ranges (8-26 km), which means the data has lower reliability. No information regarding averaging time for these profiles is included.

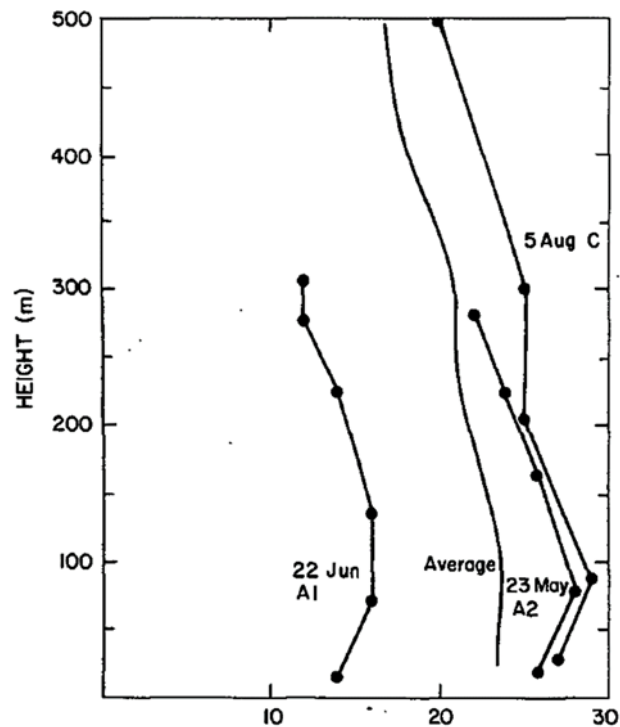


Figure 46. Doppler high resolution, vertical profiles of the radial wind differential velocity for three microbursts and the average curve for six cases. Source: Wilson et al. (1984)

Hjelmfelt (1988) published the first studies with a more in-depth analysis of the vertical structure characteristics of maximum TS events that had more practical applicability to the wind engineering, and for that reason these datasets are commonly used to validate downburst models. Datasets captured in the JAWS experiment and another subsequent project called Classify, Locate, and Avoid Wind Shear (CLAWS) Project (MCCARTHY; WILSON; HJELMFELT, 1986) were used to create idealizations of downbursts profiles and ultimately estimate with more precision TS wind profiles. No information about the acquisition sampling was made available in the publications.

The lifecycles of these downbursts were also analyzed, and it was found that organized lines of microbursts produce longer-lasting wind shears when compared to isolated downburst cases. Similar conclusions were found in modeling developments of Ponte and Riera (2010). The differential maxima velocities registered identified that microbursts have as an important internal feature internal pulsations within the downdraft that helps to define variations in velocity, lifetime, and/or diameter.

Hjelmfelt (1988) focused on developing empirical models based on the full-scale measurements. In Figure 47 is shown the idealized schematic of the downburst downdraft, in

this case the areas with higher dBZ rates (hatched) showed clearly higher wind speeds. In Figure 48 is shown the schematic version of the proposed model with parameters used to define the downdraft current. It was found for the maximum wind velocity (V_{max}) a typical value of 24 m/s, which typically occurs at height of 1.8 km and at 1.5 km diameter (D). This diameter is normally referred as 1D and it represents the distance from one point to another of maximum wind velocity within the outflow. It was also found on these analysis that the typical height of the maximum winds was at 80 m or 100m, still varying significantly from one event to another (KIM AND HANGAN, 2007). The ground average maximum velocity found was of (\bar{V}_{max}) 12m/s and the outflow depth, representing the outflow from the ground to the returning wind field above it was of 0.7 km.

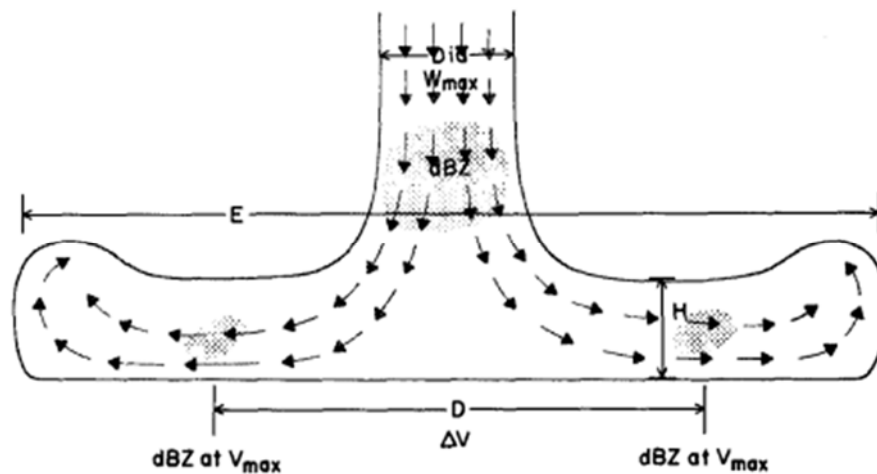


Figure 47. Typical schematic of a downburst per radar reflectivity. Source: Hjelmfelt (1988).

**SCHEMATIC JAWS MICROBURST STRUCTURE
AT MAXIMUM INTENSITY**

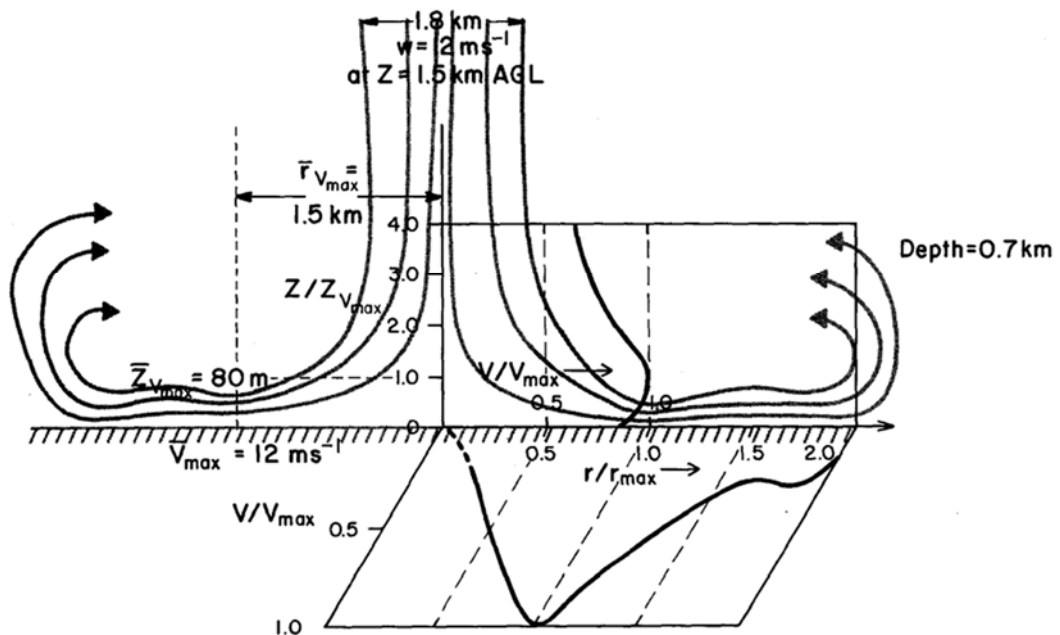


Figure 48. Schematics of typical JAWS microburst structure at maximum intensity. Source: Hjelmfelt (1988).

In Figure 49 are presented the a) maximum radial velocity profiles for the microburst cases investigated by Hjelmfelt (1988), where the solid thick line represents the average profile of the events. In the same Figure in b) is showed the maximum diameter for each event. Note that the velocity profile presented is the radial differential velocity, which is given by the difference between the two maximum points of the velocity vortex ring. In practical terms, this velocity should be divided by two considering an axisymmetric downburst event.

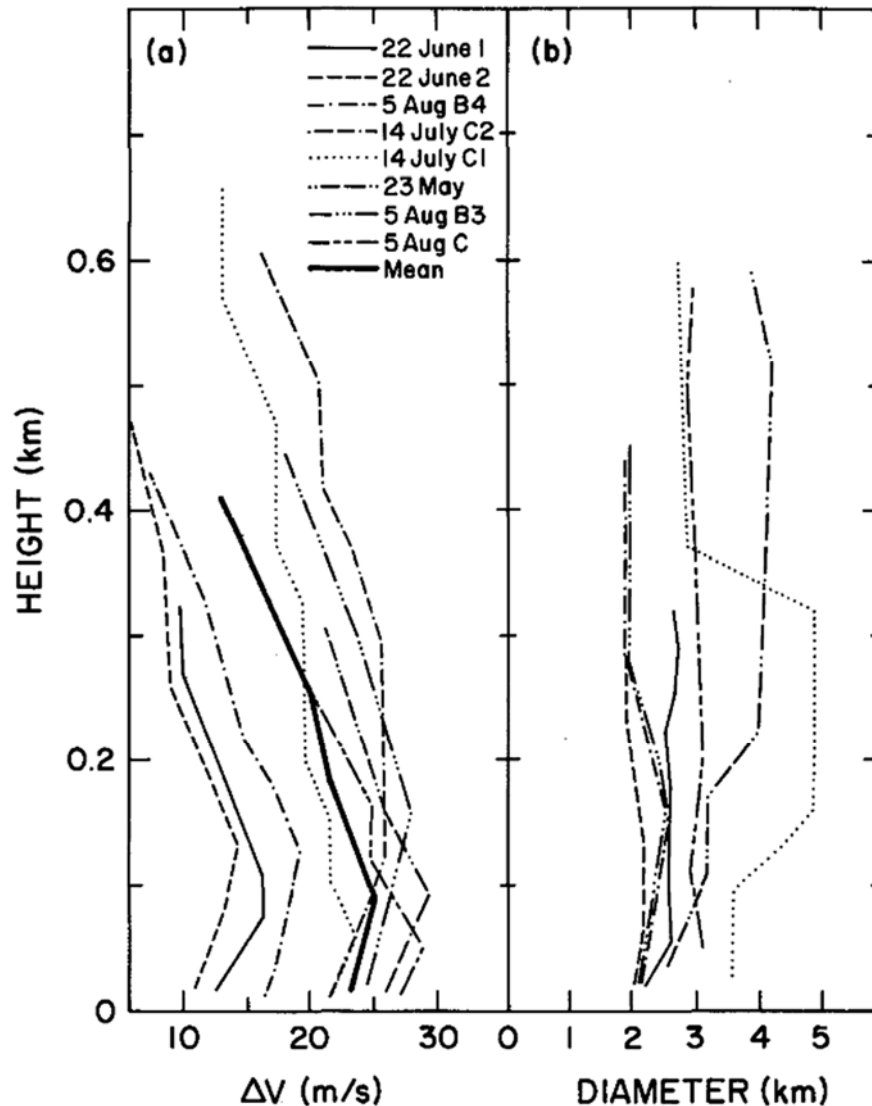


Figure 49. In a) is shown the maximum radial velocity profiles for the microburst cases investigated by Hjelmfelt (1988) and in b) the maximum diameter for each event. Source: Hjelmfelt (1988).

Even though Hjelmfelt (1988) profiles did not reach the most significant maximum captured velocities, these studies resulted in significant advances to understand the dynamics and evolution of such events. Figure 50, in a) is presented the variation of radial velocity of normalized with V_{\max} over the time of duration the event. It is noticeable that a microburst typically increases in strength nearly linearly from the divergence point to the maximum velocity, decreasing closer to linearly or even more rapidly. Some events might decrease but still present small pulses of velocity.

In Figure 50 b) is presented the normalized velocity profile of V_{\max} along Z axis, scaled to V_{\max} for 12 microburst analyzed cases. It is also presented the mean average profile observe on

these cases and the profile observed on the wall jet experiment by Poreh *et al.* (1967). V_{max} occurs at about 1.5 to 2 times the downdraft radius, as estimated from multiple-Doppler analysis, observed certain concordance between the modeled profile and the wall jet experiment.

In Figure 50 c) the presented normalized radial velocity along the V_{max} azimuth versus scaled to the radius of maximum velocity ($r_{v_{max}}$). It is also shown the mean profile expected along with the wall jet experiment from (POREH *et al.*, 1967) . Note how the wall jet profile is a reasonable approximation for the normalized downburst profiles. Passing the maximum velocity, the velocity profile decay of the observed downbursts happens more rapidly than the wall jet experiment, at a rate proportional to $1/r^2$. Hjelmfelt (1988) suggests that one of the reasons why the wall jet fails to simulate correct this part of the experiment is due to the typical stationary conditions of the wall jet experiment and the non-stationarity characteristic of the downbursts.

In Figure 50 d) is presented the typical time of expansion and dissipation of the investigated downbursts. Even though there is a wide range of dimension possibilities in the development outflows, it is clear that there is a small trend in which downbursts usually grow linearly until about 4 km and persist at that constant size before start dissipating, this trend categorizes them as microbursts. Also note that some outflows may persist and grow, reaching out to a macroburst dimension but with smaller velocities. Note that most part of these events are axisymmetric and non-stationary and the analysis in this case focuses on the side with the highest intensity.

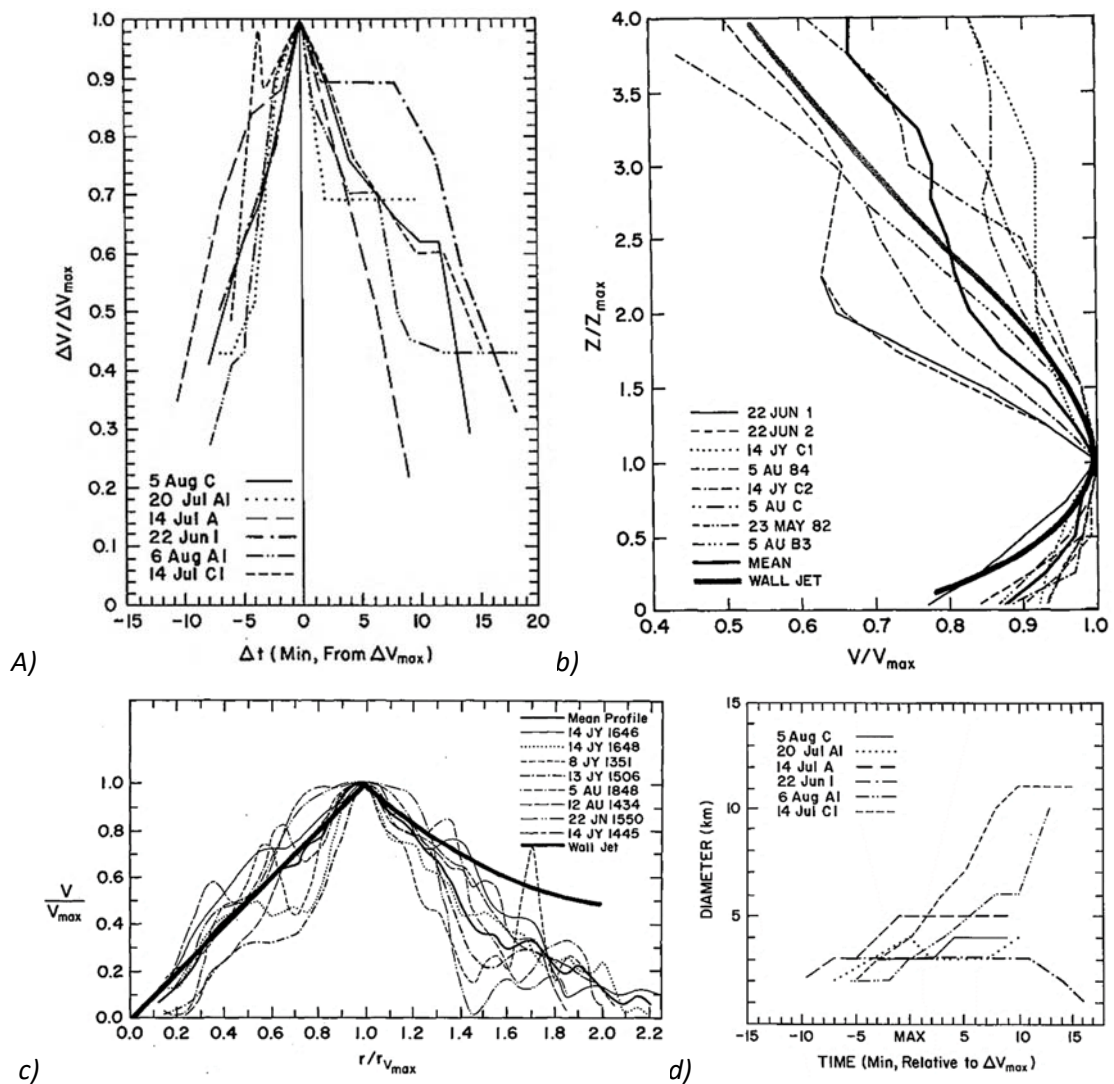


Figure 50. Different analysis of typical downburst profiles, where in a) is showed time variation to reach normalized V_{max} ; in b) is showed microburst velocity profile normalized to V_{max} ; in c) is showed normalized radial velocity along the V_{max} azimuth versus scaled to the radius at maximum velocity ($r_{V_{max}}$); and in d) typical time of expansion and dissipation of downbursts. Source: Hjelmfelt (1988).

In Figure 51, Hjelmfelt (1988) drafted a typical downburst timeline, note that the lifespan of the microburst starts when the winds touch the ground, reaching to V_{max} at approximately 5 minutes. In this case the outflows normally extend with microburst intensity winds until typically 10 min, and usually dissipates at about 13 min.

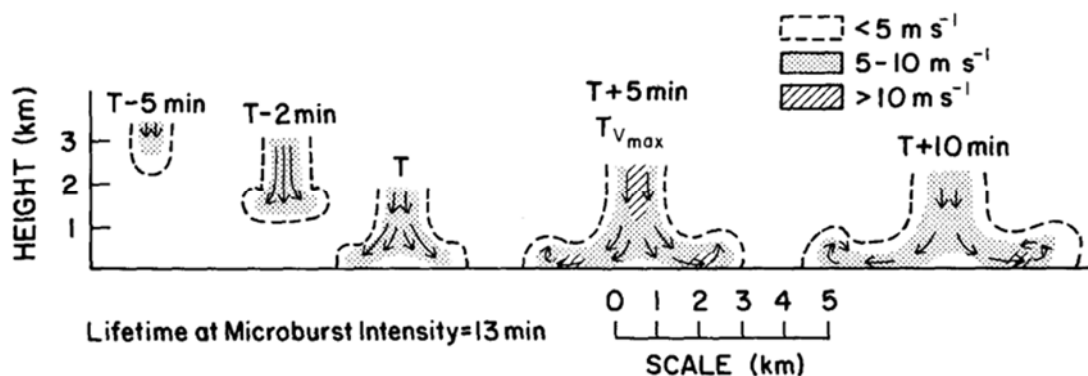


Figure 51. Typical microburst lifespan. Source: Hjelmfelt (1988).

Until this point, the focus of the research in downburst was to obtain vertical profiles of downbursts for aeronautical industry applications. Little was done in mind of wind engineering and structural safety. Sherman (1987) presented the first modern measurement of a weak downburst in Australia, using a 200 m tall tower with 1 Hz wind speed sensors and temperature at various levels. Meteorological analyzes were performed coupled with data from SWSs, Doppler Radar imagery, and vertical sounding. In this study an isolated thunderstorm passed through an instrumental tower at Bald Hills, in Australia, on 5 of November 1977. The terrain was flat covered with grass with a few scattered trees, equivalent to a Category II at NBR 6123. Two downdrafts were observed at this event with the second one being more expressive.

In Figure 52 is shown the 1-s peak wind speeds at 20:15 (Local Time) of an isolated downburst event at different levels of the tower. This was a mild event that passed through the site associated with a gust front, increasing the wind speed from about 6 to 11 m/s for the levels of 58 to 104 m, with less well-defined increases at other levels. Within the same density current outflow, a second gust was captured at approximately 90 seconds after the first gusts, this time accompanied by the most marked increased in wind speed, from 11 to 18 m/s at the same levels as mentioned in the first peak of velocity.

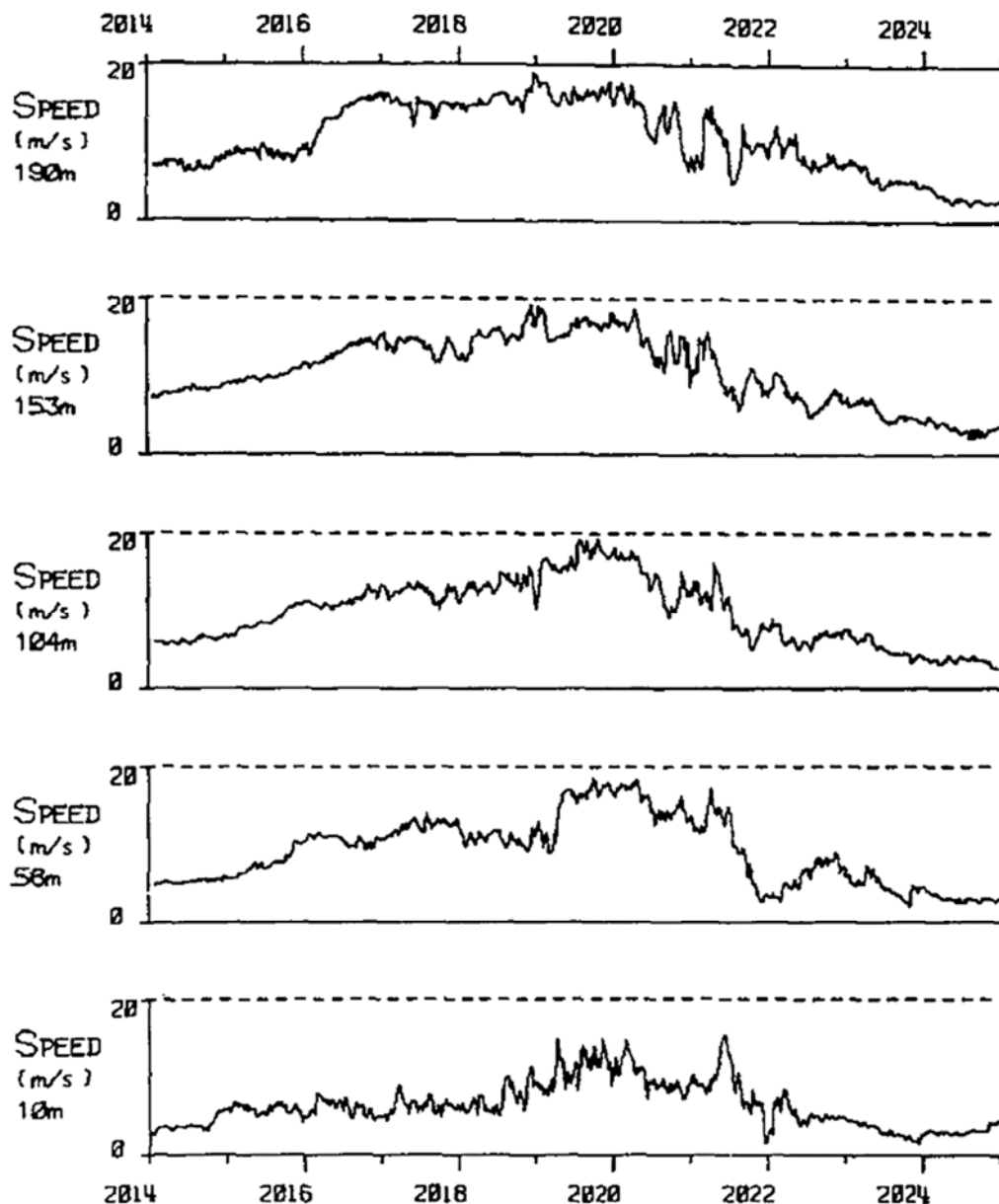


Figure 52. Graphs of wind speed (1-sec instant values) at each level on the tower around the time of passage of the downburst. Source: Sherman (1987).

Nelson *et al.* (1994) observed wide spreads occurrence of large blowdowns (larger than 30 ha) in the mature Amazon Forest caused by downbursts. Garstang *et al.* (1998) continued to study such phenomena using four 40 m towers in the middle of the jungle 50 km apart. The research was conducted for 45 days, in which 15 of these days, intense winds over 10 m/s were taken at one-second interval, from which one-minute averages were compiled. This study explored the variation of environmental parameters during the occurrence of strong outflows, helping characterize downburst recurrence in wet tropical zones of the equatorial belt. Even though

towers were used to capture the structure of the storm outflows, only surface data was made available in the publication.

In the 2000s, full-scale measurement investigations started to focus on the effects of TS winds in the wind engineering parameters. Choi and Hidayat (2002) analyzed the differences in the wind gust factor due to TS events and monsoon systems using data obtained from two surface weather stations and two towers equipped of anemometers. The focus in this study was to understand the influence of averaging periods to calculate the Gust Factors (G) of TS events, which is given by the maximum wind speed of duration t and average wind speed for an averaging period T .

One tower was 20 m tall with four cup-type anemometers at 4 Hz sampling frequency ($G_{0.25,T}$) and the other tower was 125 m tall with three ultrasonic anemometers at 50 Hz sampling frequency ($G_{0.25,3000}$). The authors separated high wind speed values and classified them as TS and Monsoon systems based on abrupt changes in wind direction record and found that most part of the high gust speeds events happen during TS events. One of the events analyzed is shown in Figure 53. In a) is shown the wind speed for three different heights for both 30-s and 10 min intervals and in b) the same is presented but for wind.

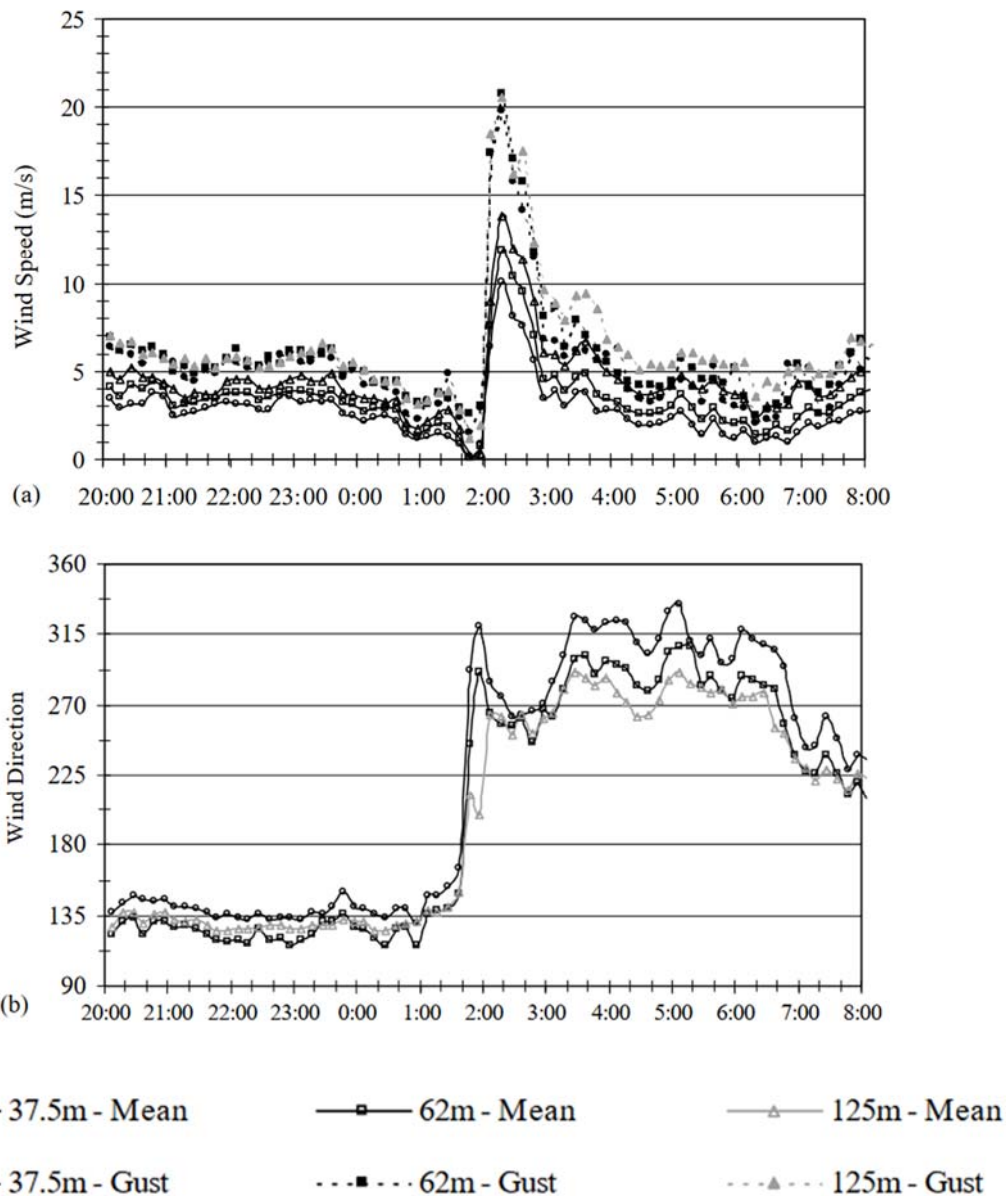


Figure 53. in a) shown the wind speed for three different heights for both 30-s and 10-min intervals, and in b) the same is presented but for wind. Source: Choi and Hidayat (2002).

The results showed that the G for TS winds were significantly higher than those G of monsoon winds. The G values are found to be higher as the measurement is done closer to the center of the thunderstorm event. The analysis of the G from both monsoons and TS events showed that TS winds are more turbulent than EPS winds and because of the small-time scale of these events averaging time of 5 to 10 minutes (or less) are preferable over the traditional 1-hour used for synoptic winds.

In Brazil Paluch *et al.* (2003) registered a TS event from a 40 m tall tower at the City of Passo Fundo – RS. The horizontal velocities of the record obtained are shown in Figure 54 for 3

anemometers at 20, 30, and 40 meters. Based on the sudden peaks of velocity at all three levels of data obtained and the change in direction of the wind this TS event was classified as a downburst, although the intensity of the wind lead to the collapse of the anemometric tower (PONTE AND RIERA, 2010).

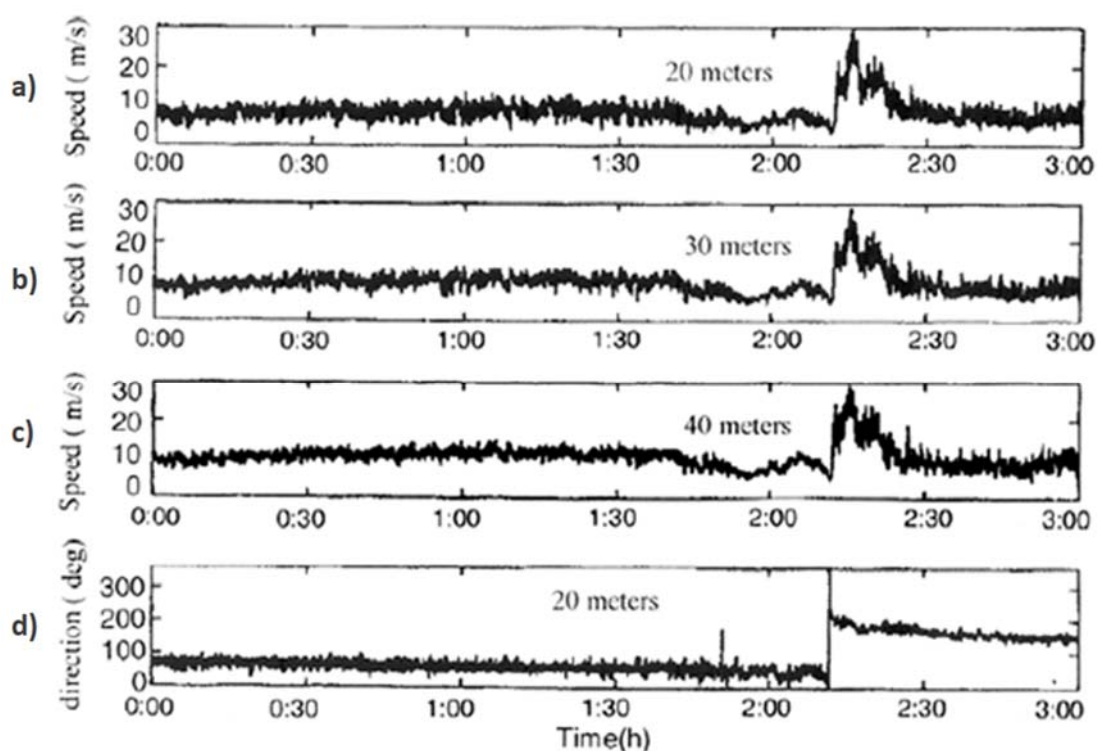


Figure 54. Velocity-time record during a TS event in Passo Fundo – RS at a) 20 meters; b) 30 meters, and c) 40 meters and change in wind direction. Source: Paluch et al. (2003) apud Ponte and Riera (2010).

Gast (2003) conducted a field experiment using seven mobile towers installed along a 1600 meters array at Reese Technology Center – see towers schematically presented in Figure 55. Tower 1 captured all meteorological parameters using a sampling rate of 1 Hz, the other towers used a sampling rate of 2 Hz. Tower 4 consisted of anemometers used at 5 different levels, tower 5 had wind anemometers at three different heights, and other towers had one single anemometer installed at 10 meters. Some towers used propeller anemometers; others used ultrasonic anemometers.

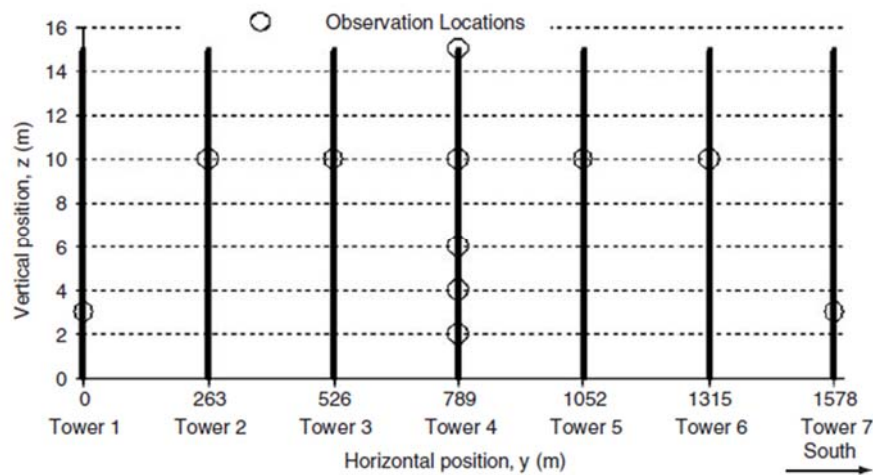


Figure 55. Seven towers configuration utilized in Gast (2003) during the register of the RFD and Derecho. Source: Chen and Letchford (2006).

The focus of this experiment was to understand the TS outflow properties at lower levels of the atmosphere, closer to the ground, focusing on thermodynamics and kinematic properties. Besides the tower datasets, data from a Doppler Radar and from the West Texas Mesonet Station were also used to classify and study the TS event, which was conducted in 2002 during a field experiment named Thunderstorm Outflow Experiment. Gast (2003) obtained high-resolution data from the RFD and derecho and analyzed the wind profile and turbulence intensity for both events. In Figure 56, is presented the wind speeds registered during the RFD a) and Derecho b) at 10 m in an isometric view.

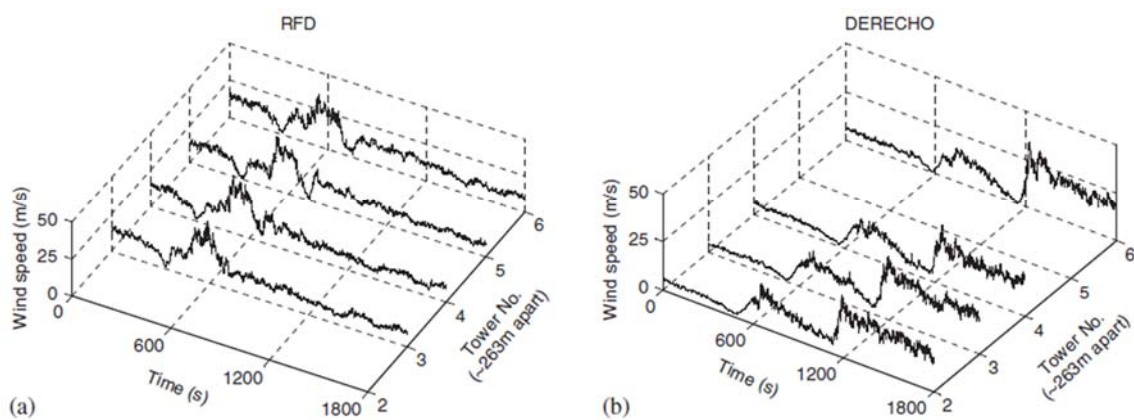


Figure 56. Isometric view of wind speed for a) RFD and b) Derecho at various at 10 m in height. Source: Chen and Letchford (2006).

Gast (2003) confirmed with the data obtained from the full scale measurements that many of the pre-existing theories in TS winds were valid, including that a) the conversion of wind speeds from 3-m heights to 10-m height using log wind profile produces erroneous results; b) the use of traditional turbulence methods cannot be applied to non-stationary events, though for some events, the time averaging method can be used to generate stationary segments of a non-stationary time history event; c) the existence of a two peaks surge for RFDs cases during the maximum wind peaks, lasting about 6.5 minutes and varying greatly over distances of roughly 800 meters; d) the kinematic structures of TS wind events vary from event to event.

Gast (2003) also analyzed the thermodynamics of the TS wind events. The RFD case presented a characteristic increase in temperature and a small decrease in relative humidity, suggesting various forcing mechanisms besides precipitation and evaporative cooling. For the derecho, the reverse was observed, the temperature decreased, and the relative humidity increased. The barometric pressure fluctuated drastically during both events, presenting an initial non-hydrostatic increase during the downdraft, followed by a rapid decrease during peak gust, ending in a hydrostatic increase of the pressure.

Figure 57 and Figure 58 presents the wind profiles obtained in Gast's study the RFD and the derecho, respectively, at different times. Both profiles were obtained from two-minute mean ($U_{Mean} = 120 \text{ sec}$) and presented similar transitioning aspects from the beginning of the event to the end. Also, both profiles were very different of each other, where the RFD profile had more of a linear shape and this fact shows how difficult it can be to defining a typical wind profile for TS events specially at lower levels of the atmosphere that suffer major influence of the terrain.

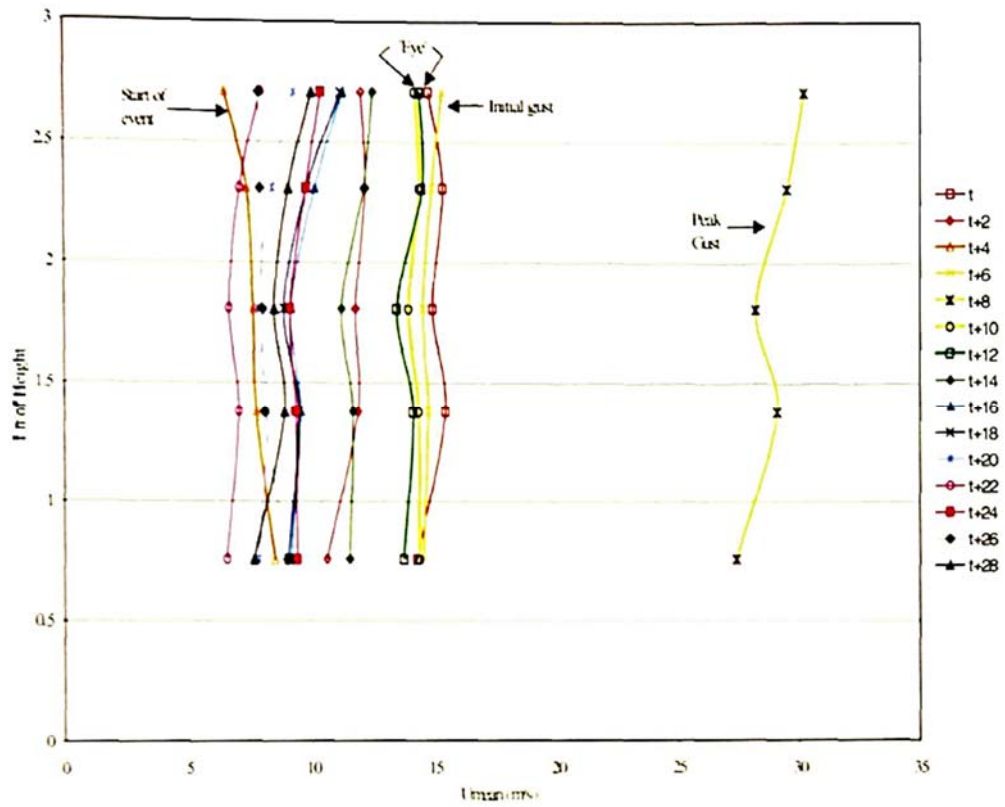


Figure 57. RFD event Vertical mean wind profile (U_{mean}) at different time steps. Height is given in natural logarithm. Source: Gast (2003).

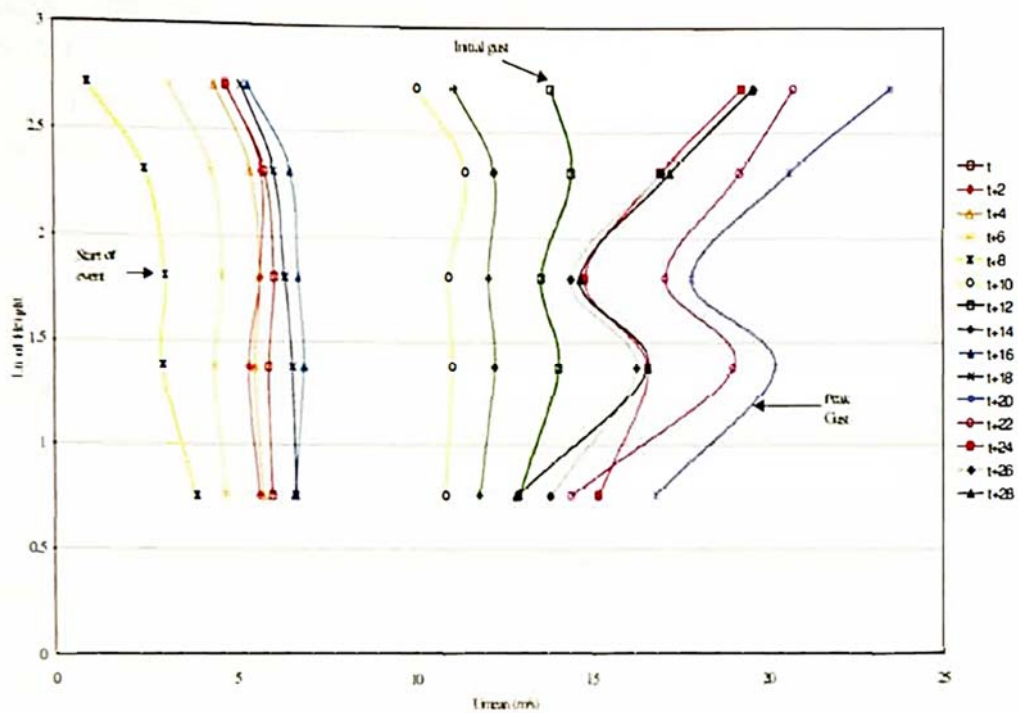


Figure 58. Derecho event vertical Wind Profile (U_{mean}) at different time steps. Height is given in natural logarithm. Source: Gast (2003).

Choi (2004) performed studies in Singapura using a 150 m tall meteorological tower in which horizontal and vertical wind speeds, wind direction, temperature and humidity, barometric pressure and rainfall are monitored at 100 Hz. For normal conditions, 10-min statistics are recorded, although during high-wind days, raw data is recorded for further evaluation. In this experiment, 5-min peak mean wind speed are used to study the transient characteristics of 36 thunderstorms. It was found that the highest wind speed is observed sometimes at the lower levels, but other times at the highest levels. The factors found to influence the most the wind profiles are the location of the thunderstorm cell center, the intensity of the storm (kinematic and thermodynamic properties), and ground roughness.

Using the exponent law obtained from a non-thunderstorm (NTS) profile, Choi (2004) analyzed how the TS profiles obtained may fit the typical NTS power exponent profile and proposed four main profiles in this case. For Type I, all data points fit reasonably well with the power profile of the NTS exponent, and with the highest wind speed at the top level. For Type II, the highest wind speeds occurred at the lower levels. Wind speeds at all levels fall within the NTS power exponent profile fitted to the lowest level data point. Type III is like Type II except that wind speeds at other levels exceed the profiles fitted to lowest level and the top-level data points. For Type IV, the highest wind speed is recorded at the top level. All wind speeds are less than the profile fitted to the top-level data point but exceed the profile fitted to the bottom point.

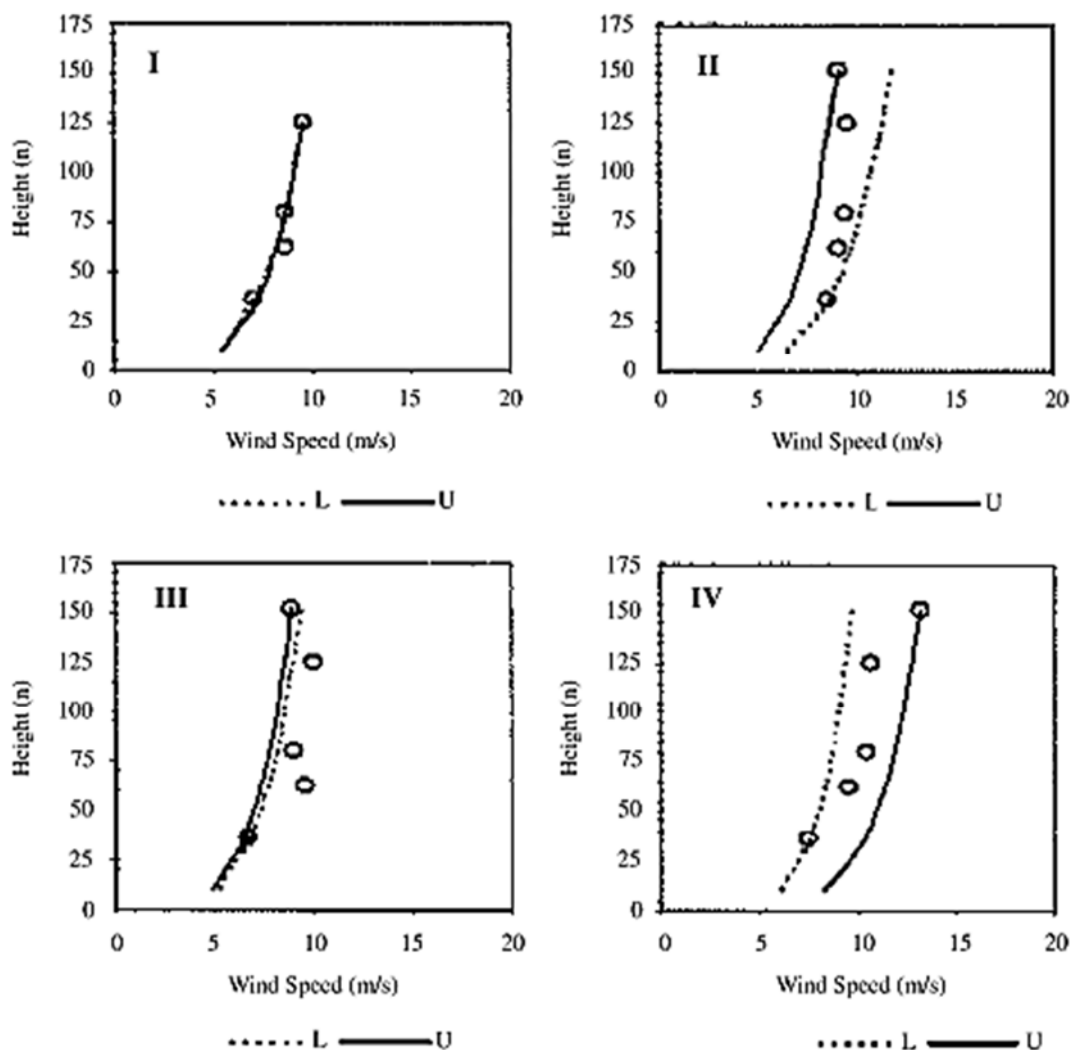


Figure 59. Four types of TS wind profiles (dashed line) proposed comparatively to non-thunderstorm events (continuous line). Source: Choi (2004).

To acquire further insight into the different profiles, the movement and location of the thunderstorm cell (s) was further studied. It was found significant variations of thunderstorm cell movement and location within each type of profile; however, certain trends of variations were observed. In Figure 60, is shown four typical profile configurations are presented, where the gray continuous line represents the 5-min average velocity and the dotted dark line represents the 3-sec peak gust event. In the same figure, in a) is shown the Type I profile captured in 03/23/2001 and it represents a profile observed when the storm center is far away (10 km or more) from the measuring station. In the same figure, in b) and in c) events captured in 12/25/2000 and 01/29/2001 are shown respectively and they represent type II and Type III, in which the storm cell is very close to the observation station. In d) is shown the event

captured in 05/21/2002 Type IV profiles that are more random, they may occur further away or closer to the station.

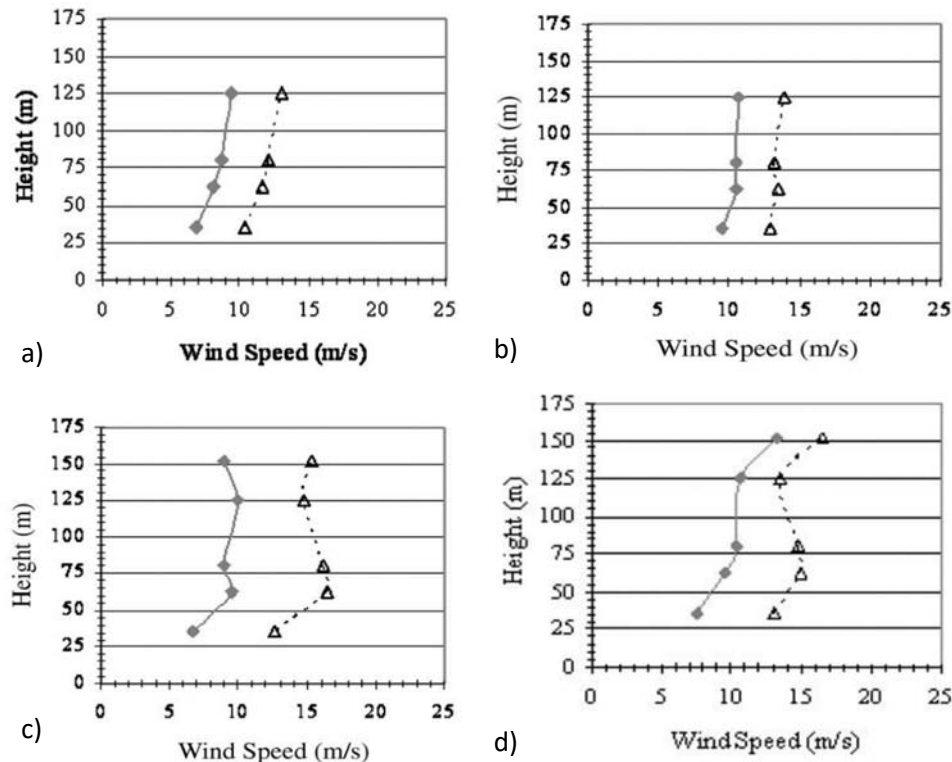


Figure 60. Typical TS outflow profiles identified by Choi (2004). Source: Adapted from Choi (2004).

Skinner *et al.* (2012) used the Texas Tech University ka band Mobile Doppler Radars Mobile Doppler–TTUKa to scan the outflow characteristics of a RFD event generated by a supercell, occurred in Dumas – State of Texas, US; and a MSC System thunderstorm event in the Reese Center–Texas the focus of this study was to validate the use of this technology to study to characterize thunderstorms outflows. No vertical profiles of such measurements were published.

Later, Gunter and Schroeder (2015) as part of the same group, advanced the investigation of three outflow events using a similar methodology. A field project called Project SCOUT was designed to target the collection of engineering-relevant data in organized thunderstorms. Because of the novelty of the method proposed, two validation experiments were conducted near the 200 m tall instrumental tower at the National Wind Institute field site at Reese Technology Center in Lubbock, Texas. The results showed a degree of overestimation greater than approximately 50 m (mean error approx. 2.2m/s), but acceptable confidence for

applications at heights above 50 m (with error approx. 1 m/s), moreover there was a great similarity in the profile shapes between both measurement methods.

Given the validity of the method proposed by Gunter and Schroeder (2015), three thunderstorm events were investigated in different localities in the United States and extensive data of their vertical properties were made available. The maximum profile of each event is showed in Figure 61 for 1-min averaging time, 10-min averaging time, and event mean, whereas in a) is presented the profile for the event observed in Syracuse – Kansas or (SYR), in b) Truscott – Texas (TRUS), and in c) Pep – Texas (PEP).

SYR event was developed into a multicellular complex that propagated into southwestern Kansas, the area was characterized by Exposure C (ASCE, 2010), while TRUS event was a non-severe thunderstorm outflow associate with a large squall line associated with a cold front passed through central Texas, this profile presented a power exponent profile, close to a typical ABL profile. Finally, PEP event was the most intense one, the outflow product of a large thunderstorm complex formed in New Mexico, which traveled across west Texas producing widespread damage over the location primarily characterized by flat open terrain (Type II)

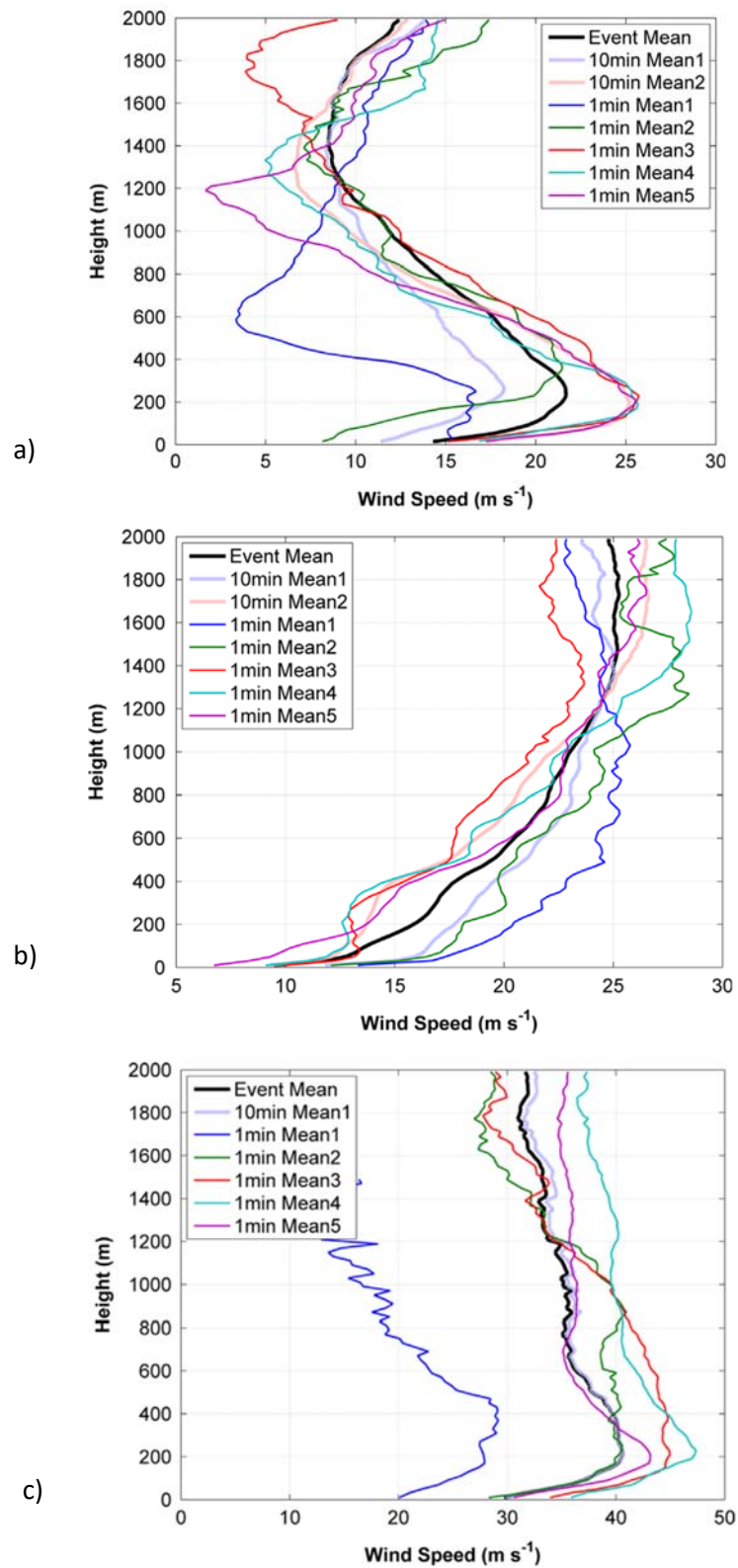


Figure 61. Various dual-Doppler mean 1-min mean wind speed profiles from and 10-min mean profiles for a) Syracuse – Kansas (SYR), b) Truscott – Texas (TRUS) and c) Pep – Texas (PEP). Source: Gunter and Schroeder (2015)

Lombardo *et al.* (2014) performed a series of typical maximum ABL events measurements at Texas Tech University from 2003 to 2010 at the Wind Engineering Research Field Laboratory (WERFL), using a 50 m tower instrumented at 5 levels in an open "Category C" exposure "ASCE, 2010) sampling data at a frequency rate of 50 Hz. Later, in partnership with Reese Technology Center 8 major outflow events were captured using a 200 meters tower instrumented at 10 levels, with the support of Doppler Radar data, automated weather stations data (ASWS), and the West Texas Mesonet. None of the profiles obtained fully resembled the time story of AAFB downburst (FUJITA, 1985) nor existing downburst models. This may be as previously suggested by Holmes *et al.* (2008) that none of the events have passed directly through the measuring point. Also, the secondary wind speed has practically no consequence to the wind engineering compared to the overall peak wind speed.

In Figure 62 are showed the maximum profiles obtained by Lombardo for four of the most severe events. The profiles are presented at 5 different averaging times (3s, 8s, 34s, 68s, and 136s), with 3-s profiles, where the right side of each chart and 136s to the far left. In these observations, the maximum profile was the one on June 4, 2009, and it resembles an ABL profile for all averaging times. This storm was produced by a bow-echo/super cell thunderstorm (organized storm). For May 21st, 2008, the TS event has generated a uniform profile (straight up) assuming a log profile at $t > 34$ -s. The events of March 08, 2010, and August 12, 2009, assume a ABL shaped profile for averaging $t > 68$ seconds for the former and $t < 136$ for the latter. These finds highlight the importance of adopting a shorter time scale in thunderstorm-prone areas. For 3-s, the overall peak gust occurred between 40 and 80 m. As a rule of thumbs, the use of 20-s to 30-s moving averages is enough to capture typical intermediate fluctuations properties of TS wind (LOMBARDO *et al.*, 2014; MASON, 2017; SOLARI *et al.*, 2015).

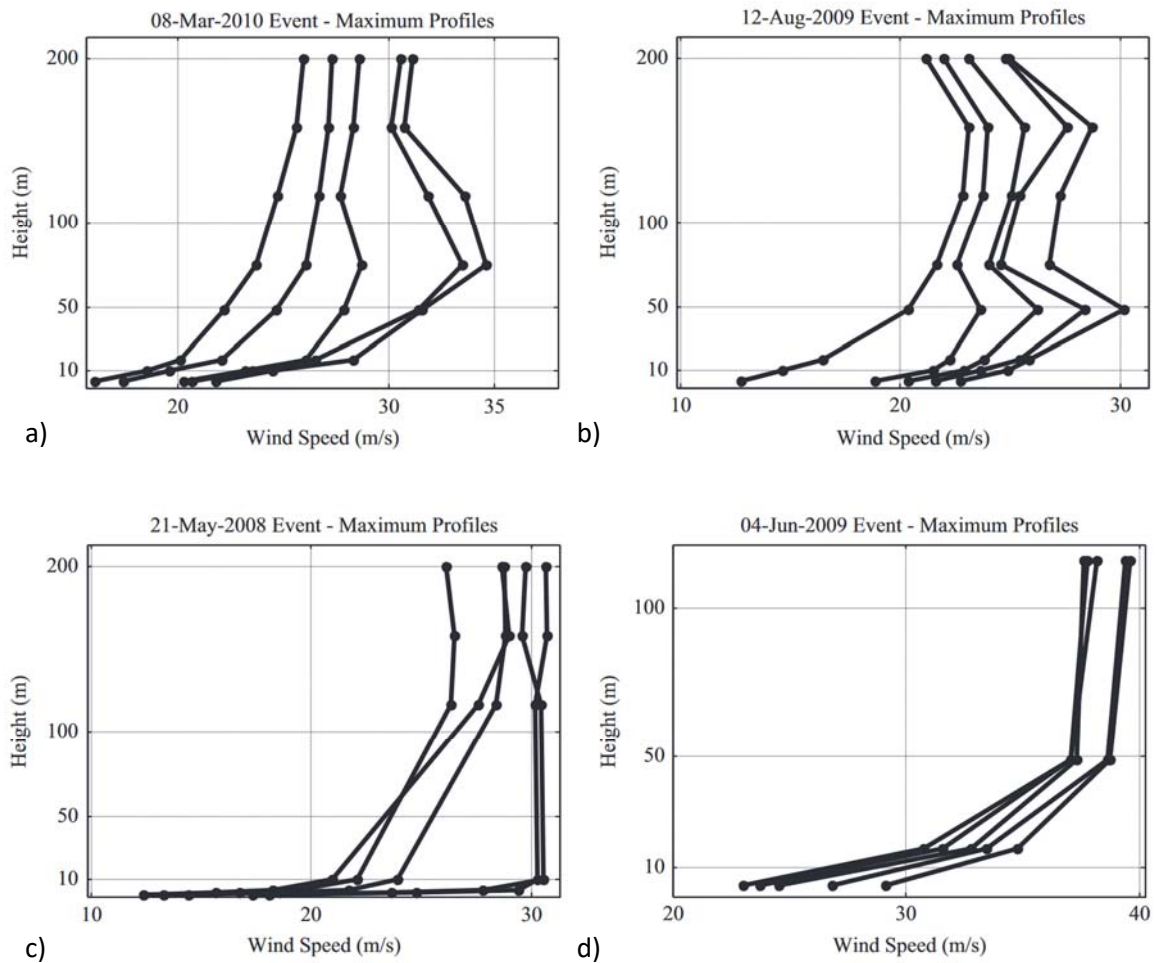


Figure 62. Maximum gust profiles for averaging times of 3s, 8s, 34s, 68s, and 136s. The maximum profile is the far right and increasing averaging times continue to the left. In a) is shown the profile for the event in 08. Source: Lombardo *et al.* (2014).

Solari *et al.* (2015) as part of the European Project "Wind and Ports" used in-situ wind monitoring network composed of 22 ultrasonic anemometers at various heights, 3 LiDAR's and an extensive surface weather stations network. The anemometers' sampling rate was of to 10 Hz attending specific to the dominant characteristics to the concerns of wind engineering. Using a semi-automated procedure implemented by Gaetano *et al.* (2014), 64 thunderstorms events were identified, resulting in 93 thunderstorm records using 15 m/s as a threshold.

Vertical measurements of a thunderstorm wind profile were made available in Burlando *et al.* (2017, 2017a) and Solari *et al.* (2020), in these works a downburst event occurred in Port of Livorno, in September 13th, 2015 is discussed in details. In Figure 63 a) is shown the wind speed velocity over time at 120 m above ground. In b) these wind profiles are plotted at three-time steps. The nose-like shape profile appears clearly during the ramp-up phase (in which the flow

is developing and increasing in velocity) at about 295-s and the use of 20-s, 30-s, and 40-s moving averages were capable to capture the typical thunderstorm outflow profile. Note that in this case there was a second absolute maximum wind speed at about 500-s, but the authors suggested that the peak velocity was likely due to the heavy rain that followed the downburst, affecting the LiDAR and reading creating an erroneous reading, therefore it should be ignored.

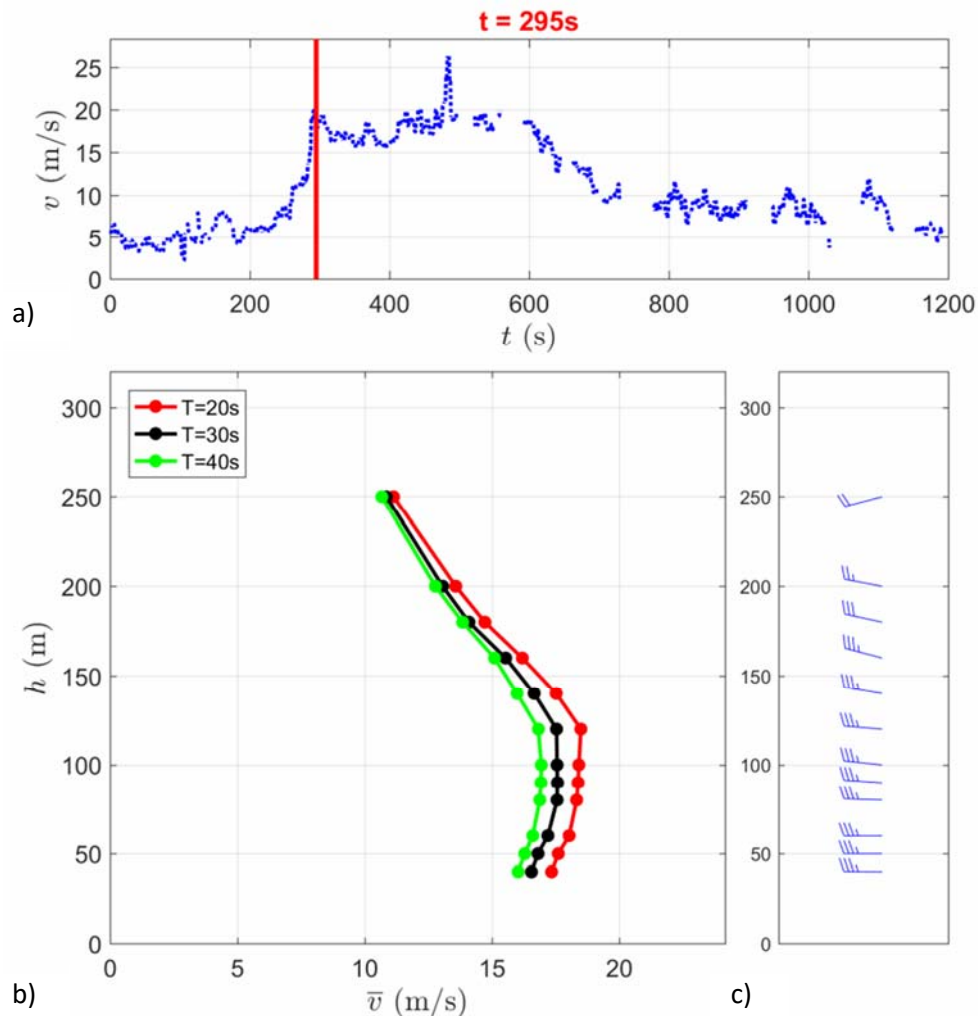


Figure 63. LiDAR profiler measurements in the Port of Livorno, 13 September 2015: a) velocity at 120 m above ground; b) evolutionary vertical wind velocity profile at time 295-s, for different time averaging, and c) wind direction at time 295-s. Source: Burlando et al. (2017a).

Repetto et al. (2018) used Global Information System (GIS) web-based platform to promote safe management and risk assessment of complex structural systems exposed to extreme mixed climates. The non-synoptic thunderstorm event shown in Figure 64 was captured using LiDAR technology on June 14th, 2014. The profile on the left shows the vertical wind records (downwards) for the downdraft; and the profile in the right shows the horizontal outflow velocity. The gray line in the far right represents the maximum dataset for 1-s measurements,

whereas the empty gray circles are instant measurements along the 10 min average. The 10-min horizontal profiles in the center represented the filled black dots. Note that in this example, the 10-min averaging presented maximum velocity values captured between 60 and 70 m.

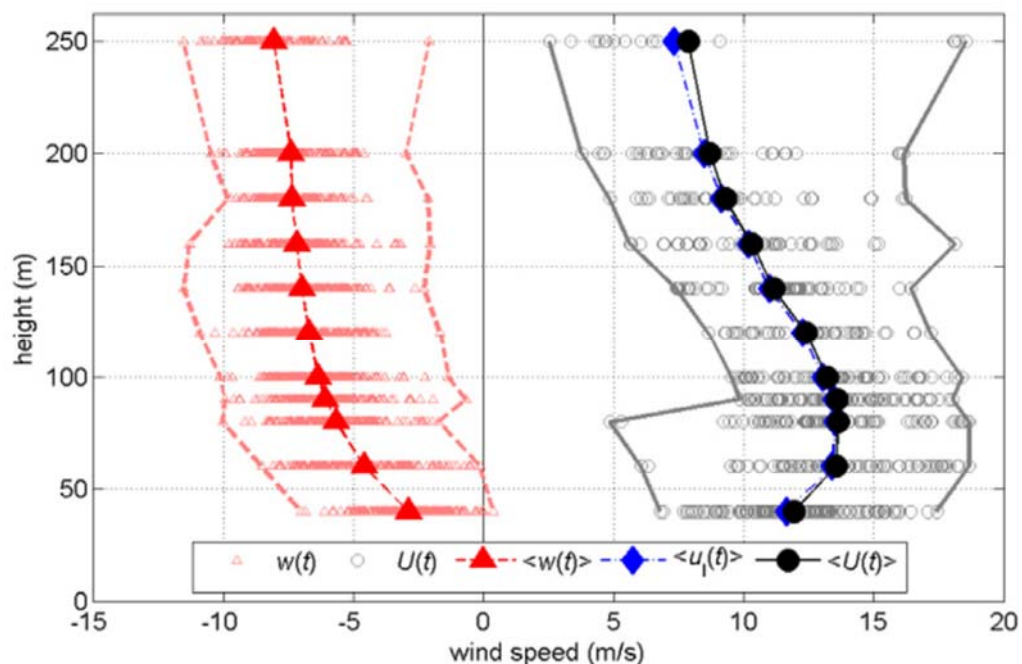


Figure 64. Intense non-synoptic event detected by LIDAR in Port of Livorno on June 14th, 2014. In the Left is shown 10-min mean vertical wind velocity and, in the right, it is shown the 10-min mean horizontal wind velocity. The hollow triangles and circles are the 1 sec measurements along the 10 maximum min average. Source: Repetto *et al.* (2018).

Using the same monitoring network, Zhang *et al.* (2018) continued the work of Solari *et al.* (2015a) and Gaetano *et al.* (2014) and captured a wide dataset of 277 wind velocity records of transient winds characterized as thunderstorm outflows. An extensive statistical analysis was developed aiming to propose a new parametrization for the turbulent fluctuations of TS winds, although the focus herein was not to capture the profiles properties, rather to characterize surface the TS wind properties of these measurements.

In northern German, Stengel and Thiele (2017) proposed an innovative way to capturing the wind data from a presumable downburst by installing sensors along two spans of overhead transmission lines. In this experiment, signals from 13 anemometers and inclinometers were continually recorded with sampling rate of 25 Hz aiming to measure the vertical misalignment of the sensors during intense wind events. A strong TS wind event occurred in the fall of 2015 causing the collapse of towers close to the place of measurement. The authors suspect the

data obtained was a product of the outflow from the referred downburst. In Figure 65 is presented the measurement points along the conductors of the three suspension towers. In this example a vertical wind profile could not either be reconstructed from the dataset made available, but it represents an important step towards characterizing the effects of TS event on transmission lines.

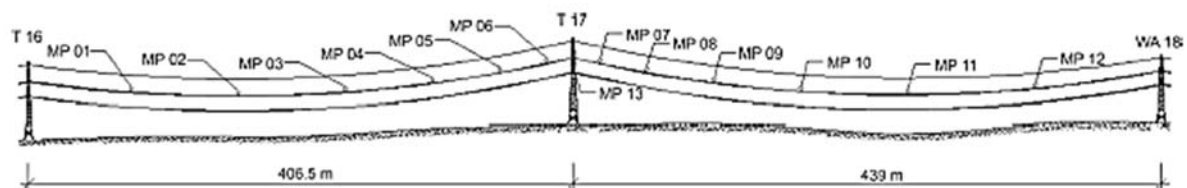


Figure 65. Elevation of test section with measurement points. Source: Stengel and Thiele (2017).

Figure 66 shows the wind data recorded over time in an isometric view of the referred event. It is noticeable the simultaneous increase in wind speed with height and time in all the sensors. At the beginning, the wind speed was almost zero and suddenly increased from 20 to 30 m/s, it kept varying at high wind speeds for approximately 10 minutes until decay to the initial values. It was also observed that there was a rapid decay in temperature (about 10° C) and change in wind direction.

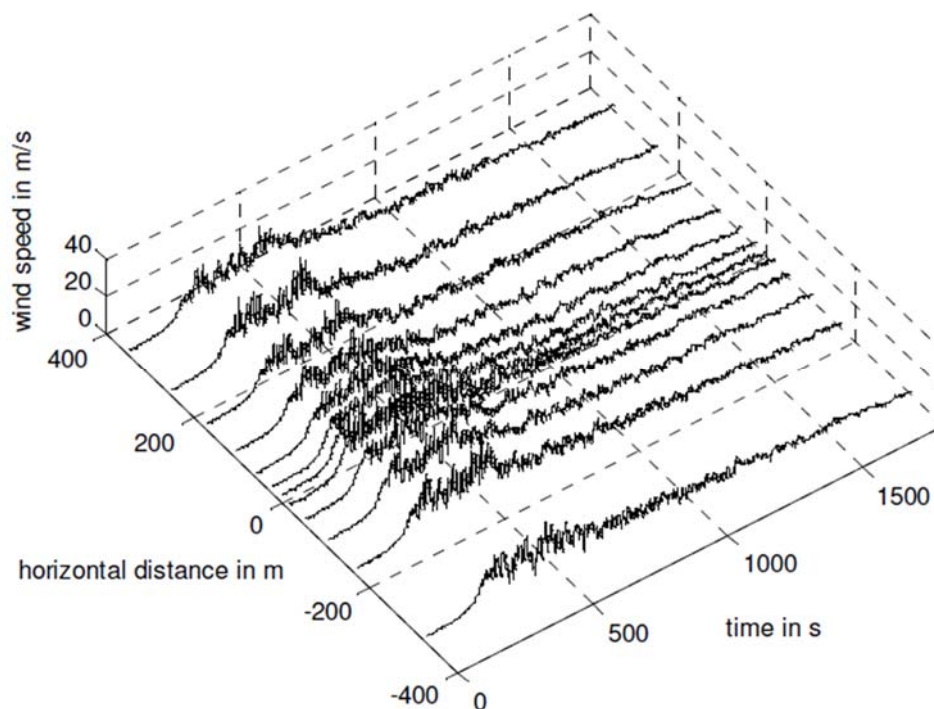


Figure 66. Wind speed time history on 12 positions along the time during a downburst event in Northern Germany in the fall of 2015. Source: Stengel and Thiele (2017).

Zhang *et al.* (2019) analyzed the vertical profile of 70 thunderstorms using nine ultrasonic continuously collecting wind speed data simultaneously with a sampling rate of 10 Hz placed in on a tower at nine different heights from 8 m to 280 m. The terrain category is referred as terrain C (urban area) according to the Chinese National Standard "Load Code For The Design of Building Structures" (GB50009-2012), in which there are 4 categories of ground roughness, where A is used for sea and lake; B for open countryside; C for towns and cities; and D for center of large cities (JIN *et al.*, 2012).

It is further interpreted in this study that Category C would be equivalent to Category IV in the NBR 6123, although it is important to note that further analysis of the terrain where the tower is located has shown that the structure it is in fact embedded in a highly dense urban environment, composed of a park with trees and lower building (Category IV as per NBR 6123) that runs in the west-east directions, but there are several high rises are in the vicinity of the building, see northern and southern boundaries buildings (Category V as per NBR 6123), which can drastically affect the final maximum profile.

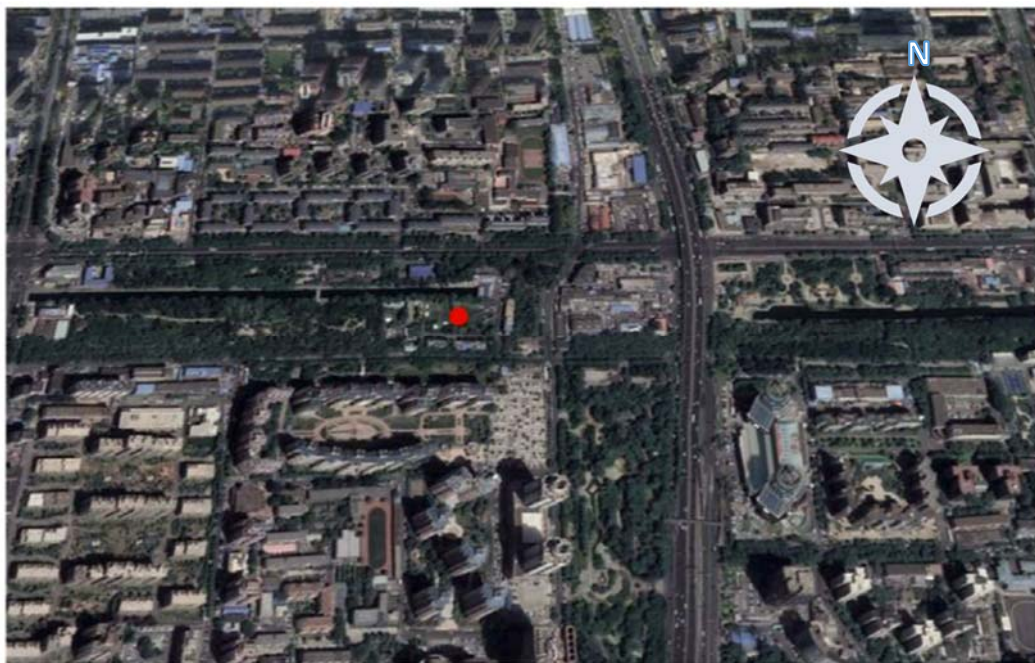


Figure 67. Picture of the urban environment in Beijing where the anemometric tower used to capture the TS wind profile event in Zhang *et al.* (2019). Source: Zhang *et al.* (2019).

Zhang *et al.* (2019) analyzed not only the slowly varying wind profile from such registers but also analyzed the wind direction, turbulence intensity, reduced turbulent fluctuations, turbulence integral length scale, power spectral turbulence intensity modulation or such TS

wind events. Some of the finds highlight that this tower in particular is in a highly dense urban environment, which creates greater turbulence intensity closer to the ground when compared to studies such as the Wind, Ports, and Sea Programs. It was shown that moving averages of 32-s or less are needed to capture the structure of the flow due to the transient characteristics of thunderstorms outflows, also the most intense part of the thunderstorms was observed between 143 to 333-s from the beginning of the ramp up measurements.

One thunderstorm outflow event was examined in the published research and is further analyzed in this work. In Figure 68 the thunderstorm outflow record that occurred in Beijing on June 10, 2016, is shown for its 1-min moving average wind speed. In a) the record is shown the evolution over time at different heights; in b) is shown the same information, but as a 2D profile for 30-s moving average and in c) is shown the evolution of the profile direction over time. Like what was observed in Burlando *et al.* (2017), the sudden appearance and dissolution of the nose-shape profile was also identified in these measurements. Note that there are two moments in which the record achieves a maximum profile: the first one at time step 15:00 and the second one at 15:01. It is highlighted that the first one presented the typical nose-like profile, with maximum velocity between 140 and 200 m, although in the next minute the profile assumes a more linear shape with velocities of about 20 m/s from 50 m to 250 m, it is thought that this occurs due to the influence of the surrounding buildings that affects the considerably once there was a drastic change in wind direction.

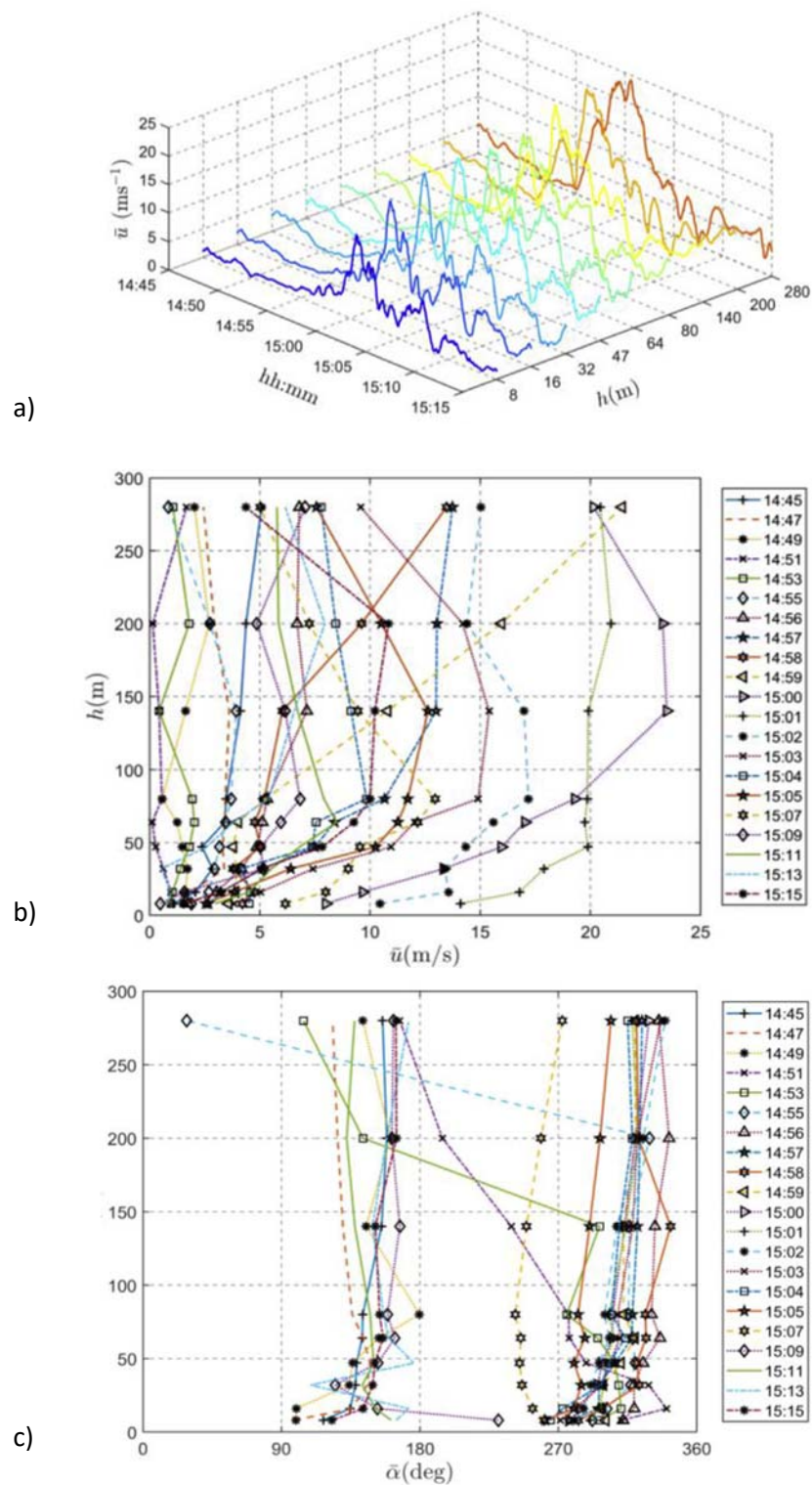


Figure 68. Shown the 30-min long record of the thunderstorm outflow in Beijing on June 10, 2016. In a) the data is shown in an isometric chart with the tower's height increasing in the z axis $h(\text{m})$ (colored graphs), time is presented in the x axis and velocity in the y axis. In b) the same data but presented in a 2D graph for different time steps of the outflow and c) is shown the evolution of the profile direction over time. Source: Zhang et al. (2019).

In Figure 69 is shown a compilation of four full-scale from Mason (2017) of vertical TS wind measurements from Hjelmfelt *et al.* (1989), Lombardo *et al.* (2014), Gunter and Schroeder (2015), and Repetto *et al.* (2017) at their maximum stage. Different methods were deployed to capture the shown datasets, equipment had different sampling rates, and averaging times were different from event to event. Even though they vary significantly, it is still possible to assess several similarities within these measurements, such as the horizontal wind speed profiles presented similar magnitudes, besides that they also showed the typical nose-like profile, and higher velocities at lower levels comparatively to ABL profiles.

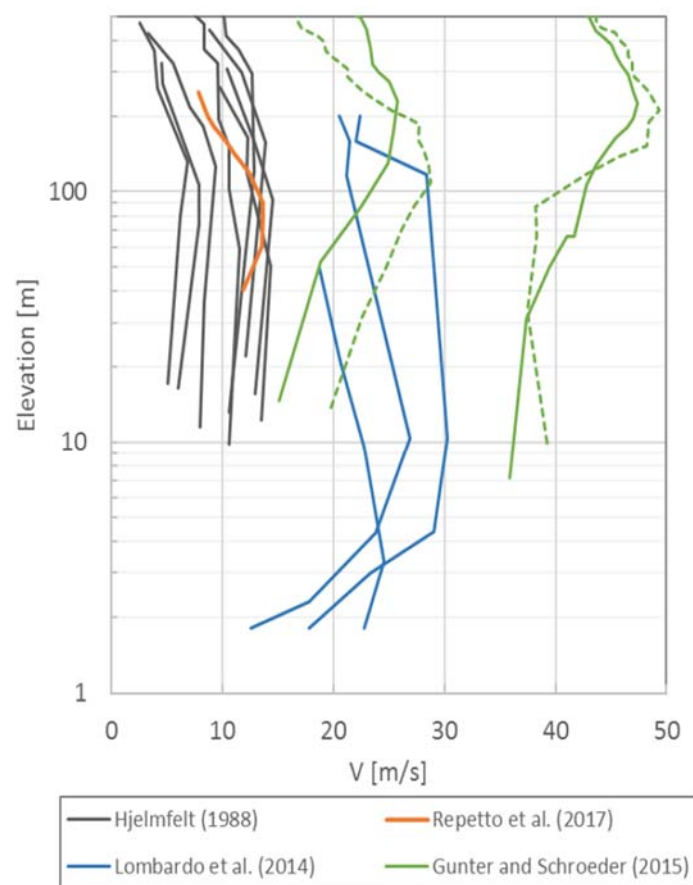


Figure 69. Compilation of four maximum TS wind outflow profiles. Where black lines are Hjelmfelt *et al.* (1989) TS wind profiles from various events; blue lines are Lombardo *et al.* (2014) TS wind profiles; green lines are Gunter and Schroeder (2015), where dash lines represent the divergent flow velocities; and orange line refers to Repetto *et al.* (2017) profile. Source: Mason (2017).

Regarding the information presented in this section, in the following some of the preliminary finds on TS wind speed profiles are presented.

- a) TS winds generate wind speed peaks at lower levels when compared to ABL profiles, these peaks may occur anywhere between 50 and 250, eventually extending until 300 to 350 meters, depending on the roughness effects to the profile.
- b) TS wind profiles vary significantly from one event to another. These profiles usually show either a nose-like profile or a more linear-like profile.
- c) The averaging time chosen to depict profiles is crucial when aiming to capture the transient characteristics of TS winds. Most authors showed that 1-min (BURLANDO *et al.*, 2017a) and 30-s (SOLARI *et al.*, 2015) or less are ideal to capture the transient characteristics of TS winds.
- d) The stronger the background wind, the closer the profile presented is of a typical log or power ABL profile.
- e) The height in which the maximum wind speed is shown varies also with time as the event evolves, therefore there are events in which exist over one single maximum profile.

The analysis of the profiles discussed in this section makes it clear that thunderstorms events produce wind vertical profiles that significantly differ from the typical properties of synoptic wind events. Given the large variability in properties from one event to another, full-scale measurements are the most reliable way to the basic properties of these events, but field studies and equipment are costly and institutional funding is still limited. Although, with recent advances and refinement in technologies—such as Doppler Radar, LiDAR technologies, mesoscale weather station networks, and ultrasonic anemometers have brought a renewed perspective on TS winds properties, including a better understanding of the typical variability of such properties from one event to another.

Strategies to select the right instrumentation and capturing strategies to obtain full-scale measurements are a key element to advancing the knowledge regarding the properties of TS wind profiles. Each one of the methods adopted within a wide-range array of research developed has pros and cons regarding their capturing resolution and reliability. For instance,

the *in-situ* datasets taken from multi-level ultrasonic anemometers towers tend to present better resolution and accuracy, and for that reason, are preferred over remote sensing technologies specially for study of wind-structures interactions. Although, it is important to highlight that remote sensing technologies are rapidly catching up, and they present various advantages such as the fact that these systems can obtain dataset information from distance points, they also have the option of being built mobile, therefore increasing the chances of capturing wind data of rapidly and small-scale outflow events.

In Appendix B is presented a complete discussion on thunderstorm outflow modeling, and in Chapter 4, some of the full-scale profiles are analyzed in detail aiming to propose best fit functions that best describe the maximum TS wind profiles available in the literature. Lastly, in Table 2 is presented a summary of the datasets cited in this section. This table is divided into two portions, the first includes the reference, the nomenclatures chosen to refer to each TS event, the year, method, and place of observation of the TS event. In the second portion of the same table, information pertinent to the maximum event is included, such as the maximum velocity captured in the field measurement (at any height), then the averaging time in which this dataset is presented, the terrain exposure (adapted to the equivalent in the NBR 6123), and the storm configuration (either isolated or organized storm).

Table 2. Table of vertical profile measurements of TS wind outflows available in the literature discovered within the scope of this research. Source: Author.

#	Reference	Nomenclature Utilized	Year of Event	Observation Method	Place	Project or Institution Related	Max Event			
							V _{Max} [m/s] at any height)	Averaging time <i>t</i>	Assumed Terrain Exposure NBR 6123	Storm Configuration
1	Foster (1958) ⁷	Downdraft winds	1955	Upper-air Sounding	US – KA State	US National Weather Service	47	N.I.	N.I.	N.I.
2	Sinclair et al. (1973) ⁷	6 Gust Front	1973	150 Tower	US – OK & FL States	NASA	32+	1-sec	Cat II	Isolated
3	Fujita (1976) ⁷	1 Downburst	1975	Radar & SWS	US – NY City	JFK Airport	28	1-min	N.I.	Organized (Hook Echo)
4	Fujita and Wakimoto (1981) ⁷	Multiple Microburst Events Analyzed	1980	Doppler Radar & Ballistic Analysis	US – Cities of Chicago Detroit	University of Chicago	63 ± 10	N.I.	N.I.	Organized
5	Fujita (1983) ⁷	Microburst	1983	SWS	US AAFB ³	University of Chicago	67	N.I.	N.I.	Organized
6	Wilson et al. (1984) ⁷	Microburst	1982	Doppler Radar	US – CO State	NCAR – NSF ¹	48	Gust Peak	N.I.	N.I.
7	Fujita (1985a) ⁷	Microburst	1978 to 1982	Doppler Radar & SWS	Northern Illinois / Denver - CO	University of Chicago &	31.3 (NIMROD) & 32.5 (JAWS)	1-min	N.I.	N.I.
8	Hjelmfelt (1988)	27 Cases of Microbursts Isolated and Inline	1982 to 1984	Radar & SWS	US – CO State	JAWS Project	Average 26 (in line) 12 (isolated)	2-min (Radar update Rate)	N.I.	Organized (in line) Isolated

#	Reference	Nomenclature Utilized	Year of Event	Observation Method	Place	Project or Institution Related	Max Event			
							V_{Max} [m/s] (at any height)	Averaging time t	Assumed Terrain Exposure NBR 6123	Storm Configuration
9	Sherman (1987)	Microburst	1977	190 m Tower	Australia	Aeronautical Research Laboratories	18	1-s	Cat II	Isolated
10	Garstang et al. (1998)	31 Convective Gusts > 10m/s	1987	Four 40 m towers	Brazil - Amazon Basin	University of Virginia	17	1-min	Cat V	N.I.
11	Choi and Hidayat (2002)	2 TS events	1983 to 1997	20 m and 125 m Towers & SWS	Singapore	Nanyang Technological University	23.1	30-s	Cat IV	N.I.
12	Gast (2003) & Orwig-Gast and Schroeder (2005)	1 RFD 1 Derecho (MCS)	2002	7 Tower & Radar & Mesonet	US – Texas State	TTU ⁴	40 (RFD) & 35 (Derecho)	2-min	Cat II	Organized
13	Paluch et al. (2003)	1 TS Event	2007	Tower	Brazil - RS State	UPF ⁵	30	3-s	Cat II	N.I.
14	Choi (2004)	36 TS Events	2001 to 2002	Tower & Radar	Singapore	Nanyang Technological University	16	3-s	Cat IV	Organized
15	Skinner et al. (2012)⁷	1 MCS & 1 RFD	2012 & 2010	Tower & Radar	US – TX State	TTU ⁴	40 (RFD) & 24 (MCS)	20-s	N.I.	Organized

#	Reference	Nomenclature Utilized	Year of Event	Observation Method	Place	Project or Institution Related	Max Event			
							V_{Max} [m/s] (at any height)	Averaging time t	Assumed Terrain Exposure NBR 6123	Storm Configuration
16	Gunter and Schroeder (2015)	3 TS Outflows	2011, & 2012	Radar & Towers	US – TX	TTU ⁴	26 (SYR) & 47 (PEP)	1-min	Cat III (SYR) & Cat II (PEP)	Organized (both events)
17	Lombardo et al. (2014)	8 TS Ramp-up Events	2003 to 2009	2 Towers	US	Rensselaer Polytechnic Institute & TTU	36	3-s	Cat III	Organized
18	Burlando et al. (2017, 2017a), & Solari et al. (2020)	1 Downburst	2015	LiDAR, & SWS	Italy	University of Geneva, Beijing Jiaotong University, & WindEEE	20	Presented as 20-s 30-s 40-s	Cat II (System coming from Sea)	Organized
20	Repetto et al. (2017)	1 non-synoptic event	2014 and 2015	LiDAR	Italy	University of Geneva	30	1-s	Cat II	Organized
21	Zhang et al. (2019)	70 TS Events	2013 to 2017	325 m tower	China	Chinese Academy of Sciences (CAS)	23.5	1-min	Cat V (Intensely Urbanized)	Organized

¹ National Center for Atmospheric Research - National Science Foundation

² SWS – Surface Weather Station

³ AAFB - Andrews Air Force Base

⁴ TTU – Texas Tech University

⁵ UPF - Universidade de Passo Fundo

⁶ BAM - Federal Institute for Materials Research and Testing

⁷ Profile not made available or cannot be used for wind engineering purposes.

N.I. – Not Informed

3.2. TURBULENCE CHARACTERISTICS OF NON-TORNATIC THUNDERSTORM WINDS

Turbulent flow is characterized by randomness or irreproducibility of motion of individual particles at determined time and space stamps and it can only be defined statistically. It occurs naturally depending on the viscosity of the fluid; the flow turns unstable because of its inertial components that have high potential energy gradients when the flow is moving at higher speeds beyond a critical velocity.

Turbulence characteristics can be essentially defined by the four main criteria:

1. Increase or periodic disturbance of velocity, temperature, and pressure.
2. Development of bi-dimensional instabilities.
3. Development of tridimensional vortices and high frequency of harmonics.
4. Establishment of an aleatory process transferring energy from larger to smaller scales.

In Figure 70 a) is shown a typical wind record, the horizontal line on the upper middle of the record represents the average sum of wind speed (\bar{v}) and each data point is given by the random fluctuation of velocity v' around the mean added to \bar{v} . In b) is shown the typical frequency distribution chart (left) formed by this wind record considering a Δt interval, where the highest frequency of values is found within the center part of the curve, which statistically represents the average speed of the flow, meanwhile the remaining velocity values are considered to be the fluctuations of the flow.

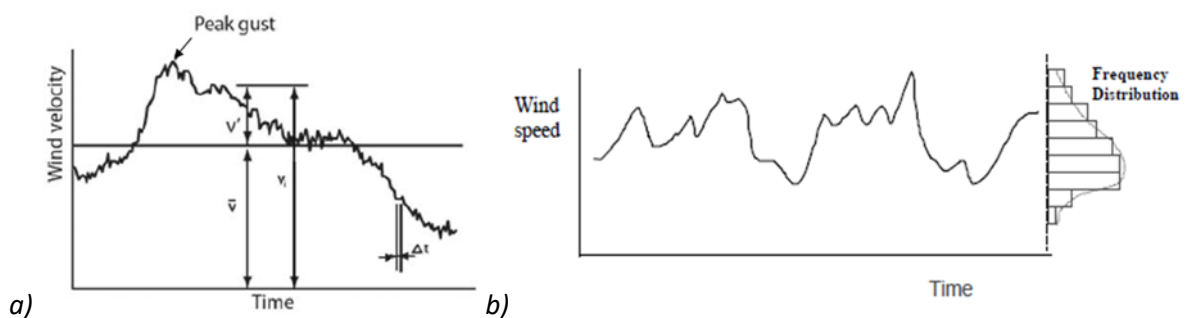


Figure 70. Typical wind records over the length of the record in which a) is showed the random fluctuation of velocity around the mean and in b) is showed the typical frequency distribution where the highest frequency of values is found within the center part of the curve. Source: Liu (1990).

The wind frequency and probability distribution vary depending on the characteristics of the wind datasets and length of the record available. For instance, a short-term distribution of an extreme wind record around the average is represented by a much narrower and symmetric

Gaussian function, as shown in Figure 71. The longer the datasets are available more the probability density function stretches to the left curve presenting a skewed tail at the right end of the curve representing the extreme wind values.

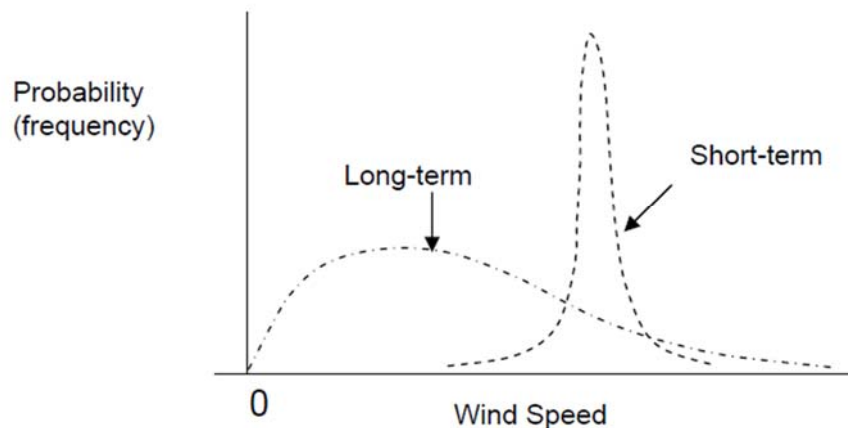


Figure 71. Long-term and short-term probability distributions of wind speed. Source: Liu (1990).

A typical series of synoptic wind records is characterized by the long-term distribution due to their strong and steady wind characteristics with stationary statistical properties. Also, for synoptic-scale phenomena, the mean wind velocity is characterized by a vertical profile in equilibrium with an atmospheric boundary layer. They typically occur in a neutrally stable atmosphere with enough spacing to the complete development of the flow. This layer varies from 1 km to 3 km and turbulence varies in typical the time intervals vary of 10 min to 1 hour and these fluctuations are stationery and Gaussian.

TS winds in contrary are characterized by a short-term distribution and they present rapid three-dimensional wind speed changes in time and space only lasting a few minutes. The turbulence associated with convective gusts differs considerably from the traditional turbulence observed in the ABL winds due to the intrinsic kinematics and dynamic properties of the latter. Convective thunderstorms outflow present varying and unique velocity and direction vertical profile, they increase rapidly in speed and impose an atypical load on structures designed for ABL winds. These winds are statistically non-stationary processes and conventional turbulence approaches cannot quantify the gustiness of these winds (LIN *et al.*, 2007). Since buildings and structures are flexible, they may exhibit resonant amplification, which is induced by the wind turbulence, therefore it is important to learn to simulate such

characteristics in wind tunnels when aiming to quantify such excitations loads in structures (SIMIU, 1981a).

Even though it is hard to describe transient phenomena like TS winds, random phenomena still present certain signature characteristics which will be discussed in this section. The first step to start this discussion comes with the decomposition of the wind velocity into its vectorial components u, v, w in their mean (\bar{u}) and fluctuating (u') parts component as showed in Equation 2, Equation 3, and Equation 4:

$$u = \bar{u} + u' \quad \text{Equation 2}$$

$$v = \bar{v} + v' \quad \text{Equation 3}$$

$$w = \bar{w} + w' \quad \text{Equation 4}$$

Holmes *et al.* (2008) indicated that the fluctuating wind speeds generated by downbursts events are represented dominantly by low frequency running mean with superimposed random turbulences of higher frequencies. Therefore, considering the resultant wind velocity V is decomposed into the horizontal component $v(t)$, which given by the sum of the slowly varying mean velocity $\bar{v}(t)$ plus the residual fluctuation $v'(t)$, expressed in Equation 5 and Equation 6, respectively.

$$v(t) = v'(t) + \bar{v}(t) \quad \text{Equation 5}$$

$$v'(t) = \tilde{v}'(t) \times \sigma_v(t) \quad \text{Equation 6}$$

Where in the Equation 5 $\bar{v}(t)$ is the deterministic component and it is related to the low frequency content of the wind velocity, which is driven by the large-scale flow, and the statistic component; and $v'(t)$ is the component induced by a small scale non-stationary random processes and represent the high frequency component of the wind velocity. Note that the same logic is valid for the other components u and v . In Equation 6, $\sigma_v(t)$ is the slowly varying standard deviation of $v'(t)$ and considering the medium scale turbulence of the fluctuation at the scale of the turbulence is driven by the mean wind velocity at large scale, making it approximately a deterministic property. Finally, $\tilde{v}'(t)$ is the reduced to a turbulent fluctuation, which it is then considered the small scale turbulence with zero mean and unit standard deviation (CHEN AND LETCHFORD, 2004).

On the attempt to describe the turbulence of TS winds the Gust Factor $G_{t,T}$ is possibly the most common deployed relationship once it described the gustiness the wind. This parameter

is simply given by the difference between the sustained wind speeds and the gusting wind speeds, in other words, it describes the instant fluctuations of the wind record around its mean value. The relationship that defines $G_{t,T}$ is shown in Equation 7:

$$G_{t,T} = \frac{u_t}{\bar{u}_T} \quad \text{Equation 7}$$

Where u_t is the wind gust speed registered using the typical wind speed acquisition time t which varies typically from 3 to 0.25-s. The average wind speed \bar{u}_T is the value obtained considering a the moving average time period T , which assumes typical values of 10 to 60 min for EPS winds analysis and but these values are much lower for TS winds. Solari *et al.* (2015a) suggests T for TS winds should stay within 20 to 40-s (SOLARI *et al.*, 2015a) and the greater these values get statistics become more unstable (SCHROEDER; SMITH, 2003). Solari *et al.* (2015a) observed that due to the highly non-stationary properties of these winds, Gust Fronts should not be compared to the mean wind velocity any longer, instead of the mean value \bar{U} should be replaced by a the time-varying mean wind velocity \bar{u} . Consequently, G in thunderstorms is then turned as function of moving average period T , resulting in the relationships showed in Equation 8 and Equation 9:

$$G_{max} = \frac{u_{max}}{\bar{u}_{max}} \quad \text{Equation 8}$$

$$\hat{G} = \frac{\hat{u}}{u_{max}} \quad \text{Equation 9}$$

In which u_{max} , \hat{u} , and \bar{u}_{max} are respectively, the maximum sampled value of the wind velocity for 1-s peak wind velocity; the maximum value of the slowly varying mean wind velocity averaged over $T = 30$ seconds; and \hat{G} refers to the gust factor of thunderstorms winds as function of moving average period T . Solari *et al.* (2015a) found that for TS winds the mean results for G ranged from mean $G_{60} = 2.58$, $G_{10} = 1.86$ and $\hat{G} = 1.20$; and for synoptic winds $G_{60} = 1.6$, $G_{10} = 1.49$ and $\hat{G} = 1.19$.

The Turbulence Intensity (I_v) is especially important for structures that are sufficiently flexible to exhibit a large oscillatory response under wind loads, such as transmission lines (SIMIU, 1981B; ORWIG-GAST AND SCHROEDER, 2005). I_v is given by combining both Equation 5 and Equation 6, which results in Equation 10.

$$I_v(t) = \frac{\sigma_v(t)}{\bar{v}(t)} \quad \text{Equation 10}$$

Orwig-Gast and Schroeder (2005) analyzed the two TS wind events (RFD and Derecho) presented in Gast (2003) and observed that because of the non-stationary characteristics of these winds the relative high values of I and Gust Factors was not due to the ground (mechanically generated, as in EPS winds), instead they were a typical characteristic of the phenomena thermally generated within the outflow event. In Figure 72 a) is presented the I over the event's life for both events, where blue represents the RFD event and red represents the Derecho; and in b) the same is valid, but in y-axis is given the I for different averaging times T . Note a close to linear relationship between I and moving average period T .

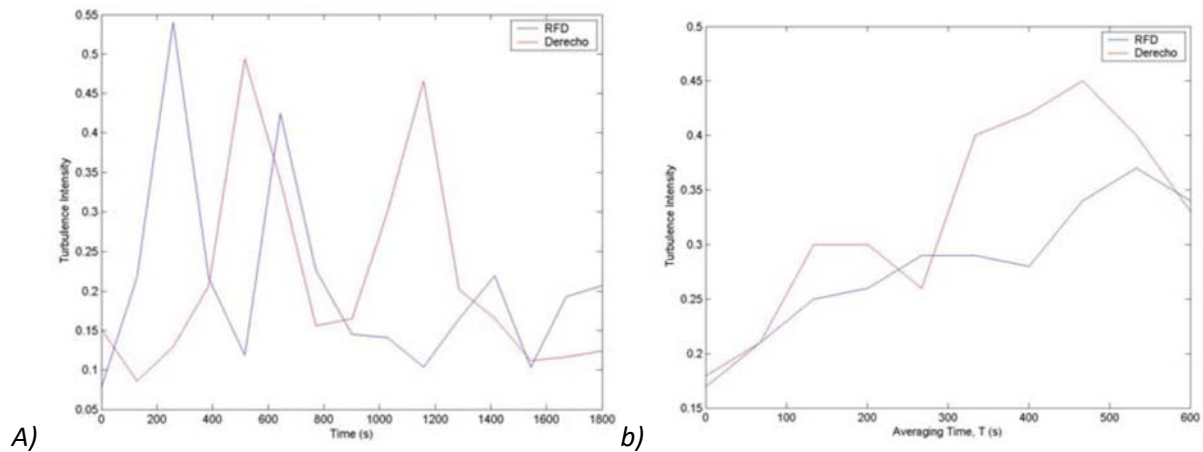


Figure 72. Turbulence Intensity for the RFD and Derecho Events. In a) the TI time series (120s s mean) and in b) the I of both events compared for different I . Source: Orwig-gast and Schroeder (2005).

Turbulence Intensity of TS winds have not being agreed upon since there are many discrepant results from independent analysis of TS wind events, for instance, Solari *et al.* (2015a) proposed to express the turbulence intensity in thunderstorm winds using a non-dimensional function named $\mu(t)$ given by Equation 11:

$$\mu(t) = \frac{I_v(t)}{\bar{I}_v} \quad \text{Equation 11}$$

Where, \bar{I}_v is the I_v averaged over a 10-minute interval. In Figure 73 is shown the non-dimensional parameter μ for all thunderstorm's records centered at $t=300$ s, where the thick line corresponds to the mean value obtained for $\mu(t)$.

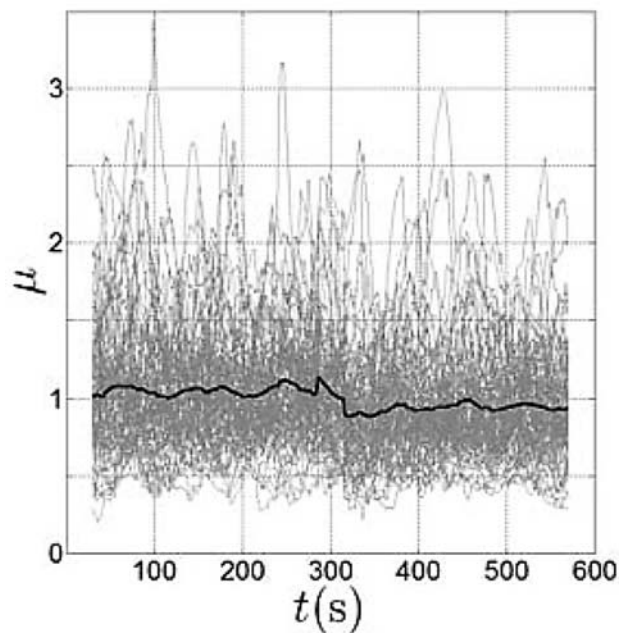


Figure 73. Ensemble of the diagrams of $\mu(t)$ for all thunderstorm records investigated and their mean values (thick line). Source: Solari *et al.* (2015a).

Solari *et al.* (2015a) found that I_v does not exhibit any relevant dependency on the wind direction and in mean terms and the average value of the turbulence intensity is nearly independent of averaging time period utilized, therefore $\bar{I}_v = I_v$.

Though the approach above, Solari *et al.* (2015a) found that in practice I is smaller for TS events ($I_v = 0.12$) than for synoptic events ($I_v = 0.17$) and much smaller than the previous found in Orwig-Gast and Schroeder (2005), agreeing more with values of mean turbulence intensity found in Chen and Letchford (2006), typically varying from 0.08 to 0.11. Thus Solari *et al.* (2015a) proposed a more realistic approach to obtain I empirical relationship that includes the parametrization of Equation 11 of the planetary boundary layer length and the roughness length of the terrain as shown in Equation 12 – which again, goes in contrary to that was proposed in Orwig-Gast and Schroeder (2005) – leaving an important lacune of knowledge to be explored once more TS wind full-scale measurements become available.

$$I_{v,n} = \frac{1}{\ln\left(\frac{z}{z_o}\right)} \quad \text{Equation 12}$$

The reduced turbulent fluctuation \tilde{v}' is found to have similar characteristics of synoptic events (CHEN AND LETCHFORD, 2004; HOLMES *et al.*, 2008), but there is still a limited understanding regarding the integral length scale of \tilde{v}' (ORWIG AND SCHROEDER, 2007; LOMBARDO *et al.*, 2014). The estimation of integral length scale of thunderstorms turbulence I_v is done by

applying the power spectral density (PSD) to the \tilde{v}' , which returns in average much lower L_v for thunderstorms than what is seen in synoptic events, possibly because the average size of outflows within the TS winds. Solari *et al.* (2015a) points out that this possibly happens because of the proximity of thunderstorms to the ground, generating smaller in size eddies comparatively to the ones observed in synoptic events. Although further studies in this subject are needed as also reported in Lombardo *et al.* (2014) and Orwig and Schroeder (2007)

The response of a structure to turbulence depends more on the sequence of intermittent gust, than of eddies isolated, therefore the larger the eddy, the more energy it has within, but lower it is the frequency of these events. The dimension of the whirlwinds define which elements of the structure are more vulnerable, for instance, smaller whirlwinds tend to cause major effects on the building façade, meanwhile larger whirlwind imposes larger dynamic effects on the building structure. In wind engineering these edges are called *Vorticity Sheds* and they are responsible for creating lateral response on the building oscillation. When simulating a flow in wind tunnel, the mean velocity, the turbulence intensity, spectra of turbulence and integral scale must be similar in order to artificially replicate the effects the wind on the prototype. By not knowing these components of the flow, it is impossible to determine the dynamic interactions of wind-structures.

Based on the discussed, consequently the integral length scale of turbulence in thunderstorm events is on average much lower than in synoptic events, averaging 123 m for the latter and $L_v = 35$ m for the former. Solari *et al.* (2015a) defined in qualitative terms that this difference is due to outflows of thunderstorms events occur next to the ground and both maximum and averaging sizes of their eddies are potentially smaller than those observed on synoptic events. Consequently, when adopting a reduced frequency of the maximum value of the mean wind speed, it is observed a decrease on the integral length scale of thunderstorms. In addition, the integral length scale of turbulence of thunderstorms and synoptic events seem to exhibit relevant dependence on the ratio between the height above ground and the roughness length of the terrain.

The PSD mean value of reduced turbulent fluctuation \tilde{v}' of a thunderstorm event is shown in Figure 74 superimposed with the Von Karman Spectrum. It shows the reduced frequency function (f) for all thunderstorms records detected in Solari *et al.* (2015a). Such curve has an

excellent fit in the inertial sub-range (0.5 to 10 Hz), but it does not model the same precision for lower frequencies (≤ 0.5 Hz). This can be in part due to the PSD turbulence model chosen or due to the thermodynamic properties of the thunderstorm.

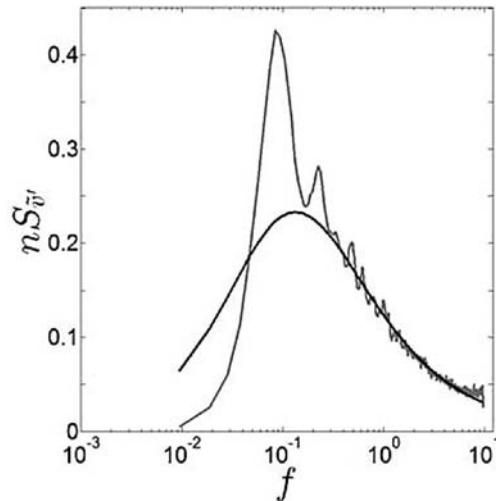


Figure 74. PSD reduced turbulent fluctuation \tilde{v}' as a function of the reduced frequency f for all thunderstorms records detected in Solari et al. (2015a). Source: Solari et al. (2015a).

Chen and Letchford (2006) analyzed a full-scale dataset and noticed slowly variable wind speed presented small variations from 2 to 15 meters in both events. The standard deviation of the fluctuating velocity over time was proportional to the mean-varying speed and the turbulence intensity averaged about 0.1. Finally, assuming the fluctuating velocity of the wind record as the ratio of fluctuating velocity and variable standard deviation, the spectral density signals of the normalized fluctuating velocity are similar in both events. In Figure 75 is presented the power spectral function at 10 meters of the data obtained for the a) RFD and b) derecho and the data is then compared to the Harris–Von Karman spectrum.

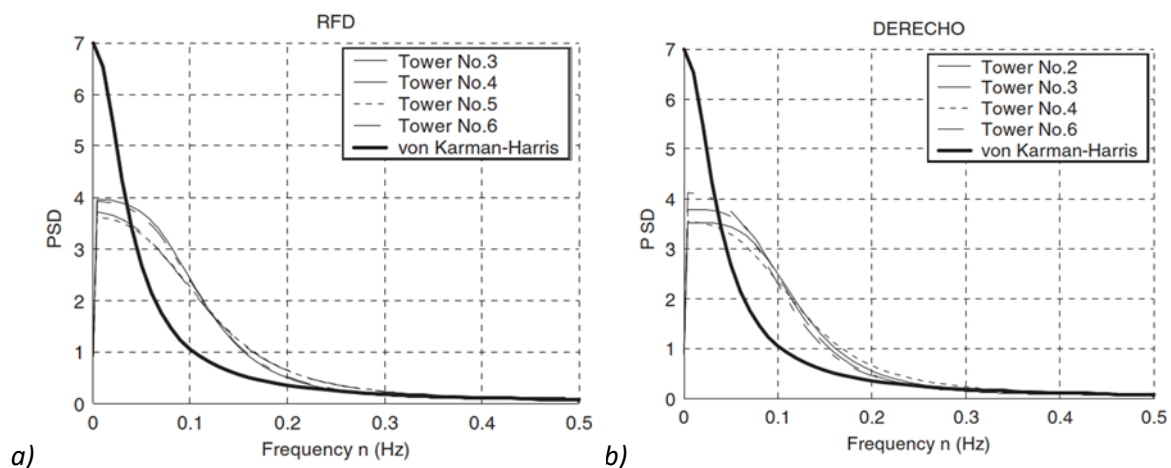


Figure 75. Estimated PSD as stationary process for a) RFD and b) derecho overlaid with Karman-Harris PSD (thicker line) Source: Chen and Letchford (2006).

Durañona *et al.* (2007) inferred from the dimensional analysis through the application of wavelet analysis to some thunderstorms wind events that higher energy spectrums are detected at lower time scales, which corresponds to an increase of energy largely due to wind speed. Assuming the temporal variability of extreme wind events is the result of the energy contained in distinct structures within the flow, is expected that the vortex stretching induces energy into smaller length scales.

Järvi *et al.* (2007) observed a microburst event passing through a micrometeorological station in Helsinki. The authors noted the turbulence spectra before and after the event were consistent with the traditional ABL turbulence spectral theory. It was also observed that the effects in aerosol particle concentration and observed carbon dioxide atypically increased due to the turbulent mixing caused by the TS wind event.

Zhang *et al.* (2019) analyzed the turbulence spectra of full-scale events in Beijing–China and compare the results with measurements in the Mediterranean. In the results from the 325 m tall tower showed that closer much more turbulence is observed closer to ground on the present experiment when compared to the Italian data because of the urbanization, which is not observed on the Italian experiment because the thunderstorms usually flow from the ocean inland. Therefore, the application of roughness coefficients to simulate the turbulence into the wind profile generated by TS winds has several limitations, mostly because there is not one specific profile for thunderstorm winds and not all possibilities have been met to this point, which makes the task of creating a model that fits as well as for the logarithmic profile for EPS winds much harder to achieve.

The efforts to define all the complexity of the speed profile and the turbulence characteristics of downburst winds are not accomplished yet and are ongoing in the wind engineering community for decades. Even though a few full-scale measurements of TS winds are available, there are still uncertainties on how representative of the nature of the phenomena. Models and simulations have improved the overall understanding of thunderstorm outflows but there is not a clear consensus on this subject.

3.3. THUNDERSTORM WIND CODES PROVISIONS AND STANDARD SPECIFICATIONS

Thunderstorm winds tend to dominate the extreme wind climate in most parts of the world, especially at mid-latitudes and away from coastlines (LOMBARDO, 2012; GAETANO *et al.*, 2014; MASON, 2017). These finds have taken research institutions of several countries to work towards including TS winds specifications in national standards and wind codes provisions. When examining the implementation of TS winds to building codes, Mason (2017) proposed two questions regarding the differences between the effects of structures for localized windstorms and synoptic winds:

1. Will the difference between outflow and standard ABL velocity and turbulence profiles lead to different pressure loads on structures?
2. Given the transient nature of outflow events, will the rapid changes in wind speed, wind direction, ambient pressure, and velocity/turbulence profiles change due to the building aerodynamics?

For the first question, researches have indicated some similarities between the effects of steady thunderstorm wind flow models in structures and ABL wind flows, except when the structures are located beneath to the vertical jet area– which at moment none of the existing wind codes have implemented this sort of analysis (ABD-ELAAL *et al.*, 2013b). Therefore, the literature has suggested that methods applied to study ABL winds effects in structures can also be applied to study TS winds effects in structures (LETCHFORD AND CHAY, 2002; SENGUPTA *et al.*, 2008; MASON *et al.*, 2009).

The second question reveals a greater issue; when transient flow is applied to structures, it causes maximum dynamic wind pressures that can reflect in unexpected reactions within the structure. This assumption has been widely adopted for steady ABL studies, but for TS winds,

Mason (2017) highlights that it remains unclear if the unexpected dynamic loads due to the unsteady thermodynamic nature of TS winds flow and the variability over time of their vertical profile will ever be able to be simulated in a wind tunnel environment.

Even aware of such concerns, tornados as a specific type of TS wind, have been considered in standard of building codes since 2011. For instance, the ANSI/ANS-2.3-2011 (AMERICAN NATIONAL STANDARDS INSTITUTE, 2011) requires the consideration of tornado wind for nuclear structures and the same is valid for the ASCE 7-16 (AMERICAN SOCIETY OF CIVIL ENGINEERS, 2016). The latter also provides design guidance under discretion of the designer/owner to consider tornado loads in typical structures. Although, because of the elevated costs, such additional safety measures are typically neglected.

In 2022, ASCE included for the first time a chapter dedicated to consider loads due to tornadic winds to the ASCE's Minimum Design Loads and Associated Criteria for Buildings and Other Structures (ASCE 7-22) (ASCE, 2022). In this new edition, variables such as rain and building size (the greater a chance it has of being struck and environmental loads) are included, and snow, for instance, is neglected since TS winds are a typical characteristic of warmer climates. Although, in the United States as well in other countries, the inclusion of these specifications to standards developed by professional organizations do not actually mandates the use until adopted in law by code provisions at various jurisdiction levels, such as municipal or state.

Even though tornadoes can produce the most intense winds, straight outflow winds are more frequent and it are widely accepted to cause more damage in the United States (FUJITA, 1990; HOLMES, 2002; SOLARI *et al.*, 2015a) the same is believed to be true in other parts of the world where TS wind dominates the extreme wind climate. Taking the last statement in consideration, it would be coherent to also develop standard specifications for straight-line outflow winds, specially taking in consideration that standards are meant primarily to provide economical design criteria that would create acceptable levels of protection to the built environment within the needs of society at large.

The Australia/New Zealand Design Code AS/NZS1170.2 (2010) and the International Organization for Standardization (ISO) 4354 (ISO, 2009) have been the first entities to incorporate in their provisions outflow-type convective winds. But such initiatives involve challenges, especially when trying to simply a phenomenon as discussed here with such great

variation in properties from one event to another, such as wind speed, turbulence, rate of occurrence, and trigger mechanism.

The ISO 4354 provides a framework for several types of structures. It first looks to identify if the site location is within mixed wind climate and what is the structure's serviceability (residential, hospital, etc.). The ISO 4354 then proposes different profiles to calculate the ultimate load limit for safety and for serviceability, considering separately the probability of exceedance of each event, whichever is dominant. The standard does not provide specific turbulence, intensity, spectra, or correlations. No event-specific shape factors are proposed and only a single steady profile is adopted. Although, specific external and internal shape factors for structures over 25 m are introduced.

The AS/NZS 7000-2016 code only provides a framework for the design of overhead power lines in Australia and New Zealand taking in consideration localized TS winds. It provides a map where localized storms are observed in those countries and provides storm specific wind speeds, a unique typical downdraft profile, different span reduction factors for synoptic or thunderstorms winds, and topographic multipliers for storm profiles—which are found to vary from event to event, but staying about less than 20% of the ABL flow (MASON, 2017).

Similarly to the way other national wind codes treat wind tropical cyclones with the creation of zones where these events are possible or not to be observed, the AS/NZS 7000 proposes a map with 3 Zones: Zone 1, areas where extreme wind events have mostly synoptic origins; Zone 2, areas where extreme wind events are defined by localized downdraft; and Zone 3, areas where extreme wind events have origin from both synoptic and thunderstorm events, therefore both types of winds must be considered.

Due to the lack of agreement in turbulence characteristics of TS winds events, both ISO 4350 the AS/NZS do not provide a specific turbulence intensity and aerodynamic shape factors for study in buildings. They also ignore the effects of the surface roughness, since it has been shown the little influence of the this factor to the wind speed (CHOI, 2004; XU AND HANGAN, 2008). Although they account for effects of topographic amplifications to the flow,

Mason (2017) synthesized the envelope profile of both ISO 4350 and AS/NSZ 7000 in Figure 76 and compared them to the three full-scale TS winds measurements by Holmes *et al.* (2008),

Lombardo *et al.* (2014) and Gunter and Schroeder (2015). The profiles are normalized to their respective speeds at 10 m, resembling the typical approach adopted in ABL wind analysis. The analysis of Figure 76 shows that ISO 4354 is less conservative, below 10 m than AS/NZS 7000, but the former becomes more conservative as it goes higher. Furthermore, AS/NZS 7000 matches reasonably better observations from 10 to 30 m, but its counterpart becomes more conservative at higher elevations.

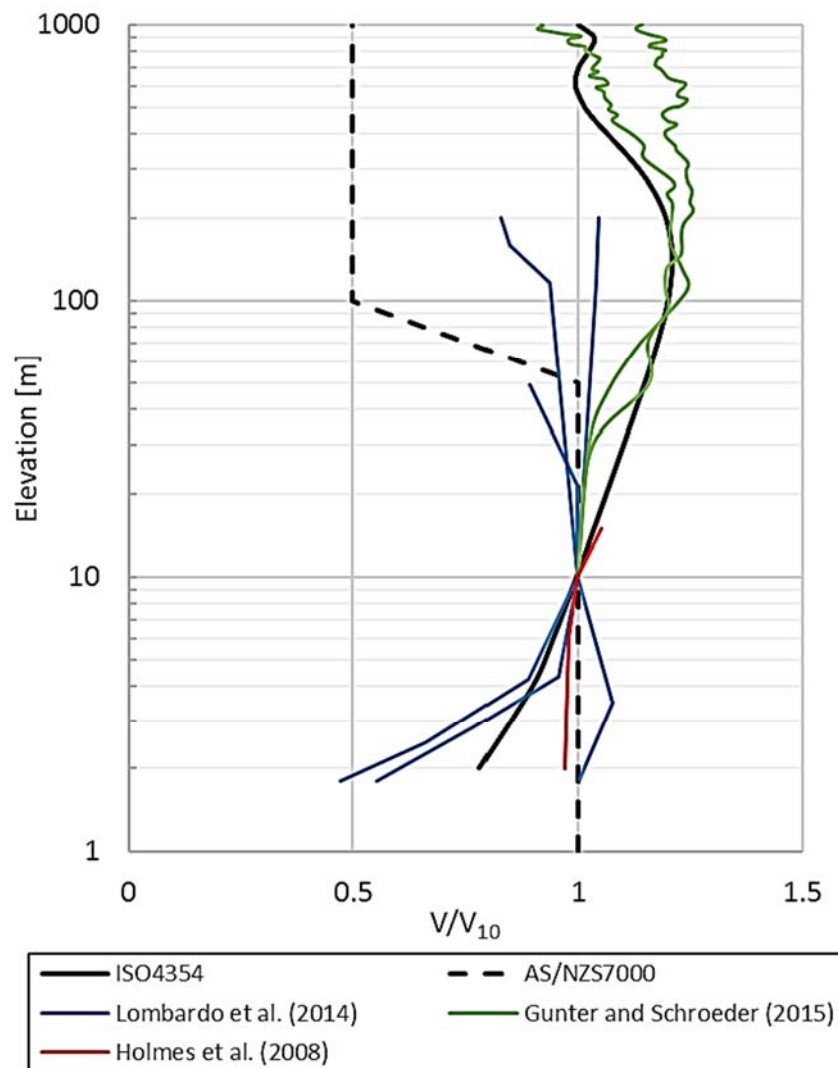


Figure 76. Envelope wind speed profiles from ISO 4354 and AS/NZS 7000 compared to three full-scale measurements of TS winds. Source: Mason (2017) apud Holmes *et al.* (2008); Lombardo *et al.* (2014); Gunter and Schroeder (2015).

3.4. DISTINGUISHING AND CLASSIFYING THUNDERSTORM WIND SIGNALS FROM MIXED DATASETS

Normally wind datasets are found amongst mixed and uncategorized formats, therefore a common practice for the development of wind codes and standard specifications is the application of techniques of extreme wind climate analysis. These identification methods were developed with aiming to segregate extreme wind registers based on their respective causal mechanisms. The need perform this sort of analysis was first identified by Gomes and Vickery (1978) who initially proposed to apply the extreme-analysis method of Gumbel to the observations of annual maximum wind speeds in mixed climates in Australia.

After that, several other techniques emerged involving various other approaches and nomenclatures. For instance Twisdale and Vickery (1992) utilized the criteria of thunderday and non-thunderday to identify TS winds; Choi and Hidayat (2002) utilized thunder and rain to define a TS wind event; and Cook *et al.* (2003) utilized the annotation “thunderstorm seen or thunder heard”. Other methods deployed satellite reanalysis data, LiDAR, and Doppler radar, and lighting mapping to identify TS winds (CANEPA *et al.*, 2020 BROWN AND DOWDY, 2021). In this section is discussed some of the existing methodologies developed to decompose wind signals as per their originating events, classify outputs, and some preliminary results of these procedures, with focus on wind engineering applications.

Fujita (1985b) first proposed a practical method to identify downburst induced wind records based on the 1-min maximum wind speed and the pre-peak mean wind speed, plus the post-peak mean speed. The focus on this work was to analyze the wind records simultaneously in different time steps before and after the record’s peak. Some of these conditions deployed are shown below:

- Condition 1: Center wind should be faster than 10 m/s.
- Condition 2: Center wind should be at least 5 m/s faster than \overline{w}_+ .
- Condition 3: Center wind should be at least 5 m/s faster than \overline{w}_- .
- Condition 4: Center wind should be at least $1.25\overline{w}_+$ or faster.
- Condition 5: Center wind should be at least $1.25\overline{w}_-$ or faster.

- Condition 6: \overline{w}_+ should not exceed $1.25\overline{w}_+$.

Where \overline{w}_+ is the post-peak mean and \overline{w}_- is the pre-peak mean, expressed as the average of seven registers before and after the peak velocity happens, excluding the first ones (\overline{w}_{+1} and \overline{w}_{-1}). Figure 77 shows very briefly the system proposed by Fujita, which ultimately would depend upon human analysis.

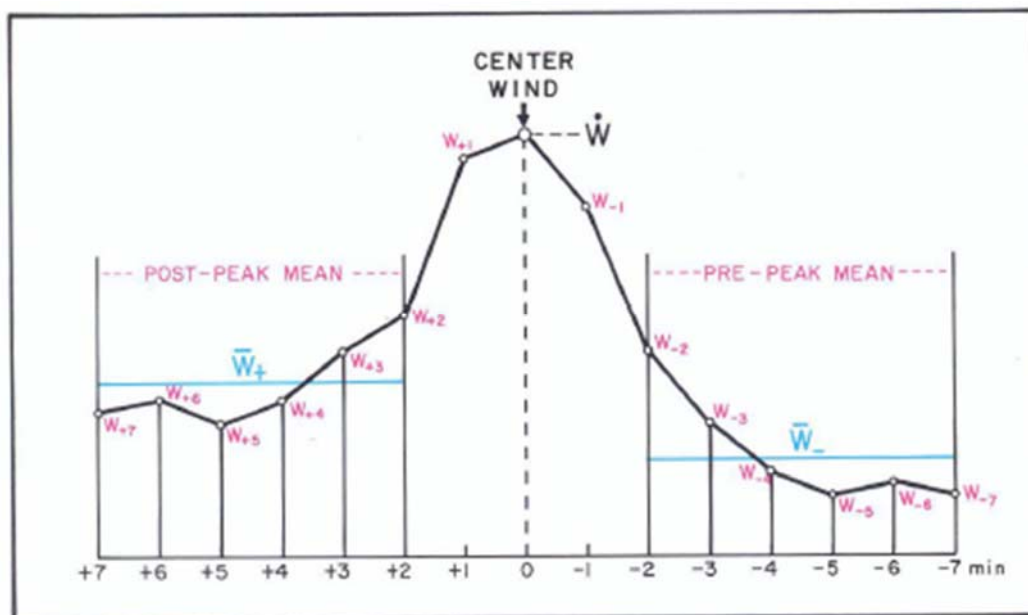


Figure 77. Typical wind speed pattern is used to illustrate the method aimed at identifying downburst winds within surface wind records. Source: Fujita (1985b).

Riera and Nanni (1989) used the following criteria to identify TS wind records in Brazil:

1. Duration and intensity of the wind record, which was considered not to exceed 5 minutes for thunderstorm events.
2. The occurrence of thunder and/or lighting.
3. Observation of cells of cumulonimbus clouds.
4. Rainfall accompanying sudden decrease in temperature.

Lombardo *et al.* (2009) proposed automated methods that would promptly differentiate non-thunderstorm winds events from thunderstorm winds and hurricane winds, counting with minimum human supervision, and for the whole Automated Surface Observing System (ASOS) in the United States, which is composed of one thousand standardized weather stations. In this experiment was applied the spectral analyses method to the entire datasets allowing to

separate stationary turbulence from the steady part of the wind record. In this method the time varying mean is removed from the dataset and the remaining residual turbulence is called time-varying residual turbulence, allowing the segmentation algorithm to identify if a record was due to a EPS or TS event (LOMBARDO *et al.*, 2009). In Figure 78 a) is shown a dataset in which the time-varying mean was removed and the residual turbulence u' on t averaging time is then expressed in Equation 13.

$$u' = u - \tilde{u}_t \quad \text{Equation 13}$$

Where u is the original wind record and \tilde{u}_t is the time-varying residual turbulence. The method proposed by Lombardo *et al.* (2009) consists on separating the record in small averaging times, such as 17-s (not over 34-s) to ensure the mean residual turbulence was approximately zero. Each time history was analyzed using the reverse arrangement test with a significance level of 0.01. The time history was broken up in eighteen parts and the algorithm continue to jump to the next segment until it detects non-stationarity, this point is then called "changing point". As one example of the system implemented, Lombardo *et al.* (2009) discussed the application of this method for the New York City area which was made of three main steps: a) classification of peak gust wind data and thunderstorm observation from the reports; b) classification of wind data as TS winds and non-TS winds; and c) definition of datasets separated by specified minimum time intervals to ensure statistical independence by deploying distribution of extreme values analysis.

This algorithm was then run for 500 events and a probability density function was estimated for the distribution of changing points. In Figure 78 b) is shown the density function and c) the residual turbulence applied for a random data with zero mean and time-varying variance, the actual change points in variance can be visually inspected in changing points at 60, 400, and 700 seconds, showing the effective occurrence of non-stationary events. This method does not only allow the identification of thunderstorms winds within the ordinary wind dataset, but by removing the stationary residual turbulence of each segment and the time varying mean from that segment it is possible to obtain other wind engineering parametrization parameters (e.g., turbulence intensity, gust factor).

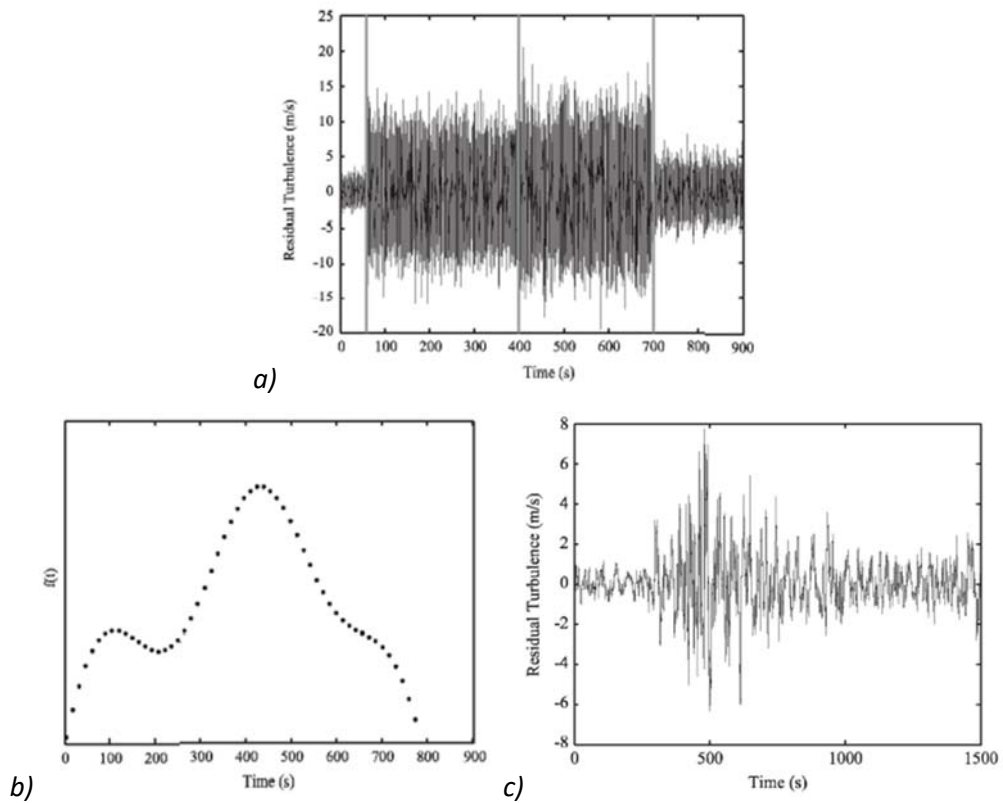


Figure 78. A sample of a dataset in which a) the time-varying mean that has been removed, b) the density function of such series and c) the residual turbulence after removing the stationary residual turbulence. Source: Lombardo et al. (2009).

The results showed for the studied area that thunderstorms winds were dominant for the returns period of 50 years to a such extended that non-thunderstorms winds speeds can be completely disregarded of the analysis. In Figure 79 is shown the assessments using the Generalized Pareto Distribution (GPD) fitting method for a mixed distribution for the Newark Airport.

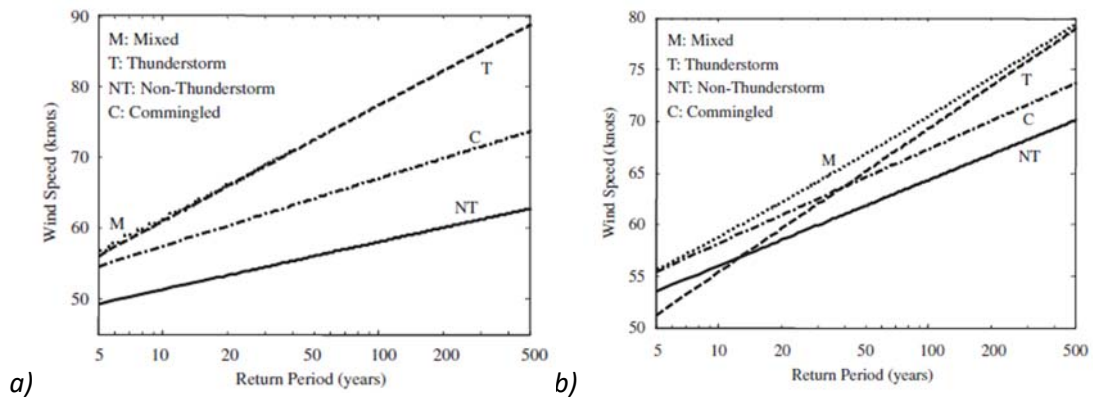


Figure 79. In a) are shown the assessments of wind speeds for various return period for the Newark Airport using a mixed distribution (M), thunderstorms winds (T), non-thunderstorm winds (NT), and commingled winds (C) in b) are shown the same analysis for the La Guardia Airport. Source: Lombardo et al. (2009).

Where T represents here in this figure thunderstorm winds, M represents here mixed winds (the wind series are not separated), NT represents here non-thunderstorm winds, and C represents here commingled winds, meaning all wind speeds exceeding threshold being considered are included, regardless the origin. Note that Figure 79 a) shows that the mixed climatology analysis is entirely dominated for all return period by T winds in the climate for Newark Airport. In contrast, in b) NT winds dominate the extreme climate for smaller returns periods, but after that, for extended return period of approximately 50 years, TS winds dominates the extreme wind climate for La Guardia Airport, even though this airport is not even 25 km away from Newark, which presented a completely different extreme climate.

Considering that traditional synoptic weather station networks do not fully capture the rapid and transient TS winds (DISTEFANO, 1983), Gaetano *et al.* (2014) deployed data from a high acquisition frequency mesoscale weather networks and used an extensive dataset of high frequency anemometers (between 2 and 10 Hz) in Italy, for the project "Wind and Ports". The events were classified in three different categories:

1. Stationary Gaussian Synoptic Events: neutral atmospheric events, with large mean velocities and small gust factors.
2. Non-stationary, non-Gaussian Events: thunderstorms, with large peak velocities and gust factors, but relatively small mean velocities.
3. Stationary non-Gaussian events: corresponding to unstable atmospheric conditions, with relatively small mean velocities, but large picks and gust factors. Referred as gust fronts or intermediate events (KASPERSKI, 2002).

In Figure 80 are shown three distinct cases for each type of winds identified by Gaetano *et al.* (2014) cited above. On the right side is shown a typical 1-hour record wind speed and on the left side is shown the histogram and Gaussian Density Function (GDF) of the respective event. The red dots represent the maximum observed wind gust. In Figure 80 a) and b) are shown typical results for a Stationary Gaussian Event observed during a depression within a neutral atmospheric event. On these events, it is usually observed a relatively high mean wind velocity, meanwhile on this specific case, it was observed a one-hour average $V_{m60} = 15.03$ m/

and the 1-sec gust peak $V_{p10} = 22.46$, resulting on a Gust Factor $G_{60} = 1.49$, where $G_{60} = V_{p10} / V_{m60}$. The Skewness and kurtosis observed were $\gamma_{60} = 0.22$ and $\kappa_{60} = 3.08$, respectively.

For the same Figure 80 in c) and d) is presented a typical one-hour record of a non-stationary and non-Gaussian event, characterizing a typical thunderstorm event. In this event, a relatively low wind speed of $V_{m60} = 7.33$ m/s is observed, and a very high 1-s gust peak of $V_{p10} = 33.36$ m/s was captured, which results in a Gust Factor $G_{60} = 4.55$. The Skewness and kurtosis observed were $\gamma_{60} = 1.20$ and $\kappa_{60} = 5.60$, respectively.

For the same Figure 80 in e) and f), it is presented a typical one-hour record of a stationary and non-Gaussian event during an unstable gust front. In this event, a typical low wind speed of $V_{m60} = 5.51$ m/s and a relatively intense 1-s gust peak $V_{p10} = 15.68$ m/s, which results in a $G_{60} = 2.85$. The Skewness and kurtosis observed were $\gamma_{60} = 0.63$ and $\kappa_{60} = 3.61$, respectively.

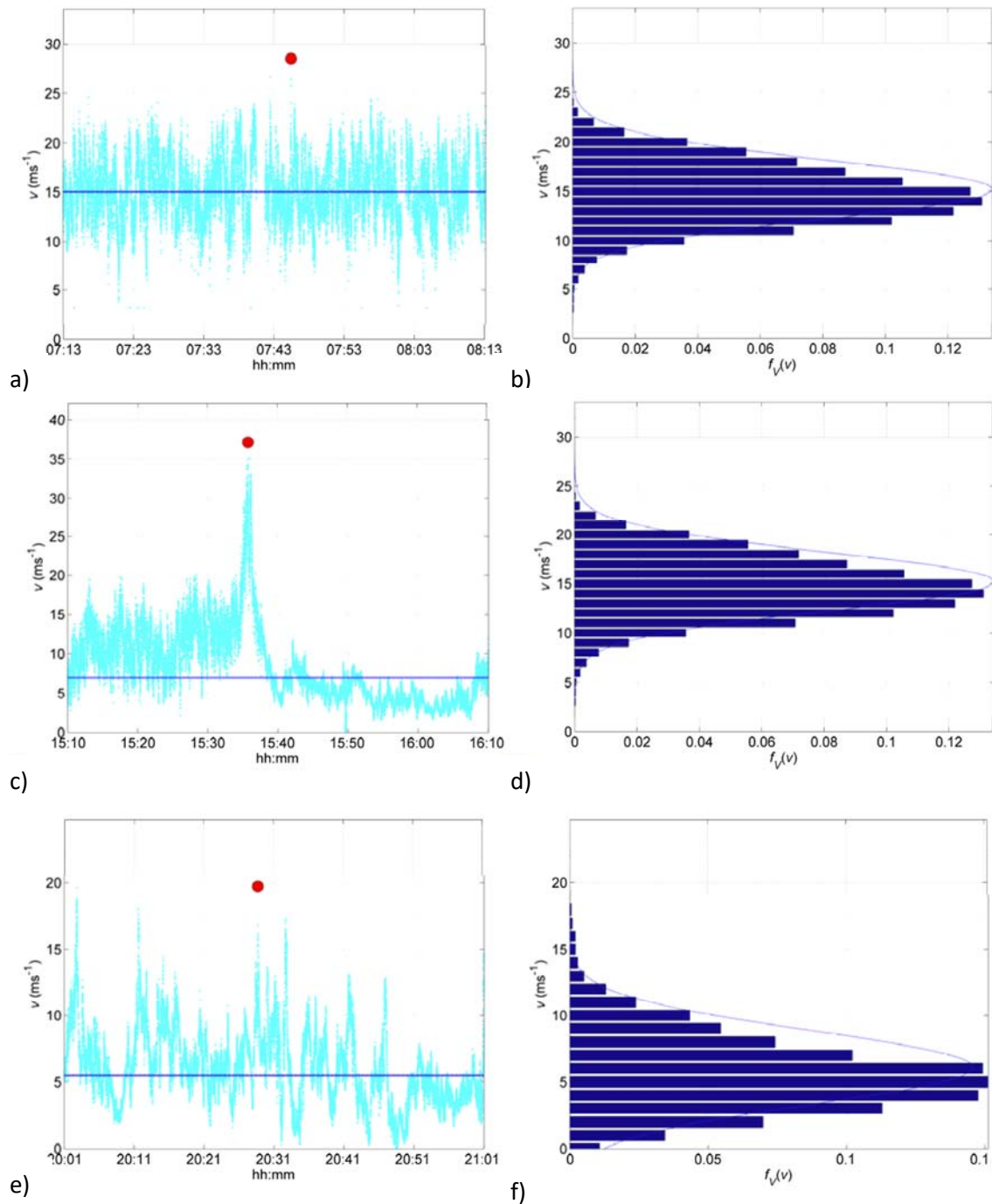


Figure 80. Three distinct cases of a typical 1-hour record of a) a stationary gaussian event; in b) it is almost perfectly superimposed histogram density function of the recorded wind speed. This event corresponds to a neutral atmospheric event; in c) a non-stationary and non-gaussian event and in d) the histogram density function changed because a gust peak relative to the mean wind speed, corresponding to a Thunderstorm. In e) a typical 1-hour record of a Stationary Non-Gaussian event and a moderately non-Gaussian distribution, corresponding to an unstable gust front. Source: Gaetano et al. (2014)

This process deployed by Gaetano et al. (2014) is inspired on Cook (1982) and it is composed of 15 steps as showed in Figure 81. These steps ultimately lead to obtaining the statistical

parameters cited above. In complement to the already discussed parameters, V_{p10} is the peak velocity averaged on $\tau = 1$ s, V_{m10} is mean velocity with $T = 10$ min, and α is the mean direction.

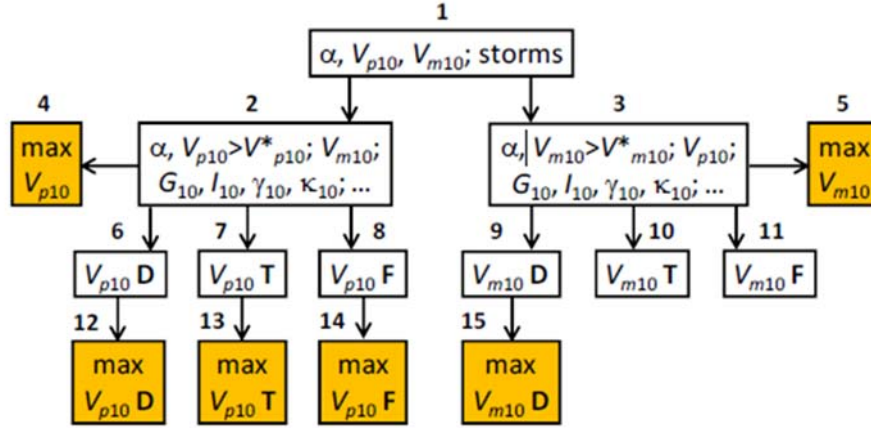


Figure 81. Conceptual scheme of transforming datasets associated with the different wind events.
Source: Gaetano et al. (2014).

The flowchart showed in Figure 81 is used to process raw datasets obtained in the monitoring network from an anemometer, representing Step 1. In sequence, two datasets are created, denoted by steps 2 and 3, in which 2 contains $V_{p10} \geq V_{p10}^*$ and step 3 contains $V_{m10} \geq V_{m10}^*$, where $V_{p10}^* = 15$ m/s and $V_{m10}^* = 10$ m/s. Both datasets also perceive to obtain gust factor (G_{10}), which is given by $G_{10} = \frac{V_{p10}}{V_{m10}}$ with the Turbulence intensity I_{60} , skewness Υ_{60} , and kurtosis κ_{60} in a 60-min interval centered around T_{10} . Ultimately, events were classified using the intervals of the parameter relationships cited below:

1. $\frac{G_{60}}{G_{60}^0} \leq 1.10 \therefore$ Depression (D) and strongly stationery and Gaussian over 1 hour
2. $\frac{G_{60}}{G_{60}^0} \leq 1.25 \cap \frac{G_{10}}{G_{10}^0} \leq 1.10 \therefore$ Depression (D) strongly stationery and Gaussian over 10-minutes intervals, although they exhibit some variability over 1- hour intervals.
3. $\frac{G_{60}}{G_{60}^0} > 1.25 \therefore$ Thunderstorm (T) or Gust Front (F)
4. $\frac{G_{60}}{G_{60}^0} < 1.25 \cap \frac{G_{10}}{G_{10}^0} > 0.80 \therefore$ Depression (D)

Events that do not qualify in any of these categories go through a qualitative analysis involving other distinguishing parameters, such as skewness and kurtosis. The last step of this method is the independent maxima extraction, when, for example, depressions present an

independent maxima interval and shall be separated by 72 hours. For thunderstorms, this value is 1 hour and for gust fronts this interval stays between 1 and 24 hours.

The application of this procedure is represented in the example showed in Figure 82, during the two events observed in the Port of the Northern Tyrrhenian Sea during the Project "Wind and Ports", where in a) a typical EPS record does "not" present any abrupt change in direction for the 17 seconds averaged segment. In contrast, in b) is shown the rapid and expressive change in wind speed, showing the occurrence of a downburst event at the time at about 15:30 (GAETANO *et al.*, 2014; SOLARI *et al.*, 2015a).

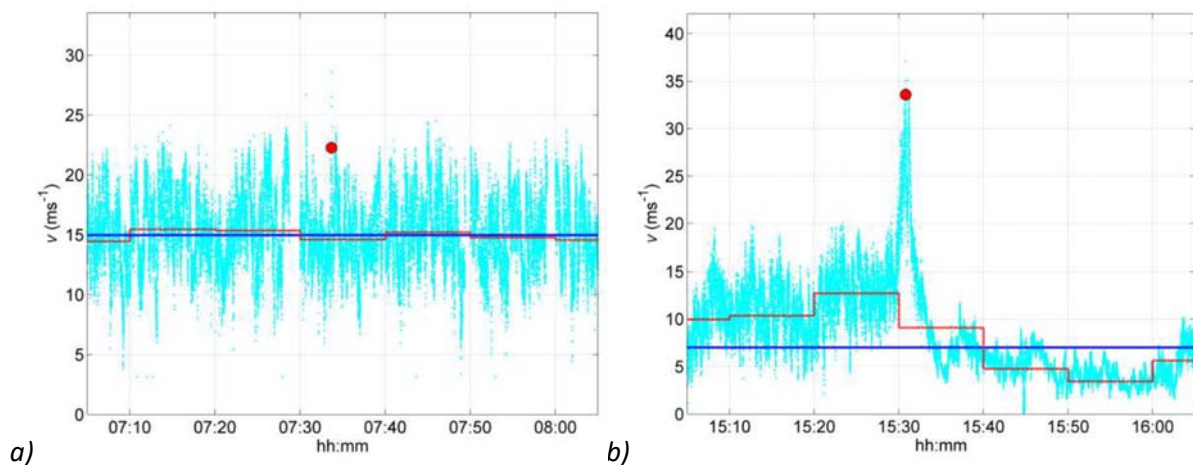


Figure 82. Two wind records of a) EPS event and b) downburst event from the Port of the Northern Tyrrhenian Sea during the Project Wind and Ports. Where the blue line represents the mean wind speed, the red line the moving average speed, and the red dot the maximum wind record captured. Source: Gaetano *et al.* (2014).

Other classifications methods include Gunter *et al.* (2017) in which it was proposed to the separate thunderstorm wind series in five segments of 40 seconds moving average of wind direction, aiming to identifying the zero-derivative points on both sides of the abrupt changes in the wind series. This method assumes that the thunderstorm velocity records are necessarily associated with changes in wind directions, which might not be necessarily true for all thunderstorms events (ROMANIC *et al.*, 2020). Holmes *et al.* (2018) proposed to separate synoptic wind events from non-synoptic wind events by analyzing the ratio between the peak speed and the mean gust speed for 2 hours before and after the suspected peak event. If the ratio was greater than 2, such an event was classified as non-synoptic.

More recently, Romanic *et al.* (2020) developed an extensive analysis of the transient characteristics of TS winds using an aim method of change points in velocity records on 41

records from 19 thunderstorms events from Europe, United States, and Australia. The method proposed to analyze not only the instantaneous velocity records but also the decomposed time series in the form of slowly varying moving mean, moving standard deviation, moving turbulence intensity, and residual turbulence. Also, under previous finds i.e. Gaetano *et al.* (2014), the systematic analysis of the records suggests that the changes in velocity fluctuation often precede and proceed the abrupt change in the mean flow.

Even though these classification methods discussed above can be applied to identify TS winds in the midst of mixed climate datasets in different parts of the world, Romanic *et al.* (2020) observed that the thresholds may vary because of changes in climate for different geographic regions, and they may even vary over time due to climate variability. For example, in Europe, storms are more isolated, and the maximum velocity during the thunderstorms peak is usually between 2 to 4 times larger than the mean wind speed before the events. In the United States, the ratios seem to be larger since TS events are more organized, but results are still inconclusive and further research is needed to categorize these events (ROMANIC *et al.*, 2020).

3.5. THE CASE FOR THE DEVELOPMENT OF BRAZIL'S EXTREME WIND CLIMATOLOGY

Because of the increased frequency and severity of wind related accidents in Brazil, major efforts have been developed to define its extreme wind climate. In this session, it is discussed initiatives performed in Brazil towards understanding the influence of severe thunderstorm events to this country's extreme wind climate and subsequent efforts to update its wind code called Norma Brasileira (NBR) 6123 - Forças devidas ao vento em Edificações.

Riera and Nanni (1989) pioneered the studies of extreme wind climate in Brazil by applying their own method as discussed in beginning of the previous section. The goal was to obtain the mean recurrence period of extreme wind velocities in two cities in Southern Brazil. In Figure 83 are shown the results from that experiment for the mean recurrence period in years for extreme wind velocity clustered in sectors groups for the cities of a) Bagé and b) Porto Alegre, both in the State of Rio Grande Sul. In a) are indicated the windiest sectors 3 and 7 for Bagé, in this case EPS winds were found to dominate the extreme wind climate for lower return periods, although TS winds dominate when performing these analyzes for higher wind speeds, such as 50-years return periods, which in fact is the typical design criteria used for the

calculation of loads due to wind in structures. In b) is shown the analysis of extreme winds per sector for Porto Alegre. Here is not shown a predominant direction for the extreme winds and the TS wind events were found to define the extreme wind climate for all return periods. This initial study showed 40 years ago that TS winds defined the typical wind design criteria for that region.

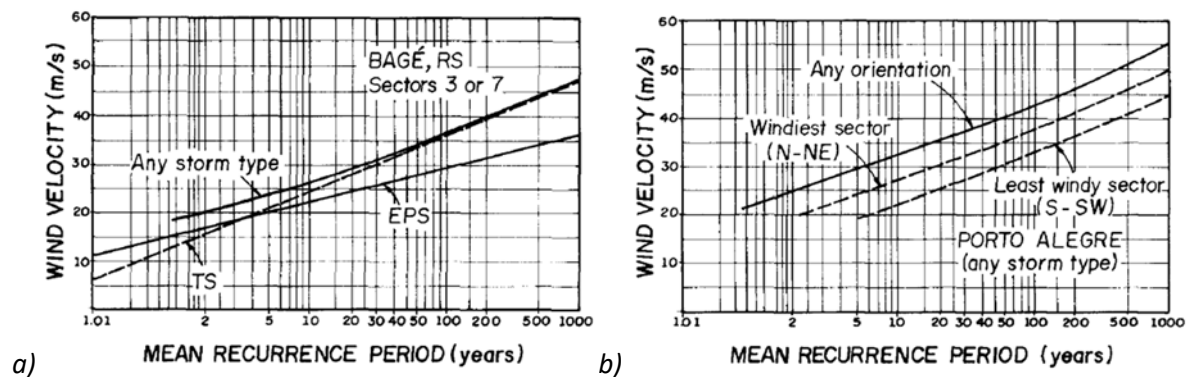


Figure 83. Mean recurrence period in year for extreme wind velocities in sector groups for a) Bagé, and b) Porto Alegre. Source: Riera and Nanni (1989) .

After Riera and Nanni (1989), Brazil's extreme wind climate studies were advanced by Santos (1989), Almeida (2010), Ponte and Riera (2010), Beck and Corrêa (2013), and more recently by Vallis (2019). Almeida (2010) used ASWS datasets and performed a Gumbel Extreme Value Analysis using maxima values from meteorological reports in conventional weather stations resulting on an isopleth map with values ranging from 60 to 90 m/s. Almeida's study took in consideration a greater amount of wind datasets, but it was free of data control process resulting in erroneous results (VALLIS, 2019). Similar conclusions are true for Beck and Corrêa (2013), but the results showed to be more similar to Padaratz (1977), ranging from 28 to 42 m/s, although little was done for data quality control as well.

Vallis (2019) made significant advances in defining the climatology of extreme winds in Brazil. In this work was selected datasets from 692 weather stations with length varying from 3 years to 27 years were selected to develop this analysis—note that in fact 7 years is minimum suitable for an extreme value analysis. These datasets included wind (direction, velocity, and gust speed), temperature, and present weather data, all these parameters helped in the identification to define the extreme wind events (TS or EPS). Extensive quality control techniques were applied to these datasets, including filters looking to exclude several types of errors, and data course cross-reference technique (different data providers, satellite

reanalysis, radar, and others) aiming to identify possible errors due to transmission issues or decoding. The data was then ranked according to the wind speed for each station and was statistically analyzed.

Preexisting methodologies such as the ones proposed by Choi and Hidayat (2002), Lombardo and Smith (2009) and Gaetano *et al.* (2014) showed to be unsuitable for the study considering datasets constraints, therefore specific algorithms tailored to each weather station were developed, the process was defined in four phases as summarized in Figure 84.

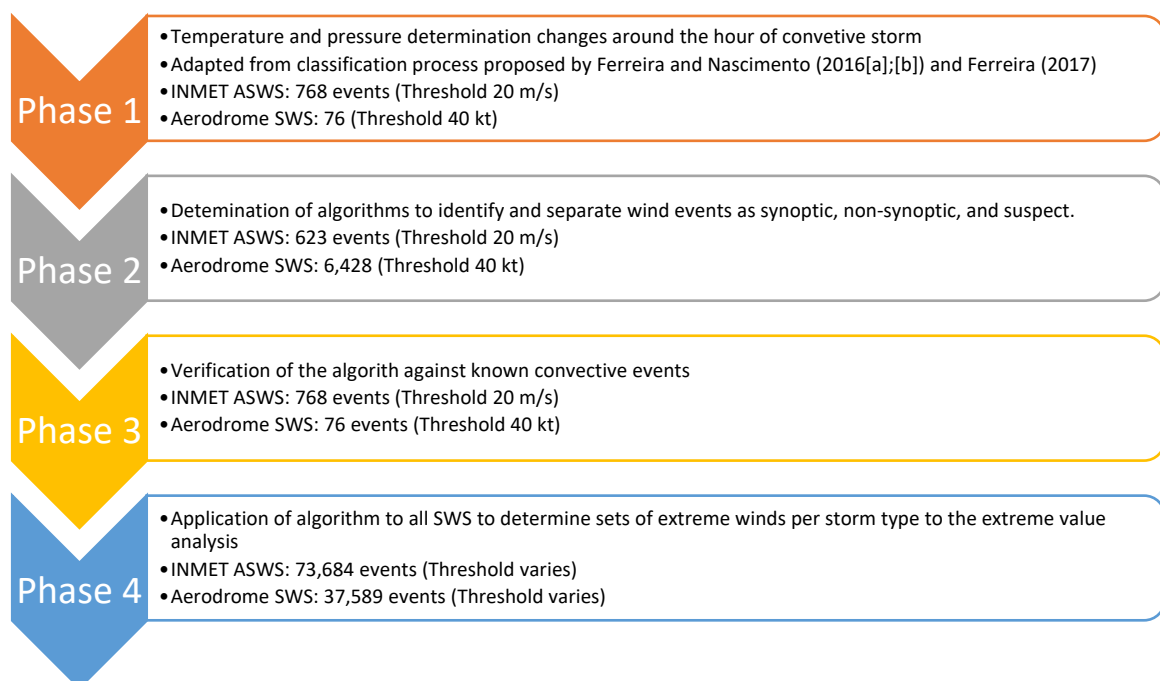


Figure 84. Summary of four phases adopted to perform the dataset classification proposed by Vallis (2019). Source: Author. Data extracted from Vallis (2019).

Once the wind datasets were classified according to their type (synoptic or non-synoptic winds) a few extreme value analysis methods were evaluated. Because of limitations of the datasets, only the Method of Independent Storms (MIS-BR) developed in Engineering Sciences Data Unit (ESDU, 1990) showed to be more of a suitable approach for this study. A Generalized Extreme Value Distribution (GEVD) - Type I was found to be the best to represent the existing datasets, being deployed to elaborate on the proposed isopleth method. The extreme values analysis methods and distribution methods considered by Vallis (2019) for the analysis of Brazil's extreme wind climatology are summarized in Table 3.

Table 3. Summary of extreme values analysis methods and distribution methods considered by Vallis (2019) for the analysis of Brazil's extreme wind climatology. Source: Author. Data extracted from Vallis (2019).

Classification		Action	Comments
Distribution Type	Fréchet distribution GEVD Type-II with $k > 0$	Not adopted	Actual NBR 6123. Results were too conservative and the wind speeds unrealistically high.
	GEVD Type-III/Weibull	Not adopted	"Culture shock" moving from existing $k > 0$ to $k < 0$
	GEVD-Type I/Gumbel, with $k = 0$	Adopted	Linear distribution and unbounded at higher return periods. Favoring safety without being too conservative.
Extreme Value Analysis Method (EVAM)	Method of Independent Storms (MIS) (COOK, 1982; HARRIS, 1999)	Not adopted	Require identification of approx. 100 events/year, regardless of the storm type. Not reached in the present data analysis.
	Lieblein's Best Linear Unbiased Estimator (BLUE) method	Not adopted	Identified tendency of high values being censored by some INMET ASWS datasets. Since this method highly favours mid-range values and reduces influence of tail values to determine the model, lowering wind speeds, it was not adopted.
	GPD Method	Not adopted	Emphasis on $k < 0$
	MIS (ESDU, 1990)	Adopted	Storm numbers threshold adopted: 20 storms with 48 hrs interval between successive events

Vallis (2019) confirmed previous finds in terms of Brazil's extreme wind climate being defined by non-synoptic wind in the most part of the Brazilian territory for a return period of 50-years. Finally, Valis presented two proposals of isopleth maps for the basic wind V_0 that could be adopted to the update of the NBR-6123. The first map presents a format of zones that would be using homogeneous values for the areas within each zone. The second map is composed of isopleths that are generated from the polynomial regression modeling of the local average values of V_0 determined by dominant data points.

The research developed by Valis represented a great advancement in the understanding Brazil's extreme wind climate, but it has a few limitations for its direct application, such as systemic issues with source datasets, short and inconstant meteorological records, the non-consideration of cyclones tropical—such as the Hurricane Catarina that impacted Santa

Catarina State shoreline—and reduced V_0 values at few punctual cities to produce the final isopleth map.

The early adoption of a basic wind map for each type of phenomena may induce to erroneous engineering applications, since little is known about the interactions of non-synoptic interaction with structures. First, a wind profile or a group of profiles (well-accepted wind model) should be defined so aerodynamic coefficients for common buildings and structures can be obtained, which as per what has been discussed, the present state-of-art is far from achieving such developments, especially in Brazil where little is known about the vertical structure of TS winds. Also, the existing weather data sampling is far from being able to capture superior quality datasets from a meteorological meso-scale data standpoint since the typical synoptic scale weather networks present poor spatial and time resolution.

In response, Loredou-Souza *et al.* (2021) proposed a "transitioning approach" that is composed of an updated map that does not separate wind extreme values (for a 50-year return period) as per their origin types. Instead, this method considers a "climatologic approach" in which uses Brazil's climatologic regions to defined areas prone to maximum wind record because of TS, non-TS or both wind type events, as showed in Figure 85.

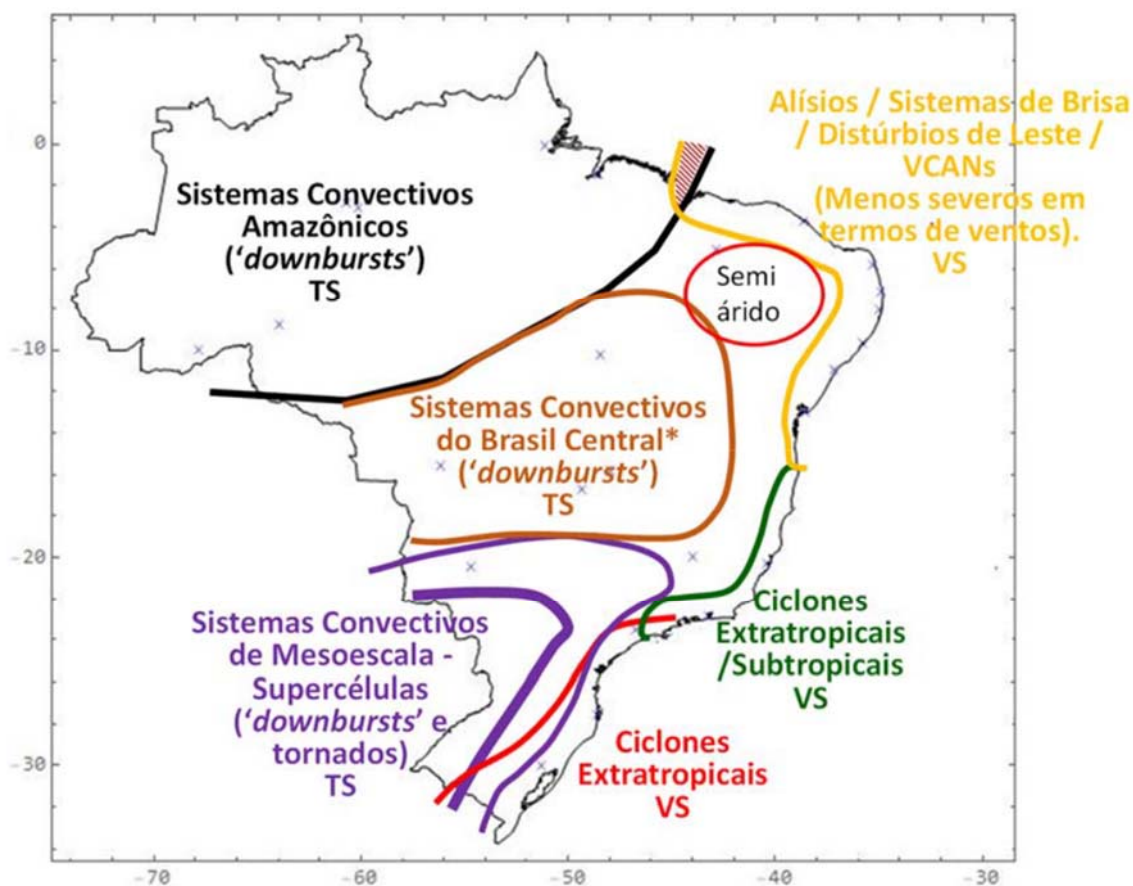


Figure 85. Climatic regions are based on the type of associated phenomena that originate them.
Source: Loredou-Souza et al. (2021).

Instead of polynomial regression for local averages, maximum V_0 values for each region were used, which are based on the representative maximum data points (weather stations) captured by Vallis. This is a conservative approach since it recognizes limitations in data sampling and data quality and assumes that the whole region around those extreme values is susceptible to observe the same extreme type of winds, not specifically only where those values, where in fact captured by sparse weather stations systems.

In Figure 86 is shown the basic wind velocity (V_0) proposed for the NBR 6123 which is called a "transitioning map" which kept the same isopleth format as in its previous format. In this new map, the physical characteristics of the typical meteorological phenomena shown in Figure 85 are maintained.

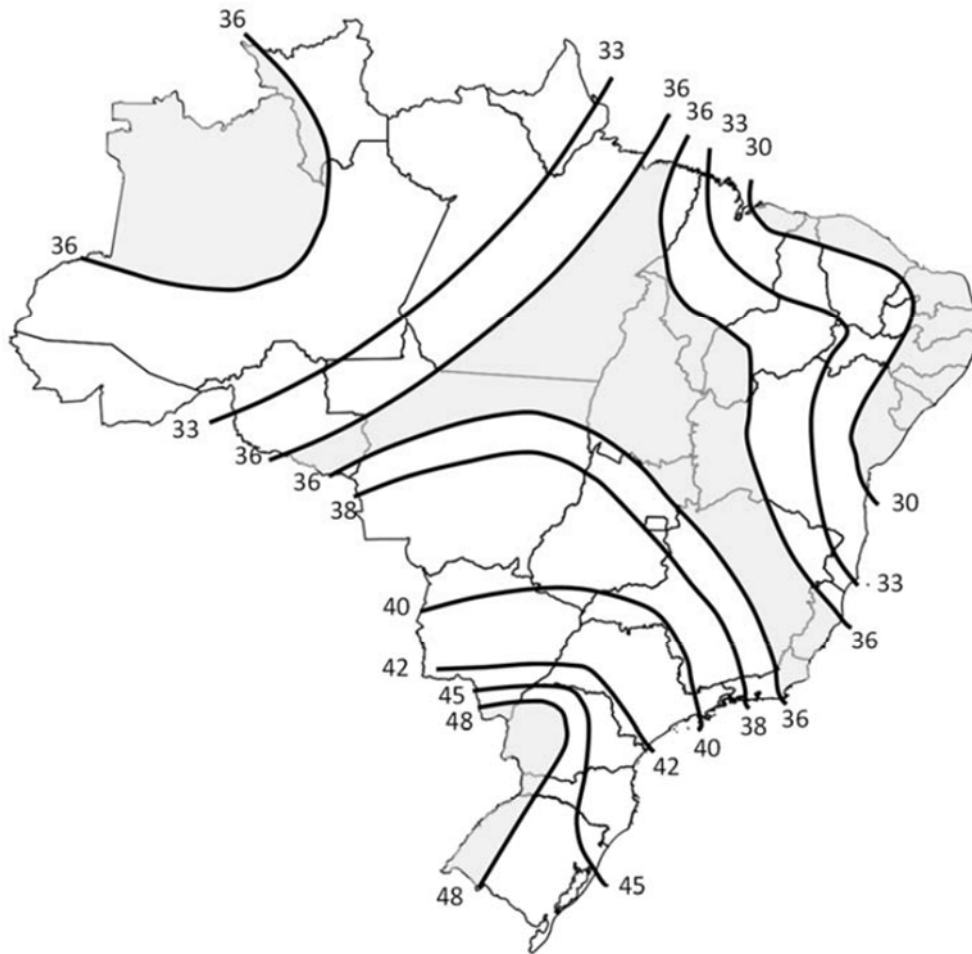


Figure 86. Isopleth map for basic velocity V_0 (m/s) considering proposed “transitioning map” approach. Source: Loredou-Souza et al. (2021).

4. PROPOSITION OF MAXIMUM THUNDERSTORM WIND FITTING CURVE PROFILE FUNCTIONS FOR MEAN VELOCITY BASED ON FULL-SCALE MEASUREMENTS

Existing approaches and techniques to simulate downbursts are discussed in Appendix B and an extensive list of models is summarized at the end of the same Appendix (Item E). Intending to contribute to the state-of-art in TS wind outflow modeling, in this Chapter existing full-scale measurements of thunderstorm wind profiles (discussed in Chapter 3.1) from those datasets are in-depth analyzed; and are proposed empirical analytical solutions for profiles at their maximum stages using best fitted curve functions.

4.1. DESCRIPTION OF METHOD DEVELOPED

The approach developed adopts a systematic analysis and further comparison of several TS wind profiles against each other at their worst-case stage—which is herein considered when they reach their maximum velocities. This assumption comes from the idea that by adopting a vertical TS wind profile at its maximum stage, a more conservative approach could be developed in order to calculate the maximum loads imposed by extreme TS wind events on structures.

In Section 3.1 a list of TS wind vertical profiles datasets was presented, and in this section, some of these profiles are further analyzed and selected aiming to propose best fitted curve models at maximum stage. The profiles were selected considering two criteria: 1) quality and resolution of the datasets for wind engineering applications and 2) extent of vertical TS wind event measurement length.

The models are described here as a $y = f(x)$ function, where x is the wind profile velocity given in m/s and y is the vertical height given in meters. Note that the model functions were set to not intercept zero at the origin because that would affect the fitted curve shape. Finally, R-squared values are used to estimate the tightness of the best-fit equation to the field data – the closer R-Squared gets to 1, the best that equation describes the field data points.

In Figure 87, the representation of the workflow to normalize profiles is shown schematically. On the left chart several velocity profiles are shown together at their maximum stage and on the right side these profiles are also together, but at this time they are shown normalized to their velocity at the height of 10 meters, which is the standard height that weather data

(including wind data) is normally captured and made available in extreme wind climatologies. Note that the profile with the highest speed (on the left) does not necessarily maintain its shape when normalized (on the right), that is because when applying normalization techniques to the wind speed profile, the shape of the profile assumes a factored proportion related to the velocity assumed at 10 m, tending to get modified.

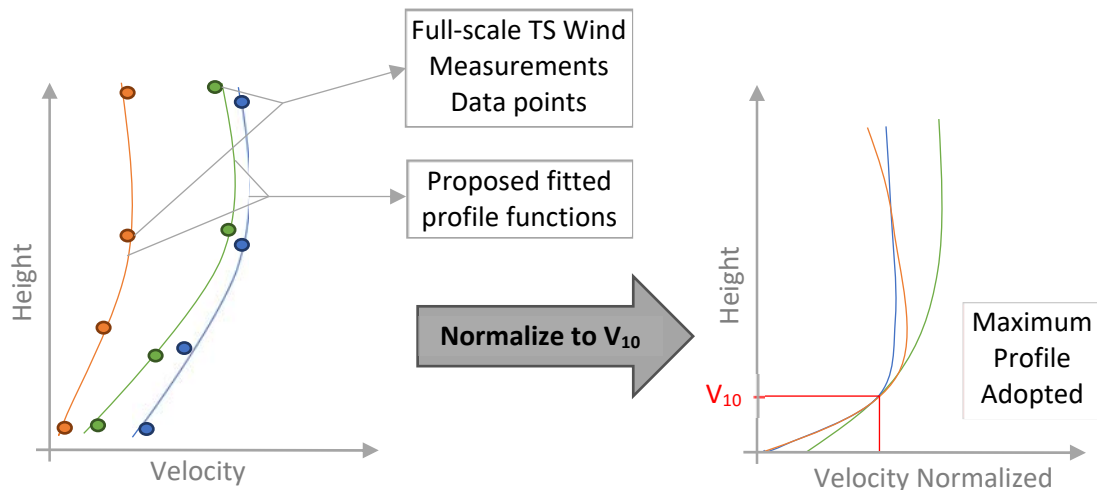


Figure 87. Visual representation of the process to obtain the profiles proposed here. Source: Author.

Below are presented assumptions taken in consideration to develop the fitted curve profiles presented in section 5.2:

1. **Function of velocity at 10m and use for climatologic studies:** The goal of this study is to propose profiles that can be coupled with general extreme wind climatologies, such as the study developed by Vallis (2019). These climatologies are developed using as reference the wind properties at the standard height of 10 meters from the ground. Therefore, the functions presented herein as described as factors related to that height and only profiles with velocity available starting at 10 m or below can be considered.
2. **Terrain influence:** profiles are categorized according to the terrain roughness characteristics described by the author in each paper using as reference the roughness definitions described on NBR 6123.
3. **Varying phenomena, same physical processes:** Every TS wind profile is the result of a series of elements that generate a thunderstorm event, these profiles carry out the typical local characteristics of thunderstorm outflows near ground. Here is assumed that these outflows are governed by the same principles, and while no regional data

on TS wind profiles becomes available, it is assumed that they can be interchangeably applied for different regions of the world.

4. **Storm Type:** In this study, the full-scale measurement profiles were classified as a product of major organized storms or isolated storms. This classification was performed by using the description of the storm (directly or not) in the original reference. This is an important characteristic to consider, since it has been previously reported that organized storms tend to generate profiles that impose a major impact on structures, e.g., Riera (2016).
5. **Maximum wind profile:** The task of considering only one profile becomes challenging amidst so many variations that the outflow profile can assume over time. Peak velocities of wind profiles may not reach maximum levels simultaneously. These values also vary at different elevations and time (MASON *et al.*, 2009). Therefore, there are cases in which more than one maximum profile will occur for one thunderstorm event, and in these cases both profiles are taken into consideration.
6. **Composite profiles not allowed:** The wind profiles presented in this study are analysis of observed data from full-scale measurements at various instants and they are not the composite of maximum velocities at different instants, therefore it assumed that if they were captured, they are physically possible.
7. **Data obtaining method:** Data obtained from different methods, such as LiDAR, anemometric tower, and radar were analyzed together without distinction.
8. **Fitting modeling method:** The best fitting profile function is not necessarily the one with the smaller R, but the one that best represents the maximum points of the profile, without underestimating the maximum wind profile velocities preferably at any point.

Limitations of this research include:

1. **Time averaging conversion not allowed:** In this study, datasets are presented on their original time averaging and no conversion was performed. Solari *et al.* (2015) recommends time averaging of 30-s or less to capture the transient characteristics of TS wind outflow.

2. **Dependency of wind speed to the height:** In this study it is considered that the fitted curves are the product of sole wind speed varying with the height, not other meteorological parameters are taken into consideration. The height is here expressed as the variable y and it is assumed therefore the velocity profile (expressed here as the variable x) is enough to characterize the TS wind profile.
3. **Structural analysis not performed:** Structural analysis of thunderstorm winds and structures interactions is not performed in this work. Also, the profiles herein discussed should be used with caution, especially for dynamic analysis. This item comes relevant once considering that the evolving characteristics, turbulence, and wind velocities profiles of typical thunderstorms may cause extreme longitudinal dynamic excitation in susceptible structures, specialty for slender buildings, transmission lines, or long span buildings.
4. **Focus on the horizontal wind components:** The downdraft is mostly composed of vertical downwards moment, but after it impinges on the ground, it becomes mostly horizontal flow (outflow). The focus of this work is to simulate solely the maximum wind speeds of the outflow at its horizontal stage, because this is the stage that represents a major threat to the built environment.
5. **Turbulence not analyzed:** Considering the lack of agreements in terms of turbulence characteristics, this study refrains from including these factors. Instead, in Section 3.2 is developed an overview of the present understanding of the topic for non-tornadic thunderstorm winds.
6. **Probability of occurrence not analyzed:** Due to the low availability of TS wind profiles datasets it is not developed an analysis of probability of exceedance for the TS wind profiles for typical structural design return periods (e.g., 50-years).
7. **Background wind and storm motion not decomposed:** In this study the background wind is not decomposed in terms of background wind and storm motion contributions.
8. **Distance to touchdown:** In this study is not analyzed the distance of the downdraft touchdown to the point of the measurement. As Choi and Hidayat (2002) discussed, considering the constant evolution of thunderstorms profiles, it is plausible that the

wind profile had developed a maximum profile at a different point in the space that was not captured by the instruments. It is noted here that for future studies would be of major interest to know the estimated distance from the touchdown for the development of the maximum TS wind profiles.

9. **Extrapolation is not allowed:** due to the increased degree of uncertainty and randomness characteristics of TS wind profiles, data should not be extrapolated beyond the limits of the proposed fitted curve of the observed datasets (YOE, 1996).

4.2. ANALYSIS OF VERTICAL FULL-SCALE PROFILE DATASETS AND PROPOSED CURVE FITTING FUNCTIONS

Considering the method described in Section 5.1; a revision of the profiles discussed in Section 3.1 was performed to choose profiles that could meet the criteria proposed. Using automated applications such as <https://apps.automeris.io/> or through the manual analysis of wind data measurements records, the following datasets were extracted and analyzed.

4.2.1. Sherman (1987)

In Sherman (1987) an anemometric tower was used to collect the wind datasets, there were two major peaks of velocities that are very similar. Here it was found that the first peak of velocity at various levels was the most expressive at all captured heights and it was then herein taken for further analysis. In Figure 88 is shown the field data record extracted from Sherman (1987) (dashed orange line) and proposed model (continuous blue line).

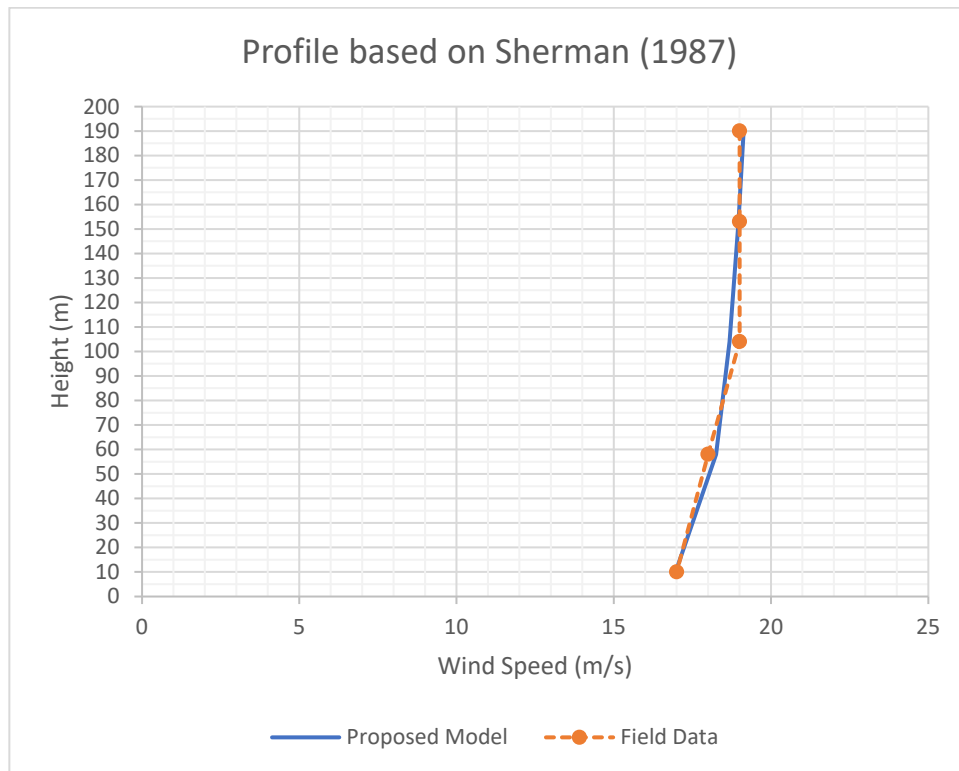


Figure 88. Proposed model (continuous blue line) and field data (dashed orange line) from vertical TS wind event extracted from Sherman (1987). Source: Author.

The proposed model is given by the logarithmic fitted function defined by Equation 14 and R-squared 0.88. The model overestimates wind speed at lower levels, underestimates in mid-levels, and overestimates the wind speed above 150 m. R-squared presented good adherence to field data.

$$x = 07348 \ln(y) + 15.272$$

Equation 14

$$R^2 = 0.88$$

4.2.2. Hjelmfelt *et al.* (1988)

In Figure 88 is shown field data record extracted from Hjelmfelt *et al.* (1988) (dashed orange line) and the proposed fitted curve (continuous blue line). As previously stated in this document, measurements taken during Fujita's studies have limited resolution in lower levels of the atmosphere and should be used with caution.

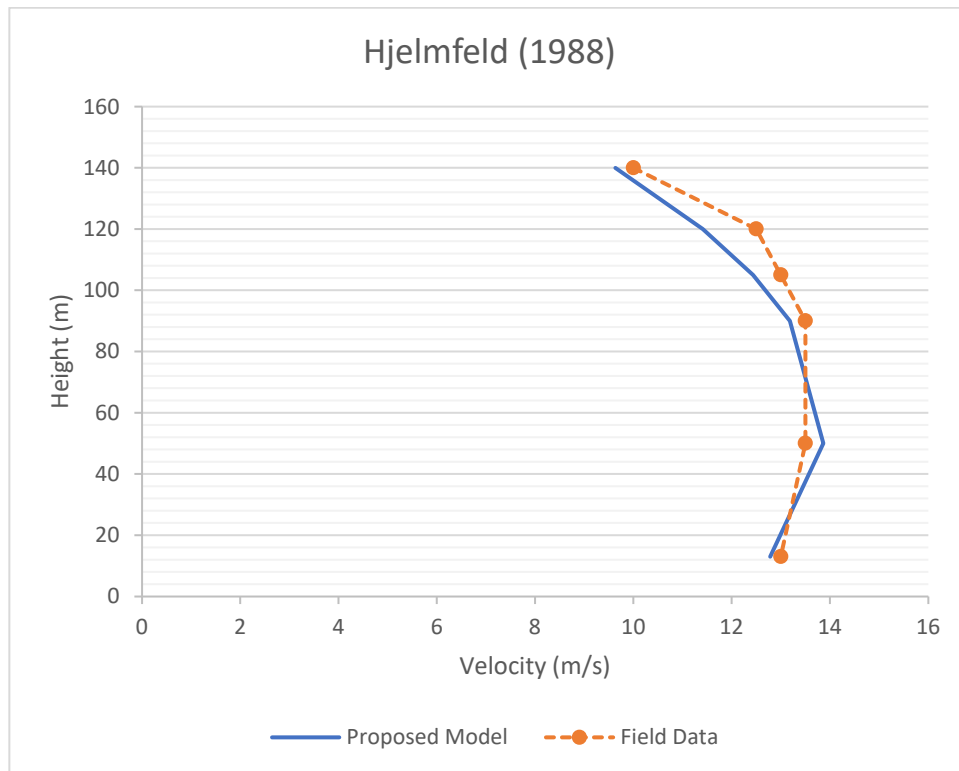


Figure 89. Proposed model (continuous blue line) and field data (dashed orange line) from vertical TS wind event extracted from Hjelmfelt (1988). Source: Author.

The proposed fitted curve is given by a second-order polynomial function defined by Equation 15 and R-Squared 0.92. It assumes an almost linear shape below 100 m and then the velocity decreases above that height. The use of this equation is not recommended since the maximum wind profile registered does not extend until 10 m and due to the lower resolution of purpose of those measurements.

$$x = -0.0006y^2 + 0.067y + 12.014 \quad \text{Equation 15}$$

$$R^2 = 0.92$$

4.2.3. Choi and Hidayat (2002)

In Figure 88 is shown field data record extracted from Choi and Hidayat (2002) (dashed orange line) and proposed fitted curve (continuous blue line).

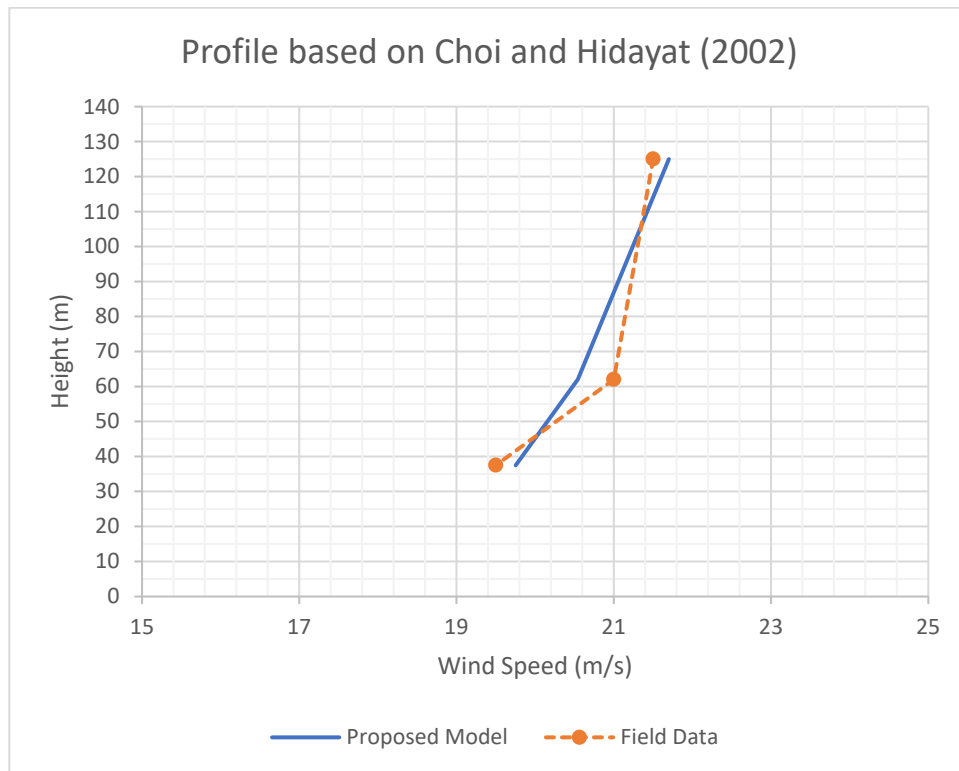


Figure 90. Proposed model (continuous blue line) and field data (dashed orange line) from vertical TS wind event extracted from Choi and Hidayat (2002). Source: Author.

The proposed fitted curve is given by the power curve equation defined in Equation 16 with R-squared of 0.86.

$$x = 14.883y^{0.0781} \quad \text{Equation 16}$$

$$R^2 = 0.86$$

The proposed fitted curve is given by a power function. This function slightly overestimates the wind speed at lower levels, it under estimates at mid-levels, and over estimates wind speed above 100m. The use of this equation is not recommended since the maximum wind profile registered does not extend up to 10 m.

4.2.4. Paluch *et al.* (2003)

In Figure 91 is shown the field data record extracted from Paluch *et al.* (2003) (dashed orange line) and proposed fitted curve (continuous blue line). The wind data modeled from this dataset show a model approximately linear with $x = 30 \text{ m}$ from 20 m to 40 m. These values are approximated because of the low resolution of the graph used to extract the dataset. Also, during the measurement of this TS event, the tower was damaged by the force of the wind,

potentially compromising the dataset. Since no measurement is available at 10 meters, this dataset cannot be further used to the purpose of this research.

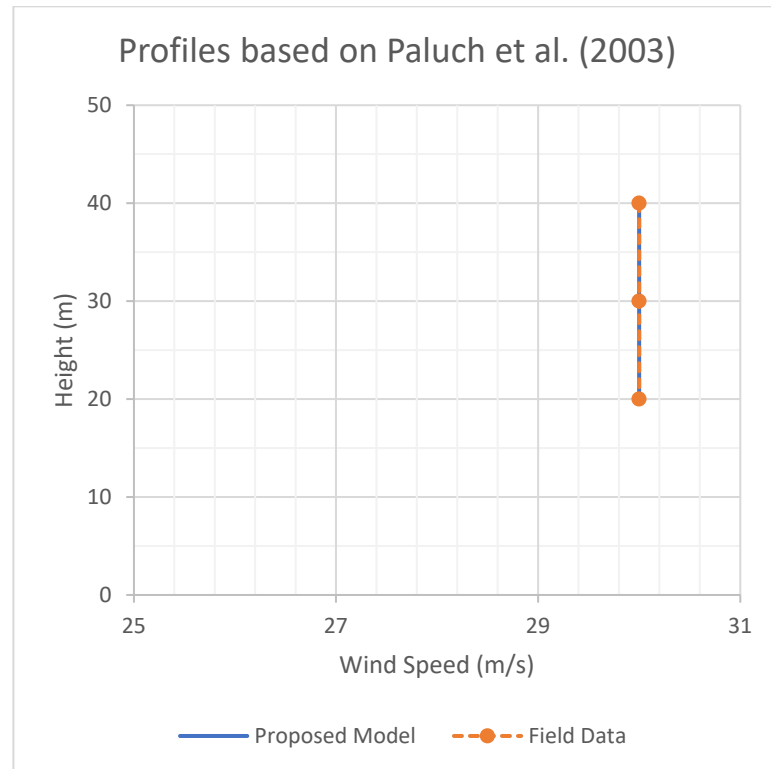


Figure 91. Proposed model (continuous blue line) and field data (dashed orange line) from vertical TS wind event extracted from Paluch et al. (2003). Source: Author.

4.2.5. Gast (2003) – RFD and Derecho Events

In Figure 92 is shown the field data record extracted from Gast (2003) for the RFD and for Derecho events (dashed blue and orange lines, respectively). Proposed fitted curves (continuous blue and orange lines, respectively) are also shown for each of the wind events.



Figure 92. Proposed model (continuous blue line) and field data (dashed blue line) from vertical TS wind event extracted from Gast (2003) for RFD event and proposed model (continuous orange line) and field data (dashed orange line) from vertical TS wind event extracted from Gast (2003) for Derecho event. Source: Author.

Proposed fitted curve for RFD event is given by the logarithmic function defined by Equation 17 and R-squared 0.66:

$$x = 1.412 \ln(y) + 25.977 \quad \text{Equation 17}$$

$$R^2 = 0.66$$

Proposed fitted curve for Derecho event is given by the linear equation defined by Equation 18 and R-squared 0.75.

$$x = 0.4362 y + 16.385 \quad \text{Equation 18}$$

$$R^2 = 0.75$$

Both proposed models have limited use since the anemometric towers sampled data only until 16 m. Also, equation proposed presents low adherence to the field data.

4.2.6. Choi (2004)

In Choi (2004) four events were analyzed, two events that presented maximum values were further analyzed, they occurred on the days of 25/12/2001 and 29/01/2001. In Figure 93 are shown the full-scale dataset and the two proposed fitted curve.

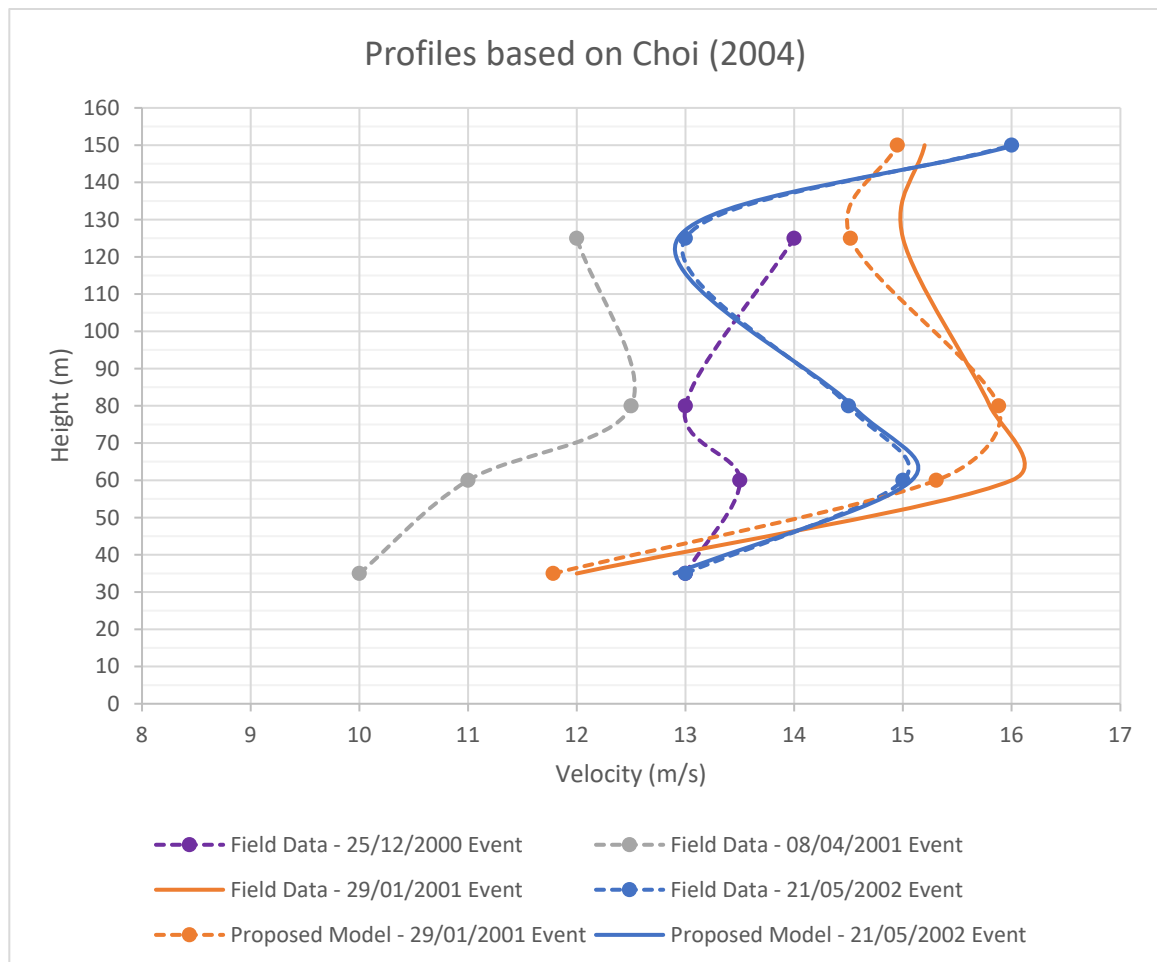


Figure 93. Thunderstorm events observed by Choi (2004). Each dashed line represents a different event observed. The two continuous lines represent best fit models proposed for two maximum et 29/01/2001 and 21/05/2022 events. Source: Author.

The proposed fitted curve for the dataset extracted from Choi (2004) for the thunderstorm event in 29/01/2001 is given by the third-degree polynomial function defined by Equation 19 and R-squared defined below:

$$x = 0.00001762y^3 - 0.0056y^2 + 0.5488y - 1.35 \quad \text{Equation 19}$$

$$R^2 = 0.99$$

For the event in 05/21/2002 the model is defined by the third-degree polynomial Equation 20 and R-squared below:

$$x = 0.0000268 y^3 - 0.0072y^2 + 0.589y \quad \text{Equation 20}$$

$$R^2 = 0.99$$

The proposed fitted curve is described by third-degree polynomial function and presented great fit to the field datasets, but they cannot be further used since the original datasets were not sampled at or around 10 m and the normalization equation is not going to work for the purpose of this exercise.

4.2.7. Lombardo *et al.* (2014)

In Figure 94 are presented four maximum profiles based on Lombardo *et al.* (2014) measurements. One equation is proposed for the two most significant events, one on 03-Aug-2010 and another one 06-Jun-2009. The event in 21-May-2009 presented a classic approximately linear profile, which when normalized and compared to the other profiles it does not represent the worst-case scenario and the 12-Aug-2009 was an overall weaker event and it is not further analyzed.

In blue is presented the maximum profile for the event in 03-Aug-2010, in which the dashed line with points represents the field datapoints and the continuous blue line represents the proposed fitted curve based on the best fitting curve. Similarly, the orange line represents the maximum profile for the event in 06-Jun-2009, in which the dashed line is the field data, and the continuous orange line is the proposed fitted curve. The full yellow line with dots representing the field data for the event in 21-May-2009 and the green line with dots representing the event in 12-Aug-2009 are also showed in Figure 94.

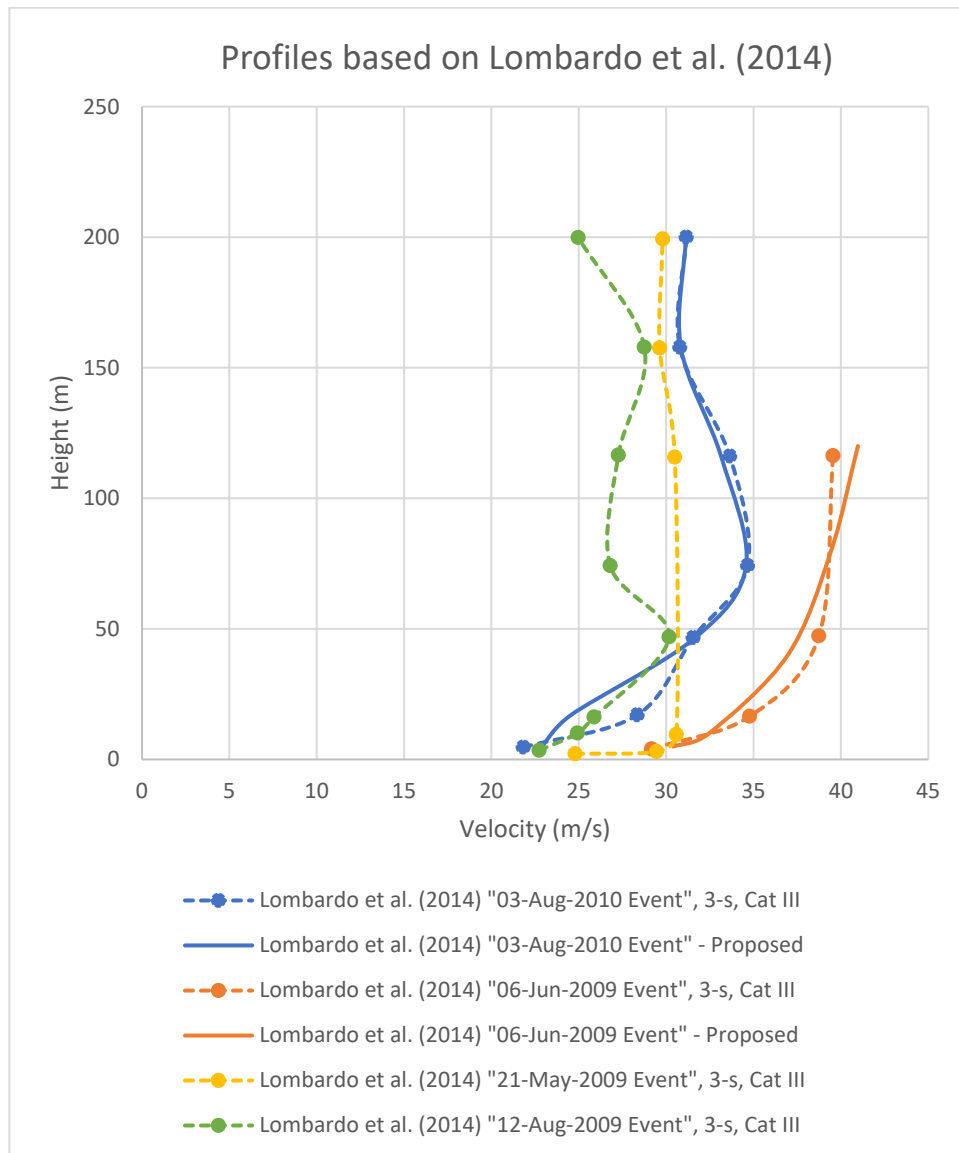


Figure 94. Two maximum profiles based on Lombardo et al. (2014) datasets. In this case the Maximum Profile 1 is showed in Blue, and the Maximum Profile 2 is showed in orange. In both cases the proposed model is given by the continuous line and the field data is given by the dashed line.

Source: Author.

The proposed fitted curve of 06-Jun-2009 (orange) is defined by the power function given by Equation 21 with R-squared 0.94.:

$$x = 26.1481y^{0.0938} \quad \text{Equation 21}$$

$$R^2 = 0.94$$

The proposed fitted curve of 03-Aug-2010 is given by a third-degree polynomial equation defined by Equation 22 with R-squared 0.96:

$$x = 9.0135E - 06y^3 - 0.0035y^3 + 0.39369y + 20.9633$$

Equation 22

$$R^2 = 0.96$$

4.2.8. Gunter and Schroeder (2015)

In Figure 95 are presented two maximum profiles based on Gunter and Schroeder (2015). Two profiles were extracted from this full-scale measurement since they presented very distinguished maximum values at three distinct levels. In blue is presented the maximum profile for "PEP" event, in which the dashed line with points represents the field datapoints and the continuous blue line represents the proposed model – based on the best fitting curve for such dataset. Similarly, the orange line presents the maximum profile for "SYR", where the line is the field data, and the continuous orange line is the proposed model.

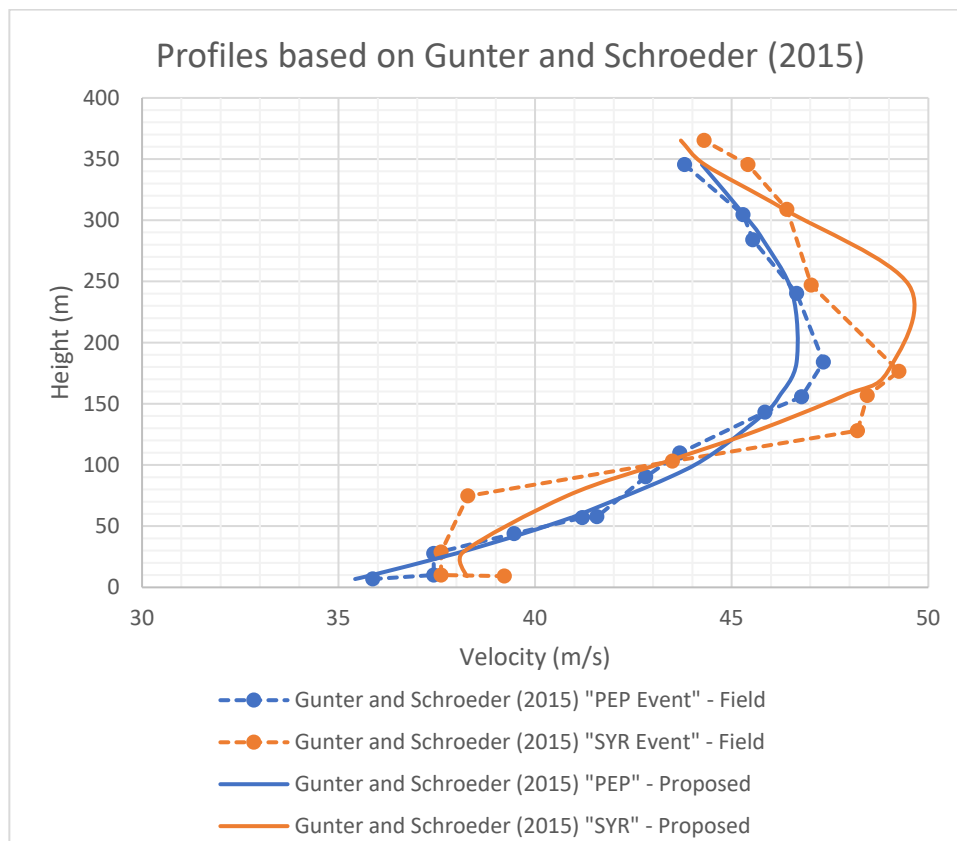


Figure 95. Two maximum profiles based on Gunter and Schroeder (2015) datasets. In this case the Maximum Profile 1 is showed in Blue, and the Maximum Profile 2 is showed in orange. In both cases the proposed model is given by the continuous line and the field data is given by the dashed line.

Source: Author.

The proposed fitted curve of PEP Event (blue line) is defined by the third-order polynomial showed in Equation 23 of third order and R-squared 0.98:

$$x = 1.3628E-07y^3 - 0.000309y^2 + 0.1142y + 35.37$$

Equation 23

$$R^2 = 0.98$$

The proposed fitted curve of SYS Event (orange) is defined by the fourth-order polynomial showed in Equation 24 and R-squared showed below:

$$x = 1.44E-08y^4 - 1.10E-05y^3 + 0.00245y^2 - 0.110y + 39.044$$

Equation 24

$$R^2 = 0.92$$

4.2.9. Burlando *et al.* (2017)

In Figure 96 is shown the field data record extracted from Burlando *et al.* (2017) (dashed orange line) and proposed fitted curve (continuous blue line).

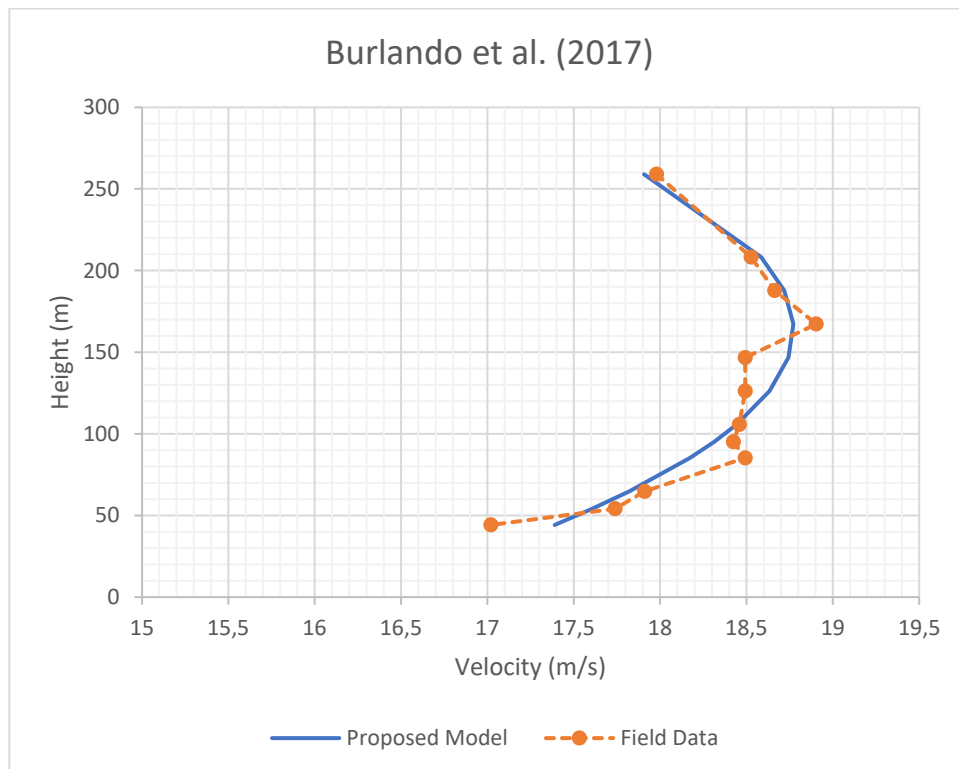


Figure 96. Proposed model (continuous blue line) and field data (dashed orange line) from vertical TS wind event extracted from Burlando *et al.* (2017). Source: Author.

The proposed fitted curve function is given by the second-degree polynomial function defined by Equation 25 and R-squared showed below:

$$x = 0.00005y^2 + 0.0284y + 16.368$$

Equation 25

$$R^2 = 0.85$$

The proposed fitted curve slightly overestimates velocity below 80 m and slightly underestimates above this level. Although, this case is not be further analyzed since the original dataset was not sampled at or around 10 m and the normalized equation does not work for the purpose of this exercise.

4.2.10. Repetto (2018)

In Figure 97 is shown the profile measurement of one extreme thunderstorm outflow event for 1-s averaging time (blue) and 10-min averaging time (orange), where the dashed lines represent field measurements and the continuous line represent the proposed models. Note that even though the profile decreased in magnitude from 1-s to 10-min time averaging, the equation shape maintained similar format, specially at lower levels, although these profiles are not taken for further analysis since there is no measurement available at or close to 10 meters height.

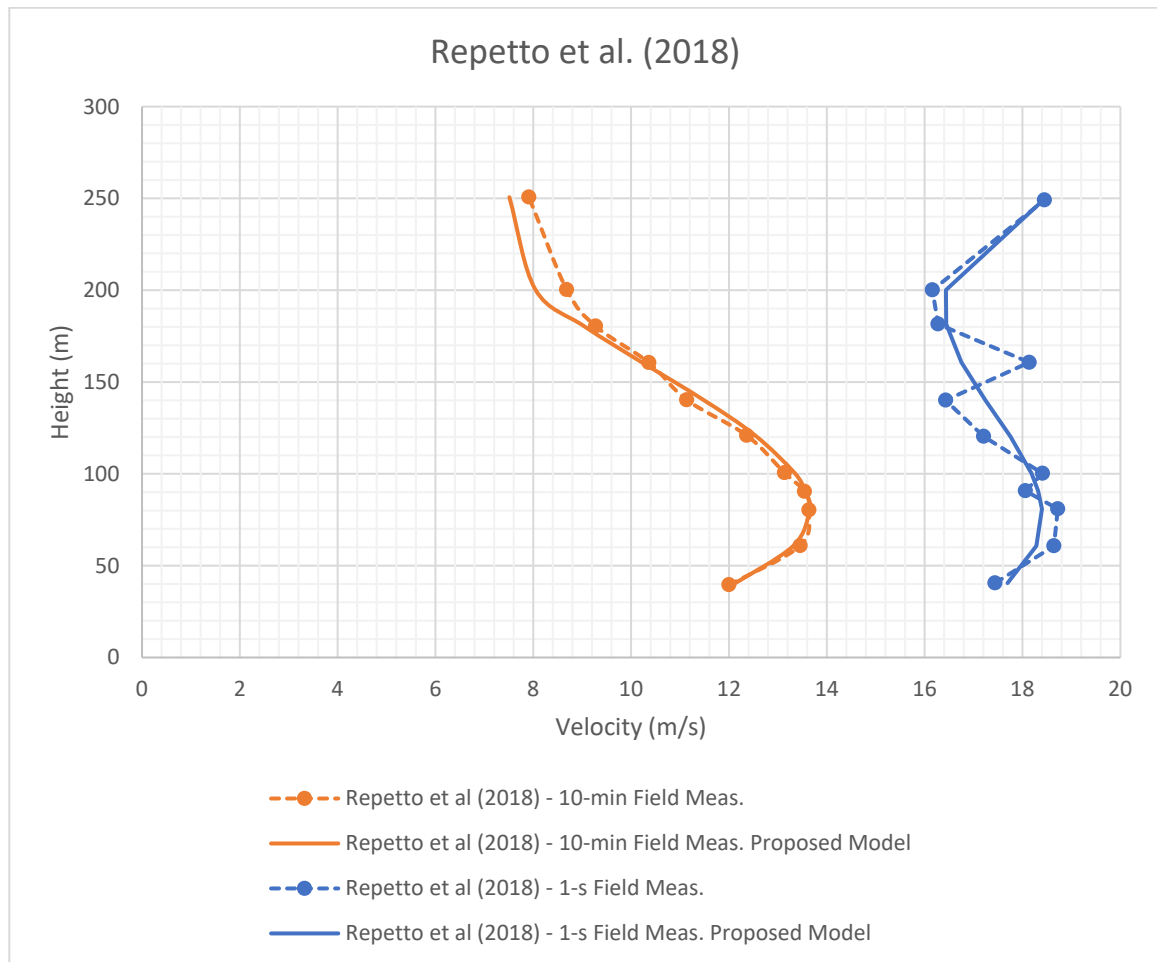


Figure 97. Profile measurements of Repetto et al. (2018) at maximum stage for both 1-s (blue) and 10 min (orange) averaging time. where the dashed lines represent field measurements and the continuous line represent the proposed models. Source: Author.

The 1-s averaging time proposed fitted curve is defined by a third-degree polynomial function given by Equation 26 with a squared-R of 0.65.

$$x = 2.642E - 06y^3 - 0.0011y^2 + 0.1161y + 14.556 \quad \text{Equation 26}$$

$$R^2 = 0.65$$

The 10-min averaging time proposed fitted curve is also defined by a third-degree polynomial function given by Equation 27 with a squared-R of 0.99.

$$x = 3.16E - 06y^3 - 0.0015y^2 + 0.174y + 7.427 \quad \text{Equation 27}$$

$$R^2 = 0.65$$

4.2.11. Zhang et al. (2019)

In Figure 94 are presented two maximum profiles based on Zhang et al. (2019). Two profiles were extracted from the full-scale measurement since they presented very distinguished

maximum values at different levels instants, even though they were only one minute apart. In blue is presented the maximum profile at 15:00 Local Standard Time (LST), referred as Zhang *et al.* (2019) "15:00 Meas.", in which the dashed line, the points represent the field datapoints and the continuous blue line represents the proposed fitted curve – based on the best fitting curve for such dataset. Similarly, the orange line presents the profile at 15:01 Local Standard Time (LST) one minute apart, referred as Zhang *et al.* (2019) "15:01 Meas.", where the dashed line is the field data, and the continuous orange line represents the proposed fitted curve.

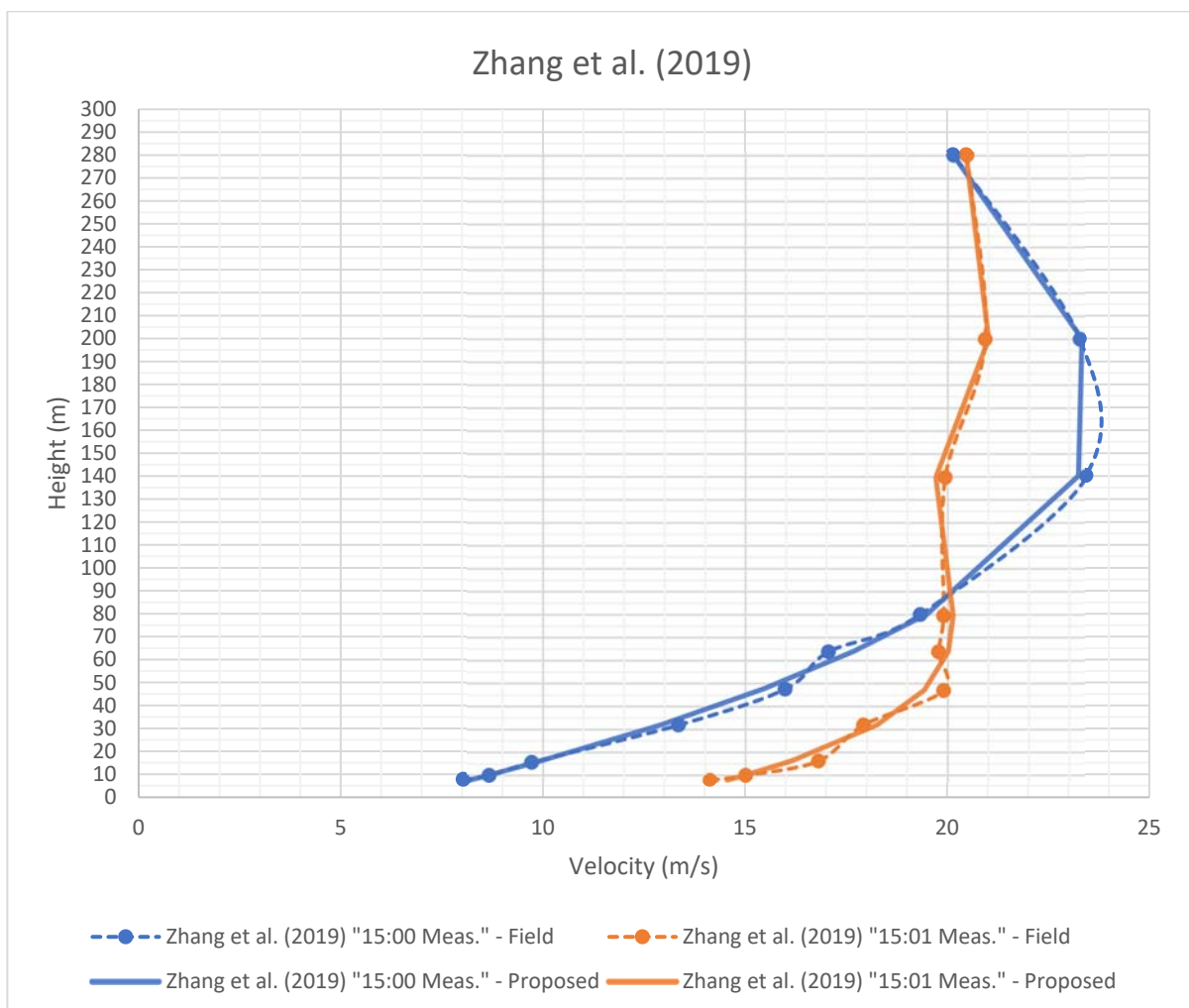


Figure 98. Proposed model (continuous blue line) and field data (dashed orange line) from vertical TS wind event extracted from Zhang *et al.* (2019). Source: Author.

The proposed fitted curve of Maximum Profile 1 (blue) defined by the third order polynomial function showed in Equation 28 with R-squared showed below:

$$x = 1E - 06x^3 - 0.001x^2 + 0.2324x + 6.44 \quad \text{Equation 28}$$

$$R^2 = 0.99$$

The proposed fitted curve of Maximum Profile 2 (orange) is given by the fourth order polynomial function showed in Equation 29 with R-squared below:

$$x = -3E - 08x^4 + 2E - 05x^3 - 0.0031x^2 + 0.2595x + 12.71 \quad \text{Equation 29}$$

$$R^2 = 0.98$$

4.3. ANALYSIS OF FULL-SCALE THUNDERSTORM WIND PROFILES AND RESPECTIVE PROPOSED FITTING PROFILE CURVE FUNCTIONS

In this section full-scale TS wind profiles are further analyzed altogether. In Figure 99 all maximum profiles extracted from different sources in the literature are showed together independently of their averaging time and terrain roughness, where in the y-axis is shown height and in the x-axis is shown wind speed. In this same figure, call-outs were added to each profile highlighting the time averaging applied to the original datasets, as well as terrain category where those datasets were acquired from.

The profiles in Figure 99 highlights the wide range of magnitudes and shapes TS wind outflow profiles may assume at their maximum stage. From the altogether analysis, a few conclusions can be proposed, in general they all presented the "nose-like" profile independently of the time averaging approach applied; there is a trend in which profiles in smother terrains tend to develop higher wind speeds at lower levels, which makes sense considering the lesser of the effect of the terrain roughness to these outflows. All TS outflow events were the result of more intense and organized storms, with exception of Sherman (1987), which from a weaker and isolated thunderstorm event.

Regarding the proposed TS wind profile functions, Figure 99 makes evident that there is not what it is called "one model fits all", although it is noticeable that most of the field measurements fitted a curve normally defined by a third-degree polynomial function. This is most likely because this equation can simulate the typical downburst "nose-like" profile at lower levels and it decreases the vertical velocity above at higher levels.

Additionally, in Table 5, these same profiles are listed, where in the five left columns, the main characteristics of the full-scale measurements are summarized; and in the other six remaining columns to the right of the same table, considerations about actions taken towards the development of the final proposed fitted curve profile functions are presented.

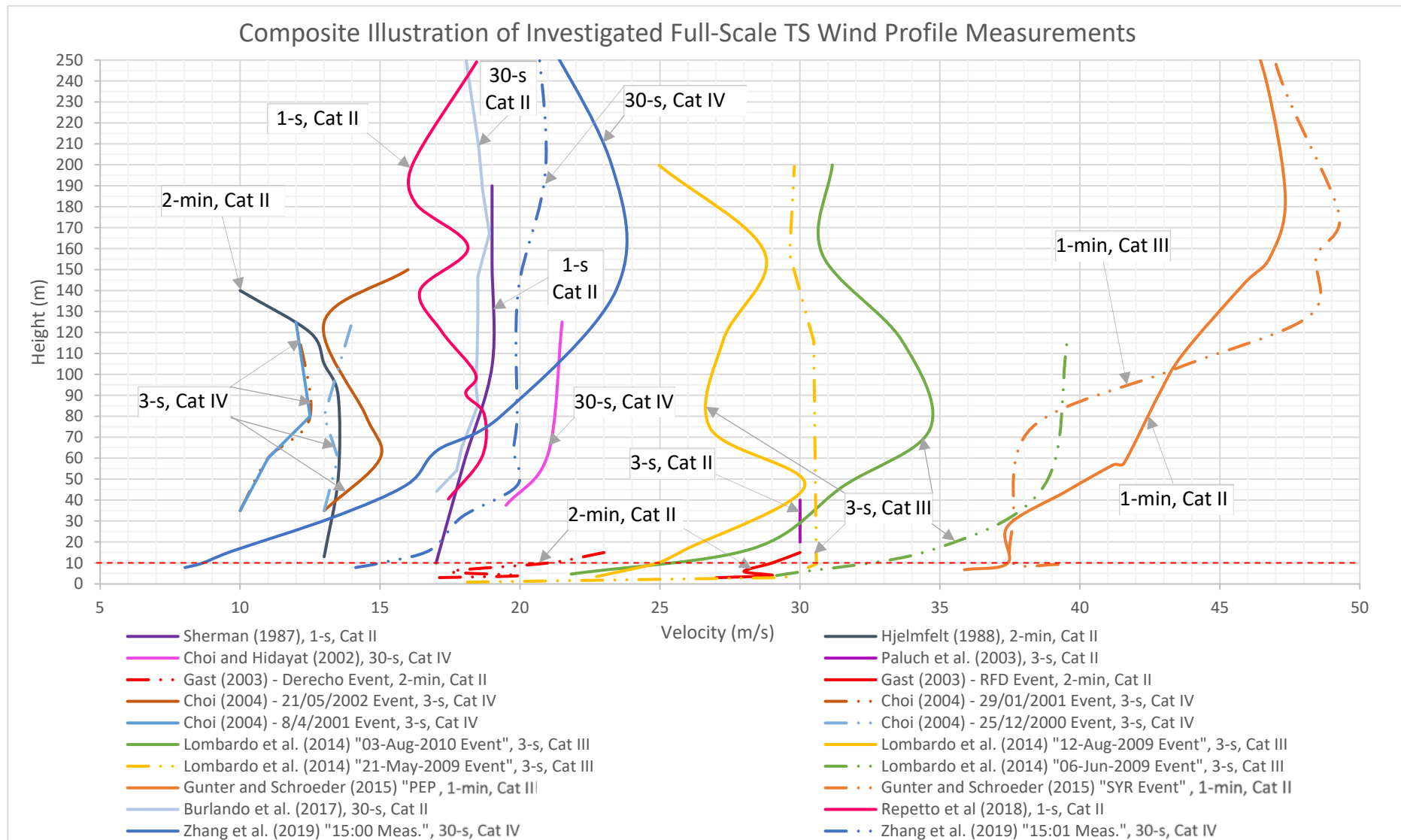













Figure 99. Composite illustration of wind outflow profiles field measurements investigated in this study. Each color represents the maximum profile from each source. It also showed time averaging and terrain category as per NBR 6123 in which each dataset was acquired from. Source: Author.

Table 4. Summary of all full-scale measurements and proposed fitted curve profile considerations. Source: Author.

Full-scale Measurements					Proposed Fitted Curve Profile Considerations					
#	Author	Time Ave	Terrain (NBR 6123)	TS Type	Measure at 10 m	Measure at 50+ m	Fitting Eq. Type	R	Allowable Requirement	Comments/Actions
1	Sherman (1987)	1-s	Cat II	Isolated	Yes	Yes	Logarithmic	0.88	✓	
2	Hjelmfelt (1988)	2-min	Cat II	Organized	None	Yes	Polynomial Order 2	0.92	⊘	Lower resolution measurements. Aeronautical Industry Applications.
3	Choi and Hidayat (2002)	30-s	Cat IV	Organized	None	Yes	Power	0.86	⊘	No measurement at 10 m.
4	Paluch <i>et al.</i> (2003)	3-s	Cat II	Organized	None	Yes	Linear	1	⊘	Tower damaged during the event. Low Resolution of dataset.
5	Gast (2003) - RFD Event	2-min	Cat II	Organized	Yes	None	Logarithmic	0.66	⊘	No measurement above 16 m. Used only for velocity below 10 m.
6	Gast (2003) - Derecho Event	2-min	Cat II	Organized	Yes	None	Linear	0.75	⊘	No measurement above 16 m. Used only for velocity below 10 m.
7	Choi (2004) - 29/01/2001 Event	3-s	Cat IV	Organized	None	Yes	Polynomial Order 3	0.97	⊘	No measurement at 10 m.
8	Choi (2004) - 21/05/2002 Event	3-s	Cat IV	Organized	None	Yes	Polynomial Order 3	0.99	⊘	No measurement at 10 m.
9	Choi (2004) - 8/4/2001 Event	3-s	Cat IV	Organized	None	Yes	Polynomial Order 2	0.91	⊘	No measurement at 10 m.

Full-scale Measurements					Proposed Fitted Curve Profile Considerations					
#	Author	Time Ave	Terrain (NBR 6123)	TS Type	Measure at 10 m	Measure at 50+ m	Fitting Eq. Type	R	Allowable Requirement	Comments/Actions
10	Choi (2004) - 21/05/2002 Event	3-s	Cat IV	Organized	None	Yes	Polynomial Order 3	1		No measurement at 10 m.
11	Lombardo <i>et al.</i> (2014) ""3-Aug-2010 Event""	3-s	Cat III	Organized	Yes	Yes	Polynomial Order 3	0.95		
12	Lombardo <i>et al.</i> (2014) ""2-Aug-2009 Event""	3-s	Cat III	Organized	Yes	Yes	Polynomial Order 3	0.67		Proposed Fitted Curve Equation not representative.
13	Lombardo <i>et al.</i> (2014) "21-May-2009 Event"	3-s	Cat III	Organized	Yes	Yes	Linear	0.6		Proposed Fitted Curve Equation not representative.
11	Lombardo <i>et al.</i> (2014) "6-Jun-2009 Event"	3-s	Cat III	Organized	Yes	Yes	Power	0.94		
12	Gunter and Schroeder (2015) "PEP Event"	1-min	Cat II	Organized	Yes	Yes	Polynomial Order 3	0.98		
13	Gunter and Schroeder (2015) "SYR Event"	1-min	Cat III	Organized	Yes	Yes	Polynomial Order 3	0.92		
14	Burlando <i>et al.</i> (2017)	30-s	Cat II	Organized	None	Yes	Polynomial Order 2	0.85		No measurement at 10 m.
15	Repetto <i>et al.</i> (2018)	1-s	Cat II	Organized	None	Yes	Polynomial Order 3	0.65		Proposed Fitted Curve Equation not representative.
16	Zhang <i>et al.</i> (2019) "15:00 Meas."	30-s	Cat V	Organized	Yes	Yes	Polynomial Order 3	0.99		
17	Zhang <i>et al.</i> (2019) "15:01 Meas."	30-s	Cat V	Organized	Yes	Yes	Polynomial Order 4	0.98		

4.3.1. Proposed fitted curves meeting allowable requirements

Out of the seventeen full-scale measurement profiles datasets analyzed in this study, only seven profiles were found to suffice the requirements described in Section 5.1. In Figure 100, the fitted curve profiles functions (note, not full-scale measurements any longer) meeting criteria summarized in Table 5 are shown together. Note that it would be incorrect to extrapolate the values of the equations herein presented beyond the limits of available data due to the randomness characteristics of TS wind, therefore profiles from Hjelmfelt (1988), Choi and Hidayat (2002), Paluch *et al.* (2003), Choi (2004), and Burlando *et al.* (2017), Repetto *et al.* (2018) were excluded from further analysis due to the fact that the original full-scale datasets do not contain measurements taken at or below 10 m. Gast (2003) measurements are excluded because of low height range in which these datasets were captured/available. This exercise highlights not only the importance of acquiring TS wind full-scale measurements at the standard height of 10 m, but also the need to acquire data at higher elevations, in general, of at least 150 m when aiming to improve knowledge on the thunderstorm winds effects to tall buildings.

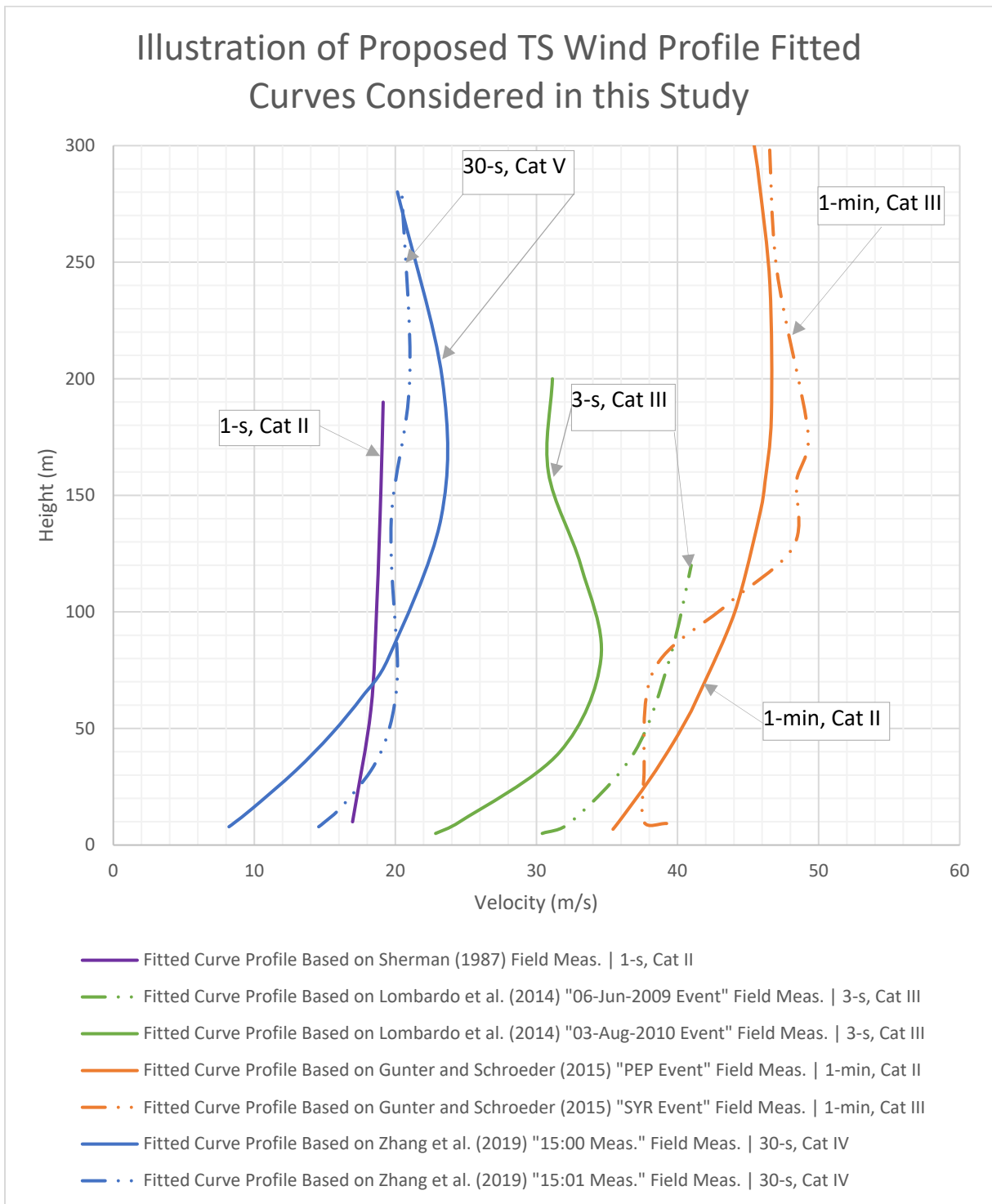


Figure 100. Illustration of proposed TS wind profile fitted curves based on full-scale measurements considered in this study. Source: Author.

In Figure 101, the same profiles are now showed normalized to their corresponding wind speeds at 10 meters. By analyzing such figures, the measurements taken by Zhang *et al.* (2019) "15:00 Meas." represents a global worst-case scenario, following a shape very atypical when compared to other measurements. As mentioned in Section 3.1 the influence of the terrain

and surrounding buildings may have led to modifications in the TS outflow profile, causing significantly higher normalized factors, as seen in Zhang *et al.* (2019) measurement at 15:00.

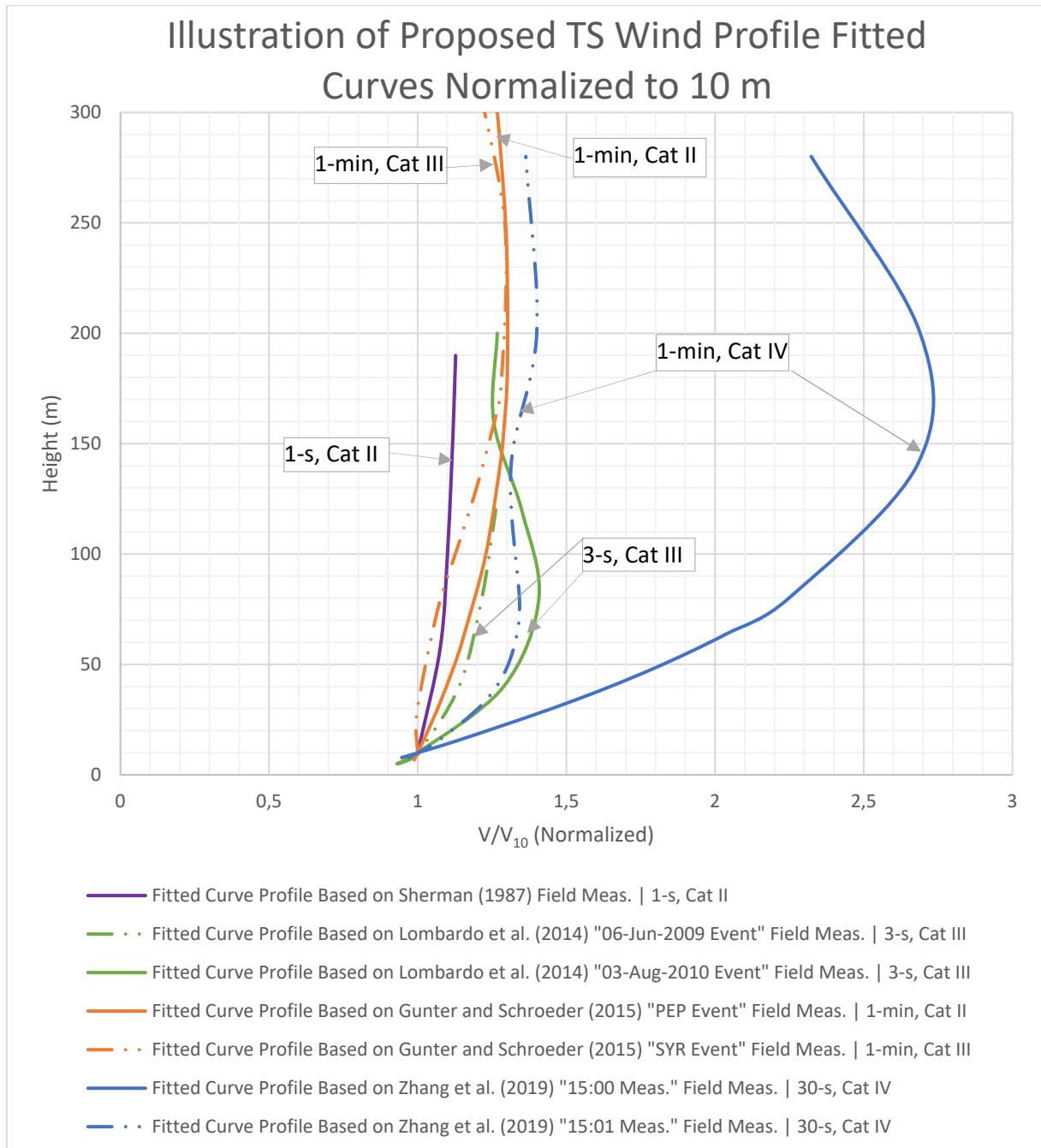


Figure 101. Illustration of proposed TS wind profile fitted curves based on full-scale measurements considered in this study. Datasets are normalized to their wind speed at 10 m. Source: Author.

4.3.2. Proposed fitted curves at levels below 10 meters

The wind speed measurements below the standard normalized height of 10 meters showed in Figure 101 are now zoomed into the 10 m surroundings in Figure 102. Note that this time,

it is added to this figure the profiles of the TS events (RFD and derecho) by in Gast *et al.* (2013), which as previously discussed were captured only at relatively lower elevations. Here, all profiles tend to show slightly decrease of velocity below 10 m, but considering limitations of these measurements and unknown effects of the terrain roughness to the final wind profile; aiming for a conservative outlook, it is suggested to use the TS wind velocity captured at 10 meters as a reference for future structural analysis with no reductions allowed.

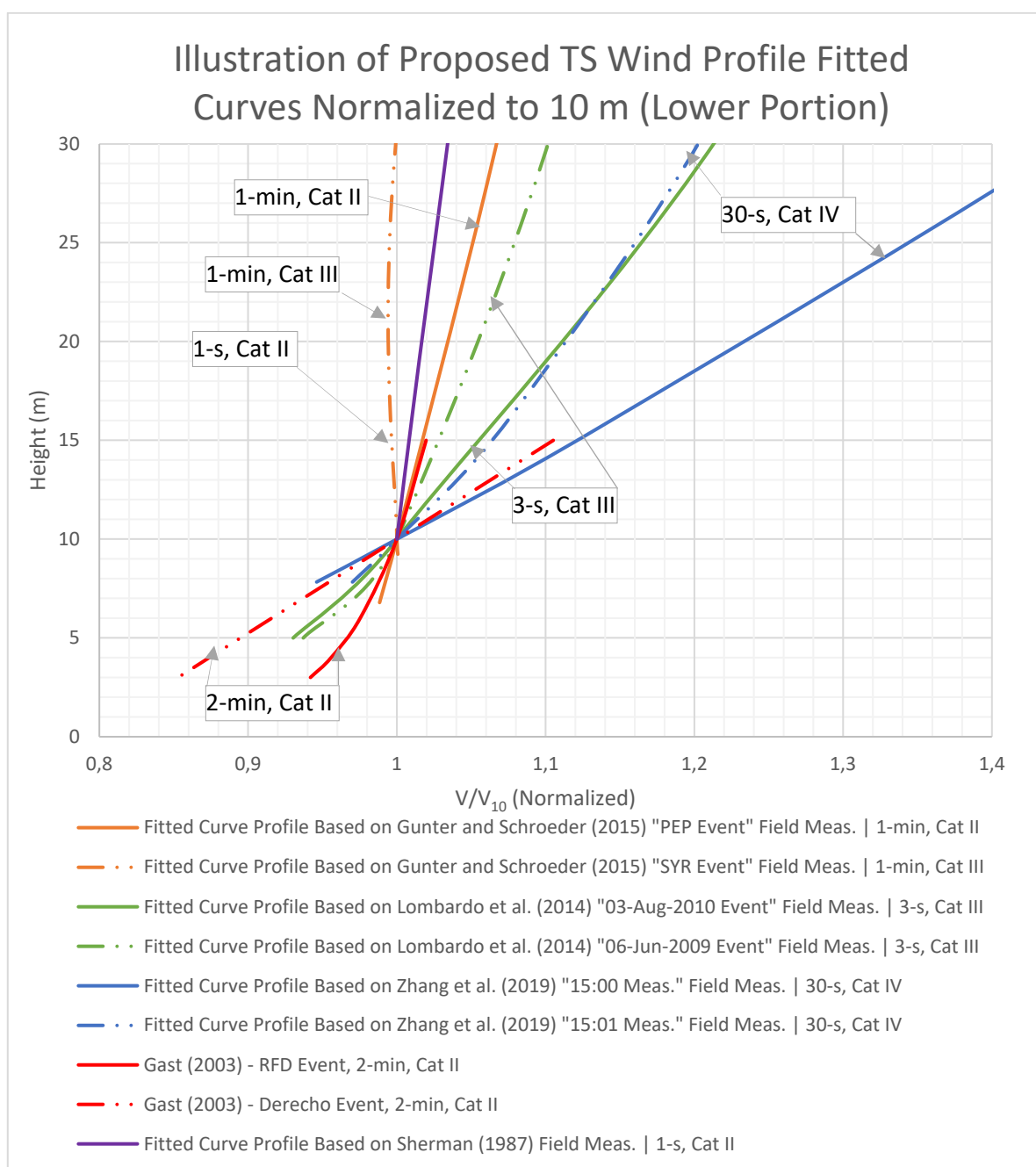


Figure 102. Illustration of proposed TS wind profile fitted curves based on full-scale measurements considered in this study. Datasets are normalized to their wind speed at 10 m. Only the lower portion of the profile is shown. Source: Author.

4.4. COMPARASION OF PROPOSED FITTED CURVE PROFILES TO EXISTING ANALYTICAL THUNDERSTOM WIND MODELS

In this section, four downburst models commonly referred to in the literature are now compared against the proposed fitted curves. With exception of Zhang *et al.* (2019) "15:00 Meas.", all modeled curve functions presented a similar shape and magnitude of the model profile proposed in Ponte Junior (2005) for k (background wind contribution) varying from 0.35 to 1. The agreement with Ponte Junior (2005) model for $k=0.35$ shows consistency with the typical contribution of background wind as recently proposed by Riera (2016, 2020).

For the other models analyzed, which are Osegura & Bowles (1988), Vicroy (1992), and Wood & Kwok (2000), were more similar to more intense event showed in Zhang *et al.* (2019) "15:00 Meas.", with an exception that the maximum speed in the existing models was found to be at lower levels comparatively to the proposed fitted curve. Note that these many of these models used full-scale measurements to validate their outputs from datasets mostly developed for aeronautical applications and as discussed previously, there are limitations of these datasets at lower levels. Considering these finds, a more in-depth comparisons of existing downburst models to more recent full-scale datasets is therefore suggested.

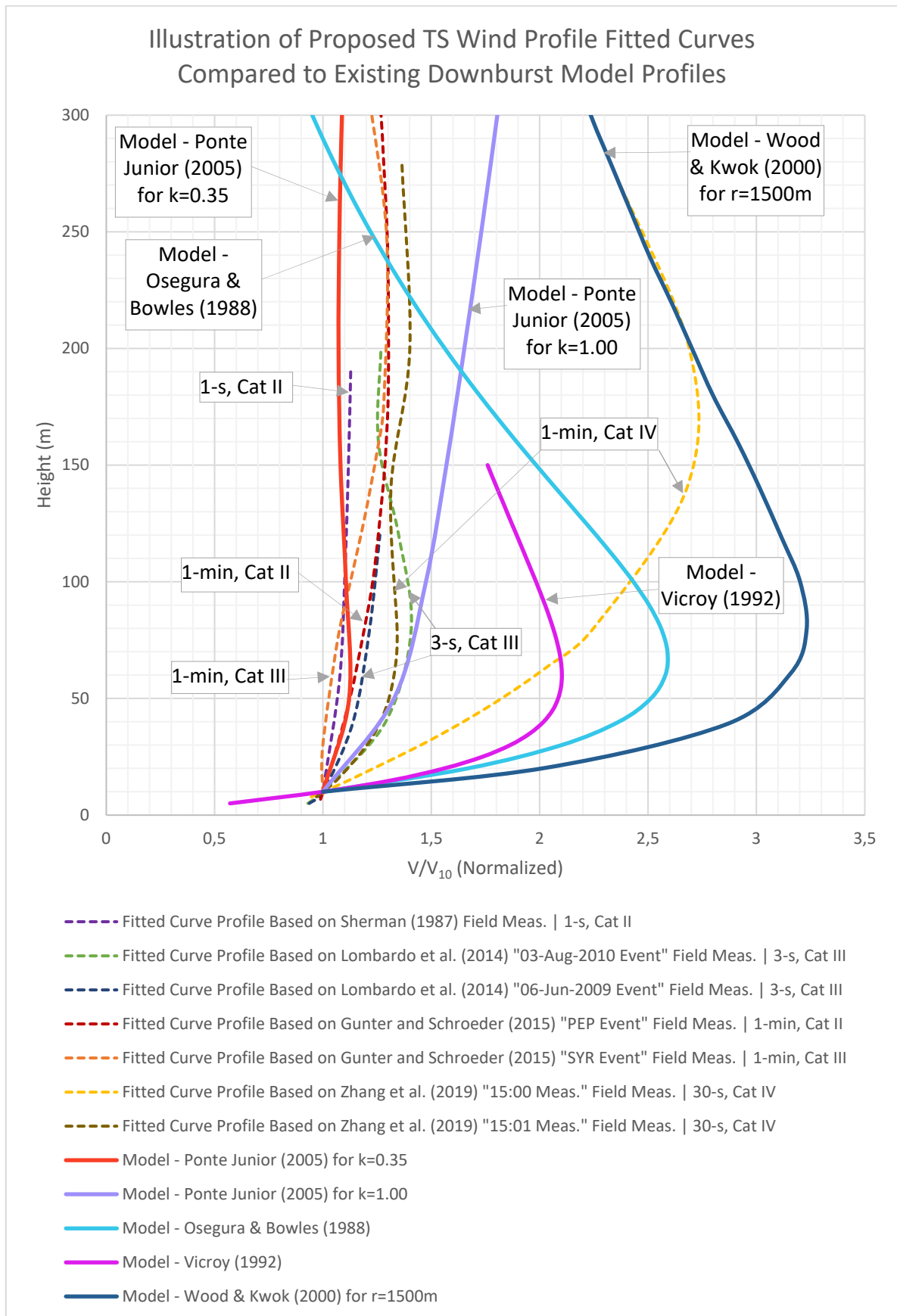


Figure 103. Illustration of proposed TS wind profile fitted curves based on full-scale measurements considered compared to other existing TS wind models normalized to V_{10} . Source: Author.

4.5. PROPOSED FITTING CURVE PROFILE FUNCTIONS COMPARED TO EXISTING WIND CODES

In this section, the obtained fitted curve profile functions for TS wind profiles are taken to further discussion and analyzed against the NBR 6123 synoptic wind profiles and two other TS wind profiles that have to date attempted to implement TS wind provisions within codes and standards.

4.5.1. Results comparison to TS wind codes and standards: ISO 4354 and AS/NZS 7000

As discussed in Section 3.3, there are only two wind standards that have included provisions for TS wind outflows, these standards are the ISO 4354 and AS/NZS 7000. In Figure 104 the fitted profile curve functions for TS wind profiles are shown together with the profiles proposed in ISO 4354 and AS/NZS 7000 for an open flat terrain (equivalent to Category II as per NBR 6123) and 3-s time averaging, with all profiles normalized to their velocities at 10 meters (AS/NZS1170.2, 2011; ISO 4354, 2009). Note that AS/NZS 7000 underestimated significantly the wind load at almost all levels, with the exception of below 10 meters, although ISO 4354 presents great adherence to the fitted functions herein presented.

Note that neither of these codes specifies storm-specific turbulence intensity, aerodynamic shape factors, and considerations of terrain roughness impacts to the profiles. They do consider modifier factors, such as topographic multipliers or regional factors, which can lead to slightly modified profiles.

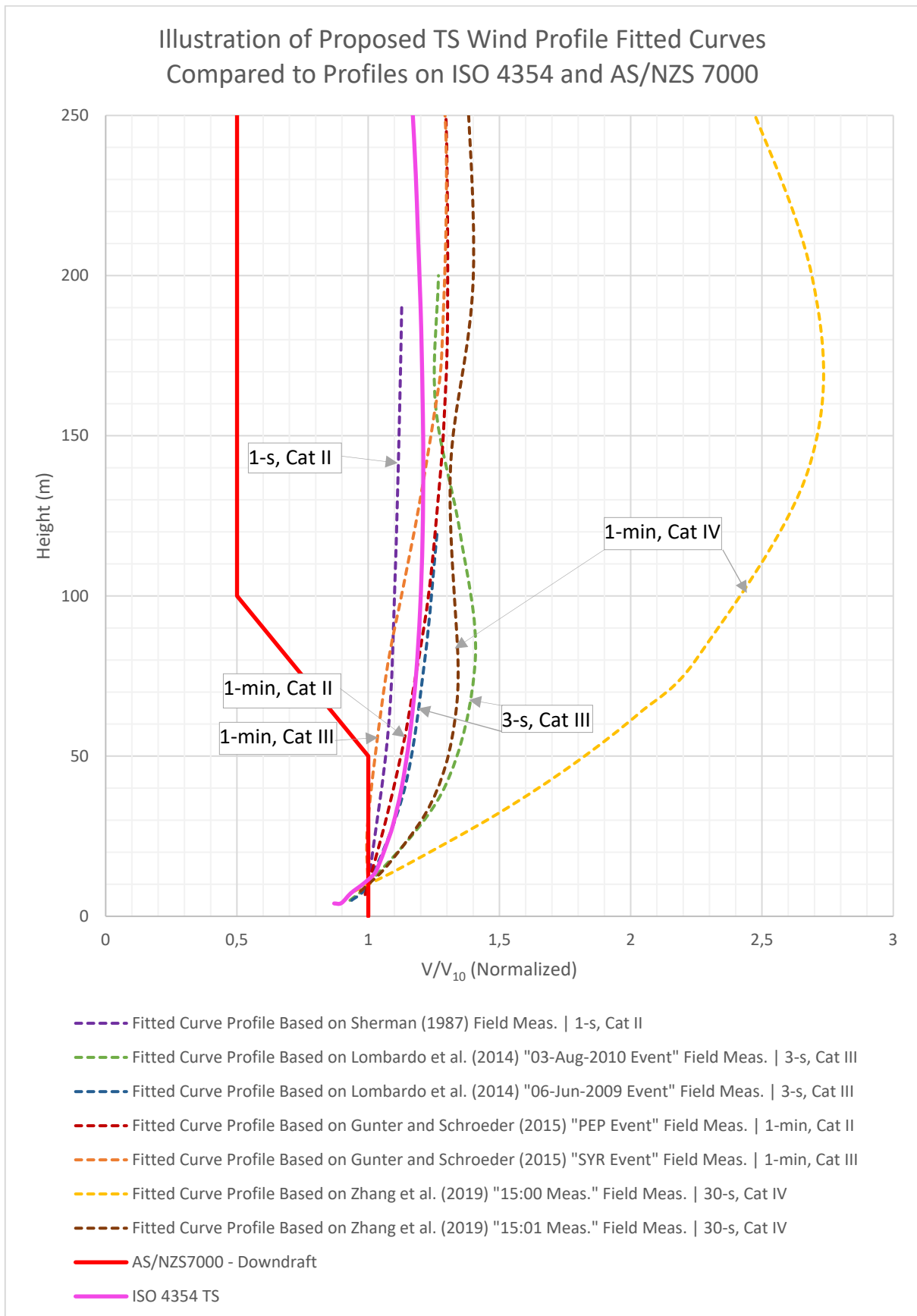


Figure 104. Illustration of proposed TS wind profile fitted curves based on full-scale measurements considered in this study compared to TS profiles on ISO 4354 and AS/NZS 7000. Source: Author.

4.5.2. Results investigation against NBR 6123 profiles

The comparison of proposed fitted curve profiles obtained are now analyzed against the typical ABL wind profiles established in NBR 6123. In this exercise is brought a more practical perspective of how the TS measurements compare with the present industry standards of structural design in Brazil. In Figure 105, Figure 106, and Figure 107 are presented the proposed fitted curve profiles against the corresponding NBR 6123 profiles for categories II, III, and IV respectively.

In Figure 105 is shown the fitted curve profiles for Gunter and Schroeder (2015) "PEP Event" and Sherman (1987) along with various NBR 6123 Category II profiles for various time averaging. Sherman (1987) measured profiles presented velocities significantly lower than the existing NBR 6123 for 3-s averaging time (closest available), therefore the latter represents a more conservative approach. This is aligned with previous findings that indicated that ABL wind profiles represent the most conservative approach than TS wind profiles generated by isolated and weaker storm outflows.

The same is not observed for Gunter and Schroeder (2015) "PEP Event". This event was the result of an intense and organized thunderstorm outflow that generated a wind speed profile with higher intensity higher, varying between 10 and 20% higher the 60-s time averaging profile of NBR 6123. Although it is interesting to note that the profile shape of the proposed fitted curve extracted for this TS wind event is near to the power law profile proposed in the NBR 6123 for that same terrain at lower levels. Also, a "nose-like" maximum is formed between 150 and 200 meters, and it decreases to lower values than what is established by the NBR 6123 at heights above 300 meters.

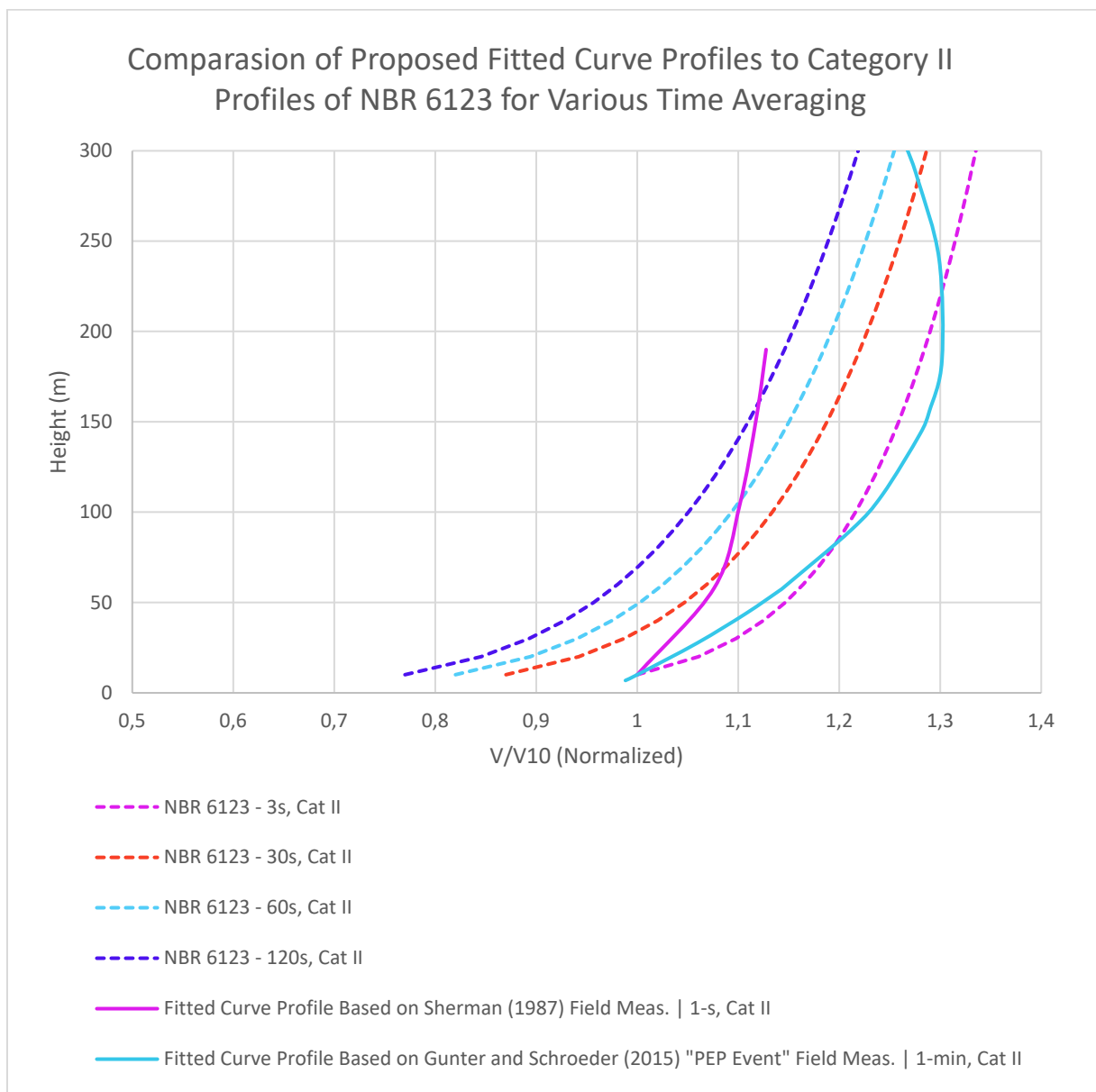


Figure 105. Comparison of proposed fitted curve profiles to category II profiles of NBR 6123 and various time averaging. Source: Author.

In Figure 106 the maximum fitted curve profiles of Gunter and Schroeder (2015) "SYR Event" and Lombardo *et al.* (2014) for both 03-Aug-2010 and 06-Jun-2009 events are presented along with the NBR 6123 Category III profiles for various time averaging. Note that all the proposed fitted curve profiles for the TS wind events analyzed presented higher wind speed magnitude for their respective applied time averaging methods when compared to the profiles established by NBR 6123. This time, the profiles had a major variation in shape (compared to Category II) and a larger discrepancy in magnitude compared to the NBR 6123 profiles. Also, it is noticeable the effect of the terrain in the profiles dragging up higher the "nose-like" profiles of the downburst events.

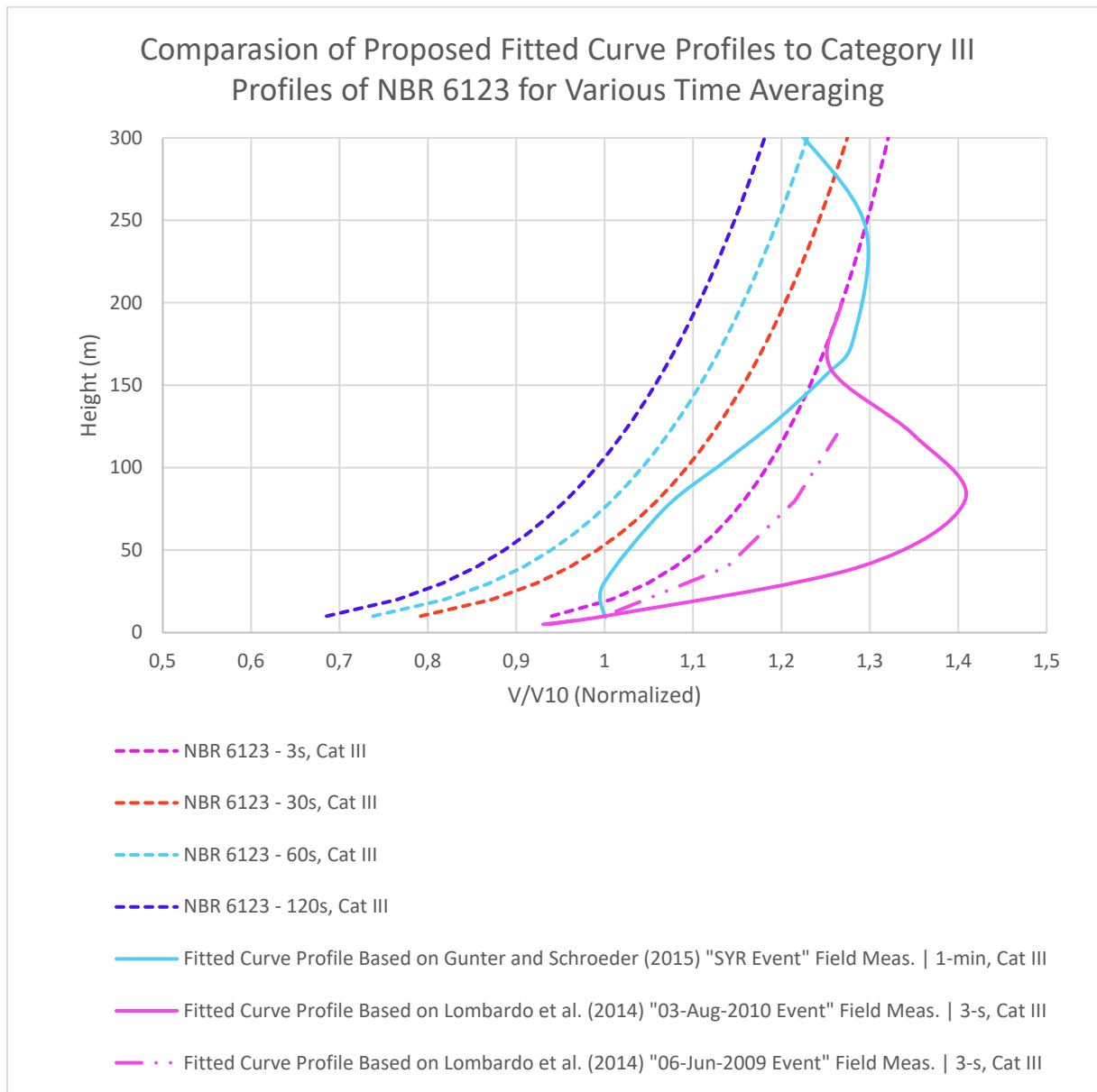


Figure 106. Comparison of proposed fitted curve profiles to category III profiles of NBR 6123 and various time averaging. Source: Author.

Gunter and Schroeder (2015) "SYR Event" was the only profile for 60-s time averaging, it in fact represents the worst-case scenario with a "nose-like" profile with maximum velocities between 150 and 250 meters. Lombardo *et al.* (2014) measurement for 03-Aug-2010 event resulted in the worst-case scenario for the 3-s time averaging, with a very predominant "nose-like" profile reaching a maximum velocity between 50 and 100 meters. Note that no transformation between different time averaging can be made for the proposed maximum profiles, therefore without further analysis, these profiles cannot be compared.

In Figure 107, are presented the profiles of Zhang *et al.* (2019) at two different instants, 15:00 and 15:01 for a Category IV terrain. Although, it is worth mentioning that at the north and south areas of the measurement tower would be better described as Category V as per the NBR 6123. As previously mentioned in Section 3.1, the terrain where this tower is located may have led to the generation of questionable results for maximum profiles; for instance, local vortices may have generated relative maximum local velocities that are not representative of the outflow profile, or in contrary they could have captured the potential effect of the buildings significantly increasing the wind speed at specific situations due to the Bernoulli effect. Nevertheless, the profile proposed by Zhang *et al.* (2019) at 15:00 is suggested to not be used as a reference for TS wind profiles until further research is developed, although the profile at 15:01 follows a magnitude and shape more similar to previous examples here analyzed, producing velocities of 20 to 30% higher in magnitude compared to the NBR 6123 profile of same averaging time. Finally, due to the limited data available, more research is needed to define TS wind profiles in terrains equivalent to Categories IV and V (as per the NBR 6123).

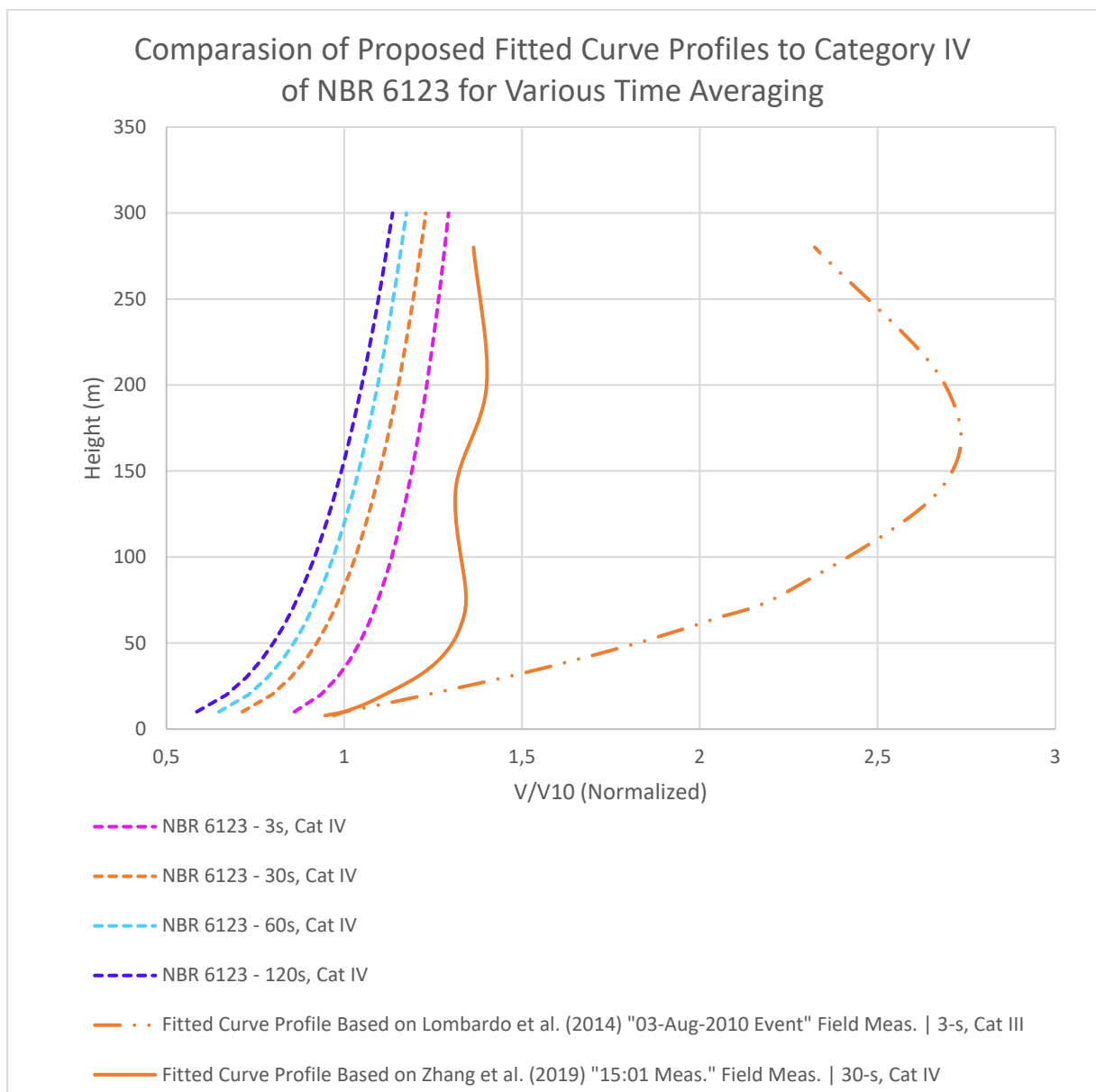


Figure 107. Comparison of proposed fitted curve profiles to category IV profiles of NBR 6123 and various time averaging. Source: Author.

Considering the previously discussed profiles and in the attempt to provide a non-dimensional Factor S_2 normalized to V_0 at 10 meters as in NBR 6123, in Table 5 are presented proposed factors for the fitted curves of thunderstorms wind profiles based on the full-scale measurements analyzed in this research work. These profiles are further categorized according to their terrain categories (as per NBR 6123) and time averaging (as per their original authors). No conversion from different time averaging and terrain categories are allowed at this moment without further investigation.

Table 5. Factors based on proposed TS wind fitted curve profiles. The highlighted gray cells show the normalized maximum values for the obtained profiles. Source: Author.

Height (m)	Sherman (1987) Proposed 1-s Cat II	Gunter and Schroeder (2015) "PEP Event" Proposed 60-s Cat II	Gunter and Schroeder (2015) "SYR Event" Proposed 60-s Cat III	Lombardo et al. (2014) "03-Aug-2010 Event" Proposed 3-s Cat III	Lombardo et al. (2014) "06-Jun-2009 Event" Proposed 3-s Cat III	Zhang et al. (2019) "15:00 Meas." Proposed 30-s Cat IV	Zhang et al. (2019) "15:01 Meas." Proposed 30-s Cat IV
10	1.00	1.00	1.00	1.00	1.00	1.00	1.00
20	1.03	1.03	1.00	1.12	1.07	1.24	1.12
30	1.05	1.07	1.00	1.22	1.11	1.45	1.20
40	1.06	1.10	1.01	1.29	1.14	1.65	1.26
50	1.07	1.12	1.02	1.34	1.16	1.82	1.30
60	1.08	1.15	1.04	1.38	1.18	1.98	1.33
70	1.08	1.17	1.06	1.40	1.20	2.12	1.34
80	1.09	1.19	1.08	1.41	1.22	2.25	1.34
90	1.10	1.21	1.10	1.40	1.23	2.36	1.34
100	1.10	1.23	1.13	1.39	1.24	2.45	1.33
110	1.10	1.24	1.15	1.37	1.25	2.53	1.32
120	1.11	1.26	1.17	1.35	1.26	2.59	1.32
130	1.11	1.27	1.20	1.32	-	2.64	1.31
140	1.11	1.28	1.22	1.30	-	2.68	1.31
150	1.12	1.29	1.24	1.27	-	2.71	1.32
160	1.12	1.29	1.26	1.26	-	2.72	1.33
170	1.12	1.30	1.27	1.24	-	2.73	1.34
180	1.13	1.30	1.28	1.24	-	2.72	1.36
190	1.13	1.30	1.29	1.25	-	2.71	1.38
200	-	1.30	1.30	1.27	-	2.69	1.40
210	-	1.30	1.31	-	-	2.66	1.42
220	-	1.30	1.31	-	-	2.63	1.44
230	-	1.30	1.30	-	-	2.59	1.46
240	-	1.30	1.30	-	-	2.54	1.47
250	-	1.30	1.29	-	-	2.49	1.47
260	-	1.29	1.28	-	-	2.44	1.45
270	-	1.29	1.27	-	-	2.38	1.42
280	-	1.28	1.26	-	-	2.32	1.36
290	-	1.27	1.24	-	-	2.26	1.28
300	-	1.27	1.23	-	-	2.20	1.16

4.6. PROPOSED FITTED CURVE MODEL DISCUSSIONS

A thorough examination of several full-scale TS wind profiles has been presented; in this section conclusions about this research are then summarized. Finds herein showed that there is still a large inconsistency and lack of standardization in the attempt to describe TS winds, including full-scale measurements approaches, downburst modeling, and TS wind codes. The comparison of the selected profiles to existing downburst analytical models showed that all profiles – with exception of Zhang *et al.* (2019) "15:00 Meas." – agreed in shape and magnitude to the profile model proposed by Ponte Junior (2005) for k (background wind contribution) varying from 0.35 to 1, but other models generated factors significantly higher than the proposed fitted curves found in this work. The agreement with Ponte Junior (2005) model for $k=0.35$ shows consistency with the typical contribution of background wind as recently proposed by Riera (2016, 2020).

Due to the typical characteristics of TS wind, it is extremely challenging if not impossible to define one typical TS wind profile; instead, TS wind profiles are better defined as a "family of profiles" (RIERA, 2016) that can be grouped considering various characteristics, such as storm type, terrain, application for design criteria, and outflow characteristics. In this work it was attempted to propose some of "these families" according to their storm type (organized or isolates), terrain roughness properties (according to NBR 6123), and time averaging applied by the original author of the full-scale measurement, finally these measurements are summarized in Table 5.

To regard the comparison to other TS wind codes, the proposed best fitting profile curves presented similar shape and magnitude of the profiles proposed in ISO 4354. A more in-depth analysis was performed against the NBR 6123. With exception of the measurement proposed by Sherman (1987), all analyzed full-scale measurements resulted from organized storms and as extensively mentioned these events presented significantly higher profile magnitude when compared to the NBR 6123. This serves as a case study that shows that isolated thunderstorms will generate weaker TS wind profiles than the presently proposed for ABL wind in the NBR 6123. Additionally, it would be expected that the wind profile speed magnitude for the time averaging of 1-s would be higher than the 60-s profile, but in this case this assumption was

shown to be true, which reveals some inconsistency in the traditional ABL theory and what is in fact observed in the field, requiring further analysis.

Considering the final results and recommendations for terrain category II, the fitted curve profiles based on **Gunter and Schroeder (2015) "PEP Event"** presented a maximum profile (most conservative) at all the elevations and it is proposed here as a TS wind profile for 1-min time averaging. For Category III, results are mixed. **Lombardo et al. (2014) "03-Aug-2010 Event"** presented a maximum profile for a 3-s time averaging and **Gunter and Schroeder (2015) "SYS Event"** for 1-min time averaging, overall is proposed to consider **Lombardo et al. (2014) "03-Aug-2010 Event" as the maximum event**. These profiles presented maximum heights at distinct levels, but both showed the "nose-like" shape. Finally, for Category IV, it is suggested to use as reference the profile of **Zhang et al. (2019) "15:01 Meas."**, since it was considered to be a more realistic TS wind profile for 30-s time averaging.

For the TS wind speed profile at or below 10 m height, *Gast et al. (2003)* measurements showed some reduction in wind speed from 10 m, but the model based on *Lombardo et al. (2014)* measurements showed a slight increase in the wind speed at lower levels. Therefore, considering these varying results and the effects of the terrain to the final wind speed profiles, it is proposed herein to use the same wind velocity at 10 meters reference height as a design reference, as suggested in the NZ/AUS 7000.

Most profiles herein analyzed presented a "nose-like" shape and are typically described by a third-degree polynomial equation. The height in which the maximum wind speed is observed will vary according to the terrain characteristics and it will acquire an ABL-like shape as the time averaging increases, revealing the importance of using lower time averaging when analyzing TS wind profiles. Peak velocities happen at lower elevations when compared to traditional ABL profiles and they vary significantly over time, typically staying between 50 and 250 meters, depending on the terrain roughness. Although, as described by *Mason (2017)* the profile shape tends to be maintained when different time averaging is applied, but not in magnitude aspects, this can be seen in the *Choi (2005)* and *Repetto (2018)* measurements.

Lastly, considering the arguments developed in this section, in Figure 108 are shown the maximum proposed fitted curve profiles for TS winds based on full-scale measurements found in this study for Terrain Categories II, III, and IV and time averaging 1-min, 3-s, and 30-s,

respectively. It is suggested the adoption of these profiles for further wind/structure interaction analysis and apply this methodology here proposed to newer full-scale measurements of TS winds outflows. Once more datasets of TS wind vertical measurements become available it is expected to reach to a more refined understanding of these types of winds, as well as a clearer understanding of the impact of the variability due to various other factors such as time averaging, terrain categories, terrain topography, and others.

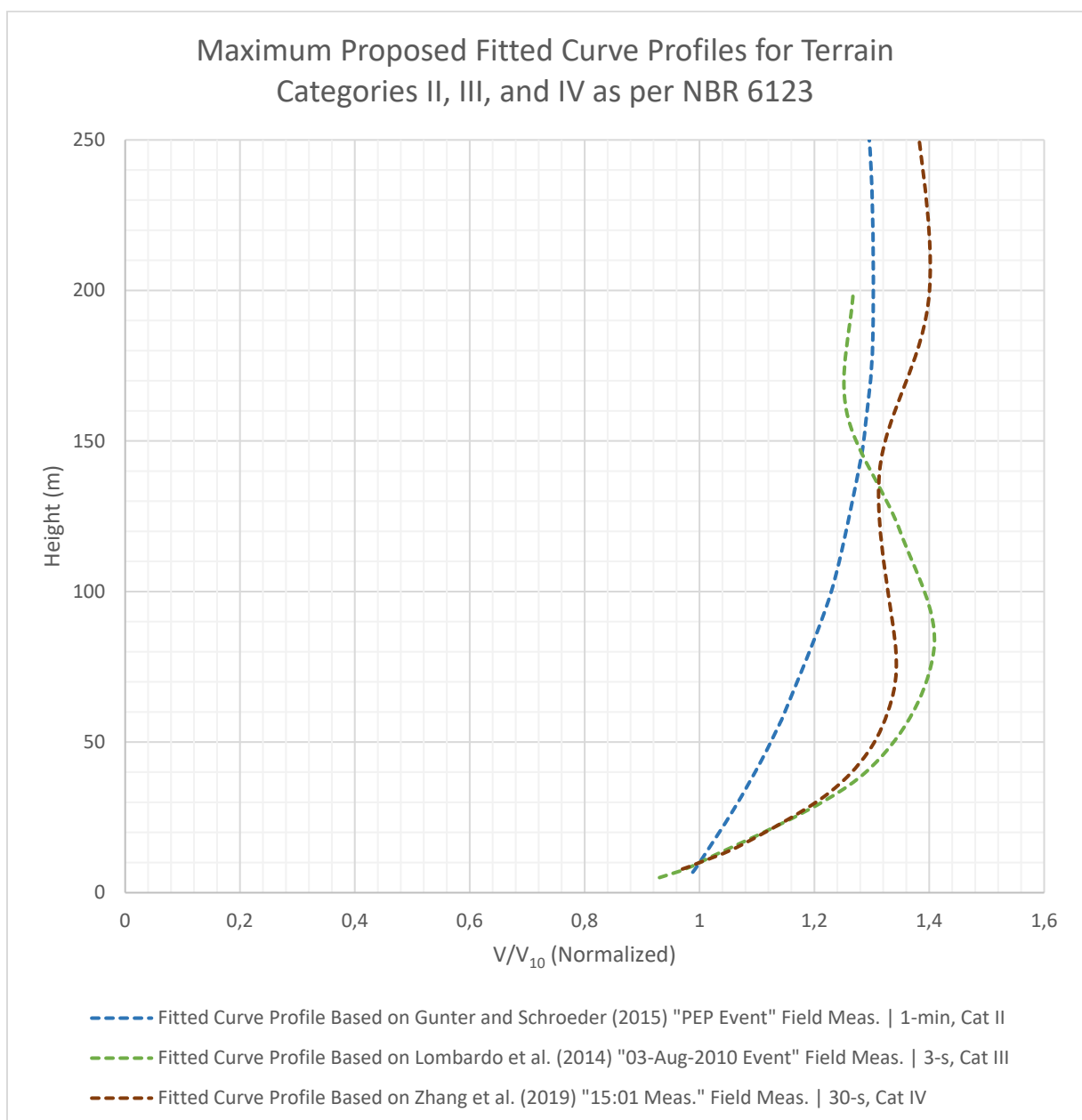


Figure 108. Maximum proposed fitted curve profiles found in this study for Terrain Categories II, III, and IV and time averaging 1-min, 3-s, and 30-s, respectively. Source: Author.

5. CONCLUSIONS

Solari (2020) reported the need for studies on the state-of-the-art in downburst modeling and thunderstorm winds with an eye towards application in wind engineering. Existing research in this area is still fragmented, and there is a major knowledge gap. Moreover, the lack of field measurements of vertical wind profiles makes it even harder to synthesize the intrinsic and transient characteristics of the event. This single factor is a major obstacle to progress towards codifying thunderstorm winds.

This work aimed to address the need for a comprehensive literature review of thunderstorm winds, discussing their properties, modeling approaches, and proposing analytical models of thunderstorm wind profiles based on existing full-scale measurements. Additionally, an extended survey of downburst reports in Brazil was presented, indicating areas where thunderstorm winds pose a major risk to the built environment. It is hoped that this work can serve as a guide to emphasize the importance of studying thunderstorm winds in engineering practice and help the community to understand the effects of these winds on the built environment, thereby contributing to the development of more resilient and safer structures.

Downbursts were first proposed as a distinct weather phenomenon by Fujita after investigating a series of aircraft accidents in the US, Europe, and Japan. Initially, the concept of a localized, strong, and cold downward current of air followed by a radial expansion was met with skepticism from the academic community. However, after several field studies, downbursts have become widely accepted, and their impact on the built environment is an important subject of research in wind engineering nowadays.

TS winds are essentially convectively generated by meso-scales weather phenomena, such as tornadoes, RFD, FFD, wind gusts, and others. The characteristics of this type of winds vary drastically from one event to another, presenting rapid variations in time and spatial scales, leaving behind extensive pattern damages that differ from what is normally seen by traditional extreme EPS wind events. Velocity peaks might reach super-high values in pockets called burst watches, which is one of the various components of a downburst morphology.

Downbursts descend from a convective cloud as a strong downdraft almost like a one-dimensional flow, impinging at the ground, and subsequently diverging as a highly non-

stationary three-dimensional outflow, also called outburst or outflow. These winds present a horizontal "nose-type" velocity profile with maximum values near to the ground, ranging from 15 m to 250 m and typically decreasing with height after reaching this peak.

The turbulence characteristic of these events is still not completely agreed upon. There are divergent finds, the most recent research has shown that comparatively to EPS outflows it is assumed that the turbulence intensity in TS wind outflows is lower, meanwhile the correlation is higher. The outflow winds assume low turbulence profiles near the impinging locations, acquiring more turbulence as the boundary layer develops. The downburst outflow is "slowly" affected by the terrain roughness and the height of the peak velocity increases as the roughness of the terrain increases due to the mechanic turbulence component imposed by the terrain (SKINNER *et al.*, 2012). Riera (2016) assumes the turbulence to be similar to the ABL winds, meanwhile Solari (2016) suggests that the simple exponential model used for synoptic winds can be applied to account for the coherence factor in TS winds.

Downbursts can happen isolated, in line, along with other meso-scale phenomena, or embedded within major tropical or extratropical cyclones. When embedded in larger synoptic systems, downbursts are found to be at their most destructive stage and are estimated to in average contribute to approximately 65% of the captured outflow velocity (RIERA, 2016). These zones are commonly referred as mixed climates regions and represent a major concern especially to temperate climate zones. The typical maximum wind speed varies significantly from one event to another, ranging from 10 m/s to 67 m/s at 10 meters. Cook (1984) estimated that 20 m/s outflows can cause some damage in structures, meanwhile 32.5 m/s cause is already enough to cause major structural damage.

Foster (1958) first studied downdraft winds, but it was not until the 70's that Sinclair (1973) and Fujita and Wakimoto (1981) investigated TS winds thoroughly and obtain horizontal and vertical full-scale measurements using various methods, including Radar Doppler, SWS, and Meteorological Towers. More recent projects, such as the Thunderstorm Outflow Project (ORWIG AND SCHROEDER, 2007; LOMBARDO *et al.*, 2014), the Wind and Ports, and Winds, Ports, and Sea (SOLARI *et al.*, 2015) have made available dozens of TS wind event datasets by deploying advanced capturing networks compounded typical of mesoscale weather stations networks, high resolution meteorological towers, and LiDAR technology. Such innovations

lead to a significantly better-quality data and increased number of datasets available for further studies, particularly at lower levels of the atmosphere. For instance, in this research only 21 projects accompanied by respective publications have been found in the literature and extensively discussed along the document.

In the present work, it was briefly discussed the process of creating extreme wind climate analysis distinguishing such records according to their originating events. This need was first identified by Gomes and Vickery (1978) and since then several techniques to separate wind datasets have been created. These techniques use not only wind data to help with the identification process, but also other meteorological parameters are deployed to classify entire datasets according to their patterns around the time of the peak wind gust. The application of such methods to various localities in the world has shown that TS winds dominate the extreme wind climate in most parts of the globe for the typical design return periods of 50 years. The same is observed in Brazil, where TS winds are found to dominate the extreme wind climate for return periods as little as 10-years.

Aware of such issue, Vallis (2019) used historical weather data records from various places in Brazil and proposed a new extreme wind climate for this country. Besides the limitations of synoptic weather station network to capture mesoscale weather events, the finds from Vallis (2019) have revealed the need to scrutinize extensive historical wind datasets before the development of extreme wind climatologies. A modified version of the ESDU (1990) Method of Independent Storms Extreme Value Method (referred as RB-MIS) was developed and modified to such experiment because there were many weather stations with short sampling periods and time-series with discontinuities. A proposed basic velocity V_o map with regions for synoptic and non-synoptic winds was presented by Vallis (2019). Presently, further research is now under development which takes the datasets previously analyzed by Vallis (2019) and applies considerations of climatic regions in Brazil (LOREDO-SOUZA *et al.*, 2021). This more recent study also suggests that – instead of acquiring V_o using a polynomial function for local averages – a more conservative approach would be to use representative maximum data points to trace the new wind basic speed isopleth map (LOREDO-SOUZA *et al.*, 2021), which would ultimately increase V_o for most part of the regions in Brazil susceptible to TS winds.

A detailed investigation presented in Appendix A of several downburst reports in Brazil was developed in this present study and similar trend found in previous research was encountered. Here it was showed a much higher frequency of reports in the southern half of Brazil, especially in the area adjacent to the La Plata Basin. Therefore, in the States of Rio Grande do Sul, Santa Catarina, Paraná, São Paulo, and Rio de Janeiro downbursts represent a threat to the built environment and should be considered in the structural design process. With lower intensity, downbursts were also reported in the Northern States of Pará and Amazonas, and in the Northeast State of Pernambuco. For the north and northeastern states of Brazil, downbursts have been observed to be weaker and more isolated.

Considering the limited full-scale measurements of downbursts, modeling approaches have been shown to be an excellent alternative to understand the properties of these phenomena, helping to understand the effects of such extreme, rapid, and non-stationary winds to structures. A detailed investigation of existing modeling approaches is presented in Appendix B. It was identified four main approaches to simulate TS winds, they are: experimentally, analytically, numerically, and data-driven statistically; besides these main approaches, there is a myriad of methods within the approaches above discussed which are extensively discussed in this document as well.

Experimental facilities offer the possibility of simulating downburst outflows and directly measure static and dynamic pressure induced by the flow in structures, but they normally consider scale effects due to the need of using reduced models for such experiments. There are three main methods to simulate downburst-like flows in laboratories: *Ad-hoc* impinging wall jet facilities, *Ad-hoc* fluid release models, and modified traditional wind tunnels. Within a myriad of finds available in the literature, normally the mean peak wind speeds occur at a distance of about one downdraft diameter from the jet axis. Buildings located directly under a downdraft experience direct reactions downwards, which can be devastating for houses and garblers with spaced support spans. Experimental models were also extensively used to investigate the effects of topography to the downburst flow and calculate aerodynamic coefficient, a remarkable find includes the fact that surrounding building neighborhood and increased terrain roughness tend to move upward the downburst nose and in consequence

decrease the maximum velocity at lower levels (ABOSHOSHA; BITSUAMLAK; EL DAMATTY, 2015).

Due to the nature of downbursts, impulsively impinging jet studies have shown to be more faithful than the other techniques in the experimental modeling realm since it reproduces very well the gustiness of the leading edge of the outflow. Furthermore, by adding the translation component to the jet, it is observed a significant increase to the final TS wind speed and adherence to full-scale measurements. Advanced wind tunnels, such as the WindEEE, have been developed in recent years generating significant advances on the study of TS winds and their interactions with structures. Also, solutions such as modified ABL wind tunnels are a promising technique to be explored since they may be easily implemented in existing facilities.

Analytical models are mathematical expressions that normally derive from primary fluid dynamic equations and steady flow, aiming to propose simplified mathematical solutions for the vertical and radial components of the wind speed. These models present the ability to easily evaluate different downburst parameters, such as diameters, age of events, and varying initial locations. Parametric methods aim to solve these models entirely based on analytical methods or on hybrid stochastic-deterministic models. Several models for vertical wind profile and radial development are available in the literature and were extensively discussed.

Nonparametric Deterministic-Stochastic Hybrid (NDESH) Models compose the most recent developments in this realm and these methods aim to divide the flow in two parts, one deterministic aiming to simulate the mean part of the flow, and another part stochastic aiming to simulate the fluctuating part of the flow. In this method, the fluctuations are said to be induced by small-scale turbulent models and calculated as a stochastic process using turbulence power spectral functions and coherence functions. The development of these modeling methods has helped significantly with the understanding of the TS wind turbulence.

CFD simulations of downbursts have been extensively developed after substantial increase in computational processing power seen over the last decades. Besides lowering the costs, numerical simulation eliminates scale effects as seen in experimental laboratory approaches. A myriad of CFD models and turbulence model are promptly available for many uses and due to their flexibility, they can be easily adapted to downburst modeling and are often deployed parallelly to evaluate/validate experimental and analytical models. There are typically three

methods of CFD models commonly deployed. They are, full-cloud models, which simulate the whole cloud structure that originates TS winds; sub-cloud or cooling source models, which emulate an axisymmetric cooling forcing function equivalent to the thermodynamic processes within the cloud that generate the downburst outflow; and the CDF impinging wall jet models, that simulate the downdraft outflow solely mechanically.

Each modeling approach adopts different CFD and turbulence models to solve the problem in different contexts. Full-cloud CFD models have a lot of advantages when aiming to simulating downbursts at higher resolutions, which can be extremely useful for to the wind engineering since the generated wind loads will be faithful result of the cloud physics that generates the downdraft within the cloud (ORF *et al.*, 2012). Although, these models may be expensive and require large computational capacity, commercial packages can be expensive, but they are becoming more popular and accessible. In summary, it is widely accepted that CFD simulations are a vital tool to improving the simulation of downburst outflows and studies of their effects in structures (MASON, 2017).

Data-driven models simulate the time-frequency domain of TS winds using Monte-Carlo data-driven approaches. Differently than in NDESH models procedures, the entire non-stationary wind field is simulated all-together, without separating it in deterministic and stochastic components. These methods have been applied to determine the wind-excited response of slender structures by time domain-integration of the equation motions (SOLARI *et al.*, 2017). The Gust-Front factor approach developed by Kwon and Kareem (2009) adopts a similar approach to the typical synoptic winds formulation and the authors have made available an online tool to guide designers applying such technique to TS wind structural analysis; a semi-analytical approach proposed by Canor *et al.* (2016) evaluates statistically the structural response to the transient characteristics of the downburst; and Solari *et al.* (2015b) proposed the Thunderstorm Response Spectrum method as a derived technique from the seismic loading analysis.

With the intent to add to the research in downburst modeling, in this present work it was proposed a method to analyze existing vertical full-scale measurements and propose fitted curves to best describe these profiles using analytical equations. The approach proposed adopts a systematic analysis and further comparison of several TS wind profiles against each

other at their worst-case stage—which is herein considered when they get to their maximum velocities. An in-depth analysis of seventeen (17) full-scale TS wind measurements and respective fitted curves were proposed. Although, taking into consideration established criteria and delimitations, only seven profiles were deemed to suffice the requirements to propose fitted curve profiles that could be coupled to the standard reference height of 10 meters, which is the typical reference height used for extreme wind climate studies.

Due to the typical characteristics of TS wind, it is extremely challenging to define one typical TS wind profile for a nature event with extreme randomness. Instead, TS wind profiles are better defined as a "family of profiles" (RIERA, 2016) and they can be grouped considering various characteristics, such as storm type, terrain, application for design criteria, and outflow characteristics. In general, the full-scale measurements herein analyzed presented a "nose-like" shaped profile typically described by a third-degree polynomial equation and peak varying in each case, but with velocities at lower heights (between 50 and 250) when compared to traditional ABL profiles. In TS wind profiles the terrain roughness plays an important role in defining the height of the peak of velocity.

When compared against existing downburst models with exception of Zhang *et al.* (2019) "15:0 Meas.", all the proposed fitted curves agreed in shape and magnitude with the model proposed by Ponte Junior (2005) for k (background wind contribution) varying from 0.35 to 1. Although when analyzes with older stablished downburst models, the proposed profiles presented significant lowere velocities. Finally, comparying to existing TS wind Codes, proposed profiles presented similar shape and magnitude to the profiles in ISO 4354, but not when compared to the NZ/AUS 7000.

The analysis of the proposed fitted curve profiles against the NBR 6123 showed that all profiles obtained from organized storms presented higher magnitudes when compared to the ABL profiles from NBR 6123. Therefore, it was found here that this wind code only provides a more conservative provision for TS winds generate by isolated thunderstorms, agreeing with previous finds of Riera (2016).

General recommendations for the TS wind profiles were proposed in this work and grouped using as reference terrain categories and time averaging as per the NBR 6123. For Terrain Category II, the fitted curve profiles based on **Gunter and Schroeder (2015) "PEP" Event**

presented a maximum profile (most conservative) at all the elevations and it is proposed here as a TS wind profile for 1-min time averaging. For Terrain Category II, results are mixed; the fitted curve profiles based on **Lombardo et al. (2014) "03-Aug-2010 Event"** presented a maximum profile for a 3-s time averaging and **Gunter and Schroeder (2015) "SYS Event"** for 1-min time averaging. These profiles presented maximum heights at distinct levels, but both showed the typical "nose-like" shape; considering the time-averaging approach and overall maximum values is suggested herein to adopt **the former** as the extreme profile for this terrain category. Finally, for Category IV, it is suggested to use as reference the fitted curve profile based on 15:01, since it was considered being a more realistic TS wind profile 30-s time averaging. No conclusions are found for Terrain Categories I and V of NBR 6123.

It was not within the scope of this investigation to further advance the study of these profiles onto structures interactions. Although, a few finds in the literature review show that the types of structures most susceptible to downbursts are transmission lines, transmission towers, low-rising buildings, and long-span structures. There is a myriad of reasons why transmission lines are highly susceptible to downbursts-like winds, for instance the application of very localized wind loads to a long span transmission line-like structure intuitively causes large longitudinal momentum between two points within a short span, imposing patterns that differ from the typical homogenous ABL wind loads design, leading eventually to the typical type of failure seen in those structures (ZHANG, 2013).

Low rising buildings are also very susceptible to TS winds due to the "inversion" of maximum wind speeds loads typical of the downburst "nose-profile" shape, which increases the wind speed at lower levels, creating higher loads than what it was designed for utilizing typical ABL profiles. Intense downburst vertical downdrafts can be extremely harmful when they fall within low-rise buildings, for instance ASCE 7-05 gable-roof building models could experience almost the double in surface pressures under downburst-like wind at the leading edge of the flow (at $X/D \approx 0.50$), although when the impinging downdraft outflow is further away from the downburst core, these loads tend to agree considerably with the standard practice (ZHANG, 2013b).

In conclusion, this work is a product of the joint effort between the wind engineering and atmospheric sciences research that aimed to contribute to the knowledge very much needed

to ensure the design of safer structures and it was previously identified by Solari *et al.* (2015a, 2020). Considering the extensive discussions that have been developed herein, the transient characteristics of the downburst are still one of the main challenges of modern engineering. The complexity of TS winds is not only within their formation and characteristics, but how they come to interact with structures. Understanding the velocity profile of TS winds is only the first step to further comprehending their interactions with structures.

5.1. SUGGESTION FOR FUTURE WORK

In this section are presented some suggestions of future work that would be contributing to the development of the knowledge in this topic.

1. **Advocate for more resources in TS winds full-scale measurements:** Advocate for public resources or private partnerships to create a meso-scale weather station network with tall meteorological towers in southern Brazil and South America, with focus on the most susceptible regions to TS winds, which could represent excellent opportunities to capture relevant full-scale measurements for the scientific community. Good quality data and more datasets from static sources or field campaigns that include anemometric towers, LiDAR, Doppler Radar, etc., would help creating more representative TS wind profiles for these susceptible regions and help creating significant probability of exceedance analysis for such events.
2. **Study effects of proposed profiles onto structures:** Recreate the TS wind profiles herein proposed in wind tunnels or CFD environment to investigate the effects of these profiles on structures.
3. **Propose Aerodynamic Coefficients:** Obtain aerodynamic coefficients from the TS wind profiles herein proposed for different types of structures and compare them to existing aerodynamic coefficients in the wind code.
4. **Turbulence analysis:** Use existing full-scale measurements to identify characteristics of atmospheric turbulence features relevant to wind engineering, such as integral turbulence scales, turbulence intensity, spectra, and cross-spectra.

5. **Model comparisons research:** Continue an in-depth comparison of existing downburst modeling approaches, aiming to perfect modeling performance and validate these models against more recent TS wind full-scale measurement datasets.
6. **Averaging time and terrain conversion:** investigate and test methods to convert TS wind measurements from different time averaging and terrain categories.
7. **Background wind contribution:** Develop more in-depth investigations regarding the magnitude of TS and EPS contributions to the final TS wind record.
8. **Distance to touchdown:** Investigate the distance of the downdraft touchdown to the point of the TS wind measurement.
9. **Climate changes:** Improve understanding of how a changing climate will affect the recurrence and intensity of extreme TS wind events in Brazil and map the vulnerability of Brazil's infrastructure to TS winds.
10. **Local TS wind surveys:** Consistently develop structural failure surveys after extreme wind events looking to improve understanding of TS wind characteristics and mitigate risk of future accidents.

REFERENCES

- ABD-ELAAL, El-Sayed; MILLS, Julie E.; MA, Xing. A Simplified Design Charts for the Vertical Profile of Horizontal Downburst Wind Speeds. *Em: EIGHTH ASIA-PACIFIC CONFERENCE ON WIND ENGINEERING, 2013. Proceedings of the Eighth Asia-Pacific Conference on Wind Engineering*. [S. l.]: Research Publishing Services, 2013. p. 511–521. Disponível em: <http://rpsonline.com.sg/proceedings/9789810780111/html/181.xml>. Acesso em: 9 fev. 2021.
- ABOSHOSHA, Haitham; BITSUAMLAK, Girma; EL DAMATTY, Ashraf. Turbulence characterization of downbursts using LES. *Journal of Wind Engineering and Industrial Aerodynamics*, [s. l.], v. 136, p. 44–61, 2015.
- ALMEIDA, LO. **Estudo para atualização do mapa de ventos da NBR6123**. 2010. Master Thesis - Engenharia de Infraestrutura Aeronáutica, Instituto Tecnológico de Aeronáutica, São José dos Campos, Brasil, 2010.
- AMERICAN SOCIETY OF CIVIL ENGINEERS. **Minimum Design Loads and Associated Criteria for Buildings and Other Structures—ASCE/SEI 7-16**. Reston, VA: American Society of Civil Engineers, 2016. *E-book*. Disponível em: <http://ascelibrary.org/doi/book/10.1061/9780784414248>.
- ANSI (AMERICAN NUCLEAR SOCIETY). Estimating Tornado, Hurricane, and Extreme Straight Line Wind Characteristics at Nuclear Facility Sites: An American National Standard. *Em:* , 2011, La Grange Park, IL. **Anais [...]**. La Grange Park, IL.: ANSI/ANS–2.3–2011, 2011.
- ASCE. **ASCE 7-22 wind load standard adds tornado chapter**. [S. l.], 2022. Disponível em: <https://www.asce.org/publications-and-news/civil-engineering-source/civil-engineering-magazine/article/2022/02/asce-7-22-wind-load-standard-adds-tornado-chapter>. Acesso em: 19 mar. 2022.
- AS/NZS1170.2. Structural design actions Part 2: Wind Actions. **Australia-New Zeland Standard**, [s. l.], 2011.
- ATKINS, Nolan T; WAKIMOTO, Roger M. Wet microburst activity over the southeastern United States: Implications for forecasting. *Weather and Forecasting*, [s. l.], v. 6, n. 4, p. 470–482, 1991.
- BARRETT, E. W.; RIEHL, Herbert. Experimental verification of entrainment of air into cumulus. *Journal of Meteorology*, [s. l.], v. 5, n. 6, p. 304–307, 1948.
- BECK, André T.; CORRÊA, Márcio R. S. New design chart for basic wind speeds in Brazil. *Latin American Journal of Solids and Structures*, [s. l.], v. 10, n. 4, p. 707–723, 2013.
- BLESSMANN, Joaquim. **O vento na engenharia estrutural**. [S. l.]: Editora da Universidade/UFRGS, 1995.
- BRAHAM, Roscoe R. The Water And Energy Budgets Of The Thunderstorm And Their Relation To Thunderstorm Development. *Journal of Meteorology*, [s. l.], 1952.
- BRAUN, Alexandre Luis; AWRUCH, Armando Miguel. Numerical investigation of the wind action over low- rise buildings using large eddy simulation and a synthesized turbulence generator. *Mecânica Computacional*, [s. l.], v. 30, p. 2609–2626, 2011.

BROOKS, Harold E; LEE, James W; CRAVEN, Jeffrey P. The spatial distribution of severe thunderstorm and tornado environments from global reanalysis data. **Atmospheric Research**, [s. l.], v. 67–68, p. 73–94, 2003.

BROWN, Andrew; DOWDY, Andrew. Severe convection-related winds in Australia and their associated environments. **Journal of Southern Hemisphere Earth Systems Science**, [s. l.], 2021.

BROWN, Rodger A.; LEWIS, John M. PATH TO NEXRAD: Doppler Radar Development at the National Severe Storms Laboratory. **Bulletin of the American Meteorological Society**, [s. l.], v. 86, n. 10, p. 1459–1470, 2005.

BURLANDO, Massimiliano; DE CIO, Andrea; PIZZO, Marina; SOLARI, Giovanni. Analysis of wind vertical profiles of thunderstorm events in the Mediterranean. [s. l.], 2017a.

BURLANDO, Massimiliano; ROMANIĆ, Djordje; SOLARI, Giovanni; HANGAN, Horia; ZHANG, Shi. Field Data Analysis and Weather Scenario of a Downburst Event in Livorno, Italy, on 1 October 2012. **Monthly Weather Review**, [s. l.], v. 145, n. 9, p. 3507–3527, 2017b.

BYERS, Horace Robert; BRAHAM, Roscoe R. **The thunderstorm: Report of the Thunderstorm Project**. [S. l.]: US Government Printing Office, 1949.

BYERS, Horace R; HULL, Edwin C. Inflow patterns of thunderstorms as shown by winds aloft. **Bulletin of the American Meteorological Society**, [s. l.], p. 90–96, 1949.

CALOTESCU, I. Overview of recent wind-induced damage in Romania based on mass-media reports. *Em:* , 2018. **International workshop on wind-related disasters and mitigation, Sendai, Japan**. [S. l.: s. n.], 2018. p. 11–14.

CANEPA, Federico; BURLANDO, Massimiliano; SOLARI, Giovanni. Vertical profile characteristics of thunderstorm outflows. **Journal of Wind Engineering and Industrial Aerodynamics**, [s. l.], v. 206, p. 104332, 2020.

CANOR, Thomas; CARACOGLIA, Luca; DENOËL, Vincent. Perturbation methods in evolutionary spectral analysis for linear dynamics and equivalent statistical linearization. **Probabilistic Engineering Mechanics**, [s. l.], v. 46, p. 1–17, 2016.

CARACENA, Fernando; HOLLE, Ronald L; III, Charles A Doswell. Microbursts A Handbook for Visual Identification. [s. l.], p. 15, 1989.

CARACENA, Fernando; MAIER, Michael W. Analysis of a microburst in the FACE meteorological mesonet network in southern Florida. **Monthly weather review**, [s. l.], v. 115, n. 5, p. 969–985, 1987.

CHARBA, Jess. Application of gravity current model to analysis of squall-line gust front. **Monthly Weather Review**, [s. l.], v. 102, n. 2, p. 140–156, 1974.

CHEN, Lizhong. **Vector Time-Varying Autoregressive (TVAR) Models and Their Application to Downburst wind Speeds**. 2005. 252 f. Doctoral Thesis - Texas Tech University, [s. l.], 2005.

CHEN, Lizhong; LETCHFORD, Chris W. A deterministic–stochastic hybrid model of downbursts and its impact on a cantilevered structure. **Engineering Structures**, [s. l.], v. 26, n. 5, p. 619–629, 2004.

CHEN, L.; LETCHFORD, C.W. Multi-scale correlation analyses of two lateral profiles of full-scale downburst wind speeds. **Journal of Wind Engineering and Industrial Aerodynamics**, [s. l.], v. 94, n. 9, p. 675–696, 2006.

CHOI, Edmund C.C. Field measurement and experimental study of wind speed profile during thunderstorms. **Journal of Wind Engineering and Industrial Aerodynamics**, [s. l.], v. 92, n. 3–4, p. 275–290, 2004.

CHOI, Edmund C.C; HIDAYAT, Ferry A. Gust factors for thunderstorm and non-thunderstorm winds. **Journal of Wind Engineering and Industrial Aerodynamics**, [s. l.], v. 90, n. 12–15, p. 1683–1696, 2002.

CHOWDHURY, Junayed. Transient Analysis of Full Scale and Experimental Downburst Flows. [s. l.], p. 143, 2018.

COCHRAN, Leighton. Wind issues in the design of buildings. *Em:* , 2012. **Anais [...]**. [S. l.]: American Society of Civil Engineers, 2012.

COOK, N. J. Towards better estimation of extreme winds. **Journal of Wind Engineering and Industrial Aerodynamics**, [s. l.], v. 9, n. 3, p. 295–323, 1982.

DAMATTY, Ashraf El; ELAWADY, Amal; HAMADA, Mohamed. Transmission Line Failures during Tornadoes and Downbursts- Can they be avoided. *Em:* , 2016. **Anais [...]**. [S. l.: s. n.], 2016. p. 7.

DAVENPORT, A G. The Application of Statistical Concepts to the Wind Loading of Structures. **Proceedings of the Institution of Civil Engineers**, [s. l.], v. 19, n. 4, p. 449–472, 1961.

DEMPSEY, D.; WHITE, H. Winds wreak havoc on lines. **Transmission and Distribution World**, [s. l.], v. 48, n. 6, p. 32–37, 1996.

DISTEFANO, John Thomas. **Analysis of a thunderstorm downburst**. 1983. Master Thesis - Massachusetts Institute of Technology, [s. l.], 1983.

DOSWELL, Charles A. (org.). **Severe convective storms**. Boston, Mass: American Meteorological Society, 2001. (Meteorological monographs, v. v. 28, n. 50).

DURAÑONA, Valeria. Extreme wind climate of Uruguay. **Reportes Técnicos; 263**, [s. l.], 2015.

DURAÑONA, Valeria; STERLING, Mark; BAKER, Christopher J. An analysis of extreme non-synoptic winds. **Journal of Wind Engineering and Industrial Aerodynamics**, [s. l.], v. 95, n. 9–11, p. 1007–1027, 2007.

EILTS, Michael; DOVIK, Richard. Oklahoma Downburst and Their Asymmetry. **Journal of Climate and Applied Meteorology**, [s. l.], v. 26, p. 10, 1986.

ELLROD, Gary. Environmental conditions associated with the Dallas microburst storm determined from satellite soundings. **Weather and forecasting**, [s. l.], v. 4, n. 4, p. 469–484, 1989.

ELLROD, Gary P.; NELSON III, James P.; WITIW, Michael R.; BOTTOS, Lynda; ROEDER, William P. Experimental GOES sounder products for the assessment of downburst potential. **Weather and forecasting**, [s. l.], v. 15, n. 5, p. 527–542, 2000.

EMANUEL, Kerry A. A similarity theory for unsaturated downdrafts within clouds. **Journal of the Atmospheric Sciences**, [s. l.], v. 38, n. 8, p. 1541–1557, 1981.

ESDU. **Data Unit 87034 – World-wide extreme wind speeds. Part 1: Origins and Methods of Analysis.** ENGINEERING SCIENCES DATA UNIT, , 1990.

FAWBUSH, Ernest J.; MILLER, Robert C. A Basis for Forecasting Peak Wind Gusts in Non-Frontal Thunderstorms. **Bulletin of the American Meteorological Society**, [s. l.], v. 35, n. 1, p. 14–19, 1954.

FERREIRA, V; NASCIMENTO, EL. Convectively-induced severe wind gusts in southern Brazil: Surface observations, atmospheric environment, and association with distinct convective modes. *Em: 28TH CONFERENCE ON SEVERE LOCAL STORMS, 2016. Anais [...].* [S. l.: s. n.], 2016. p. 7–11.

FOSTER, Donald S. Thunderstorm Gusts Compared with Computed Downdraft Speeds. **Monthly Weather Review**, [s. l.], v. 86, n. 3, p. 91–94, 1958.

FUJITA, T. T. Andrews AFB microburst. **Chicago IL - University of Chicago**, [s. l.], v. SMRP Res., n. Paper No 205, p. 38, 1983.

FUJITA, T Theodore. Downbursts: Meteorological features and wind field characteristics. **Journal of wind engineering and industrial aerodynamics**, [s. l.], v. 36, p. 75–86, 1990.

FUJITA, Tetsuya Theodore. Spearhead echo and downburst near the approach end of a John F. Kennedy Airport runway, New York City. [s. l.], 1976.

FUJITA, TT. The downburst, microburst and macroburst, satellite and mesometeorology research project (SMRP). **Research Paper**, [s. l.], v. 210, 1985a.

FUJITA, TT. The downburst, report of Projects NIMROD and JAWS. **University of Chicago**, [s. l.], 1985b.

FUJITA, T Theodore. The downburst-Micoburst and Macroburst. **Report of Projects NIMROD and JAWS**, [s. l.], 1985.

FUJITA, T Theodore. Tornadoes and downbursts in the context of generalized planetary scales. **Journal of the Atmospheric Sciences**, [s. l.], v. 38, n. 8, p. 1511–1534, 1981.

FUJITA, T Theodore; BYERS, Horace R. Spearhead Echo and Downburst in the Crash of an Airliner. **Monthly Weather Review**, [s. l.], v. 105, n. 2, p. 18, 1977.

FUJITA, T Theodore; CARACENA, Fernando. An Analysis of Three weather-Related Aircraft Accidents. [s. l.], v. 58, n. 11, p. 18, 1977.

FUJITA, Tetsuya Theodore; NEWSTEIN, Herman; TEPPER, Morris. **Mesoanalysis: An important scale in the analysis of weather data.** [S. l.]: US Government Printing Office, 1956.

FUJITA, T Theodore; WAKIMOTO, Roger M. Five scales of airflow associated with a series of downbursts on 16 July 1980. **Monthly weather review**, [s. l.], v. 109, n. 7, p. 1438–1456, 1981.

GAETANO, Patrizia De; REPETTO, Maria Pia; REPETTO, Teresa; SOLARI, Giovanni. Separation and classification of extreme wind events from anemometric data. **Journal of Wind Engineering and industrial aerodynamics**, [s. l.], n. 126, p. 132–143, 2014.

GARDINER, Barry; BLENNOW, Kristina; CARNUS, Jean-Michel; FLEISCHER, Peter; INGEMARSSON, Fredrik; LANDMANN, Guy; LINDNER, Macus; MARZANO, Mariella; NICOLL, Bruce; ORAZIO, Christophe. Destructive storms in European forests: Past and forthcoming impacts. [s. l.], 2010.

GARSTANG, M.; WHITE, S.; SHUGART, H. H.; HALVERSON, J. Convective cloud downdrafts as the cause of large blowdowns in the Amazon rainforest. **Meteorology and Atmospheric Physics**, [s. l.], v. 67, n. 1–4, p. 199–212, 1998.

GAST, Kirsten Deann. **A comparison of extreme wind events as sampled in the 2002 thunderstorm outflow experiment**. 2003. - Texas Tech University, [s. l.], 2003.

GOFF, R. Vertical structure of thunderstorm outflows. **Monthly Weather Review**, [s. l.], v. 104, n. 11, p. 1429–1440, 1976.

GOMES, L.; VICKERY, B.J. Extreme wind speeds in mixed wind climates. **Journal of Wind Engineering and Industrial Aerodynamics**, [s. l.], v. 2, n. 4, p. 331–344, 1978.

GOMES, L.; VICKERY, B.J. On the prediction of extreme wind speeds from the parent distribution. **Journal of Wind Engineering and Industrial Aerodynamics**, [s. l.], v. 2, n. 1, p. 21–36, 1977.

GUNTER, W Scott; SCHROEDER, John L. High-resolution full-scale measurements of thunderstorm outflow winds. **Journal of Wind Engineering and Industrial Aerodynamics**, [s. l.], v. 138, p. 13–26, 2015.

GUNTER, W. Scott; SCHROEDER, John L.; WEISS, Christopher C.; BRUNING, Eric C. Surface measurements of the 5 June 2013 damaging thunderstorm wind event near Pep, Texas. **Wind and Structures**, [s. l.], v. 24, n. 2, p. 185–204, 2017.

HANSEN, J.; RUEDY, R.; SATO, M.; LO, K. Global Surface Temperature Change. **Reviews of Geophysics**, [s. l.], v. 48, n. 4, 2010. Disponível em: <https://agupubs.onlinelibrary.wiley.com/doi/abs/10.1029/2010RG000345>. Acesso em: 30 jun. 2020.

HARRIS, R. I. Improvements to the Method of Independent Storms'. **Journal of Wind Engineering and Industrial Aerodynamics**, [s. l.], v. 80, n. 1–2, p. 1–30, 1999.

HJELMFELT, Mark R. Structure and life cycle of microburst outflows observed in Colorado. **Journal of Applied Meteorology**, [s. l.], v. 27, n. 8, p. 900–927, 1988.

HJELMFELT, M.; ROBERTS, R.; ORVILLE, H.; CHEN, Jen-Ping; KOPP, F. Observational and Numerical Study of a Microburst Line-Producing Storm. **Journal of Atmospheric Sciences**, [s. l.], v. 46, p. 2731–2744, 1989.

HOLMES, John D. A re-analysis of recorded extreme wind speeds in region A. **Australian Journal of Structural Engineering**, [s. l.], v. 4, n. 1, p. 29–40, 2002.

HOLMES, JD; HANGAN, HM; SCHROEDER, JL; LETCHFORD, CW; ORWIG, KD. A forensic study of the Lubbock-Reese downdraft of 2002. **Wind and Structures**, [s. l.], v. 11, n. 2, p. 137–152, 2008.

HOLMES, J.; WANG, C. H.; OLIVER, S. Extreme winds for six South Australian locations. *Em: , 2018. 19th Australasian Wind Engineering Society Workshop, April 4-6, 2018, Torquay, Australia. [S. l.: s. n.], 2018.*

HOUZE, Robert A. **Cloud dynamics**. Second edition. Amsterdam ; New York: Academic Press is an imprint of Elsevier, 2014.

HOUZE, Robert A. Mesoscale convective systems. **Reviews of Geophysics**, [s. l.], v. 42, n. 4, 2004. Disponível em: <http://doi.wiley.com/10.1029/2004RG000150>. Acesso em: 24 out. 2018.

INSURANCE INFORMATION INSTITUTE. **Facts + Statistics: Tornadoes and thunderstorms | III**. [S. l.], 2020. Disponível em: <https://www.iii.org/fact-statistic/facts-statistics-tornadoes-and-thunderstorms>. Acesso em: 30 jun. 2020.

INTERNATIONAL ORGANIZATION FOR STANDARDIZATION, ISO 4354. **Wind action on structures**. Geneve, Switzerland: International Organization for Standardization: [s. n.], 2009.

JÄRVI, Leena; PUNKKA, Ari-Juhani; SCHULTZ, David M.; PETÄJÄ, Tuukka; HOHTI, Harri; RINNE, Janne; POHJA, Toivo; KULMALA, Markku; HARI, Pertti; VESALA, Timo. Micrometeorological observations of a microburst in southern Finland. *Em: ATMOSPHERIC BOUNDARY LAYERS*. [S. l.]: Springer, 2007. p. 187–203.

JIN, Xinyang; GE, Yaojun; CAO, Shuyang. Chinese Country Report 2012-Revision of wind loading code and wind tunnel test guidelines. *Em: , 2012. Proceedings of APEC-WW2012 Workshop*. [S. l.: s. n.], 2012.

JOHNS, Robert H; DOSWELL III, Charles A. Severe local storms forecasting. **Weather and Forecasting**, [s. l.], v. 7, n. 4, p. 588–612, 1992.

JOHNSON, Richard H.; CHEN, Sue; TOTH, James J. Circulations associated with a mature-to-decaying midlatitude mesoscale convective system. Part I: Surface features—Heat bursts and mesolow development. **Monthly weather review**, [s. l.], v. 117, n. 5, p. 942–959, 1989.

KAŇÁK, Ján; BENKO, Martin; SIMON, André; SOKOL, Alois. Case study of the 9 May 2003 windstorm in southwestern Slovakia. **Atmospheric Research**, [s. l.], v. 83, n. 2–4, p. 162–175, 2007.

KASPERSKI, Michael. A new wind zone map of Germany. **Journal of Wind Engineering and Industrial Aerodynamics**, [s. l.], v. 90, n. 11, p. 1271–1287, 2002.

KIM, Jongdae; HANGAN, Horia. Numerical simulations of impinging jets with application to downbursts. **Journal of Wind Engineering and Industrial Aerodynamics**, [s. l.], v. 95, n. 4, p. 279–298, 2007.

KINGSMILL, David E.; WAKIMOTO, Roger M. Kinematic, dynamic, and thermodynamic analysis of a weakly sheared severe thunderstorm over northern Alabama. **Monthly Weather Review**, [s. l.], v. 119, n. 2, p. 262–297, 1991.

KNUPP, Kevin Robert. **Precipitating convective cloud downdraft structure: A synthesis of observations and modeling**. 1985. - Colorado State University. Libraries, [s. l.], 1985.

KWON, Dae-Kun; KAREEM, Ahsan. Gust-Front Factor: New Framework for Wind Load Effects on Structures. **Journal of Structural Engineering**, [s. l.], v. 135, n. 6, p. 717–732, 2009.

LEE, Jean Theodore. **A summary of field operations and data collection by the National Severe Storms Project in spring 1961**. [S. l.]: US Weather Bureau, 1962.

LETCHFORD, C.W; CHAY, M.T. Pressure distributions on a cube in a simulated thunderstorm downburst. Part B: Moving downburst observations. **Journal of Wind Engineering and Industrial Aerodynamics**, [s. l.], v. 90, n. 7, p. 733–753, 2002.

LETCHFORD, C W; LOMBARDO, F T. Is codification of non-synoptic wind loads possible?. *Em*: 14TH INTERNATIONAL CONFERENCE ON WIND ENGINEERING, 2015, Porto Alegre, Brazil. **Anais [...]**. Porto Alegre, Brazil: [s. n.], 2015. p. 25.

LI, C.Q. A stochastic model of severe thunderstorms for transmission line design. **Probabilistic Engineering Mechanics**, [s. l.], v. 15, n. 4, p. 359–364, 2000.

LILLY, D K. The Dynamical Structure and Evolution of Thunderstorms and Squall Lines. **Annual Review of Earth and Planetary Sciences**, [s. l.], v. 7, n. 1, p. 117–161, 1979.

LIN, W. E.; ORF, L. G.; SAVORY, E.; NOVACCO, C. Proposed large-scale modelling of the transient features of a downburst outflow. **Wind and structures**, [s. l.], v. 10, n. 4, p. 315–346, 2007.

LIU, Henry. **Wind engineering: A handbook for structural engineering**. [S. l.]: Pearson Education, 1990.

LOMBARDO, Franklin T. Improved extreme wind speed estimation for wind engineering applications. **Journal of wind engineering and industrial aerodynamics**, [s. l.], v. 104, p. 278–284, 2012.

LOMBARDO, Franklin T.; MAIN, Joseph A.; SIMIU, Emil. Automated extraction and classification of thunderstorm and non-thunderstorm wind data for extreme-value analysis. **Journal of Wind Engineering and Industrial Aerodynamics**, [s. l.], v. 97, n. 3–4, p. 120–131, 2009.

LOMBARDO, Franklin T; SMITH, Douglas A. Analysis and interpretation of non-stationary wind flow on a bluff body. *Em*: 11TH AMERICAS CONFERENCE ON WIND ENGINEERING, SAN JUAN, PUERTO RICO, 2009. **Anais [...]**. [S. l.: s. n.], 2009.

LOMBARDO, Franklin T; SMITH, Douglas A; SCHROEDER, John L; MEHTA, Kishor C. Thunderstorm characteristics of importance to wind engineering. **Journal of Wind Engineering and Industrial Aerodynamics**, [s. l.], v. 125, p. 121–132, 2014.

LOREDO-SOUZA, Acir Mércio; PFEIL, Michèle Schubert; NASCIMENTO, Ernani de Lima; RIERA, Jorge Daniel; FISCH, Gilberto Fernando. Proposta de um novo mapa de isopletas para a NBR-6123 com base em uma abordagem climatológica. **Not Published**, [s. l.], p. 22, 2021.

MARCELINO, Isabela; NASCIMENTO, Ernani; FERREIRA, Nelson Jesus. Tornadoes in Santa Catarina State (southern Brazil): Event documentation, meteorological analysis and vulnerability assessment. [s. l.], 2005.

MARKOWSKI, Paul; RICHARDSON, Yvette. **Mesoscale Meteorology in Midlatitudes**. Chichester, UK: John Wiley & Sons, Ltd, 2010. *E-book*. Disponível em: <http://doi.wiley.com/10.1002/9780470682104>. Acesso em: 29 mar. 2020.

MASON, M. S. Towards Codification of Localised Windstorms: Progress and Challenges. *Em*: , 2017. **Proceedings of 9th Annual Asia-Pacific Conference on Wind Engineering. Auckland, New Zealand, 3-7 December**. [S. l.: s. n.], 2017.

MASON, Matthew S.; WOOD, Graeme S.; FLETCHER, David F. Numerical simulation of downburst winds. **Journal of Wind Engineering and Industrial Aerodynamics**, [s. l.], v. 97, n. 11–12, p. 523–539, 2009.

MCCANN, Donald W. WINDEX—A new index for forecasting microburst potential. **Weather and forecasting**, [s. l.], v. 9, n. 4, p. 532–541, 1994.

MCCARTHY, P.; MELSNESS, M. Severe weather elements associated with September 5, 1996 hydro tower failures near Grosse Isle, Manitoba, Canada. **Manitoba Environmental Service Centre, Environment Canada**, [s. l.], p. 21, 1996.

MCCARTHY, John; WILSON, James W. The Joint Airport Weather Studies Project ". [s. l.], v. 63, p. 8, 1982.

MCCARTHY, John; WILSON, James W.; HJELMFELT, Mark R. Operational Wind Shear Detection and Warning: The "CLAWS" Experience at Denver and Future Objectives. **SAE Transactions**, [s. l.], p. 1446–1450, 1986.

MUNICH RE. **Facts + Statistics: U.S. catastrophes**. [S. l.: s. n.], 2019. Disponível em: <https://www.iii.org/fact-statistic/facts-statistics-us-catastrophes>. .

NACCARATO, K.; MACHADO, L. Brazil BrasilDAT Lightning Network Data. Version 1.0. UCAR/NCAR - Earth Observing Laboratory, , 2019. Disponível em: <https://data.eol.ucar.edu/dataset/553.024>. Acesso em: 4 jul. 2020. CSV: Comma Separated Value (ASCII) (text/csv)

NASCIMENTO, E. L. Previsão de tempestades severas utilizando-se parâmetros convectivos e modelos de mesoescala: Uma estratégia operacional adotável no Brasil. **Revista Brasileira de Meteorologia**, [s. l.], v. 20, n. 1, p. 121–140, 2005.

NATIONAL RESEARCH COUNCIL. **Low-altitude wind shear and its hazard to aviation**. [S. l.]: National Academies Press, 1983.

NELSON, Bruce W; KAPOs, Valerie; ADAMS, John B; OLIVEIRA, Wilson J; BRAUN, Oscar PG. Forest disturbance by large blowdowns in the Brazilian Amazon. **Ecology**, [s. l.], v. 75, n. 3, p. 853–858, 1994.

NOAA. **Delta Flight 191 Incident at DFW Airport**. [S. l.], 2020. Disponível em: <https://www.weather.gov/fwd/delta191>. Acesso em: 27 jun. 2020.

NULLIS, Clare. **WMO certifies Megaflash lightning extremes**. [S. l.], 2020. Disponível em: <https://public.wmo.int/en/media/press-release/wmo-certifies-megaflash-lightning-extremes>. Acesso em: 30 jun. 2020.

ORLANSKI, Isidoro. A rational subdivision of scales for atmospheric processes. **Bulletin of the American Meteorological Society**, [s. l.], p. 527–530, 1975.

ORWIG, Kirsten D.; SCHROEDER, John L. Near-surface wind characteristics of extreme thunderstorm outflows. **Journal of wind engineering and industrial aerodynamics**, [s. l.], v. 95, n. 7, p. 565–584, 2007.

ORWIG-GAST, KD; SCHROEDER, JL. Extreme wind events observed in the 2002 thunderstorm outflow experiment. *Em: PROCEEDINGS OF THE TENTH AMERICAS CONFERENCE ON WIND ENGINEERING, BATON ROUGE, LA, 2005. Anais [...]*. [S. l.: s. n.], 2005.

PALUCH, M. J.; TOAZZA, A.; ROCHA, M. M.; MARROQUIM, A. I. O laboratório anemométrico da Universidade de Passo Fundo. *Em: , 2003. III Workshop Brasileiro de Micrometeorologia; UFSM, Universidade Federal de Santa Maria, Santa Maria, RS, Brasil.* [S. l.: s. n.], 2003. p. 201–205.

PENALBA, Olga C.; ROBLEDO, Federico A. Spatial and temporal variability of the frequency of extreme daily rainfall regime in the La Plata Basin during the 20th century. **Climatic Change**, [s. l.], v. 98, n. 3–4, p. 531–550, 2010.

PEREIRA FILHO, Augusto José; PEZZA, Alexandre Bernardes; SIMMONDS, Ian; LIMA, Raquel Silva; VIANNA, Marcio. New perspectives on the synoptic and mesoscale structure of Hurricane Catarina. **Atmospheric Research**, [s. l.], v. 95, n. 2–3, p. 157–171, 2010.

PITA, Gonzalo L.; DE SCHWARZKOPF, María L. A. Urban downburst vulnerability and damage assessment from a case study in Argentina. **Natural Hazards**, [s. l.], v. 83, n. 1, p. 445–463, 2016.

PONTE, Jacinto; RIERA, Jorge D. Simulation of extreme wind series caused by thunderstorms in temperate latitudes. **Structural Safety**, [s. l.], v. 32, n. 4, p. 231–237, 2010.

POREH, Michael; TSUEI, YG; CERMAK, Jack E. Investigation of a turbulent radial wall jet. **Journal of Applied Mechanics**, [s. l.], v. 34, n. 2, p. 457–463, 1967.

POTTS, Rodney J. Low Windshear at Major Australian Airports and the Risks to Aviation. *Em: , 2007. Conference on Aviation, Range, and Aerospace Meteorology.* [S. l.]: American Meteorological Society, 2007. p. 45.

POVOLEDO, Elisabetta. Genoa's New Bridge Nears Completion, Turning Tragedy Into Hope. **The New York Times**, [s. l.], 28 abr. 2020. World. Disponível em: <https://www.nytimes.com/2020/04/28/world/europe/italy-new-genoa-bridge.html>. Acesso em: 29 abr. 2020.

PROCTOR, Fred H. Numerical simulations of an isolated microburst. Part I: Dynamics and structure. **Journal of the atmospheric sciences**, [s. l.], v. 45, n. 21, p. 3137–3160, 1988.

PROCTOR, Fred H. Numerical Simulations of an Isolated Microburst. Part II: Sensitivity Experiments. **Journal of Atmospheric Sciences**, [s. l.], v. 46, n. 14, p. 23, 1989.

PRYOR, Kenneth L. Microburst nowcasting applications of GOES. **ArXiv preprint arXiv:1106.2143**, [s. l.], 2011.

PRYOR, Kenneth L. Microburst windspeed potential assessment: Progress and developments. **ArXiv preprint arXiv:0810.1622**, [s. l.], 2008.

PRYOR, Kenneth L. Progress and developments of downburst prediction applications of GOES. **Weather and Forecasting**, [s. l.], v. 30, n. 5, p. 1182–1200, 2015.

PRYOR, Kenneth L. Recent developments in microburst nowcasting using GOES. **ArXiv preprint arXiv:1009.0687**, [s. l.], 2010.

PRYOR, Kenneth L; ELLROD, Gary P. WMSI-A new index for forecasting wet microburst severity. **National Weather Association Electronic Journal of Operational Meteorology**, [s. l.], 2004.

REBOITA, Michelle Simões; GAN, Manoel Alonso; ROCHA, Rosmeri Porfírio da; AMBRIZZI, Tércio. Regimes de precipitação na América do Sul: Uma revisão bibliográfica. **Revista Brasileira de Meteorologia**, [s. l.], v. 25, n. 2, p. 185–204, 2010.

REPETTO, Maria Pia; BURLANDO, M.; SOLARI, G.; DE GAETANO, P.; PIZZO, M. Integrated tools for improving the resilience of seaports under extreme wind events. **Sustainable cities and society**, [s. l.], v. 32, p. 277–294, 2017.

REPETTO, Maria Pia; BURLANDO, Massimiliano; SOLARI, Giovanni; DE GAETANO, Patrizia; PIZZO, Marina; TIZZI, Marco. A web-based GIS platform for the safe management and risk assessment of complex structural and infrastructural systems exposed to wind. **Advances in Engineering Software**, [s. l.], v. 117, p. 29–45, 2018.

RIERA, Jorge D. Sobre a Definição do Vento para projecto estrutural na ABNT NBR 6123 (1989) e outras normas Sulamericanas. **Revista Sul-Americana de Engenharia Estrutural**, [s. l.], v. 13, n. 3, 2016.

RIERA, J. D.; NANNI, L. F. Pilot study of extreme wind velocities in a mixed climate considering wind orientation. **Journal of Wind Engineering and Industrial Aerodynamics**, [s. l.], v. 32, n. 1–2, p. 11–20, 1989.

RIERA, J.D.; VIOLLAZ, A.J.; REIMUNDIN, J.C. Some recent results on probabilistic models of extreme wind speeds. **Journal of Wind Engineering and Industrial Aerodynamics**, [s. l.], v. 2, n. 3, p. 271–287, 1977.

ROBERTS, J. F.; CHAMPION, A. J.; DAWKINS, L. C.; HODGES, K. I.; SHAFFREY, L. C.; STEPHENSON, D. B.; STRINGER, M. A.; THORNTON, H. E.; YOUNGMAN, B. D. The XWS open access catalogue of extreme European windstorms from 1979 to 2012. **Natural Hazards and Earth System Sciences**, [s. l.], v. 14, n. 9, p. 2487–2501, 2014.

ROMANIC, Djordje; CHOWDHURY, Junayed; CHOWDHURY, Jubayer; HANGAN, Horia. Investigation of the Transient Nature of Thunderstorm Winds from Europe, the United States, and Australia Using a New Method for Detection of Changepoints in Wind Speed Records. **Monthly Weather Review**, [s. l.], v. 148, n. 9, p. 3747–3771, 2020.

SALIO, Paola; NICOLINI, Matilde; ZIPSER, Edward J. Mesoscale Convective Systems over Southeastern South America and Their Relationship with the South American Low-Level Jet. **Monthly Weather Review**, [s. l.], v. 135, n. 4, p. 1290–1309, 2007.

SANTOS, Mario Luis Wunderlich dos. Regionalização das velocidades extremas e temperaturas dos ventos no centro-sul do Brasil. [s. l.], 1989.

SAVORY, Eric; PARKE, Gerard A.R; ZEINODDINI, Mostafa; TOY, Norman; DISNEY, Peter. Modelling of tornado and microburst-induced wind loading and failure of a lattice transmission tower. **Engineering Structures**, [s. l.], v. 23, n. 4, p. 365–375, 2001.

SCHROEDER, John L.; SMITH, Douglas A. Hurricane Bonnie wind flow characteristics as determined from WEMITE. **Journal of Wind Engineering and Industrial Aerodynamics**, [s. l.], v. 91, n. 6, p. 767–789, 2003.

SENGUPTA, Anindya; HAAN, Fred L.; SARKAR, Partha P.; BALARAMUDU, Vasanth. Transient loads on buildings in microburst and tornado winds. **Journal of Wind Engineering and Industrial Aerodynamics**, [s. l.], v. 96, n. 10–11, p. 2173–2187, 2008.

SHERLOCK, R. H.; STOUT, M. B. Wind Structure in Winter Storms. **Journal of the Aeronautical Sciences**, [s. l.], v. 5, n. 2, p. 53–61, 1937.

SHERMAN, Douglas J. The passage of a weak thunderstorm downburst over an instrumented tower. **Monthly weather review**, [s. l.], v. 115, n. 6, p. 1193–1205, 1987.

SHOWALTER, A. K. A Stability Index for Thunderstorm Forecasting. **Bulletin of the American Meteorological Society**, [s. l.], v. 34, n. 6, p. 250–252, 1953.

SILVA DIAS, Maria A. F. An Increase in the Number of Tornado Reports in Brazil. **Weather, Climate, and Society**, [s. l.], v. 3, n. 3, p. 209–217, 2011.

SIMIU, Emil. Modern developments in wind engineering: Part 1. [s. l.], p. 9, 1981a.

SIMIU, Emil. Modern developments in wind engineering: Part 2. [s. l.], p. 7, 1981b.

SINCLAIR, Russell William; ANTHES, Richard A.; PANOFSKY, Hans A. Variation of the low level winds during the passage of a thunderstorm gust front. [s. l.], 1973.

SKINNER, Patrick S; WEISS, Christopher C; GUNTER, W Scott; SCHROEDER, John L. Near-surface thunderstorm outflow characteristics observed by the TTUKa mobile Doppler radars. [s. l.], p. 10, 2012.

SOLARI, Giovanni. Thunderstorm Downbursts and Wind Loading of Structures: Progress and Prospect. **Frontiers in Built Environment**, [s. l.], v. 6, p. 63, 2020.

SOLARI, Giovanni; BURLANDO, Massimiliano; GAETANO, Patrizia; REPETTO, Maria Pia. Characteristics of thunderstorms relevant to the wind loading of structures. **Wind and Structures**, [s. l.], v. 20, n. 6, p. 763–791, 2015.

SOLARI, Giovanni; BURLANDO, Massimiliano; REPETTO, Maria Pia. Detection, simulation, modelling and loading of thunderstorm outflows to design wind-safer and cost-efficient structures. **Journal of Wind Engineering and Industrial Aerodynamics**, [s. l.], v. 200, p. 104142, 2020.

SOLARI, Giovanni; GAETANO, Patrizia; REPETTO, Maria Pia. Thunderstorm response spectrum: Fundamentals and case study. **Journal of Wind Engineering and Industrial Aerodynamics**, [s. l.], v. 143, p. 62–77, 2015.

SOLARI, Giovanni; RAINISIO, Davide; DE GAETANO, Patrizia. Hybrid simulation of thunderstorm outflows and wind-excited response of structures. **Meccanica**, [s. l.], v. 52, n. 13, p. 3197–3220, 2017.

SQUIRES, P. Penetrative Downdrafts in Cumuli. **Tellus**, [s. l.], v. 10, n. 3, p. 381–389, 1958.

SRIVASTAVA, R. C. A Model of Intense Downdrafts Driven by the Melting and Evaporation of Precipitation. **Journal of the Atmospheric Sciences**, [s. l.], v. 44, n. 13, p. 22, 1987.

SRIVASTAVA, R. C. A Simple Model of Evaporatively Driven Downdraft: Application to Microburst Downdraft. **Journal of Atmospheric Sciences**, [s. l.], v. 42, n. 10, p. 20, 1985.

STENGEL, Dominik; THIELE, Klaus. Measurements of downburst wind loading acting on an overhead transmission line in Northern Germany. **Procedia Engineering**, [s. l.], v. 199, p. 3152–3157, 2017.

TWISDALE, Lawrence A.; VICKERY, Peter J. Research on thunderstorm wind design parameters. **Journal of Wind Engineering and Industrial Aerodynamics**, [s. l.], v. 41, n. 1–3, p. 545–556, 1992.

VALLIS, Matthew. **Brazilian Extreme Wind Climate**. 2019. 419 f. Doctoral Thesis - Universidade Federal do Rio Grande do Sul, Porto Alegre, Brazil, 2019.

VARGAS JR, V. R.; CAMPOS, C. R. J. Severe Events on Rio Grande do Sul from 2004 to 2008. **Anuário do Instituto de Geociências—UFRJ**, [s. l.], v. 38, n. 1, p. 137, 2015.

VIANA, Denilson Ribeiro; AQUINO, Francisco Eliseu; MUÑOZ, Viviana Aguilar. Avaliação de desastres no Rio Grande do Sul associados a complexos convectivos de mesoescala. **Sociedade & Natureza**, [s. l.], v. 21, n. 2, p. 91–105, 2009.

VILLANI, Paola M. Chiara. Dynamics and causes of the collapse of the Morandi viaduct in Genoa. **Catalogo Pubblicazioni POLIMI**, [s. l.], v. 07 ALTRO, n. 07.12 Altro, 2019. Disponível em: <https://re.public.polimi.it/retrieve/handle/11311/1102900/414271/IP0294-Villani-E-Full.pdf>. Acesso em: 4 fev. 2020.

WAKIMOTO, Roger M. Forecasting Dry Microburst Activity over the High Plains. **Monthly Weather Review**, [s. l.], v. 113, p. 13, 1985.

WAKIMOTO, Roger M. Kinematic, Thermodynamic, and Visual Structure of Low-Reflectivity Microbursts. **Monthly Weather Review**, [s. l.], v. 122, 1994.

WAKIMOTO, Roger M; BRINGI, V. N. Dual-Polarization of Microburst Associated with Intense Convection: The 20 July Storm during the MIST Project. **Monthly Weather Review**, [s. l.], v. 116, p. 19, 1988.

WALLACE, John M.; HOBBS, Peter Victor. **Atmospheric science: An introductory survey**. 2nd eded. Amsterdam ; Boston: Elsevier Academic Press, 2006. (International geophysics series, v. v. 92).

WANG, Lijuan; MCCULLOUGH, Megan; KAREEM, Ahsan. A data-driven approach for simulation of full-scale downburst wind speeds. **Journal of Wind Engineering and Industrial Aerodynamics**, [s. l.], v. 123, p. 171–190, 2013.

WANG, Lijuan; MCCULLOUGH, Megan; KAREEM, Ahsan. Modeling and simulation of nonstationary processes utilizing wavelet and Hilbert transforms. **Journal of Engineering Mechanics**, [s. l.], v. 140, n. 2, p. 345–360, 2014.

WIKIPEDIA. **Category: Airliner accidents and incidents caused by microbursts**. Em: WIKIPEDIA. [S. l.: s. n.], 2018. Disponível em: https://en.wikipedia.org/w/index.php?title=Category:Airliner_accidents_and_incidents_caused_by_microbursts&oldid=841913179. Acesso em: 30 jun. 2020.

WILSON, James W; ROBERTS, Rita D.; KESSELMEIER, Cathy; JOHN, McCarthy. Microburst Wind Structure and Evaluation of Doppler Radar for Airport Wind Shear Detection. **Journal of Climate and Applied Meteorology**, [s. l.], 1984.

WOLFSON, M M. Characteristics of Microbursts in the Continental United States. **The Lincoln Laboratory Journal**, [s. l.], v. 1, n. 1, p. 26, 1988.

WOLFSON, Marilyn M.; DELANOY, Richard L.; FORMAN, Barbara E.; HALLOWELL, Robert G.; PAWLAK, Margita L.; SMITH, Peter D. Automated microburst wind-shear prediction. **Lincoln Laboratory Journal**, [s. l.], v. 7, n. 2, 1994.

WOLFSON, Marilyn Mitchell; IACONO, Michael J. **A comparison of PAM-II and FLOWS mesonet data during COHMEX**. [s. l.]: Lincoln Laboratory, Massachusetts Institute of Technology, 1987.

WOOD, Graeme S; KWOK, Kenny CS; MOTTERAM, Nicholas A; FLETCHER, David F. Physical and numerical modelling of thunderstorm downbursts. **Journal of Wind Engineering and Industrial Aerodynamics**, [s. l.], v. 89, n. 6, p. 535–552, 2001.

XU, Zhuyun; HANGAN, Horia. Scale, boundary and inlet condition effects on impinging jets. **Journal of Wind Engineering and Industrial Aerodynamics**, [s. l.], v. 96, n. 12, p. 2383–2402, 2008.

YOE, Charles E. **An Introduction to Risk and Uncertainty in the Evaluation of Environmental Investments**. [s. l.]: ARMY ENGINEER INST FOR WATER RESOURCES FORT BELVOIR VA, 1996.

ZHANG, Yan. **Study of microburst-like wind and its loading effects on structures using impinging-jet and cooling-source approaches**. 2013. Doctoral Thesis - Iowa State University, Ames, Iowa, 2013.

ZHANG, Yan; HU, Hui; SARKAR, Partha P. Modeling of microburst outflows using impinging jet and cooling source approaches and their comparison. **Engineering Structures**, [s. l.], v. 56, p. 779–793, 2013.

ZHANG, Shi; SOLARI, Giovanni; DE GAETANO, Patrizia; BURLANDO, Massimiliano; REPETTO, Maria Pia. A refined analysis of thunderstorm outflow characteristics relevant to the wind loading of structures. **Probabilistic Engineering Mechanics**, [s. l.], v. 54, p. 9–24, 2018.

ZHANG, Shi; YANG, Qingshan; SOLARI, Giovanni; LI, Bo; HUANG, Guoqing. Characteristics of thunderstorm outflows in Beijing urban area. **Journal of Wind Engineering and Industrial Aerodynamics**, [s. l.], v. 195, p. 104011, 2019.

ZIPSER, E. J.; CECIL, Daniel J.; LIU, Chuntao; NESBITT, Stephen W.; YORTY, David P. Where are the most intense thunderstorms on earth?. **Bulletin of the American Meteorological Society**, [s. l.], v. 87, n. 8, p. 1057–1072, 2006.

APPENDIX A - INVESTIGATION OF DOWNBURSTS-LIKE EVENTS INCIDENCE IN BRAZIL

Brazil is highly vulnerable to the effects of extreme winds. Modern studies of accidents due to extreme wind events gained traction in Brazil with Blessman, who investigated reported on 355 major accidents from 1979 to 1982 in the State of Rio Grande do Sul. The most part of these accidents were observed in the northwest and northeast part of this state. Blessman (1991) points out that several accidents could have been avoided if the right aerodynamic coefficient had been adopted for the design, but in those analysis, it was also argued that the wind speeds that could have been exceptionally higher and could have presented different shapes of profiles.

It was not until the 2000s that tornadoes and downbursts began to be considered part of the Brazil's climatology (SILVA DIAS, 2011) and considered nationwide a leading cause of natural disasters (MARCELINO *et al.*, 2005; NASCIMENTO, 2005A). Although, when these events make to the news, they are usually generically named "windstorms" or simply "thunderstorms," rarely receiving the right classifications and a throughout meteorological analysis. Even though Brazil's territory is within one the most convective active zones of the world (BROOKS *et al.*, 2003; NASCIMENTO, 2005), databases with extreme wind events are incomplete, making it difficult to tracking, characterizing, and statically describing TS events for that country.

While tornadoes are intrinsically different of downbursts, they share similar precursors and have been more consistently investigated worldwide. Therefore, the investigation of tornadoes may bring some insights into the frequency of extreme wind events generated by downbursts. Marcelino *et al.* (2005) found that between 1976 and 2003, at least 45 episodes of tornadoes were observed only at the southern state of Santa Catarina. In Rio Grande do Sul State Vargas Jr and Campos (2015) found that between 2004 and 2008, 43% of the 276 severe weather events were due to windstorms.

At the Brazilian Integrated Disaster Database (S2iD) there are approximately 2500 natural disaster entries of events caused by convective-local windstorms from 1982 to 2016, plus 72 tornadoes and waterspouts cases in Brazil (S2id, 2020). There is no specific classification for

downbursts events within this database, possibility because of the lack of knowledge of such phenomena by the authorities resulting in erroneous classifications.

Silva Dias (2011) identified 158 cases total of tornadoes and waterspouts reports in Brazil from 1960 to 2008 and developed the frequency map showed in Figure 109 with the distribution of these cases in Brazil. It is important to note that tornadoes usually depend upon observational proof in order to be recorded and there is a proportional relationship between events and the area's population. There is clear evidence on the increase in reports over the last years, which can be as a result of several factors, such as population growth, significant increase of mass-media stations, easier access to crowdsourcing applications, popularization of smartphones and internet; and finally, climate changes. Therefore, using these datasets to prescribe a climatological trend of these extreme events without a throughout analysis and consideration of the mentioned factor may result in biased outputs.

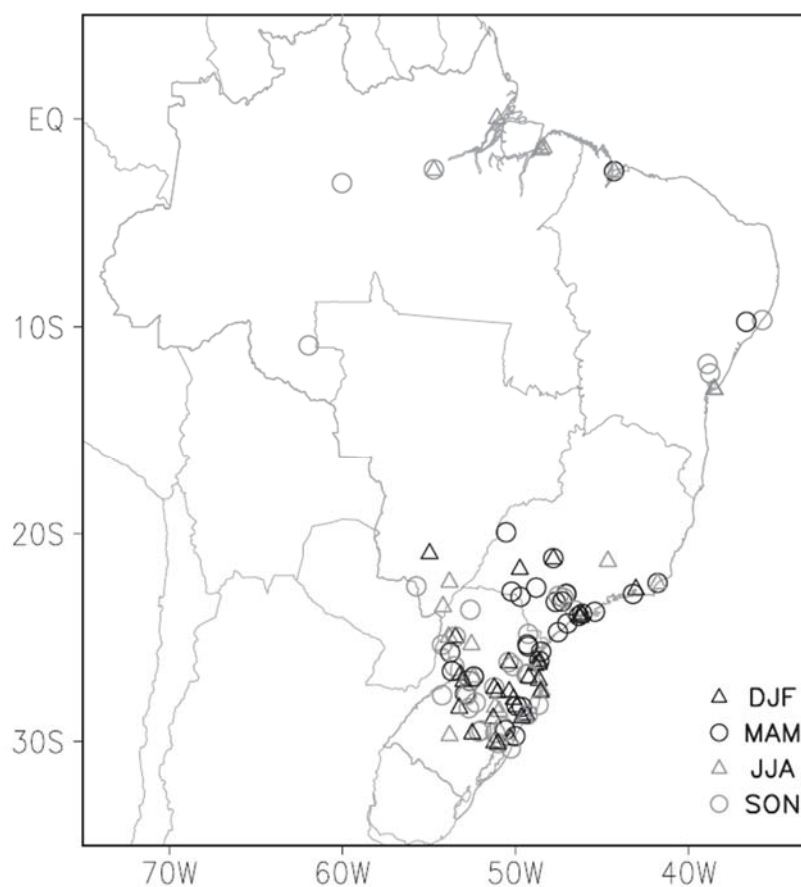


Figure 109. Location and season of tornadoes and waterspouts reports. December–February (DJF) is summer, March–May (MAM) is fall, June–August (JJA) is winter, and September–November (SON) is spring. Source: Silva Dias (2011).

The research into downbursts or downburst-like incidence events in Brazil is a little more recent. The first reports of downbursts in Brazil dates to 1991. An investigation among scientific literature and news magazines found a report of a severe weather event in Itú, State of São Paulo (SP), questioning if such event was due to a tornado or microburst and briefly discussing Fujita's research (MASSAMBANI *et al.*, 1991). Later, downbursts occurrence started to be investigated in the Amazon with Nelson *et al.* (1994) using satellite imagery, leading to the identification of 330 large blowdowns in the Brazilian Amazon of at least 100-ha size classes each for one specific year.

Later, Garstang *et al.* (1998) investigated the occurrence of downbursts in the Central Amazon Basin using four 40 meters tall towers for 45 days temporarily installed in the region. Based on the data obtained, typical meteorological parameters during the occurrence of downbursts in the Amazon Basin were defined, and a small frequency analysis based on satellite imagery of the phenomena occurrence was proposed. The forests disturbances caused by density driven downdrafts from convective clouds and measured winds gust speed averaged 12 m/s, one only case out of 31 reached the maximum of 17 m/s. The authors argued that, based on damages patterns, the winds could have reached 30 m/s at the core area of the strong downdrafts.

In Figure 110 is shown the geographic distribution of blowdowns occurrence over the Brazilian Amazon, where the distribution of large events is expressed as square kilometers per Landsat scene (28,000 km²) with isolines ranging from 5 to 85 km² per scene in intervals of 5 km². In b) is shown a more recent work developed by Taszarek *et al.* (2021), using ERA5 global reanalysis data of annual mean of hours favorable to the development of severe thunderstorm environments based on CAPE. Note how the blowdown events analysis developed by Garstang in 1998 matches closely to the more recent analysis for severe thunderstorm environments definition in that specific region.

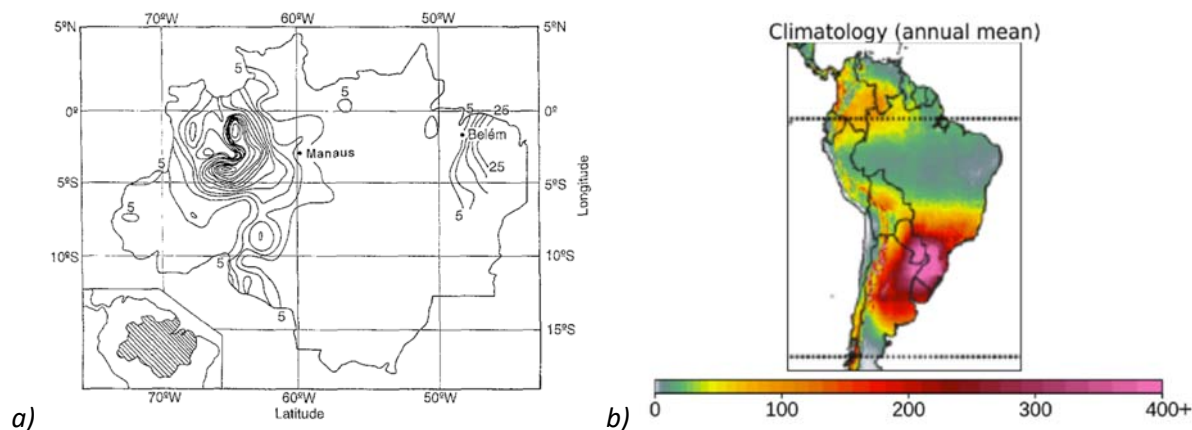


Figure 110. In a) shows Garstang (1998) estimation of downburst distribution in the Amazon based on satellite analysis and in b) a more recent work from Taszarek et al. (2021) shows the annual mean climatology of severe thunderstorm environments in hours. Note how the blowdowns analysis matches very closely the more recent climatologic studies. Source: Adapted from Taszarek et al. (2021) and Garstang (1998).

Downburst events began to be associated to severe weather event in Brazil more frequently in southern Brazil in the 2000s and more diligently investigated in 2010's with the works of Lima and Loredo-Souza (2015); and later with a small climatological for southern Brazil developed by Ferreira (2017), in which several major convectively induced low level gusts were identified using reanalysis data from the Climate Forecast System Reanalysis (CFSR) and Climate Forecast System Version 2 (CFSv2).

In terms of major downburst events noticed in news outlets, an event occurred in 25/11/2010 in Caçador, State of Santa Catarina (SC), was diligently surveyed and damages that characterizes to have been caused by convectively induced straight-lined winds were extensive surveyed by the Agribusiness Research and Rural Extension Company of Santa Catarina State (EPAGRI/SC). Figure 111 shows one of the pictures taken at the event.



Figure 111. Agribusiness Research and Rural Extension Company of Santa Catarina (EPAGRI/SC) news article, discuss the pattern of damages after a severe storm in the State. Source: EPAGRI (2010).

Areas in Brazil with radar coverage have the strategic advantage of promptly offer significantly more quality of information to help track, identify, and report downburst events to local communities. A great example was the downburst observed in 06/13/2020 in Presidente Getúlio – SC, the analysis of divergent wind patterns of this event from radar imagery and damage survey allowed researchers to show the exact occurrence of downburst(s) during a severe weather event and assertively inform the authorities, communities, and mass media. The Radar imagery and the damages survey are presented in Figure 112 and in Figure 114, respectively.

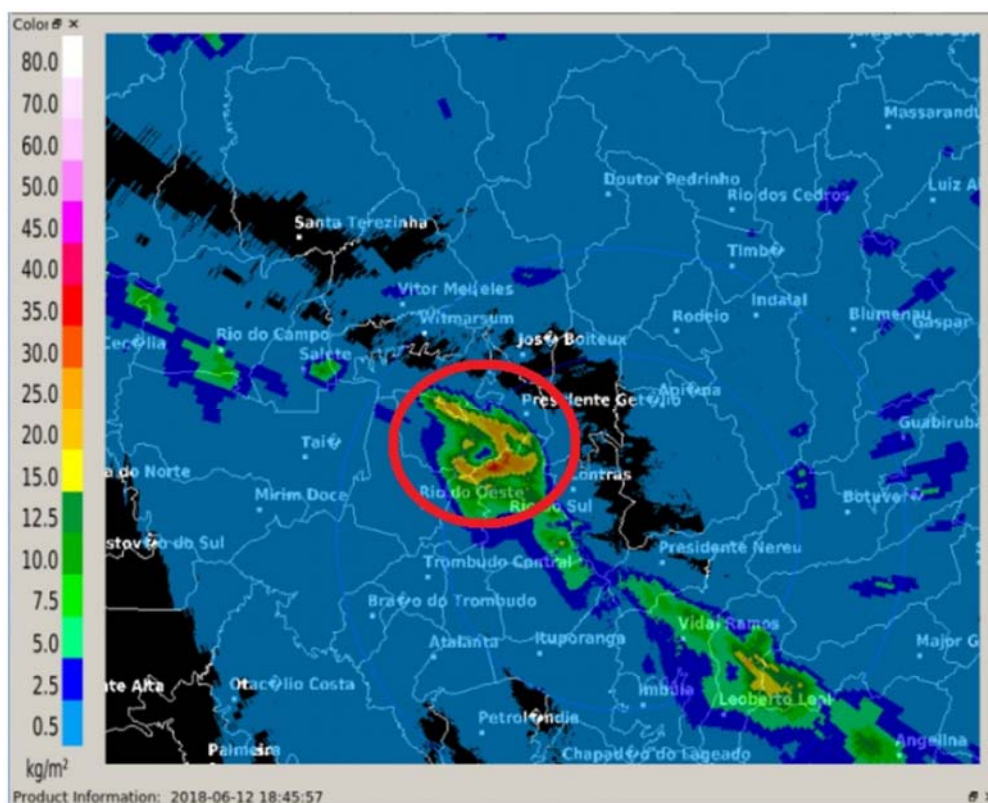


Figure 112. Capture of a downburst event in Presidente Prudente – SC. Notice the divergent wind pattern highlighted in the Radar capture. Source: O Município (2018).

Radars became an essential tool to help meteorologists and civil defense to provide reliable forecasting and help to alert and protect communities from extreme weather events. Radar can also estimate precipitation and winds within its quantitative ranges and help understand better the structures of the storms at certain regions. Brazil has a relative extensive network of radars coverage over its lands but lack of availability of Doppler Radars of S-band, which are

the most efficient type of radars that can be used to detect severe weather, including the typical non-stationary convective wind gusts under study on this document.

Figure 113 presents the coverage of Meteorological Radars in Brazil's territory identified according to their respective managing entities. Some are under state administration, others belong to federal entities, including some with private funding in both cases. These radars network are independently but collaborate to promote radar surveillance in Brazil. The system has become more integrated over the last years (ANGELIS *et al.*, 2006) and there are four main sources of radar data information in Brazil:

- The Department of Airspace Control (DECEA). The institution has the most extensive radar network in Brazil.
- National Center for Monitoring and Early Warning of Natural Disasters (CEMADEN).
- Amazon Surveillance System (SIPAM).
- National Institute for Space Research (INPE).

Brazil has also several regional public and private entities that have and offer radar products:

- Agricultural Research and Rural Extension of the state of Santa Catarina (EPAGRI/CIRAM).
- Foundation for Meteorology and Water Resources in the State of Ceará (FUNCEME).
- Meteorological System in the State of Paraná (SIMEPAR).
- Institute for Meteorological Research of the University of the State of São Paulo (IPMET-UNESP).
- State Environmental Institute in the State of Rio de Janeiro (INEA).
- Geotechnical Institute Foundation in the State of Rio de Janeiro (Geo-Rio).
- Department of Water and Electricity in the State of São Paulo – (DAEE).

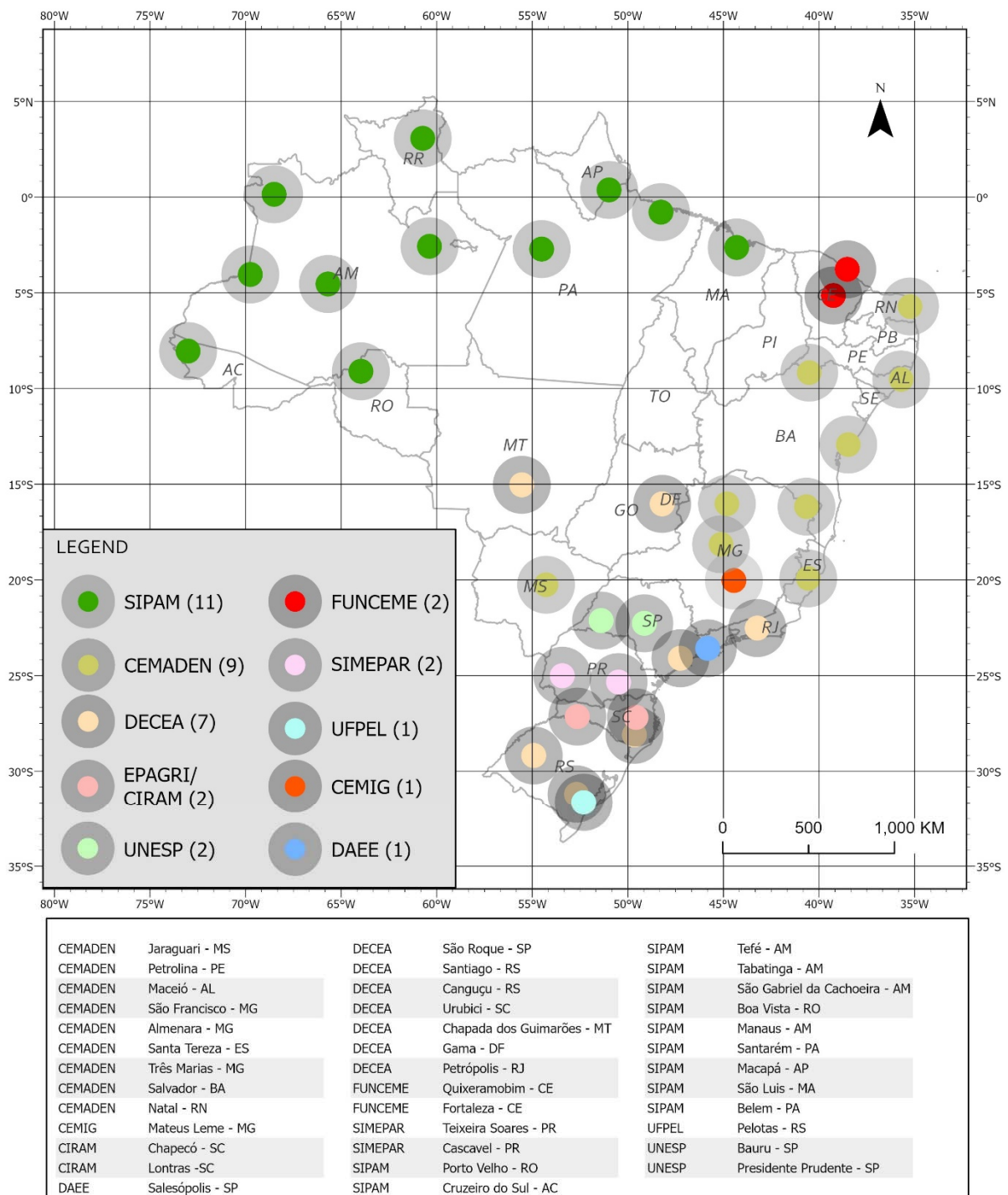


Figure 113. Existing radar network in Brazil colored according to their respective managing entities. Source: Created by Author. Data extracted from: Naccarato and Camargo (2019) and Tropical Atlantic (2020).



Foto: Marcos Fernandes/Especial

Figure 114. Damage survey after a downburst event in President Prudente – SC. Photo by Marcos Fernandes. Source: O Município (2018).

More recently, with the advent of cameras and cellphones, several pictures and videos registering the recurrence of downbursts became available in Brazil. For example, two macrobursts events were captured during a sudden precipitation event in Morro Agudo – SP and in Torres – RS during a supercell event. These events are depicted in Figure 115 and Figure 116, respectively.



Figure 115. Picture of a downburst event in Morro Agudo on 12/11/19. Source: Climaavivo.com (2019)



Figure 116. Downburst event photographed in Torres – RS. Source: sajoaquimonline.com (2019).

Loredo-Souza *et al.* (2019) provided an analysis of the downburst occurrence in Brazil and surveyed the typical damage in buildings in the wake of a downburst event in Porto Alegre – RS on January 29, 2016. It was noticed common damage patterns after thunderstorm events, including to the roof level of houses or buildings, roof tiles, steel sheet, partial or overall roof-lift and partial removal of cladding and facades. In Figure 117 a) is showed the aftermath picture of one building façade and in b) is showed the wind tunnel laboratory testing results. It is noticeable that most part of the damage occurred in the areas of the building with the highest wind intensity incidence according to the wind tunnel laboratory testing results.

The analysis of this incident shows that localized intense winds due to the thunderstorm events were responsible for causing such damages, although ABL wind tunnel testing was an efficient tool capable to identify in this case the most susceptible areas of the building's façade to extreme TS wind events.

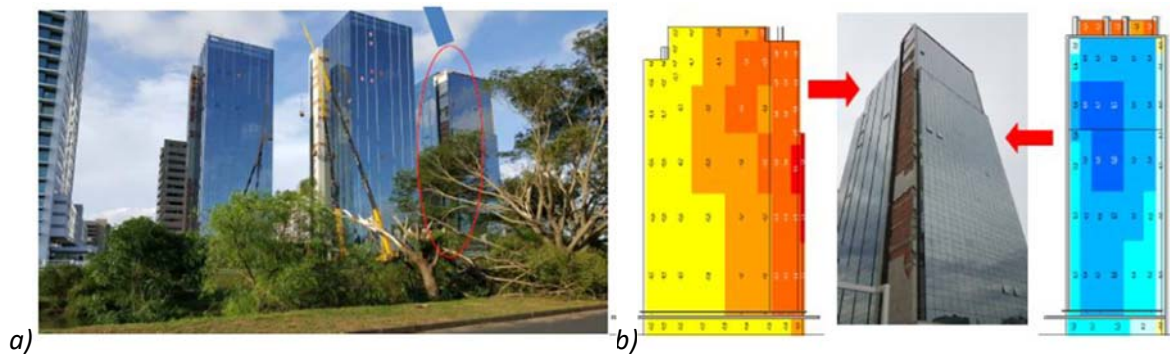


Figure 117. In a) is shown the full-scale damage caused by a downburst event in Porto Alegre and in b) the laboratory testing showing records of the same building, where the red and orange areas represent the side that was mostly damaged by the same thunderstorm event. Source: Loredou-Souza *et al.* (2019).

Here a study was developed considering the key terminologies, *microexplosão*, downbursts, microbursts, and blowdowns, aiming to investigate how many times this phenomena has been used to describe accidents or extreme events in Brazil. Extensive search in various platforms, including academic and commercially available websites, found at least 41 downburst events reported in Brazil until mid-2020. Furthermore, other 361 more blowdowns observations in the Amazon by Nelson *et al.* (1994) and Garstang *et al.* (1998). Figure 118 shows the distribution of these throughout Brazil. The colored squares show the year ranges in which these events have happened. The expressive amount of downburst reported over the last decade raises the question if this is correlated to effects of climate changes or if it is merely because of popularization of the knowledge about downbursts as previously discussed.

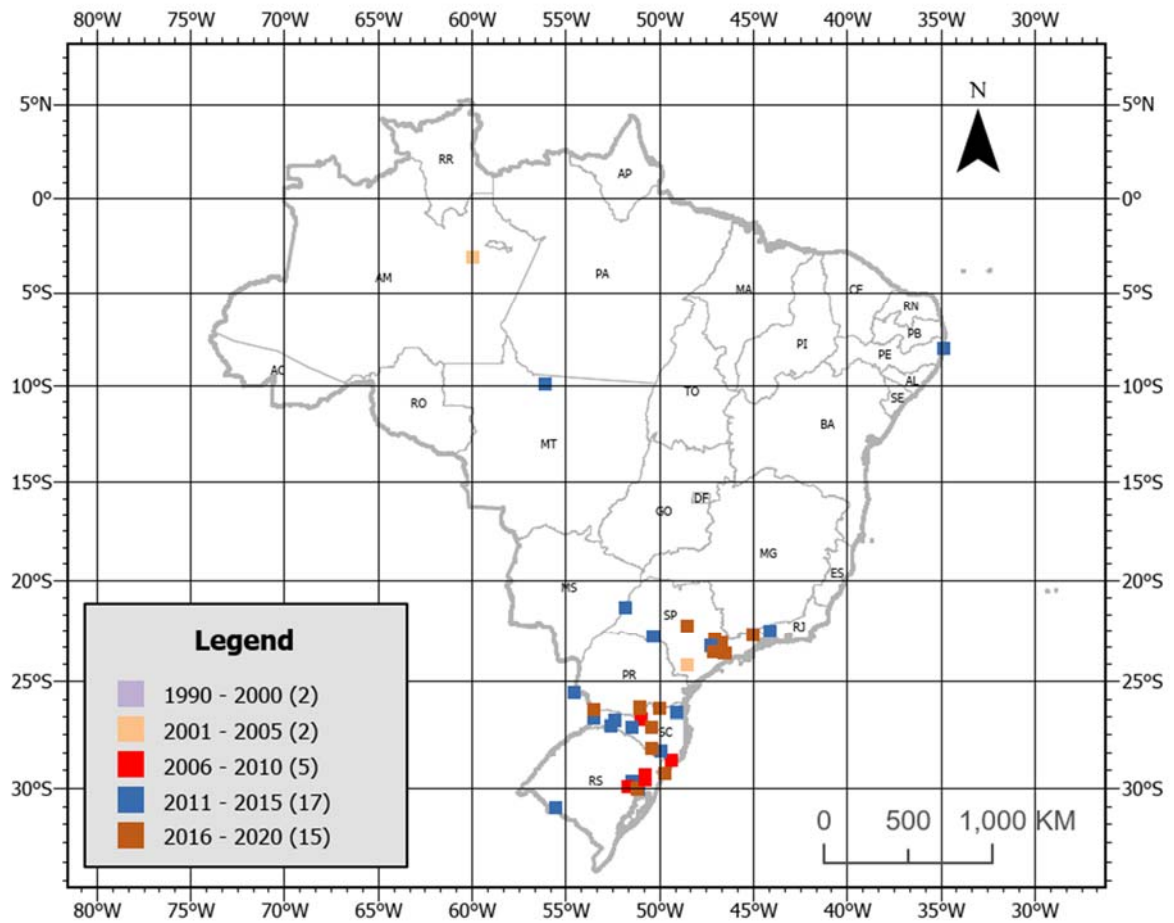


Figure 118. Downburst cases reported in Brazil within different year ranges. Source: Author.

It is noticeable that most part of the downburst events were reported in the southern part of Brazil, in Figure 119 is presented a chart with these cases sorted by State. The states of Rio Grande do Sul, Santa Catarina, and São Paulo presented the greatest number of cases: 11 each. In this study, only a few downburst events were registered in the State of Paraná, which contradicts the fact that this state is known for frequently experiencing severe wind events, showing a limitation of this sort of analysis to track areas prone to the occurrence of downbursts.

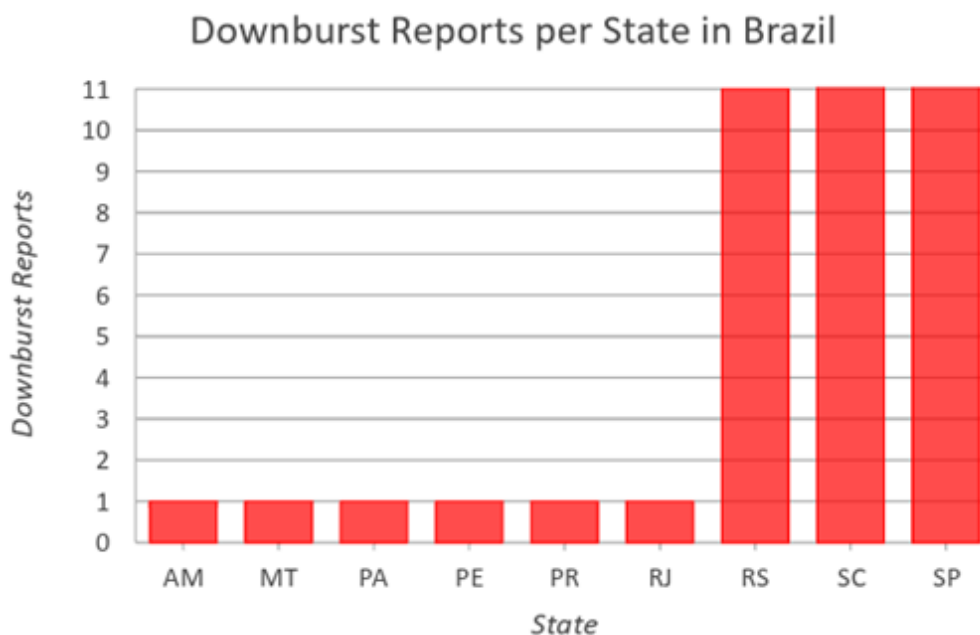


Figure 119. Downburst cases reported in Brazil until 2020 per State. Source: Author.

In this research it was also analyzed the maximum wind gusts speed reported in each event based on available reports. The amazon basin and the northeastern downburst cases are not showed since they did not present significantly higher speed when compared to the events in the southern states of Brazil. The downburst case reports showed wind speeds of up to 42 m/s for the states of Santa Catarina, Rio Grande do Sul, Paraná, and São Paulo. A case of downbursts reported in Alta Floresta, State of Mato Grosso (MT), registered maximum wind gusts of 39 m/s, which shows how the North portion of the Country can also be vulnerable to TS wind events. Although, it is important to remember this data was obtained from synoptic weather stations, and because of their low spatial and temporal resolutions, the actual velocity could have been higher than the registered one.

Figure 120 shows the maximum wind speed gust reported during the downburst report events for the southern portion of Brazil overlay with Brazil's population density (1 km² resolution). Areas with higher density population are shown in darker orange and lower density population in light yellow. It is noticeable the correlation but not causation that the urbanization effect and higher amount of downburst events reported over the last decade, this can be explained because of various factors, including popularization of knowledge regarding downbursts as a specific weather phenomenon among the scientific community and communications mass media; the popularization of cameras among the local communities; and possibly adverse effects of climate changes. It is important to note that this downburst events analysis was

based mostly on reports from news outlets and scientific research, no extensive meteorological analysis was developed on this study, leaving an opportunity for the development of future work.

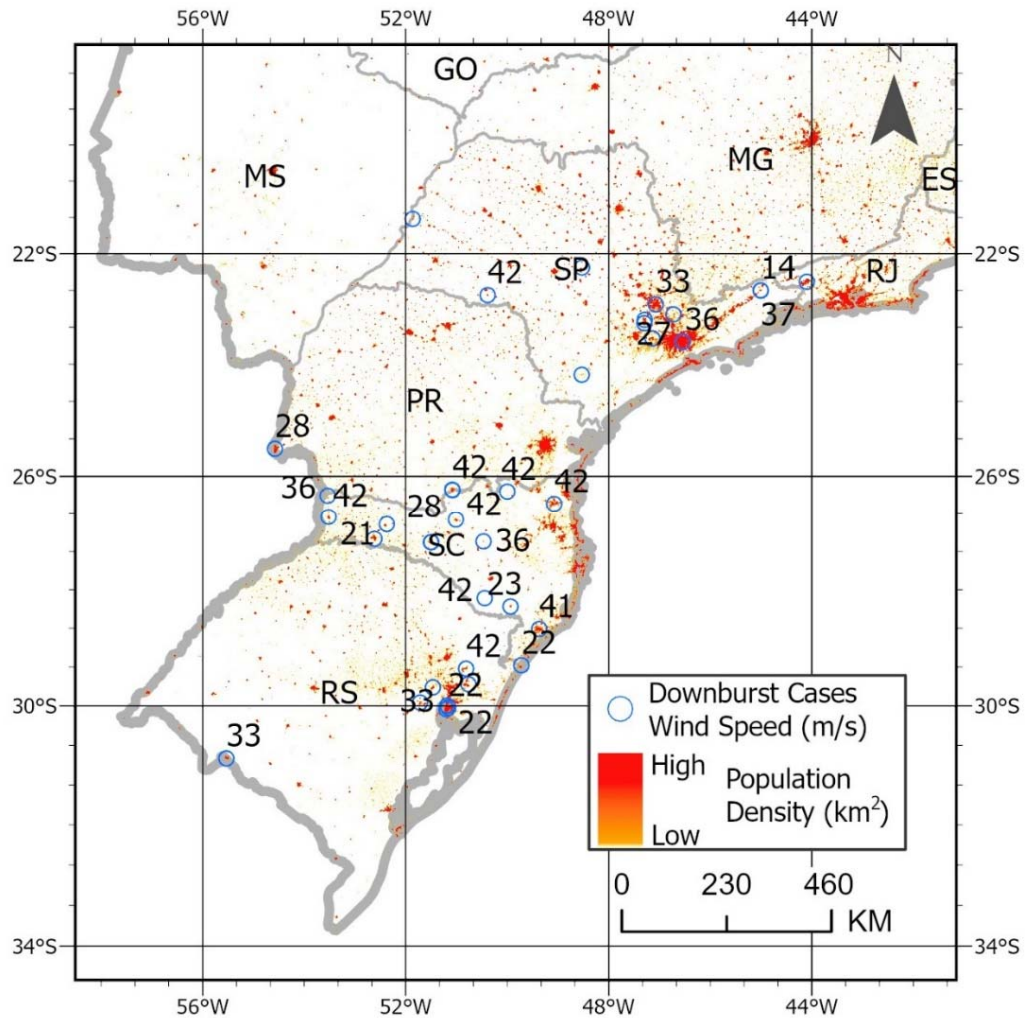


Figure 120. Downburst reports maximum wind gust speed overlaid above population density in Brazil. Focus is given to southern portion of Brazil since is where most part of the cases are located. Source: Author. Data extracted from: Wind data extracted from several downburst events analysis and population density information from WorldPop.org (WORLDPOP, 2021).

REFERENCES - INVESTIGATION OF DOWNBURTS-LIKE EVENTS INCIDENCE IN BRAZIL

AMBIENTE BRASIL. **Meteorologista aponta "tempestade severa" em São Francisco de Paula/RS** Ambientebrasil - Notícias, 14 mar. 2017. Disponível em: <<https://noticias.ambientebrasil.com.br/clipping/2017/03/14/135950-meteorologista-aponta-tempestade-severa-em-sao-francisco-de-paulars.html>>. Acesso em: 2 jul. 2020

ANGELIS, Carlos Frederico; MACHADO, Luiz Augusto Toledo; MORALES, Carlos Augusto; SILVA, Sergio Antonio Alves; ROBERTO HENRIQUES, Carlos; NOGUEIRA, Jimmy. **Rede de Radars Meteorológicos: Ação Conjunta DECEA – INPE/CPTEC**. [s. l.], p. 6, 2006.

APAC - AGÊNCIA PERNAMBUCANA DE ÁGUAS E CLIMA. **Ventos fortes em Olinda**. Disponível em: <http://www.apac.pe.gov.br/noticias.php?noticia_id=453>. Acesso em: 30 jun. 2020.

BOCAINA INFORMA. **Morador de Jaú faz foto de fenômeno "down buster", micro-explosão Bocaina Informa**, 1 out. 2019. Disponível em: <<https://bocainainforma.com.br/tempo-e-temperatura/morador-de-ja-u-faz-foto-de-fenomeno-down-buster-micro-explosao/>>. Acesso em: 2 jul. 2020

BROOKS, Harold E; LEE, James W; CRAVEN, Jeffrey P. **The spatial distribution of severe thunderstorm and tornado environments from global reanalysis data**. Atmospheric Research, [s. l.], v. 67–68, p. 73–94, 2003.

CEPAGRI. **Meteorologista explica dificuldade na emissão de alerta de microexplosões**. Disponível em: <<https://www.cpa.unicamp.br/noticia/14/meteorologista-explica-dificuldade-na-emissao-de-alerta-de-microexplosoes>>. Acesso em: 2 jul. 2020.

CIRAM. **Estações Meteorológicas de Criciúma**. Disponível em: <www.ciram.com.br/siscrici/index.jsp?url=pagina/jsp/projeto.jsp/1/1>.

CLIC SOLEDADE. **Após possível tornado na Serra, temperatura despensa e chuva pode chegar a 60mm no Norte**. Disponível em: <<https://www.clicsoledade.com.br/clicnews/?pg=ler&id=2968>>. Acesso em: 30 jun. 2020.

CLIMAAOVIVO.COM. **Microexplosão em Morro Agudo / SP - 12/11/19**. Disponível em: <<https://www.climaaovivo.com.br/videos/microexplosao-em-morro-agudo-sp-121119>>. Acesso em: 2 jul. 2020.

CPTEC/INPE. **Notícias - CPTec/INPE**. Disponível em: <<https://www.cptec.inpe.br/noticias/noticia/9828>>. Acesso em: 2 jul. 2020.

DE OLHO NO TEMPO. **Tromba d'água avança do rio Paraná e se transforma em tornado ao destruir parte de Panorama**, 9 nov. 2015. Disponível em: <<https://jotaneves.com.br/2015/09/tromba-d-c2%b4agua-avanca-do-rio-parana-e-se-transforma-em-tornado-ao-destruir-parte-de-panorama/>>. Acesso em: 2 jul. 2020

DIÁRIO DE CANOAS. **MetSul alerta para temporal na região - Região - Diário de Canoas**. Disponível em: <http://www.diariodecanoas.com.br/index.php?id=/noticias/regiao/materia.php&cd_matia=229017>. Acesso em: 30 jun. 2020.

DIÁRIO SP. **Jarinu vira cenário de guerra após microexplosão.**

ÉDERLUIZ.COM. **Meteorologistas dizem que possivelmente uma micro-explosão atingiu Joaçaba - Éder Luiz Notícias.** Disponível em: <<https://www.ederluiz.com.br/meteorologistas-dizem-que-possivelmente-uma-micro-explosao-atingiu-joacaba>>. Acesso em: 2 jul. 2020.

EDUCADORA.AM.BR. **Microexplosão em Presidente Getúlio teve ventos estimados em mais de 150 km/h.** Disponível em: <<https://www.educadora.am.br/noticia/microexplosao-em-presidente-getulio-teve-ventos-estimados-em-mais-de-150-kmh/>>. Acesso em: 2 jul. 2020.

EPAGRI. **Clima: Epagri/Ciram afirma que microexplosão atingiu Caçador.** Disponível em: <<https://www.cacador.net/noticias/geral/2010/11/25/clima-epagri-ciram-afirma-que-microexplosao-atingiu-cacador-12651>>. Acesso em: 2 jul. 2020.

EPAGRI/CIRAM. **São Miguel do Oeste registrou microexplosão, diz Epagri/Ciram** *Notícia Hoje*, 6 fev. 2019. Disponível em: <<https://noticiahoje.net/sao-miguel-do-oeste-registrou-microexplosao-diz-epagri-ciram/>>. Acesso em: 2 jul. 2020

FERREIRA, Vanessa. **Um estudo observacional de rajadas de vento geradas por tempestades severas no sul do Brasil.** 2017. 127 f. Master Thesis - Universidade Federal de Santa Maria, Santa Maria, 2017.

G1-RS. **Estragos em Livramento podem ter sido provocados por microexplosão.** Disponível em: <<http://g1.globo.com/rs/rio-grande-do-sul/noticia/2014/12/estracos-em-livramento-podem-ter-sido-provocados-por-microexplosao.html>>. Acesso em: 2 jul. 2020.

G1-RS. **Vento teve velocidade de um furacão em Porto Alegre, diz meteorologista.** Disponível em: <<http://g1.globo.com/rs/rio-grande-do-sul/noticia/2016/02/vento-teve-velocidade-de-um-furacao-em-porto-alegre-diz-meteorologista.html>>. Acesso em: 30 jun. 2020.

G1-SC. **Microexplosão atingiu região Oeste de SC no início desta semana.** Disponível em: <<http://g1.globo.com/sc/santa-catarina/noticia/2013/01/microexplosao-atingiu-regiao-oeste-de-sc-no-inicio-desta-semana.html>>. Acesso em: 2 jul. 2020.

G1-SC. **Epagri/Ciram confirma microexplosão em Ponte Alta do Norte e Porto União.** Disponível em: <<http://g1.globo.com/sc/santa-catarina/noticia/2016/05/epagriciram-confirma-microexplosao-em-ponte-alta-do-norte-e-porto-uniao.html>>. Acesso em: 2 jul. 2020a.

G1-SC. **Fenômeno que atingiu Oeste de SC foi tornado ou microexplosão, aponta documento da Defesa Civil.** Disponível em: <<https://g1.globo.com/sc/santa-catarina/noticia/2020/06/11/fenomeno-que-atingiu-oeste-de-sc-foi-tornado-ou-microexplosao-aponta-documento-da-defesa-civil.ghtml>>. Acesso em: 2 jul. 2020.

G1-SC, D. G. **Epagri/Ciram confirma microexplosão em Ponte Alta do Norte e Porto União.** Disponível em: <<http://g1.globo.com/sc/santa-catarina/noticia/2016/05/epagriciram-confirma-microexplosao-em-ponte-alta-do-norte-e-porto-uniao.html>>. Acesso em: 2 jul. 2020b.

G1-SC. **Microexplosão foi registrada em São Joaquim, diz meteorologista.** Disponível em: <<http://g1.globo.com/sc/santa-catarina/noticia/2013/11/microexplosao-foi-registrada-em-sao-joaquim-diz-meteorologista.html>>. Acesso em: 2 jul. 2020.

G1-SC. **Quarta vítima de tornado em Xanxerê é enterrada no cemitério municipal.** Disponível em:

<<http://g1.globo.com/sc/santa-catarina/noticia/2015/05/quarta-vitima-de-tornado-em-xanxere-e-enterrada-no-cemiterio-municipal.html>>. Acesso em: 30 jun. 2020a.

G1-SC. **Inmet confirma passagem de tornado em Chapecó, SC; houve feridos.** Disponível em: <<http://g1.globo.com/sc/santa-catarina/noticia/2015/11/inmet-confirma-passagem-de-tornado-em-chapeco-sc-houve-feridos.html>>. Acesso em: 2 jul. 2020b.

GARSTANG, M.; WHITE, S.; SHUGART, H. H.; HALVERSON, J. Convective cloud downdrafts as the cause of large blowdowns in the Amazon rainforest. **Meteorology and Atmospheric Physics**, [s. l.], v. 67, n. 1–4, p. 199–212, 1998.

GAUCHAZH. **Temporal em Porto Alegre pode ter sido causado por downburst; entenda o fenômeno.** Disponível em: <<https://gauchazh.clicrbs.com.br/porto-alegre/noticia/2018/02/temporal-em-porto-alegre-pode-ter-sido-causado-por-downburst-entenda-o-fenomeno-cjdgitcpb00lq01rv8h1rb91j.html>>. Acesso em: 2 jul. 2020.

INPE. **Temporais no Sul do Brasil.** Disponível em: <http://www.cptec.inpe.br/~rupload/arquivo/RS_11092008.pdf>. Acesso em: 2 jul. 2020.

JORNAL CRUZEIRO DO SUL. **Temporal causou estragos no bairro Canguera.** Disponível em: <https://www2.jornalcruzeiro.com.br/materia/705786/um-morre-e-dez-ficam-feridos-em-sao-roque>.

LIMA, D. R.; MENEZES, W. F. **Queda de estruturas de linha de transmissão de energia elétrica em cachoeira paulista (SP) e a ocorrência de tempestades severas –um estudo de caso.** 22 jul. 2000

LIMA, E G; LOREDO-SOUZA, Acir Mércio. **Analysis of Downburst Occurrence in Brazil.** [s. l.], p. 10, 2015.

LOREDO-SOUZA, Acir M.; LIMA, Elias G.; VALLIS, Matthew B.; ROCHA, Marcelo M.; WITTEWER, Adrián R.; OLIVEIRA, Mario G.K. **Downburst related damages in Brazilian buildings: Are they avoidable?** Journal of Wind Engineering and Industrial Aerodynamics, [s. l.], v. 185, p. 33–40, 2019.

MASSAMBANI, O.; CARVALHO, L. M. V. DE; VAZQUEZ, M. A. **Tornado ou microexplosão? um diagnóstico via radar do evento de Itu- São Paulo.** Congresso Brasileiro de Meteorologia. Anais...30 set. 1991Disponível em: <https://repositorio.usp.br/item/000838981>

MARCELINO, Isabela; NASCIMENTO, Ernani; FERREIRA, Nelson Jesus. Tornadoes in Santa Catarina State (southern Brazil): **Event documentation, meteorological analysis and vulnerability assessment.** [s. l.], 2005.

METSUL. **Temporais com incríveis frentes de rajada deixam 1 milhão sem luz Metsul Blog - Meteorologia.** Disponível em: <https://www.diariodecanoas.com.br/_conteudo/2015/10/noticias/regiao/229017-ja-caiu-granizo-no-centro-do-estado-metsul-alerta-para-temporal-na-regiao.html>.

NASCIMENTO, E. L. **Previsão de tempestades severas utilizando-se parâmetros convectivos e modelos de mesoescala: Uma estratégia operacional adotável no Brasil.** Revista Brasileira de Meteorologia, [s. l.], v. 20, n. 1, p. 121–140, 2005.

NELSON, Bruce W; KAPOs, Valerie; ADAMS, John B; OLIVEIRA, Wilson J; BRAUN, Oscar PG. Forest disturbance by large blowdowns in the Brazilian Amazon. *Ecology*, [s. l.], v. 75, n. 3, p. 853–858, 1994.

NGUYEN, Hieu Huy. **The influence of thunderstorm downbursts on wind turbine design**. [s. l.], 2012.

NSC TOTAL. **Tornado ou microexplosão pode ter atingido RS**. Disponível em: <<https://www.nsctotal.com.br/noticias/tornado-ou-microexplosao-pode-ter-atingido-rs>>. Acesso em: 2 jul. 2020.

O MUNICÍPIO. **Fenômeno que atingiu Presidente Getúlio foi uma microexplosão, diz Defesa Civil O Município**, 13 jun. 2018. Disponível em: <<https://omunicipio.com.br/fenomeno-que-atingiu-presidente-getulio-foi-uma-microexplosao-diz-defesa-civil/>>. Acesso em: 7 jul. 2020

PARAGUACITY.COM. **Fenômeno “microburst” causa grandes estragos em Cândido Mota - Paraguacity - Notícias de Paraguaçu Paulista SP e região hoje**. Disponível em: <<http://www.paraguacity.com/?b=18196>>. Acesso em: 2 jul. 2020.

POPA/COM.BR. **Tornado destrói hangar do Yacht Club de Santo Amaro**. Disponível em: <<https://acervo.popa.com.br/diversos/ydsa.htm>>. Acesso em: 2 jul. 2020.

PORTAL JIPA. **Microexplosão deixa um morto, feridos, desaparecidos e estragos em cinco municípios do oeste do Pa - Blog - Seu Guia Virtual**. Disponível em: <<https://www.portaljipa.com.br/noticias/politica-1/microexplosao-deixa-um-morto-feridos-desaparecidos-e-estragos-em-cinco-municipios-do-oeste-do-pa-16548>>. Acesso em: 30 jun. 2020.

RADIO CATARINENSE. **Meteorologia indica que microexplosão atingiu Joaçaba**. Disponível em: http://www.radiocatarinense.com.br/portal/noticias_detalhe.php?id=4675 1/1 Acesso em: 30 jun. 2020.

GLOBO TV TEM. **Após chuva e vendaval em Salto, escolas e creches ficam sem aulas**. Disponível em: <http://g1.globo.com/sao-paulo/sorocaba-jundiai/noticia/2015/09/apos-chuva-e-vendaval-em-salto-escolas-e-creches-ficam-sem-aulas.html>. Acesso em: 30 jun. 2020.

S2ID. **Séries Históricas :: Sistema Integrado de Informações sobre Desastres - S2ID**. [S. l.], 2020. Disponível em: <https://s2id-search.labtrans.ufsc.br/>. Acesso em: 6 jul. 2020.

SAOJOAQUIMONLINE.COM. **Supercélula assustadora se forma nos céus de Torres/RS em questão de minutos**. Disponível em: <<https://saojoaquimonline.com.br/destaque/2019/12/12/supercelula-assustadora-se-forma-nos-ceus-de-torres-rs-em-questao-de-minutos/>>. Acesso em: 2 jul. 2020.

SILVA DIAS, Maria A. F. **An Increase in the Number of Tornado Reports in Brazil**. *Weather, Climate, and Society*, [s. l.], v. 3, n. 3, p. 209–217, 2011.

TASZAREK, Mateusz; ALLEN, John T.; MARCHIO, Mattia; BROOKS, Harold E. Global climatology and trends in convective environments from ERA5 and rawinsonde data. *npj Climate and Atmospheric Science*, [s. l.], v. 4, n. 1, p. 1–11, 2021.

TERRA.COM. **Ventos de quase 140 km/h em Alta Floresta (MT)**. Disponível em: <<https://www.terra.com.br/noticias/climatempo/ventos-de-quase-140-kmh-em-alta-floresta-mt,57a9e8ad266035cb1270af8a7faf2019u6bpirl7.html>>. Acesso em: 2 jul. 2020.

TROPICAL ATLANTICO. **Radars - Tropical Atlantic**. [S. l.], 2020. Disponível em: <http://tropicalatlantic.com/radars/#americas>. Acesso em: 3 jul. 2020.

UOL. **“Microexplosão” capaz de derrubar avião causou queda de árvores em SP - 29/12/2014 - Cotidiano**. Disponível em: <http://www1.folha.uol.com.br/cotidiano/2014/12/1568571-queda-de-arvores-foi-causada-por-microexplosao-capaz-de-derrubar-aviao.shtml>. Acesso em: 2 jul. 2020.

VARGAS JR, V. R.; CAMPOS, C. R. J. Severe Events on Rio Grande do Sul from 2004 to 2008. **Anuário do Instituto de Geociências—UFRJ**, [s. l.], v. 38, n. 1, p. 137, 2015.

VEJA. **Tempestade matou meio bilhão de árvores na Amazônia**. Disponível em: <https://veja.abril.com.br/ciencia/tempestade-matou-meio-bilhao-de-arvores-na-amazonia/>. Acesso em: 30 jun. 2020.

WORLDPOP. **WorldPop**. [S. l.], 2021. Disponível em: <https://www.worldpop.org/about>. Acesso em: 12 mar. 2021.

APPENDIX B - MODELING TECHNIQUES OF THUNDERSTORM WIND OUTFLOW

In this work it was extensively discussed the differences between TS wind and EPS winds and how they impact the built environment. In this Appendix is developed an extensive discussion on modeling approaches utilized to simulate TS such winds for the further study of wind interactions with structures and use existing full-scale datasets or even other model's outputs to validate innovative efforts in this realm. From this inference, several efforts have been made to better understand thunderstorm winds in the different forms they can exist, such as tornadoes, gust fronts, RFD, downburst, and others.

These efforts are commonly defined as downbursts modeling, even though it is worth mentioning that there are other types of non-tornadic TS wind phenomena (MARKOWSKI AND RICHARDSON, 2010) in which models herein discussed may be apply for. Here is presented the advance in modeling techniques since they started to be deployed for the study of convective gusts initially for aviation industry applications and later extended/adapted to the wind engineering industry.

The rationally to discuss these models was initially proposed by Solari (2020) who named four main clusters of modeling approaches, which they are A.2) Wind Modeling Facilities (Laboratory tests); 2) Analytical Models; 3) Computational Fluid Dynamics (CFD) simulation modeling; 4) Data-driven models. From that point, in this work, these clusters are subdivided in methods and specific techniques to better describe different ways of modeling these phenomena. In Figure 121 is presented a summary of the models herein discussed.

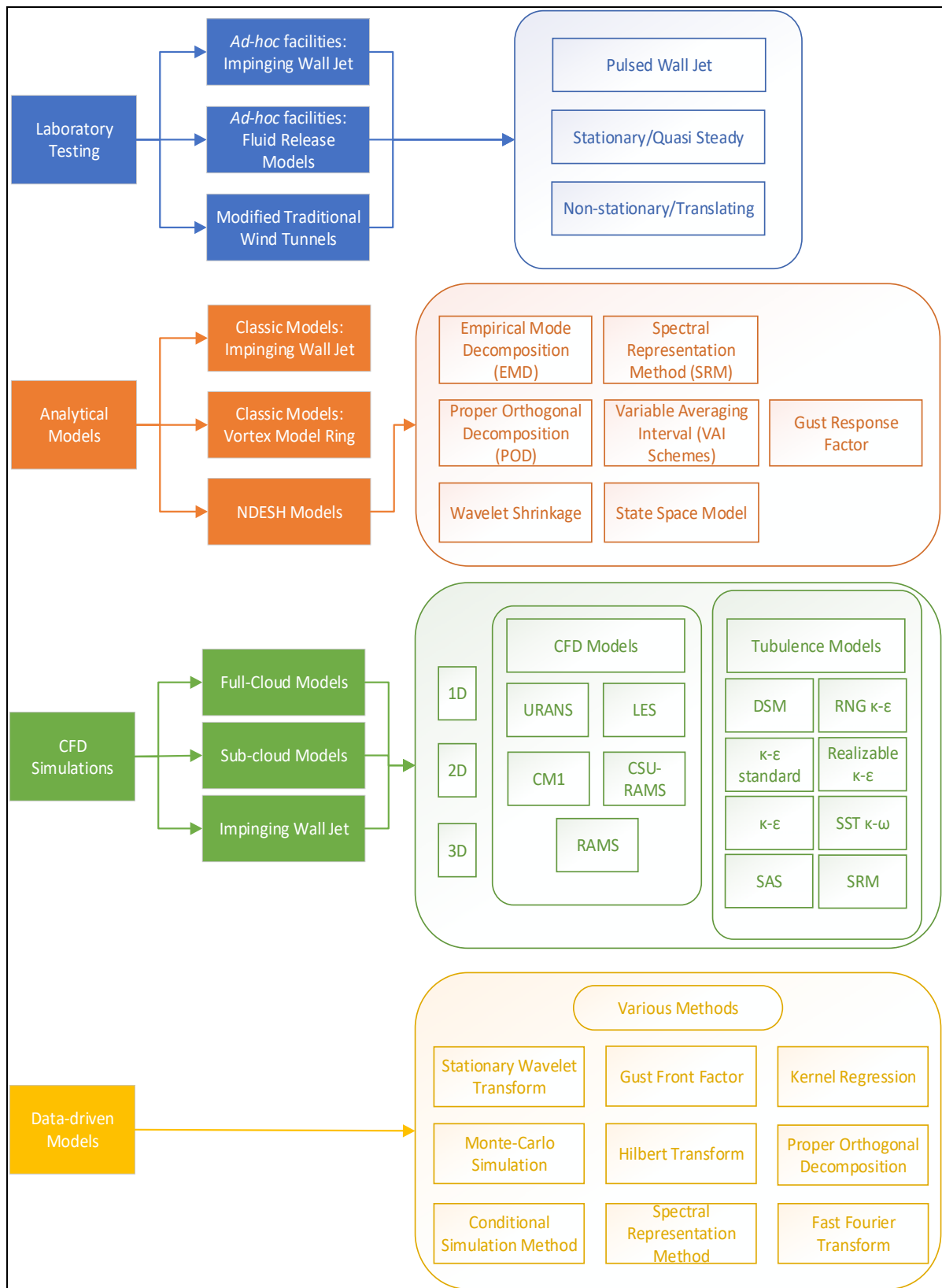


Figure 121. Summary of downburst modeling approaches clusters (first level), methods (second level), and specific techniques (third level). Source: Author.

A. LABORATORY TESTING AND THUNDERSTORM WINDS MODELING FACILITIES

Empirical models were the first attempt to simulate downburst flows. There are three methods of experimental facilities designed to simulate downburst-like winds. The first method and most common are the *ad hoc* facilities, which are equipped to release specific types of fluid over another fluid with different density, simulating on the bottom surface of the laboratory apparatus the downburst flow. The second method is the impinging wall jet *ad hoc* facilities, which are the most common applications. Last, the third method is the traditional wind tunnel facilities, which are equipped with especial devices capable of reproducing thunderstorm outflows.

A.1 Ad hoc Facilities: Fluid Release Experiments

These experiments consist of analyzing the density perturbation driven by the downdraft, in which a cylindrical parcel of fluid is released in a slightly less dense ambient fluid. When applied to the study of downbursts, the denser parcel falls onto a horizontal plate and spreads radially driven by buoyancy forces simulating the effects of the vortex ring.

Middleton (1966)¹ started analyzing the interaction between denser fluids being released over less dense solutions. Simpson (1969, 1972)^{2,3} *apud* Solari (2020) applied the concept to study the geometry of frontal regions and up-current ahead of thunderstorms outflows and showed empirically the application density currents theory to atmospheric studies.

Charba (1974)⁴ used full-scale measurements of gust fronts taken by a 444 m tall tower to study the properties of cold fronts and cold air masses. Given these analyzes, it was showed that the structural characteristics of squall lines are found to be closely represented by laboratory-produced gravity currents, agreeing with empirical and dynamical theory of gravity currents. In Figure 122 a) is presented a gravity current (or density current) simulated by Simpson (1969) along with the classification of the main regions of the flow (turbulent mixing, head, and nose), and in b) is presented a schematic representation by Charba (1974) of a density current scaled to the dimensions of the gust front event

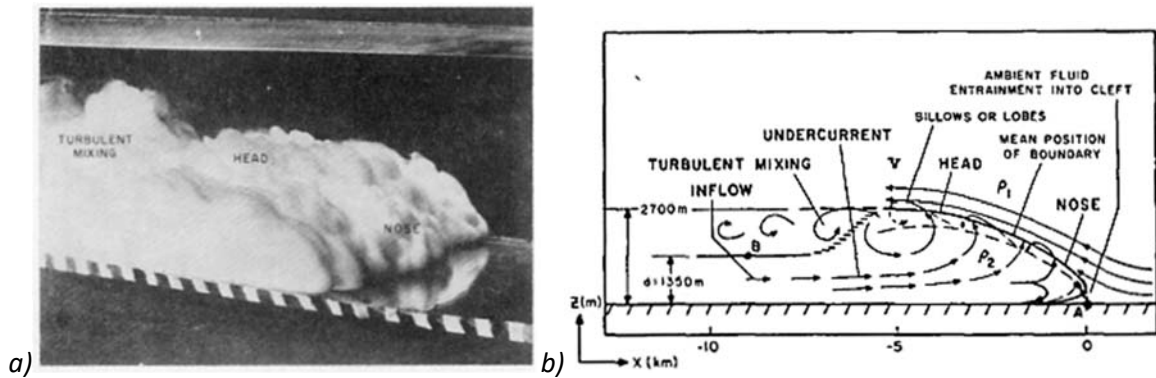


Figure 122. Depicts a) gravity current (or density current) simulated in a laboratory experiment utilizing the fluid release approach and in b) the structure of a gust front event. Source: a) Simpson (1969) and b) Charba (1974).

Landreth and Adrian (1990)⁵ used a PIV to capture the field resultant of a circular water jet onto a flat surface. By capturing high-resolution velocity components, it was allowed the development of flow structures as small as 1 to 2 mm in size and mean vorticity, also mean rate-of-strain maps that showed the process of boundary layer information. Results have shown that the primary vortex weakens as it propagates downstream before spawning the secondary vortex at or near 1.8 diameters from the jet centerline. These studies continue using liquid state fluids, which were discussed in item 6.1.1. A schematic representation of the apparatus deployed by Landreth and Adrian (1990) is presented in Figure 123. The PVI system is shown at the lower part of the boundaries, while the water pumping system is shown at the top, releasing the fluid onto the flat plate.

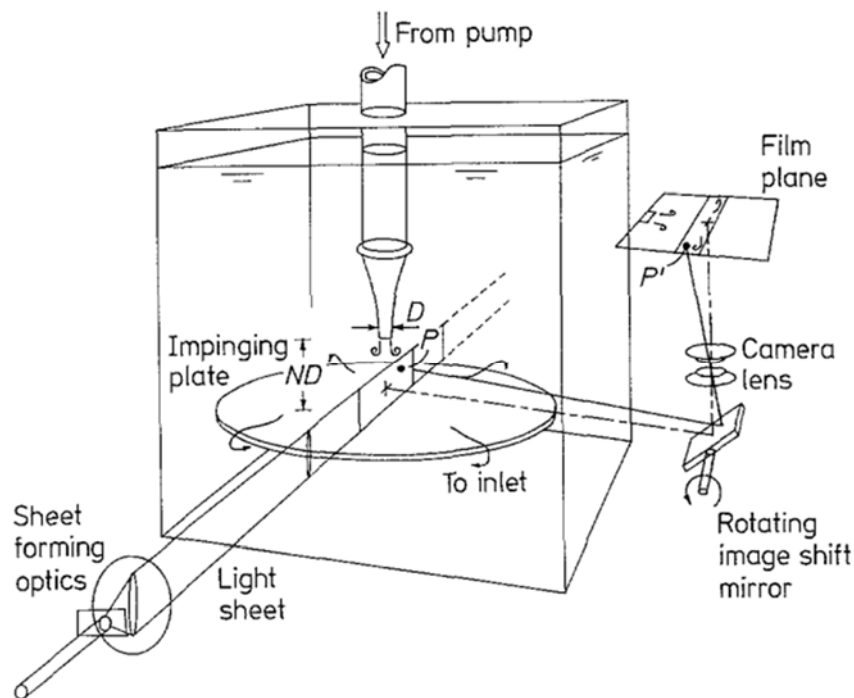


Figure 123. Recording stage of PIV system deployed for circular water jet flow impinging on a flat plate. Source: Landreth and Adrian (1990).

Lundgren *et al.* (1992)⁶ applied the concept of fluid release to the study of downbursts dropping a parcel of saltwater solution (simulating cold and heavy air) over fresh water in a flat plate (simulating the ground). In this experiment, it was found that vorticity develops on the sides of the downward parcel released onto a horizontal plate, causing to roll up into a turbulent vortex ring, which impinges on the ground and exhibits many of the features of a typical downburst.

Yao and Lundgren (1996)⁷ continued investigations with saltwater, looking to better understand the interactions of the vortex within the ground. In this experiment it was proposed a simple relationship where the maximum velocity beneath the microburst is four times the velocity of advance of the microburst front. The authors identified the presence of a secondary vortex generated at the leading edge of the vortex, close to the surface. This counter rotating vortex results from the friction between the shear layer of wind and steady ground surface.

Alahyari and Longmire (1994)⁸ improved the capturing capability of the flow field to a higher resolution by utilizing a Particle Image Velocimeter (PVI). This new method was less intrusive as well when comparing to hot-wire anemometers and allowed the variation in the index of refraction within the flow by matching the refractive indices of the lighter and the heavier

fluids, while maintaining minimum density differences of 4%. The method was optimized by deploying an aqueous solution of glycerol and potassium phosphate, which was used to achieve precise index matching in the presence of mixed and unmixed constituents of a laboratory simulated downburst.

In Figure 124 is depicted the modeling facility used to develop Alahyari and Longmire's experiment. Here the jet is placed at the top of the squared boundary filled with a different density fluid at the bottom. The scaled data from this experiment showed that the wind velocities can reach up to 70 m/s beneath the primary vortex-ring and be short-lived within a small spatial range, showing how difficult it can be to capture the downbursts peak of velocities in full-scale investigations.

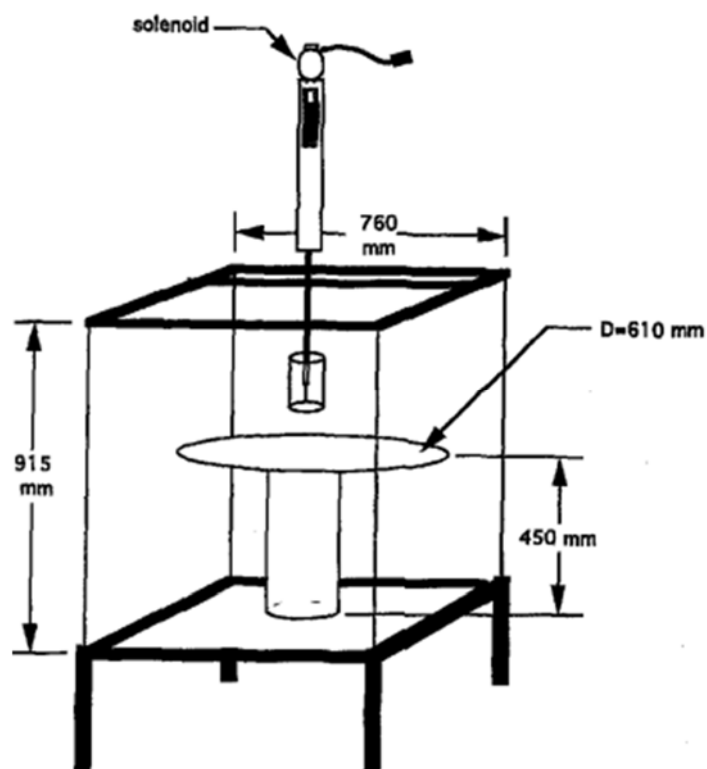


Figure 124. Representation of the fluid release structure used in Alahyari and Longmire (1994).
Source: Alahyari and Longmire (1994).

A.2 Ad hoc Facilities: Impinging Wall Jet Experiments

Impinging wall jet experiments are relatively simple and can provide reasonable resolution on the surface (ZHANG *et al.* 2013a). These experiments use laboratory testing techniques to

simulate downbursts. It reproduces the phenomena by projecting a jet onto a flat surface in order to create an impinging wall radial flow and vortex ring with a nose-like shape of the vertical wind profile. This method received a lot of attention for structures applications due to the capacity of better simulating winds loads at the vortex within the surface when compared to other experimental methods (HOLMES AND OLIVER 2000; SAVORY *et al.* 2001).

Bakke (1957)⁹ developed experimental simulations of a low-speed jet air spreading out radially over a flat smooth plate, defining the first attempts to reproduce in laboratory what would later be associated to downbursts outflows. Among other contributions, Bakke (1957) proposed the rate of change of velocity and width of the jet can be expressed by simple power-law. Investigations of turbulent characteristics of wall jet experiment are found in Chun and Schwarz (1967)¹⁰ and Poreh *et al.* (1967)¹¹. Donaldson and Snedeker (1971)¹² established the mean properties of the flow issuing from a circular convergent nozzle, for different conditions, such as various angles, distances, and surfaces shapes. Launder and Rodi (1983)¹³ and Cooper *et al.* (1992)¹⁴ found good degree of internal consistency for the mean and turbulent impinging flow and proposed two-dimensional (2D) and three-dimensional (3D) numerical solutions starting from the Navier-Stokes equations to describe such event.

Didden and Ho (1985)¹⁵ extensively documented the velocity and pressure fields of the impinging wall jet experiment, looking to better understand the unsteady wall-jet boundary layer separation evolution into a primary and secondary vortex in such experiment similar to what is commonly observed in downbursts. It was found that the unsteady wall pressure gradient produced by the perturbations in the inviscid region retards the flow in the viscous region, forming a local shear layer at the viscous-inviscid interface. The vorticity in the shear layer results in a primary vortex that protrudes into the inviscid region moving downstream in the radial mean flow direction. Therefore, the unsteady separation originated from a local shear layer, which was started by the unsteady adverse pressure gradient produced by the primary vortex.

Much of the impinging wall jet simulations developed experimentally in the 60, 70s, and 80s mostly intended to be apply to the advancement of the wall jet theory, other studies that were developed to the downburst research were mostly designed to understand the effects of such phenomena to aircraft. In the 90s, literature on the scale of interest for wind engineering

started being developed with Holmes (1992)¹⁶ in which the wall jet facility for physical modeling of thunderstorm downbursts. A new generic empirical equation that describes the development of the velocity profile over a flat board was proposed. Analysis of different radii, distance to wall and embankment (height and slope) were developed.

Wood *et al.* (2001)¹⁷ and Wood and Kwok (1998)¹⁸ used the wind tunnel schematically presented in Figure 125 to simulate a steady downburst model. In this experiment the focus was to understand the development of the wind profile by obtaining such values at various points of the terrain, for various terrain conditions, aiming to identify how topographic conditions influence the downburst flow (LETCHFORD *et al.*, 2002). The topographic speed-up factor for the embankment configuration showed that the Australian Wind Code loading was a conservative for most of the tested points, except for height near ground level above the embankment crest.

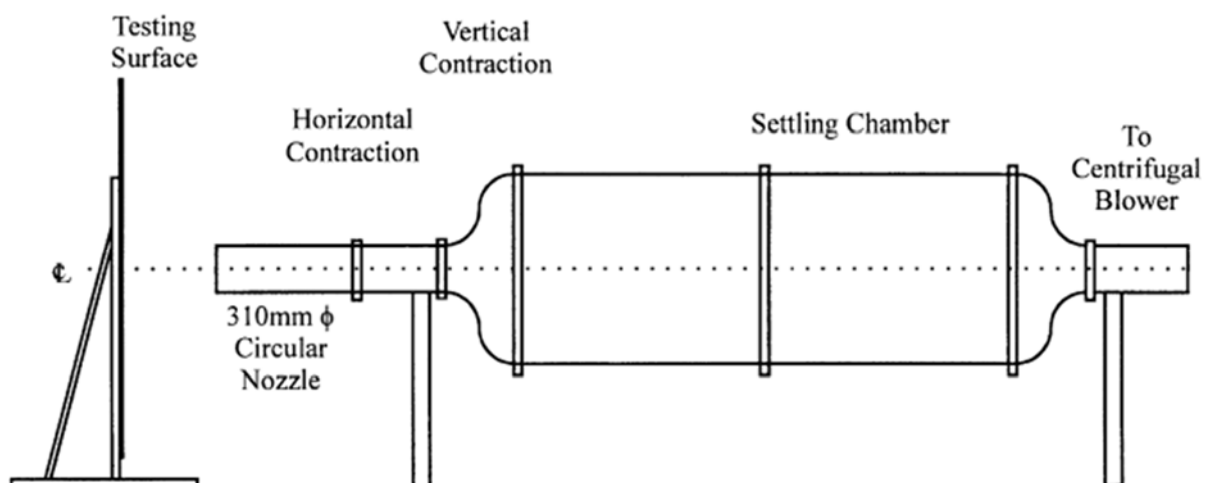


Figure 125. Schematic layout of the deployed thunderstorms wind tunnel in Wood *et al.* (2001) and Wood and Kwok (1998). Source: Wood *et al.* (2001).

CFD modeling and full-scale measurements were used by Wood *et al.* (2001) to validate the results obtained experimentally. It was found that increasing the surface roughness changes the turbulence profile, causing a more rapid decay in the flow velocity, and increasing the height of the peak velocity of the wall jet. It was also found that above two diameters (D) of the jet, the shape velocity profiles were insensitive to the magnitude of the inlet velocity and therefore the height of maximum wind (H) speed would not change, as shown in Figure 126.

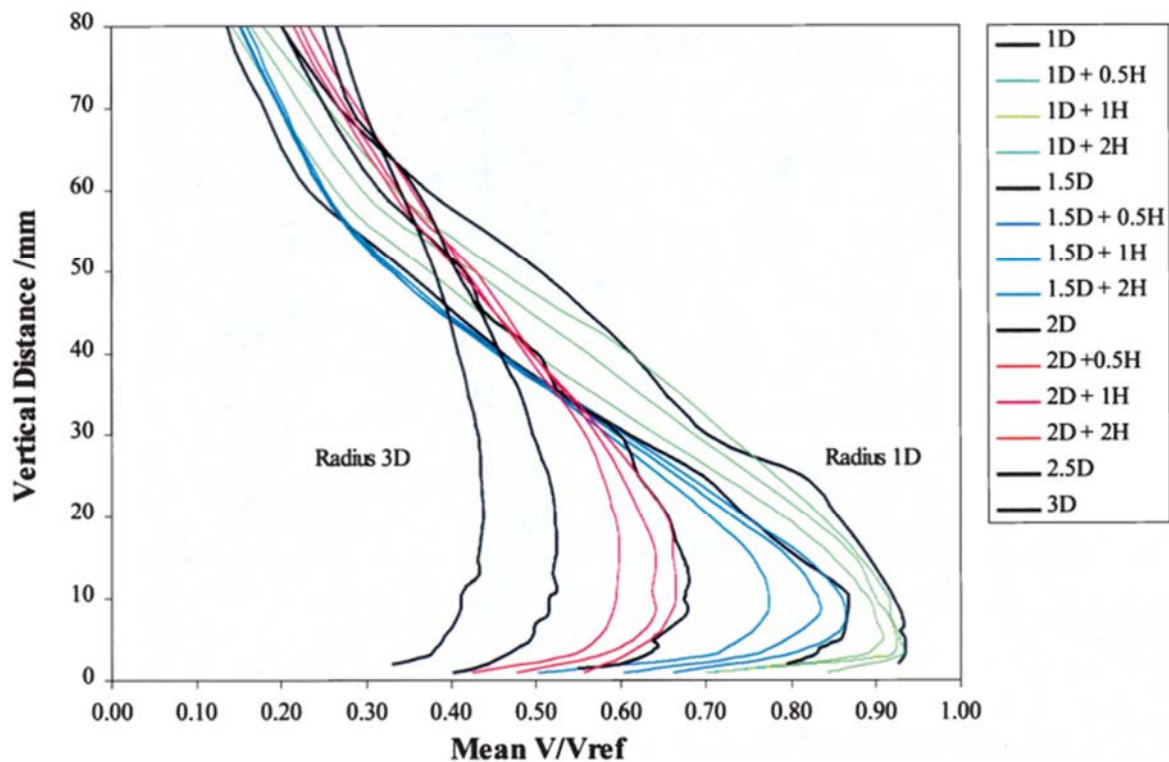


Figure 126. Radial development of the mean velocity profile for wall jet experiment. Source: Wood *et al.* (2001).

Wood *et al.* (2001) found that the simulated downburst profiles tend to stabilize at 1.5D, therefore the maximum mean velocity (V_{\max}) is defined Equation 30, based on the normalized data:

$$\frac{V}{V_{\max}} = 1.55 \left(\frac{z}{\delta}\right)^{1/6} \left[1 - \operatorname{erf}\left(0.70 \frac{z}{\delta}\right)\right] \quad \text{Equation 30}$$

Where V is the velocity at height z , velocity is equal to half its maximum value δ , and erf is the error function. Further finds on this research are discussed in Letchford *et al.* (2002)¹⁹.

Chay and Letchford (2002)²⁰ and Letchford and Chay (2002)²¹ investigated the simulated flow structure and proposed of a stationary downburst proposed a transient downburst model. They investigated the mean pressure generated over a cube immersed in the flow and found that the transient experiment presented more similarities to full-scale measurements of downbursts.

The moving wall jet in Letchford and Chay (2002) experiment is shown in Figure 127. The moving structure aimed to replicate the typical transient characteristics of recorded downburst winds to overcome the lack of dynamic similarity between full scale observations

and quasi-steady downburst simulations. It used translation speeds of approximately 20% of the downdraft speed, the simulated winds resulted from the summation of the downburst and gust front winds. The dynamic pressure location and static pressure varies significantly compared to the quasi-steady experiment.

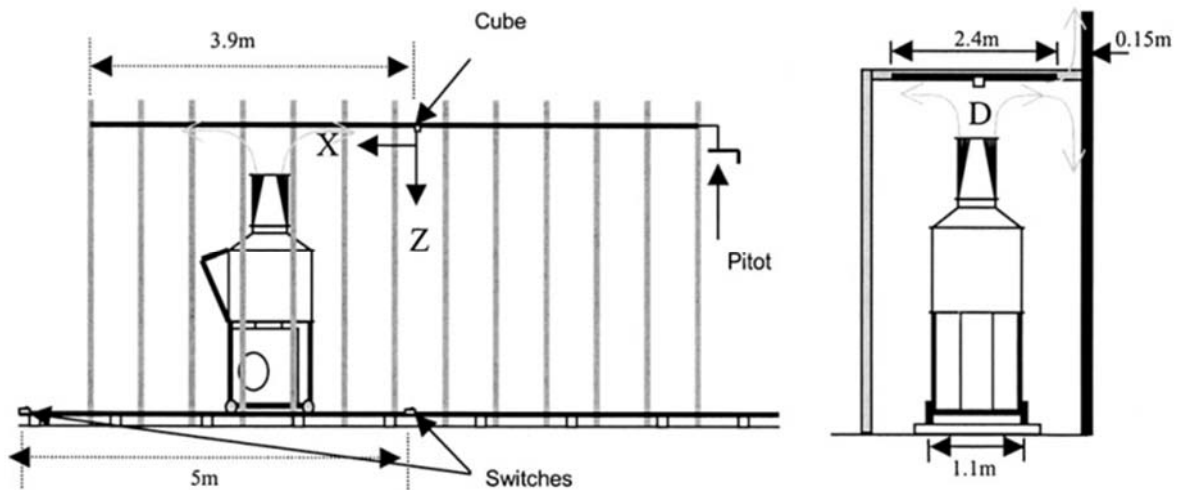


Figure 127. *The moving jet wind tunnel. Source: Letchford and Chay (2002).*

Sarkar and Haan (2002)²² developed a wind simulator at the Iowa State University capable of replicating straight-line thunderstorm winds and tornado-like winds all-in-one single apparatus. The flow structure was compared to experimental profiles, presenting close agreement. Figure 128 is presented both a) the jet simulator and in b) the jet with smoke added to allow visualization of the flow.

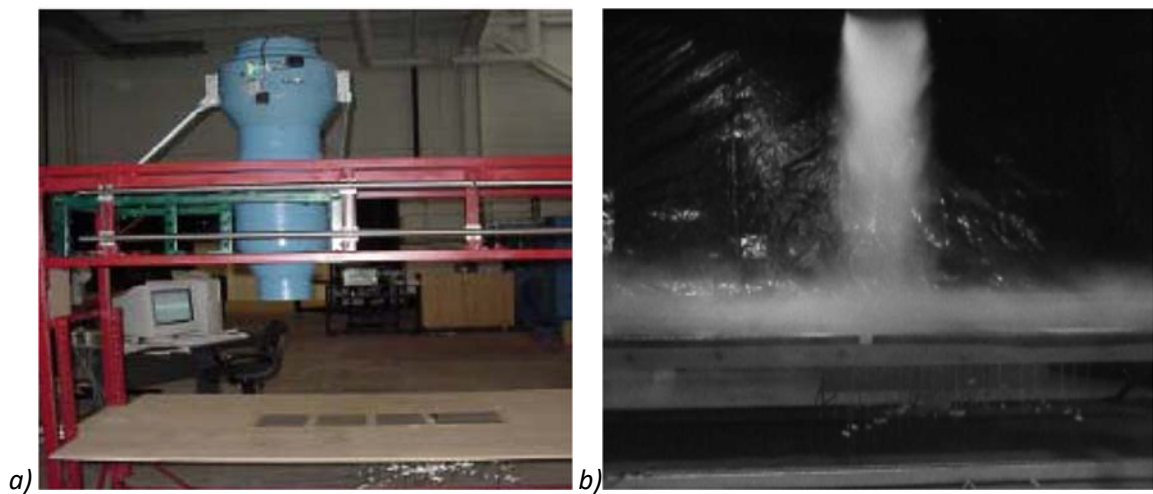


Figure 128. *Sarkar and Haan (2002) downburst wind simulator in a) the jet simulator and in b) the jet with added smoke to allow visualization of the flow. Source: Sarkar and Haan (2002).*

Mason *et al.* (2005)²³ proposed a stationary-pulsed wall jet apparatus capable of simulating a downburst outflow and analyzed the influence of the jet angle to understand non-axisymmetric outflows. A detailed investigation of the flow and corresponding generated vortexes was presented. The flow velocity and the acceleration fluctuating peaks presented great similarity to the full-scale measurement of the TS wind event captured in Gast (2003). The comparison of Gast's records at 10 m of the event in Lubbock, Texas, on June 4th, 2002; and the experimental replication of Mason *et al.* (2005) experiment results is shown in Figure 129. To maintain reciprocity of flows, focus was given to replicate the turbulence from 15 to 30 m/s and the rise and fall of the record. Furthermore, the scaling ratios adopted on a maximum full-scale velocity of 38.75 m/s are length of 1/3000, velocity 1/1.7, and time 1/1750. Figure 129 shows great adherence to the full-scale measurement and replication of the transient flow time history, with exception on initial time between initial acceleration and velocity increase. Such results proved that the proposed technique can successfully create a primary vortex at the leading edge of the impinging and divergent flow, being able to reproduce the distinctive positive and negative pressure transition as it would be expected with passing a horizontal vortex.

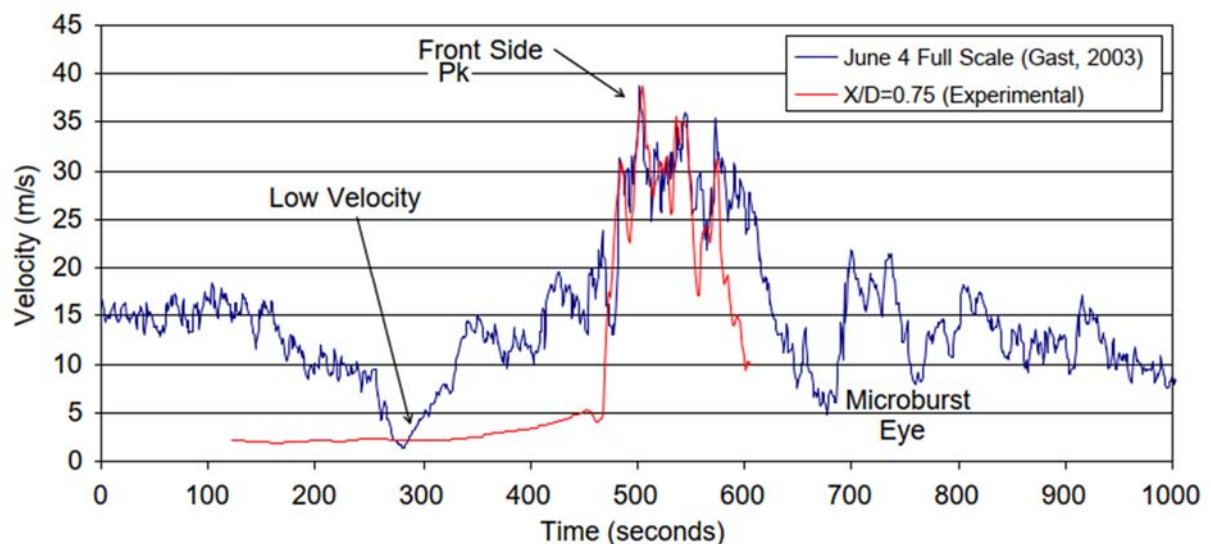


Figure 129. Graph comparing Gast's full-scale microburst wind record measurement at 10 m above ground (blue line) and Sarkar and Hann's record considering and experimentally jet at $X/D = 0.75$ and $Z/D = 0.01$ (representing approximately 15 m in full scale). Source: Mason *et al.* (2005).

The centrifugal blower jet used in Mason *et al.* (2005) was the same as the one deployed in Letchford and Chay (2002) experiment, although it was added an entertainment-reducing outlet composed of 16 sheet metal blades, capable to producing the pulsing characteristic of

the downburst flow, see Figure 130. The jet experiment replaced the buoyantly driven natural downburst force by the inverted forced fan, following the same scheme presented in Figure 127, but without the translating feature.

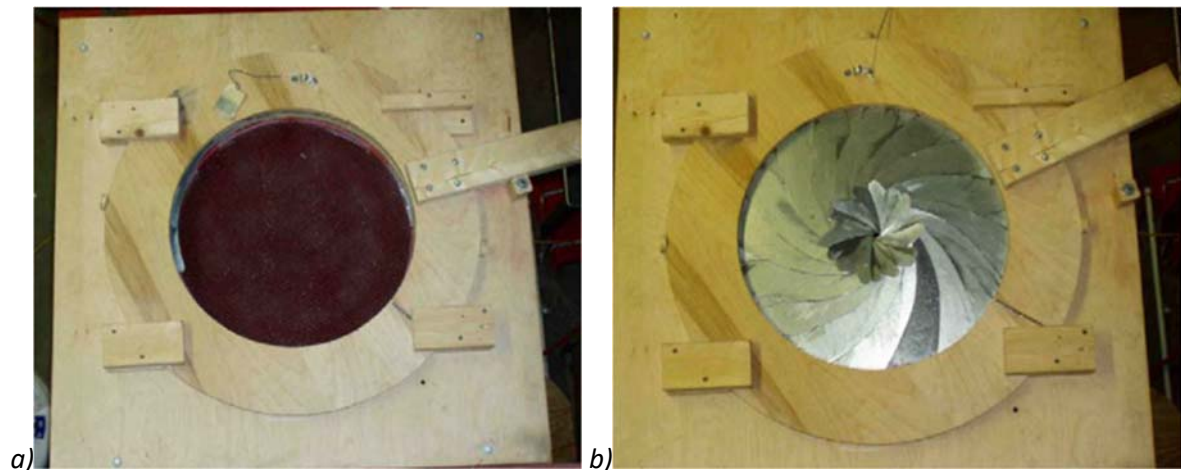


Figure 130. Pulsing aperture in a) open position and in b) close position. Source: Mason et al. (2005).

Choi (2004)²⁴ captured velocity profiles from over 50 thunderstorms using a 150 m tall tower and developed an experimental impinging wall jet model to simulate such winds. Choi used these measurements to test their own impinging wall jet experiment helping to show that the measured velocity reflects the vector sum of the thunderstorm outflow plus the boundary layer profile wind of the originating weather system. It was confirmed again that the peak profile velocities are found at lower elevations compared to the ABL profile and velocities decrease as they go further away the observations of the center of the jet.

Xu and Hangan (2008)²⁵ investigated the axial orthonormal impinging jet flow to different scales using as reference RE to compare to full-scale observations. In this experiment it analyzed different inflow and Boundaries conditions, such as jet to surface distance, surface roughness, and radial and axial confinements. Measurements were obtained using hot-wire anemometers and pressure if taken with the installation of pressure taps. In Figure 131 is presented a schematically representation of a the impinging wall jet experiment developed by Xu and Hangan (2008), Where D is the diameter of the jet pipe; H is the axial distance (height) between jet and impinging surface.

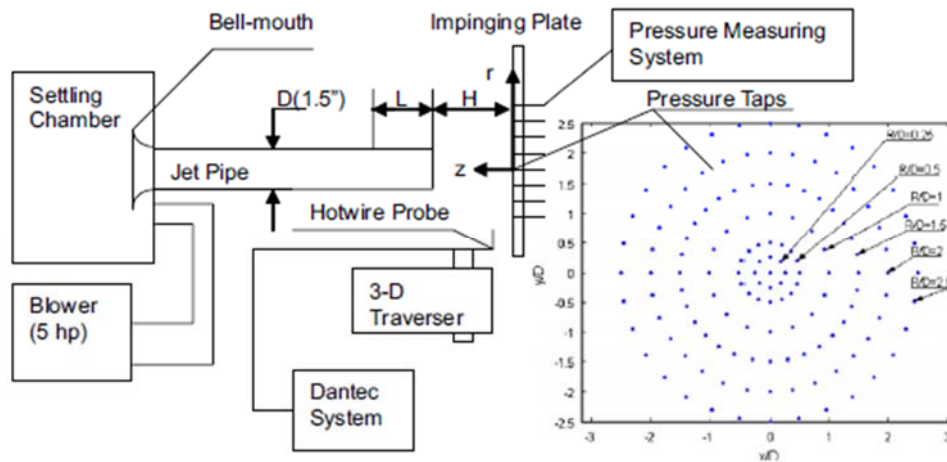


Figure 131. Schematic arrangement of an impinging wall jet experimental setup. Source: Xu and Hangan (2008).

Xu and Hangan (2008) experimentally investigated distinct aspects of an axial orthonormal impinging jet flow taking in consideration the Scale (Reynolds Number), Boundary Conditions (Jet-to-surface distance, surface roughness, and radial and axial confinements), and Inflow conditions. It was shown that with the distance nozzle-to-plate lower than $1D$ tends to induce stronger pressure-strain mechanism that results in increased maximum radial velocities and normal stress. Also, the radial confinement of the jet being lower than $10D$ is found to affect the surface pressure distribution. Finally, it was showed that for RE of one order above the critical value makes the flow to be dependent only on the surface roughness, showing that in such conditions it is possible to extend laboratory testing to full-scale applications.

McConville *et al.* (2009)²⁶ discussed the feasibility of using larger scale simulator to generate downburst winds. The results were coherent with previous investigations and empirical relationships, including the mean velocity profile, being a function of the distance between the impingement zone and the nozzle height represented (X/D). Figure 132 shows sketches along with dimension of the three arrangements of the nozzles located at a) $1.0D$, in b) $1.5D$, and c) $2.0D$.

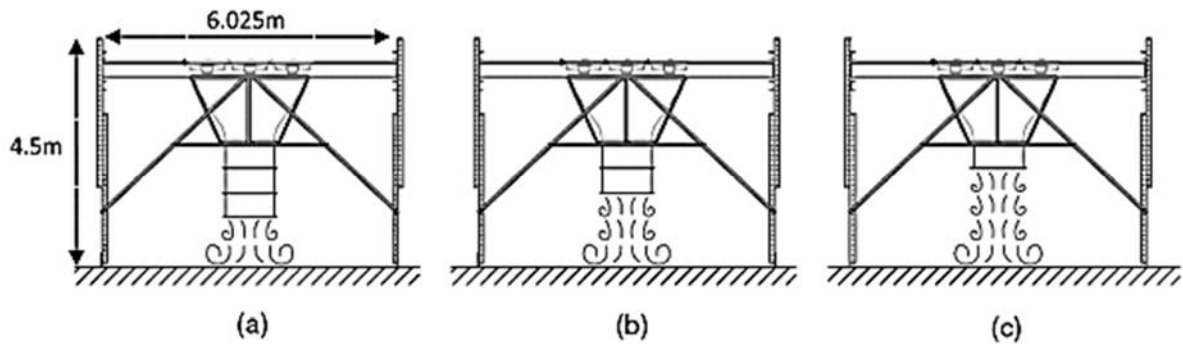


Figure 132. Nozzle height arrangements utilized in McConville *et al.* (2009) experiment. In a) the nozzle is located a $1.0D$, in b) $1.5D$, and in c) $2.0D$. Source: McConville *et al.* (2009).

In this experiment, it was used three different methods to recreate the transient motion of the gust front and it was analyzed how they affect the magnitude of the primary radial vortex of the downburst. These methods were: a) acceleration of the flow by controlling the rotational speed of the fans; b) acceleration through a plane mechanism perpendicular to axis of the jet; c) acceleration for a mechanism that opens in the jet's direction. Tests showed the latter method develops a flow with more transient characteristics.

Zhang *et al.* (2013b)²⁷ developed an impinging wall jet experiment focused on achieving dynamic similarity of loads because of downburst induced flow when acting on low-rise gable-roof buildings, results were then compared to conventional ABL winds. Measurements using PIV technology showed that the vertical flow rapidly turns parallel to the ground at the impinging point, presenting the highest speed flow. A schematic picture of the simulator used in this experiment is shown in Figure 133.

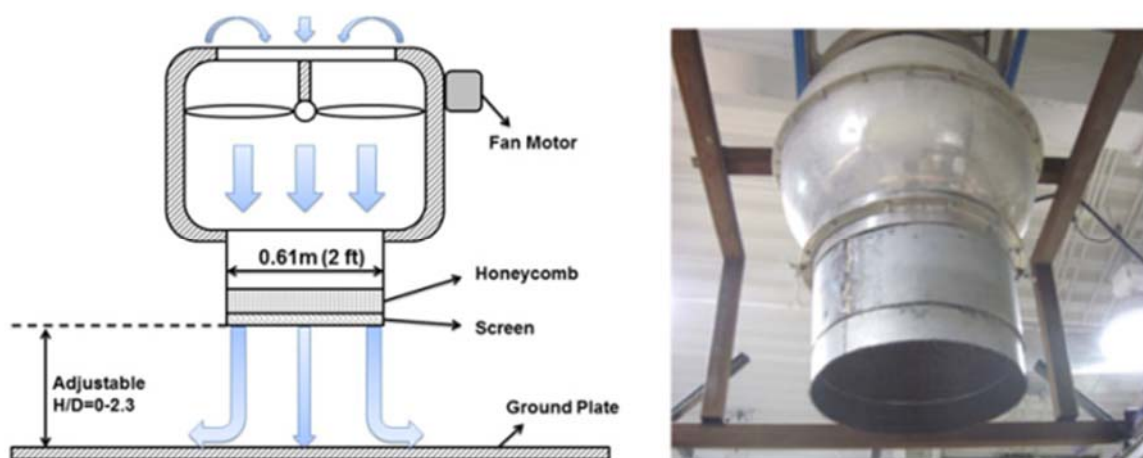


Figure 133. A schematic picture of the impinging wall jet simulator used Zhang *et al.* (2013b). Source: Zhang *et al.* (2013b).

Zhang *et al.* (2013b)²⁷ found that the high turbulence levels of the simulated flow induced significant dynamic excitations to the building models analyzed. There was a significant change in the resultant aerodynamic forces depending on the location of the roof comparatively to the flow; for instance, the resultant force was downward if the roof was at the core region of the downdraft ($X/D < 1$); the resultant force was horizontal if the roof was located at $X/D = 1$, and finally the resultant was upwards if the roof was located further away. Comparatively to ASCE 7-05, gable-roof building model could experience almost the double in surface pressures under downburst-like wind at the leading edge of the flow (at $X/D \approx 0.50$), although further away from the downburst core, these loads tend to agree considerably with the standard practice.

Zhang *et al.* (2013c)²⁷ compared the results obtained in the impinging wall jet experiment to a sub-cloud to a cooling source model (ANDERSON *et al.*, 1992). The author highlights that both experiments presented similar trajectories and development of the primary vortex in radial direction in time, but the rolling up primary vortex generated in the cooling source model was more alike the full-scale measurements. The results presented in Figure 134 obtained by Zhang *et al.* (2013a) showed good agreement at lower levels at different X/D comparing to the cooling source model. The same was observed with previous experiments and full-scale measurements.

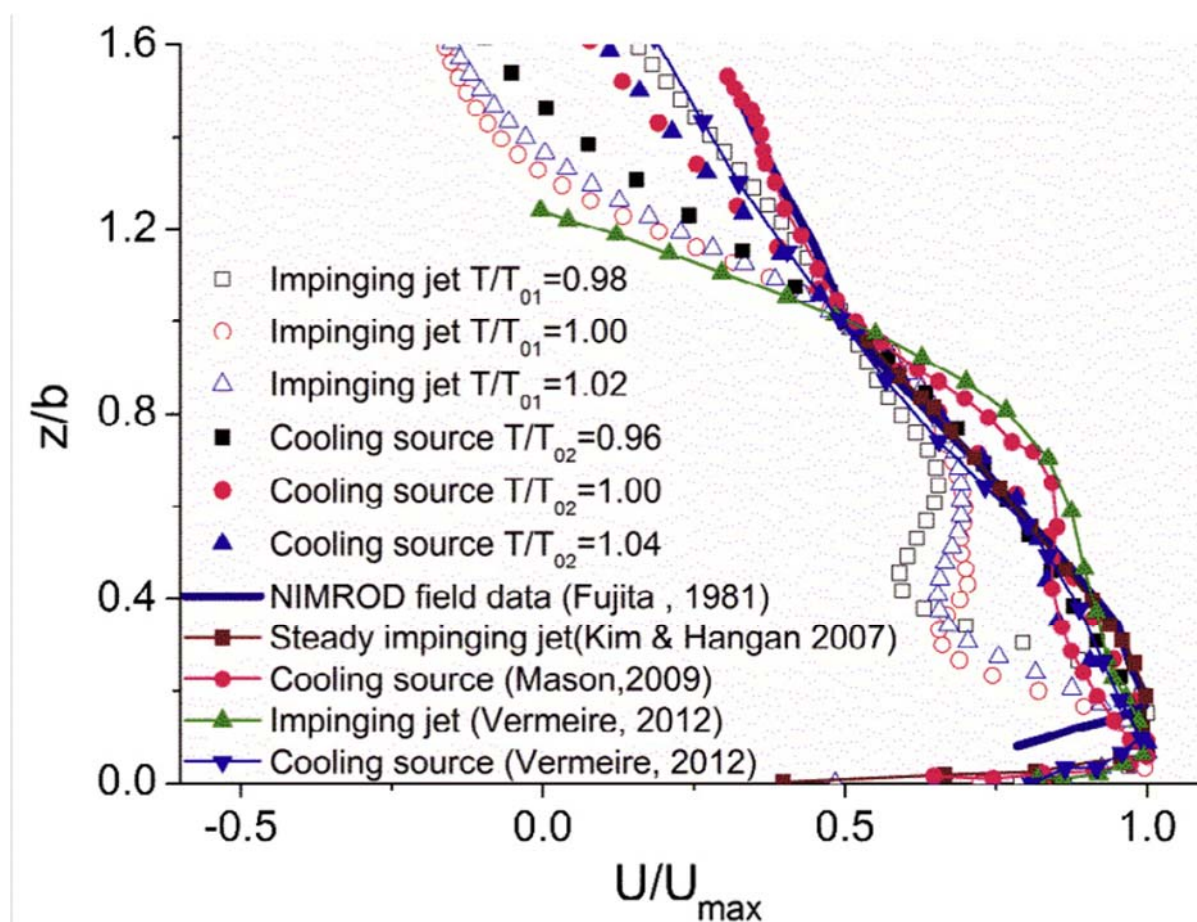


Figure 134. Results obtained by Zhang *et al.* (2013a) showing good agreement at lower levels to different X/D comparing to the cooling source model, other previous experiments, and full-scale measurement. Source: Zhang *et al.* (2013a).

Zhang *et al.* (2014)¹¹⁶ analyzed the velocity and turbulence profiles obtained in the previously mentioned experiment to the effects on the aerodynamics of low rising building models as depicted in Figure 135. The higher complexity of downburst-like winds when compared to ABL winds, suggests that if a downburst occurs nearby a low rising building, it causes higher external pressure and larger downward force in the building models analyzed. Pressure distributions suggested that flat, low-angle, and conical roof surfaces resulted in larger suction areas and larger pressure fluctuations on the roof because of the flow separation and reattachment. Finally, the analysis of the model scales led the researchers to the conclusion that low-rise structures with a more realistic scale of 1:100 to 1:150 a larger simulator, 5 to 7 times larger than the one deployed in such experiment, with models less than 0.2% blockage ratio need shall be deployed.

The investigation also included the estimation of aerodynamic coefficient for the structures shown in the figure below, the study suggested that the wind loads change in radial location,

orientation and geometric shape of the structures. Consequently, the nearer the center of the microburst, the higher pressures occur in all structures, leading to intense downward forces on the roof. Although, the distribution of pressure in the outburst region was found to be similar to those in the ABL wind, but these loads will vary depending on the intensity of the downburst. In terms of roof shapes, gable roof and conic-shaped roof experience lower drag uplift in the outburst region when compared to flat, low-angle roof and high-angle gable roof. The geometric parameters of the roof did not seem to influence significantly the wind load. Finally, model geometric scales seem to have minor influence on the structural wind load.

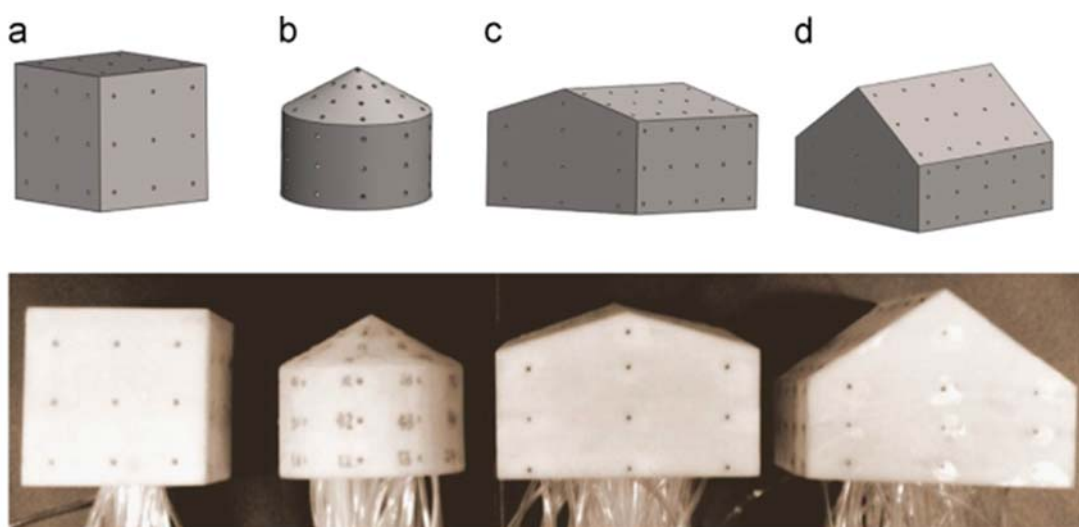


Figure 135. Modeled buildings geometry of a) Cube, b) grain bin, c) gable-roofed building (16° degrees roof slope) and d) gable-roofed building (35° roof slope). Gable roofs and conic-shaped roof experience lower drag uplift in the outburst region. The geometric parameters of the roof did not seem to influence significantly the wind load. Source: Zhang *et al.* (2014).

Richter *et al.* (2018)²⁸ proposed a wind tunnel to simulate downburst-like winds with both pulsed and continuing wall jet experiments plus additional background flow wind. The authors focused on understanding the effects on a street canyon, finding that such configuration can increase the maximum horizontal wind velocity on an average 50% when compared to tests in open flat terrain. Comparatively to the same scenario, it was also observed an increase in height of maximum velocity and longer propagation of high intense winds up to 3 times longer.

The interest in understanding extreme winds leads to the development of the more advanced *ad-hoc* facilities, such as the Wall of Wind at Florida International University in Miami, United States; and the Wind Engineering Energy and Environment (WindEEE) constructed at the Western University, London, Canada. The former is mostly focused on hurricane winds and

can generate even real scale simulation; where the latter can simulate a wide variety of wind systems and climates, including downbursts and tornadoes at larger scales than previous wind tunnels (HANGAN *et al.*, 2017).

In Figure 136 is shown a photograph taken from inside of the WindEEE wind tunnel. The chamber's dome is composed of 106 fans, and it can generate inflow or outflow through 4.5 m from the bottom to the jet at the top. The back of the chamber is made of 60 fans chamber a wall, 14 m wide x 4 m high, which can simulate the back flow of ABS components in a downburst event. These fans can be operated independently to generate the flows as desired. Figure 137 presents the annular vortex sample of particles streaks captured during a downburst simulation using the new measurement technique called Large Scale Streak Velocimeter (LSPSV)

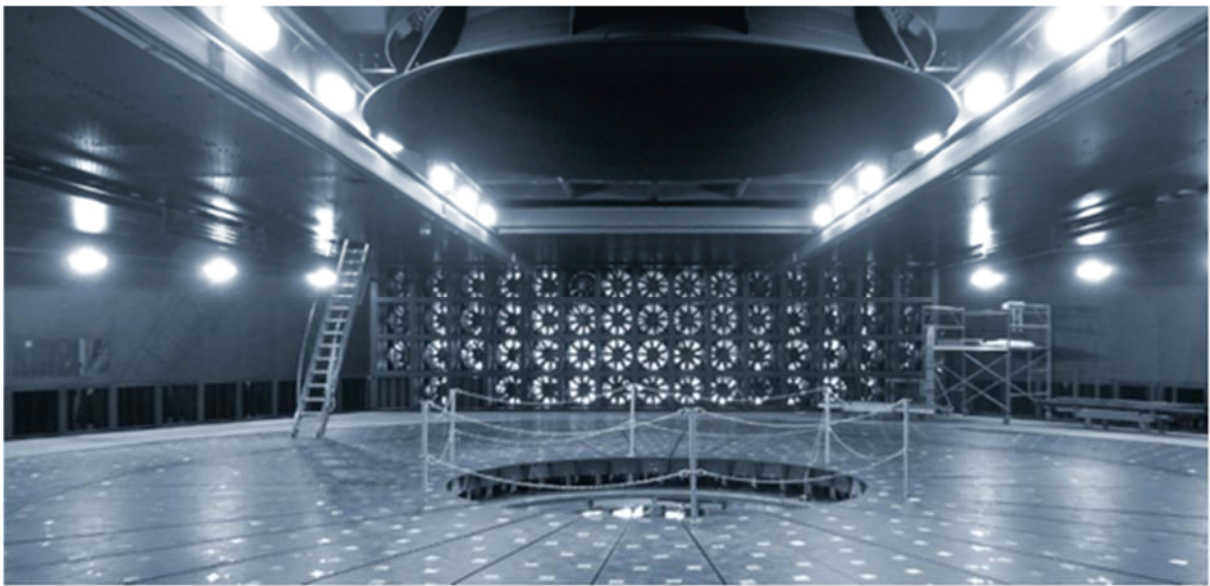


Figure 136. Photograph taken internally of the WindEEE wind tunnel. Source: Hangan *et al.* (2017).

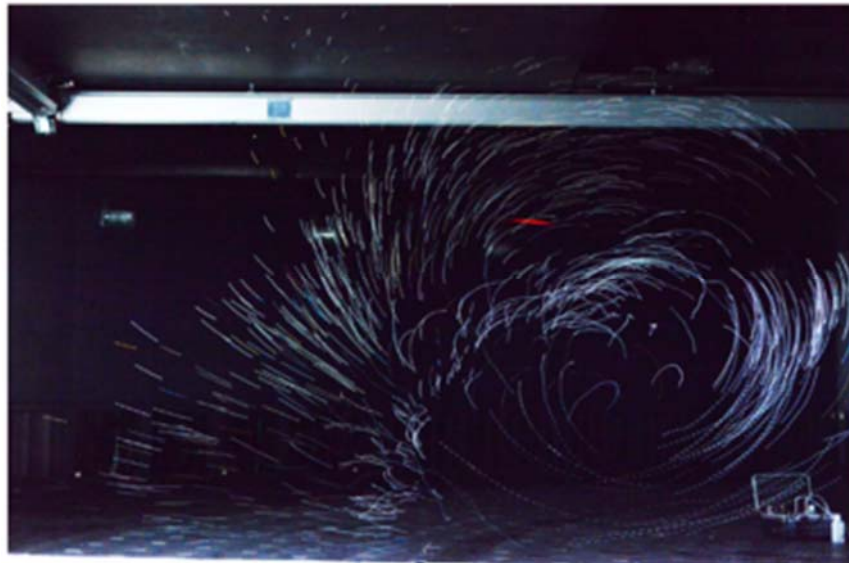


Figure 137. Downburst flow visualization in WindEEE. Source: Hangan *et al.* (2017).

Several TS wind studies have been developed discussing applications of the WindEEE to so simulate downbursts, they include Damatty *et al.* (2016)²⁹, Hangan *et al.* (2017)³⁰, and Chowdhury³¹ (2018). The profiles generated by this wind tunnel were compared with great similarity against CFD simulations and full-scale measurements.

Junayed *et al.* (2019)³² and Chowdhury (2018) compared simulations from the WindEEE Dome to the Wind and Port and Wind, Ports, and Sea Projects (SOLARI *et al.*, 2015a), showing good agreement specially for the turbulent components of the flow, where the power spectral density of the reduced turbulent fluctuations of the experiment conformed to the -5/3 law - similarly to synoptic ABL winds. In Figure 138 are presented the results from the WindEEE experiment comparing to a) the maximum wind speed and b) vortex trajectory against results obtained in Hjelmfelt (1989), Fujita (1978), and Wakimoto (1982).

Romanic *et al.* (2019)³³ analyzed the superposition of straight-line flow (SF) (representing ABL Winds) and the jet outflow (JF) (representing downburst winds) in the WindEEE. It was found that when the JF is stronger than the SF no major influence in the structure of the impinging jet is observed, but changes to the profile become noticeable when the SF overpowers the JF by increasing the shearing in the long direction. This finding leads to the conclusion that by increasing the strength of the JF leads the SF to gradually decrease. Although the differences are not uniformly distributed throughout the impinging jet.

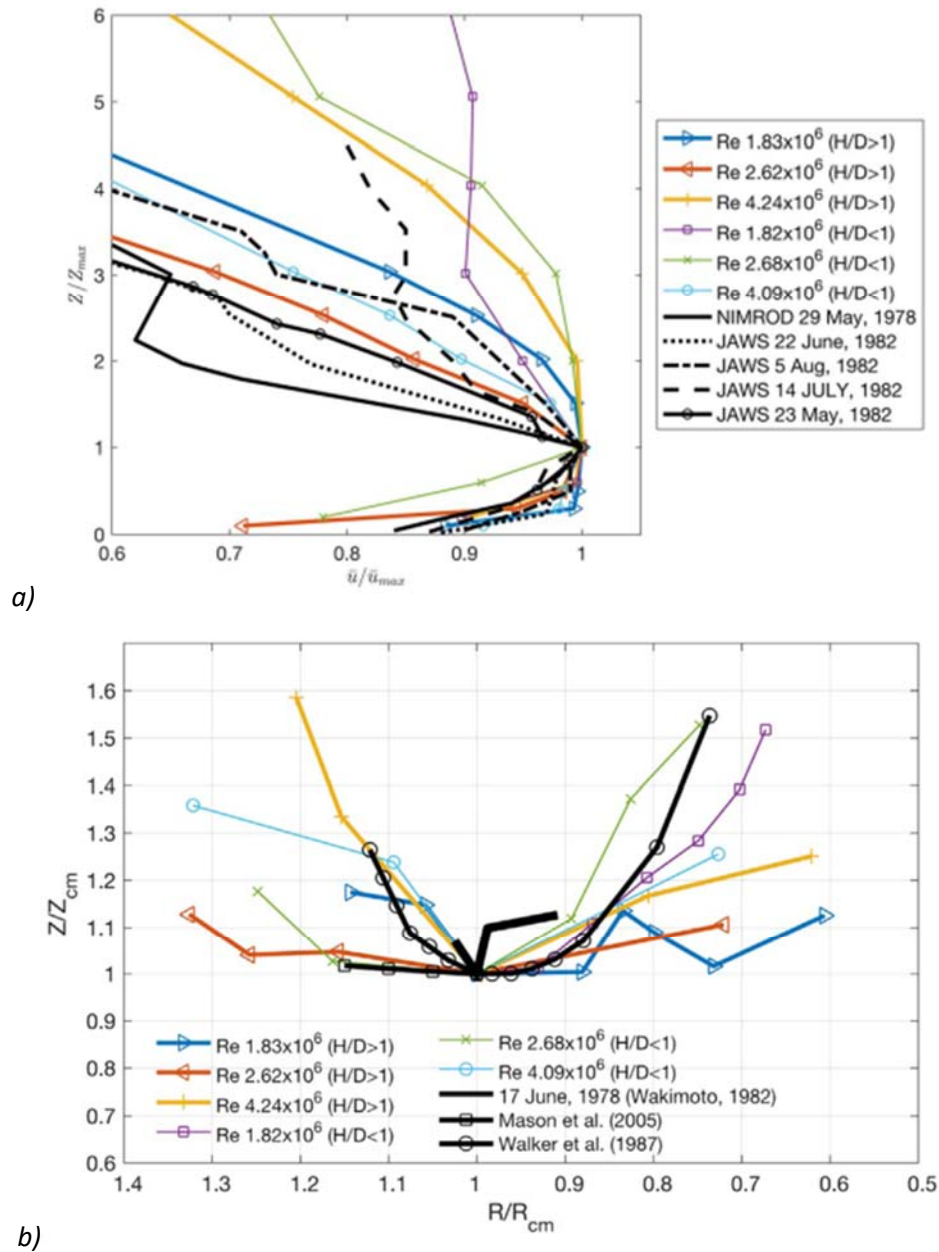


Figure 138. Normalized velocity profiles from full scale events from Hjelmfelt (1989) and Fujita (1978). Source: Junayed et al. (2019).

A.3 Traditional Wind Tunnels Modified with Especial Devices

The third method of experimental laboratory tests comprehends modifying the axis of flow in classic wind tunnel to reproduce thunderstorm outflows. The merit of traditional wind tunnel modified with especial devices (i.e., wind obstacles or blades) lies in its simplistic approach of controlling the flow with apparatus that can be easily installed in already existing ABL wind tunnels.

Cao *et al.* (2002)³⁴ deployed multiple fans that are actively and independently controlled to simulate an intermittent flow with specific speed and turbulence. Lin and Savory (2006)³⁵ implemented two-dimensional slot jets to the open-circuit ABL Wind Tunnel of the Western University to simulate the outflow region of a downburst. Profiles and turbulence were acquired with hot-wire anemometry and presented good approximation to typical downburst profile, showing to be a reliable approach to analyze the effects of TS wind in transmission lines.

Lin *et al.* (2007)³⁶ continued the approach by applying larger flow scales and allowing to better understand the effects in common structures. The slot jet sketched in Figure 139 exemplifies the design used in such experiment. In a) the slots are located at the bottom of the wind tunnel, in b) the slots are shown fully shut, and in c) they are shown fully open.

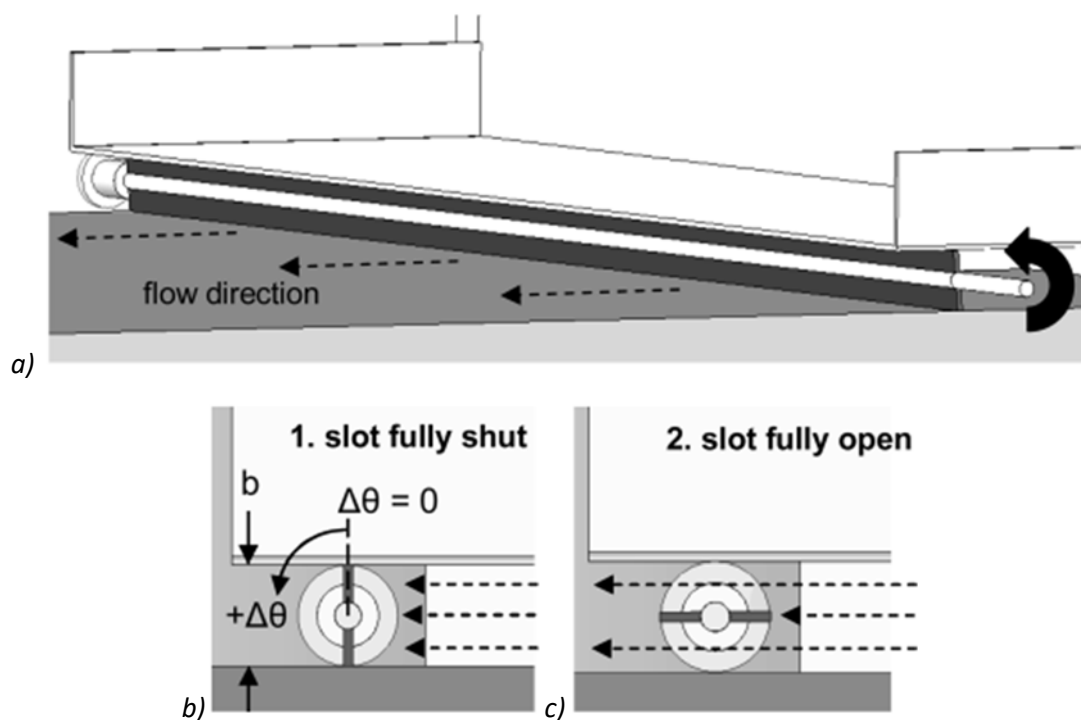


Figure 139. Sideview depicting the slot jet tunnel proposed by Lin *et al.* (2007). In a) is depicted the bottom of the tunnel, in b) and c) are shown the slots in close and open position. Source: Lin *et al.* (2007).

The results were validated against a CFD simulation using the sub-cloud module of Bryan Cloud Model (CM1) and the Andrews AFB Downburst (FUJITA, 1985b). The model was able to fairly reproduce the outflow wind directions and maximum velocity peaks of the full-scale measurement for the Andrews ABF Downburst event. This method shows that is more practical to install an ABL wind tunnel as an “add-on” than other wall jet models. Further on,

the translational capability was added to the model by moving the slots during the simulation of the whole slot jet slowly forward (translating feature) while the jet goes off with the "downburst" flow. Such technique generated wind profiles more closely related to full-scale measurements especially in the ground region, when compared to the non-translating setup.

Lin *et al.* (2015)³⁷ added a pulsed plane wall jet to an ABL wind tunnel and with a specific setup of obstacles (cubes, honeycombs, and screens) to analyze the effects of the ground roughness to a downburst-like flow. In Figure 140 is presented a cross section view along of the wind tunnel utilized to such experiment.

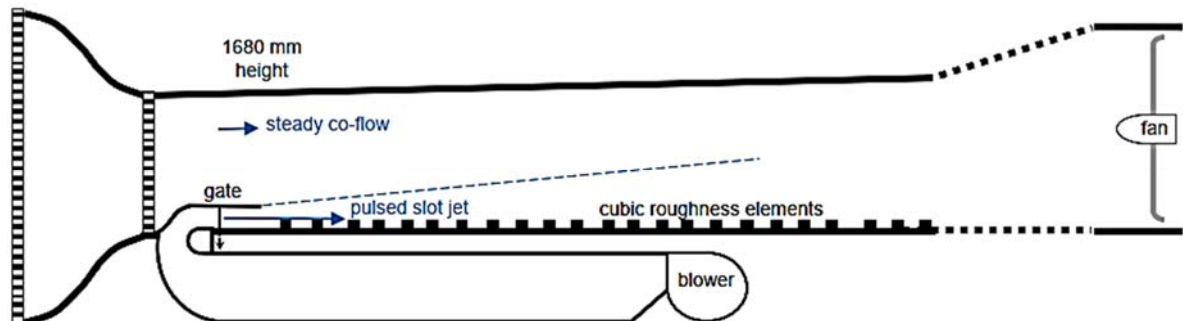


Figure 140. Elevation view of the wind tunnel used in Lin *et al.* (2015) experiment. Source: Lin *et al.* (2015).

Butler and Kareem (2007)³⁸ proposed a manually controlled pivoted flat plate in a low-speed wind tunnel facility that diverts the flow downwards because of a high angle of incidence, forcing the flow to accelerate near the defined ground surface. Not differently of the dynamic of the wall jet experiment, the flow evolves near the flat plate to the desired profile. In Figure 141 in a) and b) are shown pictures of the prototype at different angles at the pivoted flat plate at the Miyazaki University used by Butler and Kareem (2007); in c) is shown the schematic of the wind tunnel, where D in this experiment represents the height of the distance from the ground to the flat plate used as a reference for the analysis of the TS wind simulation.

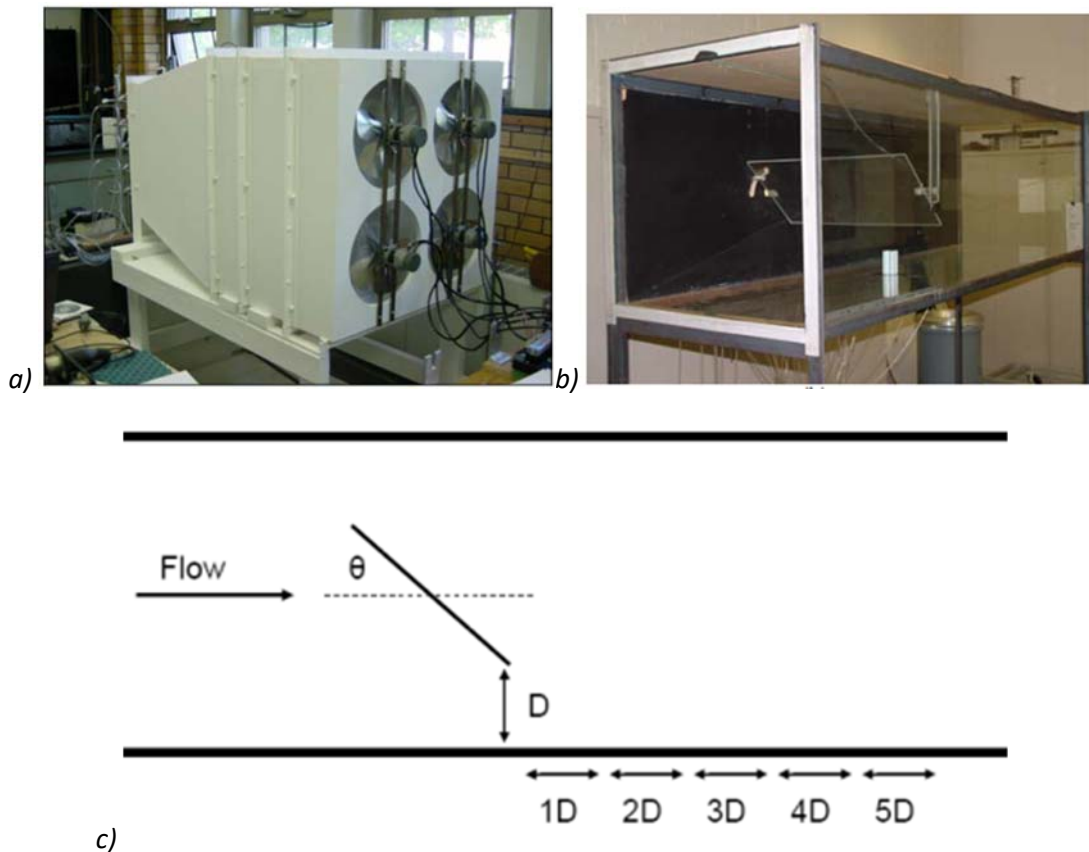


Figure 141. The prototype of the pivoted flat plate at the Miyazaki University used by Butler and Kareem (2007). D in this figure represents the height of the distance from the ground to the flat plate. Source: Butler and Kareem (2007).

This plate can be suddenly rotated to create transient effects of the flow, aiming to mimicking the kinematic and dynamic characteristics of downburst flow after impinging the surface. In Figure 142 a) the flow obtained is shown for different development stages (3D and 4D outlets heights) with the flat plate angle suddenly rotated to 30 degrees and simulated data is compared to Hjelmfelt (1988) experiments and in b) the flow obtained is compared to the boundary layer profile. The results were also compared against CFD simulation using the commercial application Fluent.

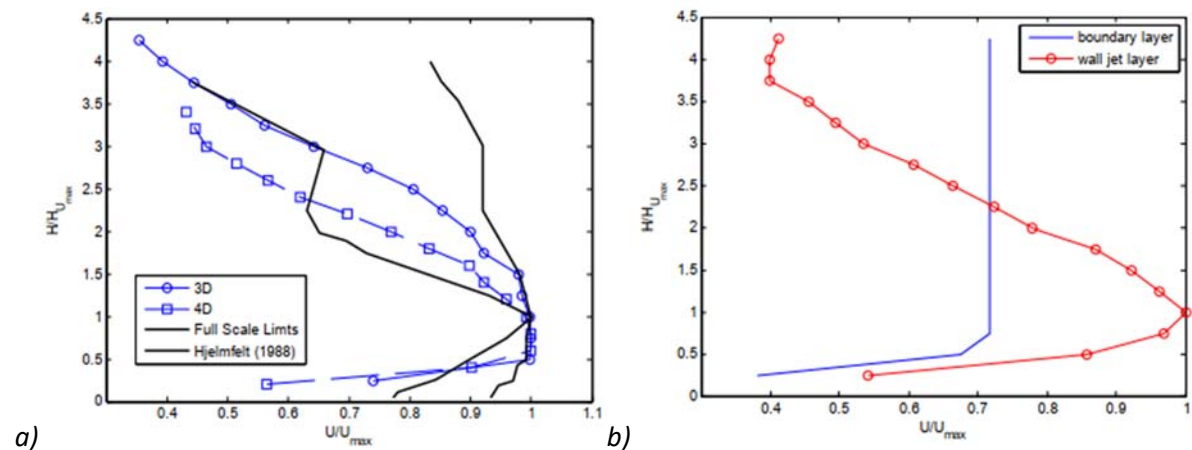


Figure 142. a) Profile development beyond a flat plate at 30° incidence and b) boundary layer profile compared during simulation attempt. Source: Butler and Kareem (2007).

Butler *et al.* (2010)³⁹ advanced the previous experiment with a multiple independently controlled fans wind tunnel constructed at the University of Miyazaki, Japan where the resulting surface pressure is captured on a suit of prismatic models. This facility is shown schematically in Figure 143, which it can tailor to the flow fields to generate a downburst-like flow in the 2D and 3D domain, reproducing along various characteristics of the atmosphere.

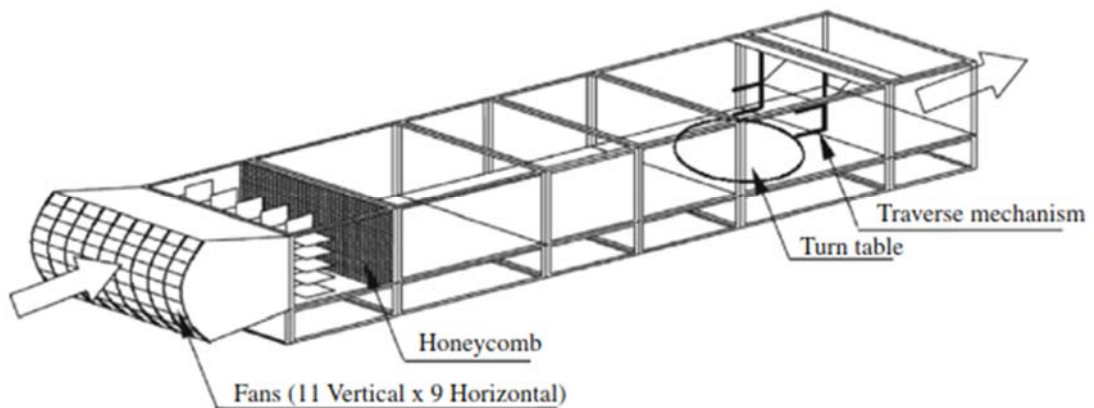


Figure 143. Configuration of the 3-D multiple fan wind tunnel. Source: Butler *et al.* (2010).

In Figure 144 a) are presented the measurements obtained from this experiment compared against the ABL velocity profiles and full-scale data from Hjelmfelt (1988), presenting fair similarity in shape especially at higher levels. For the same figure in b), is shown the turbulence intensity profile for both the initial boundary layer profile and gust flow fields, which did not match with what was found in Lin and Savory (2006), but the authors argument that there is little information regarding the full behavior of the gust front profile from which to draw accurate comparisons.

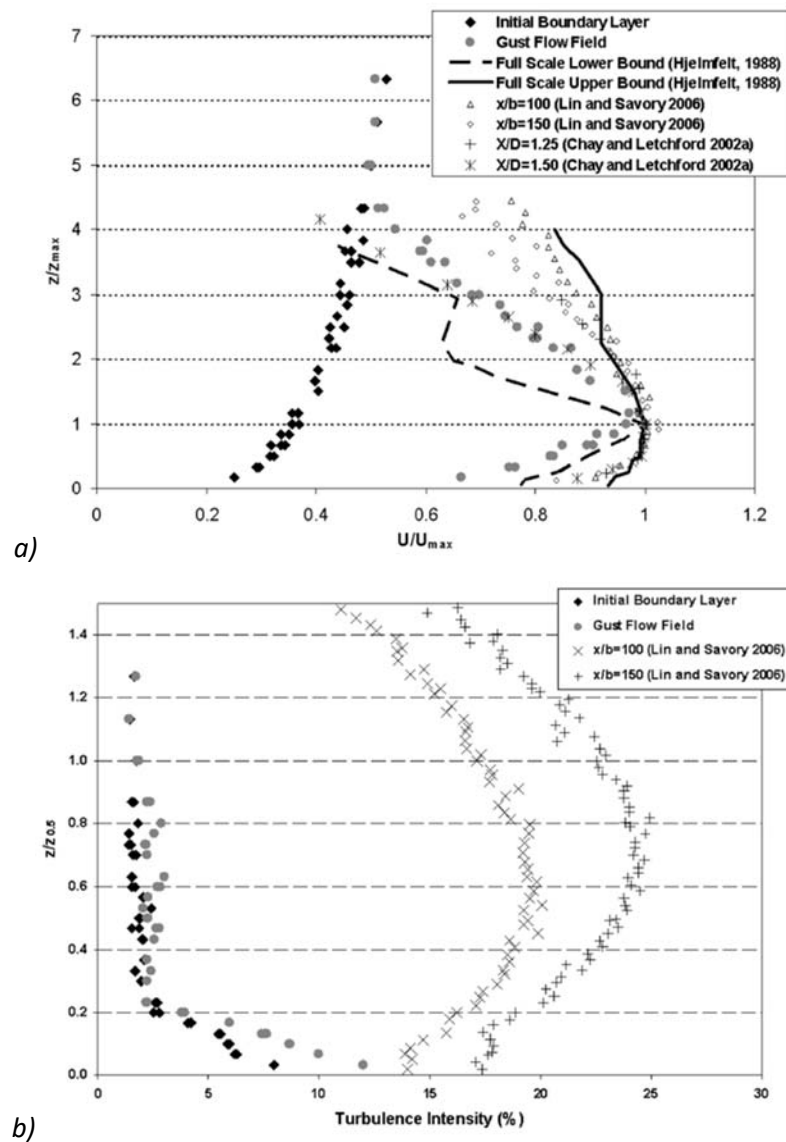


Figure 144. ABL velocity profile gust flow field compared to the full-scale data from Hjelmfelt (1988). In b) turbulence intensity profile of both the initial boundary layer profile and gust flow field. Source: Butler et al. (2010).

Aboutabikh et al. (2019)⁴⁰ designed a blade system integrated to a at the Subsonic Wind Tunnel at Ryerson University, Toronto, Canada. Pictures of experiment are shown in Figure 145 allows the modeling of downbursts outflows in conjunction with ABL simulated winds. It consists of multiple blades capable of rotating at high speed to different angles, for the same Figure in a) is shown the system with blades rotated at $+50^\circ$ and b) -30° positions. The calibration of the system was done using CFD modeling and several compositions of the blades setups were evaluated, including the fully rotating mode that would allow to recreate the non-stationary flow.

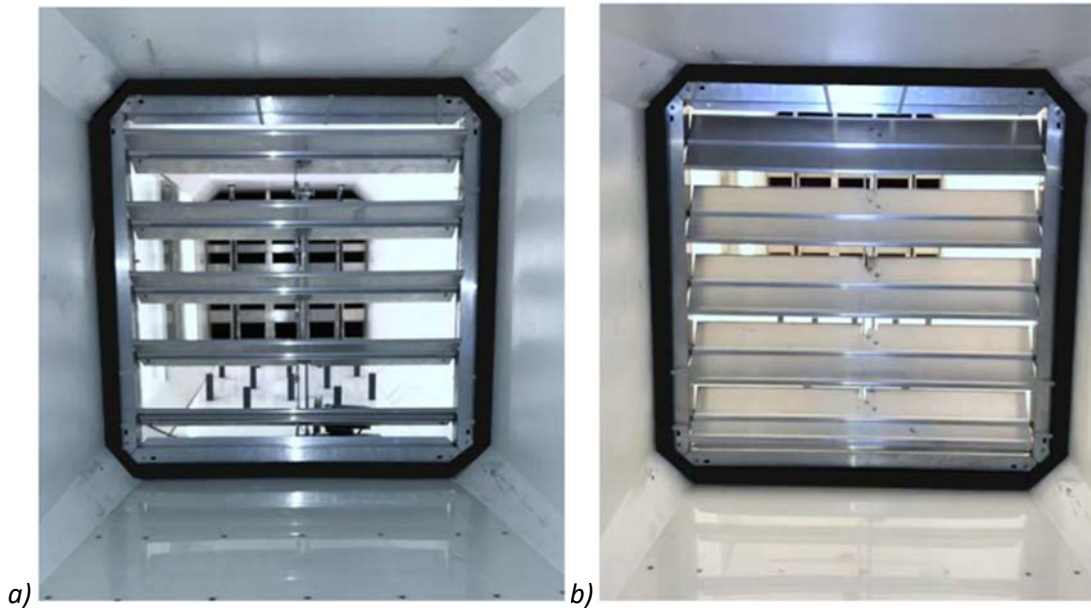


Figure 145. Multiple louvers capable of rotating at high speed to different angles in a) is shown the system with blades rotated at $+50^\circ$ and b) -30° positions. Source: Aboutabikh et al. (2019).

The data obtained was compared to full-scale measurements for vertical profile and temporal velocity variations. In Figure 146 a) is shown the maximum running-mean wind speed profile obtained with other models and full-scale measurements and in b) is shown the turbulence intensity profile compared to the ESDU open exposure profile (ENGINEERING SCIENCES DATA UNIT, 2010). A reasonable agreement (goodness of fit in the order of 90%) was observed for both the temporal and spatial variations of the running mean speed. Furthermore, the residual turbulence for both turbulence intensity and power spectral density presented good agreements with synoptic winds.

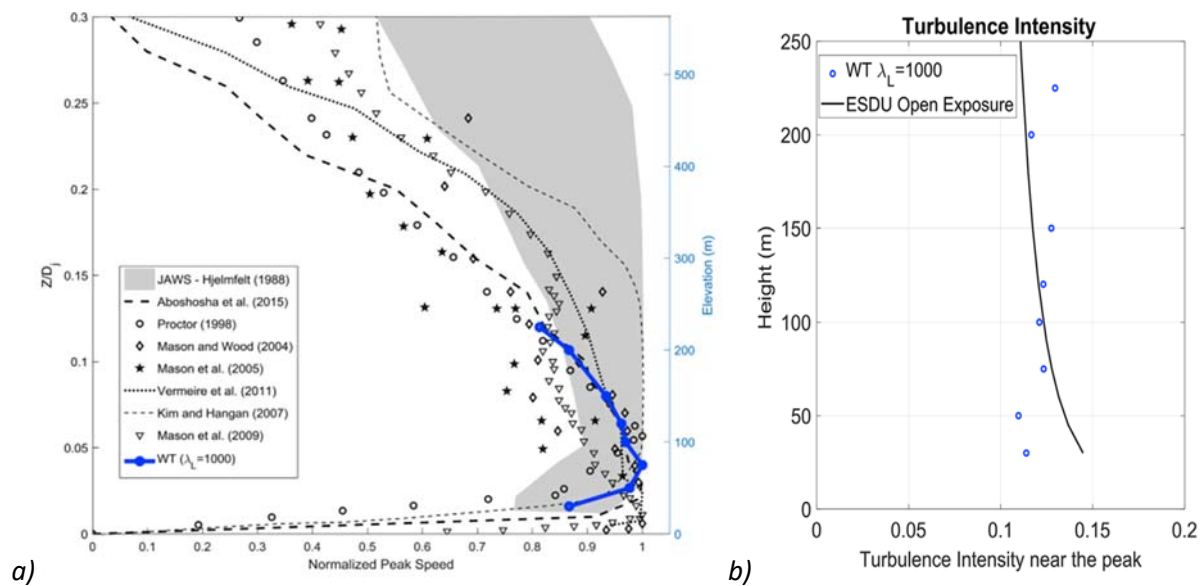


Figure 146. In a) are shown vertical wind profiles of the maximum running-mean wind speed, and in b) shown the turbulence intensity profile compared to the ESDU open exposure profile. Source: Aboutabikh (2019).

Asano *et al.* (2019)⁴¹ developed a downburst simulator capable of generating a pulsed jet and a moving downdraft either separately or together, aiming to investigate the effects of non-stationary winds on flat-roofed low-rise buildings using such simulator. The results of the modeled TS winds (2007) were compared to the effects of ABL winds in buildings and significant differences in loading because of the wind were found. The pulsed jet with or without moving characteristics produced larger negative pressures on the roof and larger positive pressures on the wall than the turbulent ABL. The building was rotated to a diagonal position and the non-stationary pulsed jet was found to cause larger peak of negative pressures, leading the authors to the conclusion that the current code and standards cannot be applied to the calculation of downburst loads in low-rising buildings.

Le and Caracoglia (2019)⁴² examined the feasibility a multi-blade device installed in the closed-circuit wind tunnel at Northeastern University, in Boston, United States. This tunnel was capable of reproducing a non-stationary outflow leading front, which in this study is referred as downburst gust front. The wind tunnel showed in Figure 147 was capable to reproduce the TS wind profiles for blades at 25°, 35°, and 45° flow redirections. These profiles are showed in Figure 148 along with other full-scale measurements and previously downburst profiles.

The proposed device was evaluated to verify adequacy of downburst features, such as nose-like horizontal velocity profile, vertical profile, the non-stationarity of different time varying

means, and the residual fluctuations. Dynamic similarity was introduced to understand how the tunnel flow approximates to the full-scale downburst event at the Andrews Air Force Base. The results showed sudden magnitude increases and the loading scenarios at selected mean flow velocity were similar to previous experiments, but limitations of the device include the 2D characteristic of the outflow, which is not comparable to the typical 3D downburst vortex.

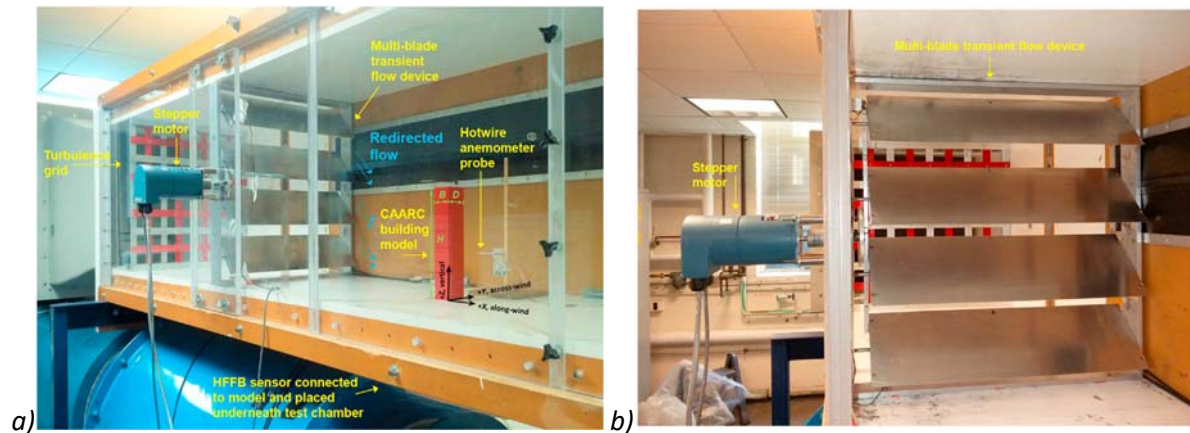


Figure 147. In a) is shown the small-scale win tunnel of the Northeastern university with multi-blade transient flow device to redirect and simulate flow at angle and in b) shown another view of the same experiment with blades in different angle. Source: Le and Caracoglia (2019).

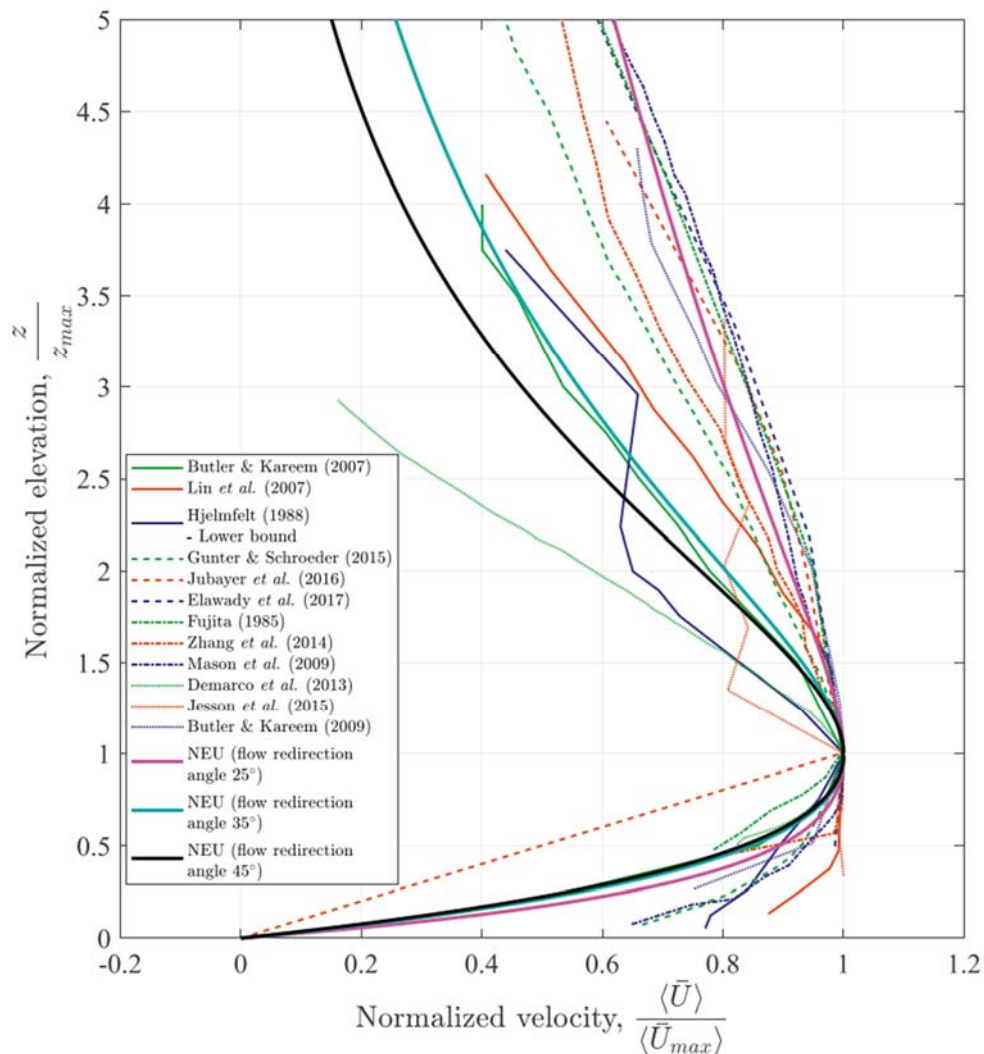


Figure 148. Comparison of the velocity profile obtained at the modified wind tunnel along with other full-scale measurements and downburst simulations. Source: Le and Caracoglia (2019).

B. ANALYTICAL MODELS

Analytical models are mathematical expressions that normally derived primary equations from fluid dynamic equations and steady flow, aiming to propose simplified mathematical solutions for the vertical and radial components of wind speed. These models can be developed either analytically or by defining hybrid stochastic-deterministic models. There are three main methods to analytically simulate downburst induced winds: the classic impinging wall jet, the classic vortex ring models, and hybrid deterministic-stochastic models, which starts from the first two classic analytical methods and adds up the stochastic portion to treat specifically the characteristics of the downburst outflow's fluctuating component.

Classic analytical vortex ring methods focus on simulating the way how the descending column of air forms an outburst prior to touching the ground. This model is more applicable when investigating the vertical loads from the downburst. After the touchdown, the radial outflow is better represented by the wall jet approach, since in this case horizontal forces control the wind field. It is recognized that wall jet models provide a better representation of the fully developed microburst outflow than vortex ring models (SAVORY *et al.*, 2001).

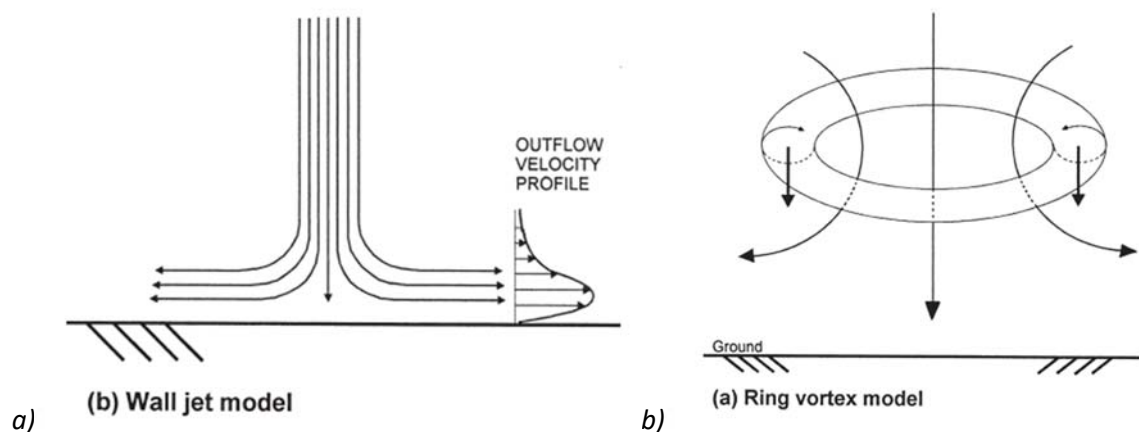


Figure 149. A graphic representation of classic analytical model a) wall jet and b) ring vortex models: Source: Savory *et al.* (2001).

Outputs from analytical models are often validated against not only full-scale measurements but also against results of other modeling approaches: laboratory, CFD, data-driven models. It is to correct to affirm that the most part of other modeling approaches converge to a form of analytical expression, since these simplified models may be easily implemented in the engineering practice and require low computational effort to further analyze the effects of such load in structures and subsequent application to the development of codes and standards.

B.1 Classic Impinging Wall Jet Models

Glauert (1956)⁴³ first proposed the theory of the wall jet experiment on a flat surface by deploying the application of basic fluid dynamic equations steady flows for both turbulent and laminar conditions. The proposed impinging jet had extensive practical purposes, ranging from industrial applications to the study of environmental phenomena – such as downbursts. The process of developing an downburst induced wind model led to implementing different mechanisms meant to introduce translation, slope, and specific pressure distribution in both analytical and experimental fronts of impinging wall jet studies (LETCFORD AND CHAY, 2002).

Oseguera and Bowles (1988)⁴⁴ applied the concepts of "Wall Jet Theory" to the study of windshear caused by downbursts. They proposed a steady state axisymmetric model from around the stagnation point, starting from Euler and Continuity Equations. The results were validated against the velocity profiles from the numerical model Termina Area Simulation System (TASS) developed by Proctor (1987) and the NIMROD full-scale measurements. Equation 31 was proposed to define the ratio of maximum outflow and downflow velocities:

$$\frac{u_m}{w_m} = \frac{0.2357R}{z^* \left(e^{-\left(\frac{z_h}{z^*}\right)^{-0.92}} \right)} \quad \text{Equation 31}$$

Where u_{\max} is the maximum horizontal velocity, w_{\max} is the maximum vertical velocity, R is the radius of the downburst shaft, z is the height of interest, and z_h is the depth of the outflow. Figure 150 shows the maximum vertical velocity obtained from the proposed analytical equation and compared against full-scale measurements from the NIMROD, TASS CFD model, and performed laboratory testing.

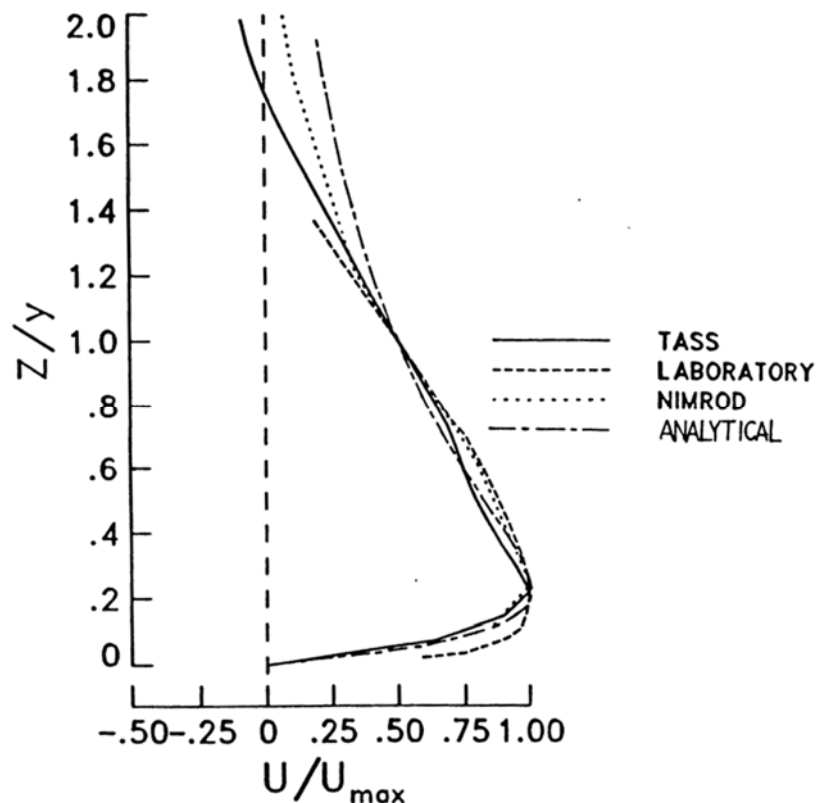


Figure 150. Comparison of Oseguera and Bowles (1988) Model to TASS, NIMROD full-scale measurements and proposed Analytical Model. Source: Oseguera and Bowles (1998).

Vicroy (1991)⁴⁵ proposed an axisymmetric, steady-state empirical model version derived from Osegura and Bowles's Model. This model used sharing functions of the wind profiles to satisfy the mass equation, simulate the boundary effects, and approximate the characteristic profile of the model to the TASS CFD simulated downburst and full-scale measurements. Figure 151 compares Vicroy (1991) outputs to Osegura/Bowles's Model, NIMROD, and JAWS full-scale measurements. It is noticeable how the new model proposed presented a better fit for both a) normalized vertical profile of horizontal winds and in b) normalized horizontal wind profiles along a radial development comparing to the full-scale measurements.

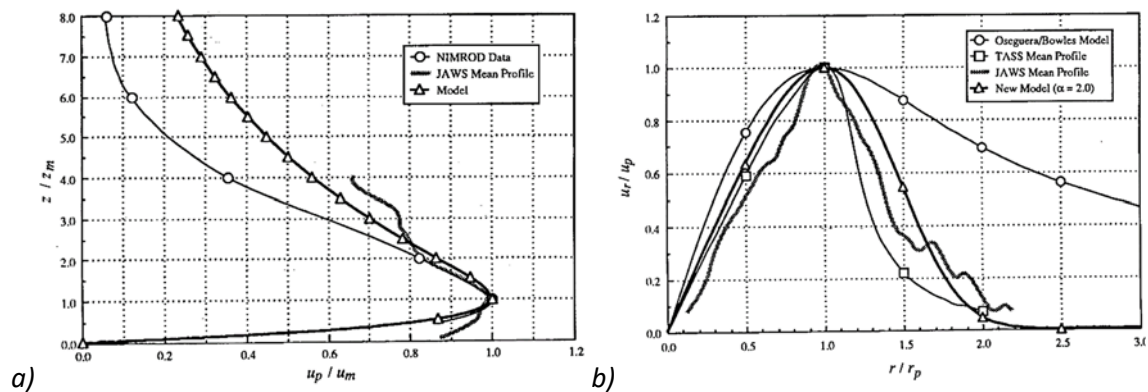


Figure 151. Vicroy (1991) outputs compared to Osegura/Bowles's Model, NIMROD, and JAWS full-scale measurements. It is noticeable how the new model proposed presented a better fit for both a) normalized vertical profile of horizontal winds and in b) normalized horizontal wind profiles along a radial development comparing to the full-scale measurements. Source: Vicroy (1991).

Holmes and Oliver (2000)⁴⁶ improved accuracies for the horizontal wind speed component of a downburst model. In this model was proposed the idea of incorporating the concept of a downburst embed to a translating thunderstorm, that leaves a "footprint" as shown in Figure 152 and it is defined as the vectorial summation of the downburst displacement in the horizontal plane and the radial velocity generated by the downburst thunderstorm itself as illustrated in Figure 153.

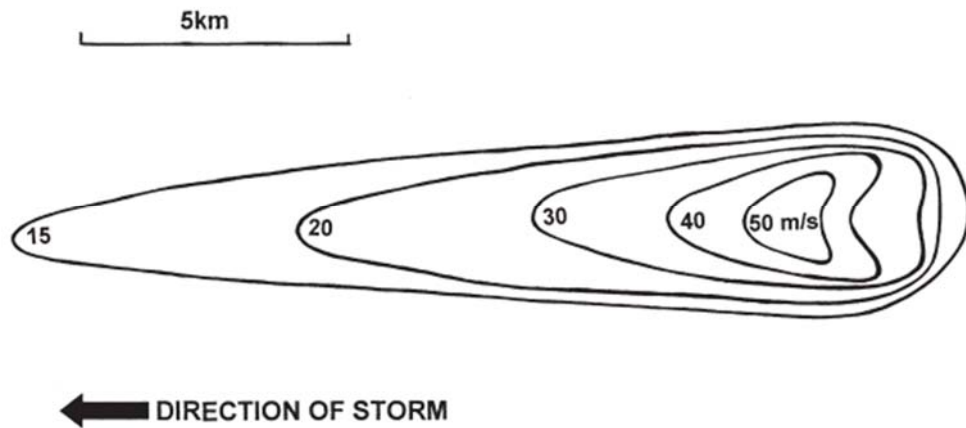


Figure 152. Contours of maximum wind speed footprint generated by the downburst passage. Source: Holmes and Oliver (2000).

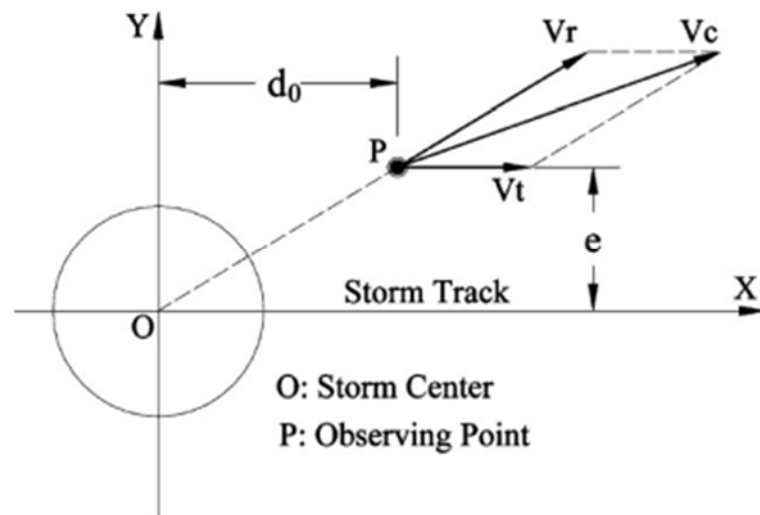


Figure 153. Vectorial summation of the downburst displacement in the horizontal plane and the radial velocity generated by the downburst thunderstorm itself. Source: Holmes and Oliver (2000).

The model's outputs were validated against full-scale measurements of the AAF Base Downburst event in 1983 and the equation of the radial velocity at a 10 m height derived from the solution for given by Schlichting and Kestin (1961) was proposed as the empirical function for the outburst radial velocity, which is expressed by Equation 32 and Equation 33

$$V_r = V_{r,max} \cdot \exp\left[\frac{-t}{T}\right] \cdot \left(\frac{x}{r_{max}}\right) \text{ for } x < r_{max} \tag{Equation 32}$$

$$V_r = V_{r,max} \cdot \exp\left[\frac{-t}{T}\right] \cdot \exp\left\{-\left[\frac{(x-r_{max})}{R}\right]^2\right\} \text{ for } x > r_{max} \tag{Equation 33}$$

Where R is the radial distance from the center of the thunderstorm V_{max} is the maximum radial velocity, r_{max} is the radial distance at the maximum radial velocity. The decay of the

downburst is simulated as an exponential time decay function. In Figure 154 a) is presented the model profile of horizontal radial wind profile and in b) the proposed equation compared to full-scale measurements and the wall jet experiment. Note how the velocity increases almost linearly until it reaches its maximum at the stagnation area and then decreases following Equation 33.

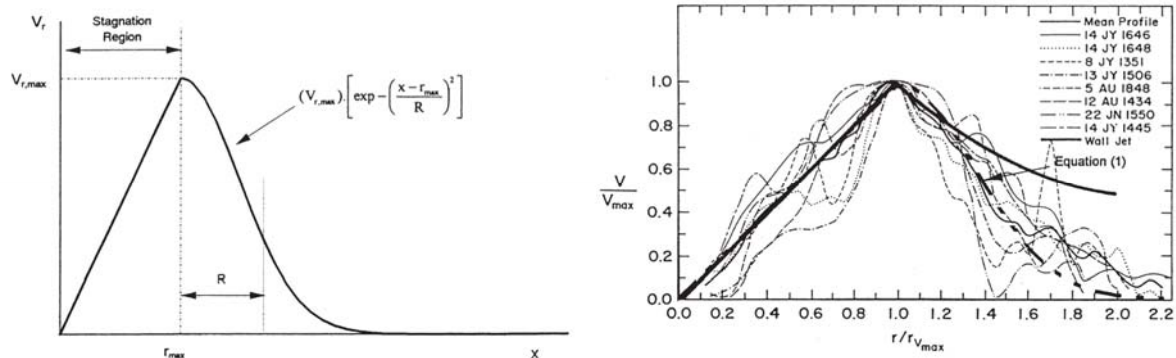


Figure 154. Results from Holmes and Oliver's model. In a) is presented the Mode's profile radial windspeed and in b) a comparison of the equation proposed to full-scale measurements. Source: Holmes and Oliver (2000).

Savory *et al.* (2001)⁴⁷ developed a parametric study to understand the effects of the scale and intensity in simulation of high intensity wind events loading response of transmission towers to tornadoes and downbursts. In this model was presented a variation of Holmes and Oliver's and Vicroy's Models, which got extrapolated to find wind profiles at different heights above the ground using a vertical profile of horizontal mean wind velocity (U), which is showed in Equation 34.

$$\frac{U}{U_{max}} = \exp\left(-0.15 \frac{z}{z_{max}}\right) - \exp\left(-3.2175 \frac{z}{z_{max}}\right) \quad \text{Equation 34}$$

Where U_{max} is the maximum horizontal velocity at any given radial distance from the microburst center and z_{max} is the height above the ground where the radial velocity reached its peak. This value is mentioned to be on average 60 m.

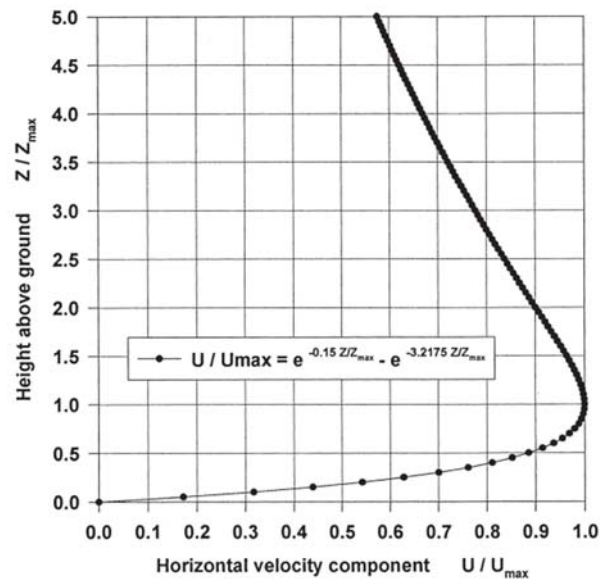


Figure 155. The vertical profile of horizontal radial outflow wind speed associated with microburst.
Source: Savory et al. (2001).

Ponte Júnior (2005)⁴⁸ and Ponte and Riera (2010)¹²¹ started from the analysis of the pressure difference caused by a TS wind event and by further applying the Bernoulli Equation obtaining a TS wind model for a stable atmosphere. It allows the estimation of the variation in time and space in a certain region of the radial and vertical axisymmetric tangential velocities. The resultant streamline flow is shown in Figure 156.

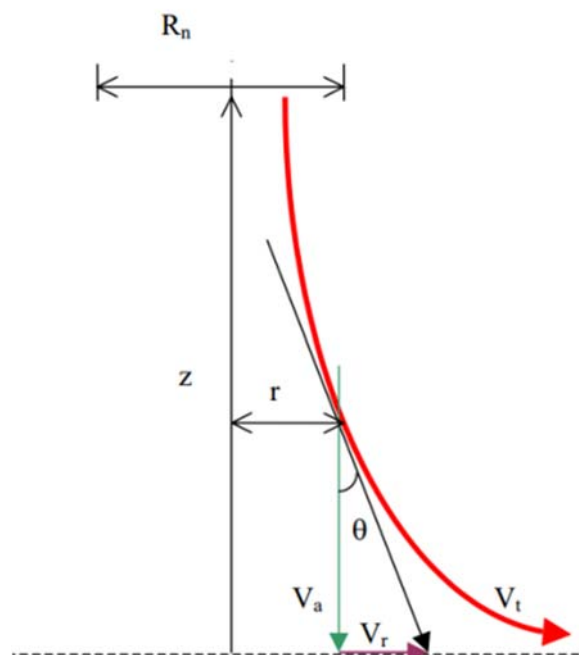


Figure 156. Flow line in the downdraft. Source: Adapted from Ponte and Riera (2010).

Where in any point the radial and axial velocities are given by Equation 35 and Equation 36:

$$V_r = V_t \left(\frac{r^4}{[r^4 + (R \cdot H_c)^2]} \right)^{1/2} \quad \text{Equation 35}$$

$$V_\alpha = V_t \left(\frac{R \cdot H_c^2}{[r^4 + (R \cdot H_c)^2]} \right)^{1/2} \quad \text{Equation 36}$$

Where, R_n is the distance from the center of the cloud to the point of interest and r is the distance of the center of the jet to the reference point and V_r is the radial velocity. This model describes the downdraft flow as stationary, to estimate the time evolution of the tangential velocity $V(t)$, considering the typical transient characteristics of the process, as in Holmes and Oliver (2000) a T parameter was then adopted, as show in Equation 37 and Equation 38

$$V(t) = 1.58V_t \left[1 - e^{\left(\frac{-t}{T}\right)} \right], \text{ for } t \leq T \quad \text{Equation 37}$$

$$V(t) = V_t e^{\left(\frac{-(t-T)}{T}\right)} \text{ for } t > T \quad \text{Equation 38}$$

Where 1.58 is the parameter to correct the initial boundary conditions; V_t is the tangential velocity at a height h and T is the storm's duration characteristic time, when $t = T$ then $V(t) = V_t$. The work of Ponte Júnior (2005) showed that the main parameter to define the TS wind characteristics is the pressure difference due to the event. The second most important characteristic was the frequency of thunderstorm events.

Li *et al.* (2012)⁴⁹ and Abd-Elaal *et al.* (2013c)⁵⁰ proposed an analytical model for steady downbursts outflows. This work also used as starting point the mass continuity equation, which included new shape functions based on experimental and full-scale downburst measurements. The latter depicts better the primary changes in shape of profiles wind speed because of the effects of nonlinear growth of boundary layer thickness and achieves more simplicity and higher accuracy than previous proposed models.

Abd-Elaal *et al.* (2013a)⁵¹ proposed an analytical model for a transient downburst by presenting a new pair of shaping functions starting from a model derived from the mass continuity equation. A downburst intensity factor was proposed to match recorded data, and the parent storm speed presented as a function of height. Abd-Elaal *et al.* (2013d)¹¹⁹ associated downburst events estimated parameters such as age, intensity period, decay period, diameter, and others to a coupled parametric-CFD study that takes into account the differences between downburst records.

Damasceno Neto (2012)⁵² proposed a hybrid model to estimate the turning moments because of downbursts loads in transmission lines towers. In this experiment it was developed a Fortran routine called SubDown and the components of the downburst model were broken down as follows: 1) vertical wind speed velocities $V_r(t)$ (WOOD AND KWOK, 1998); 2) radial velocity profile $V_r(z)$; 3) exponential decaying $V_r(z)$ (HOLMES AND OLIVER, 2000); and 4) turbulence modeling $v(z, t)$ (CHEN AND LETCHFORD, 2007).

The program calculates the maximum radial velocity of the downburst at a height (z) for the point of interest following these steps: 1) it calculates the coordinates on the horizontal plan because of the relative location of the central axis of the downburst translation, imposed by the background wind. 2) it calculates the distance from the downburst to the point of analysis. 3) calculates the radial velocity as a function of the distance from the point of analysis to the center of the downburst through the radial profile velocities. 4) it calculates the radial velocity direction at the point of analysis through the vectorial sum of speed V_o and V_r . 5) it calculates the non-stationary horizontal component and adds it to the radial velocity. 6) it calculates the horizontal components (x and y) of the downburst velocity summed to the horizontal components of the background wind.

The analysis of the downburst flows and structural interactions obtained in Damasceno Neto (2012) showed a smaller amplification coefficient for downbursts when compared to the EPS winds, but the values of the downburst winds at the base of the tower were much higher than for EPS winds, due to the typical "nose" profile shape of the former. The dynamic amplifications for the horizontal displacement and axial forces were small due to the lower turbulence intensity, ranging from 8.8 to 18%. The author concludes that for transmission towers, static analysis of downbursts wind at its critical condition is enough to evaluate the loads due to these winds in structures.

Riera (2016)⁵³ advanced the conclusion from Riera and Nanni (1989) that TS events tend to define the extreme wind climate for a return period of as little as 10-years. Miguel and Riera (2013) found that isolated downburst events rarely reach maximum wind speeds higher than 30 m/s at 10m/ and are therefore a minor structural concern, but when they happen within mesoscale convective systems and squall lines, they are in fact a major concern to the design of structures, reaching sometimes maximum velocities of 60 m/s.

To prove such theory, Miguel and Riera (2013) run a random thunderstorm model for 1-year period near a weather station for a 40 km circular diameter region. It was found that the chances of an isolated storm pass the control point was about two orders of magnitude smaller when compared to the chances of a squall line event reach the control points, in other words, 1 out 100 isolated storm modeled event were found to strike the control point. Miguel *et al.* (2018) showed that for a period of exposure and probability of occurrence of 25 years or more, TS winds would almost certainly occur within squall lines. In Figure 157 is shown the traces of twenty randomly simulated storms, which is the annual mean in the Region of the City of Porto Alegre.

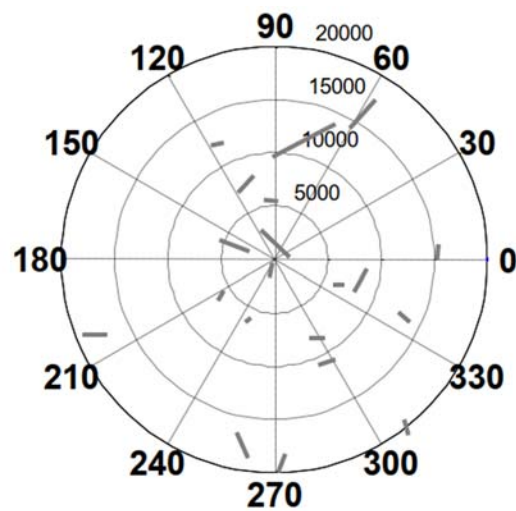


Figure 157. Path of 20 TS events in the region of interest. Source: Miguel and Riera (2013).

Riera (2016) proposed an analytical assumption that these linear paths are the result of the vectorial summation of the EPS and TS winds. Therefore, it is proposed that the initial basic velocity (V_o) of the downburst outflow is given by the vectorial sum of the axisymmetric downburst outflow (V_1), storm motion (V_2), and the atmospheric boundary flow (V_3). The highest value is obtained when all three components are in the same direction, as shown in Equation 39. In Figure 158 a) is shown a sketch representing an extra-tropical cyclone with a frontal system composed of several smaller mesoscale convective cells that can cause downbursts. In b) is shown a representation of the vectorial sum of these winds.

$$V_o = V_1 + V_2 + V_3 \quad \text{Equation 39}$$

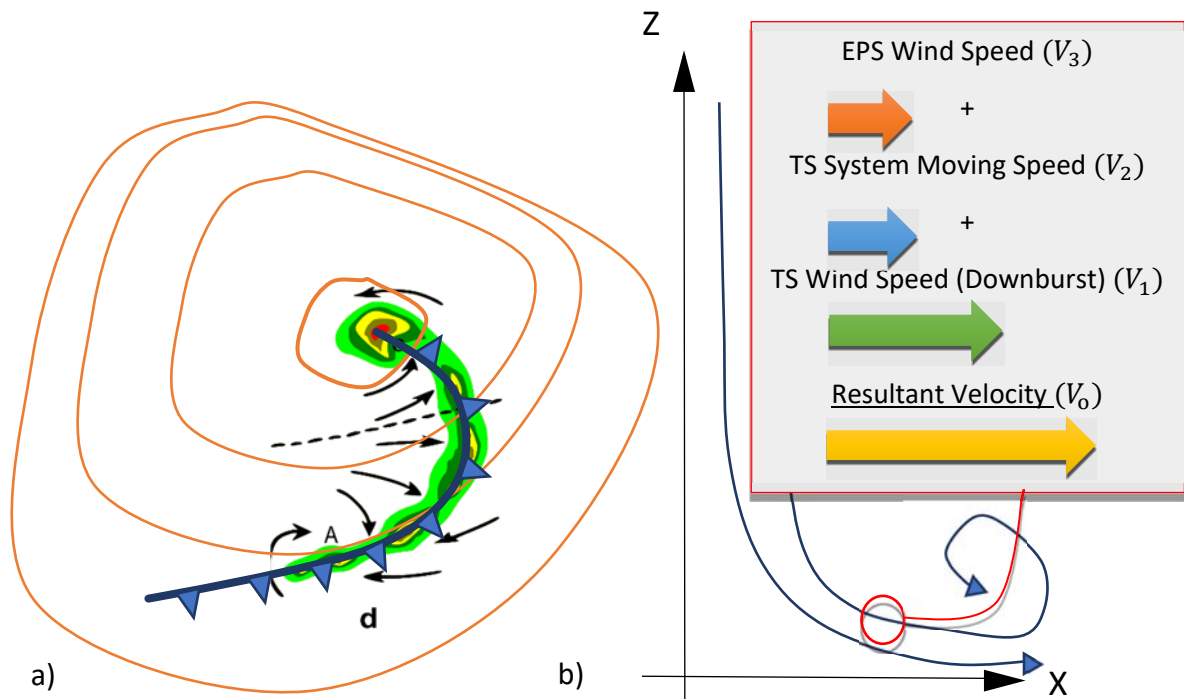


Figure 158. In a) is shown the sketch of a thunderstorm system embedded in an extratropical cyclone and in b) is shown a sketch of a theoretical vectorial sum of speed from the EPS with the thunderstorm system moving, and TS outflow speed. Source: Author.

The full-scale wind measurements are assumed to be V_0 in Equation 39. Here the TS wind component V_1 is now called V_{TS} and the EPS wind becomes the summation of the two large scale components $V_{EPS} = V_3 + V_2$, therefore Equation 39 assumes the form of Equation 40

$$V_0 = V_{EPS} + V_{TS} \quad \text{Equation 40}$$

Riera (2016) proposed the ratio V_{EPS}/V_{TS} can be obtained from the analysis of the mean wind records before and after the peak velocity (V_{EPS}) over the wind peak wind speed (V_{TS}). Riera (2016) showed with the empirical analysis of seven TS wind events showed a typical ratio V_{EPS}/V_{TS} varies from 0.3 to 0.4, the author adopts 0.35 a value of reference, as shown in Equation 41.

$$0.35 = \frac{V_{EPS}}{V_{TS}} \quad \text{Equation 41}$$

To illustrate such theory in Figure 159 is shown an example of a downburst event measured at the Porto La Spezia in 25/11/2011 by Solari *et al.* (2015b). The red line represents the 10-min average of the wind speed captured for this event. By the time the peak velocity is captured at about 35 m/s, the average wind speed is about 12 m/s, therefore the background or V_{EPS} wind contributes to about 35% of the total flow due to the storm.

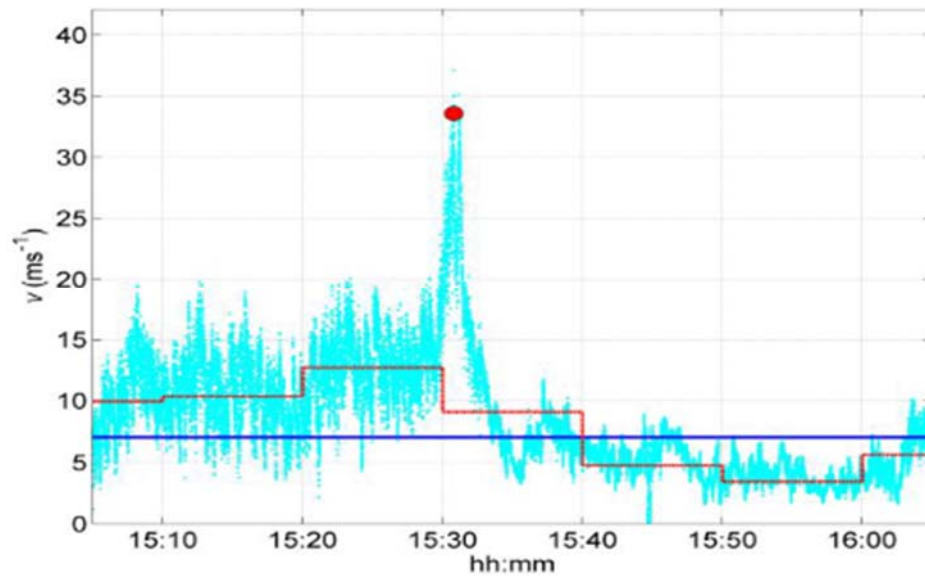


Figure 159. Horizontal component of a downburst event registered at the Porto La Spezia in 25/11/2011, where the red line represents the 10-min average flow, which is equivalent to the velocity of the thunderstorm system. Source: Solari et al. (2015b).

Riera (2016) proposed the adoption of Holmes and Oliver (2000) model, which considers the idea that in an orthogonal plane to the orientation of the squall line, the downburst flow occurs causing damages to approximately the limits of the trapezoidal cross-section with a width at ground level b , the top width is d . The length can extend to several kilometers, forming a sort of "wind tunnel" where the downburst profile can be observed, as shown in Figure 160. External to that region the flow is dominated by the EPS winds, following the typical parabolical wind profile.

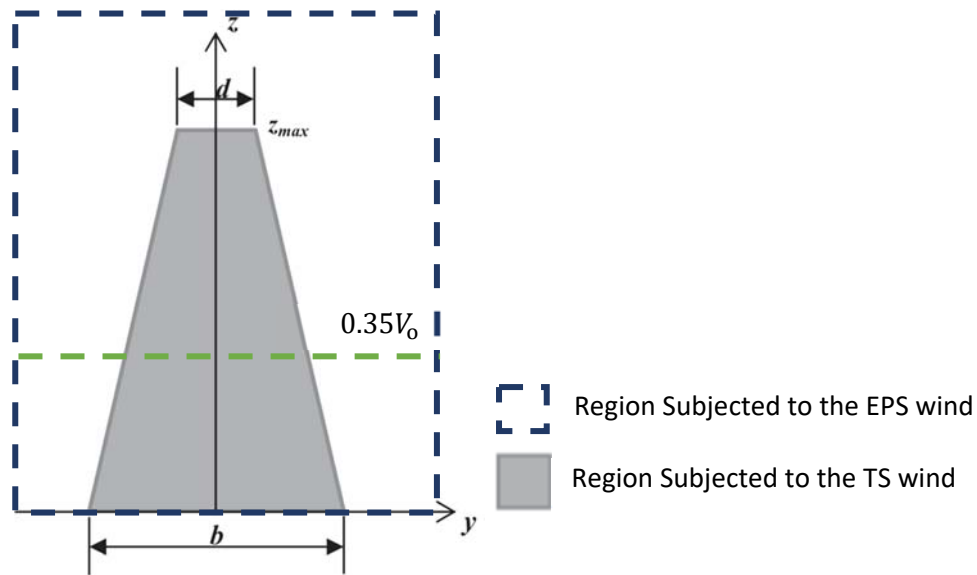


Figure 160. Horizontal wind velocity at the reference height ($z=10\text{m}$) during a typical squall line event. Source Riera (2016).

For static structural design, only the velocity profile suffices, but when analyzing the dynamic effects, a more comprehensive analysis is needed that helps determine the evaluation with time of the velocity V_0 . Riera (2016) proposed the adoption of the empirical solution of the semi stationary axisymmetric jet presented by Holmes and Oliver (2000), which was shown to satisfactory fit observed velocity records. A simplified version of Equation 32 and Equation 33 are presented in Equation 42 and Equation 43.

$$V(t) = 1,58V_t[1 - \exp(-t/T)], \text{ for } t \leq T \quad \text{Equation 42}$$

$$V(t) = V_t \exp[-(t-T)/T], \text{ for } t > T \quad \text{Equation 43}$$

Where the parameter T is defined as a characteristic time of the TS event, and it depends on the model in which T is composed of a curve of the atmospheric pressure based on the Bernoulli equation, the expansion effects of the thunderstorms, the model of development of the boundary layer for the horizontal flow of the TS, and the probabilistic distribution of the flow and the cloud's top were considered. In this approach the authors focused on understanding the influence of the regional climatology of TS winds to define the parameters of the model. They also showed that the difference in pressure due to a TS wind even is the main factor that defined the intensity of the TS wind.

Riera (2016) then proposed 5 categories of downbursts as shown in Table 6, varying from DB1 to DB5 according to the value of V_0 , and it provides the value of T to insert in the equation and

obtains the max downburst profile. Miguel and Riera (2013) and Miguel *et al.* (2018) extended the analysis of these models to understand their interactions with structures.

Table 6. Parameters of five downbursts categories for various downbursts V_0 proposed by Riera (2016). Source: Riera (2016)

Designation (DB)	V_0 (m/s)	d (m)	b (m)	Height of V_{max} z_{max} (m)	T (s)
DB 1	$V_0 \leq 30$	10	40	20	60
DB 2	$30 < V_0 \leq 40$	20	60	40	120
DB 3	$40 < V_0 \leq 50$	40	100	80	180
DB 4	$50 < V_0 \leq 60$	60	160	120	300
DB 5	$60 < V_0$	80	240	160	480

In Figure 161 a) is shown the wind profile adopted by Riera in this model, which is the same profile considered in AS/NZS 7000 and b) shows the graph representation of Equation 42 and Equation 43 with the evaluation of the velocity parameter for maximum height with time for five different time instants.

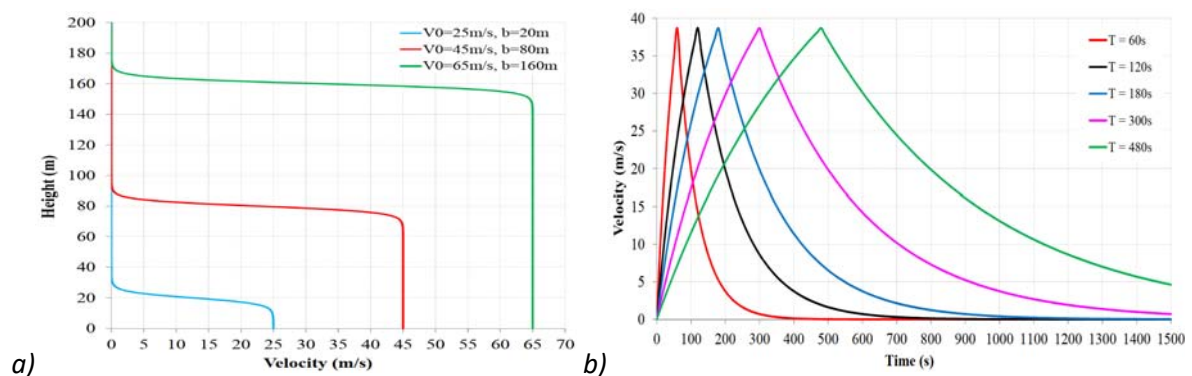


Figure 161. Evolution in time of TS component for $V_t = 38.7$ m/s and five different characteristic time T . Source: (RIERA, 2020)

XHELAIJ *et al.* (2020)¹²² proposed a novel analytical model that simulates the horizontal mean wind velocity profile and evaluation. Similar to the method proposed by Riera (2016), the final profile was considered to be a vector summation of three independent velocity fields (radial impinging jet velocity, translational velocity of downburst cell, and the downburst jet) – the work separates this process in 3 stages. In summary, the horizontal outflow mean wind velocity (stage 1) as well the parent cloud movement or traveling downburst (stage 2) was reconstructed using the Holmes and Oliver (2000) model with modifications implemented in Chay *et al.* (2006); and to reproduce the wind field near the surface novel reconstruction

approach was proposed (Stage 3). A parametric analysis was added to simulate the dimensions and relevant kinetic parameters of the flow in space and time. Results were validated against full-scale downburst measurements and captured at different anemometers and locations – which was a unique accomplishment in this aspect.

In Figure 162 the results obtained from the simulation (magenta line) are presented and compared against full-scale measurements at two different spots (blue line). In a) and b) is showed the results obtained for velocity and direction, respectively, in Anemometer SP03; and in c) and d) the same parameters are shown for Anemometer SP 02. The reconstruction results showed good adherence to the observed data in SP03. For SP02 some minor detachments in the simulation of the mean wind and direction were observed, which is possibly due to the susceptibility of the flow to the complex effects imposed by the orographic configuration of the La Spezia site, in Italy.

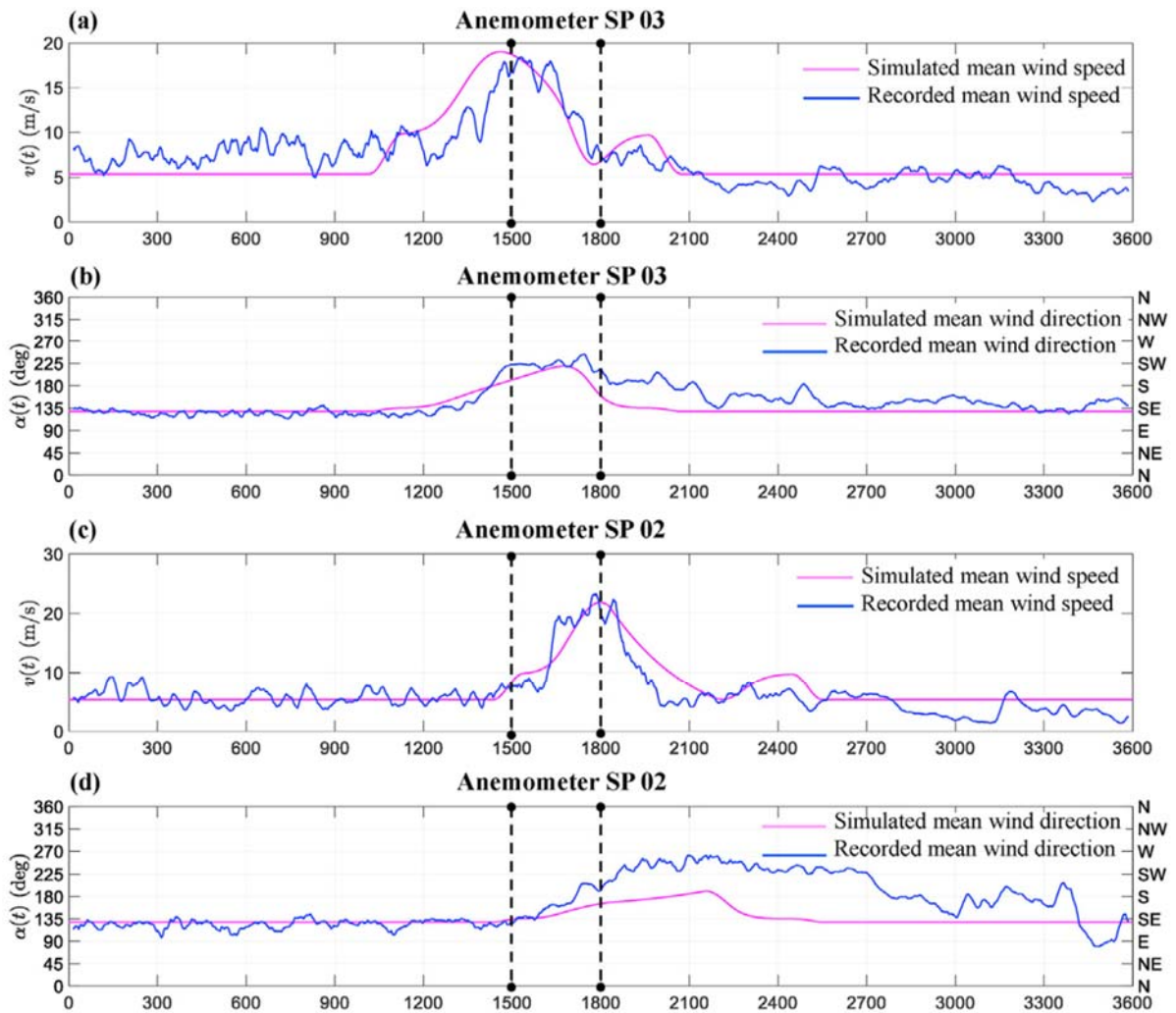


Figure 162. Simulation results of model proposed by Xhelaj et al. (2020) are presented (magenta line) and compared against full-scale measurements at two different spots (blue line). In a) and b) is showed the results obtained for velocity and direction, respectively, in Anemometer SP03; and in c) and d) the same parameters are shown for Anemometer SP 02.

B.2 Classic Vortex Ring Models

Ring vortex method assumes that the flow field patterns generated by a vortex ring near a flat plate is similar to the flow generated by a downburst. Zhu and Etkin (1985) simulated the downburst flow like a jet directed vertically downward to the ground. This synthesized model simulated the wind field near ground during the mature phase of the downburst and could be implemented to predict the effects of these winds on a flight path. The resulting velocity field was modeled as a classical ideal fluid flow generated by a suitable singularity distribution, this method called double sheet, reproduces the boundary wall by creating an image of the specular flow with respect to the ground.

Ivan (1986)⁵⁴ introduced a 3D axisymmetric circulatory flow to Zhu and Etkin's Model. This mathematical model was applied for real-time flight simulation of takeoffs and landing in low-altitude severe wind shears due to downbursts and the data was validated against full-scale measurements from the JAWS Project. The flow field developed in the vortex-ring model can be approximated by the expression showed in Equation 44.

$$\frac{0.788k^2}{(0.25 + 0.75\sqrt{1-k^2})} \quad \text{Equation 44}$$

Where for the limited range of $0 \leq k^2 \leq 1$ for the modulus $k = \frac{(r_2-r_1)}{(r_2+r_1)}$, where r_2 and r_1 denote the least and greatest distanced, respectively of the point P of divergence of the Downburst.

Schultz (1990)⁵⁵ proposed a multiple vortex ring model applying a vortex ring stream function and compared the results against the measurements of the downburst event in the Dallas - Ft. Worth's Airplane Accident. The model consists of time-invariant vortex wind filaments embedded in an irrotational flow. The vortex rings viscous cores are modeled by the potential flow theory distributing the vorticity over a small radially distance of the vortex ring filament.

Vicroy (1992)⁵⁶ proposed a simple downdraft model which is mostly frequently cited in the literature and starts from the principle of conservation of mass and assumes the vertical wind to be zero at the ground elevation, the vertical wind can be calculated as in Equation 45:

$$w = \frac{\partial w}{\partial z} z = -z \left(\frac{\partial u}{\partial r} + \frac{u}{r} \right) \quad \text{Equation 45}$$

Where, u is the wind component in the radial component r , and w is the vertical wind component. In this model the vortex ring is located above the ground and a mirrored image ring equidistant below the ground is generated to satisfy the no-flow through the ground boundary conditions. Figure 163 shows the ring-vortex and the variables used to define such function.

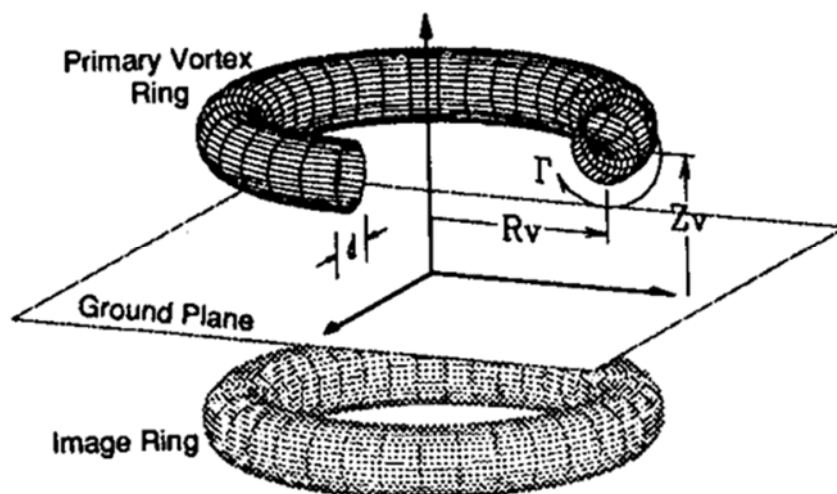


Figure 163. Ring Vortex Model. Source: Vicroy (1992).

Riera *et al.* (1998)⁵⁷ proposed a mixed numerical model starting with the analytical model of Zhu and Etkin (1985)⁵⁸. In this model it was considered the influence of the extreme wind return period of the area in analysis for the model's proposition, it was taking in consideration the cumulonimbus cloud movement due to the larger scale flow, and it was showed that the most damaging winds happen in a longer and thinner area closer to the ground. The velocity vector was calculated at a control point in between the starting and finishing point of the moving storm and with the resultant velocity field curves were adjusted to a Rayleigh distribution. The results were compared with the histogram of TS wind data frequency in one meteorological station in Brazil and it was found to be representative.

Jesson and Sterling (2018)⁵⁹ proposed a non-translating analytical downburst model, similar to Ivan (1986) ring-vortex model. In this study, both the primary and secondary vortices were modeled. It was showed that the maximum wind speed varies linearly with initial primary circulation, and it has an inverse linear relationship with the rate of decay of the primary vortex and it lifts from the ground as it weakens. The secondary vortex has a more complex behavior and less importance to structural engineering. The shape of the "nose" wind profile is showed to be dependent on the primary and secondary vortices. Due to the inviscid nature of the model and lack of accurate full-scale measurements, the near ground behavior of the wind speed (heights <10 m) is identified not be accurate.

B.3 Nonparametric Deterministic-Stochastic Hybrid (NDESH) Models

A turning point in the development of downburst models was when hybrid analytical models started to be proposed. Several variances have been developed, but it consists essentially in separating the mean (non-turbulent) winds from the fluctuations about the mean. The fluctuations are said to be induced by small-scale turbulent models and calculated as a stochastic process using turbulence power spectral functions and coherence functions, i.e., spectral density function (SDF), evolutionary power spectral density function (EPSD), and Stochastic Systems (with linear or not filters) with white noise inputs. Here are presented the downburst models developed based on the TS wind turbulence theory.

Chang and Frost (1987) first proposed the idea of applying a turbulence model to understand the spectral width broadening due to the wind shear caused by downbursts, proposing the first form of a hybrid microburst wind mode. Later, autoregressive moving average (ARMA) models started to be used to investigate the longitudinal component of EPS wind data and the turbulence associated (SMITH, 1993)

Choi and Hidayat (2002a)⁶⁰ proposed a modification of the gust response factor method (GRF) to calculate the dynamic response of structures of monsoon winds and thunderstorms winds. By separating the running-mean from its fluctuation, it was shown that the thunderstorm flows become more stationary and conventional structural analysis may be applied. It was found the best performance in 60-s mean-averaging.

This model was then improved by Chen and Letchford (2004, 2005, 2006, 2007)^{61,62,63,64} and Chay *et al.* (2008)⁶⁵, where it was proposed an empirical hybrid model approach to simulate the TS wind events oriented to applications on slender structures that are more susceptible the small scale turbulence fluctuation. An extensive discussion on vector time-varying autoregressive (TVAR) modeling is presented in the doctorate thesis of Chen (2005)⁶⁶, in which the proper orthogonal decomposition (POD), wavelet shrinkage, and state space methods used to show that downburst wind speeds are composed of both larger stationary portion and a smaller non-stationary scale and both may be characterized by TVAR models.

With the TVAR method, the deterministic part (slowly time-varying) is determined by using different moving average times and the fluctuating wind speeds are modeled as uniformly

evolutionary vector stochastic process, which is generated by using the amplitude of a stationary Gaussian vector represented by its power spectral function (PSD) matrix. The simulation of the stationary and non-stationary Gaussian stochastic processes is realized using spectral representation method (SRM).

SRM assumes that a stationary/non-stationary Gaussian process can be decomposed into a series of sine and cosine random waves with random amplitude functions. In this model, as briefly discussed in Section 4.3, a nonparametric deterministic-stochastic hybrid (NDESH) model is framed by the wind speed properties, as follows, mean and fluctuating wind speeds, standard deviation, power spectral density. Considering the wind speed $U(z, t)$ at any height and instant is described by its mean component $\bar{U}(t, z)$ plus its fluctuating component $\tilde{U}(t, z)$, as show in Equation 46.

$$U(z, t) = \bar{U}(t, z) + \tilde{U}(t, z) \quad \text{Equation 46}$$

The rapidly fluctuating velocity component $\tilde{U}(t, z)$ has a time-varying standard deviation $\tilde{\sigma}(z, t)$ that is approximately proportional to the mean speed with a factor of ~ 0.1 . Therefore, the fluctuating wind speed can be factorized as shown in Equation XX.

$$\tilde{U}(z, t) = \tilde{\sigma}(z, t) \times u(z, t) \quad \text{Equation 47}$$

Where $u(z, t)$ becomes the normalized fluctuating wind speed with unit variances or standard deviations. N Profiles (or mode shapes) can characterize the mean wind speed $\bar{\Phi}_1(z)$ and wind speed time functions $\bar{U}_1(t)$, as shown in Equation 48.

$$\bar{U}(z, t) \approx \sum_{i=1}^{\bar{N}} \bar{\Phi}_1(z) \times \bar{U}_1(t) \quad \text{Equation 48}$$

The time-varying standard deviation $\tilde{\sigma}(z, t)$ is defined by Equation 49.

$$\tilde{\sigma}(z, t) \approx \sum_{i=1}^{N_{\tilde{\sigma}}} \Phi_{\tilde{\sigma},i}(z) \times \tilde{\sigma}_i(t) \quad \text{Equation 49}$$

And the time-varying turbulence intensity assumes the form showed in Equation 50.

$$I_u(z, t) = \frac{\tilde{\sigma}(z, t)}{\bar{U}(z, t)} \quad \text{Equation 50}$$

The new normalized fluctuating wind speeds $v(t)$ can be characterized by their cross-power spectral density (XPSD) functions $S_u(z_1, z_2, \omega)$ if they are stationary or by their evolutionary cross-power spectral density (XEPSD) functions $S_u(z_1, z_2, t, \omega)$ if they are non-stationary.

Based on the discussed above, the NDESH approaches actually decomposes the model into three portions: 1) the **time-varying mean speed**, is understood as the large-scale parcel of the wind speed and it is mostly due to the storm translation or environmental flow; 2) the **time-varying standard deviation**, which is the medium scale flow and even though it is considered a stochastic property of the fluctuating speeds at turbulence scale, it is largely defined by the deterministic properties of the mean speeds of the largest scale; finally, 3) the normalized fluctuating speeds or **modulated fluctuating speeds** are understood as the smallest scale – samples of the stochastic process embedded within the flow, which are mainly due to the turbulence characteristic of the wind speed.

The time-varying standard deviation $\tilde{\sigma}(z, t)$ of $\tilde{U}(z, t)$ can assume the format in Equation 51, by applying the state space smoothing method discussed in (Chen, 2005)

$$\bar{U}(t) \approx \sum_{i=1}^{\bar{N}} \bar{\Phi}_i \times \bar{U}_i(t) \quad \text{Equation 51}$$

Where $\bar{U}(t) = \{\bar{U}(z_1, t), \bar{U}(z_2, t), \dots, \bar{U}(z_n, t)\}'$ and $\bar{\Phi}_i = \{\bar{\Phi}_i(z_1), \bar{\Phi}_i(z_2), \dots, \bar{\Phi}_i(z_n)\}'$ are the mean speed profiles or mode shapes with values only at observation positions.

Considering the Equation 46 to Equation 50, Chen and Letchford (2007) proposed an empirical form as in Equation 52:

$$U(z, t) \approx \left[\sum_{i=1}^{\bar{N}} \bar{\Phi}_i(z) \times \bar{U}_i(t) \right] \times [1 + I_u(z, t) \times u(z, t)] \quad \text{Equation 52}$$

Which can be simplified to Equation 53:

$$U^*(z, t) = \bar{\Phi}_1^*(z) \times \bar{U}_1^*(t) \times [1 + I_u^*(z) \times u(z, t)] \quad \text{Equation 53}$$

It is assumed therefore that the velocity profile is enough to characterize the time-varying mean speed field and the turbulence intensity in time is invariant.

For the vertical profile $V(z)$ may assume previously proposed models. In this work, Chen and Letchford (2004) adopted Oseguera and Bowles (1988), Vicroy (1992), and Wood and Kwok (1998). For the time function, meaning the way how the mean wind speed evolves, it is assumed that the vector summation of the radial impinging jet velocity and storm translation speed as presented in Holmes and Oliver (2000).

As discussed in Section 3.3, Chen and Letchford (2007) verified that the empiric model for the variations of turbulence intensity with height follows the traditional ABL profile, proposed on ASCE 7-98. The turbulence intensity I_{v10} at 10 meters is given by Equation 54.

$$I_v^*(z) = I_{v10} \left(\frac{10}{z} \right)^{1/6} \quad \text{Equation 54}$$

The fluctuating wind portion is the product of its time-varying standard deviation since it is considered a Gaussian process characterized by its power spectral density function/evolutionary power spectral density function evolutionary power spectral density (EPSD) and stochastic filters with white noises as inputs. Chen and Letchford (2004) used the spectrum representation method to obtain the sample functions. This method can be decomposed into a series of sine and cosine random wave forms with random amplitude functions. In Figure 164 a) is shown the simulated downburst wind speed time history at a height of 101.7 m and in b) is show the downburst fluctuation wind speed component for the same simulation.

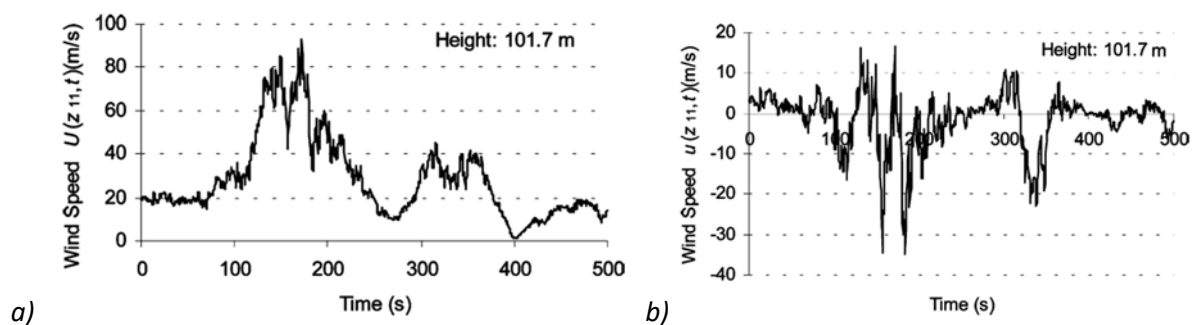


Figure 164. The simulated downburst wind speed time history at a height of 101.7 is shown in a) and in b) is shown the downburst fluctuation wind speed component for the same simulation. Source: Chen and Letchford (2004).

Chen and Letchford (2007) found that the vertical profile $\overline{\Phi}_1(z)$ was a good fit to the profile proposed in Wood and Kwok (1998) for both RFD and Derecho events. The same was not true for the spatial function $\overline{U}_1(t)$, in this case the authors suggested that using Holmes' Model

would present better fit. In Figure 165 are showed the results of the a) spatial function and in b) the vertical profile.

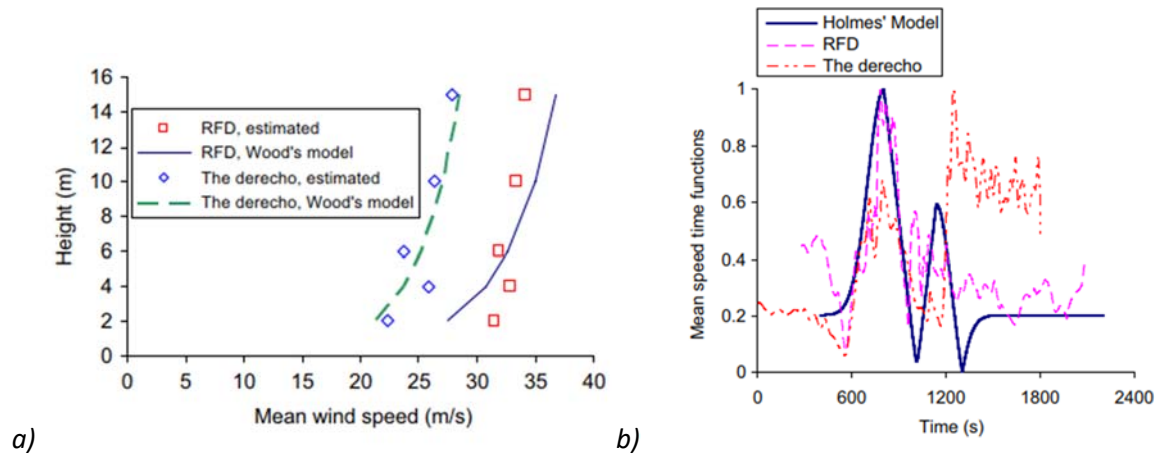


Figure 165. Results of Chen and Letchford' NDESH Model for utilizing a) Wood's vertical profile and b) Holmes's spatial function. Source: Chen and Letchford (2007).

Xu and Hangan (2008)⁷² used the empirical model decomposition (EMD) technique to characterize the non-stationary wind data during a Typhoon event, while the stationary well-behaved fluctuating wind was admitted being a stationary random process with a Gaussian distribution.

Chen and Letchford (2005) used POD technique and described the framework in four steps, named: 1) separating time-varying mean speed and fluctuating speeds through wavelet shrinkage; 2) application of POD to the time-varying means, standard deviations, and normalized fluctuations; 3) select the number of retained modes for the further approximation to a numerical mode; 4) calculation of the vertical velocity and turbulence profiles from the defined numerical model.

Chen (2008) developed a frequency domain analysis of the along-wind tall building response to transient non-stationary winds based on non-stationary random vibration theory. The hybrid model calculates the along-wind loads on building through the approaching winds by using the Strip Theory and considering the unsteady forces characteristics in terms of aerodynamic admittance and joint acceptance functions. The authors provided a quantitative analysis of the time varying mean, evolutionary spectrum, and time varying root-mean-square values of building response.

The results of Chen (2008) were validated against full-scale measurements and showed that the transient nature of these wind speeds generally leads to lower response as the result of the lack of sufficient "build-up time" to reach its steady-state value. It was found with the application of this technique that the downburst wind profile resulted on similar loads on lower buildings, but smaller loads on taller buildings when compared to the traditional ABL Approach, showing how low laying structures are more susceptible to TS wind. Huang and Chen (2009)⁶⁷; Huang *et al.* (2015)⁶⁸ continued developing hybrid-deterministic models utilizing variances of PSD and wavelet transforms.

Nguyen (2012)⁶⁹ proposed a modified version of the deterministic-stochastic model proposed by Chay *et al.* (2006) and Oseguera and Bowles (1988) applied the model to study the effects of these loads to wind turbines. The downburst touchdown locations and directions were relative to the turbine array and were modeled as random variables. The results were validated against full scale measurements from the projects NIMROD and JAWS.

McCullough *et al.* (2014)⁷⁰ proposed to use a variable averaging interval method (VAI) instead of a fixed interval method (FIM) to isolate the constant mean from the fluctuating wind component. In this same experiment, new revisions for gust factor, turbulence intensity, and turbulence integral length scale were defined to validate the new proposed method. This present model results were validated against a hurricane event and the rear-flank downdraft event from the thunderstorms outflow experiment (ORWIG-GAST AND SCHROEDER, 2005). The authors found that the VAI method using the wavelet analysis or empirical mode decomposition can represent the trends in the wind speed and can capture embedded time varying frequencies of the TS wind components, but the interval length continuous to be a parameter chosen by the user a priori. The effectiveness and robustness of VAI schemes are highly improved by increasing higher sampling rates in which measurements are acquired.

Su *et al.* (2015)⁷¹ analyzed the effect in structures for non-stationary winds with the application of three time-varying mean techniques (Kernel regression, discrete wavelet transforms, and empirical mode decomposition). An empirical formula for the maximum frequency in mean wind speed was proposed to determine the probable window size with the structural fundamental frequency. Using two full scale measurements, the evaluation of the derived mean and ensuing fluctuation should be based on three principles: 1) the time-varying

should reflect the trend of the original wind speed dataset; 2) the estimated fluctuation of the EPSD should be physically meaningful, and 3) wind-induced responses should be primarily conservative. The results showed that the discrete wavelet transform, and the empirical mode decomposition are recommended approaches to derive the mean wind speed of downbursts.

C. COMPUTER FLUID DYNAMIC MODELS

Resolving downburst flow by deploying numerical simulation approaches such Computer Fluid Dynamic (CFD) simulation rose significantly in use with the advent of computer processing power. Some advantages of numerical simulation include the capacity of simulating the actual size of the downburst and avoid scale effects (seen normally in experimental laboratory model) and also the capability of creating numerical models capable of simulating the physical (thermodynamic and kinematic) properties of the downbursts. There are three main methods for simulating a downburst using CFD: full-cloud, sub-cloud, or impinging wall jet models.

C.1 Full Cloud Models

Full-cloud models simulate the whole life cycle of the atmosphere, considering thermodynamic and microphysics processes. The first simulations to be developed in 2D and aimed to replicate the behavior of the convective phenomena in the atmosphere through the analysis of the distribution of pressure and density in an adiabatically stratified atmosphere using non-viscous Boussinesq Equations. These models include Ogura and Phillips (1962)⁷³ and Orville (1965)⁷⁴.

Hjelmfelt *et al.* (1989)¹¹⁸ deployed Ogura and Phillips (1962) and Orville (1965) models to validate full-scale measurements from the JAW Project. It was also showed that the outflow structure properties of downbursts resemble numerous features of the laboratory wall jet experiment, such as wind profile, maximum velocities, and radial development, although these same velocities were found to decay much more rapidly in the full-scale measurements than on the wall jet velocities in both experimental and CFD simulation approaches.

As more computational power become available, 3D CFD models started to be developed, including Steiner (1973)⁷⁵, Miller and Pearce (1974)⁷⁶, Clark (1979)⁷⁶ and Straka and Anderson (1993)⁷⁷ which were focused on simulating the storm development and outflow processes, since at time was not widely accepted the existence of downbursts. Knupp (1989)⁷⁸ utilized

the 3D cloud model proposed by Tripoli and Cotton (1982)⁷⁹ and investigated the necessary kinematic, dynamic, and thermodynamic process for the generation of intense downdrafts (microbursts) and less-intense downdrafts (non-microbursts). It was noted that the effects of the humidity and environmental wind shear of the boundary layer for the formation of downbursts, leading to the conclusion that the morphology of downbursts differs significantly from one event to another.

But with the limited computation power available until the 80's smaller scale phenomena such as downburst were impossible to model. With the knowledge of Fujita's finds regarding downbursts in the 80s, consequent increase in computer power, and full-scale measurements becoming available, full-cloud downburst models started to be ramp-up. Proctor (1987)⁸⁰ developed a model called Terminal Area Simulation System (TASS) capable of simulating various convective induced winds, including downbursts, tornadoes, and gust fronts. This 3D model was non-hydrostatic, non-stationary, and fluid was compressible.

Proctor (1987) model received a lot of attention since it parametrized water at different states, allowing to capture the effects because of the change of phases and solving numerically microphysical interactions. Turbulence scales greater than the solution grid size were explicitly simulated and smaller scale turbulence were parameterized by a first order of closure. Surface stresses were function of stratification, the mesh was free to translate, plus effects of the soil roughness and storm translation were taken into account. Knupp (1985) and Straka and Anderson (1993) continued working towards the development of the TASS Model.

Nicholls *et al.* (1993) proposed a 2D model called the Colorado State University–Regional Atmospheric Modeling System (CSU-RAMS). This model contained a full set of non-hydrodynamics compressible dynamic equations for water and ice-phases clouds and precipitation. This was the first attempt to use Large Eddy Simulation (LES) to simulate a thunderstorm producing a microburst. In this model, the thermal current within the developing mixed layer reaches the lifting condensation level and latent heat is released. Consequently, a downburst is produced due to the condensation of this parcel of air beneath the melting level within the cloud. The produced downdraft was simulated over a surface with modeled buildings to understand how the built environment affects the vertical profile.

Nicholls *et al.* (1993)⁸¹ experiments showed the impact of the downburst flow to structures by analyzing the generated eddies because of the separation surface layer and the effects of the surface friction to the wind profile. The authors concluded that the CFD simulation was able to successfully reproduce the full-scale downburst characteristics and recommended to further develop the downburst models in 3D. In Figure 166 is shown the two-way grids created by Nicholls *et al.* (1993) for two different scales. In a) and c) at two different scales the perturbations to the streamlines due to the buildings in b) and d) the same is shown this time for the pressure field.

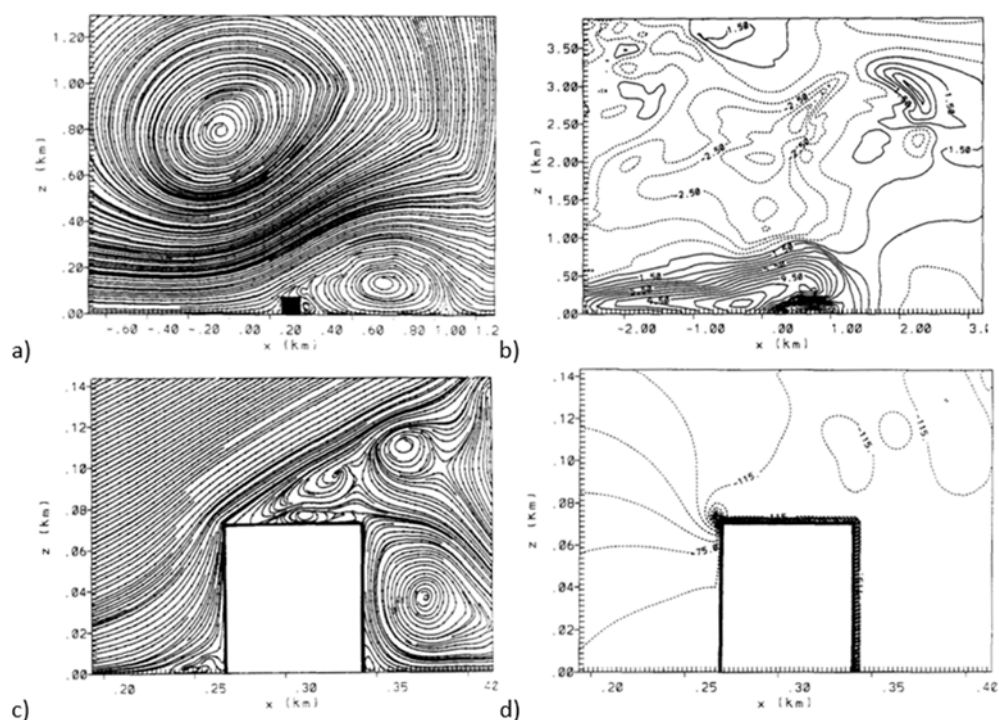


Figure 166. Outputs of Nicholls *et al.* (1993) LES model a) and c) streamlines outflows and b) and d) pressure perturbations over a building. Source: Nicholls *et al.* (1993).

Bryan and Fritsch (2002)⁸² developed the Bryan Cloud Model Version 13 (CM1) which is a 3D meteorological model that simulates the convective activity at all levels atmosphere, therefore could also serve to study the interactions of downburst winds in the scale of interest of the wind engineering. The model runs on top of massive parallel computer architecture and is flexible enough to simulate the cooling source component for either dry or wet downburst. The CM1 model includes the parametrization hydrometeors microphysics and it is a non-hydrostatic model, which allows the modeling of realistic vertical simulations by solving the vertical moment equation and successfully resolving small-scale mesoscale circulation.

Orf *et al.* (2012)⁸³ made significant advances to understand downburst wind profiles using the full cloud CM1 Model and analyzing their effects in transmission lines, joining capabilities of mesoscale meteorological models (MMM) and computational wind engineering (CWE) models. In Figure 167 is shown a picture of a complete downburst experiment causing by a completely simulated thunderstorm event.

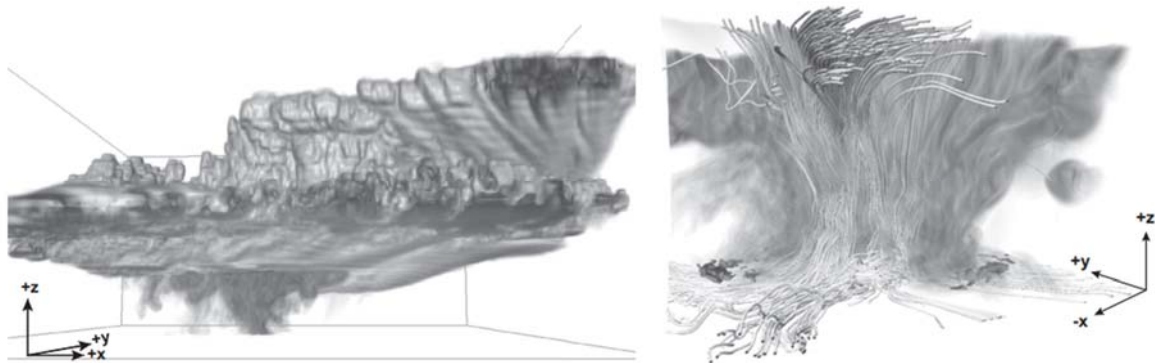


Figure 167. CM1 Model 3D volume rendering of a) a cloud developing a downburst and b) isopleths of enclosed horizontal streamline winds exceeding 25 m/s. Source: Orf *et al.* (2012).

The authors compared the results obtained with the CM1 to the impinging wall-jet and cooling source models and concluded that simplified methods do not reproduce all the complexity of downburst environments – as full-cloud CFD models do – and this fact would lead to errors, especially for structural analysis. Although, some of the results of this research showed that the well established linear relationship between circumferentially radial velocity development and peak radial velocities can successfully help modeling downburst peak winds on structures. Additionally, Yamada and Koike (2011)¹²⁰ acknowledge that even currently computational power burdens to generate these simulations are enormous and simplified models are still needed specially for practical applications to study downbursts and structures interactions.

C.2 Sub-Cloud Models

Sub-cloud models are also called cooling source models. These models focus on the dynamics of the downdrafts below the cloud base, simulating the downburst outflow without reproducing the physic processes within the cloud that generate it. Instead, these sub-cloud models simulate only the downburst downdrafts currents, using negatively buoyant cooling sources and – in some cases – the rain evaporation, which gives rise to a cold downdraft. This method tends to be less precise than the full cloud models, but present the improved

computational performance which makes them more easily replicable in practice (KIM E HANGAN, 2007),

This concept was first introduced by Mitchell and Hovermale (1977)⁸⁴ who developed the first non-hydrostatic, two-dimensional (2D) numerical model capable of simulate the negatively buoyant air produced by evaporation through local-cooling. Later on, Srivastava (1985, 1987)^{85,86} presented a simple one-dimensional time-dependent model and applied to the study of downbursts making great advancements to the study of the phenomenon. For instance, it was found that the intensity of the downdraft 1) increased with lapse rate for ambient temperature; 2) increased with the concentration of precipitation; 3) increased with the relative humidity of the environment; and 4) decreased with the mixing ratio of the environment. Srivastava's model only considered precipitation in the form of rain and since it is a one-dimensional model, could not solve the outflow structure or intensity.

These models were fundamental to study the characteristics of downbursts, for instance Srivastava (1987) found using sub-cloud models that 1) precipitation in form of ice increases the intensity of the downdraft; 2) dry and wet microbursts can occur under unstable lapses rate, but the more stable it gets, more wet downbursts with substantial ice precipitation may occur. Also, Krueger *et al.* (1986) focused on investigating the dynamics of the downdraft below cloud base and simulation of the microburst outflow.

Droegemeier and Wilhelmson (1987)⁸⁷ proposed a simplified version of TASS Program's model as a 2D numerical model that simulated thunderstorms outflow, imposing a controlled horizontal flow of cold air entering the computational domain through the contour.

Proctor (1988, 1989)^{89,90} also proposed a simplified version of TASS Program's model (previously discussed) by assigning a distribution of the precipitation at the top boundary and allowing it to fall within the domain. In these experiments was found that the intensity of a microburst depends on the vertical distribution of temperature and humidity and distribution and duration of precipitation. It was shown that particles in the form of snowflakes are more efficient in producing microbursts, since the sublimation of these particles is more effective because of their expressive lower density. Snow particles readily sublimate skipping the melting process when they are injected to a colder and drier layer of air. In this scenario, the latent heat of sublimation that is absorbed in the process is higher than either the latent heat

absorbed by melting or evaporating. The sublimation cooling takes place at higher altitude within the deep adiabatic layer, allowing the acceleration of the downward parcel of air. Proctor (1988, 1989) finds in cloud's agree microphysics cloud theories of Fujita.

Anderson *et al.* (1992)⁹¹ used the massive parallel computation model Wisconsin Model Engine (WME) to simulate full and sub-cloud downburst models to show the applicability of such apparatus for the development in understanding different geophysics problems. In this experiment was studied two colliding downbursts and the effects of the resulting flow by utilizing a sub-cloud 3D model. The finds showed how this phenomenon can create a region of violent and complicated dynamics that only CFD models can correctly describe. Figure 168 shows 3D renderings of the phenomena at different time steps in the 2km grid. The experiment was improved and repeated by Orf *et al.* (1996)⁹² and Orf and Anderson (1999)⁹³.

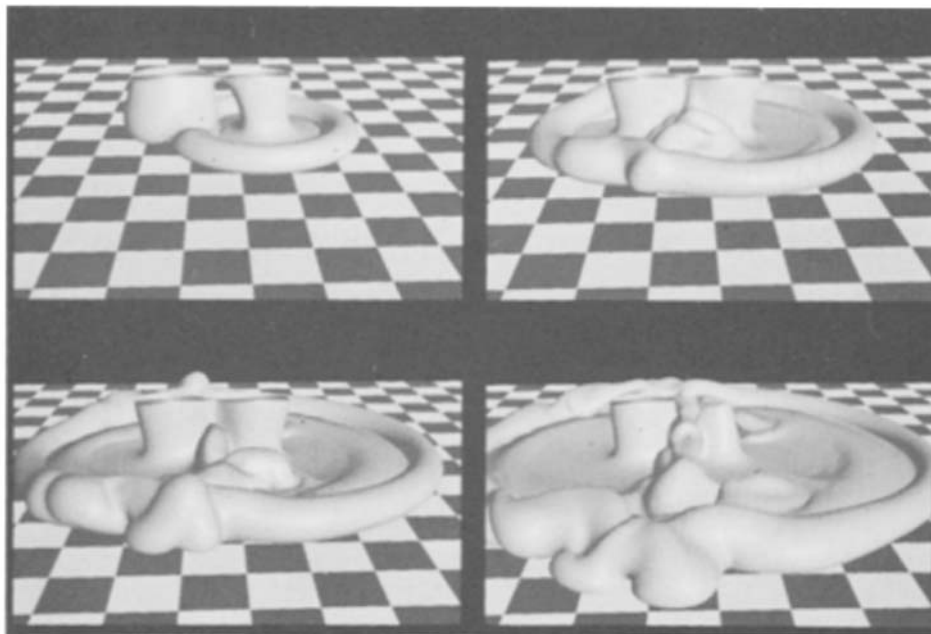


Figure 168. 3D renderings of the two colliding downbursts at different time steps in the 2km grid.
Source: Anderson *et al.* (1992).

Mason *et al.* (2009, 2010)^{94,95} focused on understanding the flow dynamics of intense and idealized downbursts using an axisymmetric, dry, non-hydrostatic thermodynamically forced numerical sub-cloud model. The model was implemented within the commercially available package ANSYS CFX11. The turbulence model used an Adaptive Scale Simulation (SAS) method, which was an improved unsteady Reynolds Averaged Navier-Stokes (URANS) method. Also, LES model was deployed to solve unsteady regions of the flow field. In this

model, vortex ring characteristics from the downburst were clearly modeled along with a secondary counter-vortex ring leading to the edge of the divergent front. The results show a good fit to experiments and full-scale measurements.

Mason *et al.* (2010) showed how the environment conditions influence the resulting downburst outflow wind. In translational downbursts, it is found an increase in speed for the forward propagation side. Topographic effects have some effect on the vertical wind profile of the downburst. The analysis in structures showed that not considering the drag effects of downbursts to mid- and high-rise structures leads to an unconservative design from an ultimate loading standpoint.

In Figure 169, the velocities of different experiments were normalized to their respective maximum values against the horizontal distance from the center of the downdraft. In the same Figure was added the range of results data obtained during the Project JAWS. It was observed agreement for all the models in lower level until it reaches peak values, but the same is not observed for higher levels. Mason *et al.* (2009, 2010) highlighted the need to acquire more full-scale measurements of downbursts for the validation of models specially with improved resolution at lower levels, since much of the existing of downburst profiles were at the time obtained from radar and mostly for aeronautical application, giving less importance to lower atmospheric levels.

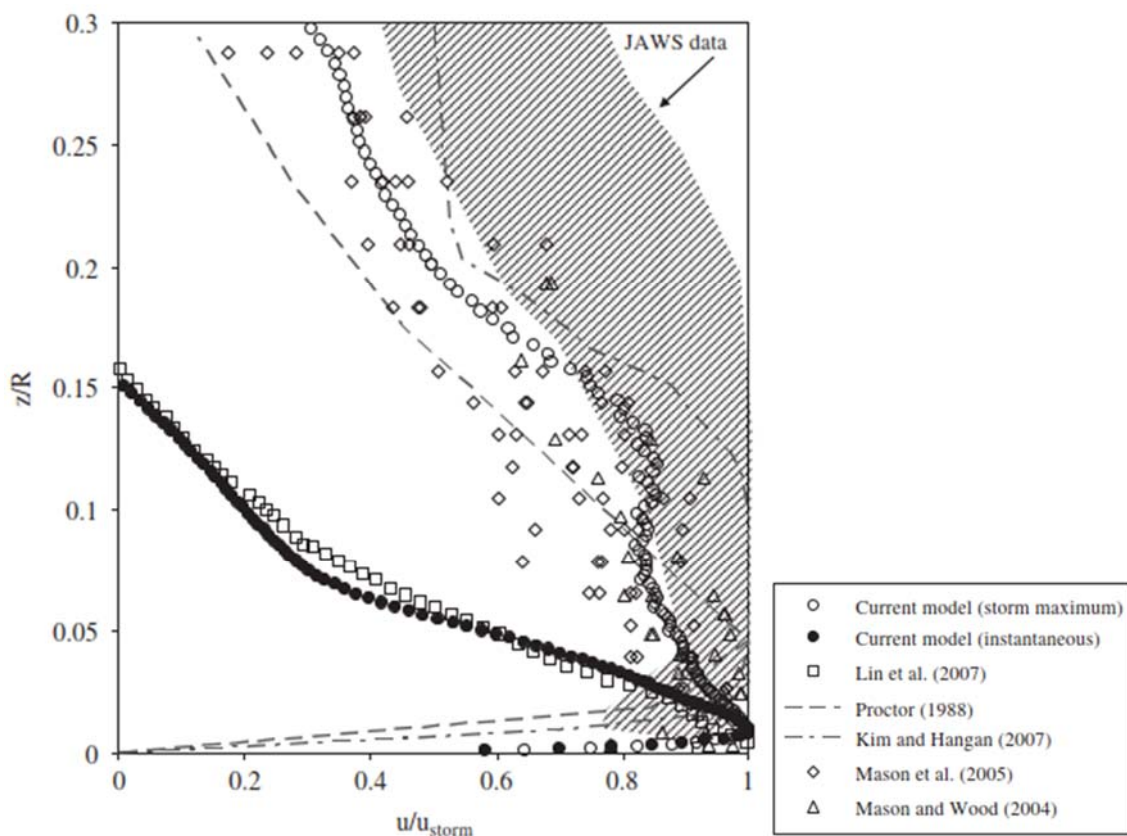


Figure 169. Comparison of results from Mason *et al.* (2009, 2010) to other experiments and full-scale measurements from the JAWS experiment. Source: Mason *et al.* (2009; 2010).

Vermeire *et al.* (2011a)⁹⁶ utilized cooling source model of Anderson *et al.* (1992) to simulate downbursts occurring isolated and as in-line. The results obtained were then compared to full scale measurements from the JAWS project, along with earlier experiments. LES showed to be more efficient than URANS (MASON *et al.*, 2009) to correctly simulate the maximum velocity near-surface. Vermeire *et al.* (2011a) also showed that downburst collisions can present an amplification factor of 1.55 and there are significantly more chances (up to 70%) for a building being subject to in-line downbursts.

C. 3 Impinging Wall Jet Models

Another type of CFD simulation includes the numerical replication of impinging wall jet laboratory tests. Similarly, to sub-cloud models or cooling source models, impinging wall jet models do not replicate all the effects within the cloud, but in this case, instead of they create a downwards jet thermodynamically, the jet is created mechanically aiming to reproduce the near-surface winds.

Selvam and Holmes (1992)⁹⁸ used a 2D model to simulate a downdraft current as an incompressible jet or air perpendicular to a surface. This model was based on the Navier-Stokes equations and the turbulence was resolved by deploying a κ - ϵ model. The results obtained reasonably matched Bakke's laboratory tests and Fujita's observations, but they showed some differences from the TASS program (PROCTOR, 1988).

Wood *et al.* (2001) used the commercial package ANSYS CFX4 package to numerically simulate an impinging wall jet and compare results to a laboratory experiment (discussed in item 6.1.1). This software package is based on the Navier-Stokes equations and two used the κ - ϵ and the differential second-moment (DSM) models to solve the turbulence. The DSM turbulence model was preferred since such model is better for simulating anisotropic flows, in which properties change depending the direction of analysis. Wood *et al.* (2001) analyzed the effects of a crest or embankment to the profile of a downburst, and even though results have shown similar speed-up coefficients, it was also found the effect dropped off behind the crest quicker compared to the ABL flow. Based on the CFD results and the accompanying experimental test, an equation that describes the mean velocity profile of the downbursts generated was obtained. In general terms, it was found that stabilization of the maximum wind profile occurs after 1.5 jet diameter, reaching its peak after 2 jet diameters.

Shehata *et al.* (2005) used an impinging wall jet numerical model to simulate the effects of a steady downburst outflow to transmission towers. The model was carried out using the commercial software Fluent 6.0, which application for downburst modeling was previously validated in Hangan *et al.* (2003) *apud* Shehata *et al.* (2005), whom also developed an experimental program to compare the numerical results to.

The schematic of the computational domain used in such a simulation is presented in Figure 170, in which the D_{jm} is the jet diameter and r_m and Z_m are the coordinates of the jet flow in the radial and axial directions, respectively. The dimensions H_T and B are the parameters that defined the location of the pressure outlet and were summed to be $H_T = 7D_{jm}$ and $Z_m = 9D_{jm}$, and H is the height of the jet exit.

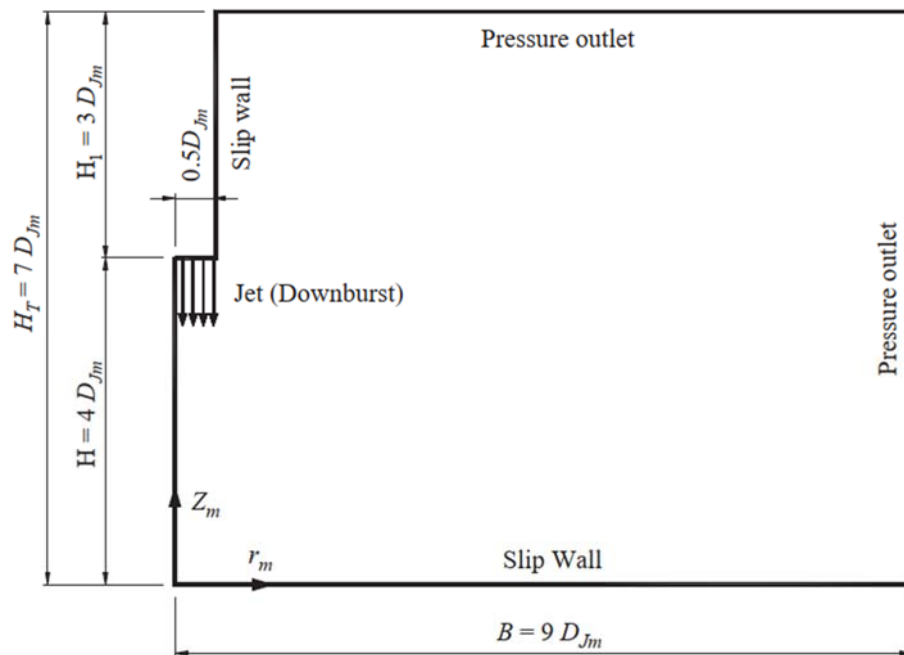


Figure 170. Schematic of the computational domain used for the CFD simulation. Source: Shehata *et al.* (2005).

Shehata *et al.* (2005)⁹⁹ found that loads in structures due to downbursts are greatly affected, depending on the touchdown distance and the angle in which winds reach the structure. Also, the peak values of the axial forces associated with the downburst exceed those because of normal wind load by a percentage ranging between 9.0% and 304%.

Chay *et al.* (2006)¹⁰⁰ looked to understand the influence of a downburst of translational velocity and the variation in intensity as the events mature and decay. In this experiment, the CFD package FLUENT 6.0 was also used to perform simulations and the turbulence was obtained with the autoregressive moving average (ARMA). The results were confirmed against downburst simulations at the Texas Tech University (TTU) downburst wind tunnel. The jet was simulated using different geometries, velocities, and time scale. In Figure 171, a) are presented vectors coming out from a numerically simulated jet impinging a flat surface and in b) is shown one profile for a radio jet diameter of maximum velocities compared to an empirically tested downburst at TTU.

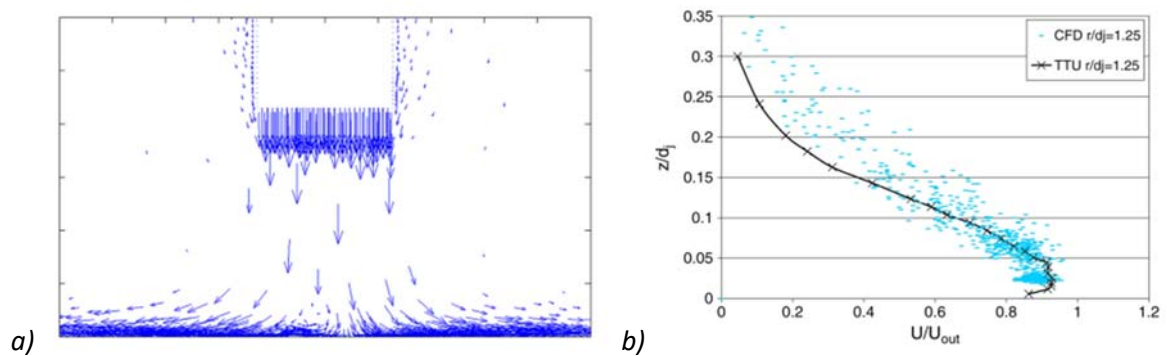


Figure 171. In a) are presented vectors coming out from a numerically simulated jet impinging a flat surface. In b) is shown one of the profiles for a radio jet diameter and maximum velocities ratio of an empirically tested downburst at TTU. Source: Chay et al. (2006).

Kim and Hangan (2007)¹⁰¹ utilized the same domain and setup for further developed URANS models, in which a flow sample is showed in Figure 170 to simulate an impinging jet downburst. The study focused on analyzing the direct dependency of Reynolds Number and the flow's unsteady separation-reattachment of the boundary layer. The scale dependency becomes less pronounced towards higher Reynolds numbers and an asymptotic behavior for wind speed is expected, with the surface roughness becoming the dominant parameter at large scales. In Figure 172 is shown the vorticity and vector snapshots of vortex-ring and the secondary vortex evolution at the non-dimensional time step $T=12.8$, for a) $RE=20,000$ and b) $RE=100,000$. Note that the higher the RE , the more expressive asymptotic behavior of the vortex (getting closer to the x-axis, but never touching it).

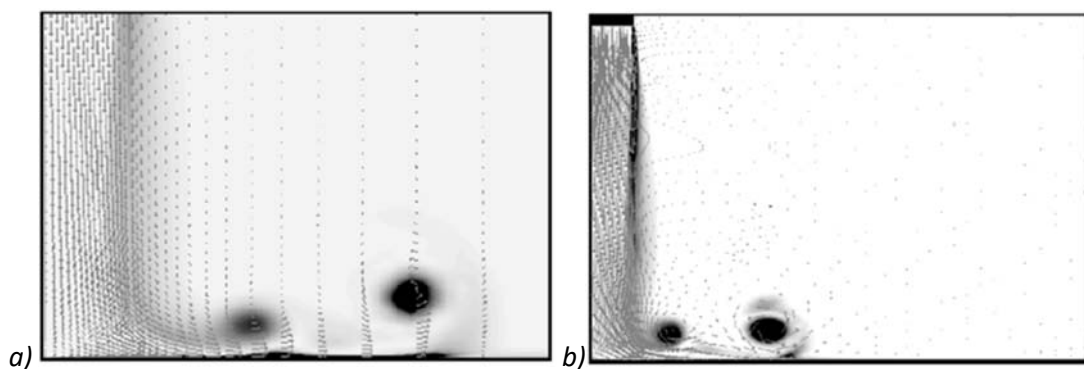


Figure 172. Vorticity and vector snapshots of vortex-ring and secondary vortex evolution at the non-dimensional time step $T=12.8$, for a) $RE=20,000$ and b) $RE=100,000$. Source: Kim and Hangan (2007).

Sengupta and Sarkar (2008)¹⁰³ focused on comparing different turbulence models, namely $\kappa-\epsilon$ standard, RNG $\kappa-\epsilon$, Realizable $\kappa-\epsilon$, SST $\kappa-\omega$, RMS, and LES (SOLARI, 2020). In this study, the velocity profile was formulated as shown in Equation 55.

$$\frac{U_{r,\max}}{V_{\text{inl}}} = \exp \left[\left(1.095 - \frac{1.858}{\frac{r}{D}} - 1.949 \ln \left(\frac{r}{D} \right) \right) \right] \quad \text{Equation 55}$$

Where $U_{r,\max}$ is the maximum horizontal wind speed at different radial locations and at the inlet. Also, D and r are the diameter of the downburst and radius to the jet axisymmetric axis.

Darwish *et al.* (2010)¹⁰³ used a 2D consistent curved frame element CFD model to study the effects of downburst-like winds in transmission conductors. The focus of this study was to include the turbulent component in the analysis, since it has been shown that turbulence magnifies the response of those components due to combined effects of the fluctuating and resonant components. The dynamic effects of TS winds in conductors are more important than in other structures, since they typically have larger fundamental frequency that is closer to the dominant periods of the turbulent component of thunderstorm outflows.

It was found that the structural response of the conductors due to the downburst generated increase significant with the increase in turbulence. Furthermore, due to the aerodynamic damping, the background component plays a key role in the quantification of the resonant component (turbulence). Hence, the quasi-static analysis is sufficient in assessing the effects of turbulence in conductors.

Vermeire *et al.* (2011b)⁹⁷ used LES to study the influence of the roughness to the flow in several downburst events, comparing the results of sub-cloud simulations to full-scale observations. It was shown in this experiment that impinging jet was not capable of capturing outflows features predicted by the cooling source method, deviating up to 56% from the cooling source (sub-cloud) model results.

Zhang *et al.* (2013a)¹⁰⁴ modeled a transient impinging jet approach at the steady impinging jet flow simulator in the Wind Simulator and Testing (WiST) Laboratory the Iowa State University. The results were compared to a cooling source axisymmetric model based on URANS and run on ANSYS FLUENT 12.1. Their finds showed that both models resemble the dynamic features of a downburst, but the cooling source model was capable of better representing the maximum radial velocity profile. Other fundamental differences were found in the generation of the outflow vortex rings, for instance, for the cooling source method, the primary vortex was found to be generated only after the cooled air descended to the ground, dominated by gravity currents, then denser air was found to roll up forming the primary vortex at the leading

edge of the outflow. Hence, in the transient impinging jet experiment, several vortices formed continuously defined by strong instability in the shear layer.

Aboshosha *et al.* (2015)¹⁰⁵ used ANSYS FLUENT 13.0 LES model to analyze the effect of the roughness on the maximum radial and envelope peak velocities. It was found that the exposure to the profile to increased roughness would cause to decrease the maximum velocity, shifting the profile peak upwards. This effect is clear in Figure 173, which shows the effects of the roughness on the instantaneous and envelope peak radial velocity profiles.

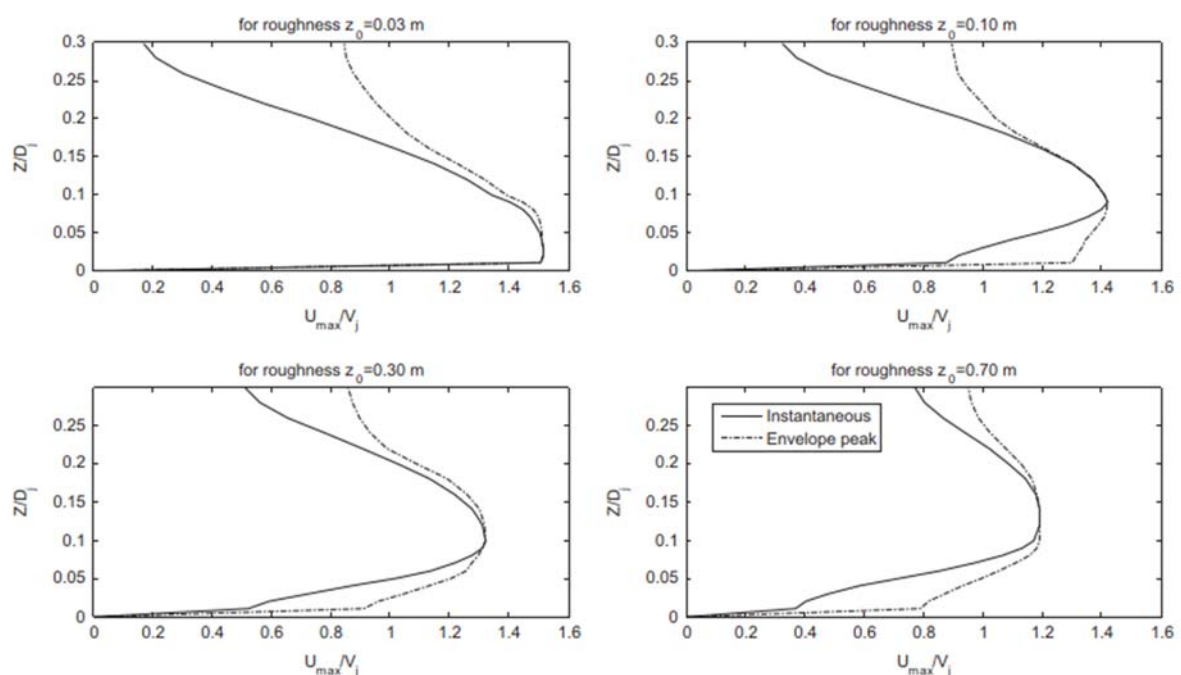


Figure 173. Effects of the roughness to the instantaneous and envelope peak radial velocity profiles. Source: Aboshosha *et al.* (2015).

Oreskovic and Savory (2018)¹⁰⁶ questioned the validity of simpler impinging wall jet models and sub-cloud models and compared the outputs from a full-cloud Bryan Cloud Model to a simplified, axisymmetric, downburst sub cloud model, which is density-driven, and based on URANS simulations with κ - ω turbulence closure the full-scale. It was found that simpler models struggle to simulate the non-linear relationship between the source due to the density perturbation in the cloud and the strength of the outflows near-ground. The authors concluded that advanced full-cloud models can provide the initial solution guide the development of more simplified CFD models in the attempt to bring these studies to the common engineering practice. Skote *et al.* (2018)¹⁰⁷ compared outputs from URANS and RANS

models and showed results of both approaches to be consistent with full-scale measurement when simulating downburst outflows.

D. DATA-DRIVEN MODELS

Data-driven downburst models aim to simulate the time-frequency domain of the entire non-stationary wind. In this case the deterministic and stochastic components are not treated separately, similarly to what is done in the NDESH Models. In this session is briefly discussed some of the most recent advances in data-driven methods for the simulation of downbursts, although it is not within the scope of this work to apply such concepts for the development of the proposed model in the Chapter 4.

Kareem (2006)¹⁰⁸ introduced the concept of numerical modeling of wind from a probabilistic perspective and discussed the wide range of simulation stochastic methods to deal with non-stationary natural phenomena. These methods usually include Monte Carlo based approaches that incorporate model simulations or information derived from observed data. The scope of the simulation cases discussed are within the application of univariate to multi-variate processes of unidimensional and multi-dimensional fields (Gaussian or non-Gaussian) mostly applied to the study of wind loads to long-span bridges.

Later, Wang (2008)¹⁰⁹ applied the concept for non-stationary transient events such as extreme winds and earthquakes. Considering the impact to structures due to extreme winds events loads, which have expressive temporal variation in frequency (especially in the inelastic range). By utilizing Hilbert and wavelets transforms, these events are modeled in the time-frequency domain framework. The results were validated against full-scale measurements and other simulation methods, resulting in the formulation of a web-based Monte Carlo simulation tool to calculate structural response and reliability analysis to transient environmental loads.

Wang *et al.* (2013, 2014)^{110,111} studied the evolutionary behavior of downbursts in the time-frequency domain using stationary wavelet transform and Hilbert transform. The stationary wavelet transform decomposes a sample of a multi-component non-stationary random processes into a set of mono-components signals, which are subsequently transformed into analytic signals with the Hilbert transform, allowing to obtain instantaneous amplitudes and frequencies of the downburst signal without the need of making customary assumptions of stationary pieces of the signal or adoption of parametric models (as seen in NDESH). The multi-

resolution decomposition of the signal through the stationary wavelet transform is given by Equation 56:

$$x(t) = \sum_{j=1}^M D_j(t) + A_M(t) \quad \text{Equation 56}$$

Where, $D_j(t)$ denotes the detail function level j , M represents the total number of decomposition levels, and $A_M(t)$ is the approximation function, which represents the trend of $x(t)$. In Figure 174 is shown the application of the stationary wavelet transform to process the RFD data from the 2002 thunderstorms outflow experiment (ORWIG AND SCHROEDER, 2007), where in a) is shown the original full-scale measured data; b) is shown the stationary decomposition approximation function and c) the flow for different detail coefficient levels of the record.

The result obtained from the application of the method above was a multi-component, non-stationary process, decomposed into the summation of mono-component processes. The Hilbert transform was then applied at each level to obtain the instantaneous amplitude $a_j(t)$ and frequency $\omega_j(t)$ for each frequency band, as shown in Equation 57:

$$x(t) = \text{Re} \left[\sum_{j=1}^M a_j(t) e^{i \int \omega_j(t) dt} \right] + A_M(t) \quad \text{Equation 57}$$

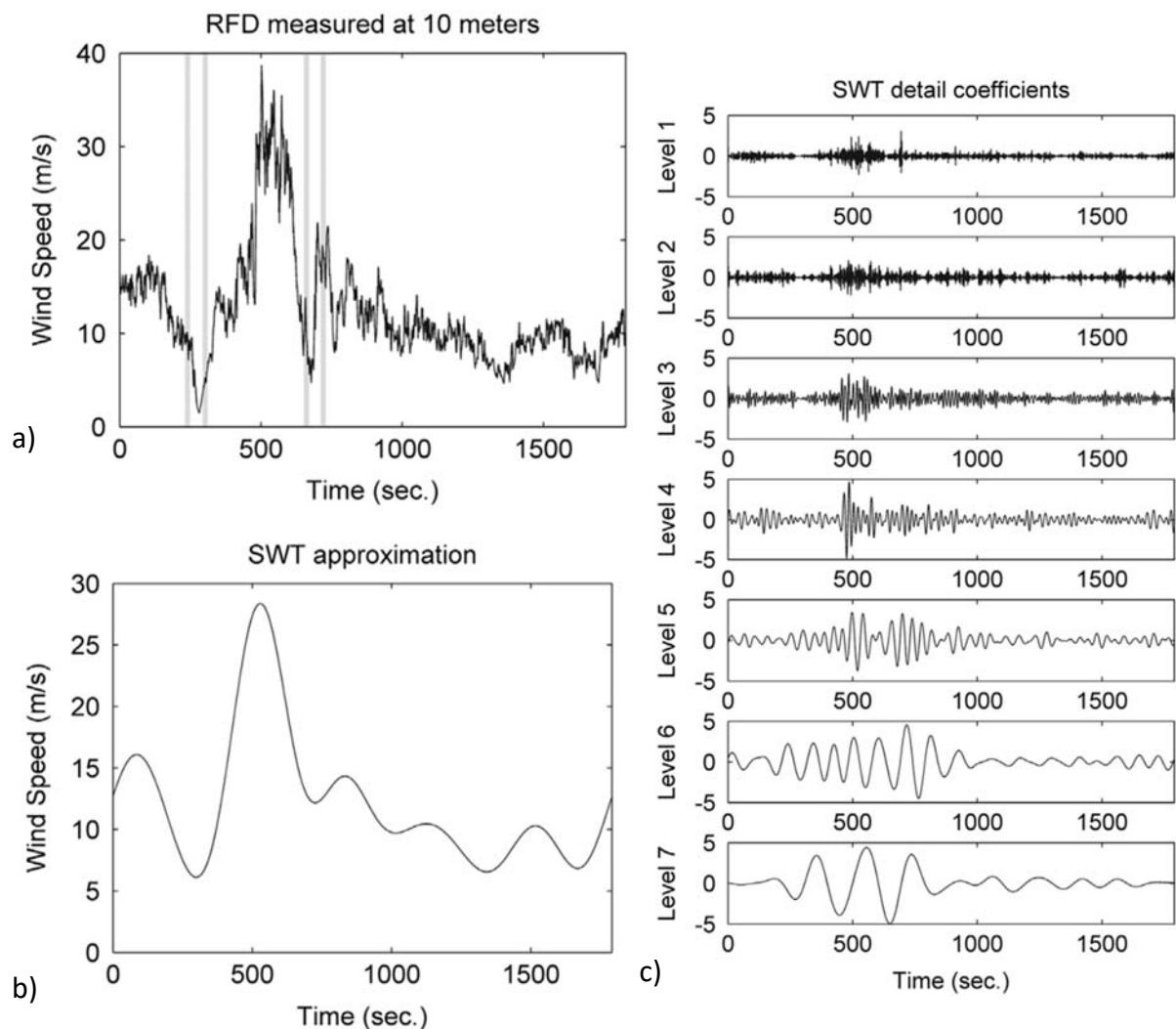


Figure 174. Application of the stationary wavelet transform to process the RFD data, where in a) is shown the original full-scale measured data; b) is shown the stationary decomposition approximation function and c) for different detail coefficient levels. Source: Orwig and Schroeder (2007).

The results were compared to numerical (CFD) simulations and have showed that the probabilistic simulation method chosen captures the evolutionary energy characteristics of the non-stationary process in time and space without stationary assumptions, modulation functions, or spectral expressions as previously seen in other models.

Huang (2014)¹¹² proposed a hybrid simulation method that involves the spectral decomposition via Fourier transform of wavelets and spectral representation method (SRM), making this process more straightforward and efficient than utilizing the Fast Fourier Transform (FFT). The results showed greater performance for scalar and vector-valued processes with real coherence functions, such as the wind speeds, in which simulation points

are close and wave passage effect may be neglected. This method was then advanced by Xu *et al.* (2014)¹¹³ *apud* Solari (2020).

Huang *et al.* (2015)¹¹⁴ utilized discrete wavelet transform and kernel regression methods to obtain the time-varying mean and variance of a non-stationary wind record. These records are examined with the application of the EPSD. The results showed that spectral variations in non-stationary wind fluctuations are relatively weak, meaning that these non-stationary fluctuations can be modeled as uniformly modulated processes.

Kwon and Kareem (2009, 2019)^{115,116} introduced a model-based and data-driven technique to deal with non-stationary winds both in the mean and standard deviation of wind fluctuation named gust-front factor. In this effort the author went a step ahead not only proposing a model for the non-stationary winds, but also presenting a solution in a code format to analyzing the effect in structures in a comparable way it has been done in codes and standards world-wide for the treatment of ABL wind. In this attempt, it included not only analytical dynamic load effects associated with gust front winds in structures, but also considered the conventional gust loading factor.

Kwon and Kareem (2009, 2019)^{115,116} presented the relationships showed in Figure 175. The conventional gust-front factor (as in ASCE 7) becomes a special case of the proposed scheme as the gust-front factor (G_{G-F}) and velocity pressure coefficient ($K_{z,G-F}$) are reduced to unity values. In the cases studied by Kwon and Kareem (2009, 2019) as a result of the gust-front winds, a higher local equivalent static wind loads distribution exists despite the fact that the dynamic effects (I_2, I_3, I_4) for the buildings analyzed were less than unity value. This find underscored the role of enhancement in the kinematic effects introduced through the kinematic effect factor I_1 and velocity pressure coefficient ($K_{z,G-F}$) for the overall design even though dynamic effects were not prevalent in studied examples.

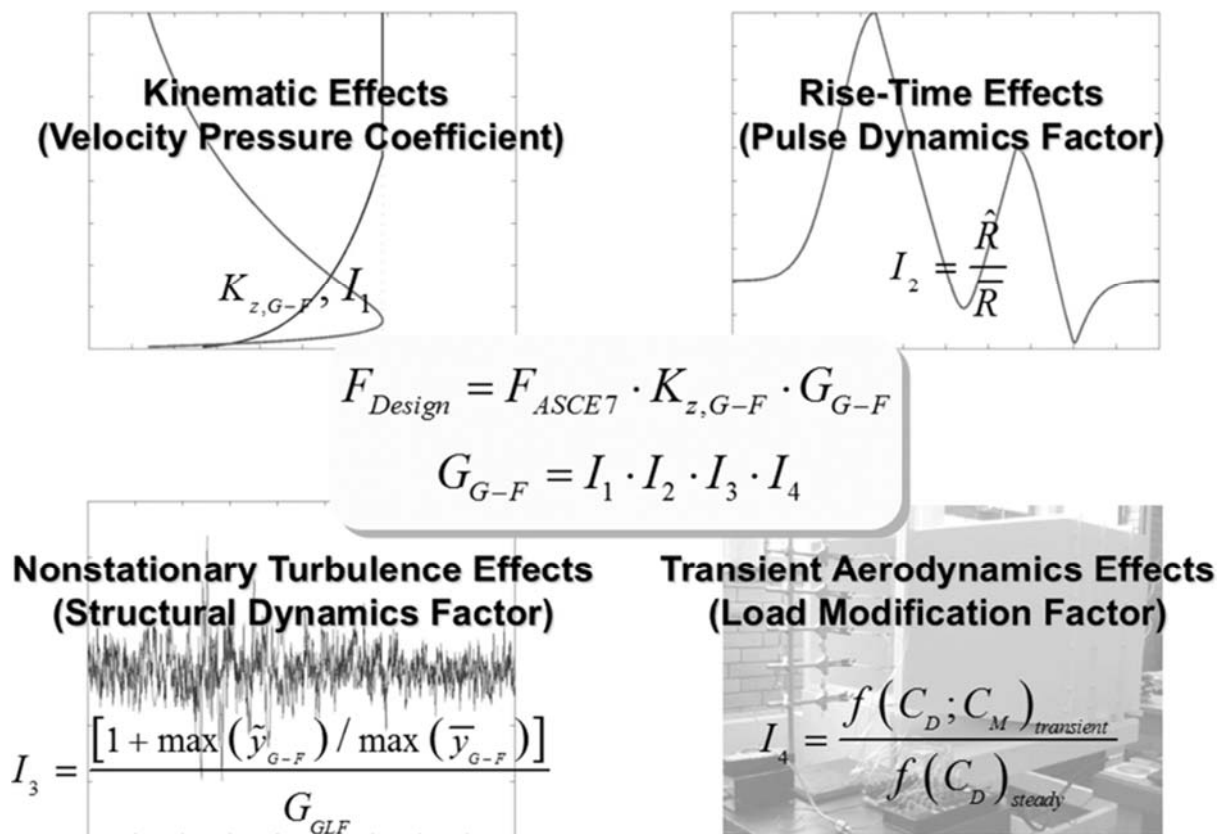


Figure 175. Schematic diagram of the new gust front factor framework proposed by Kwon and Kareem (2009). Source: Kwon and Kareem (2019).

This solution was presented in a simplified and web-enabled framework format, which helps designs to easily estimate wind load effects. This is an example of an interactive process based on the idea of “design thinking” proposed to enhance the resilience of the built environment to thunderstorm winds by providing a “simpler” tool for the development of non-stationary load analysis in structures. This tool can be accessed through the following link http://gff.ce.nd.edu/int_gff.html (KWON AND KAREEM, 2021).

Solari *et al.* (2017)¹¹⁷ utilized records from the European projects “Wind and Ports” and “Wind, Ports, and Sea” to evaluate the statistical properties of thunderstorms outflows and develop a wind-excited structures response procedure upon the evaluation of response spectrum technique similarly to what is used to in seismic loading analysis. The process developed was applied to three different slender structures and aimed to generate artificial time-histories of aerodynamic wind loading and to determine the wind-excited response of these structures by time domain-integration of the equation motions.

The process consisted of dividing the wind field into five groups according to their distinct inherent sources of randomness. These groups are: 1) those related to the wind velocity scaling have a suitable return period; 2) those related to the vertical profile of wind velocity are resolved with a parametric analysis; 3) those related to the evaluation of the wind velocity are represented by a set of full-scale measure records; 4) the mean value of turbulence intensity and gust factor are dealt through a conventional choice based on measurements; 5) Monte Carlo algorithm is applied to simulate those related fields related to the random space-time variation of the atmospheric turbulence by applying fast Fourier Transform and proper orthogonal decomposition.

E. SUMMARY TABLE - EXISTIG MODELING EFFORTS ON THUNDERSTORM WIND OUTFLOWS

ID	MODEL TYPE	AUTHOR(S)	MODEL CHARACTERISTICS	TITLE
1	Laboratory Tests	Middleton (1966)	Ad hoc Facilities: Fluid Release, Stationary/Quasi-steady	Experiments on density and turbidity currents: I. motion of the head.
2	Laboratory Tests	Simpson (1969)	Ad hoc Facilities: Fluid Release, Stationary/Quasi-steady	A comparison between laboratory and atmospheric density currents
3	Laboratory Tests	Simpson (1972)	Ad hoc Facilities: Fluid Release, Stationary/Quasi-steady	Effects of the lower boundary on the head of a gravity current
4	Laboratory Tests	Charba (1974)	Ad hoc Facilities: Fluid Release, Stationary/Quasi-steady	Application of gravity current model to analysis of squall-line gust front
5	Laboratory Tests	Landreth and Adrian (1990)	Ad hoc Facilities: Impinging Wall Jet, Stationary/Quasi-steady	Impingement of a low Reynolds number turbulent circular jet onto a flat plate at normal incidence
6	Laboratory Tests	Lundgren <i>et al.</i> (1992)	Ad hoc Facilities: Fluid Release, Stationary/Quasi-steady	Microburst modelling and scaling
7	Laboratory Tests	Yao and Lundgren (1996)	Ad hoc Facilities: Fluid Release	Experimental investigation of microbursts
8	Laboratory Tests	Alahyari and Longmire (1994)	Ad hoc Facilities: Fluid Release	Particle image velocimetry in a variable density flow: application to a dynamically evolving microburst
9	Laboratory Tests	Blakke (1957)	Ad hoc Facilities: Impinging Wall Jet, Stationary/Quasi-steady	An experimental investigation of a wall jet
10	Laboratory Tests	Chun and Schwarz 1967	Ad hoc Facilities: Impinging Wall Jet	Stability of the plane incompressible viscous wall jet subjected to small disturbances
11	Laboratory Tests	Poreh <i>et al.</i> (1967)	Ad hoc Facilities: Impinging Wall Jet, Stationary/Quasi-steady	Investigation of a turbulent radial wall jet
12	Laboratory Tests	Donaldson and Snedeker (1971)	Ad hoc Facilities: Impinging Wall Jet, Stationary/Quasi-steady	A study of free jet impingement. Part 1. Mean properties of free and impinging jets

13	Laboratory Tests	Launder and Rodi (1983)	Ad hoc Facilities: Impinging Wall Jet, Stationary/Quasi-steady	The turbulent wall jet measurements and modeling
14	Laboratory Tests	Cooper <i>et al.</i> (1993)	Ad hoc Facilities: Impinging Wall Jet	Impinging jet studies for turbulence model assessment-I. Flow-field experiments
15	Laboratory Tests	Didden and Ho (1985)	Ad hoc Facilities: Impinging Wall Jet, Stationary/Quasi-steady	Unsteady separation in a boundary layer produced by an impinging jet
16	Laboratory Tests	Holmes (1992)	Ad hoc Facilities: Impinging Wall Jet, Stationary/Quasi-steady	Physical modelling of thunderstorm downdrafts by wind tunnel jet
17	Analytical Model, CFD Simulations, Laboratory Tests	Wood <i>et al.</i> (2001)	Ad hoc Facilities: Impinging Wall Jet, CFD Model Type: Impinging Wall Jet, Stationary/Quasi-steady, Turbulence Model: κ - ϵ standard	Physical and numerical modelling of thunderstorm downbursts
18	Analytical Model, Laboratory Test	Wood and Kwok (1998)	Classic: Impinging Wall Jet	An empirically derived estimate for the mean velocity profile of a thunderstorm downburst
19	Laboratory Tests	Letchford <i>et al.</i> (2002)	Ad hoc Facilities: Impinging Wall Jet, Stationary/Quasi-steady	Thunderstorms—their importance in wind engineering, a case for the next generation wind tunnel
20	Laboratory Tests	Chay and Letchford (2002)	Ad hoc Facilities: Impinging Wall Jet, Stationary/Quasi-steady	Pressure distributions on a cube in a simulated thunderstorm downburst—Part A: stationary downburst observations
21	Laboratory Tests	Letchford and Chay (2002)	Ad hoc Facilities: Impinging Wall Jet, Non-stationary/Translating	Thunderstorms—their importance in wind engineering (a case for the next generation wind tunnel)
22	Laboratory Tests	Sarkar and Haan (2002)	Ad hoc Facilities: Impinging Wall Jet, Non-stationary/Translating	Next Generation Wind Tunnels for Simulation of Straight-Line, Thunderstorm- and Tornado-Like Winds

23	Laboratory Tests	Mason <i>et al.</i> (2005)	Ad hoc Facilities: Impinging Wall Jet, Pulsed Wall Jet, Stationary/Quasi-steady	Pulsed jet simulation of a stationary thunderstorm downburst. Part A: physical structure and flow field characterization
24	Laboratory Tests	Choi (2004)	Ad hoc Facilities: Impinging Wall Jet, Stationary/Quasi-steady	Field measurement and experimental study of wind speed profile during thunderstorms
25	Laboratory Tests	Xu and Hagan (2008)	Ad hoc Facilities: Impinging Wall Jet, Non-stationary/Translating	Scale, boundary, and inlet condition effects on impinging jets
26	Laboratory Tests	McConville <i>et al.</i> (2009)	Ad hoc Facilities: Impinging Wall Jet, Non-stationary/Translating	The physical simulation of thunderstorm downbursts using an impinging jet
27	Laboratory Tests	Zhang <i>et al.</i> (2013b,a,c)	Ad hoc Facilities: Impinging Wall Jet, Stationary/Quasi-steady	An experimental study on wind loads acting on a high-rise building model induced by microburst-like winds
28	Laboratory Tests	Richter <i>et al.</i> (2018)	Ad hoc Facilities: Impinging Wall Jet, Pulsed Wall Jet	Interaction of severe convective gusts with a street canyon
29	CFD Simulations, Laboratory Tests	Damatty <i>et al.</i> (2016)	Ad hoc Facilities: Impinging Wall Jet, Non-stationary/Translating	Transmission Line Failures during Tornadoes and Downbursts - Can they be avoided?
30	Laboratory Tests	Hangan <i>et al.</i> (2017)	Ad hoc Facilities: Impinging Wall Jet, Non-stationary/Translating	Novel techniques in wind engineering
31	Laboratory Tests	Chowdhury (2018)	Ad hoc Facilities: Impinging Wall Jet, Non-stationary/Translating	Transient Analysis of Full Scale and Experimental Downburst Flows
32	Laboratory Tests	Junayed <i>et al.</i> (2019)	Ad hoc Facilities: Impinging Wall Jet	Flow field dynamics of large-scale experimentally produced downburst flows
33	Laboratory Tests	Romanic <i>et al.</i> (2019)	Ad hoc Facilities: Impinging Wall Jet	Transient behavior in impinging jets in crossflow with application to downburst flows

34	Laboratory Tests	Cao <i>et al.</i> (2002)	Ad hoc Facilities: Modified devices	Reproduction of wind velocity history in a multiple fan wind tunnel
35	Laboratory Tests	Lin and Savory (2006)	Ad hoc Facilities: Modified devices	Large-scale quasi-steady modelling of a downburst outflow using a slot jet
36	CFD Simulations, Laboratory Tests	Lin <i>et al.</i> (2007)	Ad hoc Facilities: Modified devices, CFD Model: CM1, Non-stationary/Translating, Pulsed Wall Jet, Stationary/Quasi-steady	Proposed large-scale modelling of the transient features of a downburst outflow
37	Laboratory Tests	Lin <i>et al.</i> (2015)	Ad hoc Facilities: Modified devices, Pulsed Wall Jet	Wind velocity profiles from a pulsed wall jet over ground roughness
38	Laboratory Tests	Butler and kareem (2007)	Ad hoc Facilities: Modified devices	Physical and numerical modeling of downburst
39	Laboratory Tests	Butler <i>et al.</i> (2010)	Ad hoc Facilities: Modified devices	Surface pressure and wind load characteristics on prisms immersed in a simulated transient gust front flow field
40	Laboratory Tests	Aboutabikh <i>et al.</i> (2019)	Ad hoc Facilities: Modified devices	Designing a blade-system to generate downburst outflows at boundary layer wind tunnel
41	Laboratory Tests	Asano <i>et al.</i> (2019)	Ad hoc Facilities: Modified devices, Pulsed Wall Jet	Laboratory study of wind loads on a low-rise building in a downburst using a moving pulsed jet simulator and their comparison with other types of simulators
42	Laboratory Tests	Le and Caracoglia (2019)	Ad hoc Facilities: Modified devices	Generation and characterization of a non-stationary flow field in a small-scale wind tunnel using a multi-blade flow device
43	Analytical Model	Glauert (1956)	Classic: Impinging Wall Jet	The wall jet
44	Analytical Model	Osegura and Bowles (1988)	Classic: Impinging Wall Jet	A Simple Analytic 3-Dimensional Downburst Model Based on Boundary Layer Stagnation Flow

45	Analytical Model	Vicroy (1991)	Classic: Impinging Wall Jet, Classic: Shape Functions	A Simple, Analytical Axisymmetric Microburst Model for Downdraft Estimation
46	Analytical Model	Holmes and Oliver's (2000)	Classic: Impinging Wall Jet, Non-stationary/Translating	An empirical model of a downburst
47	Analytical Model	Savory <i>et al.</i> (2001)	Classic: Vortex Ring	Modelling of tornado and microburst-induced wind loading and failure of a lattice transmission tower
48	Analytical Model	Ponte Junior (2005)	Classic: Impinging Wall Jet	Modelagem e Simulação do Campo de Velocidade do Vento em Tormentas Elétricas
49	Analytical Model	Li <i>et al.</i> (2012)	Classic: Impinging Wall Jet	A revised empirical model and CFD simulations for 3D axisymmetric steady-state flows of downbursts and impinging jets
50	Analytical Model	Abd-Elaal <i>et al.</i> (2013c)	Classic: Impinging Wall Jet, Non-stationary/Translating	A newly developed analytical model of transient downburst wind loads
51	Analytical Model	Abd-Elaal <i>et al.</i> (2013a)	Classic: Impinging Wall Jet	An analytical model for simulating steady state flows of downburst
52	Analytical Model	Damasceno Neto (2012)	Classic: Impinging Wall Jet, NDESH Models	Estruturas de Torres sob ação de ventos originados de downbursts
53	Analytical Model	Riera (2016)	Classic: Impinging Wall Jet	Sobre a Definição do Vento para projecto estrutural na ABNT NBR 6123 (1989) e outras normas Sulamericanas
54	Analytical Model	Ivan (1986)	Classic: Doublet Sheet model, Classic: Vortex Ring	A ring-vortex downburst model for flight simulations
55	Analytical Model	Schultz (1990)	Classic: Vortex Ring	Multiple vortex ring model of the DFW microburst
56	Analytical Model	Vicroy (1992)	Classic: Vortex Ring	Assessment of microburst models for downdraft estimation

57	Analytical Model, CFD Simulations	Riera <i>et al.</i> (1998)	Classic: Rayleigh Function, Classic: Vortex Ring	Load definition for wind design and reliability assessments: extreme wind climate
58	Analytical Model	Zhu and Etkin (1985)	Classic: Doublet Sheet model, Classic: Vortex Ring	Model of the wind field in a downburst
59	Analytical Model	Jesson & Sterling (2018)	Classic: Vortex Ring	A simple vortex model of a thunderstorm downburst – A parametric evaluation
60	Analytical Model	Choi & Hidayat (2002a)	Gust Response Factor, NDESH Models	Dynamic response of structures to thunderstorm winds
61	Analytical Model	Chen and Letchford (2004)	NDESH Models, Spectral Representation Method (SRM)	A deterministic–stochastic hybrid model of downbursts and its impact on a cantilevered structure
62	Analytical Model	Chen and Letchford (2005)	NDESH Models, Proper Orthogonal Decomposition (POD), Wavelet Shrinkage	Proper orthogonal decomposition of two vertical profiles of full-scale nonstationary downburst wind speeds
63	Analytical Model	Chen and Letchford (2006)	NDESH Models, Proper Orthogonal Decomposition (POD), Wavelet Shrinkage	Multi-scale correlation analyses of two lateral profiles of full-scale downburst wind speeds
64	Analytical Model	Chen and Letchford (2007)	NDESH Models, Proper Orthogonal Decomposition (POD), Wavelet Shrinkage	Numerical simulation of extreme winds from thunderstorm downbursts
65	Analytical Model	Chay <i>et al.</i> (2008)	NDESH Models	Gust occurrence in simulated non-stationary winds
66	Analytical Model	Chen (2008)	NDESH Models	Derivation of time-varying mean for non-stationary downburst winds
67	Analytical Model	Huang and Chen (2009)	NDESH Models	Wavelets-based estimation of multivariate evolutionary spectra and its application to nonstationary downburst winds

68	Analytical Model	Huang <i>et al.</i> (2015b)	NDESH Models	Spectrum models for nonstationary extreme winds
69	Analytical Model	Nguyen (2013)	NDESH Models	Thunderstorm downburst risks to wind farms
70	Analytical Model	McCullough <i>et al.</i> (2014)	Empirical Mode Decomposition (EMD), NDESH Models, Variable Averaging Interval (VAI Schemes), Wavelet Shrinkage	Efficacy of averaging interval for nonstationary winds
71	Analytical Model	Su <i>et al.</i> (2015)	Empirical Mode Decomposition (EMD), NDESH Models, Variable Averaging Interval (VAI Schemes), Wavelet Shrinkage	Derivation of time-varying mean for nonstationary downburst winds
72	Analytical Model	Xu and Hangan (2008)	NDESH Models, Empirical Mode Decomposition (EMD)	Scale, boundary, and inlet condition effects on impinging jets
73	CFD Simulations	Ogura and Philips (1962)	2D, CFD Model Type: Full-cloud	Scale analysis of deep and shallow convection in the atmosphere
74	CFD Simulations	Orville (1965)	2D, CFD Model Type: Full-cloud	A numerical study of the initiation of cumulus clouds over mountainous terrain
75	CFD Simulations	Steiner (1973)	3D, CFD Model Type: Full-cloud	A three-dimensional model of cumulus cloud development
76	CFD Simulations	Miller and Pearce (1974)	3D, CFD Model Type: Full-cloud	A three-dimensional primitive equation model of cumulonimbus convection
76	CFD Simulations	Clark (1979)	3D, CFD Model Type: Full-cloud	Numerical simulations with a three-dimensional cloud model: Lateral boundary condition experiments and multicellular severe storm simulations
77	CFD Simulations	Straka and Anderson (1993)	CFD Model Type: Full-cloud	Numerical simulations of microburst-producing storms: Some results from storms observed during COHMEX

78	CFD Simulations	Knupp (1989)	3D, CFD Model Type: Full-cloud	Precipitating convective cloud downdraft structure: A synthesis of observations and modeling
79	CFD Simulations	Tripoli and Cotton (1982)	3D, CFD Model Type: Full-cloud	The Colorado State University Three-Dimensional Cloud-Mesoscale Model 1982. I: General Theoretical Framework and Sensitivity Experiments
80	CFD Simulations	Proctor (1987)	3D, CFD Model Type: Full-cloud	The terminal area simulation system. Volume 1: Theoretical formulation
81	CFD Simulations	Nicholls <i>et al.</i> (1993)	2D, CFD Model Type: Full-cloud, CFD Model: CSU-RAMS, nCFD Model: LES	Large eddy simulation of microburst winds flowing around a building
82	CFD Simulations	Bryan and Fritsch (2002)	CFD Model Type: Full-cloud	A benchmark simulation for moist nonhydrostatic numerical models
83	CFD Simulations	Orf et al (2012)	CFD Model Type: Full-cloud	Simulation of a downburst-producing thunderstorm using a very high-resolution three-dimensional cloud model
84	CFD Simulations	Mitchell and Hovermale (1977)	1D, CFD Model Type: Sub-Cloud	A numerical investigation of the severe thunderstorm gust front
85	CFD Simulations	Srivastava (1985)	1D, CFD Model Type: Sub-Cloud	A Simple Model of Evaporatively Driven Downdraft: Application to Microburst Downdraft
86	CFD Simulations	Srivastava (1987)	1D, CFD Model Type: Sub-Cloud	A Model of Intense Downdrafts Driven by the Melting and Evaporation of Precipitation

87	CFD Simulations	Droegemeier and Wjhlhelmsen (1987)	CFD Model Type: Sub-Cloud	Numerical simulation of thunderstorm outflow dynamics. Part I: Outflow sensitivity experiments and turbulence dynamics
89	CFD Simulations	Proctor (1988)	CFD Model Type: Sub-Cloud	Numerical simulations of an isolated microburst. Part I: Dynamics and structure
90	CFD Simulations	Proctor (1989)	CFD Model Type: Sub-Cloud	Numerical Simulations of an Isolated Microburst. Part II: Sensitivity Experiments
91	CFD Simulations	Anderson <i>et al.</i> (1992)	3D, CFD Model Type: Sub-Cloud	A 3-D model system for simulating thunderstorm microburst outflows
92	CFD Simulations	Orf <i>et al.</i> (1996)	3D, CFD Model Type: Sub-Cloud	A three-dimensional numerical analysis of colliding microburst outflow dynamics
93	CFD Simulations	Orf and Anderson (1999)	CFD Model Type: Sub-Cloud, Non-stationary/Translating, Turbulence Model: K-e	A numerical study of traveling microbursts
94	CFD Simulations	Mason <i>et al.</i> (2009)	CFD Model Type: Sub-Cloud, CFD Model: LES, Turbulence Model: SAS	Numerical simulation of downburst winds
95	CFD Simulations	Mason <i>et al.</i> (2010)	CFD Model Type: Sub-Cloud, CFD Model: LES, Turbulence Model: SAS	Numerical simulation of idealised three-dimensional downburst wind fields
96	CFD Simulations	Vermeire <i>et al.</i> (2011a)	CFD Model Type: Impinging Wall Jet	Improved modelling of downburst outflows for wind engineering applications using a cooling source approach
97	CFD Simulations	Vermeire <i>et al.</i> (2011b)	CFD Model Type: Sub-Cloud, CFD Model: CM1, CFD Model: LES	A parametric study of downburst line near-surface outflows
98	CFD Simulations	Selvam and Holmes (1992)	CFD Model Type: Impinging Wall Jet, Turbulence Model: K-e	Numerical simulation of thunderstorm downdrafts
99	CFD Simulations	Shehata <i>et al.</i> (2005)	CFD Model Type: Impinging Wall Jet	Finite element modelling of transmission line under downburst wind loading

100	Analytical Model, CFD Simulations, Data-driven Techniques	Chay <i>et al.</i> (2006)	CFD Model Type: Impinging Wall Jet	Numerical and analytical simulation of downburst wind loads
101	CFD Simulations	Kim and Hangan (2007)	CFD Model Type: Impinging Wall Jet, CFD Model: URANS, Turbulence Model: RNG κ - ϵ And CFD Model Type: Impinging Wall Jet	Numerical simulations of impinging jets with application to downbursts
102	Analytical Model, CFD Simulations, Laboratory Tests	Sengupta & Sarkar (2008)	CFD Model Type: Impinging Wall Jet, CFD Model: LES, Turbulence Model: RNG κ - ϵ , Turbulence Model: Realizable κ - ϵ , Turbulence Model: SST κ - ω , Turbulence Model: κ - ϵ standard	Improved modelling of downburst outflows for wind engineering applications using a cooling source approach
103	CFD Simulations	Darwish <i>et al.</i> (2010)	2D, CFD Model Type: Impinging Wall Jet	Dynamic characteristics of Transmission Line Conductors and Behavior under Turbulent Downburst Loading
104	CFD Simulations	Zhang <i>et al.</i> (2013a)	CFD Model Type: Impinging Wall Jet, CFD Model: URANS	Modeling of microburst outflows using impinging jet and cooling source approaches and their comparison
105	CFD Simulations	Aboshosha <i>et al.</i> (2015)	CFD Model Type: Impinging Wall Jet, CFD Model: LES	Turbulence characterization of downbursts using LES
106	CFD Simulations	Oreskovic <i>et al.</i> (2018)	CFD Model Type: Sub-Cloud, CFD Model: URANS, Turbulence Model: K-e	Evolution and scaling of a simulated downburst-producing thunderstorm outflow
107	CFD Simulations	Skote <i>et al.</i> (2018)	CFD Model Type: Impinging Wall Jet, CFD Model: RAMS, CFD Model: URANS	Temporal Variation of the Pressure from a Steady Impinging Jet Model of Dry Microburst-Like Wind Using URANS
108	Data-driven Techniques	Kareem (2006)	Monte-Carlo Simulation	Numerical simulation of wind effects: a probabilistic perspective
109	Data-driven Techniques	Wang (2008)	Hilbert Transform, Stationary wavelet transform	Stochastic modeling and simulation of transient events

110	Data-driven Techniques	Wang <i>et al.</i> (2013)	Hilbert Transform, Stationary wavelet transform	A data-driven approach for simulation of full-scale downburst wind speeds
111	Data-driven Techniques	Wang <i>et al.</i> (2014)	Hilbert Transform, Stationary wavelet transform	Modeling and simulation of nonstationary processes utilizing wavelet and Hilbert transforms
112	Data-driven Techniques	Huang (2014)	Fourier Transform, Spectral Representation Method (SRM)	An efficient simulation approach for multivariate nonstationary process: Hybrid of wavelet and spectral representation method
113	Data-driven Techniques	Xu <i>et al.</i> (2014)	Conditional Simulation Method	Conditional simulation of nonstationary fluctuating wind speeds for long-span bridges
114	Data-driven Techniques	Huang (2015)	Discrete wavelet transform, Kernel Regression	Spectrum models for non-stationary extreme winds
115	Data-driven Techniques	Kwon and Kareem (2009)	Gust front factor	Gust-Front Factor: A New Framework for Wind Load Effects on Structures
116	CFD Simulations	Zhang <i>et al.</i> (2014)	Ad hoc Facilities: Impinging Wall Jet, Stationary/Quasi-steady	Comparison of microburst-wind loads on low-rise structures of geometric variations
116	Data-driven Techniques	Kwon and Kareem (2019)	Gust front factor	Towards codification of thunderstorm/downburst using gust front factor: Model-based and data-driven perspectives
117	Data-driven Techniques	Solari (2017)	Fast Fourier Transform, Monte-Carlo Simulation, Proper Orthogonal Decomposition (POD)	Hybrid simulation of thunderstorm outflows and wind-excited response of structures
118	CFD Simulations	Hjelmfelt (1989)	2D, CFD Model Type: Full-cloud	Observational and Numerical Study of a Microburst Line-Producing Storm

119	Analytical Model, CFD Simulations	Abd-Elaal <i>et al.</i> (2013d)	Classic: Impinging Wall Jet	A coupled parametric-CFD study for determining ages of downbursts through investigation of different field parameters
120	CFD Simulations	Yamada and Koike (2011)	CFD Model Type: Full-cloud	Downscaling mesoscale meteorological models for computational wind engineering applications
121	Analytical Model	Ponte and Riera (2010)	Classic: Impinging Wall Jet	Simulation of extreme wind series caused by thunderstorms in temperate latitudes
122	Analytical Model	Xhelaj <i>et al.</i> (2020)	Classic: Vortex Ring	A general-purpose analytical model for reconstructing the thunderstorm outflows of travelling downbursts immersed in ABL flows

REFERENCES - MODELING TECHNIQUES OF THUNDERSTORM WIND OUTFLOWS

ABD-ELAAL, El-Sayed; MA, X; MILLS, JE. **A newly developed analytical model of transient downburst wind loads**. 2013. PhD Dissertation - CRC Press, [s. l.], 2013.

ABD-ELAAL, El-Sayed; MILLS, Julie E.; MA, Xing. A coupled parametric-CFD study for determining ages of downbursts through investigation of different field parameters. **Journal of Wind Engineering and Industrial Aerodynamics**, [s. l.], v. 123, p. 30–42, 2013a.

ABD-ELAAL, El-Sayed; MILLS, Julie E.; MA, Xing. An analytical model for simulating steady state flows of downburst. **Journal of Wind Engineering and Industrial Aerodynamics**, [s. l.], v. 115, p. 53–64, 2013b.

ABOSHOSHA, Haitham; BITSUAMLAK, Girma; EL DAMATTY, Ashraf. Turbulence characterization of downbursts using LES. **Journal of Wind Engineering and Industrial Aerodynamics**, [s. l.], v. 136, p. 44–61, 2015.

ABOUTABIKH, Moustafa; GHAZAL, Tarek; CHEN, Jiaxiang; ELGAMAL, Sameh; ABOSHOSHA, Haitham. Designing a blade-system to generate downburst outflows at boundary layer wind tunnel. **Journal of Wind Engineering and Industrial Aerodynamics**, [s. l.], v. 186, p. 169–191, 2019.

ALAHYARI, A.; LONGMIRE, E. K. Particle image velocimetry in a variable density flow: Application to a dynamically evolving microburst. **Experiments in Fluids**, [s. l.], v. 17, n. 6, p. 434–440, 1994.

ANDERSON, J. R.; ORF, L. G.; STRAKA, J. M. A 3-D models system for simulating thunderstorm microburst outflows. **Meteorology and Atmospheric Physics**, [s. l.], v. 49, n. 1–4, p. 125–131, 1992.

ASANO, Kazunori; IIDA, Yumi; UEMATSU, Yasushi. Laboratory study of wind loads on a low-rise building in a downburst using a moving pulsed jet simulator and their comparison with other types of simulators. **Journal of Wind Engineering and Industrial Aerodynamics**, [s. l.], v. 184, p. 313–320, 2019.

BAKKE, P. An experimental investigation of a wall jet. **Journal of Fluid Mechanics**, [s. l.], v. 2, n. 05, p. 467, 1957.

BRYAN, George H.; FRITSCH, J. Michael. A benchmark simulation for moist nonhydrostatic numerical models. **Monthly Weather Review**, [s. l.], v. 130, n. 12, p. 2917–2928, 2002.

BUTLER, Kyle; CAO, Shuyang; KAREEM, Ahsan; TAMURA, Yukio; OZONO, Shigehira. Surface pressure and wind load characteristics on prisms immersed in a simulated transient gust front flow field. **Journal of wind engineering and industrial aerodynamics**, [s. l.], v. 98, n. 6–7, p. 299–316, 2010.

BUTLER, K.; KAREEM, A. Physical and numerical modeling of downburst generated gust fronts. *Em:* , 2007. **Proceedings of the 12th International Conference on Wind Engineering, Cairns, Australia**. [S. l.: s. n.], 2007. p. 791–798.

CAO, Shuyang; NISHI, Akira; KIKUGAWA, Hironori; MATSUDA, Yuji. Reproduction of wind velocity history in a multiple fan wind tunnel. **Journal of wind engineering and industrial aerodynamics**, [s. l.], v. 90, n. 12–15, p. 1719–1729, 2002.

CHANG, Ho-Pen; FROST, Walter. **Development of a Microburst Turbulence Model for the Joint Airport Weather Studies Wind Shear Data**. [S. l.]: FWG ASSOCIATES INC TULLAHOMA TN, 1987.

CHARBA, Jess. Application of gravity current model to analysis of squall-line gust front. **Monthly Weather Review**, [s. l.], v. 102, n. 2, p. 140–156, 1974.

CHAY, M.T.; ALBERMANI, F.; WILSON, R. Numerical and analytical simulation of downburst wind loads. **Engineering Structures**, [s. l.], v. 28, n. 2, p. 240–254, 2006.

CHAY, M.T.; LETCHFORD, C.W. Pressure distributions on a cube in a simulated thunderstorm downburst—Part A: Stationary downburst observations. **Journal of Wind Engineering and Industrial Aerodynamics**, [s. l.], v. 90, n. 7, p. 711–732, 2002.

CHAY, M. T.; WILSON, R.; ALBERMANI, F. Gust occurrence in simulated non-stationary winds. **Journal of wind engineering and industrial aerodynamics**, [s. l.], v. 96, n. 10–11, p. 2161–2172, 2008.

CHEN, Xinzhong. Analysis of alongwind tall building response to transient nonstationary winds. **Journal of structural engineering**, [s. l.], v. 134, n. 5, p. 782–791, 2008.

CHEN, Lizhong. **Vector Time-Varying Autoregressive (TVAR) Models and Their Application to Downburst wind Speeds**. 2005. 252 f. Doctoral Thesis - Texas Tech University, [s. l.], 2005.

CHEN, Lizhong; LETCHFORD, Chris W. A deterministic–stochastic hybrid model of downbursts and its impact on a cantilevered structure. **Engineering Structures**, [s. l.], v. 26, n. 5, p. 619–629, 2004.

CHEN, L.; LETCHFORD, C.W. Multi-scale correlation analyses of two lateral profiles of full-scale downburst wind speeds. **Journal of Wind Engineering and Industrial Aerodynamics**, [s. l.], v. 94, n. 9, p. 675–696, 2006.

CHEN, L.; LETCHFORD, C.W. Numerical simulation of extreme winds from thunderstorm downbursts. **Journal of Wind Engineering and Industrial Aerodynamics**, [s. l.], v. 95, n. 9–11, p. 977–990, 2007.

CHEN, L.; LETCHFORD, C.W. Proper orthogonal decomposition of two vertical profiles of full-scale nonstationary downburst wind speeds. **Journal of Wind Engineering and Industrial Aerodynamics**, [s. l.], v. 93, n. 3, p. 187–216, 2005.

CHOI, Edmund C.C. Field measurement and experimental study of wind speed profile during thunderstorms. **Journal of Wind Engineering and Industrial Aerodynamics**, [s. l.], v. 92, n. 3–4, p. 275–290, 2004.

CHOI, Edmund CC; HIDAYAT, Ferry A. Dynamic response of structures to thunderstorm winds. **Progress in Structural Engineering and Materials**, [s. l.], v. 4, n. 4, p. 408–416, 2002.

CHOWDHURY, Junayed. Transient Analysis of Full Scale and Experimental Downburst Flows. [s. l.], p. 143, 2018.

CHUN, DH; SCHWARZ, WH. Stability of the plane incompressible viscous wall jet subjected to small disturbances. **The Physics of Fluids**, [s. l.], v. 10, n. 5, p. 911–915, 1967.

CLARK, Terry L. Numerical simulations with a three-dimensional cloud model: Lateral boundary condition experiments and multicellular severe storm simulations. **Journal of the Atmospheric Sciences**, [s. l.], v. 36, n. 11, p. 2191–2215, 1979.

COOPER, D; JACKSON, D C; LAUNDER, B E; LIAO, G X. Impinging jet studies for turbulence model assessment-I. Flow-field experiments. [s. l.], p. 10, 1992.

DAMASCENO NETO, Wilson Torres. **Estruturas de Torres sob ação de ventos originados de downbursts**. 2012. [s. l.], 2012.

DAMATTY, Ashraf El; ELAWADY, Amal; HAMADA, Mohamed. Transmission Line Failures during Tornadoes and Downbursts- Can they be avoided. *Em: , 2016. Anais [...]*. [S. l.: s. n.], 2016. p. 7.

DARWISH, Mohamed M; EL DAMATTY, Ashraf A; HANGAN, Horia. Dynamic characteristics of transmission line conductors and behaviour under turbulent downburst loading. **Wind and Structures**, [s. l.], v. 13, n. 4, p. 327, 2010.

DIDDEN, Norbert; HO, Chih-Ming. Unsteady separation in a boundary layer produced by an impinging jet. **Journal of Fluid Mechanics**, [s. l.], v. 160, p. 235–256, 1985.

DONALDSON, Coleman duP.; SNEDEKER, Richard S. A study of free jet impingement. Part 1. Mean properties of free and impinging jets. **Journal of Fluid Mechanics**, [s. l.], v. 45, n. 2, p. 281–319, 1971.

DROEGEMEIER, Kelvin K.; WILHELMSON, Robert B. Numerical simulation of thunderstorm outflow dynamics. Part I: Outflow sensitivity experiments and turbulence dynamics. **Journal of the Atmospheric Sciences**, [s. l.], v. 44, n. 8, p. 1180–1210, 1987.

ENGINEERING SCIENCES DATA 1 UNIT. Characteristics of Atmospheric Turbulence Near the Ground, Part I: Definitions and General Information. *Em: , 2010, London, Uk. Engineering Sciences Data Unit (ESDU) 74030*. London, Uk: [s. n.], 2010.

FUJITA, TT. The downburst, report of Projects NIMROD and JAWS. **University of Chicago**, [s. l.], 1985.

GAST, Kirsten Deann. **A comparison of extreme wind events as sampled in the 2002 thunderstorm outflow experiment**. 2003. - Texas Tech University, [s. l.], 2003.

GLAUERT, MB. The wall jet. **Journal of Fluid Mechanics**, [s. l.], v. 1, n. 6, p. 625–643, 1956.

HANGAN, Horia; REFAN, Maryam; JUBAYER, Chowdhury; ROMANIC, Djordje; PARVU, Dan; LOTUFO, Julien; COSTACHE, Adrian. Novel techniques in wind engineering. **Journal of Wind Engineering and Industrial Aerodynamics**, [s. l.], v. 171, p. 12–33, 2017.

HANGAN, H.; ROBERTS, D.; XU, Z.; KIM, J. Downburst simulation. Experimental and numerical challenges. *Em: , 2003. Proceedings of the 11th International Conference on Wind Engineering, Lubbock, Texas, Electronic Version*. [S. l.: s. n.], 2003.

HJELMFELT, M.; ROBERTS, R.; ORVILLE, H.; CHEN, Jen-Ping; KOPP, F. Observational and Numerical Study of a Microburst Line-Producing Storm. **Journal of Atmospheric Sciences**, [s. l.], v. 46, p. 2731–2744, 1989.

HOLMES, J. D. Physical modelling of thunderstorm downdrafts by wind tunnel jet. *Em: , 1992. 2nd AWES Workshop, Monash University, 21-22 February 1992*. [S. l.: s. n.], 1992. p. 29–32.

HOLMES, John D; OLIVER, SE. An empirical model of a downburst. **Engineering structures**, [s. l.], v. 22, n. 9, p. 1167–1172, 2000.

HUANG, Guoqing; CHEN, Xinzhong. Wavelets-based estimation of multivariate evolutionary spectra and its application to nonstationary downburst winds. **Engineering Structures**, [s. l.], v. 31, n. 4, p. 976–989, 2009.

HUANG, Guoqing; ZHENG, Haitao; XU, You-lin; LI, Yongle. Spectrum models for nonstationary extreme winds. **Journal of Structural Engineering**, [s. l.], v. 141, n. 10, p. 04015010, 2015.

IVAN, Michael. **A ring-vortex downburst model for flight simulations**. **Journal of Aircraft**, 1986.

JESSON, Mike; STERLING, Mark. A simple vortex model of a thunderstorm downburst – A parametric evaluation. **Journal of Wind Engineering and Industrial Aerodynamics**, [s. l.], v. 174, p. 1–9, 2018.

JUNAYED, Chowdhury; JUBAYER, Chowdhury; PARVU, Dan; ROMANIC, Djordje; HANGAN, Horia. Flow field dynamics of large-scale experimentally produced downburst flows. **Journal of Wind Engineering and Industrial Aerodynamics**, [s. l.], v. 188, p. 61–79, 2019.

KAREEM, Ahsan. Numerical simulation of wind effects: A probabilistic perspective. **JWE: 日本風工学会誌**, [s. l.], n. 108, p. 9–32, 2006.

KIM, Jongdae; HANGAN, Horia. Numerical simulations of impinging jets with application to downbursts. **Journal of Wind Engineering and Industrial Aerodynamics**, [s. l.], v. 95, n. 4, p. 279–298, 2007.

KNUPP, Kevin R. Numerical simulation of low-level downdraft initiation within precipitating cumulonimbi: Some preliminary results. **Monthly weather review**, [s. l.], v. 117, n. 7, p. 1517–1529, 1989.

KNUPP, Kevin Robert. **Precipitating convective cloud downdraft structure: A synthesis of observations and modeling**. 1985. - Colorado State University. Libraries, [s. l.], 1985.

KRUEGER, Steven K.; WAKIMOTO, Roger M.; LORD, Stephen J. Role of ice-phase microphysics in dry microburst simulations. *Em: ,* 1986. **Joint Sessions 23rd Conf. Radar Meteorology and Conf. Cloud Physics, Snowmass, CO**. [S. l.]: Am. Meteorol. Soc Boston, Mass, 1986. p. J73–J76.

KWON, Dae-Kun; KAREEM, Ahsan. Gust-Front Factor: New Framework for Wind Load Effects on Structures. **Journal of Structural Engineering**, [s. l.], v. 135, n. 6, p. 717–732, 2009.

KWON, Dae Kun; KAREEM, Ahsan. **NatHaz Gust-Front Factor**. [S. l.], 2021. Disponível em: http://gff.ce.nd.edu/int_gff.html. Acesso em: 6 abr. 2021.

KWON, Dae Kun; KAREEM, Ahsan. Towards codification of thunderstorm/downburst using gust front factor: Model-based and data-driven perspectives. **Engineering Structures**, [s. l.], v. 199, p. 109608, 2019.

LANDRETH, Christopher C.; ADRIAN, Ronald J. Impingement of a low Reynolds number turbulent circular jet onto a flat plate at normal incidence. **Experiments in Fluids**, [s. l.], v. 9, n. 1–2, p. 74–84, 1990.

LAUNDER, B. E.; RODI, W. The turbulent wall jet measurements and modeling. **Annual review of fluid mechanics**, [s. l.], v. 15, n. 1, p. 429–459, 1983.

LE, Viet; CARACOGIA, Luca. Generation and characterization of a non-stationary flow field in a small-scale wind tunnel using a multi-blade flow device. **Journal of Wind Engineering and Industrial Aerodynamics**, [s. l.], v. 186, p. 1–16, 2019.

LETCHFORD, C.W; CHAY, M.T. Pressure distributions on a cube in a simulated thunderstorm downburst. Part B: Moving downburst observations. **Journal of Wind Engineering and Industrial Aerodynamics**, [s. l.], v. 90, n. 7, p. 733–753, 2002.

LETCHFORD, C.W; MANS, C; CHAY, M.T. Thunderstorms—Their importance in wind engineering (a case for the next generation wind tunnel). **Journal of Wind Engineering and Industrial Aerodynamics**, [s. l.], v. 90, n. 12–15, p. 1415–1433, 2002.

LI, Chao; LI, Q.S.; XIAO, Y.Q.; OU, J.P. A revised empirical model and CFD simulations for 3D axisymmetric steady-state flows of downbursts and impinging jets. **Journal of Wind Engineering and Industrial Aerodynamics**, [s. l.], v. 102, p. 48–60, 2012.

LIN, William E.; MARA, Thomas G.; SAVORY, Eric. Wind velocity profiles from a pulsed wall jet over ground roughness. *Em: , 2015. 14th International Conference on Wind Engineering (Porto Alegre)*. [S. l.: s. n.], 2015.

LIN, W. E.; ORF, L. G.; SAVORY, E.; NOVACCO, C. Proposed large-scale modelling of the transient features of a downburst outflow. **Wind and structures**, [s. l.], v. 10, n. 4, p. 315–346, 2007.

LIN, W. E.; SAVORY, E. Large-scale quasi-steady modelling of a downburst outflow using a slot jet. **Wind and structures**, [s. l.], v. 9, n. 6, p. 419–440, 2006.

LUNDGREN, T. S.; YAO, J.; MANSOUR, N. N. Microburst modelling and scaling. **Journal of Fluid Mechanics**, [s. l.], v. 239, n. 1, p. 461, 1992.

MARKOWSKI, Paul; RICHARDSON, Yvette. **Mesoscale Meteorology in Midlatitudes**. Chichester, UK: John Wiley & Sons, Ltd, 2010. *E-book*. Disponível em: <http://doi.wiley.com/10.1002/9780470682104>. Acesso em: 29 mar. 2020.

MASON, M.S.; FLETCHER, D.F.; WOOD, G.S. Numerical simulation of idealised three-dimensional downburst wind fields. **Engineering Structures**, [s. l.], v. 32, n. 11, p. 3558–3570, 2010.

MASON, M. S.; LETCHFORD, C. W.; JAMES, D. L. Pulsed wall jet simulation of a stationary thunderstorm downburst, Part A: Physical structure and flow field characterization. **Journal of wind engineering and industrial aerodynamics**, [s. l.], v. 93, n. 7, p. 557–580, 2005.

MASON, Matthew S.; WOOD, Graeme S.; FLETCHER, David F. Numerical simulation of downburst winds. **Journal of Wind Engineering and Industrial Aerodynamics**, [s. l.], v. 97, n. 11–12, p. 523–539, 2009.

MCCONVILLE, A. C.; STERLING, Mark; BAKER, C. J. The physical simulation of thunderstorm downbursts using an impinging jet. **Wind and structures**, [s. l.], v. 12, n. 2, p. 133, 2009.

MCCULLOUGH, Megan; KWON, Dae Kun; KAREEM, Ahsan; WANG, Lijuan. Efficacy of averaging interval for nonstationary winds. **Journal of Engineering Mechanics**, [s. l.], v. 140, n. 1, p. 1–19, 2014.

MIDDLETON, Gerard V. Experiments on density and turbidity currents: I. Motion of the head. **Canadian Journal of Earth Sciences**, [s. l.], v. 3, n. 4, p. 523–546, 1966.

MIGUEL, LF Fadel; RIERA, J. D. Loads induced on tall structures by thunderstorm winds in temperate latitudes. **Safety, Reliability, Risk and Life-Cycle Performance of Structures and Infrastructures**, [s. l.], p. 1–6, 2013.

MIGUEL, Letícia Fleck Fadel; RIERA, Jorge Daniel; FADEL MIGUEL, Leandro Fleck. Assessment of downburst wind loading on tall structures. **Journal of Wind Engineering and Industrial Aerodynamics**, [s. l.], v. 174, p. 252–259, 2018.

MILLER, M. J.; PEARCE, R. P. A three-dimensional primitive equation model of cumulonimbus convection. **Quarterly Journal of the royal meteorological society**, [s. l.], v. 100, n. 424, p. 133–154, 1974.

MITCHELL, Kenneth E.; HOVERMALE, John B. A numerical investigation of the severe thunderstorm gust front. **Monthly weather review**, [s. l.], v. 105, n. 5, p. 657–675, 1977.

NGUYEN, Hieu Huy. The influence of thunderstorm downbursts on wind turbine design. [s. l.], 2012.

NICHOLLS, Mel; PIELKE, R.; MERONEY, R. Large eddy simulation of microburst winds flowing around a building. *Em: COMPUTATIONAL WIND ENGINEERING 1*. [S. l.]: Elsevier, 1993. p. 229–237.

OGURA, Yoshimitsu; PHILLIPS, Norman A. Scale analysis of deep and shallow convection in the atmosphere. **Journal of the atmospheric sciences**, [s. l.], v. 19, n. 2, p. 173–179, 1962.

ORESKOVIC, Christopher; SAVORY, Eric. Evolution and scaling of a simulated downburst-producing thunderstorm outflow. **Wind and Structures**, [s. l.], v. 26, n. 3, p. 147–161, 2018.

ORF, Leigh G.; ANDERSON, John R. A Numerical Study of Traveling Microbursts. **Monthly Weather Review**, [s. l.], v. 127, n. 6, p. 1244–1258, 1999.

ORF, Leigh G.; ANDERSON, John R.; STRAKA, Jerry M. A three-dimensional numerical analysis of colliding microburst outflow dynamics. **Journal of the atmospheric sciences**, [s. l.], v. 53, n. 17, p. 2490–2511, 1996.

ORF, Leigh; KANTOR, Erica; SAVORY, Eric. Simulation of a downburst-producing thunderstorm using a very high-resolution three-dimensional cloud model. **Journal of Wind Engineering and Industrial Aerodynamics**, [s. l.], v. 104–106, p. 547–557, 2012.

ORVILLE, Harold D. A numerical study of the initiation of cumulus clouds over mountainous terrain. **Journal of the Atmospheric Sciences**, [s. l.], v. 22, n. 6, p. 684–699, 1965.

ORWIG, Kirsten D.; SCHROEDER, John L. Near-surface wind characteristics of extreme thunderstorm outflows. **Journal of wind engineering and industrial aerodynamics**, [s. l.], v. 95, n. 7, p. 565–584, 2007.

ORWIG-GAST, KD; SCHROEDER, JL. Extreme wind events observed in the 2002 thunderstorm outflow experiment. *Em: PROCEEDINGS OF THE TENTH AMERICAS CONFERENCE ON WIND ENGINEERING, BATON ROUGE, LA, 2005*. **Anais [...]**. [S. l.: s. n.], 2005.

OSEGUERA, Rosa M; BOWLES, Roland L. A simple, analytic 3-dimensional downburst model based on boundary layer stagnation flow. [s. l.], 1988.

PONTE JÚNIOR, Jacinto. **Modelagem e Simulação do Campo de Velocidade do Vento em Tormentas Elétricas**. 2005. 146 f. Doctoral Thesis - Universidade Federal do Rio Grande do Sul, Porto Alegre, Brazil, 2005.

PONTE, Jacinto; RIERA, Jorge D. Simulation of extreme wind series caused by thunderstorms in temperate latitudes. **Structural Safety**, [s. l.], v. 32, n. 4, p. 231–237, 2010.

POREH, Michael; TSUEI, YG; CERMAK, Jack E. Investigation of a turbulent radial wall jet. **Journal of Applied Mechanics**, [s. l.], v. 34, n. 2, p. 457–463, 1967.

PROCTOR, Fred H. Numerical simulations of an isolated microburst. Part I: Dynamics and structure. **Journal of the atmospheric sciences**, [s. l.], v. 45, n. 21, p. 3137–3160, 1988.

PROCTOR, Fred H. Numerical Simulations of an Isolated Microburst. Part II: Sensitivity Experiments. **Journal of Atmospheric Sciences**, [s. l.], v. 46, n. 14, p. 23, 1989.

PROCTOR, F. H. The terminal area simulation system. Volume 1: Theoretical formulation. [s. l.], 1987. Disponível em: <https://core.ac.uk/reader/42837650>. Acesso em: 4 dez. 2020.

RICHTER, Alexandra; RUCK, Bodo; MOHR, Susanna; KUNZ, Michael. Interaction of severe convective gusts with a street canyon. **Urban Climate**, [s. l.], v. 23, p. 71–90, 2018.

RIERA. **Design criteria for TS winds 2020.pdf**. , 2020.

RIERA, Jorge D. Sobre a Definição do Vento para projecto estrutural na ABNT NBR 6123 (1989) e outras normas Sulamericanas. **Revista Sul-Americana de Engenharia Estrutural**, [s. l.], v. 13, n. 3, 2016.

RIERA, J. D.; NANNI, L. F. Pilot study of extreme wind velocities in a mixed climate considering wind orientation. **Journal of Wind Engineering and Industrial Aerodynamics**, [s. l.], v. 32, n. 1–2, p. 11–20, 1989.

RIERA, Jorge D.; ROCHA, Marcelo M.; DAVENPORT, Rieira and. Load definition for wind design and reliability assessments: Extreme wind climate. **Wind effects on Buildings and Structures”, Balkema, Rotterdam**, [s. l.], 1998.

ROMANIC, Djordje; CHOWDHURY, Junayed; CHOWDHURY, Jubayer; HANGAN, Horia. Investigation of abrupt changes in thunderstorm velocity record. [s. l.], p. 5, 2019.

SARKAR, Partha P; HAAN, FL. Next generation wind tunnels for simulation of straight-line, thunderstorm-and tornado-like winds. **NIST SPECIAL PUBLICATION SP**, [s. l.], p. 141–158, 2002.

SAVORY, Eric; PARKE, Gerard A.R; ZEINODDINI, Mostafa; TOY, Norman; DISNEY, Peter. Modelling of tornado and microburst-induced wind loading and failure of a lattice transmission tower. **Engineering Structures**, [s. l.], v. 23, n. 4, p. 365–375, 2001.

SCHLICHTING, Hermann; KESTIN, Joseph. **Boundary layer theory**. [S. l.]: Springer, 1961. v. 121

SCHULTZ, Thomas A. Multiple vortex ring model of the DFW microburst. **Journal of Aircraft**, [s. l.], v. 27, n. 2, p. 163–168, 1990.

SELVAM, R.; HOLMES, J.D. Numerical simulation of thunderstorm downdrafts. **Journal of Wind Engineering and Industrial Aerodynamics**, [s. l.], v. 44, n. 1–3, p. 2817–2825, 1992.

SENGUPTA, Anindya; SARKAR, Partha P. Experimental measurement and numerical simulation of an impinging jet with application to thunderstorm microburst winds. **Journal of Wind Engineering and Industrial Aerodynamics**, [s. l.], v. 96, n. 3, p. 345–365, 2008.

SHEHATA, A.Y.; EL DAMATTY, A.A.; SAVORY, E. Finite element modeling of transmission line under downburst wind loading. **Finite Elements in Analysis and Design**, [s. l.], v. 42, n. 1, p. 71–89, 2005.

SIMPSON, J. E. A comparison between laboratory and atmospheric density currents. **Quarterly Journal of the Royal Meteorological Society**, [s. l.], v. 95, n. 406, p. 758–765, 1969.

SIMPSON, John E. Effects of the lower boundary on the head of a gravity current. **Journal of Fluid Mechanics**, [s. l.], v. 53, n. 4, p. 759–768, 1972.

SKOTE, Martin; SIM, Tze; SRIKANTH, Narasimalu. Temporal Variation of the Pressure from a Steady Impinging Jet Model of Dry Microburst-Like Wind Using URANS. **Computation**, [s. l.], v. 6, n. 1, p. 2, 2018.

SMITH, Douglas A. **Stochastic Analysis of Wind Data**. 1993. Doctoral Thesis - Texas Tech University, [s. l.], 1993.

SOLARI, Giovanni. Thunderstorm Downbursts and Wind Loading of Structures: Progress and Prospect. **Frontiers in Built Environment**, [s. l.], v. 6, p. 63, 2020.

SOLARI, Giovanni; BURLANDO, Massimiliano; GAETANO, Patrizia; REPETTO, Maria Pia. Characteristics of thunderstorms relevant to the wind loading of structures. **Wind and Structures**, [s. l.], v. 20, n. 6, p. 763–791, 2015.

SOLARI, Giovanni; GAETANO, Patrizia; REPETTO, Maria Pia. Thunderstorm response spectrum: Fundamentals and case study. **Journal of Wind Engineering and Industrial Aerodynamics**, [s. l.], v. 143, p. 62–77, 2015.

SOLARI, Giovanni; RAINISIO, Davide; DE GAETANO, Patrizia. Hybrid simulation of thunderstorm outflows and wind-excited response of structures. **Meccanica**, [s. l.], v. 52, n. 13, p. 3197–3220, 2017.

SRIVASTAVA, R. C. A Model of Intense Downdrafts Driven by the Melting and Evaporation of Precipitation. **Journal of the Atmospheric Sciences**, [s. l.], v. 44, n. 13, p. 22, 1987.

SRIVASTAVA, R. C. A Simple Model of Evaporatively Driven Downdraft: Application to Microburst Downdraft. **Journal of Atmospheric Sciences**, [s. l.], v. 42, n. 10, p. 20, 1985.

STEINER, J. T. A three-dimensional model of cumulus cloud development. **Journal of the Atmospheric Sciences**, [s. l.], v. 30, n. 3, p. 414–435, 1973.

STRAKA, Jerry M.; ANDERSON, John R. Numerical simulations of microburst-producing storms: Some results from storms observed during COHMEX. **Journal of the atmospheric sciences**, [s. l.], v. 50, n. 10, p. 1329–1348, 1993.

SU, Yanwen; HUANG, Guoqing; XU, You-lin. Derivation of time-varying mean for non-stationary downburst winds. **Journal of Wind Engineering and Industrial Aerodynamics**, [s. l.], v. 141, p. 39–48, 2015.

TRIPOLI, WR; COTTON, WR. The Colorado State University Three-Dimensional Cloud-Mesoscale Model 1982. I: General Theoretical Framework And Sensitivity Experiments. [s. l.], 1982.

VERMEIRE, Brian C.; ORF, Leigh G.; SAVORY, Eric. A parametric study of downburst line near-surface outflows. **Journal of wind engineering and industrial aerodynamics**, [s. l.], v. 99, n. 4, p. 226–238, 2011a.

VERMEIRE, Brian C.; ORF, Leigh G.; SAVORY, Eric. Improved modelling of downburst outflows for wind engineering applications using a cooling source approach. **Journal of Wind Engineering and Industrial Aerodynamics**, [s. l.], v. 99, n. 8, p. 801–814, 2011b.

VICROY, Dan. A simple, analytical, axisymmetric microburst model for downdraft estimation. [s. l.], 1991.

VICROY, Dan D. Assessment of microburst models for downdraft estimation. **Journal of Aircraft**, [s. l.], v. 29, n. 6, p. 1043–1048, 1992.

WAKIMOTO, Roger M. The life cycle of thunderstorm gust fronts as viewed with Doppler radar and rawinsonde data. **Monthly weather review**, [s. l.], v. 110, n. 8, p. 1060–1082, 1982.

WANG, Lijuan. **Stochastic modeling and simulation of transient events**. [S. l.]: University of Notre Dame, 2008.

WANG, Lijuan; MCCULLOUGH, Megan; KAREEM, Ahsan. A data-driven approach for simulation of full-scale downburst wind speeds. **Journal of Wind Engineering and Industrial Aerodynamics**, [s. l.], v. 123, p. 171–190, 2013.

WANG, Lijuan; MCCULLOUGH, Megan; KAREEM, Ahsan. Modeling and simulation of nonstationary processes utilizing wavelet and Hilbert transforms. **Journal of Engineering Mechanics**, [s. l.], v. 140, n. 2, p. 345–360, 2014.

WOOD, GS; KWOK, KCS. An empirically derived estimate for the mean velocity profile of a thunderstorm downburst. *Em: PROCEEDINGS OF THE 7TH AUSTRALIAN WIND ENGINEERING SOCIETY WORKSHOP, AUCKLAND, 1998*. **Anais [...]**. [S. l.: s. n.], 1998.

WOOD, Graeme S; KWOK, Kenny CS; MOTTERAM, Nicholas A; FLETCHER, David F. Physical and numerical modelling of thunderstorm downbursts. **Journal of Wind Engineering and Industrial Aerodynamics**, [s. l.], v. 89, n. 6, p. 535–552, 2001.

XHELAI, Andi; BURLANDO, Massimiliano; SOLARI, Giovanni. A general-purpose analytical model for reconstructing the thunderstorm outflows of travelling downbursts immersed in ABL flows. **Journal of Wind Engineering and Industrial Aerodynamics**, [s. l.], v. 207, p. 104373, 2020.

XU, Zhuyun; HANGAN, Horia. Scale, boundary and inlet condition effects on impinging jets. **Journal of Wind Engineering and Industrial Aerodynamics**, [s. l.], v. 96, n. 12, p. 2383–2402, 2008.

XU, You-Lin; HU, Liang; KAREEM, Ahsan. Conditional simulation of nonstationary fluctuating wind speeds for long-span bridges. **Journal of Engineering Mechanics**, [s. l.], v. 140, n. 1, p. 61–73, 2014.

YAMADA, Tetsuji; KOIKE, Katsuyuki. Downscaling mesoscale meteorological models for computational wind engineering applications. **Journal of Wind Engineering and Industrial Aerodynamics**, [s. l.], v. 99, n. 4, p. 199–216, 2011.

YAO, J.; LUNDGREN, T. S. Experimental investigation of microbursts. **Experiments in Fluids**, [s. l.], v. 21, n. 1, p. 17–25, 1996.

ZHANG, Yan; HU, Hui; SARKAR, Partha P. Comparison of microburst-wind loads on low-rise structures of various geometric shapes. **Journal of Wind Engineering and Industrial Aerodynamics**, [s. l.], v. 133, p. 181–190, 2014.

ZHANG, Yan; HU, Hui; SARKAR, Partha P. Modeling of microburst outflows using impinging jet and cooling source approaches and their comparison. **Engineering Structures**, [s. l.], v. 56, p. 779–793, 2013.

ZHANG, Yan; SARKAR, Partha; HU, Hui. An experimental study of flow fields and wind loads on gable-roof building models in microburst-like wind. **Experiments in Fluids**, [s. l.], v. 54, n. 5, 2013a. Disponível em: <http://link.springer.com/10.1007/s00348-013-1511-9>. Acesso em: 21 out. 2018.

ZHANG, Yan; SARKAR, Partha P; HU, Hui. Comparison of Microburst-wind Loads on Structures including Scale Effects. *Em: 12TH AMERICAS CONFERENCE ON WIND ENGINEERING*, 2013b, Seattle, USA. **Anais [...]**. Seattle, USA: [s. n.], 2013. p. 19.

ZHU, Shangxiang; ETKIN, Bernard. Model of the wind field in a downburst. **Journal of Aircraft**, [s. l.], v. 22, n. 7, p. 595–601, 1985.